Characterization of Secondary Phases of Spent Nuclear Fuel under Final Geological Disposal Conditions: Theoretical and Experimental Studies

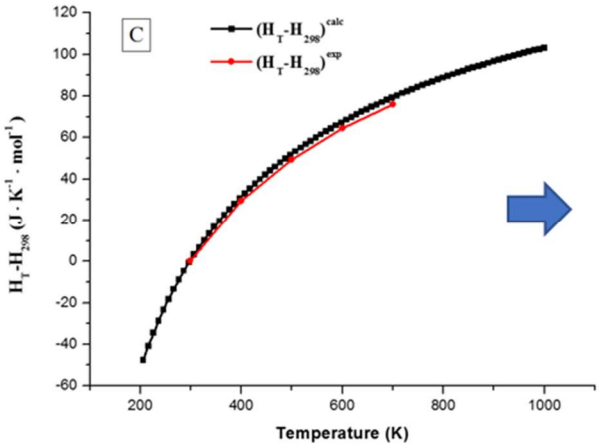

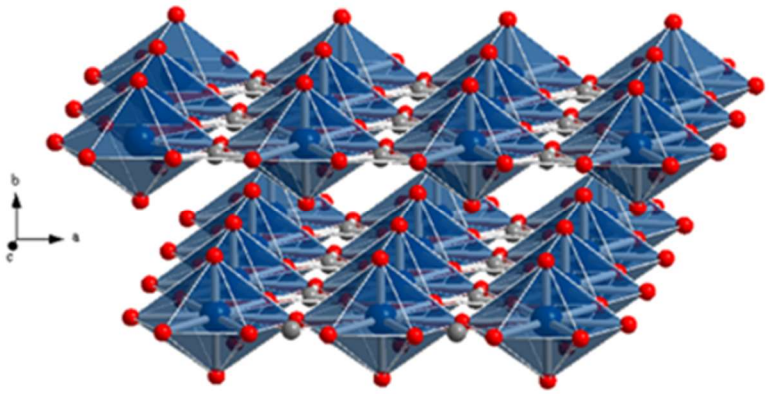

Ruthefordine

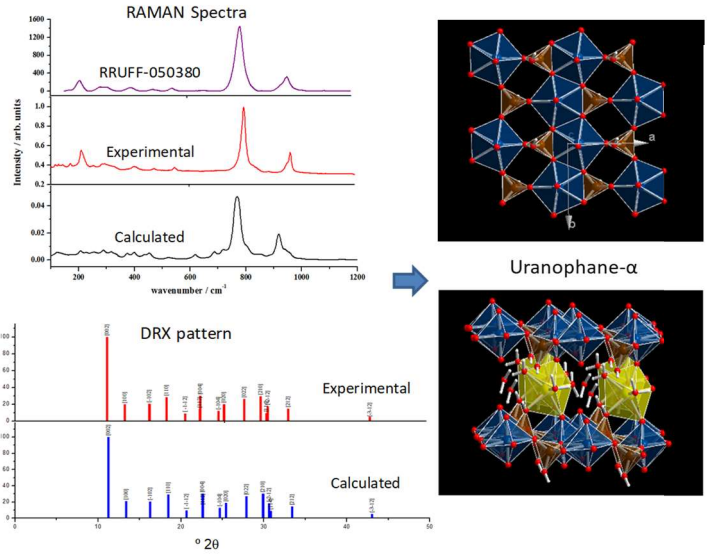

Uranophane-α

Francisco Colmenero Ruiz

Año 2017

Characterization of Secondary Phases of Spent Nuclear Fuel under Final Geological Disposal Conditions: Theoretical and Experimental Studies

Francisco Colmenero Ruiz

Supervised by:

Dr. Vicente Timón Salinero

Dr. Joaquín Cobos Sabate

This thesis has been submitted to obtain the title of Doctor in Chemistry at:

2017

La ciencia de hoy en día es la tecnología del mañana
Edward Teller

La incertidumbre es una margarita cuyos pétalos no se terminan jamás de deshojar
Mario Vargas Llosa

Con cada nueva respuesta desplegada, la ciencia ha descubierto al menos tres nuevas preguntas
Wernher von Braun

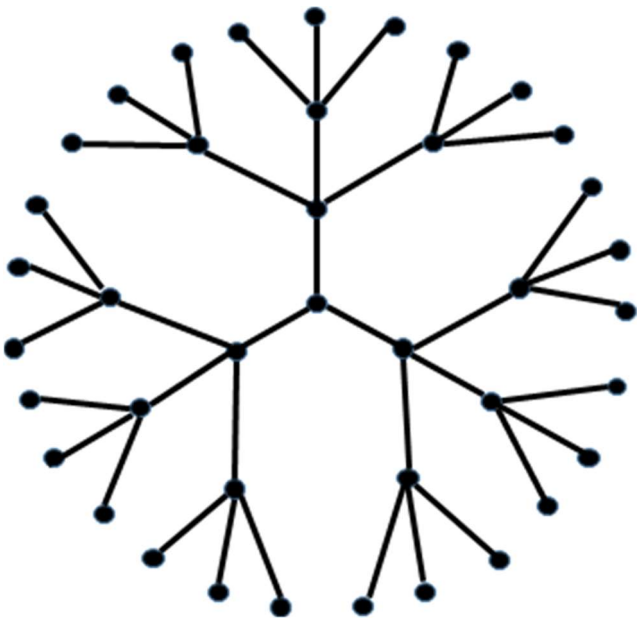

A Julia y Bartolomé por su enseñanza, paciencia y dedicación.

Summary

The resurgence of the use of nuclear energy is mainly driven by the need of more electricity for increasing populations and consumption, as well as the need of energy sources without CO_2 emissions and other greenhouse gases causing global warming. However, the management of nuclear waste is a matter of concern because it can be a source of high ecological damage, in the same way as uranium ore mining and nuclear accidents.

Nuclear fuel, commonly composed of UO_2 enriched from 0.7 to 3–5 % of ^{235}U, is obtained from natural minerals found in the rocks of the Earth´s crust. After its irradiation (one or more irradiation cycles) the fuel is considered as spent nuclear fuel (SNF) and must be managed as waste. The SNF is composed of a UO_2 matrix (> 95 %) and other radioactive elements. The latter are very hazardous, making the waste management difficult. Their hazard progressively decreases by natural processes (radioactive decay) leading, after several millions of years, to a total radioactivity that equals the radioactivity of natural uranium. Therefore, it has been proposed that the most appropriate and natural way of managing this waste is to return it to the Earth's crust. For this aim, the generally accepted solution is the burial of the SNF in a deep geological disposal for a period, at least, as long as the radioactive decay time. The design of a deep geological disposal must avoid the reaching of these radionuclides to the biosphere for such a long time by using a multi-barrier system. In this system, the radioactive waste is confined inside cladding tubes and canisters, which, in turn, are protected by introducing them into tunnels filled with buffer material and, finally, the whole system is surrounded by geological natural barriers. However, it is well-known that, after such a long time the barriers that protect the waste will be breached and SNF will be in contact with water. Thus, water could be the vehicle that mobilizes radionuclides.

Although the groundwater conditions in a repository are generally reducing, in a layer near the fuel surface, with a thickness < 50 μm, an oxidative environment has been postulated. This ambient is produced by the radiolysis of water due to the ionizing radiation associated with the fuel. The radiolysis of groundwater results in the production of oxidants as H_2O_2 among others. Therefore, uranium in the matrix of the spent nuclear fuel, composed by uranium dioxide, $U^{IV}O_2$, could oxidize to U(VI) and dissolve into the water forming uranyl groups. These uranyl groups can precipitate forming different *secondary phases*, i.e. alteration products, on the spent fuel surface depending on the local conditions and concentrations of reactive species present.

Since uranyl compounds, containing UO_2^{2+}, will appear as secondary phases at the surface of spent nuclear fuel in the final geological disposal conditions, its characterization and the determination of its properties are extraordinarily important. However, due to the radiotoxicity of these materials, the experimental study of these substances requires an extremely careful handling of the samples. The theoretical methods, based in the laws of quantum physics and chemistry studying these systems at the atomic level, are free of these difficulties and were used in this work as an interpretative tool of the experimental results and as a predictive tool for the properties of these substances inaccessible through their experimental measurement. The uranyl minerals rutherfordine, studtite, soddyite and uranophane, which have been widely recognized to be fundamental components of the paragenetic sequence of secondary phases that arises from the weathering of uraninite ore deposits and corrosion of SNF, have been studied by means of X-Ray powder diffraction and Raman spectroscopy combined with first principle calculations based on density functional theory (DFT) methods.

In the initial steps of this study, it was found that within scientific bibliography there were only a very few studies on the theoretical vibrational spectra of these materials. In fact, none of these initial studies included a complete determination of these spectra since only the phonon frequencies at gamma point were calculated and band intensities were not reported. The reasons for the very limited amount of theoretical treatments were very clear once the bibliography was

revised: 1) The high level of theory required to describe the uranium atom containing systems; 2) The large number of atoms in the unit cells of these materials; 3) The large number of valence electrons which must be described explicitly in the calculations; and 4) The absence of good norm-conserving pseudopotentials needed for the computation of the theoretical vibrational spectra. Having these difficulties in mind, it was thought that the best way to deal with these problems was the generation of a completely new pseudopotential for uranium atom. The pseudopotential should satisfy, at least, the conditions of being relativistic and norm-conserving if we desire to study the structure and spectra of these compounds with a good level of accuracy. The pseudopotential was generated and its performance was evaluated for a large series of uranium-containing minerals. The structure of these materials was determined and the resulting lattice parameters, bond lengths, bond angles and X-Ray powder pattern were found in very good agreement with experimental data. Since the structures of many of these materials (for example, soddyite and uranophane) were never studied by means of rigorous theoretical solid-state calculations, our work confirmed by the first time the structures determined experimentally by means of X-Ray diffraction techniques.

The Raman spectrum of the selected uranyl minerals (rutherfordine, studtite, soddyite and uranophane) was experimentally determined at CIEMAT and calculated theoretically using density functional perturbation theory (DFPT) at CSIC. A detailed comparison of the theoretical and experimental spectra is reported in this work. The non-scaled wave numbers of the bands of the theoretical spectrum showed very good agreement with the corresponding experimental values. This concordance in the comparison allowed for the rigorous assignment of the bands in the Raman spectra, since the theoretical methods provide microscopic scale views of the atomic motions in the corresponding normal modes. These spectra were the first published complete theoretical Raman spectra (including band wavenumbers and intensities) of uranyl-containing crystalline materials.

Since the calculations provided very good quality structures and spectra, the possibility of obtaining additional properties of these materials was considered. Due to the importance of the structures of these materials, their mechanical stability was studied. The mechanical stability and properties, as well as the equations of state of the uranyl carbonate mineral rutherfordine, and the uranyl silicate minerals soddyite and uranophane were studied theoretically for the first time. Thermodynamic properties, indispensable for the dynamic modelling of the chemical behavior of these compounds, were also determined. For the case of rutherfordine the results of the theoretical calculations of these properties showed an excellent agreement with experimental data. This fact suggest that theoretical methods constitute an excellent tool, alternative to experimental methods, for the determination of the thermodynamic properties of uranium containing materials. A side result of the study of rutherfordine mineral is that our results extended the temperature range in which the thermodynamic properties of this material were known to the range 0-700 K. The good quality of the thermodynamic properties calculated theoretically has been confirmed by the reliable results obtained in a later work of gamma uranium trioxide, γ-UO_3.

By using the calculated structures and Raman spectra of a set of uranyl containing materials, an UO bond-length to uranyl symmetric stretching Raman shift relation was obtained by a numerical fit of the calculated data. The relation, when used to determine UO bond-lengths from experimentally determined Raman shifts, provided bond-lengths of similar accuracy than other empirical relations widely used in the literature obtained by a fit to a large set of data points deduced from X-Ray diffraction and Raman spectroscopic measurements. In contrast, the relation from this work was obtained from a small set of data points deduced from first principle calculations, that is, without using any empirical information.

Because of secondary phases of SNF can reduce the release of fission products and heavier actinides contents in the SNF to the biosphere, the possibility of incorporation of fission products (the main hazard of SNF if the Advanced Nuclear Fuel Cycle is adopted) into the crystal structure of uranophane-α was also studied. It was found that the incorporation of strontium into the structure of this mineral was possible. The Sr-exchanged solid material has an X-Ray powder pattern and a Raman spectrum very close to that of normal uranophane in accordance with the

results of previous experimental studies. This study demonstrates that this uranyl silicate mineral may act as an additional barrier for the release of fission products to the biosphere.

In summary, the theoretical results, including the determination of structural, mechanical, thermodynamic and vibrational properties, suggest that theoretical methodology is a very powerful tool to perform detailed studies of the secondary phases of SNF free of the difficulties associated to its experimental handling due to their radiotoxicity. Finally, it can be concluded that the interplay of experimental and theoretical methods enhances extraordinarily the knowledge and understanding about the processes and compounds involved in the disposal of spent nuclear fuel.

Resumen

El nuevo auge en el uso de la energía nuclear es principalmente debido a la demanda de más electricidad para poblaciones en aumento con consumos por persona cada vez mayores, así como la necesidad de fuentes de energía sin emisiones de CO_2 y otros gases de efecto invernadero que causan calentamiento global. Sin embargo, la gestión de los residuos nucleares es muy importante porque puede ser una fuente de alto impacto ecológico, de la misma forma que lo pueden ser la minería del uranio y los accidentes nucleares.

El combustible nuclear, usualmente formado por UO_2 enriquecido en ^{235}U desde el 0.7 al 3–5 %, se obtiene a partir de minerales naturales que se encuentran en rocas de la corteza terrestre. Después de su irradiación (uno o más ciclos de irradiación), el combustible se considera como combustible nuclear gastado (SNF) y debe ser gestionado como un residuo. El SNF se compone de la matriz del UO_2 (> 95 %) y otros elementos radioactivos. Estos últimos son muy peligrosos, haciendo que la manipulación de los residuos sea muy complicada. Su radioactividad decrece progresivamente por medio de procesos naturales (decaimiento radioactivo) llevando, después de varios millones de años, a una radioactividad total que iguala a la radioactividad del uranio natural. Por tanto, se ha propuesto que la forma más apropiada y natural de almacenar los residuos sea retornarlos a la corteza terrestre. Con este propósito, la solución generalmente aceptada es el enterramiento del SNF en un almacenamiento geológico profundo durante un periodo de tiempo al menos tan largo como el tiempo de decaimiento radiactivo. El diseño de un almacenamiento geológico profundo consiste en un sistema multibarrera emplazado en una formación geológica a gran profundidad (~ 250-500 m), que debe evitar que los radionucleídos alcancen la biosfera. Este sistema multibarrera consiste en la contención de los residuos dentro de tubos de revestimiento y contenedores, que a su vez son protegidos mediante su introducción en túneles rellenados con materiales de sellado y rodeados por barreras geológicas naturales. Sin embargo, es bien conocido que después de este tiempo las barreras que protegen los residuos serán traspasadas y el SNF entrará en contacto con el agua. Por ello, el agua puede ser el vehículo que movilice los radionucleídos hacia la biosfera.

Aunque las condiciones del agua subterránea en un repositorio son generalmente reductoras, se ha postulado un entorno oxidativo en una delgada capa cercana a la superficie del combustible, de espesor < 50 µm. Este ambiente es producido por la radiólisis del agua debida a la radiación ionizante asociada al combustible. La radiólisis del agua lleva a la producción de oxidantes como el H_2O_2 entre otros. Por tanto, el uranio en la matriz del combustible nuclear gastado, compuesto por dióxido de uranio, $U^{IV}O_2$, podría oxidarse a U(VI) y disolverse en el agua formando grupos uranilo. Estos grupos uranilo pueden precipitar formando diferentes *fases secundarias*, es decir, productos de alteración, en la superficie del combustible gastado dependiendo de las condiciones locales y concentraciones de las especies reactivas presentes.

Ya que los compuestos uranílicos, que contienen UO_2^{2+}, aparecerán como fases secundarias en la superficie del SNF en las condiciones de almacenamiento geológico final, su caracterización y la determinación de sus propiedades es extraordinariamente importante. Sin embargo, debido a la radiotoxicidad de estos materiales, el estudio experimental de estas sustancias requiere una manipulación extremadamente cuidadosa de las muestras. Los métodos teóricos, basados en las leyes de la física y química cúantica que estudian estos sistemas a nivel atomístico, están libres de estas dificultades y se usaron en este trabajo tanto como herramienta interpretativa de los resultados de las técnicas experimentales, como herramienta predictiva para las propiedades de estas sustancias que son inaccesibles mediante su medida experimental. Los minerales uranílicos ruderfordina, studtita, soddyita y uranofana, que han sido ampliamente reconocidos como componentes fundamentales de la secuencia paragenética de las fases secundarias que surgen de la alteración de la uraninita y la corrosión del SNF, han sido estudiados por medio de difracción

de Rayos X en polvo y espectroscopia Raman combinados con cálculos de primeros principios (*ab initio*) basados en los métodos de la teoría del funcional de la densidad (DFT).

En los pasos iniciales de este estudio, se encontró en la bibliografía que existían muy pocos estudios acerca de los espectros teóricos vibracionales de estos materiales. En realidad, en ninguno de estos estudios iniciales se incluía una determinación completa de estos espectros, ya que se calculaban solo las frecuencias de los fonones en el punto gamma y no se aportaban intensidades de banda. Las razones por la que existían una cantidad tan limitada de tratamientos teóricos quedaron muy claras una vez revisada la bibliografía: 1) El alto nivel de teoría requerido para describir correctamente los sistemas que contienen el átomo de uranio; 2) El gran número de átomos en las celdas unidad de estos materiales; 3) El gran número de electrones de valencia que es preciso describir explícitamente en los cálculos; y 4) La ausencia de buenos pseudopotenciales conservadores de la norma necesarios para la computación de los espectros vibracionales teóricos. Siendo conscientes de estas dificultades, se pensó que la mejor forma de afrontar estos problemas era la generación de un pseudopotencial completamente nuevo para el átomo de uranio. Este pseudopotencial debía satisfacer, por lo menos, las condiciones de ser relativista y conservador de la norma si se deseaba estudiar la estructura y el espectro de estos compuestos con buen nivel de precisión. Se generó el pseudopotencial y se evaluó su calidad para una larga serie de minerales que contienen el átomo de uranio. Se determinó la estructura de estos materiales y se encontró que los parámetros de red, longitudes de enlace, ángulos de enlace y patrones de Rayos X en polvo obtenidos estaban en muy buen acuerdo con los datos experimentales. Ya que las estructuras de muchos de estos materiales (por ejemplo, de la soddyita y la uranofana) no habían sido nunca estudiadas por medio de cálculos teóricos rigurosos de estado sólido, este trabajo confirmó por primera vez las estructuras determinadas experimentalmente por medio de técnicas de difracción de Rayos X.

El espectro Raman de los minerales de uranilo seleccionados (rutherfordina, studtita, soddyita y uranofana) fue determinado experimentalmente en el CIEMAT y calculado teóricamente usando teoría de perturbaciones del funcional de la densidad (DFPT) en el CSIC. En este trabajo se muestra una comparación detallada de los espectros experimental y teórico. Los números de onda no escalados de las bandas del espectro teórico mostraron muy buen acuerdo con los valores experimentales correspondientes. Esta concordancia en la comparación permitió realizar una asignación rigurosa de las bandas del espectro Raman, ya que los métodos teóricos ofrecen vistas detalladas a escala microscópica de los movimientos atómicos en los modos normales correspondientes. Estos espectros fueron los primeros espectros Raman teóricos completos (incluyendo números de onda e intensidades de las bandas) publicados de materiales cristalinos que contienen el átomo de uranio.

Ya que los cálculos generaron estructuras y espectros de buena calidad, se consideró la posibilidad de obtener propiedades adicionales de estos materiales. Debido a la importancia de las estructuras de estos materiales, se estudió su estabilidad mecánica. Las propiedades y estabilidad mecánicas, así como las ecuaciones de estado, del mineral carbonato de uranilo ruderfordina y de los minerales silicato de uranilo soddyita y uranofana fueron estudiados teóricamente por primera vez. También se determinaron sus propiedades termodinámicas, indispensables para la modelización dinámica del comportamiento químico de estos compuestos. Para el caso de la ruderfordina, los resultados de los cálculos teóricos de estas propiedades mostraron un acuerdo excelente con los datos experimentales. Este hecho sugiere que los métodos teóricos constituyen una excelente herramienta, alternativa a los métodos experimentales, para la determinación de las propiedades termodinámicas de materiales que contienen el átomo de uranio. Un resultado adicional en los estudios del mineral ruderfordina es la extensión del rango de temperatura en que se conocían estas propiedades al rango entre 0 y 700 K. La buena calidad de las propiedades termodinámicas calculadas teóricamente ha sido confirmada por los excelentes resultados obtenidos en un trabajo posterior del polimorfo gamma del trióxido de uranio, γ-UO_3.

Usando las estructuras calculadas y los espectros Raman de un conjunto de materiales que contienen el ion uranilo, se ha obtenido una relación entre la distancia de enlace UO y el desplazamiento Raman asociado a la vibración de estrechamiento simétrico del uranilo por medio

de un ajuste numérico de los datos calculados. Cuando se usa esta relación para determinar longitudes de enlace UO a partir de desplazamientos Raman determinados experimentalmente, se obtienen resultados con una precisión similar a la de otras relaciones empíricas usadas ampliamente en la literatura y determinadas mediante un ajuste de un gran conjunto de datos deducidos a partir de medidas de difracción de Rayos X y de espectroscopia Raman. Sin embargo, en este trabajo la relación fue obtenida a partir de un pequeño número de datos deducidos a partir de cálculos *ab-initio*, es decir, sin utilizar ninguna información empírica.

Como las fases secundarias del SNF pueden reducir la liberación de los productos de fisión y actínidos pesados presentes en el SNF a la biosfera, en este trabajo se estudió la incorporación de productos de fisión (el principal peligro del SNF si se adopta el Ciclo del Combustible Nuclear Avanzado) en la estructura cristalina de la uranofana-α. Como resultado se encontró que la incorporación de estroncio en la estructura cristalina de este mineral es posible, y que el material cristalino sólido con estroncio en lugar de calcio tiene un patrón de Rayos X en polvo y un espectro Raman muy similares a los de la uranofana normal de acuerdo con estudios experimentales previos. Este estudio muestra que este mineral silicato de uranilo puede actuar como una barrera adicional para la liberación de productos de fisión a la biosfera.

En resumen, los resultados teóricos obtenidos, incluyendo la determinación de propiedades estructurales, mecánicas, termodinámicas y vibracionales, sugieren que la metodología teórica es una herramienta muy potente para realizar estudios detallados de las fases secundarias del SNF libre de las dificultades asociadas a la manipulación experimental debido a su radiotoxicidad. Por último, se concluye que la interacción entre los métodos experimentales y teóricos aumenta extraordinariamente el conocimiento y entendimiento de los procesos y compuestos involucrados en el almacenamiento del combustible nuclear gastado.

Agradecimientos

En primer lugar, debo agradecer la ayuda de mi compañera Ana María y de mi hija Beatriz, que me han soportado, acompañado y alentado muchísimo durante los años que he empleado en la realización de este trabajo. Os debo mucho y os quiero. Tampoco puedo olvidarme de mis cagoncetes, Pelusa, Abril y Algodón.

En segundo lugar, quiero expresar mi agradecimiento a mis hermanos César, Ana, Marta, Raquel y Constantino. Acumuleno!!!

En tercer lugar, me gustaría que estas líneas sirvieran para expresar mi más profundo y sincero agradecimiento a todas aquellas personas que con su ayuda han colaborado en la realización del presente trabajo, en especial a los Dres. Vicente Timón y Joaquín Cobos, directores de esta investigación, por la orientación, el seguimiento y la supervisión continua de la misma, pero sobre todo por la motivación y el apoyo recibido a lo largo de estos años.

También quiero agradecer la ayuda de mis compañeros del Instituto de Ciencia de Materiales del CSIC que han hecho que el tiempo entre las interminables computaciones se pasara casi sin sentirlo. En particular, quiero agradecer la ayuda del Profesor Rafael Escribano, por la acogida en su grupo y el asesoramiento en la asignación de los espectros vibracionales; y la de mis compañeros de despacho, Maite y Miguel. También quiero agradecer calurosamente la ayuda de Víctor, Isabel, Belén, Oscar, Guzmán, José María, Germán, Miguel Ángel, Ángel y muchos otros. Entre reuniones, desayunos, comidas y demás el tiempo pasa volando y se ha convertido en algo más que trabajo.

Igualmente quisiera hacer extensiva mi gratitud a mis compañeros de la Unidad de Residuos de Alta Actividad del CIEMAT y destacar su trabajo en la parte experimental de esta tesis. En particular, debo agradecer la extensa y productiva colaboración con Laura. Junto con Vicente y Joaquín hacemos un gran equipo.

Finalmente, quiero acordarme de todos mis sobrinos, de Gora y Paco y de todos Los Olvidados: Maximiano, Susana, Ángel, Pedro, Palmer, Pura, Matías, Flori, Manolo, Mero, …. que permanecen en mi memoria y no voy a olvidar jamás.

List of Publications

The content of the thesis has been published in the following papers from different Science Citation Index (SCI) Journals with permission from the publishers:

1. L. J. Bonales, F. Colmenero, J. Cobos and V. Timón, *Spectroscopic Raman characterization of Rutherfordine: a combined DFT and experimental study*. Phys. Chem. Chem. Phys. **2016**, *18*, 16575–16584.

2. F. Colmenero, L. J. Bonales J. Cobos and V. Timón, *Thermodynamic and mechanical properties of rutherfordine mineral based on density functional theory*. J. Phys. Chem. C **2017**, *121*, 5994-6001.

3. F. Colmenero, L. J. Bonales, J. Cobos and V. Timón, *Study of the thermal stability of studtite by in situ Raman spectroscopy and DFT calculations*. Spectrochim. Acta A **2017**, *174*, 245-253.

4. F. Colmenero, L. J. Bonales, J. Cobos and V. Timón, *Structural, mechanical and vibrational study of uranyl silicate mineral soddyite by DFT calculations.* J. Solid State Chem. **2017**, *253*, 249-257.

5. F. Colmenero, L. J. Bonales, J. Cobos and V. Timón, *Density Functional Theory Study of the Structural, Thermodynamic and Vibrational Properties of γ-UO_3 Polymorph,* J. Phys. Chem. C **2017,** in press.

6. F. Colmenero, L. J. Bonales, J. Cobos and V. Timón, *Structural, mechanical and Raman spectroscopic characterization of layered uranyl silicate mineral Uranophane-α by DFT methods,* Clay Minerals **2017,** submitted.

7. F. Colmenero and V. Timón, *Structural and Raman Spectroscopic Characterization of Natroxalate Mineral by Density Functional Theory*. Spectrochim. Acta A **2017**, submitted.

8. F. Colmenero, L. J. Bonales, J. Cobos and V. Timón, *Relation of uranium-oxygen bond length and uranyl symmetric stretching Raman shift obtained from theoretical DFT calculations*, J. Mol. Struct. **2017,** to be submitted.

Table of Contents

Acronyms

ACR	Advanced Candu Reactor
AFM	Atomic Force Microscopy
AGP	Almacenamiento Geológico Profundo
AGR	Advanced Gas-cooled Reactor
AO	Atomic Orbital
ATC	Almacén Temporal Centralizado
ATI	Almacén Temporal Individual
BFGS	Broyden-Fletcher-Goldfarb-Shanno
BSE	Back-Scattered Electron
BWR	Boiling Water Reactor
CANDU	CANada Deuterio Uranio
CASTEP	Cambridge Serial Total Energy Package
CCD	Charge Coupled Device
CCNN	Centrales Nucleares
CESGA	Centro de Supercomputación de Galicia
CETA	Centro Extremeño de Tecnologías Avanzadas
CIEMAT	Centro de Investigaciones Energéticas, Medioambientales y Tecnológicas
CSIC	Consejo Superior de Investigaciones Científicas
CTD	Charge Transfer Device
DFT	Density Functional Theory
DFPT	Density Functional Perturbation Theory
DGD	Deep Geological Disposal
DOE	Department Of Energy
DOS	Density Of States
DTA	Differential Thermal Analysis
DTG	Differential Thermal Gravimetry
ENRESA	Empresa Nacional de Residuos Radioactivos
EOS	Equation Of State
EPR	Electron Paramagnetic Resonance
FBR	Fast Breeder Reactor
FNR	Fast Neutron Reactor
FTIR	Fourier Transform Infrared Spectroscopy
FWHM	Full Width at Half Maximum
GEA	Gradient Energy Approximation
GGA	Generalized Gradient Approximation
GW	GigaWatt
HLW	High Radioactive Level Waste
HTGR	High-Temperature Gas-cooled Reactor
ICDD	International Center of Diffraction Data
IFBA	Integral Fuel Burnable Absorber
IPCC	Intergovernmental Panel on Climate Change
IAEA	International Atomic Energy Agency
IEA	International Energy Agency
IEM	Instituto de Estructura de la Materia
IR	InfraRed
LDA	Local Density Approximation
LILW	Low and Intermediate Level Waste
LO-TO	Longitudinal Optic (LO) and Transverse Optic (TO) effect
LSDA	Local Spin Density Approximation
LWR	Light Water Reactor
MA	Minor Actinide
MICADO	Multi-AO Imaging Camera for Deep Observations

MITYC	Ministerio de Industria, Turismo y Comercio
MOX	Mixed OXide fuel
MW	MegaWatt
NEA	National Energy Agency
NIRS	Nuclear Information and Resource Service
NMR	Nuclear Magnetic Resonance
OECD	Organisation for Economic Co-operation and Development
PBE	Perdew-Burke-Ernzerhof functional
PBEsol	Perdew-Burke-Ernzerhof functional for solids
PDF	Powder Diffraction File
PGRR	Plan General de Residuos Radioactivos
PHWR	Pressurised Heavy Water Reactor
PS	PSeudopotential
PUREX	Plutonium-Uranium Extraction
PW	Partial Wave
PW91	Perdew-Wang-91 functional
PWR	Pressurised Water Reactor
RBMK	Reactor Bolshoi Moschnosti Kanalynyi (in Russian) (Light Water Graphite-moderated Reactor)
REE	Rare Earth Element
RN	RadioNuclide
RS	Raman Spectroscopy
RRAA	Residuos Radiactivos de Alta Actividad
SE	Secondary Electrons
SIMFUEL	Simulated Used CANDU Reactor Fuel
SKB	Svensk Kärnbränslehantering AB (Swedish Nuclear Fuel and Waste Management Company)
SEM	Scanning Electron Microscopy
SNF	Spent Nuclear Fuel
TGA	Thermal Gravimetric Analysis
TRU	TRansUranium element
UN	Uranium Nitride
UNF	Used Nuclear Fuel
URRAA	Unidad de Residuos Radiactivos de Alta Actividad
VLLW	Very Low Level Waste
XC	Exchange and Correlation
XRD	X-ray Diffraction

Part I. Introduction and Overview

Chapter 1. Introduction

1.1 Introduction

The resurgence of the use of nuclear energy is mainly driven by the need of more electricity for increasing populations and consumption, as well as the need of energy sources without CO_2 emissions and other greenhouse gases causing global warming (Bruno and Ewing, 2006; Ewing, 2006, 2015). However, the management of nuclear waste is a matter of concern because it can be a source of high ecological damage, in the same way as uranium ore mining (Geipel *et al.*, 1994) and nuclear accidents (Burns *et al.*, 2012).

High-level nuclear waste, such as spent nuclear fuel (SNF) or reprocessed waste immobilized in a borosilicate glass (Ewing *et al.*, 2004), will be disposed of by burial in an underground geological repository. Contact of this waste with groundwater is expected after a time period of the order of some thousands of years (SKB-91, 1992) after closure, when the barriers that protect the waste will be breach (Ewing, 2015). The reducing conditions in the deep geological disposal will not be maintained at this time, and oxidized species near the spent fuel surface will increase due to the radiolysis of water caused by the ionizing radiation associated with the SNF (Christensen and Sunder, 1996; Shoesmith, 2000; Sunder, 1998; Roth and Johnson, 2008; Plasil, 2014). Therefore, uranium in the matrix of the spent nuclear fuel, composed by uranium dioxide, $U^{IV}O_2$, could oxidize to U(VI) and dissolve into the water forming uranyl groups. These uranyl groups can precipitate forming secondary phases, i.e. alteration products, on the spent fuel surface depending on the local conditions and concentrations of reactive species present (Plasil, 2014). These secondary phases can reduce the release of fission products and heavier actinides contained in the SNF to the biosphere (Burns *et al.*, 1997a; Shoesmith, 2000). The conceptual model of the alteration of SNF is displayed in Figure 1-1.

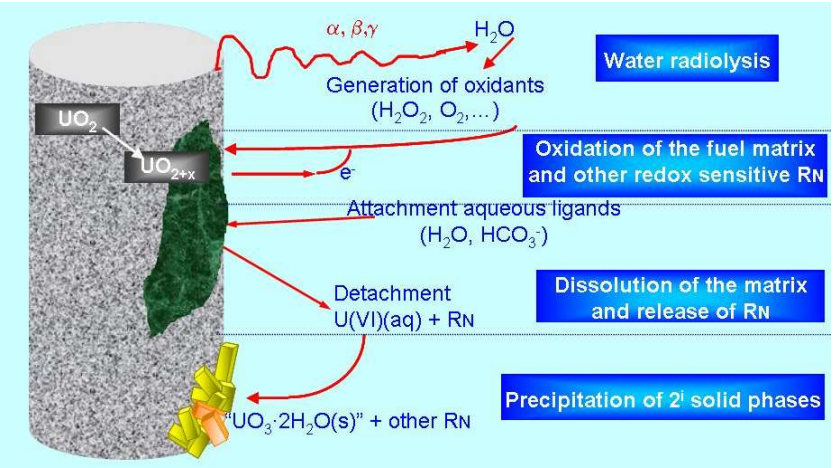

Figure 1-1. Identification of the elementary processes governing the alteration of SNF (Poinsot *et al.,* 2004).

A great amount of effort has been dedicated to the study of the reaction mechanisms to stablish the key parameters controlling the SNF corrosion (Shoesmith, 2000), such as dissolution/precipitation experiments (Amme *et al.*, 2002; Rey *et al.*, 2008; Lousada *et al.*, 2013), and uraninite mineral studies (Plasil, 2014) as a natural analogue of the SNF matrix. Due to the

difficulties in the handing of SNF, most of the experiments are carried out in analogue materials allowing the study of the transformation mechanisms in a systematic and safe way in conventional laboratories.

Minerals containing uranyl ion, UO_2^{2+}, are the result of precipitation after previous corrosion of natural uraninite or nuclear radioactive waste (Frondel 1956, 1958; Finch and Ewing, 1992; Finch *et al.*, 1992; Pearcy *et al.*, 1994; Wronkiewicz *et al.*, 1992, 1996). These minerals have an increasing interest due to its importance in the environmental, nuclear and energetic disciplines. As it has been explained, uranyl secondary phases are usually studied by analysing natural minerals containing the uranyl ion (Grenthe *et al.,* 2006), $U^{VI}O_2^{2+}$, found as alteration products of uraninite (Plasil, 2014), which is a natural analogue of the SNF matrix. In the general trend of the temporal sequence of alteration products of natural uraninites at different geochemical conditions, first recognized by Frondel (Frondel, 1956, 1958) and still widely accepted nowadays (Finch and Ewing, 1992; Pearcy *et al.*, 1994; Wronkiewicz *et al.*, 1992, 1996), uranyl oxide hydrates appear at the first place, then uranyl silicates and, less frequently, uranyl carbonates and phosphates; but as can be expected the specific alteration products depend on the local conditions. The contact with the reactive species found will produce different secondary phases depending on the pH, Eh conditions, as well as on the concentrations of the different species: silicates, carbonates, phosphates, etc. (Plasil, 2014).

Therefore, the study of these uranyl minerals is very important for the understanding of the long-term performance of a geological repository for nuclear waste. The structural characterization of uranium minerals is extraordinarily important due to the fact that the detailed understanding of their structure and bonding are key to evaluate the possible incorporation of fission products and transuranic elements into their crystal structures (Burns *et al.*, 1996, 1997a, 1997b; 2002, 2004; Jackson and Burns, 2001; Burns 1998, 1999a, 1999b, 2001, 2005; Burns and Klingensmith, 2006; Klingensmith and Burns, 2007a; Klingensmith *et al.*, 2007b), thus reducing their release and environmental impact. Also, the knowledge of the bond topology in the corresponding structures is a required step towards the understanding of the relations among the hierarchy of structures and mineral paragenesis. Despite the great amount of structural data available, the actual state of our knowledge about the crystalline chemistry and bonding of U^{6+} ion is poor and it is based on the information acquired from lighter elements. There are few quantitative theoretical works relative to the coordination chemistry of U^{6+} ion, because its theoretical study based in the application of Quantum Chemistry and Solid State methods is very complex. The number of electrons involved is very large (being necessary the use of effective potentials to describe the internal electrons), and the inclusion of relativistic effects is required.

The identification of the reaction products in the oxidation process is also very important in order to evaluate the effectiveness of a nuclear waste repository. This is a great challenge, not only due to the complexity of these materials (containing the most part of the elements of periodic table), but also due to the small amount of the products formed in the solid surface and their radiotoxicity (Bruno and Ewing, 2006). The last feature complicates the handling of these substances under security conditions and, therefore, their characterization. An additional difficulty is that the natural samples usually corresponds to mixtures of several different phases and the synthesis of these substances yield low crystallinity structures. The methods used so far to characterize the uranium containing materials cover a wide range and include, among others, X-Ray diffraction techniques, vibrational spectroscopy (infrared, Raman and even complementary far infrared methods), fluorescence and photoluminescence techniques, EPR and NMR methods (Baker, 2014).

The most appropriate technique must satisfy the following requirements: 1) The samples do not require any special preparation; 2) The technique must allow for the analysis of very small amounts of sample; and 3) The technique must be non-destructive. Two techniques satisfying these requirements are X-Ray Diffraction and Raman spectroscopy (Baker, 2014; Dubessy *et al*., 2012). Raman spectroscopy provides information about the molecular structure and its surroundings, but in order to obtain this information we need a precise assignation of the bands in the Raman spectra and models to interpret accurately the values of the Raman shifts and the

changes in these values. While Raman spectroscopy has already been employed to analyse the SNF and the associated alteration products, the needed database including the correct assignation of the different bands is still under development. We can remark the excellent works of many research groups (Amme *et al*., 2002; Sobry, 1973; Maya and Begun, 1981; Biwer *et al.*, 1990; Faulkes *et al.*, 1993, 1994, 2015a,b; Bastians *et al.*, 2004; Driscoll *et al.*, 2014), but the largest effort has been carried out by Frost *et al.* (2005-2011), which have investigated a very large number of secondary phases. Some groups have centered their research in the characterization of anhydrous uranium oxides (He and Shoesmith, 2010; Desgranges *et al.*, 2012; Manara *et al*., 2003).

On the other hand, theoretical techniques allow to perform a characterization of these materials free of the difficulties associated to experimental methods derived from their radiotoxicity. Nowadays, solid state codes are capable of optimizing the structures of complex systems and obtaining the many observable quantities comparable with those derived from experimental measurements (Clark *et al.*, 2005; Milman *et al.*, 2010; Gonze *et al.*, 2005, 2009; Paier *et al.*, 2005, 2006; Gianozzi *et al*., 2009; Pascale *et al*., 2004; Orlando *et al*., 2012; Ordejon *et al*., 1996; Artacho *et al*., 2008). This includes the determination of the crystalline structure and a great number of observables as the X-Ray pattern, the infrared and Raman spectra, the mechanical, thermodynamic, and optical properties. Besides, these methods allow for a precise assignation of the bands in the vibrational spectra, because they provide detailed microscopic scale views of the atomic motions in the corresponding vibrational normal modes (Refson *et al*., 2006).

Among the theoretical methods for which this kind of calculations are possible, the most widely employed are those based on Density Functional Theory (DFT) (Hohenberg and Kohn, 1964; Kohn and Sham, 1965, Parr and Yang, 1989) employing plane waves or atomic orbitals and pseudopotentials (Payne *et al*., 1992). The use of Density Functional Perturbation Theory (DFPT, Baroni *et al*., 1987, 2001; Gonze *et al.*, 1992, 1997) allows the prediction of infrared and Raman spectra with good levels of accuracy and cost/effectiveness ratios. However, the application to materials containing Rare Earth elements, shows difficulties not only due to the great number of atoms and valence electrons involved, but also the high level of theory required to describe these elements. Uranium is a complex atom showing four main oxidation states (+3, +4, +5, y +6) and a great size of its ions, which form complicated compounds with very high coordination numbers (Grenthe *et al*., 2006). The number of valence electrons in the external shells, which must be described explicitly is very large and it is needed to include very high angular momentum orbitals (5f shell). It is very difficult to find or generate good relativistic pseudopotentials needed to describe the inner electrons of these elements adequate to carry out vibrational studies of solids. In fact, there is very few published works on the theoretical determination of the spectra of solids containing uranium atom (Yun *et al*., 2012; Wang *et al*., 2013; Yin *et al*., 2008; Mei *et al*., 2013, 2014). These studies are limited to uranium oxides and nitrides and the unique spectral characteristic considered are the vibrational frequencies at gamma point. For example, Yun *et al*., 2012, computed the phonon spectrum of uraninite, UO_2, at gamma point and compared the resulting frequencies with the experimental ones. Nevertheless, some studies have reported other properties of these materials (Crocombette *et al*., 2001; Petit *et al*., 1998; Freyss *et al*., 2005, 2006; Beridze and Kowalski, 2014; Dudarev *et al*., 1997; Andersson *et al*., 2013; Nerikar *et al*., 2009; Wen *et al*., 2012, 2013; Kotomin *et al*. 2007, 2009; Bocharov *et al*., 2011; Chroneos *et al.*, 2013; Li *et al*., 2013; Greathouse *et al.* 2006, Weck *et al*., 2007, 2012, 2014, 2015, 2016; Ostanin y Zeller, 2007a,b; Shuller *et al*. 2010a, 2010b, 2013, 2014), and of related gas phase molecular clusters (Hay *et al*., 1998, 2000; Castro *et al.*, 2010; Shamov *et al*., 2007; Schreckenbach, *et al*., 2010; Odoh *et al*., 2013; Iche-Tarrat *et al.*, 2008; Majumdar *et al*., 2002, 2003; Chaudhuri *et al*., 2004).

One of the most relevant issues in nuclear and energetic sciences is the protection of the environment. The prediction of the behaviour of hazardous materials under diverse environmental conditions is extremely important. Fundamental thermodynamic data are the indispensable basis for a dynamic modelling of the chemical behaviour of contaminant waste components. They are needed in order to evaluate the origin and evolution of uranium ore bodies, in developing

programs for the solution mining of uranium deposits or mine dumps, in the study of spent nuclear fuel (SNF) radioactive waste and in the containment of such waste, and may also be of importance in reactions within breeder reactor (Hemingway *et al*., 1982; Langmuir, 1997; Casas *et al*., 1994; Navrotsky *et al*., 2013). The knowledge of precise thermodynamic data is basic in the development of geochemical and used fuel degradation models (Sassani *et al*., 2013)

The enormous importance of the thermodynamic information in the assessment of the safety of nuclear waste repositories is reflected by the large number of recent experimental works on this topic culminating in large reviews and updates of thermodynamic properties of uranium bearing species (Wanner and Forest, 1992; Murphy and Pabalan, 1995; Grenthe *et al*., 2004; Shvareva *et al*., 2012), and other systems containing related elements (Guillaumont, 2003). Recent studies include, among others, the important experimental determinations by means of solubility and calorimetry measurements of the thermodynamic properties of uranyl peroxide hydrates (Kubatko *et al*., 2003, 2005a; Armstrong *et al*., 2012; Guo *et al*., 2014a), uranyl carbonate minerals (Kubatko et al., 2005b), uranyl phosphate and orthophosphate minerals (Gorman-Lewis *et al*., 2009), and uranyl silicates (Nguyen *et al*., 1992; Gorman-Lewis *et al*., 2007, Shvareva *et al*., 2011; Guo *et al*., 2014b). While the thermodynamic information database of uranium bearing species is very advanced, there are many secondary phases for which the corresponding data is inaccurate due to large experimental uncertainties (Langmuir, 1997) Additionally, the range of temperature and pressure conditions for which these properties are known is quite limited.

As noted by Weck *et al*. (2015), the availability of a great amount of information on the formation, thermodynamic stability and phase transformations of alteration phases formed at the SNF surface contrasts with the paucity of data regarding the mechanical stability and properties of these phases. In fact, saving the theoretical study of the uranyl peroxide hydrates, studtite and metastudtite, by Weck *et al*. (2015), no experimental or computational studies reporting data of this kind have been carried up to date. Theoretical methods may be advantageous to determine the thermodynamic and mechanical properties of these materials, because they are free of the difficulties associated to their radiotoxicity. Whereas theoretical solid state methods may be used in order to obtain these properties, the calculations required are very complex and expensive (Beridze and Kowalski, 2014; Crocombette *et al*., 2001). For this reason, there are very few such studies and we may cite the recent works by Sassani *et al*. (2013), Weck and Kim (2014, 2016), Beridze and Kowalski (2014) and Weck *et al*. (2015).

1.2 Objectives

This PhD Thesis has been carried out within the interdisciplinary and collaborative agreement: "Caracterización experimental y teórica de fases secundarias y óxidos de uranio formados en condiciones de almacenamiento de combustible nuclear", between the Instituto de Estructura de la Materia (IEM) of the Consejo Superior de Investigaciones Científicas (CSIC) and the Unidad de Residuos Radiactivos de Alta Actividad (URRAA) del Centro de Investigaciones Energéticas, Medioambientales y Tecnológicas (CIEMAT).

The main objectives of this PhD Thesis are directed towards the structural characterization, identification and determination of the properties of secondary phases arising from alteration (oxidation/dissolution) of spent nuclear fuel in conditions of final geological disposal, when the barriers that protect this waste from contact with water have lost their integrity. These objectives are very important and lead us to the theoretical study of crystal structures, observables and spectra of the species involved including the correct assignation of the bands in the vibrational spectra.

Specifically, the main objectives are:

1. Generation of a norm-conserving relativistic pseudopotential for uranium atom adequate for the determination of vibrational spectra and properties of materials containing this atom within program CASTEP (Clark, 2005; Milman, 2010), a module of Materials Studio package (Materials Studio, 2017). The validation of this pseudopotential will be performed by means of the computation of the structures of a wide variety of uranium minerals as uranium oxides and secondary phases of SNF.

2. Structural characterization of secondary phases of SNF by means of theoretical methods, including: the uranyl carbonate rutherfordine, the uranyl peroxide studtite and the uranyl silicates soddyite and uranophane-α. It is of interest the determination of their crystalline structures, structural properties (atomic bond lengths and angles) and X-Ray diffraction powder patterns, as well as the comparison of the calculated X-Ray diffraction powder patterns with the experimental ones.

3. Determination of the theoretical Raman spectrum of these materials and comparison with the corresponding experimental spectra. Raman spectroscopy is one of main techniques used to identify the secondary phases of SNF. Therefore, the assignment and interpretation of the bands appearing in these spectra are of interest. Theoretical methods provide detailed microscopic scale views of the atomic motions in the corresponding vibrational normal modes. Thus, one of the aims of this investigation was to determine and visualize the most important Raman active vibrational normal modes.

4. Determination of the thermodynamic properties of these materials and analysis of their quality. Fundamental thermodynamic data are the indispensable basis for a dynamic modelling of the chemical behaviour of contaminant waste components, and are needed for the development of geochemical and used nuclear fuel degradation models.

5. Determination of mechanical properties and study of the mechanical stability of the structures of these materials. No experimental or computational studies reporting data of this important kind have been carried up to date, except one theoretical study of uranyl peroxide minerals studtite and metastudtite. Theoretical methods may be advantageous to determine these properties, because they are free of the difficulties associated to their radiotoxicity.

1.3 Methodology

The theoretical methods used in this work were computational techniques based in the density functional theory (DFT; Hohenberg and Kohn, 1964; Kohn and Sham, 1965; Parr and Yang, 1989) applied to periodic solids by means of the use of plane wave basis sets, and pseudopotentials (Payne *et al*., 1992) implemented in the CASTEP code (Clark *et al*., 2005; Milman *et al.*, 2010) included in the Materials Studio package (Materials Studio, 2017).

Two software packages were employed in order to generate the norm conserving relativistic pseudopotential specific for the uranium atom: OPIUM (Opium, 2004) and fhi98PP (Fuchs *et al*., 1999). The final version of the pseudopotential (Bonales *et al.*, 2016a) was obtained with the second program in cpi format and, then, it was transformed to recpot format (used by CASTEP) employing the tool cpi2recpot (Haynes and Refson, 2007). The pseudopotential is norm conserving (Troullier and Martins, 1991), being this characteristic needed to determine the vibrational spectra within CASTEP software.

The X-ray diffraction patterns were obtained from the computed atomic positions by using the software REFLEX, also included in the Materials Studio package (Materials Studio, 2017), and the programs XtalDraw (Downs, 2003) and ENDEAVOUR (Brandenburg and Putz, 2003). Further, the comparison of the experimental and theoretical spectra was carried out using the program XPowder (Martin, 2012) and the database PDF-2 (ICDD, 2003). The patterns not included in this database were determined experimentally or taken from the literature.

The vibrational spectra (infrared and Raman) were determined by using density functional perturbation theory (DFPT) (Baroni *et al*., 1987, 2001; Gonze *et al*., 1992, 1997) implemented in the software CASTEP.

The phonon spectra at different points of the Brillouin zone, needed for the computation of the thermodynamic properties, were also obtained by means of DFPT, as second-order derivatives of the total energy (Baroni *et al.*, 2001). The knowledge of the phonon spectra allows the computation of the dispersion curves and vibrational density of states and, from them, the evaluation of the thermodynamic properties in the quasi-harmonic approximation, such as free energies, enthalpies, entropies, specific heats and Debye temperatures (Baroni *et al.*, 2001; Lee and Gonze, 1995).

From the optimized structures, the elastic constants were obtained at T=0 K using stress-strain relations. With this purpose, the finite deformation technique implemented in CASTEP code was employed. In this technique symmetry-adapted finite strains (Nye, 1985) are used to extract the individual elastic constants from the elastic tensor obtained as a response of the applied deformations. In the computation of the elastic tensor, this method seems to be more efficient than energy based methods and the use of DFPT (Yu *et al.*, 2010).

The equations of state reported in this work were obtained by optimizing the different structures subject to a set of pressure values. The corresponding unit cell volumes and applied pressures where then fitted to a fourth−order Birch−Murnaghan equation of state (Birch, 1947) using the computer code EOSFIT 5.2 (Angel, 2001).

To perform the computational works, we have used a great variety of computational resources. In particular, we must mention the time spent in the supercomputers CETA-CIEMAT (Centro Extremeño de Tecnologías Avanzadas), CESGA (Centro de Supercomputación de Galicia) and TRUENO (Cluster de Cálculo Científico del CSIC, Madrid).

The experimental X-ray diffraction analyses of some materials were carried out in the laboratories of the Unidad de Residuos Radiactivos de Alta Actividad (URRAA) from CIEMAT. As it has been mentioned, a collaboration agreement CSIC-CIEMAT has been stablished for the combined experimental and theoretical study of uranium oxides and secondary phases resulting from alteration of spent nuclear fuel in conditions of final geological disposal. CIEMAT has a wide experience in the handling and characterization of these materials by means of superficial characterization techniques including X-Ray Diffraction (XRD), Raman spectroscopy (RS), Scanning Electron Microscopy (SEM) and Thermo-Gravimetric Analysis (TGA).

1.4 Structure of this PhD Thesis

In Chapter 2 (*Nuclear Fuel Cycle and Secondary Phases*), the main topics needed to understand the nuclear fuel cycle and the appearance of secondary phases in the surface of SNF are reviewed. In the first part of this chapter (*Nuclear Energy and Nuclear materials)*, the basic concepts related to nuclear energy and the materials used for its production are given. In the second part (*Nuclear Fuel Cycle and Radioactive Waste Management*), the nuclear fuel cycle and the management of radioactive nuclear waste are described. Finally, in the last part (*Spent Nuclear Fuel and Secondary Phases*), the physico-chemical characteristics and stability of spent nuclear fuel and its secondary phases are studied. The two first parts are required to know the composition of the waste generated by the use of the nuclear power. Depending on the kind of fission reactors and nuclear fuels employed as well as the option chosen for the nuclear fuel cycle, the composition of the residuals generated which must be stored in a final deep geological disposal is different. In turn, the composition of the final residuals determines the secondary phases which will appear as alteration products of the SNF and the kind of studies which must be made in order to optimize the disposal of these residuals. For example, if an Advanced Closed Nuclear Fuel Cycle (Merino Rodríguez, 2014) is adopted, the main hazard comes from generation of fission products, as

strontium and caesium, and not from the release of transuranic elements, which are the principal problem in the case of the Open Nuclear Fuel Cycle (the option chosen presently in Spain).

In Chapter 3 (*Materials and methods*) the materials and methods, experimental and theoretical, used in this work are described. The main experimental techniques employed in order to characterize the secondary phases of the SNF are first presented (*Experimental Methods and Materials*). Then, the nuclear materials used in this study (natural and synthetic samples were employed) and its management are described. Since the main purpose of this Thesis is to show that the use of theoretical methodology is a powerful tool for the study of the secondary phases of SNF, the theoretical part of this chapter (*Theoretical and Computational Methods*) is quite detailed and provides the needed background to understand the computational procedures used and the results given in the remaining chapters.

In Chapters 4 to 9 (*Results and Discussion*) the main results of this Thesis are given and discussed. Because of most of the content of this thesis has been published, the results and conclusions of each article will be summarised in separate chapters. Chapter 4 (*Rutherfordine: Structure and Raman Spectroscopy*; Bonales *et al*., 2016a) provides a structural and Raman spectroscopic study of rutherfordine, a uranyl carbonate mineral, which is an important secondary phase of SNF. It also presents the generation and validation of the norm-conserving relativistic pseudopotential, which is extensively used to study all the other secondary phases of SNF in later chapters. The calculated Raman spectrum given in this chapter is very important because it represents the first published complete theoretical Raman spectrum (including band wavenumbers and intensities) of a uranyl-containing crystalline material.

Chapter 5 (*Rutherfordine: Thermodynamic and Mechanical Properties*; Colmenero *et al.*, 2017a) involves the determination of the thermodynamic and mechanical properties of rutherfordine. This work reported very accurate thermodynamic functions of this mineral phase in the temperature range of 0-700 K. Furthermore, the mechanical properties of this mineral were reported and the mechanical stability of its structure was studied. Since there were not experimental measurements of the mechanical properties, the theoretical calculations allowed us to predict them.

In Chapter 6 (*Soddyite: Structure, Mechanical Properties, Equation of State, and Raman Spectroscopy*; Colmenero *et al.*, 2017c) a study of the structural, mechanical, and Raman spectroscopic properties of Soddyite, an important uranyl silicate mineral, is presented. This study was the first published theoretical study of this mineral and confirmed the structure obtained by means of X-Ray diffraction techniques. The Raman spectrum of soddyite was also computed and assigned. Finally, the mechanical properties of this mineral were predicted.

In Chapter 7 (*Studtite: Structure, Raman Spectroscopy and Thermal Stability*; Colmenero *et al.*, 2017b) a study of the structural and Raman spectroscopic properties of the hydrated uranyl peroxide mineral studtite is afforded. The assignation of the band corresponding to the UO bond symmetric stretching and the experimental analysis of its displacement with temperature permitted the study of the thermal stability of studtite in presence and absence of water.

Chapter 8 (*Structural, Mechanical and Raman Spectroscopic Characterization of Layered Uranyl Silicate Mineral Uranophane-α by DFT Methods*; Colmenero *et al.*, 2017e) reports a study of the structural, mechanical, and Raman spectroscopic properties of uranophane-α, the most frequently found uranyl mineral in nature after uraninite. Its structure is completely different to that of soddyite, since it is a clay-like hydrated layered uranyl silicate mineral, while soddyite has a framework crystal structure. Furthermore, this study includes an additional application of the computational methods to the study of the possible incorporation of strontium, one of the most important fission products, in the crystalline structure of uranophane-α. This study demonstrates that this uranyl silicate mineral may act as an additional barrier for the release of fission products to the biosphere.

Chapter 9 (*Uranium-Oxygen Bond-Length to Uranyl Symmetric Stretching Raman Shift relationship*; Colmenero *et al.*, 2017f) contains a compilation of the computed theoretical structures and Raman spectra of different uranyl ion containing materials. By using these

structures and Raman spectra, an UO bond-length to uranyl symmetric stretching Raman shift relation was obtained by a numerical fit of the calculated data. The relation was derived from first principle (*ab initio*) calculations, *i.e.*, without using any experimental information. The resulting parameters gave an expression with essentially the same accuracy as that derived by Bartlett and Cooney (1989), who employ a large set of experimental results.

Finally, in Chapter 10 (*Conclusions)*, the conclusions of this PhD Thesis are presented. The conclusions specific to each one of the articles given in Chapters 4-9, are presented separately and, then, the final conclusions and perspectives are indicated.

Capítulo 1. Introducción

1.1 Introducción

La reactivación del uso de la energía nuclear es principalmente debida a la necesidad de más electricidad para poblaciones en aumento y consumos por persona cada vez mayores, así como la necesidad de fuentes de energía sin emisiones de CO_2 y otros gases de efecto invernadero que causan calentamiento global (Bruno and Ewing, 2006; Ewing, 2006, 2015). Sin embargo, la gestión de los residuos nucleares es muy importante porque puede ser una fuente de alto impacto ecológico, de la misma forma que lo pueden ser la minería del uranio (Geipel *et al.*, 1994) y los accidentes nucleares (Burns *et al.*, 2012).

Los residuos nucleares de alta actividad, como el combustible nuclear gastado (SNF) o los residuos reprocesados inmovilizados en un vidrio de borosilicato (Ewing *et al.*, 2004), serán almacenados en un repositorio geológico subterráneo. Se espera que el agua subterránea entre en contacto con estos residuos después de un tiempo del orden de algunos miles de años (SKB-91, 1992) después del cierre, cuando las barreras que protegen estos residuos dejen de ser efectivas tras un posible fallo del contenedor y del almacén (Ewing, 2015). Las condiciones reductoras en el almacenamiento geológico profundo no se mantendrán en este momento, y aumentará la cantidad de especies oxidadas cerca de la superficie del combustible nuclear gastado debido a la radiólisis del agua causada por la radiación ionizante asociada al SNF (Christensen y Sunder, 1996; Shoesmith, 2000; Sunder, 1998; Roth y Johnson, 2008; Plasil, 2014). Por tanto, el uranio en la matriz del combustible nuclear gastado, compuesto por, $U^{IV}O_2$, podría oxidarse a U(VI) y disolverse en el agua formando grupos uranilo. Estos grupos uranilo pueden precipitar formando diferentes fases secundarias, es decir, productos de alteración, en la superficie del combustible nuclear gastado dependiendo de las condiciones locales y las concentraciones de las especies reactivas presentes (Plasil, 2014). Estas fases secundarias pueden reducir la liberación de los productos de fisión y actínidos pesados contenidos en el combustible nuclear gastado a la biosfera (Burns *et al.*, 1997a; Shoesmith, 2000). En la Figura 1-1, se muestra el modelo conceptual de la alteración del SNF.

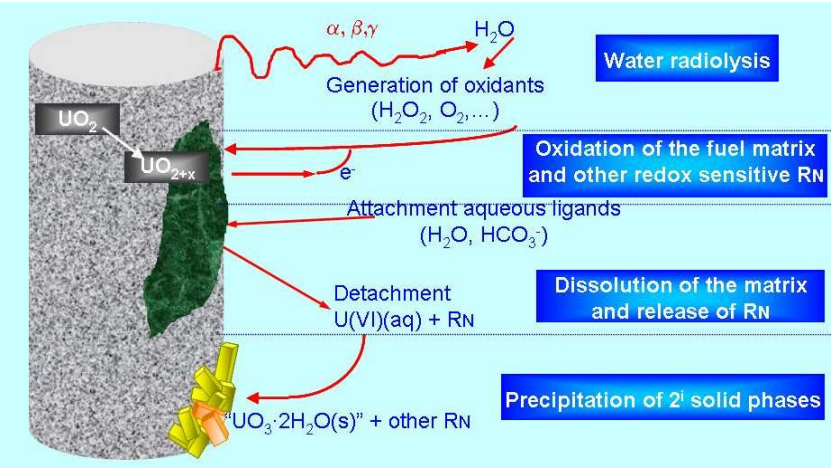

Figure 1-1. Identificación de los procesos elementales que gobiernan la alteración del SNF (Poinsot *et al.,* 2004).

Se ha dedicado un gran esfuerzo en el estudio de los mecanismos de reacción para establecer los parámetros clave que controlan la corrosión del SNF (Shoesmith, 2000), como experimentos de disolución/precipitación (Amme *et al.*, 2002; Rey *et al.*, 2008; Lousada *et al.*, 2013) y estudios del mineral uraninita (Plasil, 2014) como análogo natural de la matriz del SNF. Debido a las dificultades en la manipulación del SNF, la mayoría de los experimentos se realizan en materiales análogos que permiten el estudio de los mecanismos de transformación de forma sistemática y segura en laboratorios convencionales.

Los minerales que contienen el ion uranilo, UO_2^{2+}, son el resultado de la precipitación tras la corrosión previa de los materiales base de uranio, ya sea como uranio natural o como posible residuo radiactivo (Frondel 1956, 1958; Finch y Ewing, 1992; Finch *et al.*, 1992; Pearcy *et al.*, 1994; Wronkiewicz *et al.*, 1992, 1996). Estos minerales tienen un interés cada vez mayor debido a su importancia en las disciplinas medioambiental, nuclear y energética. En particular, las fases secundarias del SNF son usualmente estudiadas analizando minerales naturales que contienen el mineral uranilo (Grenthe *et al.,* 2006), $U^{VI}O_2^{2+}$, encontrados como productos de alteración de la uraninita (Plasil, 2014), que es un análogo natural de la matriz del SNF. En la tendencia general de la secuencia temporal de los productos de alteración de uraninitas naturales en diferentes condiciones geoquímicas, reconocida en primer lugar por Frondel (Frondel, 1956, 1958), y todavía ampliamente aceptada hoy día (Finch y Ewing, 1992; Pearcy *et al.*, 1994; Wronkiewicz *et al.*, 1992, 1996); los óxidos hidratados aparecen en primer lugar y después los silicatos de uranilo y, menos frecuentemente, los carbonatos y fosfatos de uranilo; aunque, como es de esperar, los productos de alteración específicos dependen de las condiciones locales. El contacto con las especies reactivas encontradas producirá diferentes especies secundarias dependiendo de las condiciones de pH y Eh, así como de las concentraciones de las diferentes especies: silicatos, carbonatos, fosfatos, etc. (Plasil, 2014).

Por tanto, el estudio del estos minerales uranílicos es muy importante para entender el comportamiento a largo plazo de un almacenamiento geológico de residuos nucleares. La caracterización estructural de los minerales de uranio es extraordinariamente importante debido al hecho de que un entendimiento detallado de su estructura y enlace son clave para evaluar la posible incorporación de productos de fusión y elementos transuránicos en sus estructuras cristalinas (Burns *et al.*, 1996, 1997a, 1997b; 2002, 2004; Jackson y Burns, 2001; Burns 1998, 1999a, 1999b, 2001, 2005; Burns y Klingensmith, 2006; Klingensmith y Burns, 2007a; Klingensmith *et al.*, 2007b), reduciendo su liberación e impacto ambiental. También, el conocimiento de la topología de enlaces en las correspondientes estructuras es un paso necesario hacia el entendimiento de las relaciones entre las jerarquías de estructuras y la paragénesis mineral. A pesar de la gran cantidad de datos estructurales sobre la simetría cristalina, el estado actual de nuestro conocimiento sobre la química cristalina y enlace del ion U^{6+} ion es pobre y se basa en la información adquirida para elementos más ligeros. Existen pocos trabajos cuantitativos relativos a la química de coordinación del ion U^{6+} debido a que su estudio teórico, basado en la aplicación de los métodos de la Química Cuántica y de la Física del Estado Sólido, es muy compleja. El número de electrones involucrados es muy largo, siendo necesario el uso de potenciales efectivos para describir los electrones internos, y la inclusión de efectos relativistas.

La identificación de los productos de reacción en el proceso de oxidación es también muy importante para evaluar la efectividad de un repositorio de residuos nucleares. Este es un gran desafío, no solo debido a la complejidad de estos materiales (conteniendo la mayor parte de los elementos de la tabla periódica), sino también debido a la pequeña cantidad de los productos formados en la superficie sólida y su radiotoxicidad (Bruno y Ewing, 2006). La última característica complica la manipulación de estas sustancias bajo condiciones de seguridad y, por tanto, su caracterización. Una dificultad adicional es que las muestras naturales normalmente corresponden a mezclas de diferentes fases y la síntesis de estas sustancias produce estructuras de baja cristalinidad. Los métodos usados hasta ahora para caracterizar los materiales que contienen el ion uranilo cubren un amplio rango e incluyen, entre otros, técnicas de difracción de Rayos X, espectroscopia vibracional (infrarrojo, Raman, e incluso métodos complementarios de infrarrojo lejano), técnicas de fluorescencia y fotoluminiscencia, métodos de EPR y NMR. (Baker, 2014).

La técnica más apropiada debe satisfacer los siguientes requisitos: 1) Las muestras no requieren ninguna preparación especial; 2) La técnica debe permitir el análisis de cantidades muy pequeñas de muestra; y 3) La técnica debe ser no destructiva. Dos técnicas que satisfacen estos requerimientos son la difracción de Rayos X y la espectroscopia Raman (Baker, 2014; Dubessy *et al*., 2012). La espectroscopia Raman aporta información sobre la estructura molecular y su entorno, pero para obtener esta información necesitamos una asignación precisa de las bandas en el espectro Raman y modelos para interpretar precisamente los valores de los desplazamientos Raman y cambios en estos valores. Aunque la espectroscopia Raman ya ha sido empleada para analizar el SNF y los productos de alteración asociados, la base de datos necesaria incluyendo la asignación correcta de las bandas está todavía en desarrollo. Podemos remarcar los excelentes trabajos de muchos grupos de investigación (Amme *et al*., 2002; Sobry, 1973; Maya y Begun, 1981; Biwer *et al*., 1990; Faulkes *et al.*, 1993, 1994, 2015a,b; Bastians *et al.*, 2004; Driscoll *et al.*, 2014), pero el mayor esfuerzo ha sido llevado a cabo por Frost *et al.* (2005-2011), que han investigado un gran número de fases secundarias. Algunos grupos han centrado su investigación en la caracterización de óxidos de uranio anhidros (He *et al*., 2010; Desgranges *et al.*, 2012; Manara *et al*., 2003).

Por otra parte, las técnicas teóricas permiten realizar una caracterización teórica de estos materiales libre de las dificultades asociadas a los métodos experimentales que derivan de su radiotoxicidad. Hoy día, los códigos de estado sólido son capaces de optimizar las estructuras de sistemas complejos y de obtener muchas cantidades observables comparables con las que se derivan de medidas experimentales (Clark *et al.*, 2005; Milman *et al.*, 2010; Gonze *et al.*, 2005, 2009; Paier *et al.*, 2005, 2006; Gianozzi *et al*., 2009; Pascale *et al*., 2004; Orlando *et al*., 2012; Ordejon *et al*., 1996; Artacho *et al*., 2008). Esto incluye la determinación de la estructura cristalina, los patrones de Rayos X, los espectros de infrarrojo y Raman, y las propiedades termodinámicas, mecánicas y ópticas. Además, estos métodos permiten realizar una asignación precisa de las bandas en los espectros vibracionales ya que proveen vistas a escala microscópica de los movimientos atómicos en los modos normales correspondientes (Refson *et al*., 2006).

Entre los métodos teóricos para los cuales este tipo de cálculos es posible, los más ampliamente utilizados son los basados en la Teoría del Funcional de la Densidad (DFT) (Hohenberg y Kohn, 1964; Kohn y Sham, 1965, Parr y Yang, 1989), que emplean ondas planas u orbitales atómicos y pseudopotenciales (Payne *et al*., 1992). El uso de Teoría de Perturbaciones del Funcional de la Densidad (DFPT) (Baroni *et al*., 1987, 2001; Gonze *et al.*, 1992, 1997) permite la predicción de espectros de infrarrojo y Raman con buenos niveles de precisión y radios coste/efectividad. Sin embargo, la aplicación a materiales que contienen elementos de Tierras Raras presenta dificultades, no solo debido al gran número de electrones de valencia sino también al alto nivel de la teoría requerido para describir estos elementos. El uranio es un átomo complejo que muestra cuatro estados de oxidación (+3, +4, +5, y +6). Sus iones poseen un gran tamaño y forman compuestos complejos con números de coordinación muy altos (Grenthe *et al*., 2006). El número de electrones de valencia en las capas externas que deben ser descritos explícitamente es muy grande y se necesita incluir orbitales de momento angular muy alto (capa 5f). Es muy difícil encontrar o generar buenos pseudopotenciales relativistas necesarios para describir los electrones internos de estos elementos que sean adecuados para llevar a cabo estudios vibracionales de sólidos. En realidad, existen muy pocos trabajos publicados sobre la determinación teórica de espectros vibracionales de sólidos que contienen el átomo de uranio (Yun *et al*., 2012; Wang *et al*., 2013; Yin *et al*., 2013; Mei *et al*., 2013, 2014). Estos estudios se limitan a óxidos y nitruros de uranio, y las únicas características vibracionales consideradas son las frecuencias vibracionales en el punto gamma. Por ejemplo, Yun *et al*., 2012, obtuvieron el espectro de fonones de la uraninita, UO_2, en el punto gamma y compararon las frecuencias resultantes con las experimentales. No obstante, algunos estudios han descrito otras propiedades de estos materiales (Crocombette *et al*., 2001; Petit *et al*., 1998; Freyss *et al*., 2005, 2006; Beridze y Kowalski, 2014; Dudarev *et al*., 1997; Andersson *et al*., 2003; Nerikar *et al*., 2009; Wen *et al*., 2012, 2013; Kotomin *et al*. 2007, 2009; Bocharov *et al*., 2011; Chroneos *et al.*, 2013; Li *et al*., 2013; Greathouse *et al.* 2006, Weck *et al*., 2007, 2012, 2014, 2015, 2016; Ostanin y Zeller, 2007a,b; Shuller *et al*. 2010a, 2010b, 2013, 2014), y de clústeres moleculares en fase gas (Hay *et al*., 1998,

2000; Castro *et al.*, 2010; Shamov *et al*., 2007; Schreckenbach, *et al*., 2010; Odoh *et al*., 2013; Iche-Tarrat *et al.*, 2008; Majumdar *et al*., 2003, 2004; Chaudhuri *et al*., 2004).

Uno de los problemas más relevantes en las ciencias nucleares y energéticas es la protección del medio ambiente. La predicción del comportamiento de los materiales contaminantes bajo condiciones ambientales diversas es extremadamente importante. Los datos termodinámicos fundamentales son la base indispensable para la modelización del comportamiento químico de los componentes contaminantes existentes en los residuos. Estos datos son necesarios para evaluar el origen y la evolución de los yacimientos de uranio, para desarrollar programas para la minería y el control de los depósitos de uranio, en el estudio del combustible nuclear gastado, y también pueden ser de importancia en las reacciones existentes en los reactores nucleares de alimentación rápida (Hemingway *et al*., 1982; Langmuir, 1997; Casas *et al*., 1994; Navrotsky *et al*., 2013). El conocimiento de datos termodinámicos precisos es básico para el desarrollo de modelos geoquímicos y de degradación del combustible usado (Sassani *et al*., 2013).

La enorme importancia de la información termodinámica en la evaluación de la seguridad de los almacenamientos de residuos radioactivos nucleares se refleja en la gran cantidad de trabajos experimentales recientes sobre este tema, que han culminado en largas revisiones y actualizaciones de las propiedades termodinámicas de especies que contienen el átomo de uranio (Wanner y Forest, 1992; Murphy y Pabalan, 1995; Grenthe *et al*., 2004; Shvareva *et al*., 2012) y otros sistemas que contienen elementos relacionados (Guillaumont, 2003). Estudios recientes incluyen, entre otros, las determinaciones experimentales por medio de medidas de solubilidad y calorimetría de las propiedades termodinámicas de diversos minerales como los peróxidos hidratados de uranilo (Kubatko *et al.*, 2003, 2005a; Armstrong *et al*., 2012; Guo *et al.*, 2014a), los carbonatos de uranilo (Kubatko *et al.*, 2005b), los fosfatos y ortofosfatos de uranilo (Gorman-Lewis *et al.*, 2009) y los silicatos de uranilo (Nguyen *et al*., 1992; Gorman-Lewis *et al*., 2007, Shvareva *et al*., 2011; Guo *et al*., 2014b). Aunque la base de datos termodinámica está muy avanzada, existen todavía muchas fases secundarias para las que los datos correspondientes son imprecisos debido a grandes incertidumbres experimentales (Langmuir, 1997). Además, el rango de condiciones experimentales de temperatura y presión para el que se conocen estas propiedades es bastante limitado.

Por otra parte, como fue apreciado por Weck *et al.* (2015), la disponibilidad de una gran cantidad de información sobre la formación, estabilidad termodinámica, y transformaciones de fase de los productos de alteración en la superficie del combustible nuclear gastado, contrasta enormemente con la completa ausencia de datos referentes a la estabilidad y propiedades mecánicas de estas fases. Esto es muy sorprendente debido a la importancia de estas propiedades, que determinan la respuesta de los materiales frente a los diferentes modos de deformación e interacción con el entorno y, en gran medida, la estabilidad termodinámica. En realidad, exceptuando una investigación teórica de los peróxidos de uranilo hidratados, studtita and metastudtita, de Weck *et al*. (2015), no existe ningún otro estudio ni teórico ni experimental que aporte datos mecánicos como compresibilidades, módulos de Young, constantes elásticas, factores de anisotropía, coeficientes de Poisson, índices de ductilidad y dureza, etc. La ausencia de determinaciones experimentales de estas propiedades es debida principalmente a la radiotoxidad de estos materiales, lo que dificulta enormemente su manipulación. Por ello, el uso de métodos teóricos de estado sólido, libres de estas dificultades, puede ser ventajoso para la obtención de las propiedades termodinámicas y mecánicas. Aunque los métodos de estado sólido pueden usarse para obtener estas propiedades, los cálculos requeridos son muy caros y complicados (Beridze y Kowalski, 2014; Crocombette *et al*., 2001). Por esta razón, existen muy pocos estudios y podemos citar los recientes trabajos de Sassani *et al*. (2013), Weck y Kim (2014, 2016), Beridze y Kowalski (2014) y Weck *et al*. (2015).

1.2 Objetivos

Esta Tesis Doctoral ha sido llevada a cabo en el marco de un proyecto de colaboración interdisciplinar "Caracterización experimental y teórica de fases secundarias y óxidos de uranio formados en condiciones de almacenamiento de combustible nuclear" entre el Instituto de Estructura de la Materia (IEM) del Consejo Superior de Investigaciones Científicas (CSIC) y la Unidad de Residuos Radiactivos de Alta Actividad (URRAA) del Centro de Investigaciones Energéticas, Medioambientales y Tecnológicas (CIEMAT).

Los principales objetivos de esta tesis se dirigen hacia la caracterización estructural, identificación y determinación de las propiedades de óxidos de uranio y fases secundarias que surgen de la alteración (oxidación/disolución) del combustible nuclear gastado en condiciones de almacenamiento definitivo, cuando las barreras que protegen los residuos hayan perdido su integridad y entren en contacto con el agua. Como ya se ha explicado en la anterior sección, estos objetivos son muy importantes y nos llevan al estudio teórico de las estructuras cristalinas, observables y los espectros de las especies involucradas, incluyendo la asignación correcta de bandas en los espectros vibracionales.

Específicamente, los objetivos de esta Tesis Doctoral son:

1. Generación de un pseudopotencial relativista conservador de la norma para el átomo de uranio adecuado para la determinación de espectros vibracionales y propiedades usando el programa CASTEP (Clark, 2005; Milman, 2010), un módulo del software Materials Studio (Materials Studio, 2017). Se validará de este pseudopotencial por medio de la computación de las estructuras de una amplia variedad de minerales de uranio como los óxidos de uranio y fases secundarias del SNF.

2. Caracterización estructural de las fases secundarias del SNF por medio de métodos teóricos, incluyendo en este estudio las siguientes fases secundarias: el carbonato de uranilo ruderfordina, el peróxido de uranilo studtita y los silicatos de uranilo soddyita y uranofana-α. Se determinarán sus estructuras cristalinas, propiedades estructurales (longitudes y ángulos de enlace), y patrones de difracción de Rayos X en polvo; y se compararán los patrones de difracción de Rayos X calculados con los experimentales.

3. Determinación del espectro Raman teórico de estos materiales y comparación con los correspondientes espectros experimentales. La espectroscopia Raman es una de las principales técnicas usadas para identificar las fases secundarias del SNF. Como los métodos teóricos generan vistas detalladas a escala microscópica de los movimientos atómicos en los correspondientes modos normales vibracionales; se asignarán e interpretarán las bandas que aparecen en estos espectros. Con este propósito, se deben determinar y visualizar los modos normales activos al Raman.

4. Determinación de las propiedades termodinámicas de estos materiales y análisis de la calidad de las propiedades calculadas. Los datos termodinámicos fundamentales son la base indispensable para la modelización dinámica del comportamiento químico de los residuos contaminantes, y son necesarios para el desarrollo de modelos geoquímicos y modelos de degradación del combustible nuclear usado.

5. Determinación de las propiedades mecánicas y estudio de la estabilidad mecánica de las estructuras de estos materiales. Hasta la fecha no se ha publicado ningún estudio ni experimental ni computacional que determine propiedades tan importantes como las mecánicas; excepto un estudio teórico de los minerales peróxidos de uranilo, studtita y metastudtita. El uso de los métodos teóricos puede ser ventajoso para la determinación de estas propiedades, ya que están libres de las dificultades asociadas a su radiotoxicidad.

1.3 Metodología

Los métodos utilizados en este trabajo son técnicas computacionales basadas en la Teoría del Funcional de la Densidad (DFT; Hohenberg y Kohn, 1964; Kohn y Sham, 1965; Parr y Yang, 1989) aplicadas a sólidos periódicos mediante el empleo de bases de ondas planas y pseudopotenciales (Payne *et al*., 1992) implementadas en el código CASTEP (Clark *et al*., 2005; Milman *et al.*, 2010), incluido en el paquete de software Materials Studio (Materials Studio, 2017).

Para la generación del pseudopotencial relativista conservador de la norma específico del átomo de uranio se emplearon los paquetes de software: OPIUM (Opium, 2004) y fhi98PP (Fuchs *et al*., 1999). La versión final del pseudopotencial (Bonales *et al.*, 2016) fue obtenida con el segundo programa en formato cpi y entonces se transformó al formato recpot utilizado por CASTEP usando la herramienta cpi2recpot (Haynes and Refson, 2007). El pseudopotencial es conservador de la norma (Troullier and Martins, 1991), siendo esta característica necesaria para la determinación de los espectros vibracionales en el software CASTEP.

Los espectros de difracción de Rayos X fueron obtenidos, a partir de las coordenadas atómicas computadas, usando el software REFLEX también incluido en el paquete Materials Studio (Materials Studio, 2017), y los programas XtalDraw (Downs, 2003) y ENDEAVOUR (Brandenburg y Putz, 2003). Asimismo, la comparación con los espectros experimentales fue realizada usando el programa XPowder (Martin, 2012) y la base de datos PDF-2 (ICDD, 2003). Los espectros ausentes de esta base de datos fueron determinados experimentalmente o tomados de la literatura.

Los espectros vibracionales (Infrarrojo y Raman) fueron determinados usando la Teoría de Perturbaciones del Funcional de la Densidad (Density Functional Perturbation Theory, DFPT) (Baroni *et al*., 1987, 2001; Gonze *et al*., 1992, 1997) implementada en el software CASTEP.

Los espectros de fonones en diferentes puntos de la zona de Brillouin, necesarios para la computación de las propiedades termodinámicas, fueron también obtenidos mediante DFPT, como derivadas de segundo-orden de la energía total (Baroni *et al.*, 2001). El conocimiento de los espectros de fonones permite la obtención de las curvas de dispersión y la densidad de estados vibracional y, a partir de ellos, la evaluación de las propiedades termodinámicas en la aproximación cuasi-harmónica, como las energías libres, entalpias, entropías, calores específicos y temperaturas de Debye (Baroni *et al.*, 2001; Lee and Gonze, 1995).

A partir de las estructuras optimizadas, las constantes elásticas fueron obtenidas a T=0 K usando relaciones de tensión-deformación. Con este propósito, se utilizó la técnica de deformaciones finitas, implementada en CASTEP. En esta técnica se usan deformaciones finitas adaptadas a la simetría (Nye, 1985) para extraer las constantes elásticas individuales a partir del tensor elástico obtenido como respuesta a las deformaciones aplicadas. Para el cálculo del tensor elástico este método parece ser más eficiente que los basados en energías y el uso de DFPT (Yu *et al.*, 2010).

Las ecuaciones de estado presentadas en este trabajo fueron obtenidas optimizando las diferentes estructuras sometidas a un conjunto de valores de la presión. Los correspondientes volúmenes de la celda unidad y las presiones aplicadas fueron entonces ajustadas a una ecuación de estado de tipo Birch−Murnaghan de cuarto orden (Birch, 1947), usando el código EOSFIT 5.2 (Angel, 2000).

Para la realización de los trabajos computacionales, se han empleado una gran variedad de recursos computacionales. En particular, se debe mencionar el tiempo empleado en los supercomputadores CETA-CIEMAT (Centro Extremeño de Tecnologías Avanzadas), CESGA (Centro de Supercomputación de Galicia), y TRUENO (Clúster de Calculo Científico del CSIC, Madrid).

Los análisis por difracción por rayos X fueron realizados en los laboratorios de la Unidad de Residuos Radiactivos de Alta Actividad (URRAA) del CIEMAT. Como se ha mencionado, se ha establecido un convenio de colaboración CSIC-CIEMAT para el estudio combinado teórico y

experimental de los óxidos de uranio y fases secundarias resultantes de la alteración del combustible nuclear gastado en las condiciones finales de un almacenamiento de residuos radiactivos definitivo. CIEMAT tiene una dilatada experiencia en la manipulación y caracterización de estos materiales mediante técnicas de caracterización superficial incluyendo Diffraccion de Rayos X (XRD), Espectroscopia Raman (RS), Microscopía Electrónica de Barrido (SEM) y Análisis Termo-Gravimétrico (TGA).

1.4 Estructura de esta Tesis

En el Capítulo 2 (*Nuclear Fuel Cycle and Secondary Phases*), se revisan los temas principales necesarios para entender el ciclo del combustible nuclear y la aparición de fases secundarias en la superficie del SNF. En la primera sección de este capítulo (*Nuclear Energy and Nuclear materials)*, se describen los conceptos principales relacionados con la energía nuclear y los materiales usados para su producción. En la segunda parte (*Nuclear Fuel Cycle and Radioactive Waste Management*), se describen el ciclo del combustible nuclear y la gestión de los residuos nucleares radioactivos. Finalmente, en la última parte (*Spent Nuclear Fuel and Secondary Phases*), se estudian las características físico-químicas y la estabilidad del combustible nuclear gastado y sus fases secundarias. Las dos primeras partes son necesarias para conocer la composición de los residuos generados por el uso de la energía nuclear. Dependiendo de la clase de reactores de fisión y los combustibles usados, así como de la opción elegida para el ciclo de combustible nuclear, la composición de los residuos generados que deben ser confinados en un almacenamiento geológico profundo son diferentes. A su vez, la composición de los residuos finales determina las fases secundarias que aparecerán como productos de alteración del SNF y la clase de estudios que deben hacerse para optimizar el almacenamiento de estos residuos. Por ejemplo, si se adopta un Ciclo del Combustible Nuclear Cerrado Avanzado (Merino Rodríguez, 2014) el problema de contaminación es el que proviene principalmente de los productos de fisión, como el estroncio y el cesio, y no el proveniente de la liberación de elementos transuránicos que son principal problema en el caso del Ciclo del Combustible Nuclear Abierto (opción elegida actualmente en España).

En el Capítulo 3 (*Materials and methods*) se describen los materiales y métodos, experimentales y teóricos, usados en este trabajo. Las técnicas experimentales empleadas para caracterizar las fases secundarias del SNF se presentan en el primer lugar (*Experimental Methods and Materials*). A continuación, se describen los materiales nucleares usados en este estudio (se usaron muestras naturales y sintéticas) y su preparación. Ya que el principal propósito de esta Tesis es mostrar que el uso de la metodología teórica es una herramienta extremadamente potente para el estudio de las fases secundarias del SNF, la parte teórica de este capítulo (*Theoretical and Computational Methods*) es bastante detallada y proporciona la base necesaria para entender los procedimientos computacionales utilizados y los resultados que se darán en los restantes capítulos.

En los Capítulos del 4 al 9 (*Results and Discusion*) se describen y se discuten los resultados principales de esta Tesis. Ya que se ha publicado la mayor parte del contenido de esta Tesis, se hará un resumen de los resultados y conclusiones de cada artículo en capítulos separados. El Capítulo 4 (*Rutherfordine: Structure and Raman Spectroscopy,* Bonales *et al*., 2016a) contiene un estudio estructural y espectroscópico Raman de la ruderfordina, un mineral carbonato de uranilo que es una importante fase secundaria del SNF. También presenta la generación y validación de un pseudopotencial relativista conservador de la norma, que será utilizado extensivamente para estudiar todas las demás fases secundarias del SNF en capítulos posteriores. El espectro Raman calculado que se da en este Capítulo fue muy importante porque fue el primer espectro Raman teórico completo (incluyendo los números de onda e intensidades) publicado de un material cristalino que contiene el ion uranilo.

El Capítulo 5 (*Rutherfordine: Thermodynamic and Mechanical Properties,* Colmenero *et al.*, 2017a) incluye la determinación de las propiedades termodinámicas y mecánicas del mismo mineral que en el capítulo anterior. En este trabajo se describen funciones termodinámicas muy

precisas de la ruderfordina, extendiéndose el rango de temperaturas en el que se conocen estas propiedades a 0-700 K. Además, se calcularon las propiedades mecánicas de este mineral y se estudió la estabilidad mecánica de su estructura. Ya que no existían medidas experimentales de las propiedades mecánicas, los cálculos teóricos nos permitieron predecir sus valores.

En el Capítulo 6 (*Soddyite: Structure, Mechanical Properties, Equation of State, and Raman Spectroscopy,* Colmenero *et al.*, 2017c) se presenta un estudio de las propiedades estructurales, mecánicas y espectroscópicas Raman de la soddyita, un importante mineral silicato de uranilo. Este estudio representa el primer estudio teórico de este mineral y confirma la estructura obtenida por medio de técnicas de difracción de Rayos X. Se calcularon y asignaron las bandas del espectro Raman de la soddyita y se predijeron las propiedades mecánicas de este mineral.

En el Capítulo 7 (*Studtite: Structure, Raman Spectroscopy and Thermal Stability,* Colmenero *et al.*, 2017b) se determinan las propiedades estructurales y espectroscópicas Raman del mineral peróxido de uranilo studtita. La asignación de la banda correspondiente al estrechamiento simétrico del enlace UO y el análisis experimental de su desplazamiento con la temperatura permitieron el estudio de la estabilidad térmica de la studtita en presencia y ausencia de agua.

El Capítulo 8 (*Structural, Mechanical and Raman Spectroscopic Characterization of Layered Uranyl Silicate Mineral Uranophane-α by DFT Methods*; Colmenero *et al.*, 2017e) es análogo al estudio del mineral soddyita (Capítulo 6) pero para la uranofana-α, el mineral uranílico más frecuente en la naturaleza después de la uraninita. Sin embargo, la estructura de la uranofana es completamente diferente a la de la soddyita ya que es un mineral silicato de uranilo hidratado con una estructura laminar similar a la de las arcillas, mientras que la estructura de la soddyita es tridimensional. Además, este estudio incluye una aplicación adicional de los métodos computacionales para estudiar la posible incorporación de estroncio, uno de los más importantes productos de fisión, en la estructura cristalina de la uranofana-α. Como se explicó en el primer párrafo de esta sección, los productos de fisión constituyen el principal riesgo de los residuos nucleares radioactivos si se adopta el Ciclo del Combustible Nuclear Avanzado. Este estudio demuestra que este mineral puede actuar como una barrera adicional en la liberación de los productos de fisión hacia la biosfera.

El Capítulo 9 (*Uranium-Oxygen Bond-Length to Uranyl Symmetric Stretching Raman Shift relationship*; Colmenero *et al.*, 2017f) contiene una compilación de las estructuras y espectros Raman teóricos para diferentes materiales que contienen el ion uranilo. Usando estas estructuras y espectros, se obtuvo una relación entre la longitud de enlace UO y el desplazamiento Raman asociado a la vibración de estrechamiento simétrico mediante un ajuste numérico de los datos calculados. La relación fue derivada a partir de los resultados de cálculos de primeros principios (cálculos *ab initio*), es decir sin usar ninguna información experimental. Los parámetros resultantes dieron una expresión con esencialmente la misma precisión que la obtenida por Bartlett y Cooney (1989), quienes emplearon un gran conjunto de datos experimentales.

Finalmente, en el Capítulo 10 (*Conclusions)*, se presentan las conclusiones de esta Tesis Doctoral. Las conclusiones específicas de cada uno de los artículos presentados en los Capítulos 4-9, se detallan separadamente y, a continuación, se exponen las conclusiones finales y las perspectivas de este trabajo.

Chapter 2. Nuclear Fuel Cycle and Secondary Phases

2.1 Nuclear Energy and Nuclear Materials

2.1.1 Radioactivity

Radioactivity is defined as the spontaneous disintegration or decay of the nucleus of an atom by emission of particles, usually accompanied by electromagnetic radiation (L'Annunziata, 2007). The energy produced by radioactivity has important energetic, industrial and military applications. However, the rays emitted by radioactive substances can cause radiation sickness and, therefore, such substances must be handled with extreme care.

Natural radioactivity is exhibited by several elements, including radium, uranium, and other members of the actinide series and by some isotopes of lighter elements, such as carbon-14, used in radioactive dating. Radioactivity may also be induced, or created artificially, by bombarding the nuclei of normally stable elements in a particle accelerator.

The radiation produced during radioactivity is predominantly of three types, designated as alpha, beta, and gamma rays. These types differ in velocity, in the way in which they are affected by a magnetic field, and in their ability to penetrate or pass through matter. Alpha rays have the least penetrating power, move at a slower velocity than the other types, and are deflected slightly by a magnetic field in a direction that indicates a positive charge. Alpha rays are nuclei of ordinary helium atom. Beta rays are more penetrating than alpha rays, move at a very high speed, and are deflected considerably by a magnetic field in a direction that indicates a negative charge; analysis shows that beta rays are high-speed electrons. Finally, gamma rays have very great penetrating power and are not affected at all by a magnetic field. They move at the speed of light and have a very short wavelength (or high frequency); thus, they are a type of electromagnetic radiation.

Natural radioactivity was first observed in 1896 by A. H. Becquerel (Becquerel, 1986, 1903), who discovered that when salts of uranium are brought into the vicinity of an unexposed photographic plate carefully protected from light, the plate becomes exposed. The radiation from uranium salts also causes a charged electroscope to discharge. In addition, the salts exhibit phosphorescence and are able to produce fluorescence. Since these effects are produced both by salts and by pure uranium, radioactivity must be a property of the element and not of the salt. This discovery marked the birth of nuclear physics. In 1899 E. Rutherford (Rutherford, 1899, 1908; Rutherford and Soddy, 1903) discovered and named alpha and beta radiation, and in 1900 P. Villard (1900a, 1900b) identified gamma radiation. Marie and Pierre Curie (P. Curie and M. Curie, 1898a, 1898b; P. Curie, 1905) extended the work on radioactivity, demonstrating the radioactive properties of thorium and discovering the highly radioactive element radium in 1898. Frédéric and Irène Joliot-Curie (F. Joliot and I. Joliot-Curie, 1935; Von Halban *et al*., 1939) discovered in 1934 the first example of artificial radioactivity by bombarding non-radioactive elements with alpha particles.

The nuclei of elements exhibiting radioactivity are unstable and are found to be undergoing continuous disintegration (i.e., gradual breakdown). The disintegration proceeds at a definite rate characteristic of the particular nucleus; that is, each radioactive isotope or radioisotope has a definite lifetime.

The product of a radioactive decay may itself be unstable and undergo further decays, by either alpha or beta emission. Thus, a succession of unstable elements may be produced, the series continuing until a nucleus is produced that is stable. Such a series is known as a radioactive disintegration, or decay, series. The original nucleus in a decay series is called the parent nucleus, and the nuclei resulting from successive disintegrations are known as daughter nuclei.

There are four known radioactive decay series, the members of a given series having mass numbers that differ by jumps of 4. The mass number of every isotope in these chains can be represented as A = 4*n*, A = 4*n* + 2, and A = 4*n* + 3, and A = 4*n* + 1, respectively. The long-lived starting isotopes of the three first series are, respectively, ^{232}Th, ^{238}U and ^{235}U, and have existed since the formation of the earth. The series beginning with ^{238}U and ending with ^{206}Pb is known as the 4*n*+2 series because all the mass numbers in the series are 2 greater than an integral multiple of 4 (e.g., 238=4×59+2, 206=4×51+2). The 4*n*+1 series, which begins with ^{237}Np, is not found in nature because the half-life of the parent nucleus (about 2 million years) is many times less than the age of the earth, and all naturally occurring samples have already disintegrated. The 4*n*+1 series is produced artificially in nuclear reactors.

Because the rates of disintegration of the members of a radioactive decay series are constant, the age of rocks and other materials can be determined by measuring the relative abundances of the different members of the series. All the decay series end in a stable isotope of lead, so that a rock containing mostly lead as compared to heavier elements would be very old.

The human being live together with natural radioactivity, coming from radioactive isotopes present in the earth's crust and from the nuclear processes occurring in exterior space. The human organism itself contains radioactive isotopes as carbon and potassium. To this kind of radioactivity, we must add the radiation produced by the radon we inhale during respiration coming from disintegration of radium and thorium.

The use of radioactivity has increased extraordinarily from its discovery and it has a wide spectrum of applications ranging from its use in the production of electric energy (for example, in 2004, the nuclear power provided approximately 15.7% of the world's electricity) to its utilization in medicine (as a diagnostic and therapeutic tool), food applications (treatment and processing), agriculture (improvement of the efficiency of cultivations), industry (for example in measuring and imaging technologies) and research. In any case, the use of radioactivity generates waste that must be handled with extreme care.

2.1.2. Nuclear power

2.1.2.1 Fission

In nuclear physics and nuclear chemistry, nuclear fission is either a nuclear reaction or a radioactive decay process in which the nucleus of an atom splits into smaller parts (lighter nuclei). The fission process often produces free neutrons and gamma photons, and releases a very large amount of energy even by the energetic standards of radioactive decay (DOE, 1993a, 1993b).

In 1932, the physicist Ernest Rutherford (Oliphant *et al*., 1933) discovered that when lithium atoms were "split" by protons from a proton accelerator, immense amounts of energy were released in accordance with the principle of mass-energy equivalence. The same year, his doctoral student James Chadwick (Chadwick, 1932) discovered the neutron, which was immediately recognized as a potential tool for nuclear experimentation because of its lack of an electric charge. Experimentation with bombardment of materials with neutrons led Frédéric and Irène Joliot-Curie to discover induced radioactivity in 1934 (F. Joliot and I. Joliot-Curie, 1935), which allowed the creation of radium-like elements at much less the price of natural radium. Further work by Enrico Fermi in the 1930s (Fermi *et al*., 1934a, 1934b) focused on using slow neutrons to increase the effectiveness of induced radioactivity. Fermi concluded that his experiments had created new elements with 93 and 94 protons, which the group named ausonium and hesperium.

Nuclear fission of heavy elements was discovered on December 17, 1938 by German Otto Hahn and his assistant Fritz Strassmann (Hann and Strassmann, 1939; Hann, 1946), and explained theoretically in January 1939 by Lise Meitner and her nephew Otto Robert Frisch (Meitner and Frisch, 1939; Frisch, 1939). These authors conducted experiments with the products of neutron-

bombarded uranium, as a means of further investigating Fermi's claims. They determined that the relatively tiny neutron split the nucleus of the massive uranium atoms into two roughly equal pieces, contradicting Fermi. This was an extremely surprising result: all other forms of nuclear decay involved only small changes to the mass of the nucleus, whereas this process involved a complete rupture of the nucleus. Frisch (Meitner and Frisch, 1939; Frisch, 1939) named the process by analogy with biological fission of living cells. It is an exothermic reaction which can release large amounts of energy both as electromagnetic radiation and as kinetic energy of the fragments (heating the bulk material where fission takes place). In order for fission to produce energy, the total binding energy of the resulting elements must be less negative (higher energy) than that of the starting element.

Apart from fission induced by a neutron, a natural form of spontaneous radioactive decay (not requiring a neutron) is also referred to as fission, and occurs especially in very high mass number isotopes. That is, nuclear fission can occur without neutron bombardment. Spontaneous fission was discovered in 1940 by Flyorov, Petrzhak and Kurchatov in Moscow (Flerov and Petrzhak, 1940), when they decided to confirm that, without bombardment by neutrons, the fission rate of uranium was indeed negligible. As predicted by Niels Bohr; it wasn't.

Numerous scientists, including Leo Szilárd, who was one of the first, recognized that if fission reactions released additional neutrons, a self-sustaining nuclear chain reaction could result (Szilard, 1934). Once this was experimentally confirmed and reported in the journal *Nature* by Frédéric Joliot-Curie and co-workers in 1939 (Von Halban *et al*., 1939), scientists in many countries (including the United States, the United Kingdom, France, Germany, and the Soviet Union) petitioned their governments for support of nuclear fission research for the development of a nuclear weapon. On 25 January 1939, a Columbia University team conducted the first nuclear fission experiment in the United States. The members of the team were Herbert L. Anderson, Eugene T. Booth, John R. Dunning, Enrico Fermi, G. Norris Glasoe, and Francis G. Slack (Anderson *et al*., 1939). Fermi and Szilárd, both emigrated to the United States, created the first man-made reactor, known as Chicago Pile-1, which achieved criticality on December 2, 1942 (Fermi and Szilard, 1955). This work became part of the Manhattan Project, which made enriched uranium and built large reactors to breed plutonium for its use in the first nuclear weapons, which were used on the cities of Hiroshima and Nagasaki in 1945 (Rhodes, 1986).

The United Kingdom, Canada, and the USSR proceeded over the course of the late 1940s and early 1950s. Electricity was generated for the first time in US by a nuclear reactor on December 20, 1951, at the EBR-I experimental station near Arco, Idaho, which initially produced about 100 kW (Michal, 2001). In 1953, US President Dwight Eisenhower gave his "Atoms for Peace" speech at the United Nations (Eisenhower, 1953), emphasizing the need to develop "peaceful" uses of nuclear power quickly. This was followed by the 1954 Amendments to the Atomic Energy Act which allowed rapid declassification of US reactor technology and encouraged development by the private sector.

Installed nuclear capacity initially rose relatively quickly, rising from less than 1 gigawatt (GW) in 1960 to 100 GW in the late 1970s, and 300 GW in the late 1980s. Since the late 1980s worldwide capacity has risen much more slowly, reaching 366 GW in 2005. Between around 1970 and 1990, more than 50 GW of capacity was under construction (peaking at over 150 GW in the late 1970s and early 1980s). More than two-thirds of all nuclear plants ordered after January 1970 were eventually cancelled. A total of 63 nuclear units were cancelled in the USA between 1975 and 1980. During the 1970s and 1980s rising economic costs (related to extended construction times largely due to regulatory changes and pressure-group litigation) and falling fossil fuel prices made nuclear power plants then under construction less attractive. In the 1980s (U.S.) and 1990s (Europe) electricity liberalization also made the addition of large new baseload capacity unattractive. In the 1970s there were large protests against nuclear power in Germany, France and North America.

Far-reaching fission power reactor accidents, or accidents that resulted in medium to long-lived fission product contamination of inhabited areas, have occurred in Generation I and II reactor designs, blueprinted between 1950 and 1980. These include the Chernobyl disaster which occurred in 1986 (Yablokov *et al*., 2009), the Fukushima Daiichi nuclear disaster (Lipscy *et al*., 2011), and the more contained Three Mile Island accident in 1979 (Samuel, 2004). There have also been some nuclear submarine accidents. In terms of lives lost per unit of energy generated, analysis has determined that fission-electric reactors have caused fewer fatalities per unit of energy generated than the other major sources of energy generation. Energy production from coal, petroleum, natural gas and hydroelectricity has caused a greater number of fatalities per unit of energy generated due to air pollution and energy accident effects. Four years after the Fukushima-Daiichi accident, there have been no fatalities due to exposure to radiation, and no discernible increased incidence of radiation-related health effects are expected among exposed members of the public and their descendants. The Japan Times estimated that 1.600 deaths were the result of evacuation, due to physical and mental stress stemming from long stays at shelters, a lack of initial care as a result of hospitals being disabled by the tsunami, and suicides.

Since about 2001 the term *nuclear renaissance* (IEA, 2009) has been used to refer to a possible nuclear power industry revival, driven by rising fossil fuel prices and new concerns about meeting greenhouse gas emission limits. In 2012, the World Nuclear Association reported that nuclear electricity generation was at its lowest level since 1999. As of January 2016, however, 65 new nuclear power reactors were under construction. Over 150 were planned, equivalent to nearly half of capacity at that time. In 2015, ten new reactors were connected to the grid, seven reactors were permanently shut down, 441 reactors had a worldwide net capacity of 382 GW of electricity and 67 new nuclear reactors were under construction. Most of the new activity is in China, where there is an urgent need to control pollution from coal plants.

2.1.2.1.1 Chain Reaction

In engineered nuclear devices, essentially all nuclear fission occurs as a "nuclear reaction", a bombardment driven process that results from the collision of two subatomic particles. In nuclear reactions, a subatomic particle collides with an atomic nucleus and causes changes to it. Nuclear reactions are thus driven by the mechanics of bombardment, not by the relatively constant exponential decay and half-life characteristic of spontaneous radioactive processes. Nuclear fission differs importantly from other types of nuclear reactions, in that it can be amplified and sometimes controlled via a nuclear chain reaction. In such a reaction, free neutrons released by each fission event can trigger yet more events, which in turn release more neutrons and cause more fissions (see Figure 2-1).

The chemical element isotopes that can sustain a fission chain reaction are called nuclear fuels, and are said to be fissile. The most common nuclear fuels are ^{235}U (the isotope of uranium with an atomic mass of 235) and ^{239}Pu (the isotope of plutonium with an atomic mass of 239). These fuels break apart into a bimodal range of chemical elements with atomic masses centering near 95 and 135 (fission products). Most nuclear fuels undergo spontaneous fission only very slowly, decaying instead mainly via an alpha-beta decay chain over periods of millennia to eons. In a nuclear reactor or nuclear weapon, the overwhelming majority of fission events are induced by bombardment with another particle, a neutron, which is itself produced by prior fission events.

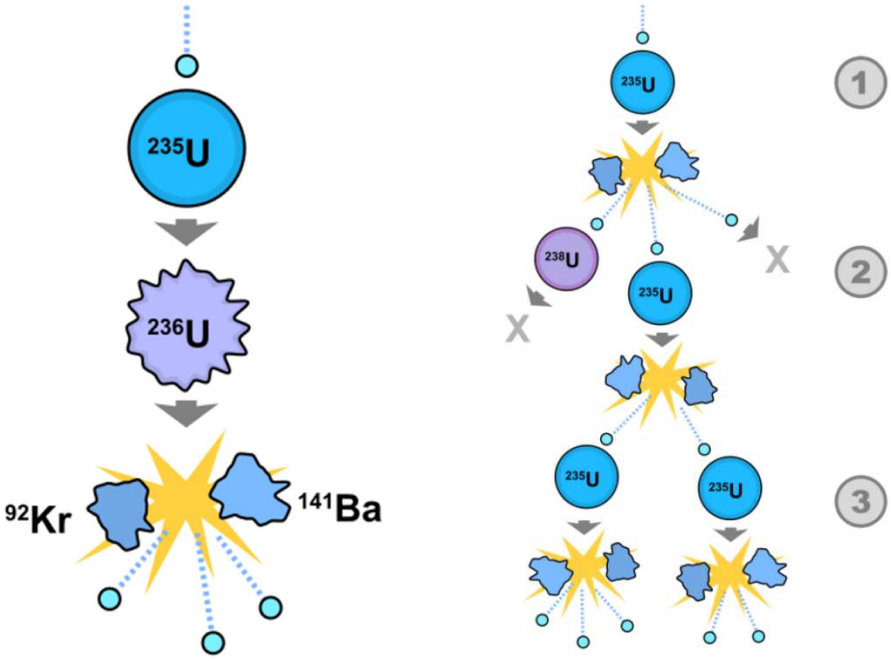

Figure 2-1. Left: An induced fission reaction. A neutron is absorbed by a ^{235}U nucleus, turning it briefly into an excited ^{236}U nucleus, with the excitation energy provided by the kinetic energy of the neutron plus the forces that bind the neutron. The ^{236}U, in turn, splits into fast moving lighter elements (fission products) and releases three free neutrons. At the same time, one or more "prompt gamma rays" (not shown) are produced, as well. Right: A schematic nuclear fission chain reaction. (1) A ^{235}U atom absorbs a neutron and fissions into two new atoms (fission fragments), releasing three new neutrons and some binding energy. (2) One of those neutrons is absorbed by an atom of ^{238}U and does not continue the reaction. Another neutron is simply lost and does not collide with anything, also not continuing the reaction. However, one neutron collides with an atom of ^{235}U, which then fissions and releases two neutrons and some binding energy. (3) Both of those neutrons collide with ^{235}U atoms, each of which fissions and releases between one and three neutrons, which can then continue the reaction.

Nuclear fissions in fissile fuels are the result of the nuclear excitation energy produced when a fissile nucleus captures a neutron. This energy, resulting from the neutron capture, is a result of the attractive nuclear force acting between the neutron and nucleus. It is enough to deform the nucleus into a double lobed "drop," to the point that nuclear fragments exceed the distances at which the nuclear force can hold two groups of charged nucleons together and, when this happens, the two fragments complete their separation and then are driven further apart by their mutually repulsive charges, in a process which becomes irreversible with greater and greater distance.

This process can also occur in other fissionable (non-fissile) isotopes (such as ^{238}U, the most abundant form of uranium), but in order to fission, these isotopes require additional energy provided by fast neutrons (such as those produced by nuclear fusion in thermonuclear weapons). ^{238}U has a near zero fission cross section for neutrons of less than one MeV energy. If no additional energy is supplied by any other mechanism, the nucleus will not fission, but will merely absorb the neutron, as it happens when ^{238}U absorbs slow and even some fraction of fast neutrons, to become ^{239}U. These nuclei decay by beta emission to ^{239}Np which then decays again by the same process to ^{239}Pu (this process is used to manufacture ^{239}Pu in breeder reactors). In-situ plutonium production also contributes to the neutron chain reaction in other types of reactors after sufficient ^{239}Pu has been produced, since ^{239}Pu is also a fissile element which serves as fuel. It is estimated that up to half of the power produced by a standard "non-breeder" reactor is produced by the fission of ^{239}Pu produced in place, over the total lifecycle of a fuel load. Thus, fissionable nonfissile isotopes can be used as fission energy source even without a chain reaction.

The remaining energy to initiate fission in fissionable (non-fissile) isotopes can be supplied by other mechanisms as the increase of the kinetic energy of the incoming neutron, which become increasingly able to fission a fissionable heavy nucleus as it exceeds a kinetic energy of one MeV or more (so called fast neutrons). Such high-energy neutrons are able to fission ^{238}U directly (in thermonuclear weapons for example). However, this happens only to a small extent in a nuclear reactor, as only a fraction of fission neutrons will have enough energy to efficiently fission ^{238}U (fission neutrons have a medium mode energy of 0.75 Mev). Therefore, fissionable, non-fissile isotopes can be used as fission energy source even without a chain reaction as long as the external neutron source is present. Some small part of the ^{238}U is "burned up" in all nuclear fuels, especially in fast breeder reactors that operate with higher energy neutrons. That same fast fission effect is used to increase the energy released by modern thermonuclear weapons. The explosive effects of nuclear fission chain reactions can be reduced by using substances like moderators which slow down the speed of secondary neutrons.

The free neutrons produced by the fission in fissionable and fissile isotope, may escape rapidly from the fuel and become a free neutron, with a mean lifetime of about 15 minutes before decaying to protons and beta particles. However, neutrons almost invariably impact and are absorbed by other nuclei in the vicinity long before this happens. Newly created fission neutrons move at about 7% of the speed of light, and even moderated neutrons move at about 8 times the speed of sound. Some neutrons will impact fuel nuclei and induce further fissions, releasing yet more neutrons. If enough nuclear fuel is assembled in one place, or if the escaping neutrons are sufficiently contained, then these freshly emitted neutrons outnumber the neutrons that escape from the assembly, and a *sustained nuclear chain reaction* will take place.

An assembly that supports a sustained nuclear chain reaction is called a *critical assembly* or, if the assembly is almost entirely made of a nuclear fuel, a *critical mass*. The word "critical" refers to a cusp in the behaviour of the differential equation that governs the number of free neutrons present in the fuel: if less than a critical mass is present, then the number of neutrons is determined by radioactive decay, but if a critical mass or more is present, then the number of neutrons is controlled instead by the physics of the chain reaction. The average number of neutrons released per nucleus that go on to fission another nucleus is referred to as k. Values of k larger than 1 mean that the fission reaction is releasing more neutrons than it absorbs. The actual mass of a critical mass of nuclear fuel depends strongly on the geometry and surrounding materials.

Summarizing, nuclear fission produces energy for nuclear power and drives the explosion of nuclear weapons. Both uses are possible because certain substances called nuclear fuels undergo fission when struck by fission neutrons, and in turn emit neutrons when they break apart. This makes possible a self-sustaining nuclear chain reaction that releases energy at a controlled rate in a nuclear reactor or at a very rapid uncontrolled rate in a nuclear weapon.

The amount of free energy contained in nuclear fuel is millions of times the amount of free energy contained in a similar mass of chemical fuel such as gasoline, making nuclear fission a very dense source of energy. The products of nuclear fission, however, are on average far more radioactive than the heavy elements which are normally fissioned as fuel, and remain so for significant amounts of time, giving rise to a *nuclear waste problem*. Concerns over nuclear waste accumulation and over the destructive potential of nuclear weapons are a counterbalance to the peaceful desire to use fission as an energy source, and give rise to ongoing political debate over nuclear power.

2.1.2.2. Fission Reactors

Just as many conventional thermal power stations generate electricity by harnessing the thermal energy released from burning fossil fuels, nuclear power plants convert the energy released from the nuclei of the atoms via continuous nuclear fission that takes place in a nuclear reactor (DOE, 1993a, 1993b). The heat produced is removed from the reactor core by a cooling system that uses the heat to generate steam, which drives a steam turbine connected to a generator producing electricity.

Fission-electric power stations are one of the leading low carbon power generation methods of producing electricity, and in terms of total life-cycle greenhouse gas emissions per unit of energy generated, has emission values lower than "renewable energy" when the latter is taken as a single energy source (IEA, 2009). Since all electricity supplying technologies use cement, etc., during construction, emissions are yet to be brought to zero. A 2014 analysis of the carbon footprint literature by the Intergovernmental Panel on Climate Change (IPCC, 2014) reported that the embodied total life-cycle emission intensity of fission electricity has a median value of 12 g CO_2 eq/kWh, which is the lowest out of all commercial baseload energy sources, and second lowest out of all commercial electricity technologies known, after wind power, which is an intermittent energy source with embodied greenhouse gas emissions, per unit of energy generated of 11 g CO_2 eq/kWh. Each result is contrasted with coal and fossil gas at 820 and 490 g CO_2 eq/kWh. With this translating into, from the beginning of fission-electric power station commercialization in the 1970s, having prevented the emission of about 64 billion tonnes of carbon dioxide equivalent, greenhouse gases that would have otherwise resulted from the burning of fossil fuels in thermal power stations.

Critical fission reactors are the most common type of nuclear reactor. In a critical fission reactor, neutrons produced by fission of fuel atoms are used to induce yet more fissions, to sustain a controllable amount of energy release. Devices that produce engineered but non-self-sustaining fission reactions are *Subcritical fission reactors*. Such devices use radioactive decay or particle accelerators to trigger fissions.

Critical fission reactors are built for three primary purposes, which typically involve different engineering trade-offs to take advantage of either the heat or the neutrons produced by the fission chain reaction. *Power reactors* are intended to produce heat for nuclear power, either as part of a generating station or a local power system such as a nuclear submarine. *Research reactors* are intended to produce neutrons and/or activate radioactive sources for scientific, medical, engineering, or other research purposes. *Breeder reactors* are intended to produce nuclear fuels in bulk from more abundant isotopes. The better known fast breeder reactor makes ^{239}Pu (a nuclear fuel) from the naturally very abundant ^{238}U (not a nuclear fuel). Thermal breeder reactors previously tested using ^{232}Th to breed the fissile isotope ^{233}U (thorium fuel cycle) continue to be studied and developed.

Criticality in nature is uncommon. At three ore deposits at Oklo in Gabon, sixteen sites (the so called *Oklo Fossil Reactors*) have been discovered at which self-sustaining nuclear fission took place approximately 2 billion years ago. Unknown until 1972, but postulated by Paul Kuroda in 1956 (Kuroda, 1956), when French physicist Francis Perrin (Cowan, 1976) discovered the Oklo Fossil Reactors, it was realized that nature had beaten humans to the punch. Large scale natural uranium fission chain reactions, moderated by normal water, had occurred far in the past and would not be possible now. This ancient process was able to use normal water as a moderator only because 2 billion years before the present, natural uranium was richer in the shorter lived fissile isotope ^{235}U (about 3%), than natural uranium available today (which is only 0.7%, and must be enriched to 3% to be usable in light water reactors).

2.1.2.2.1 Fission Reactor Designs and Generations

Nowadays, reactors derived from designs originally developed for propelling submarines and large naval ships generate about 85% of the world's nuclear electricity. The main design is the pressurised water reactor (PWR) which has water at over 300°C under pressure in its primary cooling/heat transfer circuit, and generates steam in a secondary circuit. All Nuclear Power plants active in Spain have this design. The less numerous boiling water reactor (BWR) makes steam in the primary circuit above the reactor core, at similar temperatures and pressure. Both types use water as both coolant and moderator, to slow neutrons. Since water normally boils at 100°C, they have robust steel pressure vessels or tubes to enable the higher operating temperature. Pressurized heavy water reactors (PHWR) generally use natural uranium (0.7% ^{235}U) oxide as fuel and hence need an efficient moderator as heavy water (D_2O). Hence the term 'light water' is used to differentiate the first two ones from the latter (LWR, light water reactor).

There are several components common to most types of reactors:

Fuel. Uranium is the basic fuel. Usually pellets of uranium dioxide (UO_2) are arranged in tubes to form fuel rods. The rods are arranged into fuel assemblies in the reactor core. In a 1000 MWe class PWR reactors there might be 51.000 fuel rods with over 18 million pellets. In a new reactor with new fuel a neutron source is needed to get the reaction going. Usually, this is beryllium mixed with polonium, radium or another alpha-emitter. Alpha particles from the decay cause a release of neutrons from the beryllium as it turns to carbon-12. Restarting a reactor with some used fuel may not require this, as there may be enough neutrons to achieve criticality when control rods are removed.

Moderator. Material in the core which slows down the neutrons released from fission so that they cause more fission. It is usually water, but may be heavy water or graphite.

Control rods. These are made with neutron-absorbing material such as cadmium, hafnium or boron, and are inserted or withdrawn from the core to control the rate of reaction, or to halt it. In fission, most of the neutrons are released promptly, but some are delayed. These are crucial in enabling a chain-reacting system to be controllable and to be able to be held precisely critical. In some PWR reactors, special control rods are used to enable the core to sustain a low level of power efficiently. Secondary control systems involve other neutron absorbers, usually boron in the coolant – its concentration can be adjusted over time as the fuel burns up.

Coolant. A fluid circulating through the core to transfer the heat from it. In light water reactors, the water moderator functions also as primary coolant. Except in BWRs, there is secondary coolant circuit where the water becomes steam.

Pressure vessel or pressure tubes. Usually a robust steel vessel containing the reactor core and moderator/coolant, but it may be a series of tubes holding the fuel and conveying the coolant through the surrounding moderator.

Steam generator. Part of the cooling system of pressurised water reactors (PWR & PHWR), where the high pressure primary coolant bringing heat from the reactor is used to make steam for the turbine, in a secondary circuit. Essentially, a heat exchanger like a motor car radiator. These are large heat exchangers for transferring heat from one fluid to another – here from high-pressure primary circuit in PWR to secondary circuit where water turns to steam. Reactors have up to six 'loops', each with a steam generator. Since 1980 over 110 PWR reactors have had their steam generators replaced after 20-30 years of service, 57 of these in USA.

Containment. The structure around the reactor and associated steam generators which is designed to protect it from outside intrusion and to protect those outside from the effects of radiation in case of any serious malfunction inside. It is typically a metre-thick concrete and steel structure.

Newer Russian and some other reactors install core melt localisation devices or 'core catchers' under the pressure vessel to catch any melted core material in the event of a major accident. There are several different types of reactors as indicated in table 2-1.

Table 2-1. Nuclear power plants in the world (WNA, 2017b).

Reactor type	Main countries	Number	GWe	Fuel	Coolant	Moderator
Pressurised water reactor (PWR)	US, France, Japan, Russia, China, Spain	282	264	enriched UO_2	water	water
Boiling water reactor (BWR)	US, Japan, Sweden	78	75	enriched UO_2	water	water
Pressurised heavy water reactor (PHWR)	Canada, India	49	25	natural UO_2	heavy water	heavy water
Gas-cooled reactor (AGR & Magnox)	UK	14	8	natural U (metal), enriched UO_2	CO_2	graphite
Light water graphite reactor (RBMK & EGP)	Russia	11 + 4	10.2	enriched UO_2	water	graphite
Fast neutron reactor (FNR)	Russia	3	1.4	PuO_2 and UO_2	liquid sodium	none
	TOTAL	441	384			

Several generations of reactors are commonly distinguished. Generation I reactors were developed in 1950-60s and only one is still running today. They mostly used natural uranium fuel and used graphite as moderator. Generation II reactors are typified by the present US fleet and most in operation elsewhere. They typically use enriched uranium fuel and are mostly cooled and moderated by water. Generation III are the Advanced Reactors evolved from these, the first few of which are in operation in Japan and others are under construction and ready to be ordered. They are developments of the second generation with enhanced safety. There is no clear distinction Gen II to Gen III. Generation IV designs are still on the drawing board and will not be operational before 2020 at the earliest, probably later. *Generation IV reactors will tend to have closed fuel cycles and burn the long-lived actinides now forming part of spent fuel, so that fission products are the only high-level waste.* Of seven designs under development, 4 or 5 will be fast neutron reactors. Four will use fluoride or liquid metal coolants, hence operate at low pressure. Two will be gas-cooled. Most will run at much higher temperatures than today's water-cooled reactors.

Fast neutron reactors (FNR; only one in commercial service) do not have a moderator and utilise fast neutrons, generating power from plutonium while making more of it from the ^{238}U isotope in or around the fuel. While they get more than 60 times as much energy from the original uranium compared with the normal reactors, they are expensive to build. Further development of them is likely in the next decade, and the main designs expected to be built in two decades are FNRs. If they are configured to produce more fissile material (plutonium) than they consume they are called Fast Breeder Reactors (FBR).

More than a dozen (Generation III) advanced reactor designs are in various stages of development. Some are evolutionary from the PWR, BWR and PHWR designs and some are more radical departures. The former includes the Advanced Boiling Water Reactor, a few of which are now operating with others under construction. The best-known radical new design has the fuel as large rods and uses helium as coolant, at very high temperature, possibly to drive a turbine directly. *Considering the closed fuel cycle, Generation 1-3 reactors recycle plutonium (and possibly uranium), while Generation IV are expected to have full actinide recycle.*

2.1.3 Nuclear Fuels

Most reactors need to be shut down for refuelling, so that the pressure vessel can be opened up. In this case refuelling is at intervals of 1-2 years, when a quarter to a third of the fuel assemblies are replaced with fresh ones. The CANDU (CANadá Deuterio Uranio; a PHWR type of reactor developed in Canadá) and RBMK types have pressure tubes (rather than a pressure vessel enclosing the reactor core) and can be refuelled under load by disconnecting individual pressure tubes.

Enriched uranium has the proportion of the fissile isotope (^{235}U) increased by a process called enrichment, commonly to 3.5 - 5.0%. In this case, the moderator can be ordinary water, and such reactors are collectively called light water reactors. Because the light water absorbs neutrons as well as slowing them, it is less efficient as a moderator than heavy water or graphite. During operation, some of the ^{238}U is changed to plutonium, and ^{239}Pu ends up providing about one third of the energy from the fuel.

If graphite or heavy water is used as moderator, it is possible to run a power reactor on natural instead of enriched uranium. Natural uranium has the same elemental composition as when it was mined (0.7% ^{235}U, over 99.2% ^{238}U).

In most reactors, the fuel is ceramic uranium oxide (UO_2 with a melting point of 2800°C) and most is enriched. The fuel pellets (usually about 1 cm diameter and 1.5 cm long) are typically arranged in a long zirconium alloy (zircaloy) tube to form a fuel rod, the zirconium being hard, corrosion-resistant and transparent to neutrons. Zirconium is an important mineral for nuclear power, where it finds its main use. It is, therefore, subject to controls on trading. It is normally contaminated with hafnium, a neutron absorber, so very pure 'nuclear grade' Zr is used to make the zircaloy, which is about 98% Zr plus about 1.5% tin, also iron, chromium and sometimes nickel to enhance its strength.

A significant industry initiative is to develop accident-tolerant fuels which are more resistant to melting under conditions, such as those found in the Fukushima accident, and with the cladding being more resistant to oxidation with hydrogen formation at very high temperatures under such conditions.

Numerous rods form a fuel assembly, which is an open lattice and can be lifted into and out of the reactor core. In the most common reactors these are about 4 metres long. A BWR fuel assembly may be about 320 kg, a PWR one 655 kg, in which case they hold 183 kg uranium and 460 kgU respectively. In both, about 100 kg of zircaloy is involved.

Burnable poisons are often used in fuel or coolant to even out the performance of the reactor over time from fresh fuel being loaded to refuelling. These are neutron absorbers, which decay under neutron exposure, compensating for the progressive build-up of neutron absorbers in the fuel as it is burned. The best known is gadolinium, which is a vital ingredient of fuel in naval reactors where installing fresh fuel is very inconvenient, so reactors are designed to run more than a decade between refuellings. Gadolinium is incorporated in the ceramic fuel pellets. An alternative is zirconium diboride integral fuel burnable absorber (IFBA) as a thin coating on normal pellets. Gadolinium, mostly at up to 3g oxide per kilogram of fuel, requires slightly higher fuel enrichment to compensate for it, and also after burn-up of about 17 GWd/t it retains about 4% of its absorptive effect and does not decrease further. The ZrB IFBA burns away more steadily and completely, and has no impact on fuel pellet properties. It is now used in most US reactors and a few in Asia. China has the technology for AP1000 reactors.

Nuclear fuel processing is one of the most important fields in nuclear power production. The nuclear fuel processing covers a large number of steps, from the mining to the reprocessing procedures of spent nuclear fuel. A comprehensive discussion of nuclear fuel processing may be found in an article of Wallace W. Schulz (Schulz, 2017).

2.1.3.1 Uranium Ore Mining

The Earth's crust contains about two parts per million uranium, reflecting a wide distribution in nature. The oceans are estimated to contain 4.5×10^9 tons of the element. Uranium occurs as a significant constituent in more than 150 different minerals and as a minor component of another 50 minerals. Primary uranium minerals, found in magmatic hydrothermal veins and in pegmatites, include *uraninite* and *pitchblende* (the latter a variety of uraninite). The uranium in these two ores occurs in the form of uranium dioxide, which—owing to oxidation—can vary in exact chemical composition from UO_2 to $UO_{2.67}$. Other uranium ores of economic importance are *autunite*, a hydrated calcium uranyl phosphate; *torbernite*, a hydrated copper uranyl phosphate; *coffinite*, a black hydrated uranium silicate; and *carnotite*, a yellow hydrated potassium uranyl vanadate.

It is estimated that more than 90 percent of known low-cost uranium reserves occur in Canada, South Africa, the United States, Australia, Niger, Namibia, Brazil, Algeria, and France. About 50 to 60 percent of these reserves are in the conglomerate rock formations of Elliot Lake, located north of Lake Huron in Ontario, Canada, and in the Witwatersrand goldfields of South Africa. Sandstone formations in the Colorado Plateau and Wyoming Basin of the western United States also contain significant reserves of uranium.

Uranium ores occur in deposits that are both near-surface and very deep (e.g., 300 to 1200 metres). The deep ores sometimes occur in seams as thick as 30 metres. As is the case with ores of other metals, surface uranium ores are readily mined with large earth-moving equipment, while deep deposits are mined by traditional vertical-shaft and drift methods.

2.1.3.2 Uranium Extraction

Uranium ores typically contain only a small amount of uranium-bearing minerals, and these are nor amenable to processing by direct pyro-metallugical methods; instead, hydro-metallurgical procedures must be used to extract and purify the uranium values. Physical concentration would greatly reduce the load on hydro-metallurgical processing circuits, but none of the conventional beneficiation methods typically employed in mineral processing—e.g., gravity, flotation, electrostatics, and even hand sorting—are generally applicable to uranium ores. With few exceptions, concentration methods result in excessive loss of uranium to tailings.

The hydro-metallurgical processing of uranium ores is frequently preceded by a high-temperature calcination step. Roasting dehydrates the clay content of many ores, removes carbonaceous materials, oxidizes sulfur compounds to innocuous sulfates, and oxidizes any other reductants that may interfere in subsequent leaching operations.

Roasted uranium ores are leached of their uranium values by both acidic and alkaline aqueous solutions. For the successful operation of all leaching systems, uranium must either be initially present in the more stable hexavalent state or be oxidized to that state in the leaching process. Prior to further processing, solutions resulting from either acidic or carbonate leaching must be clarified. Large-scale separation of clays and other ore slimes is accomplished through the use of effective flocculants, including polyacrylamides, guar gum, and animal glue. As a general rule, solvent extraction is preferred over ion-exchange methods for acidic leachates containing more than one gram of uranium per litre. Solvent extraction is not useful for recovery of uranium from carbonate leach liquors, however.

Prior to final purification, uranium present in acidic solutions produced by the ion-exchange or solvent-extraction processes described above, as well as uranium dissolved in carbonate ore leach solutions, is typically precipitated as a polyuranate. From acidic solutions, uranium is precipitated by addition of neutralizers, such as sodium hydroxide, magnesia, or (most commonly) aqueous ammonia. Uranium is usually precipitated as ammonium diuranate, $(NH_4)_2U_2O_7$. From alkaline solutions, uranium is most often precipitated by addition of sodium hydroxide, producing an insoluble sodium diuranate, $Na_2U_2O_7$. It can also be precipitated by acidification (to remove

carbon dioxide) and then neutralization (to remove the uranium) or by reduction to less soluble tetravalent uranium.

In all cases, the final uranium precipitate, commonly referred to as *yellow cake*, is dried. In some cases—*e.g.,* with ammonium diuranate—the yellow cake is ignited, driving off the ammonia and oxidizing the uranium to produce *uranium trioxide* (UO_3) or the more complex *triuranium octoxide* (U_3O_8). In all cases, the final product is shipped to a central uranium-purification facility.

2.1.3.3 Refining. Purification and Enrichment

Uranium meeting nuclear-grade specifications is usually obtained from yellow cake through a tributyl phosphate solvent-extraction process. First, the yellow cake is dissolved in nitric acid to prepare a feed solution. Uranium is then selectively extracted from this acid feed by tributyl phosphate diluted with kerosene or some other suitable hydrocarbon mixture. Finally, uranium is stripped from the tributyl phosphate extract into acidified water to yield a highly-purified uranyl nitrate, $UO_2(NO_3)_2$.

Uranyl nitrate is produced by the ore-processing operations described above as well as by solvent extraction from irradiated nuclear reactor fuel (described below, see Reprocessing). In either case, it is an excellent starting material for conversion to uranium metal or for eventual enrichment of the ^{235}U content (IAEA, 1999). Both of these routes conventionally begin with calcining the nitrate to *uranium trioxide,* UO_3, and then reducing the trioxide with hydrogen to *uranium dioxide* (UO_2). Subsequent treatment of powdered UO_2 with gaseous hydrogen fluoride (HF) at 550° C (1025 F) produces uranium tetrafluoride (UF_4) and water vapour, as in the following reaction:

$$UO_2 + 4\,HF \rightarrow UF_4 + 2H_2O \tag{2.1}$$

This hydrofluorination process is usually performed in a fluidized-bed reactor.

Conversion to uranium metal is accomplished through the Ames process, in which UF_4 is reduced with magnesium (Mg) at temperatures exceeding 1300° C,

$$UF_4 + 2\,Mg \rightarrow U + 2\,MgF_2 \tag{2.2}$$

Because the vapour pressure of magnesium metal is very high at 1300° C, the reduction reaction is performed in a refractory-lined, sealed container, or “bomb”. When the bomb is cooled to ambient temperature, the massive uranium metal obtained is, despite its hydrogen content, the best-quality uranium metal available commercially, and is well suited for rolling into fuel shapes for nuclear reactors.

Uranium tetrafluoride can also be fluorinated at 350° C with fluorine gas to volatile uranium hexafluoride (UF_6), which is fractionally distilled to produce high-purity material for isotopic enrichment. Any of several methods—gaseous diffusion, gas centrifugation, liquid thermal diffusion—can be employed to separate and concentrate the fissile ^{235}U isotope into several grades, from low-enrichment (2 to 3 percent ^{235}U) to fully enriched (97 to 99 percent ^{235}U. Low-enrichment uranium is typically used as fuel for light-water nuclear reactors.

After enrichment, UF_6 is reacted in the gaseous state with water vapour to yield hydrated uranyl fluoride ($UO_2F_2 \cdot H_2O$). Hydrogen reduction of the uranyl fluoride produces powdered UO_2, which can be used to prepare ceramic nuclear reactor fuel (see below: Oxide fuels). In addition, UO_2 obtained from enriched UF_6 or from UF_6 that has been depleted of its ^{235}U content can be hydrofluorinated to yield UF_4, and the tetrafluoride can then be converted to uranium metal in the Ames process described above.

2.1.3.4 Reprocessing. Conversion to Plutonium.

The nonfissile ^{238}U can be converted to fissile ^{239}Pu by the following nuclear reactions:

$$^{238}\mathrm{U} \xrightarrow{n} {}^{239}\mathrm{U} \xrightarrow{\beta^-} {}^{239}\mathrm{Np} \xrightarrow{\beta^-} {}^{239}\mathrm{Pu} \qquad (2.3)$$

In this equation, ^{238}U, through the absorption of a neutron (n) and the emission of a quantum of energy, known as a gamma ray (γ), becomes the isotope ^{239}U. Over a certain period of time (23.5 minutes), this radioactive isotope loses a negatively charged electron, or beta particle (β^-); this loss of a negative charge raises the positive charge of the atom by one proton, so that it is effectively transformed into the element neptunium (Np with and atomic number of 93 one more than uranium). ^{239}Np, in turn, undergoes beta decay, being transformed into ^{239}Pu (atomic number 94).

Uranium and plutonium are recovered from irradiated nuclear fuel through the widely-practiced plutonium-uranium extraction, or PUREX, process. In this solvent-extraction process, the fuel cladding encasing nuclear fuel elements (typically made of aluminium, magnesium, or zirconium alloys) is removed either chemically or mechanically, and the metal or oxide fuel is dissolved in nitric acid, HNO_3 (Naylor and Wilson, 1983: US-DOE, 1982). Plutonium and uranium are then coextracted into a tributyl phosphate solution, while practically all the fission products and nonradioactive components are left in the aqueous solution. The loaded organic extract is contacted with an aqueous phase containing any of several possible reductants to separate the plutonium from the uranium, and uranium is stripped from the tributyl phosphate solution into a dilute nitric acid solution. Additional extraction-strip cycles are performed as needed with the separated uranium and plutonium streams in order to complete purification from each other and from traces of coextracted fission-product zirconium and ruthenium.

Purified uranium nitrate is calcined to an oxide (either *uranium trioxide* UO_3 or *triuranium octoxide* U_3O_8) for subsequent conversion to UF_6 and enrichment of the ^{235}U content, as described above. Purified plutonium nitrate is converted to plutonium dioxide (PuO_2), either for conversion to plutonium metal (weapons-grade plutonium) or for recycling into nuclear reactor fuel. Like uranium, metallic plutonium is usually obtained by high-temperature reduction of a halide salt (plutonium tetrafluoride or plutonium trifluoride) with calcium metal. Much use is also made of the so-called direct oxidation-reduction process, whereby PuO_2 is reduced with calcium metal to plutonium metal and a calcium oxide slag:

$$\mathrm{PuO_2} + 2\,\mathrm{Ca} \rightarrow \mathrm{Pu} + 2\,\mathrm{CaO} \qquad (2.4)$$

2.1.3.5 Fission Fuels

Pellets made of low-enrichment *uranium dioxide*, UO_2, are universally employed as fuel in commercial light-water reactors that produce electrical energy. The pellets are made by blending appropriate quantities of enriched and natural or depleted UO_2 powders, mechanically compacting them, adding an organic binder, pressing into pellets, heating to burn off the binder, and, finally, sintering at high temperature to 95 percent theoretical density. Fuel pins are fabricated by loading the pellets into a Zircaloy tube. Similar procedures are employed to fabricate mixed uranium-plutonium dioxide (MOX) pellets for use in fast-neutron breeder reactors. Unirradiated *Mixed Oxide Fuel* (MOX) typically contains 20 to 35 percent plutonium dioxide.

Various *uranium and plutonium carbides* are known, including the monocarbides (UC, PuC), the sesquicarbides (U_2C_3, Pu_2C_3), and the dicarbides (UC_2, PuC_2). Because they are highly refractory, these compounds have been much investigated for use as fuels for nuclear reactors. For example, the fuel in the high-temperature gas-cooled reactor (HTGR) consists of highly enriched uranium, together with thorium as a fertile material; each is in the form of carbide pellets embedded in a dense form of graphite. Finally, uranium forms a mononitride (UN) and two higher nitride phases (alpha- and beta-sesquinitrides; $\alpha = U_2N_3$ and $\beta = U_2N_3$), whereas plutonium forms only a

mononitride. Both *uranium and plutonium nitrides* are brittle, refractory compounds that melt at temperatures generally above 2000° C (3600° F). This latter property makes the mononitrides attractive as possible high-performance nuclear reactor fuels.

2.1.4 Nuclear Power Debate

There is a social debate about nuclear power. The nuclear power debate concerns the controversy which has surrounded the use of nuclear fission reactors to generate electricity from nuclear fuel for civilian purposes. The debate about nuclear power peaked during the 1970s and 1980s, when it "reached an intensity unprecedented in the history of technology controversies", in some countries (Murphy, 1976). Proponents, such as the World Nuclear Association and Environmentalists for Nuclear Energy, contend that nuclear power is a safe, sustainable energy source that reduces carbon emissions and increases energy security by decreasing dependence on imported energy sources. Proponents claim that nuclear power produces virtually no conventional air pollution, such as greenhouse gases and smog, in contrast to the chief viable alternative of fossil fuel. Nuclear power can produce base-load power unlike many renewables which are intermittent energy sources lacking large-scale and cheap ways of storing energy (IEA, 2009). Proponents claim that the risks of storing waste are small and can be further reduced by using the latest technology in newer reactors, and the operational safety record in the Western world is excellent when compared to the other major kinds of power plants. Opponents, such as Greenpeace International and NIRS (Nuclear Information and Resource Service), contend that nuclear power poses many threats to people and the environment. These threats include the problems of processing, transport and storage of radioactive nuclear waste, the risk of nuclear weapons proliferation and terrorism, as well as health risks and environmental damage from uranium mining. They also contend that reactors themselves are enormously complex machines where many things can and do go wrong; and there have been serious nuclear accidents. Critics do not believe that the risks of using nuclear fission as a power source can be fully offset through the development of new technology. They also argue that when all the energy-intensive stages of the nuclear fuel chain are considered, from uranium mining to nuclear decommissioning (dismantling), nuclear power is neither a low-carbon nor an economical electricity source. Arguments of economics and safety are used by both sides of the debate.

2.1.5 Nuclear Power in Spain

Spain has five active nuclear plants with seven reactors producing 21% of the country's electricity as of 2017 (WNA, 2017a; See Figure 2-2 and Table 2-2). All these nuclear power reactors are of PWR type.

As shown, nuclear power plants in Spain are located in the northern half. This is because the area is of less seismic impact of the peninsula, and where the presence of large rivers Tajo and Ebro meet their needs for water used for cooling. Spain has a total of 10 nuclear installations within their mainland, among which there are a total of seven nuclear units: Almaraz I and II, Ascó I and II, Cofrentes, Trillo, and Vandellós II. Vandellós I, José Cabrera (Guadalajara) and Garoña units are being dismantled. There are no plans for either expansion or accelerated closure of nuclear plants.

Spain also possesses a nuclear fuel factory in Salamanca (Juzbado) and a storage facility for radioactive waste, low and intermediate level in Córdoba (El Cabril). State owned Empresa Nacional de Residuos Radiactivos S.A. was established in 1984, and is the responsible outfit for radioactive waste disposal and decommissioning. Spain stores nuclear waste at the reactor sites for ten years with no reprocessing. There is a temporary dry storage facility at the Trillo Nuclear Power Plant. A temporal centralized storage is now under construction (Almacén Temporal Centralizado, ATC) in Villar de Cañas (Cuenca). Research for a long term geological repository

is been carried out. The amount of radioactive waste produced nowadays in Spain is detailed in Figure 2-3.

ENUSA is a company in Spain with various holdings in uranium mining. A uranium mine in Saelices el Chico was operated for some time, but is now decommissioned. Nowadays, Spain imports all the nuclear fuel.

Figure 2-2. Nuclear power plants in Spain. Note that Garoña nuclear power plant was shut in December 2012 (WNA, 2017a).

Table 2-2. Nuclear power plants in Spain (WNA, 2017a).

Reactors	Type	Net MWe	First power	Commercial operation	Owner (%); operator	Licenced to
Almaraz 1	PWR	1011	1981	1981	Iberdrola 53%, Endesa 36%, Gas Natural Fenosa 11%; CNAT	6/2020
Almaraz 2	PWR	1006	1983	1984		6/2020
Asco 1	PWR	995	1983	1984	Endesa (100%); ANAV	10/2021
Asco 2	PWR	997	1985	1986	Endesa (85%), Iberdrola (15%); ANAV	10/2021
Cofrentes	BWR	1064	1984	1985	Iberdrola (100%); Iberdrola	3/2021
Vandellos 2	PWR	1045	1987	1988	ENDESA (78%), Iberdrola (28), ANAV	7/2020
Trillo 1	PWR	1003	1988	1988	Iberdrola (48%), Gas Natural Fenosa (34.5%), EDP (15.5%); CNAT	11/2024

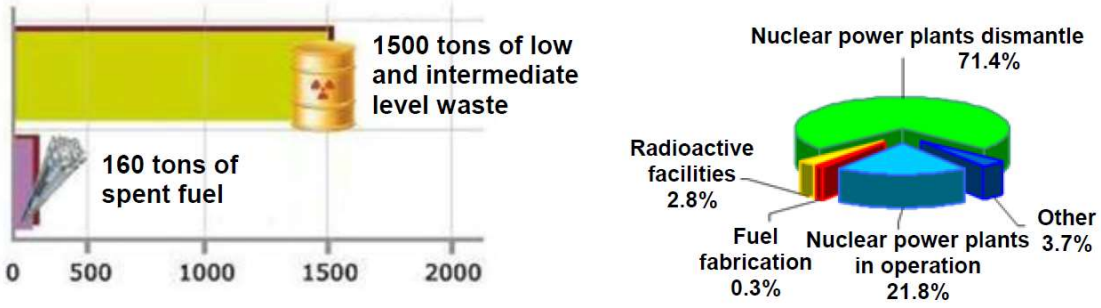

Figure 2-3. Detailed annual production of radioactive waste in Spain (Royuela, 2014).

2.2 Nuclear Fuel Cycle and Radioactive Waste Management

The use of nuclear fission as energy source, demands a program for the management of the nuclear waste generated. While the amount of radioactive wastes is insignificant compared with the volume of non-radioactive waste generated by modern industry, the radiotoxic characteristics and the great social impact of these wastes demand that a careful management different from that of any other kind of dangerous wastes. The efforts must be driven towards the search of a definitive site for its storage, assuring their immobilization and isolation from the environment during times guaranteeing the absence of radiologic risk for the persons and the biosphere. The radioactive wastes are classified according to several factors including their physical state (solid, liquid or gas), the kind of radiation emitted (α, β, or γ), semidisintegration period (short or large) and its specifical activity (high, medium or short). However, from the point of view of its final management there is not a unique international classification for all the radioactive wastes.

Radioactive waste is defined by the International Atomic Energy Agency (IAEA, 2003) as any waste that contains or is contaminated with radionuclides at concentrations or activities greater than clearance levels as established by the regulatory body. It is classified according to international standards (IAEA, 2009) as follows:

Very low level waste (VLLW): Radioactive waste considered suitable by the regulatory body for authorized disposal, subject to specified conditions, with ordinary waste in facilities not specifically designed for radioactive waste disposal.

Low and intermediate level waste (LILW): Radioactive waste that has a low concentration of radioactive materials, due fundamentally to the presence of radionuclides with half-lives of less than 30 years, and a very low and limited content of long-lived radionuclides. This waste ceases to be dangerous to health in a few hundred years.

High level waste (HLW): Radioactive waste containing high concentrations of short and medium-lived radionuclides and a considerable concentration of long-lived radionuclides. Additionally, the radioactive decay of these radionuclides generates large amounts of heat. Although its activity decreases with time, it takes thousands of years to reach levels that are not harmful to health or the environment.

In Spain, the VI plan general de residuos radiactivos (MITYC, 2006; referred to as VI PGRR) summarizes the national regulations for the management of this kind of waste. In this plan, the radioactive waste is classified in two groups, the first one including the low and medium activity radioactive wastes and the second including the high activity ones. The characteristics of each of these groups are showed in Table 2-3.

Table 2-3. Characteristics of Low, Medium and High level radioactive wastes (MITYC, 2006).

Low and Medium Level Radioactive Wastes	High Level Radioactive Wastes
Low or intermediate β/γ activity	High β/γ activity
Insignificant α activity	Significant α activity
Insignificant heat production	Significant heat production
Low or intermediate radioactivity	High radioactivity

The management of low and medium level radioactive waste may be considered a technologically solved problem, since, nowadays, it is carried out in a low deep geological storage or in surface installations guaranteeing a minimal containment period of 300 years, the estimated time for a radioactivity decay to acceptable activity values, in accordance with the stablished standard radiological levels. Before the storage, there is a preparation step, in which the waste volume is reduced by compaction and they are fixed to a solid matrix, generally of cement or concrete (polymeric resins and bitumen are also used), and packed in metallic containers. In Spain, the storage of this kind of wastes is performed in surface modules in El Cabril facility, Córdoba (ENRESA, 1995).

High level radioactive nuclear wastes are formed mainly by the irradiated nuclear fuel (referred to as spent nuclear fuel, SNF, in what follows) and high level glasses coming from the chemical treatment (reprocessing) of the SNF used in order to recuperate the plutonium which may be used in the weapon fabrication or the obtention of the Mixed OXide fuel (MOX). In Spain, only a small part of the wastes is vitrified and come from the Vandellos I nuclear plant which is now being dismantled.

For the case of high level nuclear wastes, the VI PGRR stablishes that the management of the main component will be carried out following the option of an Open Nuclear Fuel Cycle (Figure 2-4), also called "once through concept". This plan fixes a time period in a temporal wet storage (in the pools of the nuclear plant), followed by a centralized dry storage. In the final storage, the fuel elements will be send to one Almacén Temporal Centralizado (ATC, under construction, see Figure 2-5), while a definitive waste management is being developed and new technologies (separation and transmutation) are developed in order to reduce the volume and radioactivity of these wastes. One of the main options for the definitive waste management (MITYC, 2006; Wilson, 1996) is the construction of a Deep Geological Disposal (DGD; Almacenamiento Geológico Profundo, AGP, see Figure 2-6). In some of the Spanish nuclear plants, there are individual temporal storages (Almacenes Temporales Individuales, ATI), as a consequence of the saturation of the pools. These ATI are waiting to send the combustible elements to the ATC. Independently of the selected option, the management of the high level nuclear waste requires a construction of a definitive repository. In the case of the alternative strategy of the *Closed Nuclear Fuel Cycle*, the SNF is reprocessed and the recovered uranium and plutonium are directed to fabrication steps (see Figure 2-4). The *Advanced Nuclear Fuel Cycle* (closed fuel cycle with advanced reprocessing, separation and transmutación) is also shown in Figure 2-4.

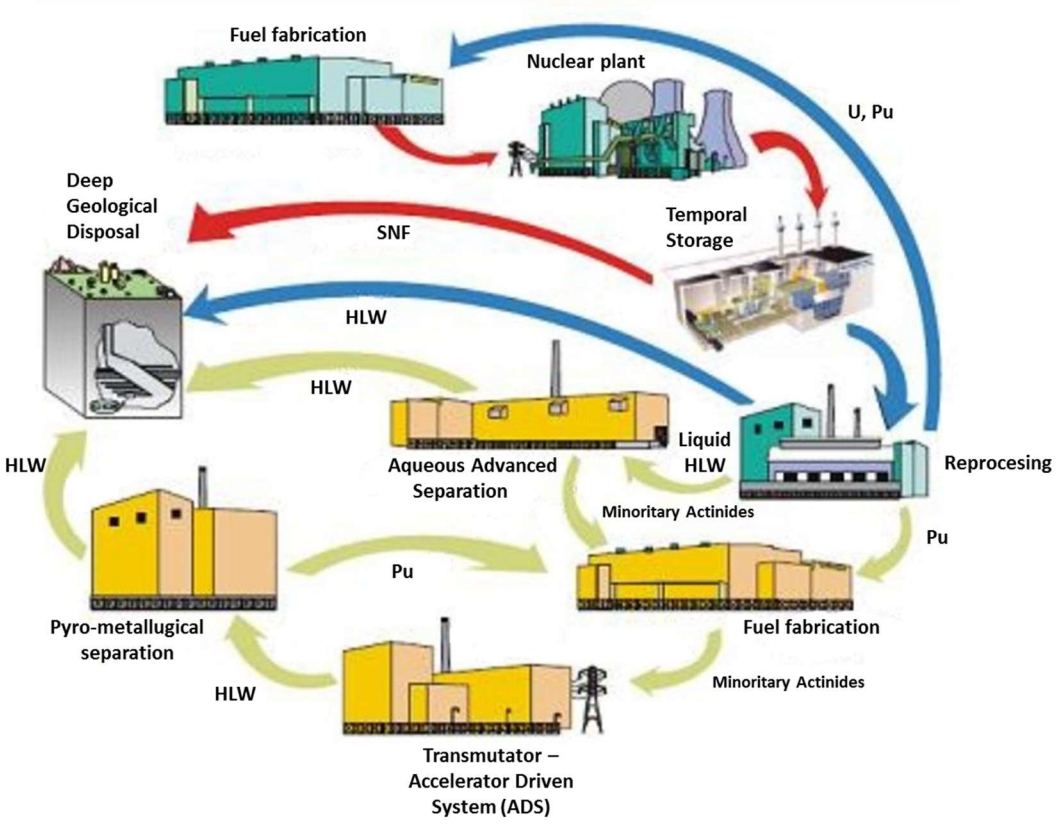

Figure 2-4. Nuclear fuel cycle. Red: Open fuel cycle; Blue: Closed fuel cycle; Green: Advanced closed fuel cycle.

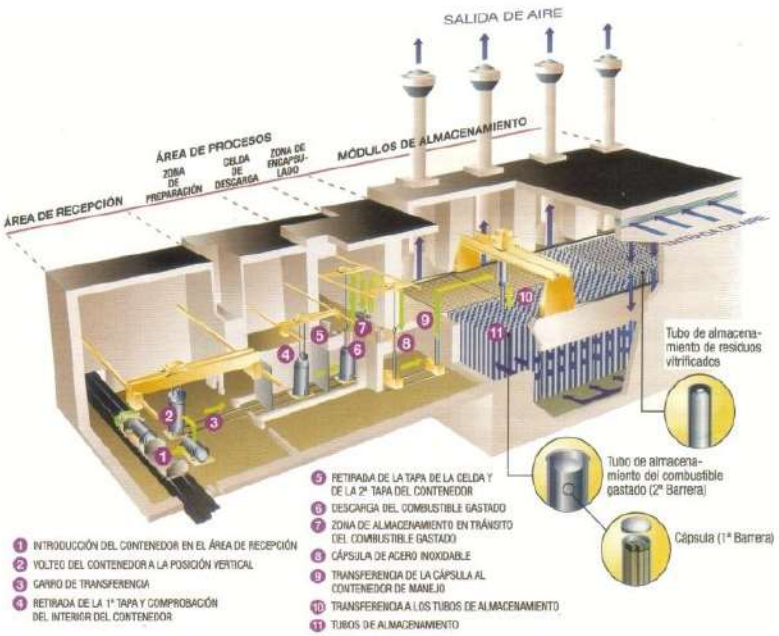

Figure 2-5. Scheme of the design of the Spanish ATC (CSN, 2017).

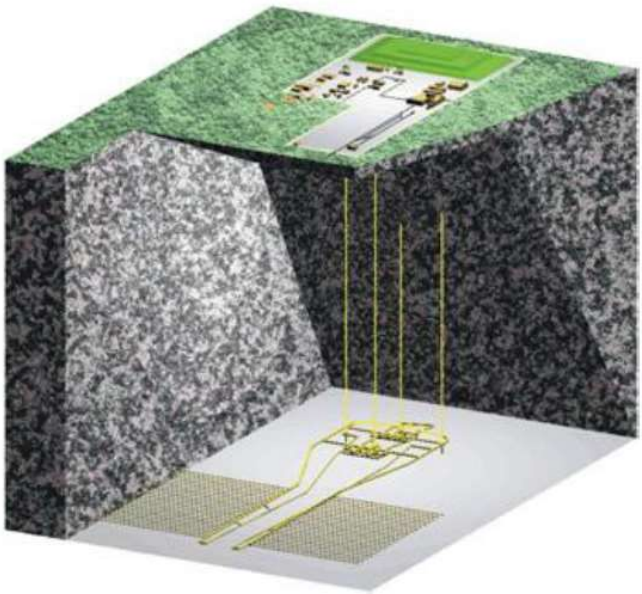

Figure 2-6. Scheme of a possible design of the DGD in granitic rock (ENRESA, 1997a; Astudillo Pastor, 2001).

2.2.1 Deep Geological Disposal

In the management of radioactive waste, we must combine technical solutions with economic, environmental, social and political aspects. The combination of all these factors is not an easy task as it is demonstrated by the investigations about the different options performed in the last decades. The most of these options have been discarded definitively.

The disposal of these wastes in sediments of the ocean underground (Hollister and Nadis, 1998) was one of the options studied during the decade of 80's. The viability and security of this disposal were studied carefully and large difficulties were found. The waste disposal in marine trenches placed in the union of tectonic plates (Fyfe *et al*., 1984) was discarded due to the geological instability of the zone. The sending of the wastes to the exterior space (McMenamin, 1997) was also studied and discarded due to the high risk associated to a possible failure during the blast-off.

Actually, there is a wide international consensus that a very good solution for the definitive waste management is the confinement of the waste at a repository constructed at a high deep (between 300 and 1000 metres) in stable geological formations (see Figure 2-6). This disposal has the objective of isolating the wastes by means of the interposition of a series of natural and artificial barriers (Savage, 1995) avoiding the liberation of radioisotopes during a large time, so that the activity of the waste is decreased to levels inoffensive for the man and the biosphere (see Figure 2-7).

The first of these barriers is the waste itself. The SNF is a very insoluble material, chemically inert, mechanically resistant, and thermally stable at high temperatures. The SNF is arranged within a cladding tube made with a Zirconium alloy (zircaloy) being hard, corrosion-resistant and transparent to neutrons. The second barrier is the container (canister) in which the SNF is introduced. The use of canisters made with Cu is one of the best choices because cooper is one of the most inert metals. However due to its high price, other possibility is the use of containers with walls of higher thickness and made with other materials as Pb, steel, Fe or concrete. Another option is the utilization of a Fe-Ti alloy, a highly inactive material due to the passivation shell formed in its surface. The final decision on the composition will be taken attending to technical and economic factors. In Spain, the Empresa Nacional de Residuos Radioactivos (ENRESA), has selected the carbon steel for the construction of the canisters. The waste containers are introduced in galleries excavated in rocks at a great profundity (300-1000 meters). These galleries are filled with an absorbing material and sealed. This material constitutes the third security barrier. Good candidates for this barrier are clay minerals. Due to their great plasticity, they can minimize the mechanical effects of possible seismic motions over the containers. They also behave as filters of small particles and colloids and as tampons of the chemical composition of the underground waters (Savage, 1995). Finally, since they have low thermal conductivity, they will reduce the thermal gradient stablished between the containers and the geological formation in the first years after the closure of the repository. Bentonite is the most widely studied material to construct this barrier. Bentonites are clays rich in expansible minerals as montmorillonite and are excellent sealing materials because they have low permeability and a great capacity to retard the transport of dissolved radionuclides (Grauer, 1990).

The fourth and last barrier is the receiving geologic formation. It is a natural barrier and should avoid or retard the migration of radionuclides released to the biosphere in the case that they have surpassed the other three barriers. We need to search a geologic environment able to minimize the release of the radionuclides until a time in which their activity level has decreased to acceptable values. The requirements that should be met by the geologic formation are a high geologic stability (absence of seismic motions) and a minimal hydrologic activity (to avoid the waste dissolution and return to the biosphere). The first three barriers constitute the *near field*, that is the zone of geosphere directly affected by the construction of a DGD. The geological barrier, or *far field*, is the natural media between the near field and the biosphere.

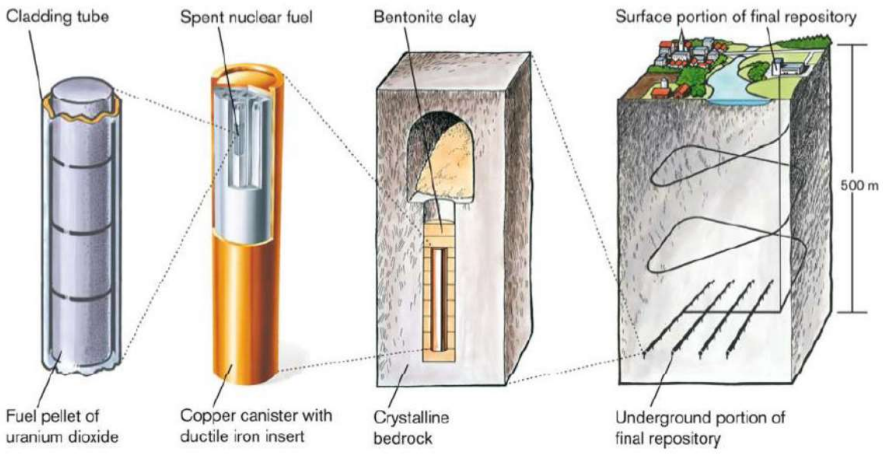

Figure 2-7. The different barriers in the Deep Geological Repository (SKB, 2017).

2.2.1.1 Geological Environments

As it has been mentioned, the selection criteria for the site selection for a repository respond fundamentally to geological aspects as the stability and hydrologic activity. Taking these aspects into account, there are three main geologies which are good candidates for a DGD. These are the granitic, clayey and saline environments. Each geological environment present advantages and inconvenients and the final choice will depend, finally, on the geological availability of each country. A fourth type of environment (Krauskopf, 1986), in extremely arid regions, was selected by EEUU, the repository of Yucca Mountain. Some researchers consider erroneous this choice because the hydrologic system is about 100 metres below the repository location. The possibility of a pluvial water infiltration could have great implications in the repository safety.

Granitic environment.

Advantages:

- ✓ High chemical and mechanical stability.
- ✓ Low water content.
- ✓ Presence of secondary minerals with good adsorption capacity, as oxides and clays.

The main *disadvantages* of this environment, adopted by Sweden and Canada, are related to the granite fracturation and the water circulation through these fractures.

Clayey environment.

Advantages:

- ✓ Low porosity and permeability.
- ✓ Great adsorption capacity of radionuclides.
- ✓ Great capacity of fracture sealing.

The main *disadvantages* of this environment are the presence of waters coming from infiltrations, the low stability of excavations, and the low physical resistance of the material.

Saline environment.

Advantages:

- ✓ Low water content.
- ✓ Great elasticity which confers to the formation a high geologic stability.
- ✓ Relatively dense and impermeable.

The main *disadvantages* of this environment, selected by Germany, is the corrosion due to the high concentration of dissolved ions.

2.2.1.2. Groundwater System

The geological repository will be, in most cases, below the underground hydrologic system. This means that in a certain moment during the construction of the DGD, the flux of groundwater will be interrupted. After the flux is restablished and after a few decades the repository is closured, the water will enter in the tunnels through the fissures of the adjacent rocks. Multibarrier system will help to retard the motion of the water in the interior of the repository and the corrosion process of the containers. However, after a time period of the order of thousands of years, the waste will be in contact with groundwater and will begin to dissolve in it. In the risk evaluation of a repository, the effects of this dissolution process and those of the liberation of radionuclides due to a possible (although improbable) accident must be taken into account. With this purpose, all the relevant processes controlling the fuel matrix dissolution at the repository conditions must be studied.

The study of the water-fuel interaction allows to obtain information on the possible mechanisms controlling the behaviour of the matrix at the different groundwater system parameters, the redox potential and the chemical composition. On the other hand, the study of the water-rock interaction will help to obtain information on the possible retention mechanisms of the radionuclide (Miller *et al*., 1994), as precipitation, adsorption, ionic exchange, etc. All these processes are interconnected.

One of the more important factors affecting the UO_2 dissolution is the redox potential of the underground water. In a granitic environment at great deep, such a potential is tamponed by the rocks of this media to highly reducing values (Wikberg, 1987; Grenthe et al., 1992). At these conditions, the thermodynamically stable phase is UO_2 (Forsyth et al., 1986), which is highly insoluble in water and, therefore, the concentration of uranium dissolved in contact with solid UO2 is relatively low (10^{-7}-10^{-8} mol·dm^{-3}). However, under oxidant conditions, an oxidation layer within < 50 μm of the fuel surface, is formed at the surface of UO_2 whose solubility is larger than that of UO_2. Dissolved uranium, in the form of uranyl ion (UO_2^{2+}) form very stable complexes with many ligands as OH^-, HCO_3^-, CO_3^{2-}, SO_4^{2-}, Cl^- and F^- (Paquette and Lemire, 1981), which are present in many underground waters (Lemire, 1988). For this reason, the concentration of dissolved uranium under oxidant conditions is larger. The oxidant conditions at the SNF surface are produced by the radiolytic decomposition of water due to α radiation. Such a radiation is highly ionizing and produce oxidant and reducing species in the water film in contact with the fuel, H_2 being the dominant reducing species. Due to the relatively low reactivity and high diffusivity of H_2, it escapes without reacting and oxidant conditions are created in the SNF surface (Carbol et al., 2005; Christensen, 1991; Eriksen et al., 1995). The effect of temperature on UO_2 dissolution (Čuba, 2012; Kienzler et al., 2012; Ahn and S. Mohanty, 2007; Ikonen, 2003) should also be studied in a more complete way because, although the main characteristic data on water radiolysis are independent on the temperature up to about 100°C, their changes at higher temperatures are conspicuous and important (Čuba, 2012).

The process of oxidative alteration leads to the formation of uranyl secondary phases which may control the uranium concentration and the radionuclide liberation in the long term. Depending on the chemistry of water in contact with the waste, different secondary phases may be formed as silicates, phosphates, hydroxides, etc. This behaviour has been widely described in the literature (Stroes-Gascoyne *et al*., 1985; Wang and Katayama, 1982; Forsyth *et al*., 1986). The study of these secondary phases is one of the main objectives pursued in this work.

2.2.1.3 Natural Analogues

As it has been discussed in previous section, the first barrier in the DGD, is the UO_2 matrix itself, that is the limited solubility of UO_2 in water. In recent years, numerous investigations have been centered in the study of the mechanisms and velocities of dissolution of the SNF in a wide range of experimental conditions. Given the inherent limitations, technical and economical, these studies are carried out using chemical analogs of the fuel, as the non-irradiated UO_2 or the SIMFUEL (UO_2 matrix with inclusions of stable isotopes chemically similar to those present in the SNF). The validity of these chemical analogs has been demonstrated and their limitations discussed (Bruno *et al*., 1992; Gray *et al*., 1992). The laboratory studies related to the security evaluation of a repository allow to identify the elemental mechanisms and to determine the influence of some parameters in a well defined and controlled system. We must not forget, however, that the models developed by means of this type of experimentation are limited in time and space. Such limitations justify the necessity of studies based in natural processes which have occurred along geological times and are similar to those of interest in the security evaluation of a repository. These processes are what we know as *natural analogs*. This term also embraces the archaeological materials because although they are of artificial origin, their presence and fingerprint in the physical media demonstrate the potential stability and longevity of the technological materials used in a repository.

The natural analogs make possible the identification of the processes really active in nature, especially those arising after large times (geochemical, mechanical and thermal processes) and to calibrate the models developed which are based in laboratory experiments. Natural analogue studies carried out in the last years have allowed the compilation of information relative to the material stability and migration of elements. The behaviour of uranium in the natural media has been the principal focus of attention because it is the main constituent of spent nuclear fuel. In this sense, the *uranium deposits are good natural analogs for a radioactive waste repository since they allow to evaluate the possible migration of uranium and other radionuclides near the repository*. This fact justifies the studies performed in a large number of analogs, as those of Jackimov (Czech Republic; Cera, 1996), Palmottu (Findland; Suutarinen, 1991), Koongarra (Australia; Isobe, 1992), Shinkolobwe (Zaire; Finch and Ewing, 1989), Poços de Caldas (Brasil; MacKenzie, 1990) and Oklo (Gabon; Janeczek, 1992). The interest of studying different analogs is due to the fact that each one gives information about different geographic localities, of its environment, and about the alteration process suffered over the years in different locations.

En Poços de Caldas (Brasil; MacKenzie, 1990), the studies have been centered on the Morro de Ferro deposit, one of the more radioactive natural localities known in the world, and in the Osamo Utsumi deposit, highly eroded by the pluvial waters penetrating in the rocks through numerous fractures and producing the oxidation of the different minerals. The redox front formed is an important aspect of this natural analogue, since similar redox fronts may be produced in the proximity of the container of a high level radioactive waste repository.

Another example of surface alteration is that suffered in Shinkolobwe mine (Zaire) which converts it in one of the mines having larger amounts of both primary and secondary uranium minerals. In this mine, more than 50 uranyl secondary phases resulting from uraninite alteration have being identified.

A natural analogue extensively studied is that of Cigar Lake in Canada (Cramer, 1994), the largest and richest uranium deposit in the world. The uranium ore is placed at a deep of 450 metres under the lake and it is surrounded by clay minerals in a rock crystalline base. *The combination of different barriers at this natural analogue has been very effective and there is not any expression of radioactivity in the surface*. This fact is a good evidence of the fact that the ore has been maintained intact at this deep from the time of its formation, 1300 millions of years ago.

The most studied natural analogue in the last years is that of Oklo in Gabon, an exceptionally rich uranium deposit in which spontaneous fission nuclear reactions occurred 2000 millions of years ago. The *uraninites originated by these geological phenomena in this natural analogue, unique in the world, are one of the best natural analogs to the spent nuclear fuel, since these have suffered*

a process of fission analogue to that of SNF. It is also important to note the similarities with the clay barriers which are planned to be used in the construction of a DGD. The reaction products located in the clayey environment of the reaction zones are an evident proof of the efficiency of the geological barriers. The study of this natural analogue provides an excellent opportunity to obtain information about the stability of uranium oxide and to identify the geochemical mechanisms implied in the migration and retention of radionuclides in the geosphere in time and space scales that cannot be simulated in the laboratory.

2.2.2 Nuclear Transmutation

Nuclear transmutation is the conversion of one chemical element or an isotope into another. Because any element (or isotope of one) is defined by its number of protons (and neutrons) in its atoms, *i.e*. in the atomic nucleus, nuclear transmutation occurs in any process where the number of protons or neutrons in the nucleus is changed.

One type of natural transmutation easily observed occurs when certain radioactive elements present in nature spontaneously decay by a process that causes transmutation, such as alpha or beta decay. An example is the natural decay of ^{40}K to ^{40}Ar (Engelkemeir *et al.*, 1962), which forms most of the argon in the air. Artificial transmutation may occur in machinery that has enough energy to cause changes in the nuclear structure of the elements (as in particle accelerators). Conventional fission power reactors also cause artificial transmutation, not from the power of the machine, but by exposing elements to neutrons produced by fission from an artificially produced nuclear chain reaction.

Artificial nuclear transmutation has been considered as a possible mechanism for reducing the volume and hazard of radioactive waste. Transmutation of transuranium elements (TRUs, *i.e*. actinides minus actinium to uranium), such as the isotopes of plutonium (about 1wt% in the Light Water Reactors' spent nuclear fuel (SNF)) or the minor actinides (MAs, i.e. neptunium, americium, and curium, about 0.1wt% each in LWRs' SNF), has the potential to help solve some problems posed by the management of radioactive waste by reducing the proportion of long-lived isotopes it contains. Isotopes of plutonium and other actinides tend to be long-lived with half-lives of many thousands of years, whereas radioactive fission products tend to be shorter-lived (most with half-lives of 30 years or less). From a waste management viewpoint, transmutation (or "burning" or "incineration") of actinides eliminates a very long-term radioactive hazard and replaces it with a much shorter-term. Thist does not rule-out the need for a Deep Geological Repository (DGD) for High Radioactive Level Waste (HLW). When irradiated with fast neutrons in a nuclear reactor, these isotopes can undergo nuclear fission, destroying the original actinide isotope and producing a spectrum of radioactive and nonradioactive fission products.

Ceramic targets containing actinides can be bombarded with neutrons to induce transmutation reactions to remove the most difficult long-lived species. These can consist of actinide-containing solid solutions such as (Am,Zr)N, (Am,Y)N, (Zr,Cm)O_2, (Zr,Cm,Am)O_2, (Zr,Am,Y)O_2 or just actinide phases such as AmO_2, NpO_2, NpN, AmN mixed with some inert phases, such as MgO, $MgAl_2O_4$, (Zr,Y)O_2, TiN and ZrN. The role of non-radioactive inert phases is mainly to provide stable mechanical behaviour to the target under neutron irradiation.

In the last years, the option of the treatment of the radioactive waste by transmutation of the most dangerous radioactive isotopes into other ones having shorter lifes (easier to handle) is being researched in Spain (ENRESA, 1997b). The use of this technique, will allow to reduce the long-lived radionuclide content but it will not eliminate them completely. Thus, the use of transmutation does not avoid the need of a solution to the isolation or elimination of high level radioactive nuclear waste.

It is important to understand that the threat posed by a radioisotope is influenced by many factors including the physical, chemical and biological properties of the element. For instance, caesium has a relatively short biological half-life (1 to 4 months) while strontium and radium both have

very long biological half-lives. As a result, ^{90}Sr and radium are much more able to cause harm than ^{137}Cs when a given activity is ingested. In transmutation, the intention is to convert the actinides into fission products. The fission products are very radioactive, but the majority of the activity will decay away within a short time. The most worrying short-lived fission products are those that accumulate in the body, such as iodine-131 which accumulates in the thyroid gland, but it is hoped that, by using a good design of the nuclear fuel and transmutation processes, such fission products can be isolated from humans and their environment and allowed to decay. In the medium term the fission products of highest concern are ^{90}Sr and ^{137}Cs; both have a half-life of about 30 years. The ^{137}Cs is responsible for the majority of the external gamma dose experienced by workers in nuclear reprocessing plants and by the workers at the Chernobyl site (Yablokov *et al*., 2009).

2.3 Spent Nuclear Fuel and Secondary Phases

2.3.1 Physico-Chemical Description of Irradiated Nuclear Fuel

The irradiated nuclear fuel is a complex material that changes its chemical composition and physico-chemical characteristics with the pass of time. The nuclear fuel used in the Spanish nuclear power plants (Centrales Nucleares, CCNN), it is elaborated by means of sinterization of UO_2 powder enriched in ^{235}U between 3 – 5%. The elaborated *pellets* have a density which represents a 92–99% of the theoretical one and a grain size of 2–15 μm. The UO_2 is characterized by a slight oxygen excess (UO_{2+x}, $x \leq 0.001$), incorporated in the interstitial holes of the material. This leads to the fact that a small fraction of uranium atoms displays the U(VI) oxidation state (Esteban *et al*., 1998; Shoesmith, 2000). For the fabrication of the fuel, the pellets are inserted in the inner part of rods of a Zirconium alloy (zircaloy) which is transparent to radiation. These rods have a length of about 4 metres and a diameter of 9-13 millimeters. The remaining holes are refilled with Argon. The sealed rods are assembled by means of structural elements or gratings that maintain the form of the *fuel elements*. The form of the grating and the number of rods depend on the type of reactor in which they will be used (Wilson, 1996).

The fabricated fuel elements are then used in the reactor. The amount of actinide elements and fission products generated during the nuclear reactions accumulate in the elements up to the moment in which they interfere in the energy producing fission reactions. Then, the fuel elements must be replaced. Once the use of the fuel elements in the reactor has been finished, the SNF is composed mainly by UO_2 (95%) and, in a smaller amount, by actinide oxides, activation products and fission products. The proportion of these elements in the fuel matrix is determined by the initial enrichment of the fuel pellet (conventional ^{235}U enrichments are in the interval 3–5%) and the degree of burning of the fuel. As an example, the composition of the irradiated nuclear fuel used in the risk analyses carried out for the Spanish AGP (Astudillo Pastor, 2001; Esteban *et al*., 1998) is presented in Figures 2-8 and 2-9.

In the inner part of a fuel element (see Figure 2-10) we may distinguish three different zones: the UO_2 matrix (about 98% of the element), the grain limit, and the empty space between the UO_2 pellets and the zircaloy cladding (referred to as "huelgo"). The cracks produced in the pellets during irradiation are considered to form part of the empty space. Most of the actinide elements generated during the fission process will be retained in the matrix of the UO_2 pellets (> 90%). For this reason, the liberation of radionuclides to the biosphere will be governed by the alteration (oxidation and dissolution) of the UO_2 matrix (Astudillo, 2001; Esteban *et al*., 1998; Shoesmith, 2000). This characteristic allows to consider the SNF matrix as the first barrier against the liberation of radionuclides to the biosphere.

In order to know the behaviour of the SNF in a storage we need to know the behaviour of the UO_2 matrix for this system. In the SNF, we observe physico-chemical changes resulting from fission reactions and thermal cycles. In the SNF pellet we observe the formation of punctual defects,

vacants, cracks, recrystallization and grain grow processes, high burning structures, a possible central hole formation, formation of punctual defects associated to the migration of radionuclides giving rise to the formation of bubbles of fission gases, volatile compound segregation directed to the space between the pellet and the cladding, formation of precipitated phases (metallic phases and oxides), etc. (See Figures 2-10, and 2-11). All these changes modify the stability of the fuel in a repository (Esteban *et al*., 1998; Forsyth, 1995; Martínez Esparza *et al*., 2004b; Quiñones *et al*., 2003).

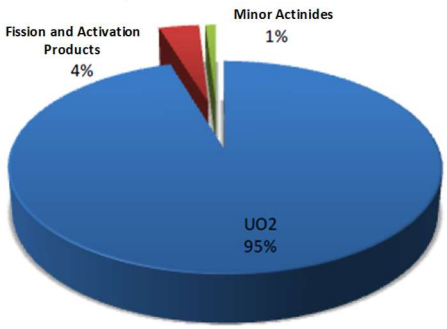

Figure 2-8. Composition of a SNF pellet with a fuel burning of 40 MW/Kg U (Astudillo, 2001).

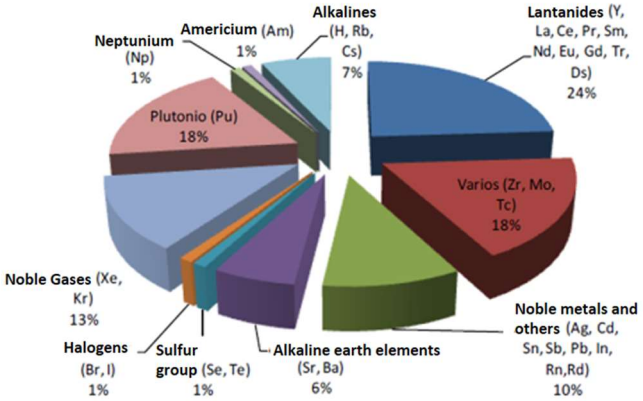

Figure 2-9. Detail of the composition of the 5% of actinide and fission products (Astudillo, 2001).

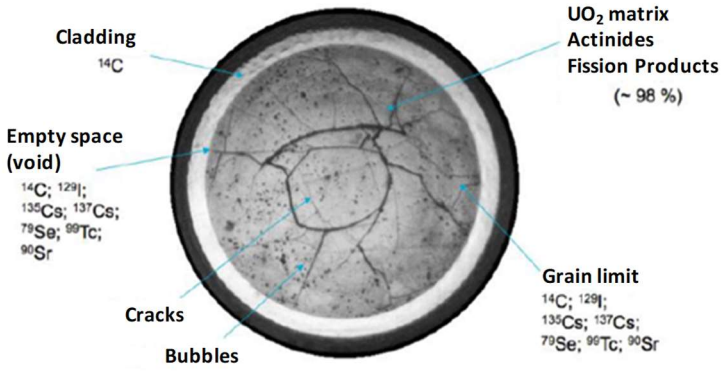

Figure 2-10. Macrography of a fuel pellet irradiated with a fuel burning of 40 MW/Kg U (Esteban *et al*., 1998).

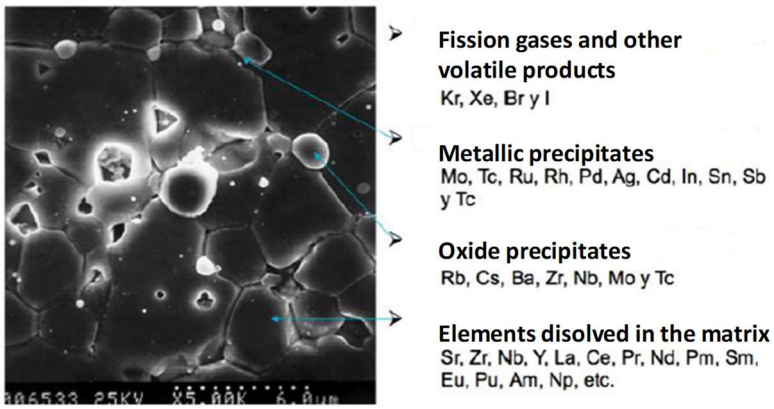

Figure 2-11. Scheme of the distribution of radionuclides within a SEM micrography of SIMFUEL (Esteban *et al*., 1998).

From the analysis of the irradiated fuel elements coming from high pressure light water reactors, we observe that they contain alloy inclusions of Mo, Ru, Rh, Pd, Ag, Cd, In, Sn, Sb and Tc elements that are segregated from the UO_2 matrix (see Figure 2-11). Inclusions formed with precipitated oxides of Rb, Cs, Ba, Zr, Nb, Mo, and Tc elements are also found. The Sr, Zr, actinides and REE form solid solutions with UO_2 in the matrix.

2.3.2 Stability of Irradiated Nuclear Fuel at Disposal Conditions. Nuclear Fuel Corrosion

In this section, the stability of the SNF at the conditions of a DGD definitive disposal are studied. It is important to note that, the conventional concept of Pourbaix has no sense here since, in the standards conditions of a repository, the solubility of $UO_2(s)$ is of 10^{-10} mol/kg of H_2O (in metallic materials and alloys, a secondary passivating phase is formed for a solubility smaller than 10^{-5} mol/kg of H_2O).

The design of the DGD is based in the isolating capacity found in some stable geologic formations during millions of years. The design of the repository is based in a multibarrier principle consisting in interposing a series of engineered barriers (fuel pellet, cladding, capsule and filling material -for example a bentonite barrier-) and a natural barrier (the geologic formation) between the high level nuclear radioactive waste (residuos radiactivos de alta actividad, RRAA) and the biosphere. In this way, if the radionuclide liberation is produced, these barriers will retard their arrival to the biosphere, and they will not alter the natural radiologic background below the minimal levels stablished by the regulator organism (Consejo de Seguridad Nuclear, CSN, in the Spanish case). The main function of the engineering barriers is to avoid that underground water reaches the SNF (Astudillo, 2001; NEA, 2000).

In the last decades, a number of research groups (France, Germany, Sweden, Finland, and United States) have performed different studies with the purpose of knowing the stability of SNF in a DGD with a failure in the engineering barriers, in which the underground water has reached the matrix of irradiated nuclear fuel.

One of the forms of evaluating the stability of the SNF is the study of natural analogs, as the uraninite mineral. Uraninite is a mineral of UO_2 generally slightly oxidized. This mineral may contain traces of different elements (Ca, Zr, Th, REE or disintegration products as Pb) retained during its formation or as a consequence of fission reactions produced in natural media. An example is the mineral localized in the Oklo deposit in Gabon, one of the most important natural nuclear reactors found. Its study has permitted to know the stability of UO_2 as a matrix and the

alteration processes which has experimented during thousands of years in its geologic environment (oxidation, secondary phase formation, etc.). The fission reaction produced 2109 years ago, caused that numerous fission products were retained in the UO_2 matrix. The works carried out have allowed to evaluate the mechanisms of migration of the radionuclides in uraninite and in in the geologic environment surrounding it for very large time periods (Finch and Ewing, 1992; Janeczek and Ewing, 1992; Janeczek *et al*., 1996). An example is shown in Figure 2-12, in which an optical micrograph obtained by means of Dark-Field Optical Microscopy (Quiñones *et al*., 2003) shows the advancement of the alteration front resulting from the interaction of groundwater with the UO_2.

In addition to the study of natural analogs, the study of the alteration of UO_2 fuel matrix (main component of the SNF), allows to predict the behaviour of the matrix in a repository. The results of different authors in the last decades have demonstrated that UO_2 is very stable at reducing conditions (see Figure 2-13). Such conditions are expected in most of the repository security studies carried out (Amme, 2002; de Pablo *et al*., 2003b; Grambow *et al*., 2010; Jégou *et al*., 2005a; Ollila, 1990; Oversby, 1999; Quiñones *et al*., 1998; Shoesmith, 2000). But these conditions will be not maintained in the proximity of the pellets.

The SNF will have a residual thermal charge (see Figure 2-14), and in its surroundings will generate an ionizing radiation field (α, β y γ) originating in the matrix due to the disintegration reactions of the generated radionuclides contained in the fuel pellet (see Figure 2-15). Such a radiation fields will vary with time in its nature and intensity. In the first times, β and γ radiation types will be predominant, diminishing up to 3 magnitude orders in the first 1000 years, when the α radiation becomes predominant (Christensen, 1998; Christensen and Sunder, 2000; Christensen *et al*., 1994; Eriksen *et al*., 1995; Eriksen *et al*., 2012; Jégou *et al*., 2005a; Jégou *et al*., 2005b; Jégou *et al*., 2007; Quiñones *et al*., 1999; Shoesmith, 2000; Shoesmith and Sunder, 1992). The interaction of the radiation coming from the SNF with the underground water will produce the water radiolysis and the generation of radiolytic products, both oxidants and reductors (see Figures 2-16 and 2-17). The concentration of these species will depend of the radiation type and the radiation dose deposited in the water (ENRESA, 2001; ENRESA, 2003). Therefore, oxidant conditions at the SNF surface will be produced by the radiolytic decomposition of water mainly due to α radiation. Such a highly ionizing radiation produces oxidant and reducing species in the water film in contact with the fuel, H_2 being the dominant reducing species. Due to the relatively low reactivity and high diffusivity of H_2, it escapes without reacting and oxidant conditions are created in the SNF surface (Christensen, 1998; Eriksen *et al*., 1995).

Figura 2-12. Image of the alteration front of an uraninite to an uranophane. Dark-Field Optical Microscopy (Quiñones *et al*., 2003).

The effect of radiation in the studies of uranium dissolution, either by the input of emitters as ^{239}Pu (α emitter) or external sources irradiating the UO_2/water interface (Christensen and Sunder, 2000; Eriksen *et al*., 2012; Garisto *et al*., 2009; Jégou *et al*., 2005a,b; Muzeau *et al*., 2009; Quiñones, 2005; Quiñones and Cobos, 2002; Quiñones *et al*., 2004a; Quiñones *et al*., 2006; Sattonnay *et al*., 2001; Sunder *et al*., 1997) have demonstrated an increase of the UO_2 dissolution rate of up to three magnitude orders when the experiments are carried out with a high α radiation dose. A similar effect was observed in the works in which the effect of γ radiation was used (Christensen and Sunder, 1996; Quiñones and Serrano, 2002; Sunder *et al*., 1992). As an example, Jégou *et al*. (Jégou *et al*., 2005a) observed that the UO_2 dissolution rate in combination of the effect of γ radiation was greater by one magnitude order when the experiments were carried out in air (oxidant conditions), than when they were carried out in inert atmosphere. Other authors have studied the effect of the radiolytic products, adding H_2O_2 to the experimental dissolutions. The concentration of such experiments was that obtained by means of radiolytic models (Nielsen *et al*., 2008), since hydrogen peroxide is one of the most important products formed by radiolysis (Amme, 2002; Clarens *et al*., 2005; Sundin *et al*., 2013). In all the cases, the addition produces an increase of dissolution rate and the formation of a zone with high concentration of U(VI) (Cobos *et al*., 2006), which could react with the ions present in water resulting in secondary phase formation and precipitation. In the presence of ligands as CO_3^{2-}, the formation of complexes with U(VI) (see Table 2-4), avoids the increase of the concentration up to that of saturation and the formation of U(VI) secondary phases (Giménez *et al*., 2005b; Shoesmith, 2000). Dissolved uranium, in the form of uranyl ion (UO_2^{2+}) form very stable complexes with many ligands such as OH^-, HCO_3^-, CO_3^{2-}, SO_4^{2-}, Cl^- and F^- (Paquette and Lemire, 1981), which are present in many underground waters (Lemire, 1988).

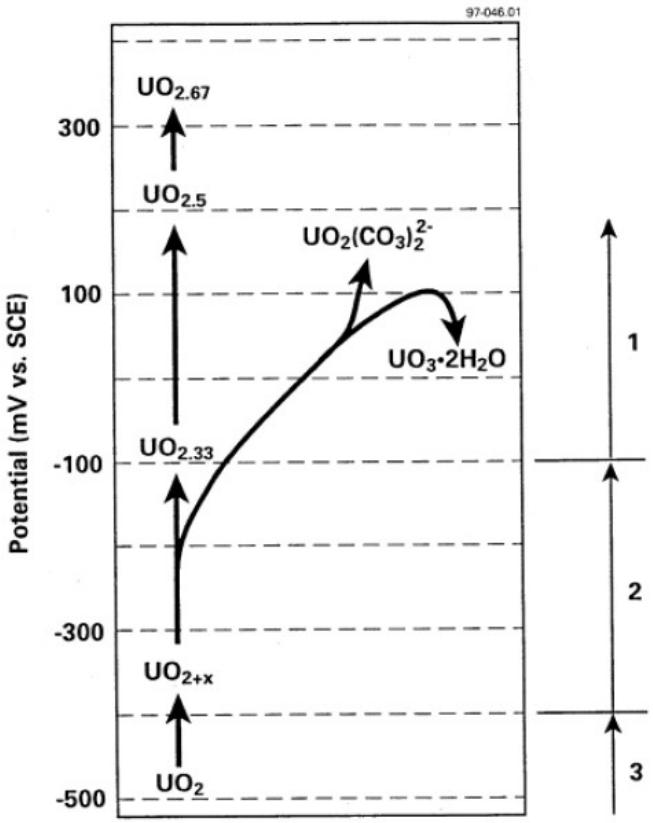

Figura 2-13. Chemistry/Electrochemistry of the oxidation/dissolution of UO_2 (Shoesmith, 2000; Sunder *et al*., 1997).

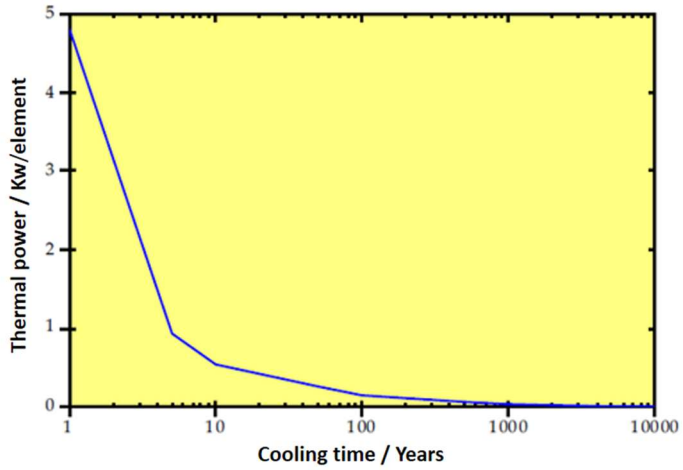

Figure 2-14. Evolution of the thermal power of a PWR fuel (3.3% ^{235}U, 33 MWd/Kg U) (Rodriguez Almazán, 2000).

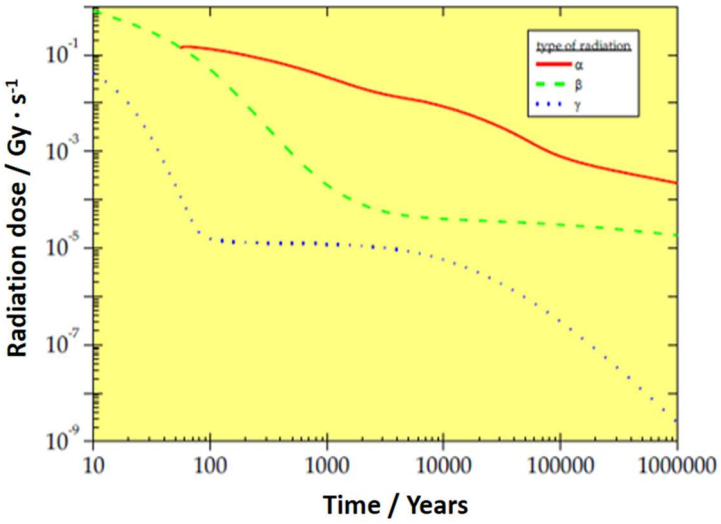

Figura 2-15. Evolution of the radiation dose in the surface of a pellet (3.3% ^{235}U, 33 MWd/Kg U) (Rodriguez Almazán, 2000).

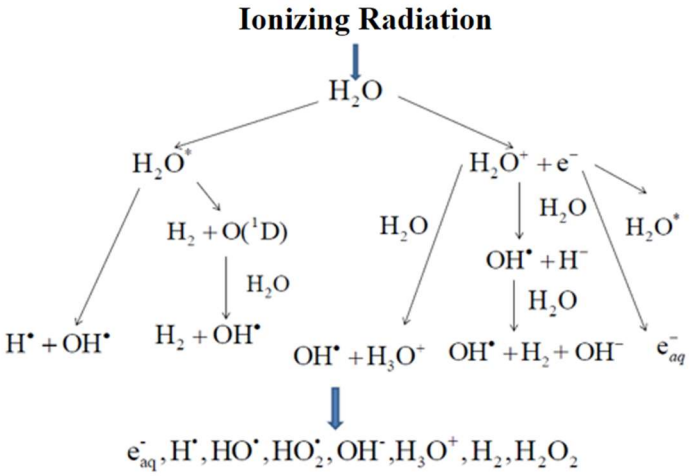

Figura 2-16. Main reactions identified in the water radiolysis (Le Caër, 2011).

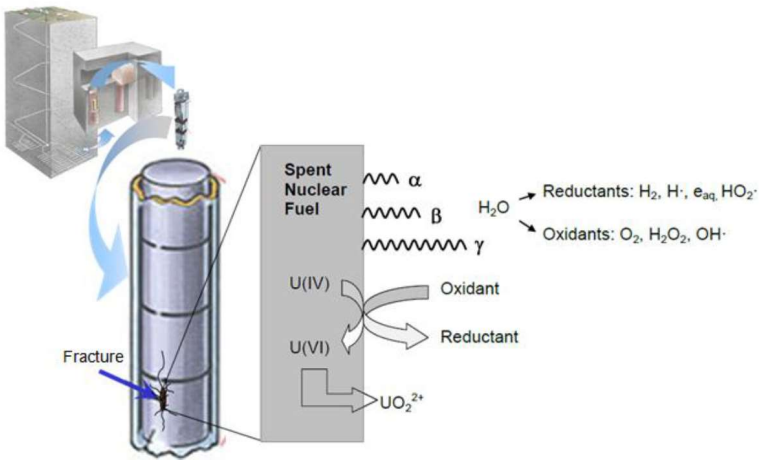

Figura 2-17. Oxidative dissolution of spent nuclear fuel in radiolytic conditions (Pehrman, 2012).

Table 2-4. Equilibrium constants of the formation of the system U(VI) – CO_3^{2-} at 298 K and I=0 (Grenthe *et al*., 2004).

Reactions	$Log_{10}K$
$UO_2^{2+} + CO_3^{2-} \rightleftarrows UO_2CO_3\ (aq)$	9.68 ± 0.04
$UO_2^{2+} + 2\ CO_3^{2-} \rightleftarrows UO_2(CO_3)_2^{2-}$	10.94 ± 0.12
$UO_2^{2+} + 3\ CO_3^{2-} \rightleftarrows UO_2(CO_3)_3^{4-}$	21.60 ± 0.05
$3\ UO_2^{2+} + 6\ CO_3^{2-} \rightleftarrows (UO_2)_3(CO_3)_6^{6-}$	54.0 ± 1.0

2.3.2.1 Uranium Corrosion

Corrosion can be defined as a chemical of electrochemical reaction between a material, usually a metal, and its environment causing a deterioration of the material and its properties (Davis, 2000). It involves the disintegration of material into its constituent atoms by chemical interactions with their surroundings. Eventually, this would cause the cracking of material producing corrosion products leading to loss of mass of metal.

Increasing the humidity can increase the corrosion rate, because moisture provides the electrolyte, which is required for corrosion reactions to take place. Corrosion rates can increase with increasing temperature. Changing temperature may change the corrosion mechanism from uniform to pitting (localized). It can also evaporate condensed moisture on metallic surfaces leaving behind corrosive contaminants (Craig *et al*., 2006).

The reaction of uranium with oxygen can be described as

$$U + \frac{2+x}{2} O_2 \rightarrow UO_{2+x} \tag{2.5}$$

The value of x is a product of the atmosphere (oxygen activity), temperature, and time. The value of x therefore varies as a function of the particular oxidizing species (oxygen, CO_2, and CO mixtures). As the oxide scale grows, the outer layer in contact with the oxide/gas interface gradually increases in the oxygen content. The oxide spalls off of the surface at a thickness of about 1 μm, leading to a reinitialization of the process (Lillard and Hanrahan, 2005). The reaction of uranium with water vapor is much faster than that of dry air or oxygen (Fig. 2-18).

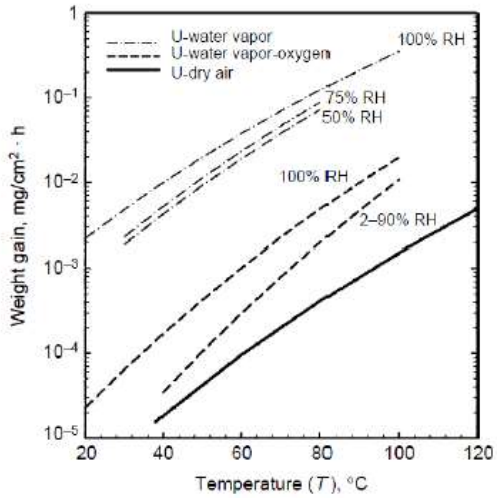

Figure 2-18. Uranium oxidation rates in dry air, oxygen-water vapor, and water vapor as a function of temperature (Lillard and Hanrahan, 2005).

In humid environments, a thin layer of water forms on a material surface and sets up an electrochemical cell. Therefore, uranium oxidation in water vapor environments is electrochemical corrosion, which is governed by anodic and cathodic reaction. The anodic reaction is the oxidation of uranium whereby uranium gives up electrons and UO_{2+x} is formed. To maintain charge neutrality, the cathodic reaction (see first eq. below) must consume the electrons generated by oxidation (Lillard and Hanrahan 2005 and references therein). The overall reaction is expressed in the second Equation:

$$O_2 + 2H_2O + 4\,e^- \rightarrow 4\,OH^- \quad (2.6)$$

$$U + O_2 + 3H_2O \rightarrow UO_2 + 3\;OH^- + 3\,H^+ \quad (2.7)$$

Water corrosivity is related to water composition, dissolved gases, pH, temperature, water velocity, and biological organisms. The presence of oxygen and sulfurous gases can increase the corrosion rate. In addition, the ions from dissolved salts most responsible for increased water corrosivity are chlorides and sulfates (Craig *et al*., 2006). pH also affects the corrosion of uranium in water. It controls the type of oxide that would be formed above the metal surface. As in the atmospheric environments, increasing temperature leads to increasing in corrosion rate.

2.3.3 Secondary Phase Formation in a Final Geological Disposal

2.3.3.1 Secondary Phases Stability

As we have already explained, due to the alteration processes of UO_2 in a DGD, given the environmental conditions, is thermodynamically possible the formation and precipitation of U(VI) secondary phases in surface of the SNF matrix. Different studies, involving the alteration of both SNF and UO_2 (Grambow *et al*., 2010; Quiñones *et al*., 2005; Quiñones *et al*., 2007) have detected the formation of secondary phases. As an example, Wronkiewicz *et al*. (1992, 1996), have exposed UO_2 at 90 °C to a simulated dripping of ground water droplets (similar to the groundwater in the area of Yucca Mountain). The analysis of the surface showed the formation of hydrated uranyl oxides (schoepite, dehydrated schoepite, becquerelite and compreignacite), uranyl silicates (uranophane, boltwoodite, soddyite and sklodowskite). Other authors have detected uranyl silicates in experiments simulating the DGD conditions in the surface of ferruginous alloys (Quiñones *et al*., 2004b).

The experimental works of Wronkiewicz *et al*. (Wronkiewicz *et al*., 1992; Wronkiewicz *et al*., 1996) propose a phase transformation sequence from the less stable compounds, as schoepite and dehydrated schoepite, to very stable minerals as boltwoodite (see Figure 2-19). In previous studies, Wilson (Wilson, 1987) identified the formation of soddyite and uranophane in experiments of dissolution of spent fuel with a burning in the range 27–30 MWd/kg U. The experiments were performed in a silicate rich media, thus favouring the formation of uranyl silicates. The formation of other types of uranyl minerals has been studied by other authors. For example, the formation of chernikovite, $H_2(UO_2)_2(PO_4)_2 \cdot 8H_2O$, was identified by Rey *et al*. (2008) in UO_2 dissolution experiments in a phosphate rich media.

This kind of studies allows to stablish stability diagrams of uranium phases in terms of the media considered, as the standard conditions expected in a repository. In Figure 2-20 the models proposed by Finch and Ewing (2003) are showed for the case of Yucca Mountain repository environmental conditions. It must be remembered that these conditions are highly oxidant and, therefore, the formation of secondary phases of U(VI) is thermodynamically favoured.

The formation of secondary phases will not be produced only in ion rich media, since it has been also confirmed in experiments performed in deionized water. In the dissolution experiments carried out in presence of radiation fields, the formation of uranyl peroxides (studtite, $UO_4 \cdot 4H_2O$, and metastudtite, $UO_4 \cdot 2H_2O$) was detected. These phases are associated to the generation of hydrogen peroxide as radiolytic product (Amme, 2002; Amme *et al*., 2005; Clarens *et al*., 2004; Clarens *et al*., 2005; Corbel *et al*., 2006; Jégou *et al*., 2005b; Quiñones *et al*., 2005; Sattonnay *et al*., 2001; Sundin *et al*., 2013). The formation of uranyl peroxides has also been documented in the dissolution of irradiated nuclear fuel and in pellets doped with Pu. McNamara *et al*. and Hanson *et al*. (Hanson *et al*., 2005; McNamara *et al*., 2004) observed that in lixiviation experiments of irradiated nuclear fuel with a burning of 30.2 MWd/kg U and times greater than two years, schoepite was the unique secondary phase formed in the UO_2 surface and that this was transformed with time in a mixture of uranyl peroxides (studtite and metastudtite). This transformation adds an intermediate step in the transformation of phases proposed by Wronkiewicz *et al*. (1992, 1996). The alteration of schoepite and other minerals as soddyite, into studtite was studied by Forbes *et al*. (Forbes *et al*., 2011) suggesting that uranyl minerals in presence of high enough concentrations of hydrogen peroxide could be transformed into studtite.

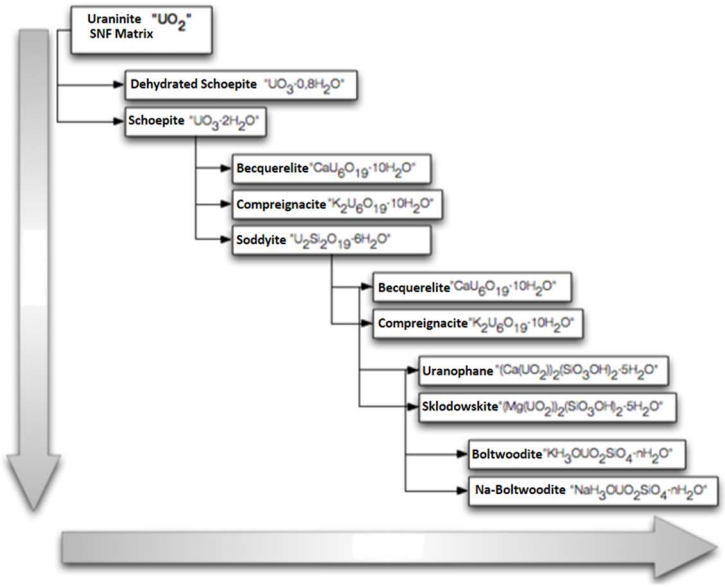

Figure 2-19. Sequence of formation and transformation of the secondary phases observed in the UO_2 surface determined by Wronkiewicz *et al.* (1992, 1996).

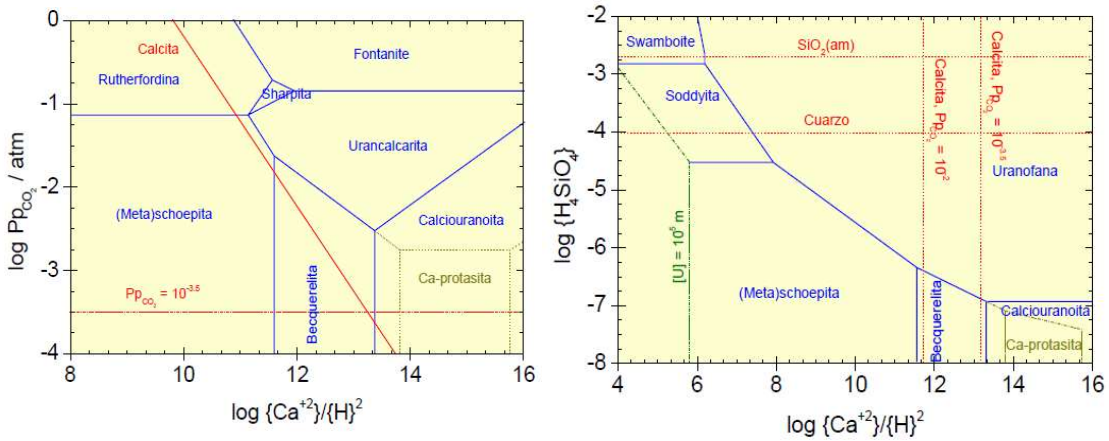

Figure 2-20. Equilibrium diagrams of U minerals in the systems: a) CO_2-CaO-UO_3-H_2O; b) SiO_2-CaO-UO_3-H_2O (Finch and Ewing, 2003).

The formation of a layer of secondary phase over the SNF could modify the corrosion process of the SNF. Shoesmith, in his documental revision of the corrosion process of the SNF in DGD conditions proposed that the formation of a layer of U(VI) mineral in the UO_2 surface of low porosity could prevent the transport of oxygen to the surface of SNF, favouring the formation of less oxidant conditions in the SNF surface. Furthermore, this deposit could diminish the surface area available for corrosion (Giménez *et al*., 2005a; Shoesmith, 2000). These conditions were also presented in the final report of the MICADO project (Grambow *et al*., 2010).

As it is concluded from the bibliographic works previously mentioned, the effects observed in the formation of secondary phases in the SNF surface, leads to the necessity of a study of the stability of such phases at the DGD conditions. These experimental studies have also permitted to perform other studies of the solubility of these secondary phases to obtain a database of the stability of these phases in a DGD (Gorman-Lewis *et al*., 2008a, 2008b), to model the experimental data and to simulate its behaviour at any desired set of environmental conditions.

2.3.3.1.1 Stability of Secondary Phases Exposed to Radiation

The presence of external radiation fields as that coming from the ions incorporated to the structure of the secondary phases will have an effect in the own structure of the secondary phases precipitated in the SNF surface. The high energy absorbed, due to the ionization electronic excitation caused by the α and β disintegration, will produce an important heating of the material (Hedin, 1997). There are different approximations in the literature in order to study these effects in the secondary phases (Deditius *et al*., 2009; Ewing *et al*., 2000; Lian *et al*., 2009, 2011; Rey *et al*., 2009b; Sureda *et al*., 2011; Utsunomiya *et al*., 2003a,b). In these approximations, the effect of α radiation was studied by means of ion irradiation and that of β radiation was studied by means of irradiation with electrons. In the works performed with uranyl silicates (Sureda *et al*., 2011; Utsunomiya *et al*., 2003a) it was observed that when the dose reaches a certain level, an amorphization of the irradiated phases is produced. For the case of irradiation of uranophane with Ca ion exchanged by Sr and Eu the irradiation was modelled with the effect of the electrons of the electronic transmission microscope on the simple. The transition from the crystalline to the amorphous structure is produced at relatively low total absorption doses, because when the doses are higher a recrystallization is observed, i.e., nucleation and grow of new crystals. The required doses for the amorphization of the four mineral phases studied in these works were of the same magnitude order (Dc ≈ 1010 Gy). This value is slightly larger than the β radiation doses generated in the SNF during the first hundred of years of a reactor discharge (107–108 Gy) (Utsunomiya *et al*., 2003a).

The effect of α radiation in synthetic uranyl phases was studied by Utsunomiya *et al*. and Lian *et al*. (Lian *et al*., 2009; Utsunomiya and Ewing, 2006). In these works, the samples were irradiated

with Kr^{2+} of 1 MeV, and the results demonstrated that uranyl carbonates presented a high instability when they were exposed to a minimal irradiation with electrons. It was observed that the most of these phases decompose and form UO_2 nanocrystals when they are exposed to irradiation of ~ 10^{13} – 10^{14} ion/cm^2 (0.006 – 0.2 dpa). From these works, Utsunomiya *et al*. proposed a formation sequence of the UO_2 nanocrystals: (i) U(VI) decomposition, and cascade displacement caused by ion flux and (ii) fast nucleation of UO_2 crystals (Utsunomiya and Ewing, 2006).

2.3.3.2 Radionuclide Retention in the Secondary Phases

The role of secondary phases is not limited to the passivation in the SNF surface since they could also modify the liberation rate of radionuclides to the medium; this retardation process is due to the incorporation of these radionuclides in the crystalline structure of the secondary phase. This possibility was studied in the works by Burns *et al*., which proposed different mechanisms of the actinide incorporation in the U(VI) phases. These authors proposed three incorporation mechanisms based in the most common structures of uranyl minerals (Burns, 2005; Burns *et al*., 1996):

- Replacement of U(VI) with charge balance needed in the chain of uranyls.

- Replacement of ions distinct to U(VI) in the uranyl chain or in the laminar structure accompanied by the exchange of other ions in order to get the charge balance.

- Incorporation in the existing vacants present in the uranyl chain and in the laminar structure.

Buck *et al*. (1997) demonstrated experimentally that the actinide liberation, concretely that of Np, could be controlled by the schoepite formation due to the retention in its structure. After these interesting experimental results, a large amount of studies were carried out about the immobilization of Np(V) in uranyl secondary phases (Burns *et al*., 2004; Burns and Klingensmith, 2006; Douglas *et al*., 2005a; Douglas *et al*., 2005b; Friese *et al.*, 2004; Klingensmith and Burns, 2007a; Klingensmith *et al*., 2007b; Shuller *et al.*, 2010a, 2010b). Due to its high mobility in oxidant underground waters and its high radiotoxicity, this radionuclide was considered one of the most important ones in the risk analyses.

One of the first works was carried by Burns *et al*. (2004). In this work, using dissolutions containing 10–500 ppm Np(V), they observed the precipitation of the following uranyl secondary phases: metaschoepite, Na-Compreignacite, uranophane and β-$(UO_2)(OH)_2$. Microstructural characterization of the precipitated phases showed that the incorporation was almost inexistent, of a small number of ppm in the hydrated uranyl phases. However, both in the uranophane and compreignacite phases great amounts of Np were incorporated. These observations are very interesting for the risk analysis of the DGD due to the implications in the retardation of the mobility of radionuclides. In later studies, these authors found similar results about the incorporation of light metals in the crystal structure of uranyl silicates and hydrated uranyl phases in synthetic mixtures of uranyl silicates and Na metaschoepite (Klingensmith and Burns, 2007a; Klingensmith *et al.*, 2007b).

The radiochemical analysis of the secondary phases detected by Hanson *et al*. (2005) revealed that metastudtite could retain elevated concentrations of fission products (^{90}Sr, ^{137}Cs and ^{99}Tc), while the retention of actinides, as ^{241}Am, ^{237}Np and ^{239}Pu is smaller (McNamara *et al*., 2005). These results were reproduced by other authors (Douglas *et al*., 2005a; Friese *et al*., 2004) by means of the synthesis of a mixed metastudtite phase in an initial Np rich media.

One of the first works in which it was demonstrated the retention capacity in uranyl peroxides was that carried out by McNamara *et al*. (2005), which using radiochemical analysis of the precipitates formed in lixiviation experiments with SNF, identified the secondary phases formed. With the aim of testing their results, Douglas *et al.* (2005a) carried out a study of metaschoepite in a dissolution with Np and its transformation to studtite when H_2O_2 was added. The results demonstrated that the most of Np remained in the lixiviant (dissolution); however, the chemical

analysis of the precipitated phase revealed that studtite contained 6500 µg Np/g. The work also studied the solubility of the Np phase and it was shown that it was possible that studtite was not controlling the mobility of Np, suggesting the need of concreting the retention mechanism of Np in studtite. In this sense, Shuller *et al*. (2010a, 2010b) carried out an evaluation of Np incorporation by means of the "Quantum-mechanical program", replacing the uranium by Np in the studtite structure. The results confirmed that the incorporation of Np^{+6}, was perfectly possible whereas the Np^{+5} or Np^{+4} incorporation was not energetically favoured.

From the point of view of the mobility control, Giménez *et al*. (2009, 2010) carried out a series of works to study the incorporation into studtite of fission products as Sr, Cs and Se(VI). With this purpose, they lixivied studtite powder in dissolutions with different pH and containing the same initial concentration of each radionuclide, 10^{-6} mol·dm^{-3}. The results demonstrated that the adsorption or Cs and Sr increase with the pH until the adsorption of the 60 y 100% of the initial concentration. However, that of Se was larger at acid pH. These authors explained the effect using the fact that at high pH, studtite presents a negative superficial charge which favours the adsorption of Cs^+ and Sr^{2+} ions. However, Se^{4+}ion is present in dissolution, as an ion with negative charge, $HSeO_4^-$, and its adsorption is favoured when the solid presents a positive superficial charge (de Pablo *et al*., 2003a; Giménez *et al*., 2009, 2010; Sureda *et al*., 2010).

2.3.3.3 Secondary Phases. Uranyl Minerals

Although uranium has four possible oxidation states (from +3 to +6), only two oxidation states exist in nature. These two states are the corresponding to uranium tetravalent U(IV) and hexavalent U(VI), which occur in reduced and oxidized environments, respectively. Therefore, the uranium minerals can be generally classified in 2 categories: The U(IV) minerals and the U(VI) minerals. In this research, we expect to have oxidizing conditions and, therefore, focus our attention on the structure and chemistry of the U(VI) minerals, which are the minerals formed in an oxidized environment.

2.3.3.3.1 Structure of U(VI) Minerals

In minerals including the U^{6+} cation, the uranium ion is present as part of the nearly linear uranyl ion UO_2^{2+} (Evans, 1963), which is the main constituent in all U(VI) phases. In the uranyl ion, the U-O bond lengths are ~ 1.8 Å, corresponding to strong covalent bonds. The U-O bonding mechanism in uranyl ion is primarily through donation of electrons from the p orbitals of the O atoms into the empty d and f orbitals of the U^{6+} cation (Craw *et al*., 1995). The uranyl ion has a formal valence of 2+, and as such, it must be coordinated by ligands in a crystal structure. The uranyl ion can be coordinated by four, five, or six ligands arranged at the equatorial corners, forming square bipyramids, pentagonal bipyramids, and hexagonal bipyramids, respectively (see Fig. 2-21). These ligands are O^{2-}, OH^-, and H_2O. The O atoms of the uranyl ion are located at the apices of the bipyramids. The equatorial bonds are longer than the uranyl U-O bonds and therefore weaker (Burns *et al*., 1996; Burns, 1999a).

The U(VI) minerals can be classified structurally according to their sheet anion topologies, which is a hierarchy suggested by Burns *et al*. (1996). The sheet anion topology contains triangles, squares, pentagons, and hexagons. It can be derived as follows (Figure 2-22):

1) Each anion that is not bonded to at least 2 anions within the sheet, and is not an equatorial anion of a bipyramid or pyramid within the sheet, is not considered a constituent of the sheet anion topology (Fig. 2-22c).

2) Cations are ignored, also the cation-anion bond, leaving an array of unconnected anions (Fig. 2-22d).

3) Anions are joined by lines, such that only anions that may be realistically considered as part of the same coordination polyhedron are connected (Fig. 2-22e).

4) Anions are removed from further consideration, leaving only a series of lines that represent the sheet anion topology (Fig. 2-22f).

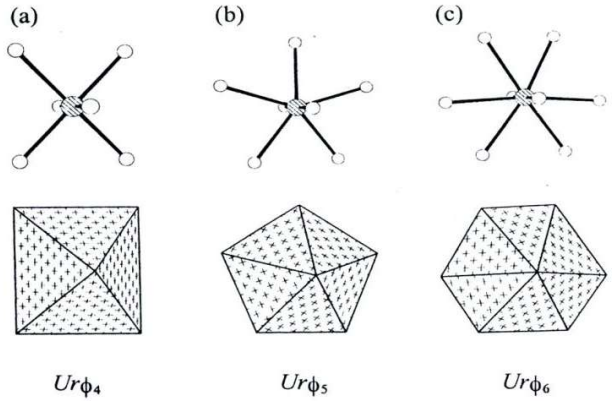

Figure 2-21. Types of coordination polyhedra observed in U(VI) minerals (Burns, 1999a).

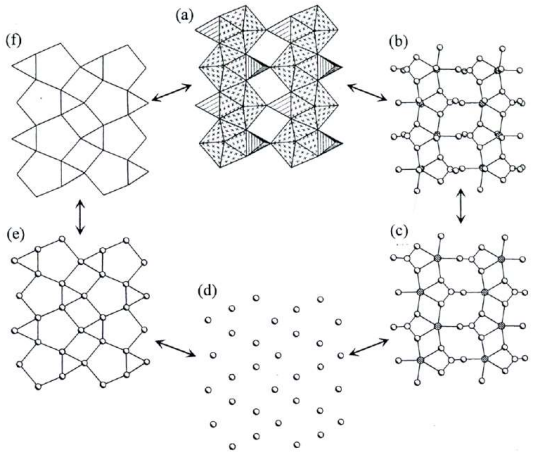

Figure 2-22. The development of a sheet anion topology (Burns *et al*. 1996).

The different minerals will be categorized by applying the concept of the hierarchy to the U(VI) minerals. For example, minerals like uranophane-α, $Ca(UO_2)_2(SiO_3OH)_2(H_2O)_5$ and ulrichite $CaCu(UO_2)(PO_4)_2(H_2O)_4$ have the same sheets that are based on anion topologies with triangles, squares, and pentagons, despite the fact that these minerals have different ligands.

2.3.3.3.2 Chemistry of U(VI) Minerals

The dissolved uranium in solution under the simulated oxidizing laboratory conditions presents the most oxidized state in nature, U^{6+}. Consequently, these conditions would lead to the formation of the uranyl ion UO_2^{2+}. The uranyl ion is the dominant aqueous species in most waters below pH 5. At higher pH, the uranyl ion hydrolyses, forming several aqueous hydroxide complexes (Finch and Murakami, 1999), according to the general hydrolysis reaction

$$UO_2^{2+} + yH_2O \rightarrow UO_2(OH)_y^{2-y} + yH^+ \quad (2.8)$$

In more U-rich solutions, polymeric U complexes could be formed:

$$xUO_2^{2+} + yH_2O \rightarrow (UO_2)_x(OH)_y^{2x-y} + yH^+ \quad (2.9)$$

Consequently, the precipitation of these solutions with dissolved U concentrations, would lead to the formation of many uranyl minerals depending mainly on the pH and the concentration of the different species dissolved. Fig. 2-23 shows the paragenesis of the main uranyl mineral groups

The uranyl or U(VI) minerals belong to different chemical groups. These minerals display remarkable structure and chemical diversity. This diversity results from different chemical conditions under which U minerals are formed. Therefore, the U minerals are excellent indicators of the geochemical environment (Finch and Murakami, 1999). The chemical groups can be classified as explained in the next section.

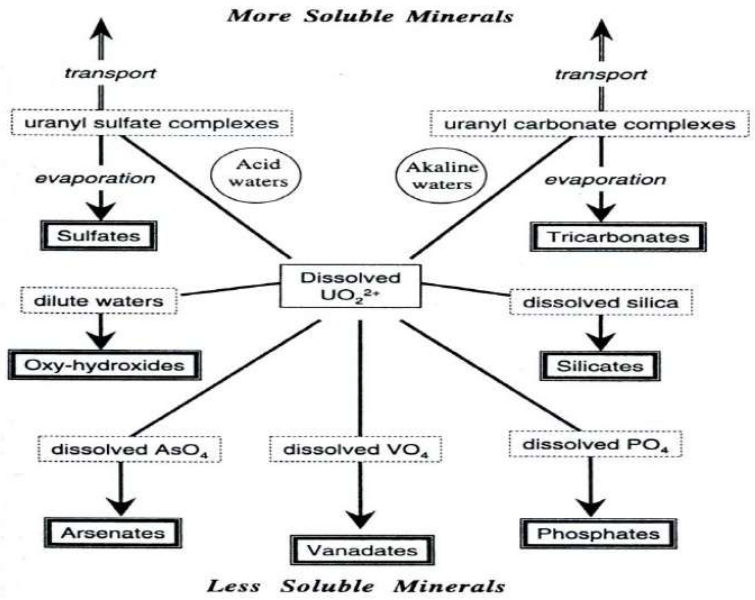

Figure 2-23. Scheme of the paragenesis of major uranyl minerals groups (Finch and Murakami, 1999).

2.3.3.3.3 Chemical Groups of U(VI) Minerals

The differences among these groups are defined by the different ligands attached in their structures. In general, the ligands can be ions as oxygens, hydroxyls, carbonates, silicates, phosphates, arsenates, vanadates, molybdates, tungstates, sulfates, selenites, or tellurites, or neutral water molecules.

2.3.3.3.3.1 Uranyl-Oxyhydroxides Group

This group of minerals can be presented by the general formula:

$$M_n\left[(UO_2)_xO_y(OH)_z\right] \cdot m\,H_2O$$

where M is the cation, generally divalent, commonly Ca^{2+}, Pb^{2+}, Ba^{2+}, Sr^{2+}, although monovalent cations as K^+ are also possible. They form in uranium rich aqueous solutions and develop early during the oxidation and corrosion of uraninite-bearing ore deposits. Table 2-5 shows some of the

common minerals from this group. Uranyl oxyhydroxides with Na or Mg were found in nature, but they were synthesized.

Table 2-5. Main minerals in the uranyl-oxyhydroxides group (Grenthe *et al.*, 2006).

Name	Formula
Agrinierite	$(K_2,Ca,Sr)(UO_2)_3O_3(OH)_2 \cdot 4H_2O$
Becquerelite	$Ca(UO_2)_6O_4(OH)_6 \cdot 8H_2O$
Billietite	$Ba(UO_2)_6O_4(OH)_6 \cdot 8H_2O$
Compreignacite	$K_2(UO_2)_6O_4(OH)_6 \cdot 8H_2O$
Schoepite	$(UO_2)_8O_2(OH)_{12} \cdot 12H_2O$
Metaschoepite	$(UO_2)_8O_2(OH)_{12} \cdot 10H_2O$
Fourmarierite	$Pb(UO_2)_4O_3(OH)_4 \cdot 4H_2O$
Vandendriesscheite	$Pb(UO_2)_{10}O_6(OH)_{11} \cdot 11H_2O$

2.3.3.3.3.2 Uranyl Peroxide Hydrates Group

There are only two uranyl peroxide minerals known. They are shown in Table 2-6.

Table 2-6. Minerals in the uranyl peroxide hydrates group (Grenthe *et al.*, 2006).

Name	Formula
Studtite	$UO_2(O_2) \cdot 4H_2O$
Metastudtite	$UO_2(O_2) \cdot 2H_2O$

2.3.3.3.3.3 Uranyl Carbonates Group

They may precipitate where evaporation is significant or where the fugacity of CO_2 is greater than the atmospheric pressure. Mono- di- and tricarbonates can precipitate from acidic to alkaline waters respectively. The monocarbonates are relatively insoluble while the di- and tri-carbonates are soluble when re-exposed to fresh water. Table 2-7 shows some of the minerals from this group.

Table 2-7. Main minerals in the Uranyl-carbonates group (Grenthe *et al.*, 2006).

Name	Formula
Blatonite	$UO_2CO_3 \cdot H_2O$
Rutherfordine	UO_2CO_3
Voglite	$Ca_2Cu(UO_2)(CO_3)_4 \cdot 6H_2O$
Fontanite	$Ca(UO_2)_3(CO_3)_2O_2 \cdot 6H_2O$
Rabbittite	$Ca_3Mg_3(UO_2)_2(CO_3)_6(OH)_4 \cdot 18H_2O$
Liebigite	$Ca_2(UO_2)(CO_3)_3 \cdot 11H_2O$

2.3.3.3.3.4 Uranyl Silicates Group

They are the most abundant group of uranyl minerals because of the ubiquity of dissolved Si in most groundwaters. Uranophane is the most common uranyl mineral, precipitating from near neutral to alkaline groundwaters that contain dissolved Si and Ca. These minerals might lose some

Ca and Si when exposed to carbonate-free waters, altering to more uranium rich minerals such as uranophane and soddyite. In more alkaline carbonate-rich waters, they may lose uranium preferentially, altering to amorphous or microcrystalline silica. Table 2-8 shows some of the minerals from this group.

Table 2-8. Main minerals in the Uranyl-silicates group (Grenthe *et al.*, 2006).

Name	Formula
Uranophane	$Ca(UO_2)_2(SiO_3OH)_2 \cdot 5H_2O$
Boltwoodite	$K(UO_2)(SiO_3OH) \cdot 1.5H_2O$
Kasolite	$Pb(UO_2)(SiO_4) \cdot H_2O$
Sklodowskite	$Mg(UO_2)_2(SiO_3OH)_2 \cdot 6H_2O$
Soddyite	$(UO_2)_2SiO_4 \cdot 2H_2O$
Weeksite	$K_2(UO_2)_2(Si_6O_{15}) \cdot 4H_2O$

2.3.3.3.3.5 Uranyl Phosphates and Arseniates Group

Dissolved phosphate is a common constituent of many groundwaters. Uranyl phosphates and arsenates precipitate from waters when dissolved phosphate, PO_4, and arseniate, AsO_4 are available and they show low solubilities. This group has approximately 70 species. Table 2-9 shows some of the minerals from this group.

Table 2-9. Main minerals in the Uranyl-phosphates group (Grenthe *et al.*, 2006).

Name	Formula
Autunite	$Ca[(UO_2)(PO_4)]_2 \cdot 10\text{-}12H_2O$
Sabugalite	$Al[(UO_2)_4(HPO_4)(PO_4)_3] \cdot 16H_2O$
Saleeite	$Mg[(UO_2)(PO_4)]_2 \cdot 10H_2O$
Bassetite	$Fe[(UO_2)(PO_4)]_2 \cdot 8H_2O$
Meta-autunite	$Ca[(UO_2)(PO_4)]_2 \cdot 6H_2O$
Metatorbernite	$Cu[(UO_2)(PO_4)]_2 \cdot 8H_2O$
Dewindtite	$Pb_3[(UO_2)_3O(OH)(PO_4)_2]_2 \cdot 12H_2O$
Ulrichite	$CaCu(UO_2)(PO_4)_2 \cdot 4H_2O$

2.3.3.3.3.6 Uranyl Vanadates, Molybdates and Tungstates Group

This group comprises the most insoluble uranyl minerals. Table 2-10 shows some of the minerals from this group.

Table 2-10. Main minerals in the Uranyl-vanadates, molybdates, tungstates group (Grenthe *et al.*, 2006).

Name	Formula
Carnotite	$K_2(UO_2)_2(V_2O_8) \cdot 3H_2O$
Tyuyamunite	$Ca(UO_2)(V_2O_8) \cdot 8H_2O$
Iriginite	$(UO_2)(Mo_2O_7) \cdot 3H_2O$
Uranotungstite	$(Ba,Pb,Fe^{2+})(UO_2)_2(WO_4)(OH)_4 \cdot 12H_2O$

2.3.3.3.3.7 Uranyl Sulfates, Selenites and Tellurites group

Dissolved sulfate in groundwater can combine with UO_2^{2+} to form stable uranyl sulphate complexes in solution. Afterwards, evaporation is required to precipitate uranyl sulfates. They can precipitate from waters with pH less than 6. Uranyl sulfates occur where uranyl carbonates are absent (and vice versa). This might reflect the different pH ranges over which uranyl sulfate and uranyl carbonate complexes are important. Table 2-11 shows some of the minerals from this group.

Table 2-11. Main minerals in the Uranyl-sulfates, selenites, tellurites group (Grenthe *et al.*, 2006).

Name	Formula
Johannite	$Cu(UO_2)_2(SO_4)_2(OH)_2 \cdot 6\text{-}8H_2O$
Uranopilite	$(UO_2)_6(SO_4)O_2(OH)_6(H_2O)_6 \cdot 8H_2O$
Meta-uranopilite	$(UO2)_6(SO_4)(OH)_{10} \cdot 5H_2O$
Haynesite	$(UO_2)_3(SeO_3)_2(OH)_2 \cdot 5H_2O$
Cliffordite	UTe_3O_9

Chapter 3. Materials and Methods

3.1 Experimental Methods and Materials

Several experimental techniques have been used in this study. These techniques dealt with solid samples of the material considered in order to identify or characterize the solid phases qualitatively and quantitatively. These are:

1- Raman Spectroscopy.

2- SEM (Scanning Electron Microscope).

3- Powder X-ray Diffraction.

4- Thermal analysis: TGA/DTG

3.1.1 Raman Spectroscopy.

The inelastic scattering of light was initially predicted by Smekal (1923), thought it was not until 1928 that Raman performed the first experiment (Raman and Krishnan, 1928) and confirmed the predictions of Smekal, obtaining the Nobel Prize in Physics in 1930. In his Nobel lecture (Raman, 1930), given on 11th December 1930, Sir C.V. Raman said: "*The frequency differences determined from the spectra, the width and character of the lines appearing in them, and the intensity and state of polarization of the scattered radiations enable us to obtain an insight into the ultimate structure of the scattering substance. […] It follows that the new field of spectroscopy has practically unrestricted scope in the study of problems related to the structure of matter*". Raman technique allows to study vibrational, rotational, and other low-frequency modes in a system. Since vibrational information provided by this technique is specific for the chemical bonds in the system studied, Raman spectroscopy provides a fingerprint by which the system can be identified.

When monochromatic radiation impact upon a sample, this light may be reflected, absorbed or scattered. Raman effect is described as a process of inelastic scattering of light with matter. From a macroscopic point of view, light scattering consists in a deviation of light from its straight trajectory (original direction of incident light, see Figure 3-1). A system scatters light because the electric field of the incident light wave forces the electrons within the system to oscillate producing oscillating electric moments leading to the reemission of radiation in all directions. Unlike 'Rayleigh scattering', which corresponds to an elastic light scattering (Strutt, 1899; the authentic name of Lord Rayleigh was John Strutt), 'Raman scattering' is an inelastic process of light due to various elementary excitations (quasi-excitations) where the energy is lost or gained during the scattering process. These excitations may be, for example, the internal vibration modes in a molecule (vibrons), phonons in an ordered crystal structure (lattice vibrations) or magnons in systems with magnetic-order transitions.

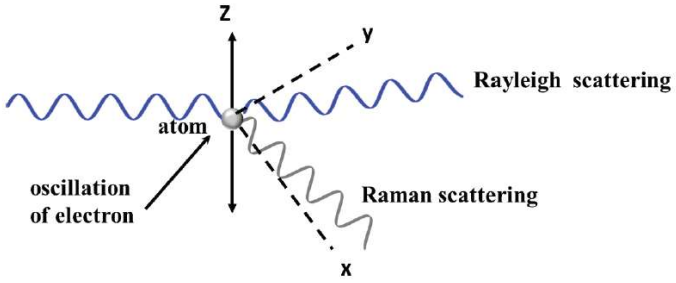

Figure 3-1. Light scattering produced by the interaction of the incident light's electric field and the electrons of the system (Bonales *et al.*, 2016b).

In conventional Raman spectroscopy, the sample is irradiated by an intense monochromatic laser beam in the UV-visible region (ν_0) and the scattered light results from two types of processes: (1) 'Rayleigh scattering' (or elastic scattering), which is strong and leads to light having the same frequency as the incident beam (ν_0); (2) 'Raman scattering' (or inelastic scattering), which is very weak (10^{-5}–10^{-8} of the incident beam intensity) and leads to light having the frequencies $\nu_0 \pm \nu_m$, where ν_m is a vibrational frequency of the system (in general the elementary excitations are: vibrons, phonons, magnons). The $\nu_0 + \nu_m$ and $\nu_0 - \nu_m$ lines are referred to as the 'Stokes' and 'Anti-Stokes' lines, respectively. Thus, in Raman spectroscopy, we measure the vibrational frequency (ν_m) as a shift from the incident-beam frequency (ν_0).

Figure 3-2 shows the basic processes which occur when light interacts with a matter sample. At room temperature, most systems, but not all, are present in the lowest-energy vibrational level (m state) (Maxwell-Boltzmann distribution law). Virtual states are not real states of the molecule but are created when the laser interacts with the electrons and causes polarization. Thus, the energy of these states is determined by the frequency of the light source used (ν_0). The Rayleigh process will be the most intense process as most photons scatter in this way. It does not involve any energy change and, consequently, the light returns to the same energy state. The Raman scattering process from the ground vibrational state m leads to the absorption of energy by the molecule and its promotion to a higher-energy excited vibrational state (n). This is called 'Stokes scattering'. However, due to thermal energy, some molecules may be present in an excited state, such as n in Figure 3-2. Scattering from these states to the ground state m is called 'anti-Stokes scattering', which involves transfer of energy to the scattered photon. The relative intensities of the two processes depend on the population of the various states of the molecule and, therefore, on temperature according to the Maxwell-Boltzmann distribution. Under normal conditions the population of molecules at state m is much larger than at state n. Thus, the 'Stokes' lines are normally stronger than the 'anti-Stokes' lines. As both give the same information, it is customary to measure only the 'Stokes' side of the spectrum.

Even though the general scheme of Figure 3-2 describes scattering phenomena in a qualitative way and highlights some key aspect of the Raman spectroscopy and its differences with the absorption process, it is worth to describe the classical treatment of the Raman scattering in order to provide a deeper insight in the frequency dependence and the microscopic origin of the scattered light. Classically (Weber and Merlin, 2000; Lewis and Edwards, 2001), the Raman scattering can be explained by the time-dependent polarizability of the system. When a system is subjected to the electric field $E = E_0\, cos(\omega t)$ of electromagnetic radiation, the dipolar moment of the molecule p is given by:

$$p = \mu_0 + \alpha\, E \tag{3.1}$$

where, μ_0 is the permanent dipolar moment and $\alpha\, E$ is the induced dipolar moment.

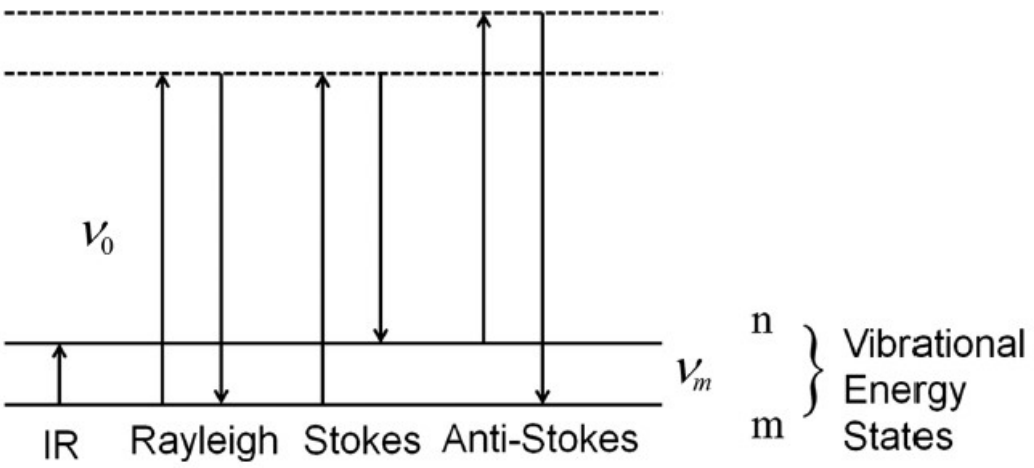

Figure 3-2. Diagram of the Rayleigh and Raman scattering processes (Rull, 2012). The lowest energy vibrational state m is shown at the bottom with states of increasing energy above it. Both the excitation energy (upward arrows, $E = h\nu_0$) and the scattered energy (downward arrows, $E = h[\nu_0 - \nu_m]$ and $E = h[\nu_0 + \nu_m]$) are much larger than the energy of a vibration ($E = h\nu_{\mathrm{m}}$).

The polarizability, α, is represented by a second-order tensor with components α_{ij}. For small vibrations assumed to be harmonic, the normal coordinates $q_n(t)$ of a vibrating molecule can be approximated as $q_n(t) = q_{n0}cos(\omega_n t)$, where q_{n0} is the amplitude, and ω_n is the vibration frequency of the normal mode n. The total dipolar moment is given by:

$$p = \mu_0 + \alpha(0)\, E_0 cos(\omega t) + \sum_{n=1}^{Q} \left(\frac{\partial \mu}{\partial q_n}\right)_0 q_{n0}\, cos(\omega t)$$
$$+ \frac{1}{2} E_0 \sum_{n=1}^{Q} \left(\frac{\partial \alpha}{\partial q_n}\right)_0 q_{n0}\, [cos(\omega + \omega_n)t + cos(\omega - \omega_n)t] \qquad (3.2)$$

where, we have made a power series expansion of q_n, μ and α, and we have taken into account only terms of first order. The second term in this equation describes the Rayleigh scattering, the third term corresponds to the infrared spectrum and the fourth term to the Raman scattering. Therefore, if $(\partial\alpha/\partial q_n)_0$ is zero, the molecular vibration is not 'Raman active'. To be Raman-active, the rate of change of polarizability with vibration must not be zero.

A symmetric tensor, as the polarizability tensor, can be expressed as the sum of two symmetric tensors,

$$\alpha = \alpha^{iso} + \alpha^{aniso} \qquad (3.3)$$

$$\alpha^{iso} = \begin{pmatrix} \alpha_{xx} & 0 & 0 \\ 0 & \alpha_{yy} & 0 \\ 0 & 0 & \alpha_{zz} \end{pmatrix} \quad \alpha^{aniso} = \begin{pmatrix} 0 & \alpha_{xy} & \alpha_{xz} \\ \alpha_{xy} & 0 & \alpha_{yz} \\ \alpha_{xz} & \alpha_{yz} & 0 \end{pmatrix} \qquad (3.4)$$

Therefore, the Raman intensity can be always represented as the sum of an isotropic part, which has no angular dependence, and an anisotropic part, which is dependent on the orientation,

$$\bar{\alpha} = \frac{1}{3}\left(\alpha_{xx} + \alpha_{yy} + \alpha_{zz}\right) \qquad (3.5.a)$$

$$\gamma^2 = \frac{1}{2}\left(\left[\alpha_{xx} - \alpha_{yy}\right]^2 + [\alpha_{xx} - \alpha_{zz}]^2 + [\alpha_{yy} - \alpha_{zz}]^2 + 6\left[\alpha_{xy}^2 + \alpha_{xz}^2 + \alpha_{yz}^2\right]\right) \qquad (3.5.b)$$

The intensity of a Raman line is determined by the scattering cross section, σ_i , of the transition between the vibrational energy levels E_0 and E_i. According to the Placzek´s classical approach,

the differential cross section for Raman scattering at right angles to the direction of an incident plane-polarized light for the vibration i, described by the normal coordinate Q_i, is given by:

$$\frac{d\sigma_i}{d\Omega} = C\ \frac{1}{45} g_i[45(\bar{\alpha}_i')^2 + 7(\gamma_i')^2] \tag{3.6}$$

where C is a constant, g_i is the degeneracy of the i vibration and the quantity $A_i = 45(\bar{\alpha}_i')^2 + 7(\gamma_i')^2$ is known as the Raman activity of the i vibration. This quantity is also known as the absolute differential Raman scattering cross section. The measured intensity under a monochromatic illumination of I_0 intensity is given by

$$I_i = I_0 \frac{(2\pi)^4}{45}\ C\ g_i A_i \frac{(\nu_0 - \nu_i)^4}{1 - exp\left\{-\frac{hc\nu_i}{kT}\right\}} \tag{3.7}$$

Measuring the intensity observed at polarizations $I_\perp$ and $I_{||}$ results in the depolarization ratio,

$$\rho = \frac{I_\perp}{I_{||}} \frac{3(\gamma_i')^2}{45\left(\bar{\alpha}_i'\right)^2 + 4\left(\gamma_i'\right)^2} \tag{3.8}$$

Much effort (mainly between the 1950s and 1980s) has been devoted to theoretical calculations of the polarizability derivatives using internal and Cartesian coordinates with the aim of obtaining absolute intensity parameters which could be transferred between molecules with similar chemical-bond characteristics.

As stated in previous paragraphs, the conditions for vibrations to be 'Raman active' are that the first derivative of the associated polarizability is non-zero. This applies to the tensor components and, thus, if at least one of the six components of the polarizability tensor are non-zero, the vibration is Raman active. For infrared spectroscopy (IR) it can similarly be seen that at least one of the three dipole moment derivatives must be non-zero. The Raman tensor and the IR dipole moment components and its derivatives with respect to normal coordinates are related directly to the molecular geometry (i.e. symmetry). For a given vibration symmetry, there is the possibility that both the Raman tensor and the IR dipole moment derivatives must be non-zero, that only one of these derivatives (Raman or IR) is non-zero or both are equal to zero. In the particular case of molecules with a centre of symmetry, the Raman activity implies non-IR activity and vice versa. This is known as the mutual exclusion rule and its application is very useful in assessing the geometry (or point group) of a molecule or molecular assemblage.

The inelastic scattering of an incident photon by the phonons (lattice vibrations) in a crystal is a process more complex than the one described above and is defined as an interaction process of the third order, which includes the electron-radiation (photon) and electron-lattice (phonon) interactions. A photon of frequency ω_0 and wave vector k_0 cannot interact directly with the lattice, but rather interacts with electrons by the electron-radiation interaction, creating in the process an electron-hole pair. Then, it creates (or destroys) a phonon of frequency ω_n and wave vector k_n via electron-lattice interaction and, finally, the electron recombines with the hole through the electron-radiation interaction. More details about the Raman spectroscopy in solids are given in later sections.

From the description of the Raman effect given above, it is easy to understand that in a conventional (or dispersive) Raman spectrometer, the main difficulty lies in separating the intense light of the Rayleigh scattering from the much weaker Raman-scattered light. Besides, because Raman scattering has low efficiency, the optimization of each of the instrumental components becomes critically important. The main components of a Raman setup are as follows:

(1) Excitation source
(2) Sample illumination systems and collection optics
(3) Wavelength selectors and separators
(4) Detector
(5) Recording device

Excitation source: Traditionally, mercury arc lamps were used as light sources until being replaced by laser sources. Laser beams are highly monochromatic, present small diameter and, with the help of different optic devices, can be focused on small samples. Different lasers can be used as the light source in Raman spectrometry. An example is the He-Ne laser producing monochromatic radiation with a wavelength of 632.8 nm. In addition, in order to enhance the laser quality, it is possible to employ a pass-band filter, designed to pass only a certain band of frequencies while attenuating all signals outside this band. This component is commonly known as interferometric filter.

Sample illumination system and collection optics: The collimation and focusing optics of the exciting radiation onto the sample depends on the experimental setup. In principle, excitation and collection from the sample can be accomplished in any geometry, although those forming angles of 90 and 180°C (backscattering) between the initial and scattered beams are more frequently employed. The use of fiber optics helps to make the spectrometers more versatile.

Wavelength selectors and/or separators: The separation or removal of the intense Rayleigh scattering can be achieved by using two different types of filters: notch and edge filters. Notch filters allow the acquisition of the anti-Stokes and Stokes Raman spectra down to ~30 cm^{-1}, but their use is expensive since they must be replaced very frequently (~2 years). For this reason, the use of edge filters is widespread. These are wide pass-band filters, which imply that the anti-Stokes Raman spectrum cannot be obtained and typical minimum wavenumbers are ~50 cm^{-1}. After the removal or suppression of the Rayleigh radiation, the separation of the different Raman radiations scattered by the sample should be performed. The first Raman spectrometers used prisms but, nowadays, these are replaced by gratings that are typically holographically produced. It is worth noting that filters can be neglected if coupling of two or three monochromators is set in a series. This configuration allows not only to separate the Raman lines but also to remove the Rayleigh scatter.

Detectors: Just like in other spectrometers, the former detectors, that is, photographic films, were substituted first by photodiode array detectors and then by charge transfer devices (CTDs) such as charge-coupled devices (CCDs). CCDs are silicon-based semiconductors arranged as an array of photosensitive elements, each one generating photoelectrons and storing them as an electrical charge. Charges are stored on each individual pixel as a function of the number of photons striking that pixel and then read by an analog-to-digital converter.

A schematic representation of a modern micro-Raman spectrometer is shown in Figure 3-3. In the micro-Raman technique, a microscope is integrated in a conventional Raman spectrometer, enabling both visual and spectroscopic measurements. As can be seen in Figure 3-3, in these types of equipment the focusing and collection optics of the scattered radiation are identical. In addition to the analysis of a single point, these spectrometers allow mapping and imaging measurements.

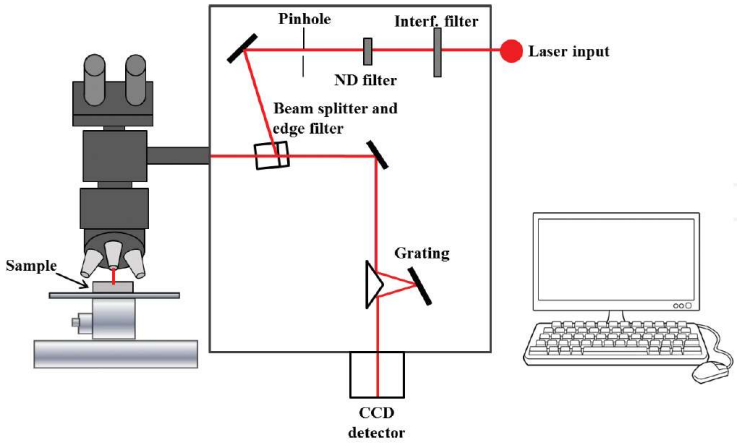

Figure 3-3. Descriptive scheme of the main components of a Raman micro-spectrometer.

3.1.1.1 *In situ* Raman Spectroscopy

In situ Raman characterization of the dehydration of studtite was carried out by using a Linkam temperature controlled pressure stage, THMS-600, coupled with the BX4 Olympus microscope of the Raman spectrometer (see Figure 3-4). The mechanical design and electronics of the Linkam stage provided precise control and temperature stability better than 0.2 K. Spectra were collected with a 50× long-range objective through a silica window (used in place of the standard quartz optical window) on the top of the stage.

Figure 3-4. Linkam THMS-600 system and the associated Linkam temperature controlled pressure stage.

A simple home cell had been specifically used to perform the *in situ* Raman measurements of studtite in contact with liquid water. This cell was mainly composed by two borosilicate glass cover slides separated by an O-ring. Therefore, the sample with water was housed between the two cover slides, separated by the O-ring.

Home-made cell

A very simple home-made cell had been used to perform the *in situ* Raman measurements of studtite in contact with liquid water. This cell is composed by two borosilicate glass cover slides of 22 mm diameter and 0.25 mm thickness separated by an O-ring of 20 mm diameter (see Fig. 3-5).

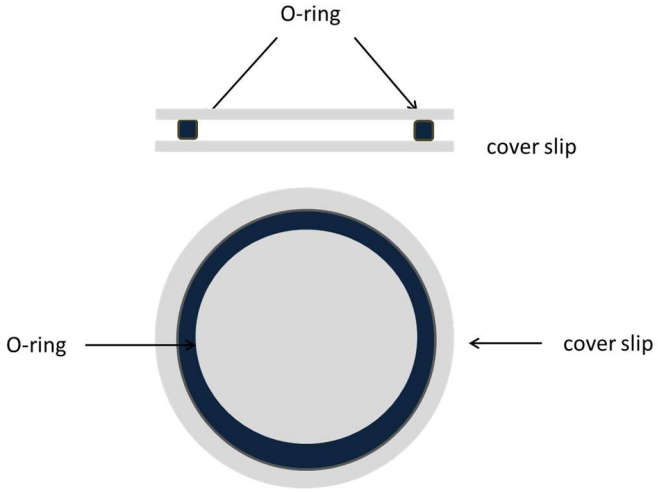

Figure 3-5. Home-made cell sketch (Colmenero *et al.*, 2017b).

In Figure 3-6 the setup is shown. First, we place an O-ring on top of a cover slip (1), then some milligrams (10-20 mg) of the solid sample is disposed on the surface of a cover slide provided with the O-ring, and a few drops of water are added over the solid (2) and, finally, the other cover slide was placed on the top the sample (studtite and water) (3). Therefore, the sample was housed between the two cover slides, separated by the O-ring.

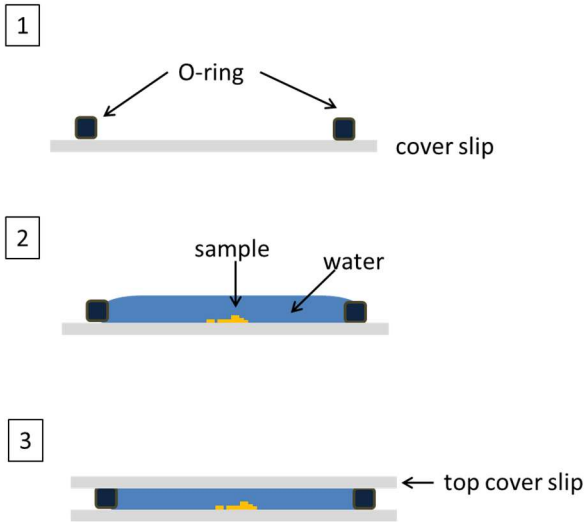

Figure 3-6. Home-made cell setup (Colmenero *et al.*, 2017b).

3.1.2 Scanning Electron Microscopy (SEM).

A scanning electron microscope (SEM) uses a focused electron beam to scan over a surface to create an image. The electrons in the beam interact with the sample, producing various signals that can be used to obtain information about the sample surface topography and composition. The scanning electron microscope is widely used in many industries and laboratories to investigate the microstructure and chemistry of a range of organic and inorganic materials. Specimens can be observed in high vacuum, in low vacuum, in wet conditions and at a wide range of cryogenic or elevated temperatures. Samples for SEM can be solid, bulk specimens of any size that will fit within the specimen chamber.

Given sufficient light, the human eye can distinguish two points 0.2 mm apart, without the aid of any additional lenses. This distance is called the resolving power or resolution of the eye. A lens or an assembly of lenses (a microscope) can be used to magnify this distance and enable the eye to see points even closer together than 0.2 mm. A modern light microscope has a maximum magnification of about 1000X. The resolving power of the microscope was not only limited by the number and quality of the lenses but also by the wavelength of the light used for illumination. White light has wavelengths from 400 to 700 nanometers (nm). The average wavelength is 550 nm which results in a theoretical limit of resolution (not visibility) of the light microscope in white light of about 200–250 nm. The electron microscope was developed when the wavelength became the limiting factor in light microscopes. Electrons have much shorter wavelengths, enabling better resolution.

The scanning electron microscope (SEM) produces images by scanning the sample with a high-energy beam of electrons. When the electron beam hits the surface of the sample, it penetrates the sample to a depth of a few microns, depending on the accelerating voltage and the density of the sample. As the electrons interact with the sample, they produce secondary electrons (SE), backscattered electrons (BSE) and characteristic X-rays. These signals are collected by one or more detectors to form images which are then displayed on the computer screen. The maximum resolution obtained in an SEM depends on multiple factors, like the electron spot size and interaction volume of the electron beam with the sample. While it cannot provide atomic resolution, some SEMs can achieve resolution below 1 nm. Typically, modern full-sized SEMs provide resolution between 1-20 nm, whereas desktop systems can provide a resolution of 20 nm or more.

The main SEM components include (see Fig. 3-7):

- Source of electrons
- Column with electromagnetic lenses
- Scan Coils
- Electron detector
- Sample chamber
- Computer and display to view the images

Electrons are produced at the top of the Column in an Electron Source by thermionic heating (for example, a tungsten filament). These electrons are then accelerated down and condensed into a narrow beam by using a combination of electromagnetic Lenses producing a focused beam of electrons which hits the surface of the sample for imaging and analysis. The sample is mounted on a stage in the Chamber area and, unless the microscope is designed to operate at low vacuums, both the column and the chamber are evacuated by a combination of pumps. The level of the vacuum will depend on the design of the microscope. The position of the electron beam on the sample is controlled by Scan Coils situated above the objective lens. These coils allow the beam to be scanned over the surface of the sample. This beam scanning, as the name of the microscope suggests, enables information about a defined area on the sample to be collected. As a result of

the electron-sample interaction, a number of signals are produced. These signals are then detected by appropriate Detectors and sent to a Computer which analyses them and generate the images. The sample chamber can include a translation stage, tilt and rotation devices, temperature stages, optical cameras, and a variety of other devices to assist in imaging the sample. Samples are generally mounted rigidly on a specimen holder using a conductive adhesive, but mechanical clamping is a possible alternative. For conventional imaging in the SEM, specimens must be electrically conductive, at least at the surface. Non-conducting materials are usually coated with an ultrathin coating of electrically conducting material.

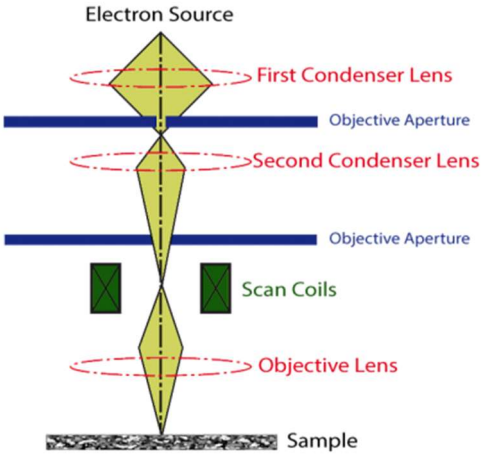

Figure 3-7. Scheme of a Scanning Electron Microscopy.

SEM images given in this work were analysed with a JEOL 5600-LV scanning electron microscope (SEM, see Figure 3-8) equipped with an Oxford Industries INCA X-sight energy dispersive X-ray spectrometer. The tablets were placed onto an aluminium sample holder and secured using adhesive carbon tape to promote conductivity between the pads and the holder. One grain is taken and then it is attached to the carbon disc and coated with liquid silver, exactly between the grain and the carbon disc. The top of the sample was coated with gold. The coatings are necessary to increase the conductivity of the samples. Since UO_2 pellets are semiconductor, the metallic coating is not necessary in this case.

Figure 3-8. JEOL 5600-LV scanning electron microscope (SEM).

3.1.3 X-ray Powder Diffraction (XRD).

Powder diffraction is a technique using X-ray, neutron, or electron diffraction on powder or microcrystalline samples for structural characterization of materials. An instrument dedicated to perform such powder measurements is called a powder diffractometer. In powder diffraction, every possible crystalline orientation is represented equally in a powdered sample. X-ray powder diffraction is used in two main areas, for the fingerprint characterization of crystalline materials and the determination of their structure. Each crystalline solid has its unique characteristic X-ray powder pattern which may be used as a "fingerprint" for its identification. Once the material has been identified, X-ray crystallography may be used to determine its structure, i.e. how the atoms pack together in the crystalline state and what are the corresponding interatomic distances and angles. X-ray diffraction is one of the most important characterization tools used in solid state chemistry and materials science.

Diffraction effects are observed when electromagnetic radiation impacts on periodic structures with geometrical variations on the length scale of the wavelength of the radiation. The interatomic distances in crystals and molecules amount to 0.15–0.4 nm, which correspond in the electromagnetic spectrum with the wavelength of X-rays having photon energies between 3 and 8 KeV. Accordingly, phenomena like constructive and destructive interference should become observable when crystalline and molecular structures are exposed to X-rays.

The unit cell is the basic repeating unit that defines the crystal structure. Parallel crystallographic planes of atoms intersecting the unit cell define directions and distances in the crystal. The Miller indices *h, k, l* defines an atomic plane *(hkl)* which intersects the crystallographic axes *a, b, c* at *x=a/h, y=b/k, z=c/k*. The crystallographic direction, *[hkl]* is perpendicular to the Miller plane *(hkl)* (see Figure 3-9). The symbol d_{hkl} denotes the distance between parallel atomic planes perpendicular to *[hkl]*. d_{hkl} is a geometric function of the size and shape of the unit cell.

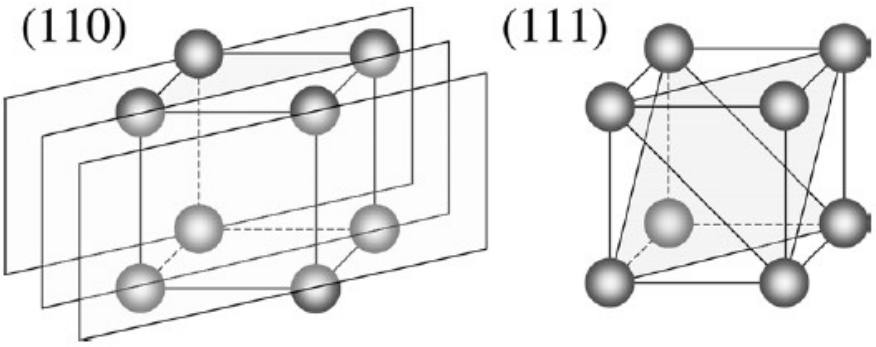

Figure 3-9. Lattice planes with Miller indices (110) and (111) in a simple cubic lattice.

Bragg's law provides a simplistic model to understand what conditions are required for diffraction, that is, the constructive interference of the radiation beams reflected by the crystal. For parallel planes of atoms, with a space d_{hkl} between the planes, constructive interference only occurs when Bragg's law is satisfied,

$$\lambda = 2\, d_{hk}\ sin\,\theta \tag{3.9}$$

The right-hand side of this equation is sometimes multiplied by an integer, n, since this condition also provides constructive interference, $n\,\lambda = 2\, d_{hkl} \sin\theta$. The difference of the path of the incident and reflected waves of each plane, $PD = 2\, d_{hk}\ \sin\theta$ is equal to some integer number n times the wavelength λ of the X-rays (see Fig. 3-10). Our convention, however, sets n = 1. When there is a path length difference of $n\,\lambda$ between adjacent planes, we change d (even though this new d may not correspond to a real interatomic distance). For example, when our diffracting planes are (100) cube faces, and

$$2\,\lambda = 2\,d_{100}\,sin\,\theta \qquad (3.10.a)$$

then, we speak of a (200) diffraction from planes separated by $d_{200} = d_{100}/2$.

$$\lambda = 2\,d_{200}\,\sin\theta \qquad (3.10.b)$$

Consequently, a family of planes *(hkl)* produces a diffraction peak only at a specific angle 2θ.

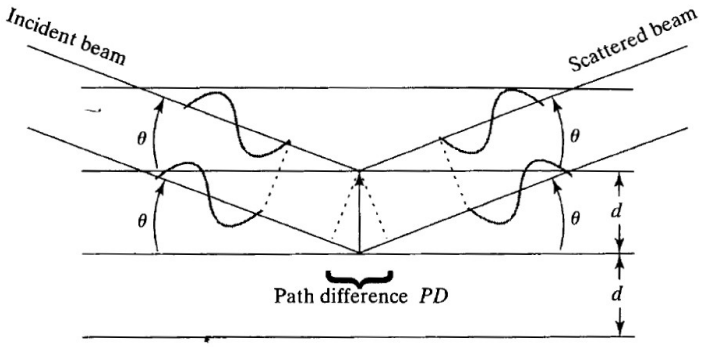

Figure 3-10. The constructive interference that leads to X-ray diffraction.

The intensity of the diffraction peaks is determined by the arrangement of atoms in the entire crystal (see Section 3.2.6). Diffraction patterns or diffractograms are collected as the absolute intensity versus 2θ but can also be reported in terms of d_{hkl}. A diffractogram is, therefore, a one-dimensional projection of three-dimensional structural information which represents a unique "fingerprint" of materials structure.

The distances among the planes, for a given set of *h, k, l* values, for each crystalline system may be obtained (in terms of the values of *h, k, l* and the lattice parameters, *a, b, c, α, β* and *γ*) from the value of $1/d_{hkl}^2$, given by the relations:

Cubic

$$\frac{1}{d^2} = \frac{h^2 + k^2 + l^2}{a^2} \qquad (3.11.a)$$

Tetragonal

$$\frac{1}{d^2} = \frac{h^2 + k^2}{a^2} + \frac{l^2}{c^2} \qquad (3.11.b)$$

Orthorhombic

$$\frac{1}{d^2} = \frac{h^2}{a^2} + \frac{k^2}{b^2} + \frac{l^2}{c^2} \qquad (3.11.c)$$

Hexagonal

$$\frac{1}{d^2} = \frac{4}{3}\left(\frac{h^2 + hk + k^2}{a^2}\right) + \frac{l^2}{c^2} \qquad (3.11.d)$$

Rhombohedral

$$\frac{1}{d^2} = \frac{(h^2 + k^2 + l^2)\,sin^2\alpha + 2\,(hk + kl + hl)(cos^2\alpha - cos\alpha)}{a^2(1 - 3\,cos^2\alpha + 2\,cos^3\alpha)} \qquad (3.11.e)$$

Monoclinic

$$\frac{1}{d^2} = \frac{h^2}{a^2\,sin^2\beta} + \frac{k^2}{b^2} + \frac{l^2}{c^2\,sin^2\beta} - \frac{2hl\,cos\beta}{ac\,sin^2\beta} \qquad (3.11.f)$$

Triclinic

$$\frac{1}{d^2} = \frac{\frac{h^2}{a^2}\,sin^2\alpha + \frac{k^2}{b^2}\,sin^2\beta + \frac{l^2}{c^2}\,sin^2\gamma + \frac{2kl}{bc}\,cos\alpha + \frac{2hl}{ac}\,cos\beta + \frac{2hk}{ab}\,cos\gamma}{1 - cos^2\alpha - cos^2\beta - cos^2\gamma + 2\,cos\alpha\,cos\beta\,cos\gamma} \qquad (3.11.g)$$

Our powder diffractometers typically use the Bragg-Brentano geometry, see Figure 3-11. The incident angle, ω, is defined as the angle between the X-ray source and the sample. The diffraction angle, 2θ, is defined between the incident beam and the detector. The incident angle ω is always 1/2 of the detector angle 2θ. In a θ:2θ instrument the tube is fixed, the sample rotates at θ °/min and the detector rotates at 2θ °/min. In a θ:θ instrument (e.g. PANalytical X'Pert), the sample is fixed, the tube rotates at a rate -θ °/min and the detector rotates at a rate of θ °/min. The mechanical assembly that makes up the sample holder and the tube and detector arms is referred to as goniometer.

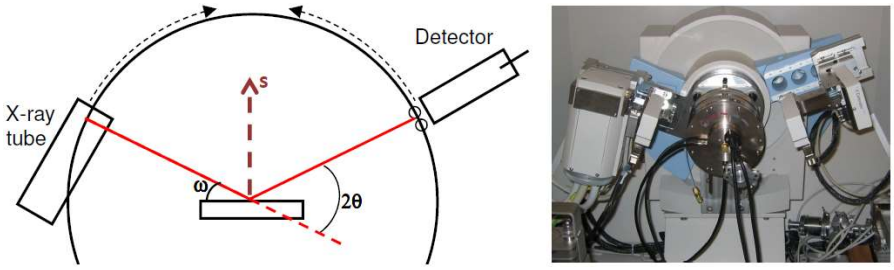

Figure 3-11. Bragg-Brentano powder diffractometer.

A polycrystalline sample should contain thousands of crystallites. Therefore, all possible diffraction peaks should be observed. In a powder diffraction, it is important to have a sample with a smooth plane surface, in order to have a random distribution of all possible *h, k, l* planes. Irradiating a large volume of material can help ensure that a statistically relevant number of grains contribute equally to the diffraction pattern.

Primary focus of X-ray powder diffraction if the phase identification, and lattice parameter and crystallite size determination. Profile fitting is the most precise way to determine diffraction peak position, intensity, and width for calculating lattice parameters and crystallite size. The resulting profile, may be recognized by comparison to known standards or international databases such as the Powder Diffraction File (PDF). Modern computer programs can help to determine what phases are present in your sample by quickly comparing your diffraction data to all the patterns in the database. The PDF contains over 300000 diffraction patterns associated to a huge amount of different crystalline phases. Each PDF card entry contains a lot of useful information, including literature references. The data usually includes mineral (common) name of the substance, chemical formula, crystalline system, and reference pattern number from the ICDD International database. Therefore, this method gives laboratories the ability to quickly analyse unknown materials and characterize them in such fields as metallurgy, mineralogy, forensic science, archaeology, and the biological and pharmaceutical sciences.

Since the diffraction pattern of a mixture is a simple sum of the scattering from each component phase, X-ray powder diffraction can also be used for quantitative phase analysis, that is for the quantitative determination of the sample composition. Temperature and pressure, substitutional doping, etc., can create changes in the pattern that may be quantified using this technique. *In-situ* X-ray diffraction can be used to study the dependence of the lattice parameters, crystallite size, composition, etc., as a function of temperature and pressure and can also yield quantitative analysis to study reaction pathways, rate constants, activation energy, and phase equilibria.

The *Rietveld method* is used to refine the crystal structure model of a material. It can be used for quantitative phase identification, lattice parameter and crystallite size calculations, and determine atom positions and occupancies. Rietveld refinement, named in honour of its pioneer, who distributed freely his method and code, represent the experimental diffraction pattern, both peaks and background, with a multi-parameter mathematical model. Rietveld refinement methods utilize the entire diffraction pattern of a crystal structure, not only one or two peaks in the diffraction pattern for obtaining certain types of information about the sample. The best set of these parameters is then found by an iterative calculation procedure that minimizes the difference between the calculated and measured diffraction patterns. A wide variety of parameters can be refined, including lattice parameters, atomic positions and crystallographic site occupancies.

In our studies, the samples were ground by a mortar to be prepared for the XRD measurement. The powder was pressed into 1 mm deep steel and brass holders (another holder of size 0.5 mm depth is chosen if the amount of the material available is small). X-ray diffraction patterns were collected using a Philips PANalytical X'Pert MPD diffractometer using Cu Kα radiation (λ = 1.54056 Å) and operating at 40 kV and 45 mA (see Fig. 3-12). Bragg-Brentano configuration geometry was used. The 2θ range covered was from 20° to 120°, with a scanning step of 0.02° and an overall exposure time of 18 hours.

Figure 3-12. Philips PANalytical X'Pert MPD diffractometer.

3.1.4 Thermal Analysis: TGA and DTG

Thermogravimetric analysis or thermal gravimetric analysis (TGA) is a method of thermal analysis in which changes in physical and chemical properties of materials are measured as a function of increasing temperature (with constant heating rate), or as a function of time (with constant temperature and/or constant mass loss). TGA measures mass changes in a material as a function of temperature (or time) under a controlled atmosphere. TGA can provide information about physical phenomena, such as second-order phase transitions, including vaporization, sublimation, absorption, adsorption, and desorption. Likewise, TGA can provide information about chemical phenomena including chemisorptions, desolvation (especially dehydration), decomposition, and solid-gas reactions (e.g., oxidation or reduction).

TGA is commonly used to determine selected characteristics of materials that exhibit either mass loss or gain due to decomposition, oxidation, or loss of volatiles (such as dehydration). Common applications of TGA are (1) materials characterization through analysis of characteristic decomposition patterns, (2) studies of degradation mechanisms and reaction kinetics, (3) determination of organic content in a sample, and (4) determination of inorganic (e.g. ash) content in a sample, which may be useful for corroborating predicted material structures or simply used as a chemical analysis. It is an especially useful technique for the study of polymer materials, including thermoplastics, thermosets, elastomers, composites, plastic films, fibers, coatings and

paints. Discussion of the TGA apparatus, methods, and trace analysis will be elaborated upon below.

Thermogravimetric analysis (TGA) relies on a high degree of precision in three measurements: mass change, temperature, and temperature change. Therefore, the basic instrumental requirements for TGA are: a precision balance with a pan loaded with the sample, and a programmable furnace. The furnace can be programmed either for a constant heating rate, or for heating to acquire a constant mass loss with time.

Though a constant heating rate is more common, a constant mass loss rate can illuminate specific reaction kinetics. Regardless of the furnace programming, the sample is placed in a small, electrically heated furnace equipped with a thermocouple to monitor accurate measurements of the temperature by comparing its voltage output with that of the voltage-versus-temperature table stored in the computer's memory. A reference sample may be placed on another balance in a separate chamber. The atmosphere in the sample chamber may be purged with an inert gas to prevent oxidation or other undesired reactions. A different process using a quartz crystal microbalance has been devised for measuring smaller samples on the order of a microgram (versus milligram with conventional TGA).

The TGA instrument continuously weighs a sample as it is heated to temperatures of up to 2000 ºC, and may be coupled to a FTIR and Mass spectrometry gas analysis. As the temperature increases, various components of the sample are decomposed and the weight percentage of each resulting mass change can be measured.

Knowing the mass of the starting material and the total mass of inclusions, such as ligands, structural defects, or side-products of reaction, which are liberated upon heating, the stoichiometric ratio can be used to calculate the percent mass of the substance in a sample. The results from thermogravimetric analysis may be presented by: (1) mass versus temperature (or time) curve, referred to as the thermogravimetric curve (TG), or (2) rate of mass loss versus temperature curve, referred to as the differential thermogravimetric (DTG) curve.

A simple thermogravimetric curve (results plotted with temperature on the X-axis and mass loss on the Y-axis) may contain the following features:

- A horizontal portion, or plateau that indicates constant sample weight
- A curved portion; the steepness of the curve indicates the rate of mass loss
- An inflection (at whichis a minimum, but not zero)

The data can be adjusted using curve smoothing, and first derivatives are often also plotted to determine points of inflection for more in-depth interpretations. This is because certain features in the TGA curve that are not readily seen can be more clearly discerned in the first derivative TGA curve. For example, any change in the rate of weight loss can immediately be seen in the first derivative TGA curve as a trough, or as a shoulder or tail to the peak, indicating two consecutive or overlapping reactions. Differential TGA curves can also show considerable similarity to differential thermal analysis (DTA) curves, which can permit easy comparisons to be made.

TGA can also be used to evaluate the thermal stability of a material. In a desired temperature range, if a species is thermally stable, there will be no observed mass change. Negligible mass loss corresponds to little or no slope in the TGA trace. TGA also gives the upper use temperature of a material. Beyond this temperature, the material will begin to degrade.

Thermal analysis experiments performed in this work were carried out by means of a Q50 thermobalance (TA Instruments, Spain, see Fig. 3-13) under a synthetic air flow with a constant rate of 60 mL per minute. The weighing precision of the thermobalance was 0.01%.

Figure 3-13. TA Instruments Q50 thermobalance.

3.1.5 Materials

Rutherfordine, soddyite and uranophane-α minerals studied in this work were obtained from a natural mineral sample. The studtite mineral was a synthetic one, whose synthesis procedure is described in detail in the next section.

The natural mineral sample is a ‘‘uraninite + gummite’’ mineral from Sierra Albarrana (Córdoba, Spain), collected during the uranium extractive activity in 1960. The sample structure corresponds to ideal gummite (Frondel, 1956) occurrence (central core black, composed by uraninite; and a yellow surrounding zone, formed by several minerals: ruthefordine, soddyite, uranophane and kasolite, see Figure 3-14). A detailed description of the mineral setting and other structural characteristics is described elsewhere (Bonales *et al*., 2015).

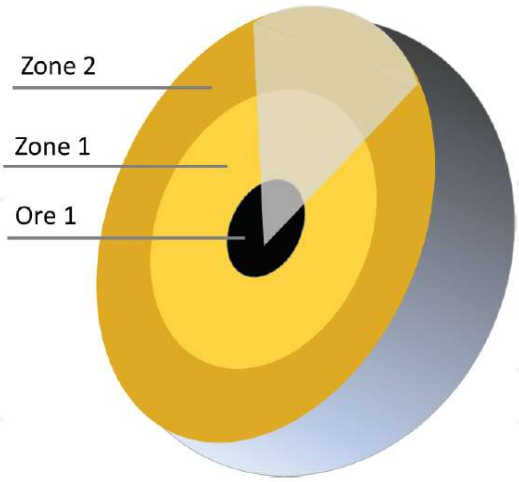

Figure 3-14. Scheme corresponding to the alteration rim of an oxidized uraninite crystal, as described by Frondel in 1956 (Bonales *et al.*, 2016b).

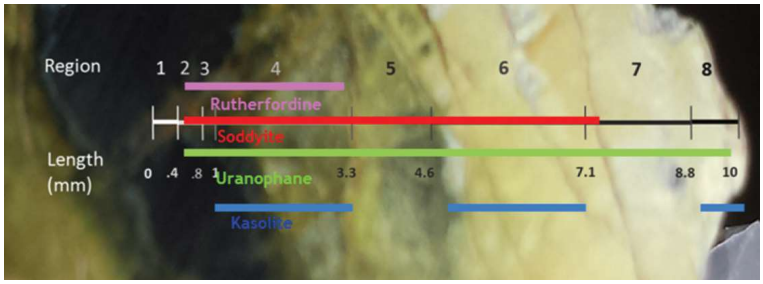

Figure 3-15. Sequence of the uraninite alteration products (Bonales *et al.*, 2016b).

This natural sample was analysed by Raman spectroscopy at different sections for characterizing each mineral. First, the natural sample was cut by using a diamond saw and polished. A polished section of the sample was analyzed via Raman spectroscopy by using a Horiba LabRam HR evolution spectrometer (Jobin Yvon Technology, see Figure 3-6). A HeNe laser with a wavelength of 632.81 nm and an operation power of 20 mW was used as the excitation source. The laser was focused onto the sample using the 100× objective of a confocal microscope (BX4 with confocal 800mm); the scattered light was collected with the same objective and then dispersed with a Jobin-Yvon spectrometer (600 grooves per mm), and detected with a Peltier cooled CCD detector (256 X 1024 pix.). The spectral resolution was about 1 cm^{-1} per pixel.

A combination of the line-mapping and step-by-step procedures were used to acquire the spectra in this kind of samples. Specifically, in this study a line mapping was performed using the automatized line-scanning tool. This tool allows Raman spectra acquisition of different sample points along a line by automatically moving the stage in one or two directions (X-Y). The microscope objective used with a magnification of 20× allows the visualization of a maximum 500 × 70-µm area. Therefore, in order to analyze the whole sample (10 mm), 20 lines with five equidistant points each have been measured, thus acquiring 100 spectra. This was performed with the step-by-step procedure, in which the motorized stage is moved 500 µm (the line-mapping length) in the x-direction to allow the analysis of the next part of the sample. The acquisition time for each spectrum was 100 s on an extended shift of 100–1200 cm^{-1}.

In order to perform a semi-quantitative analysis of the sample with the aim of detection of different phases along the sample, the spectra were processed by calculation of the second-derivative spectra in the ν_1 region (700–900 cm^{-1}). This allows to verify the existence of a minimum (corresponding to characteristic spectral peak) at each characteristic frequency. In Figure 3-15, a scheme is presented where the existence or absence of each phase at each position can be appreciated only by looking at the minimum of the second-derivative Raman spectrum.

3.1.5.1 Studtite Synthesis

Although the synthesis of uranyl peroxide hydrates from uranyl nitratres and hydrogen peroxide is known from the mid of the last century, the first work in which the precise concentrations of the reactives and the temperature conditions for the synthesis of studtite ($UO_2(O_2)\cdot 4H_2O$) and metastudtite ($UO_2(O_2)\cdot 2H_2O$) were studied was that of Sato (1963). In our work, synthetic studtite was precipitated at room temperature by adding dropwise a solution of 1M H_2O_2 (Sigma-Aldrich) over a solution of 10^{-4} M uranyl nitrate hexahydrate $UO_2(NO_3)_2\cdot 6H_2O$ (Sigma-Aldrich). This reaction yields yellow crystals, which were rinsed with cold water and dried before experiments. The precipitate was characterized by thermogravimetry (TGA), scanning electron microscopy (SEM), X-ray diffraction (XRD) and Raman spectroscopy (RS). The characterization results were reported by Colmenero *et al.* (2017b). A SEM image of the synthetic studtite crystals is given in Figure 3-16. An extended study of an alternative synthesis procedure of studtite (using uranium dioxide and hydrogen peroxide as reactives) was given by Palomo (2014).

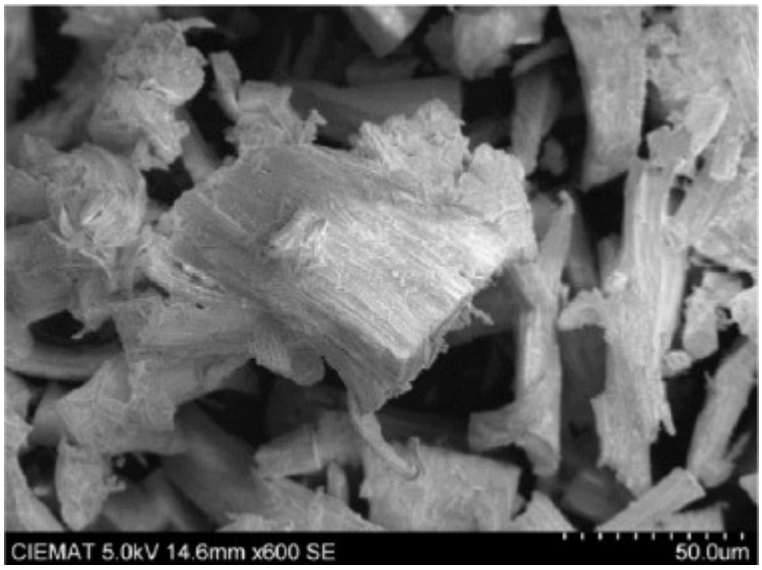

Figure 3-16. SEM image of the precipitated studtite crystals.

3.2 Theoretical and computational methods

Spectroscopic techniques are the ideal probe to investigate compositional and dynamical properties of a system at the atomic level together with structural techniques such us X-ray diffraction. In parallel with the technological development of spectroscopic instruments with improved resolution and sensitivity, the ever-growing computer capacities and performances have rendered possible the simulations of complex solid state systems with extreme precisions starting from its optimized crystalline unit cell structures.

In the context of this Thesis, the essential goal of the computer simulations is first to describe accurately the crystal unit cell of the structures of the analysed minerals in order to calculate the vibrational Raman spectrum to confront it to the experimental data measured in CIEMAT. In case of a good match, the atomic model will be considered as valid and Raman spectrum will be assigned. Further physical properties, such as mechanical and thermodynamic ones, can be predicted subsequently.

The aim of this Section is to describe the computational methods used in this work. The theoretical basis behind the DFT and the fundamental principles of the theory, which allows us to extract functions directly comparable to the experimental data, will be given. This Section starts with the description of the basis of the quantum chemistry and physics, and then, introduces very briefly the theorems and approximations at the origin of DFT. Then, the pseudopotencial approximation is depicted, which will be used to study the periodic solid state materials at atomistic level in order to predict physical properties, such us the infrared and Raman spectra, X-ray powder patterns and elastic and thermodynamical properties.

3.2.1 Quantum Chemistry and Physics

With the advent of Quantum Mechanics at the beginning of XX century, the human perception of the universe changed radically. Scientific community was highly surprised with the high degree of applicability of quantum mechanics, in spite of the difficulties associated to its application to real problems of interest. Formally, it is possible to obtain any desired information about a molecular system using Quantum Mechanics. As claimed by Dirac (1929) "The fundamental laws necessary for the mathematical treatment of a large part of physics and the whole of chemistry are thus completely known, and the difficulty lies only in the fact that application of these laws leads to equations that are too complex to be solved". In fact, we are not able to solve the Schrödinger wave equation exactly, except in a very small number of cases such as the hydrogen atom, the particle in a box and the harmonic oscillator. For larger systems, we need to use a large number of approximations to obtain a good description of the system under study.

Quantum mechanics allows to explain and predict the characteristics of ordinary matter: atoms, molecules and solids. Among these characteristics, we find: the energy, the electron density, the forces between the atoms o groups of atoms, the temporal evolution of these forces and the structural, vibrational, optical, mechanical and thermodynamic properties of these systems. The purpose of this work is precisely this: the description of solid materials by means of Quantum Mechanics. Due to the complexity of the systems studied, it is necessary to use approximations to get the best approximate solutions of the wave equations for these systems.

Despite the impressive improvements in experimental characterization of solid materials, it is difficult to interpret some experimental data and the origin of their behaviour at the atomic and molecular level. Some instrument can reach atomic-scale, e.g. atomic force microscopes (AFMs), but they require very expensive equipment to achieve this goal. Regarding the structure, it is difficult to assign unequivocally hydrogen atom positions in the crystal lattice from X-Ray diffraction (XRD) experiments, because they have smaller electron density than heavier atoms. A solution to the light atoms problem is provided by Neutron Diffraction methods, but this involves the use of another complex instrument. The interpretation of Infrared and Raman spectra of both

natural and synthetic samples can be complicated by several factors, as the presence of impurities (both in natural samples and synthetic ones), the nature and the morphology of the samples (powders or single crystals), the presence of overtones and/or combination peaks and the band broadening and overlap of signals.

Theoretical methods provide a powerful complement for the experimentalist to study different systems at nanoscale and sub-nanoscale (atomic) levels. Computational modelling theory provides a means to interpret and improve the experimental observations so that we become able to discriminate among various competing models to explain the macroscopic observation.

In the last twenty years, many works have been made coupling the experimental knowledge in mineralogy with several computational methods. The application of these approaches to the different observed phenomena is known as *computational mineralogy*, a multi-disciplinary subject where different aspects of computing science, physics, chemistry, geology and mathematics are meet. This field of research allows to reproduce and interpret experimental results and explore the behaviour of mineral systems under extreme conditions of temperature and pressure where experiments require a complex, cumbersome and expensive instrumentation and methods. The rapid growth in computing power allowed the application of theoretical simulations to study systems of increasing complexity. An account of the progress made in this field of research may be found in several excellent comprehensive reviews (Bleam, 1993; Dovesi *et al*., 2005)

3.2.2 Density Functional Theory (DFT)

Density functional theory, called DFT, it is one of the most popular and successful quantum mechanical approaches to matter (molecular and solid state) and has proven to be very powerful since its foundations in the sixties.

The beginning of DFT dates back to 1928 with the work by L. Thomas and E. Fermi (Thomas-Fermi model; Thomas, 1926; Fermi, 1928) but the real formulation was stablished by P. Hohenberg and W. Kohn in 1964 (Hohenberg and Kohn, 1964), who founded the formalism, introducing the approximations needed to model the interaction between the electrons.

Density functional theory attemps to provide a reliable approximate description of the electron distribution of the system and, therefore, it is first needed to introduce the approximation of separation of the electronic and nuclear motions, the Born-Oppenheimer approximation. Then, density functional theory will be introduced and the main approximations to the energy functional used in this work, the Perdew-Burke-Ernzerhof functional (Perdew *et al.*, 1996a), and its specialized variant for solids (Perdew *et al.*, 2008) will be described. Finally, the empirical dispersion correction of Grimme (Grimme, 2006) will be presented. The PBE functional with this empirical correction will be used for the case of systems in which non-bonded interactions are important since it improves the description of these systems significantly.

3.2.2.1. Born-Oppenheimer Approximation

The present PhD Thesis is centered in the use of full *ab initio* quantum-mechanics approach, which is based on solving the Schrödinger equation, which in the time-independent and non-relativistic formulation is given by:

$$H\Psi = E\Psi \qquad (3.12.a)$$

where, Ψ is the wavefunction (dependent on the spatial coordinates of electrons and nuclei), E is the total energy of the system and H is the Hamiltonian operator, which for a system composed of N_{el} electrons and N_{at} nuclei, is given by

$$H = -\frac{1}{2}\sum_{i=1}^{N_{el}} \nabla_i^2 - \frac{1}{2}\sum_{A=1}^{N_{at}} \frac{\nabla_i^2}{M_A} - \sum_{i=1}^{N_{el}} \sum_{A=1}^{N_{at}} \frac{Z_A}{r_{iA}} + \sum_{i<j}^{N_{el}} \frac{1}{r_{ij}} + \sum_{A<B}^{N_a} \frac{Z_A Z_B}{R_{AB}} \qquad (3.12.b)$$

where M_A and Z_A are the mass and charge of nucleus A, r_{iA} is the distance between electron i and nucleus A, r_{ij} is the distance between the electrons i and j, and R_{AB} is the distance between nucleus A and B. In this expression, all magnitudes are expressed in atomic units.

To solve this equation exactly it is not possible except in a small number of simple cases, such as hydrogen atom. In order to reduce the complexity of this equation, the first approximation which is usually made is the *Born-Oppenheimer approximation* (Born and Oppenheimer, 1927; Born and Huang, 1954). In this approximation, we consider the that since the nuclei have much larger masses, they remain nearly fixed during the electron motions. This permits to decouple the electronic and nuclear motions since the wavefunction of the system may be factorized as

$$\Psi(\boldsymbol{r}, \boldsymbol{R}) = \Psi^{el}(\boldsymbol{r}, \boldsymbol{R})\, \Psi^{N}(\boldsymbol{R}) \qquad (3.13)$$

where $\Psi^{el}(\mathbf{r}, \mathbf{R})$ and $\Psi^{N}(\mathbf{R})$ are the electronic and nuclear wavefunctions, respectively. In this equation **r** and **R** denote the coordinates of all the electrons and nuclei in the system, respectively. The nuclear wavefunction depends only on nuclear coordinates. For a fixed configuration of the nuclei, one may obtain the electronic wavefunction,

$$H^{el}\, \Psi^{el}(\boldsymbol{r}, \boldsymbol{R}) = E^{el}(\boldsymbol{R})\, \Psi^{el}(\boldsymbol{r}, \boldsymbol{R}) \qquad (3.14.a)$$

where,

$$H^{el} = -\frac{1}{2}\sum_{i=1}^{N_{el}} \nabla_i^2 - \sum_{i=1}^{N_{el}} \sum_{A=1}^{N_{at}} \frac{Z_A}{r_{iA}} + \sum_{i<j}^{N_{el}} \frac{1}{r_{ij}} = T^{el} + V^{Ne} + V^{ee} \qquad (3.14.b)$$

is the electronic Hamiltonian containing the electron kinetic energy, electron-nuclei repulsion and electron-electron repulsion terms, T^{el}, V^{Ne} and V^{ee}. Solving this equation for all nuclear positions one may determine the electronic energy $E^{el}(\boldsymbol{R})$ and utilize it as a potential in which the nuclei move,

$$H^{N}\, \Psi^{N}(\boldsymbol{R}) = E\, \Psi^{N}(\boldsymbol{R}) \qquad (3.15.a)$$

$$H^{N} = -\frac{1}{2}\sum_{A=1}^{N_{at}} \frac{\nabla_i^2}{M_A} + \sum_{A<B}^{N_a} \frac{Z_A Z_B}{R_{AB}} + E^{el}(\boldsymbol{R}) \qquad (3.15.b)$$

3.2.2.2. The Electronic Problem and DFT

The quantum mechanical approach based in the Schrödinger equation (3.14) may be described by means of the scheme:

$$H^{el} \xrightarrow{Schrödinger\ equation} \Psi^{el}(\boldsymbol{r_1}, \boldsymbol{r_2}, \ldots, \boldsymbol{r_n}) \xrightarrow{a=<\Psi|A|\Psi>/<\Psi|\Psi>} observables$$

For a given system, the electronic Hamiltonian operator of the system is constructed (for a given nuclear configuration). Then, the electronic wavefunctions may be calculated by solving the Schrödinger equation. Finally, the observables of the system are determined in terms of the corresponding wavefunctions. The properties of the system that require the knowledge of the nuclear wavefunctions may be determined by solving the electronic problem for a large set of nuclear conformations to determine the electronic potential, $E^{el}(\boldsymbol{R})$, and then solving the corresponding nuclear Schrödinger equation (3.15).

Even within the Born-Oppenheimer approximation, the solution of the electronic problem is extremely complex and numerous approximations for its solution has been devised. In this

section, we will present a short account of the Density Functional Theory (DFT), in which the full N-electron problem is replaced by a single electron approximation. The electron density of the system is an observable function that may be obtained from the electronic wavefunction from:

$$\rho(\boldsymbol{r}) = N^{el} \int d\boldsymbol{r_2} \int d\boldsymbol{r_3} \dots \int d\boldsymbol{r}_{N^{el}} \Psi^{el^*}(\boldsymbol{r_1}, \boldsymbol{r_2}, \dots, \boldsymbol{r_n}) \Psi^{el}(\boldsymbol{r_1}, \boldsymbol{r_2}, \dots, \boldsymbol{r_n}) \qquad (3.16)$$

In Density Functional Theory (Hohenberg and Kohn, 1964; Kohn and Sham, 1965; Parr and Yang, 1989), the calculation of the electronic wavefunction is replaced by the direct determination of the electron density which is a function of the coordinates of a single electron. Thus, it reduces the extremely complex N-electron problem to an effective single electron approximation. The quantum mechanical approach based in the electron density (DFT) may be described by means of the scheme:

$$\rho(\boldsymbol{r}) \xleftarrow{Kohn-Sham\ equations} E^{el}(\boldsymbol{R}) \xrightarrow{a=f(\rho A)} observables$$

In this case, the electron density is the basic variable of the system which determines the interaction potential between the electrons of the system and the corresponding observables. In this case, the full Schrödinger equation is not solved since it may be replaced by the direct self-consistent determination of the electron density. The observables of the system may be obtained directly in terms of the density. While the procedure is exact, the energy functional expressing the energy in terms of the density is not known exactly and the theory is based in approximate functionals. The fact that the electron density carries sufficient information about the ground state of the system to determine its energy (Hohenberg and Kohn (1964) theorem) raises the question of if the N-electron wavefunction ifself may be determined in terms of the electron density, leading to the reconstruction problem (Colmenero *et al*., 1993a; Colmenero *et al*., 1993b; Colmenero *et al.*, 1994). While DFT is an essentially approximate theory, its accuracy has increased extraordinarily in the last decades and it provides a powerful practical approach for the study of atoms, molecules and solids.

3.2.2.3 Density Functional Theory

Density Functional Theory tries to resolve the electronic problem in terms of the electron density function only. A simple argument may be used to rationalize the fact that the electron density carries all the required information about the system to determine its properties. If we know the electron density function of a given system, we can determine a large amount of information about this system as the nuclear positions and the number of electrons (Bader, 1990). Therefore, given an electron density we may construct the corresponding Hamiltonian operator. From the Hamiltonian, we can obtain the corresponding wavefunction and all the system observables.

Hohenberg y Kohn (1964) were the first in formulating density functional theory in a rigorous mathematical form. Their two theorems will be described now.

First theorem. Any property of an electron system in its ground state is determined in a unique way by the electron density function $\rho(\boldsymbol{r})$. In particular, the energy of the system must be a functional of the density, $E[\rho]$. This theorem is known as the energy functional existence theorem.

This theorem can also be stated in the following way. The external potential $V(\boldsymbol{r})$ acting on one electron of the system is determined, except for an additive constant, by the electron density function $\rho(\boldsymbol{r})$. Since the density also determines the number of electrons,

$$\int \rho(\boldsymbol{r}) d\boldsymbol{r} = N^{el} \qquad (3.17)$$

it follows that it determines, except for an additive constant, the Hamiltonian operator and, therefore, the wavefunction of the ground state (and the corresponding properties). Consequently, any property of the system in its ground state is determined in a unique way by the density function, as stated by the theorem:

$$\rho(\boldsymbol{r}) \rightarrow V(\boldsymbol{r}), N^{el} \rightarrow H^{el} \rightarrow \Psi^{el}$$

Since we are considering a system composed by electrons for fixed nuclear positions the dependence of external potential, $V(\boldsymbol{r},\boldsymbol{R})$, on the nuclear positions will be omitted ($V(\boldsymbol{r},\boldsymbol{R}) = V(\boldsymbol{r})$ for fixed $\boldsymbol{R}$**).**

The proof of the first theorem of Hohenberg and Kohn proceeds by *reductio ad absurdum* and it is simple if we consider a Hamiltonian of the type of equation $(3.14.b)$:

$$H^{el} = T^{el} + V^{Ne} + V^{ee} \qquad (3.14.b')$$

where, T^{el} and V^{ee} are the kinetic energy and electron interaction energy operators, and V^{Ne} is the external potential that the nuclei exert on the electrons. We have that,

$$V^{Ne} = \sum_{i}^{N_{el}} V_i(\boldsymbol{r}) \qquad (3.18.a)$$

where,

$$V_i(\boldsymbol{r}) = -\sum_{A=1}^{N_{at}} \frac{Z_A}{r_{iA}} \qquad (3.18.b)$$

Thus, the external potential acting on any electron may be written as

$$V(\boldsymbol{r}) = -\sum_{A=1}^{N_{at}} \frac{Z_A}{r} \qquad (3.19)$$

If we know $V(\boldsymbol{r})$, we may obtain V^{Ne} by summing over the electrons in the system. Further, from N^{el} we may construct T^{el} and V^{ee} because they only depend on the number of electrons (see equation $(3.14.b)$). Thus, if $\rho(\boldsymbol{r})$ determines $V(\boldsymbol{r})$ in a unique way, we may construct the Hamiltonian as stated by the theorem.

If we now suppose that two external potentials yield the same electron density, then, these two potentials give two different Hamiltonians H and H' with different wavefuntions Ψ and Ψ' and different energies E and E'. If the ground states of H and H' are non-degenerate and using the trial function Ψ for H' and Ψ' for H we obtain two equations for the energies, which are:

$$E' = \langle \Psi' \mid H' \mid \Psi' \rangle < \langle \Psi \mid H' \mid \Psi \rangle = \langle \Psi \mid H \mid \Psi \rangle + \langle \Psi \mid H' - H \mid \Psi \rangle$$
$$= E + \int dr[V'(\boldsymbol{r}) - V(\boldsymbol{r})]\rho(\boldsymbol{r})$$

$$E = \langle \Psi \mid H \mid \Psi \rangle < \langle \Psi' \mid H \mid \Psi' \rangle = \langle \Psi' \mid H' \mid \Psi' \rangle + \langle \Psi' \mid H - H' \mid \Psi' \rangle$$
$$= E' + \int dr[V(\boldsymbol{r}) - V'(\boldsymbol{r})]\rho(\boldsymbol{r})$$

In both equations, we suppose that the two potentials yield the same electron density and, therefore,

$$\rho(\boldsymbol{r}) = \langle \Psi' \mid \hat{\rho} \mid \Psi' \rangle = \langle \Psi \mid \hat{\rho} \mid \Psi \rangle$$

where, $\hat{\rho}$ is the density operator. By adding the above two equations we obtain,

$$E' + E < E' + E$$

Which is clearly false and contradicts the initial statement statement that two external potentials can give the same electron density. Therefore, each $V(\boldsymbol{r})$ can only be associated to a unique

electron density $\rho(\boldsymbol{r})$. Since there is a unique relation between the electron density of the system and its corresponding external potential and this potential determines in a unique way Ψ through the Schrödinger equation, we can say that Ψ is a function of the electron density.

Second theorem. Given an external potential, we can obtain the energy of the system from the functional $E[\rho']$ with a trial density ρ' satisfying system conditions in such a way that the energy will be larger or equal than the exact system energy, that is $E[\rho'] > E_0[\rho]$. This second theorem is known as the variational principle.

The proof of the second theorem of Hohenberg and Kohn is also straightforward and it is due to Levy (1979, 1982). Since the energy is the expectation value of the Hamiltonian using the normalized wavefuntion,

$$E[\Psi] = \langle \Psi \,|\, H^{el} \,|\, \Psi \rangle$$

and, according to the first theorem, the wavefunction is a functional of the electron density:

$$E[\Psi] = \langle \Psi[\rho] \,|\, H^{el} \,|\, \Psi[\rho] \rangle$$

the expectation value is also a functional of the density,

$$E[\Psi] = E[\rho] = \langle \Psi[\rho] \,|\, H^{el} \,|\, \Psi[\rho] \rangle = \langle \Psi[\rho] \,|\, T^{el} + V^{ee} + V^{Ne} \,|\, \Psi[\rho] \rangle$$

Since according to the first theorem, the external potential is uniquely determined by the electronic charge density $\rho(\boldsymbol{r})$, the ground state energy functional may be written as:

$$E[\rho] = \langle \Psi[\rho] \,|\, T^{el} + V^{ee} \,|\, \Psi[\rho] \rangle + \langle \Psi[\rho] \,|\, V^{Ne} \,|\, \Psi[\rho] \rangle$$

That is,

$$E[\rho] = F[\rho] + V_{ext}[\rho] \tag{3.20}$$

where,

$$F[\rho] = \langle \Psi[\rho] \,|\, T^{el} + V^{ee} \,|\, \Psi[\rho] \rangle = T_e[\rho] + V_{ee}[\rho] \tag{3.21.a}$$

and

$$V_{ext}[\rho] = \langle \Psi[\rho] \,|\, V^{Ne} \,|\, \Psi[\rho] \rangle = \int \rho(\boldsymbol{r}) V(\boldsymbol{r}) d\boldsymbol{r} \tag{3.21.b}$$

$F[\rho]$ is the *Hohenberg-Kohn universal functional*. The term universal comes from the fact that since the kinetic energy and electron repulsion operators are independent of the nuclear positions, its form must be the same for any geometry of the system.

The variational theorem of Quantum Mechanics states that the exact wavefunction minimizes the energy functional:

$$E[\Psi] = \langle \Psi \,|\, H^{el} \,|\, \Psi \rangle < E[\Psi'] = \langle \Psi' \,|\, H^{el} \,|\, \Psi' \rangle$$

where, Ψ' is a trial wavefunction. This theorem can also be written as:

$$E[\Psi] = \min_{\Psi'} \langle \Psi' \,|\, H^{el} \,|\, \Psi' \rangle$$

Thus, the exact ground state wavefunction, Ψ, is the one that minimizes the energy functional subject to the constraint that the wavefunction is properly normalized. Since the wavefunction is a functional of the density, the above principle can be expressed, using equation (3.20), as:

$$E_v[\rho] = \min_{\rho' \,(\Psi \to \rho)} (E_v[\rho']) = \min_{\rho' \,(\Psi \to \rho)} (F_v[\rho'] + V_{ext}[\rho']) \tag{3.22}$$

and the exact ground state density could be obtained by minimizing the energy functional subject to the appropriate constraints. This search of the electron density by minimizing the energy functional should be performed within a restricted class of trial electron densities not only being properly normalized (equation (3.17)) but also being *N-representable* (which may be obtained from some antisymmetric wavefunction, Eq. (3.16)) and *V-representable* (obtainable from an antisymmetric wavefunction which solves the Schrödinger equation associated to some external

potential). The *V-representability* condition can be replaced by the constraint that the energy functional be *V-representable,* that is, the functional $E_v[\rho]$:

$$E_v[\rho] = F_v[\rho] + \int \rho(\boldsymbol{r})V(\boldsymbol{r})d\boldsymbol{r} \tag{3.23}$$

must be derivable from some Schrödinger equation involving external potential $V(\boldsymbol{r})$.

The existence theorem, used in conjunction with the standard Rayleigh-Ritz variational principle of quantum mechanics leads to the fact that if the *universal functional* of the electron charge density exists, it may be minimized by the electron charge density of the ground state corresponding to the external potential $V(\boldsymbol{r})$, under the proper constraints. Furthermore, the value of the minimum coincides with the ground-state energy. This theorem provides the foundation of what is currently known as density-functional theory (Parr and Yang, 1989). It allows an enormous conceptual simplification of the quantum mechanical problem of searching for the ground-state properties of a system of interacting electrons, since it replaces the traditional description based on wave functions (which depend on $3N^{el}$ independent variables) with a much more tractable description in terms of the charge density, which depends on only three variables. Two major problems hamper a straightforward application of this remarkably simple result: (1) the form of the F functional is unknown, and (2) the conditions to be fulfilled for a function $\rho(\boldsymbol{r})$ to be considered an acceptable ground-state charge distribution (and hence the domain of the functional F) are poorly characterized. While the most important part of the second problem is fully solved (Gilbert, 1975; Ludeña *et al*., 2008), since any density satisfying the appropriate constraints is *N*-representable (that is, it can be derived from a *N*-particle wavefunction), the associated problem of the *V*-representability of the functional $F(\rho)$ is not and it can be shown to be equivalent to the problem of the *N*-representability of the second-order reduced density matrix (Ludeña *et al*., 2008). The first problem can be handled by mapping the system onto an auxiliary system of noninteracting electrons (Kohn and Sham, 1965) and by making appropriate approximations along the lines described in the next subsections.

Note that it is customary to use square brackets to indicate functional dependence (see the first equation of this section), and this notation will be employed along the next sections.

3.2.2.3.1 The Kohn-Sham Equations

The Hohenberg and Kohn theorem states that all the physical properties of a system of interacting electrons are uniquely determined by its ground-state charge density distribution. This property holds independently of the precise form of the electron-electron interaction. In particular, when the strength of the electron-electron interaction vanishes, $F[\rho]$ defines the ground-state kinetic energy of a system of noninteracting electrons as a functional of its ground-state charge-density distribution $T_0[\rho]$. This fact was used by Kohn and Sham (1965) to map the problem of a system of interacting electrons onto an equivalent noninteracting problem. To this end, the unknown functional $F[\rho]$ is cast in the form:

$$F[\rho] = T_0[\rho] + E_H[\rho] + E_{XC}[\rho] \tag{3.24.a}$$

where,

$$E_H[\rho] = \frac{1}{2}\int \frac{\rho(\boldsymbol{r})\rho(\boldsymbol{r}')}{|\boldsymbol{r}-\boldsymbol{r}'|}d\boldsymbol{r}d\boldsymbol{r}' \tag{3.24.b}$$

$E_H[\rho]$, the Hartree-energy, is the classical electrostatic self-interaction of the electron charge-density distribution. The so-called exchange-correlation energy, $E_{XC}[\rho]$, is defined by this equation (the exchange-correlation energy is the name we give to the part of the energy functional that we do not know how to calculate otherwise) and may be expressed, using equation $(3.21.a)$, as:

$$E_{XC}[\rho] = F[\rho] - T_0[\rho] - E_H[\rho] = (T_e[\rho] - T_0[\rho]) + V_{ee}[\rho] - E_H[\rho] \quad (3.25)$$

Therefore, it includes the difference of the exact and non-interacting kinetic energies.

Variation of the energy functional with respect to $\rho(\boldsymbol{r})$ with the constraint that the number of electrons be kept fixed leads formally to the same equation as would hold for a system of noninteracting electrons subject to an effective potential, also called the self-consistent field, (SCF), potential, whose form is:

$$V_{SCF}(\boldsymbol{r}) = V(\boldsymbol{r}) + \int \frac{\rho(\boldsymbol{r}')}{|\boldsymbol{r} - \boldsymbol{r}'|} d\boldsymbol{r}' + v_{XC}(\boldsymbol{r}) \quad (3.26.a)$$

where,

$$v_{XC}(\boldsymbol{r}) = \frac{\partial E_{XC}}{\partial \rho(\boldsymbol{r})} \quad (3.26.b)$$

is the functional derivative of the exchange-correlation energy, also called the exchange-correlation potential. The power of this trick is that, if one knew the effective potential $V_{SCF}(\boldsymbol{r})$, the problem for noninteracting electrons could be trivially solved without knowing the form of the noninteracting kinetic-energy functional $T_0[\rho]$. To this end, one should simply solve the one-electron Schroödinger equation:

$$\left(-\frac{1}{2m}\frac{\partial^2}{\partial \boldsymbol{r}^2} + V_{SCF}(\boldsymbol{r})\right)\psi_n(\boldsymbol{r}) = \epsilon_n \psi_n(\boldsymbol{r}) \quad (3.27)$$

The ground-state charge-density distribution and non-interacting kinetic-energy functional would then be given in terms of the auxiliary Kohn-Sham orbitals, $\psi_n(r)$

$$\rho(\boldsymbol{r}) = 2\sum_{n=1}^{N^{el}/2} |\psi_n(\boldsymbol{r})|^2 \quad (3.28.a)$$

$$T_0[\rho] = -\frac{1}{2}\sum_{n=1}^{\frac{N^{el}}{2}} 2\int \psi_n^*(\boldsymbol{r})\frac{\partial^2 \psi_n(\boldsymbol{r})}{\partial r^2} dr \quad (3.28.b)$$

In these equations, the system is supposed to be nonmagnetic, so that each of the $N^{el}/2$ lowest-lying orbital states accommodates two electrons of opposite spin. In periodic systems, the index n running over occupied states can be thought of as a double label, $n \equiv \{m, \boldsymbol{q}\}$, where m indicates the set of valence bands, and $\boldsymbol{q}$ is a wave vector belonging to the first Brillouin zone (see next sections).

The ground-state energy given by these equations can be equivalently expressed in terms of the Kohn-Sham eigenvalues:

$$E[\rho] = 2\sum_{n=1}^{N^{el}/2} \varepsilon_n - E_H[\rho] + E_{XC}[\rho] - \int \rho(\boldsymbol{r}) v_{XC}(\boldsymbol{r})\, d\boldsymbol{r} \quad (3.29)$$

The previous Schrödinger equation is a non-linear equation whose potential depends on its own eigenfunctions through the electron charge-density distribution. Once an explicit form for the exchange-correlation energy is available, this equation can be solved in a self-consistent way using a variety of methods.

The generation of approximations for E_{XC} has lead to a large and still rapidly expanding field of research. There are now many different flavours of functional available which are more or less appropriate for any particular study. The first of these approximations is the Local Density Approximation which is described in the next section.

3.2.2.3.2 Local Density Approximation (LDA)

The Kohn-Sham scheme constitutes a practical way to implement density-functional theory, provided an accurate and reasonably easy-to-use approximation is available for the exchange-correlation energy $E_{XC}[\rho]$. The simplest approach used to approximate $E_{XC}[\rho]$ is the Local Density Approximation (LDA). In their original paper, Kohn and Sham (1965) proposed the assumption that each small volume of the system (so small that the charge density can be thought to be constant therein) provides the same exchange-correlation energy as an equal volume of a homogeneous electron gas at the same density. With this assumption, the exchange-correlation energy functional and potential is:

$$E_{XC}[\rho] = \int \epsilon_{XC}[\rho]|_{\rho=\rho(\boldsymbol{r})}\, \rho(\boldsymbol{r}) d\boldsymbol{r} \tag{3.30.a}$$

$$v_{XC}[\rho](\boldsymbol{r}) = \left(\epsilon_{XC}[\rho] + \rho \frac{d\epsilon_{XC}[\rho]}{d\rho}\right)_{\rho=\rho(\boldsymbol{r})} \tag{3.30.b}$$

where $\epsilon_{XC}[\rho]$ is the exchange-correlation energy per particle in a homogeneous electron gas at density ρ. This approximation is known as the *local-density approximation* (LDA). Approximate forms for $\epsilon_{XC}[\rho]$ have been known for a long time.

In LDA we assume that the exchange-correlation energy per electron at the point $\boldsymbol{r}$ of an electron gas $\epsilon_{XC}[\rho]$ is equal to the exchange-correlation energy per electron of a homogeneous electron gas having the same electron density:

$$\epsilon_{XC}[\rho(\boldsymbol{r})] = \epsilon_{XC}^{homog}[\rho] \tag{3.31}$$

In this approximation, the exchange and correlation contributions are treated separately in the form:

$$\epsilon_{XC}^{LDA}[\rho(\boldsymbol{r})] = \epsilon_{X}^{LDA}[\rho(\boldsymbol{r})] + \epsilon_{C}^{LDA}[\rho(\boldsymbol{r})] \tag{3.32}$$

The exchange part representing the exchange energy of an electron in a homogeneous electron gas of constant density was proposed for the first time by Dirac (1930):

$$\epsilon_{X,Dirac}^{LDA}[\rho(\boldsymbol{r})] = C_X \int \rho(\boldsymbol{r})^{4/3}\, d\boldsymbol{r} \tag{3.33.a}$$

where the constant C_X is given by:

$$C_X = -\frac{3}{4}\left(\frac{3}{\pi}\right)^{\frac{1}{3}} \tag{3.33.b}$$

However, a better expression for ϵ_{XC}^{LDA} is that of Slater (1974):

$$\epsilon_{X,Slater}^{LDA}[\rho(\boldsymbol{r})] = -\frac{9}{4}\alpha\left(\frac{3}{8\pi}\right)^{1/3} \int \rho(\boldsymbol{r})^{1/3}\, d\boldsymbol{r} \tag{3.34}$$

where $\alpha = 2/3$.

For the correlation energy per particle there are several possibilities. The so called X_α method (Slater, 1974), uses $\epsilon_{C}^{LDA}[\rho(\boldsymbol{r})] = 0$ and $\alpha = 2/3$ in the expression for the exchange part ($\epsilon_{X,Slater}^{LDA}$). There are analytic expressions for the correlation part as that obtained from Monte Carlo calculations of the homogeneous electron gas at several different densities performed by Ceperley and Alder (1980). The numerical results from nearly exact Monte Carlo calculations for the homogeneous electron gas by Ceperley and Alder (1980) have been parametrized by Perdew and Zunger (1981) with a simple analytical form. More accurate parametrizations have been recently proposed by Ortiz and Ballone (1994). All these different forms are very similar in the range of electron densities relevant to condensed matter applications and yield very similar results.

The LDA is exact in the limit of high density or of a slowly varying charge-density distribution (Kohn and Sham, 1965). This approximation has turned out to be much more successful than originally expected (see, for instance, Jones and Gunnarsson, 1989), in spite of its extreme simplicity. For weakly correlated materials, such as semiconductors and simple metals, the LDA describes accurately structural and vibrational properties: the correct structure is usually found to have the lowest energy, while bond lengths, bulk moduli, and phonon frequencies are accurate to within a few percent. The LDA also has some well-known drawbacks. A large overestimate ($\sim$20%) of the crystal cohesive and molecular binding energies is possibly the worst failure of this approximation, together with its inability to properly describe strongly correlated systems, such as transition-metal oxides.

Density Functional Theory must be valid independently of the nature of the fundamental state. For example, it must describe correctly non-magnetic and spin polarized ground states. However, the dependence of the energy functional on the scalar electron density yield spin-independent equations from which information about spin-density cannot be obtained. Von Barth y Hedin (1972) extended Density Functional Theory to spin-polarized systems by replacing the electron density by spin dependent density functions (spin up and down functions, $\rho^{\downarrow}(r)$ and $\rho^{\uparrow}(r)$). This also allows the study of systems under external magnetic fields. The spin-polarized Kohn-Sham equations may be derived in a similar way as in the non-polarized case. The local spin density approach approximation (LSDA) is similar to the LDA approximation for non-polarized systems.

Much effort has been put into the search for better functionals than the LDA (see, for instance, Perdew *et al*., 1999). The LDA may be improved by introducing gradient corrections in order to describe correctly the inhomogeneities present in the electron density function. The use of *gradient corrections* (Becke, 1988; Perdew *et al*., 1996a) to the LDA has become widespread in recent years.

3.2.2.3.3 Generalized Gradient Approximation (GGA)

In the LDA approximation, it is assumed that the effects of exchange-correlation are local and depend uniquely in the electron density at each point. The next step consists in introducing density gradients in the description of the exchange-correlation effects. In this way, these effects depend on the density value at a given point and in the form in which the density vary in the proximity of that point. Kohn and Sham (1965) proposed this form to improve the LDA functional, supposing that the LDA exchange-correlation energy expression was the zero-order term in the Taylor expansion of electron density and including an additional term which introduces non-local information in the charge density (gradient expansion approximation, GEA). In the GEA, the exchange-correlation energy is given by:

$$E_{XC}[\rho] = \int \rho(\boldsymbol{r})\epsilon_{XC}[\rho(\boldsymbol{r})]d\boldsymbol{r} + \int C_{XC}[\rho(\boldsymbol{r})]\frac{\nabla\rho(\boldsymbol{r})}{\rho(\boldsymbol{r})^{4/3}}d\boldsymbol{r} \tag{3.35}$$

Unfortunately, the GEA violates the rule of conservation of the sum of exchange-correlation hole:

$$\int \rho_{XC}\,(\boldsymbol{r},\boldsymbol{r}')d\boldsymbol{r} = \mathbf{1} \qquad \forall\,\boldsymbol{r} \tag{3.36}$$

where the Exchange-correlation hole, $\rho_{XC}(\boldsymbol{r},\boldsymbol{r}')$, is the probability of finding an electron in $\boldsymbol{r}'$, if we know that the other electron is placed in $\boldsymbol{r}$.

Based on these ideas, a functional was later constructed which satisfies this rule. This approach is known as the generalized gradient approximation (GGA), and the corresponding GGA functional may be written as:

$$E_{XC}^{GGA}[\rho(\boldsymbol{r})] = \int \rho(\boldsymbol{r})\epsilon_{XC}[\rho(\boldsymbol{r})]d\boldsymbol{r} + \int F_{XC}[\rho(\boldsymbol{r}),|\nabla\rho(\boldsymbol{r})|]d\boldsymbol{r} \tag{3.37}$$

Perdew and Wang constructed a GGA functional which satisfies the rule of conservation of the sum of exchange-correlation hole, together with other exact conditions (Perdew, 1991; Perdew *et al.*, 1992; Perdew *et al.* 1996b):

$$E_{XC}^{GGA}[\rho(\boldsymbol{r})] = E_X^{GGA}[\rho(\boldsymbol{r})] + E_C^{GGA}\left[\rho^{\downarrow}(\boldsymbol{r}), \rho^{\uparrow}(\boldsymbol{r})\right] \tag{3.38.a}$$

$$E_X^{GGA}[\rho(\boldsymbol{r})] = \int \rho(\boldsymbol{r}) \epsilon_X^{LDA}[\rho(\boldsymbol{r})] F(s) d\boldsymbol{r} \tag{3.38.b}$$

$$E_C^{GGA}\left[\rho^{\downarrow}(\boldsymbol{r}), \rho^{\uparrow}(\boldsymbol{r})\right] = \int \rho(\boldsymbol{r}) \left[\epsilon_C^{LDA}[\rho(\boldsymbol{r}), \xi(\boldsymbol{r})] + H[t, \rho(\boldsymbol{r}), \xi(\boldsymbol{r})]\right] d\boldsymbol{r} \tag{3.38.c}$$

with

$$s = |\nabla\rho(\boldsymbol{r})|/2k_f \tag{3.39.a}$$

$$k_f = (3\pi\rho)^{1/3} \tag{3.39.b}$$

and

$$t \cong |\nabla\rho(\boldsymbol{r})|/2\left(k_f\right)^{1/2} \tag{3.40.a}$$

$$\xi(\boldsymbol{r}) = (\rho^{\uparrow}(\boldsymbol{r}) - \rho^{\downarrow}(\boldsymbol{r}))/\rho(\boldsymbol{r}) \tag{3.40.b}$$

The F and H functions are determined from the conditions imposed on the exchange-correlation hole. This functional, called GGA-PW91, gives better results than LDA in the study of the ground state of the system. In general, the GGA corrections improve the geometries, frequencies, and charge densities obtained with LDA. The average errors are of 6 kcal/mol in thermochemical tests and it works reasonably for systems with hydrogen bonds. It gives better equilibrium volumes and cohesion energies and also improves the results for the magnetic properties of the system. Nevertheless, as LDA, it fails in the description of complexes bonded by van der Waals forces. In order to describe correctly these interactions, it is possible, for example, to include the empirical dispersion of Grimme (2006) which is described in a later section.

3.2.2.3.3.1 Perdew-Burke-Ernzerhof Functional (PBE)

In the generalized gradient approximation (GGA) (Perdew *et al.*, 1992), we may write the exchange-correlation energy functional in the general form:

$$E_{XC}^{GGA}\left[\rho^{\downarrow}, \rho^{\uparrow}\right] = f\left[\rho^{\downarrow}, \rho^{\uparrow}, \nabla\rho^{\downarrow}, \nabla\rho^{\uparrow}\right] \tag{3.41}$$

The PW91 functional (Perdew, 1991) described in the previous subsection is an analytic fit to a numerical GGA, designed to satisfy several further exact conditions (Perdew *et al.*, 1996b). PW91 incorporates inhomogeneity effects while retaining many of the best features of LSD, but has its own problems: (1) Its derivation is complex and long; (2) The analytic function f, fitted to the numerical results, is complicated and non-transparent; (3) f is over-parametrized; (4) The parameters are not smoothly joined, leading to spurious wiggles in the exchange-correlation potential for small and large density gradients, which can give problems in the construction of GGA-based electron-ion pseudopotentials; (5) Although the numerical GGA correlation energy functional behaves properly (Perdew *et al.*, 1996b) under uniform scaling to the high-density limit, its analytic parametrization (PW91) does not; (6) Because PW91 reduces to the second-order gradient expansion for density variations that are either slowly varying or small, it describes the linear response of the density of a uniform electron gas less satisfactorily than does LSD.

This last problem illustrates the fact that the above form of E_{XC}^{GGA} is too restrictive to reproduce all the known behaviours of the exact functional (Perdew *et al.*, 1996b). In contrast to the construction of the PW91 functional, which was designed to satisfy as many exact conditions as possible, the GGA presented by Perdew, Burke and Ernzerhof (Perdew *et al.*, 1996a) satisfies only those which are energetically significant. The six problems above were solved with a

derivation of a simple new GGA functional in which all parameters selected were fundamental constants. Improvements over PW91 include an accurate description of the linear response of the uniform electron gas, correct behaviour under uniform scaling, and a smoother potential function.

The two pieces of the PBE functional, E_X^{GGA} and E_X^{GGA}, may be written in the same way as for PW1 functional (see previous subsection):

$$E_X^{GGA}[\rho] = \int \rho(\boldsymbol{r})\epsilon_X^{UNIF}[\rho(\boldsymbol{r})]F(s)d\boldsymbol{r} \tag{3.42.a}$$

$$E_C^{GGA}[\rho^{\downarrow},\rho^{\uparrow}] = \int \rho(\boldsymbol{r})\left[\epsilon_C^{UNIF}[\rho(\boldsymbol{r}),\xi(\boldsymbol{r})] + H[t,\rho(\boldsymbol{r}),\xi(\boldsymbol{r})]\right]d\boldsymbol{r} \tag{3.42.b}$$

However, the F and H are written differently. The H function can be expressed as:

$$H = \left(\frac{e^2}{a_0}\right)\gamma\phi^3 \times l_n\left\{1 + \frac{\beta}{\gamma}t^2\left[\frac{1+At^2}{1+At^2+A^2t^4}\right]\right\} \tag{3.43.a}$$

where,

$$A = \frac{\beta}{\gamma}[exp\{-\epsilon_X^{UNIF}/(\gamma\phi^3 e^2/a_0)\} - 1]^{-1} \tag{3.43.b}$$

and

$$\phi(\xi) = \left[(1+\xi)^{\frac{2}{3}} + (1-\xi)^{\frac{2}{3}}\right]/2 \tag{3.43.c}$$

And γ and β are parameters, which assume the values (deduced from the asymptotic limits, $t \to 0$ and $t \to \infty$),

$$\gamma = 0.031091 \tag{3.44.a}$$

$$\beta = 0.066725 \tag{3.44.b}$$

Likewise, the F function is written as,

$$F(s) = 1 + \kappa - \kappa(1 + \mu s^2/\kappa) \tag{3.45}$$

where μ and κ are parameters which assume the values (deduced from the asymptotic limit ($s \to 0$) and to satisfy the Lieb-Oxford bound):

$$\mu = 0.066725 \tag{3.46.a}$$

$$\kappa = 0.804 \tag{3.46.b}$$

Becke (1986) proposed this form, but with empirical coefficients ($\kappa = 0.967; \mu = 0.235$).

The PBE functional retains correct features of LSD, and combines them with the most energetically important features of gradient-corrected nonlocality. The correct but less important features of PW91 functional which have been sacrificed are: (1) correct second-order gradient coefficients for E_X and E_C in the slowly varying limit ($t \to \infty$), and (2) correct non-uniform scaling of E_X in the limit where the reduced gradient s tends to ∞. Calculations of atomization energies for small molecules also show that this functional yield essentially the same results as the PW91. Except for the improvements in the description of the linear response of the uniform electron gas, the correct behaviour under uniform scaling, and the fact that the potential function is smoother, the PBE functional is close to PW91. However, its simpler form and derivation make it easier to understand, apply, and improve.

3.2.2.3.3.2 Perdew-Burke-Ernzerhof Functional for Solids (PBEsol)

While PBE represented a high point of non-empirical functional development, much has been learned about its limitations since its development. PBE reduces the chronic overbinding of the

local spin density approximation (LSDA) but, while LSDA often slightly underestimates equilibrium lattice constants by about 1%, PBE usually overestimates them by about the same amount. Other equilibrium properties, such as bulk moduli, phonon frequencies, magnetism, and ferroelectricity, are sensitive to the lattice constant and, therefore, are also overcorrected by PBE (Wu and Cohen, 2006). Surface energies are too low in LSDA, but are made lower still by PBE (Constantin *et al*, 2006).

Attempts to construct a better GGA functional encounters the following dilemma: Those with an enhanced gradient dependence improve atomization and total energies, but worsen bond lengths, while more recent suggestions of a GGA for solids (like the very first GGA of Langreth and Mehl (1983)) have a reduced gradient dependence and typically do improve lattice parameters and/or surface energies, but worsen atomization energies. Advanced functionals as the meta-GGAs, using also the orbital kinetic-energy densities, provide greater accuracy over a wider range of systems and properties (Tao *et al.*, 2003). But current meta-GGAs do not improve lattice constants as dramatically as surface energies, and meta-GGAs are not yet available in all solid-state codes (or are included only with a reduced functionality). Besides, the use of meta-GGAs is much more time consuming.

In the work by Perdew *et al*. (2008) the origin of this dilemma is explained. They show that the GGA functionals cannot improve atomization and total energies and at the same time to improve bond lengths and lattice parameters. Accurate atomic exchange energies require violating the gradient expansion for slowly-varying densities, which is valid for solids and their surfaces. At the GGA level, one must choose. A pragmatic approach to lattice properties is therefore to use a modified functional especially for solids which recovers the gradient expansion for exchange over a wide range of density gradients, including small and moderate values as required to describe adequately these systems. Restoration of the gradient expansion for exchange requires a complementary alteration for correlation. By using the PBE form but simply altering two parameters, we retain all other exact conditions that make PBE so reliable.

Any GGA that recovers the uniform gas limit has an $F(s)$ function determining the GGA exchange functional (see previous section), of the form

$$F(s) = 1 + \mu s^2 + \cdots \quad (s \to \infty) \tag{3.47}$$

The gradient expansion that is accurate for slowly-varying electron gases (Antoniewicz and Kleinman, 1985) has

$$\mu = \mu_{GE} = 0.1235 \tag{3.48}$$

But any GGA that is accurate for the exchange energies of free neutral atoms must have $\mu \approx 2\,\mu_{GE}$ (Perdew *et al*., 2008). PBE is accurate, although its value of $\mu = 0.21951$ was found from a different non-empirical argument. The B88 functional is also accurate as it was fitted to the exchange energies of noble gas atoms (Becke, 1986). Thus, to attain accurate exchange energies of atoms any GGA must strongly violate the gradient expansion for slowly varying densities. However, the densities of real solids and their surfaces are often almost slowly varying over space. Restoring the gradient expansion should improve their description (but worsen atomization energies). The GGA is a limited form, and cannot satisfy both conditions. In PBEsol, $\mu \approx \mu_{GE}$ is chosen.

Now, for a GGA correlation functional that recovers the uniform gas limit, the gradient expansion must behave as:

$$E_C^{GGA}[\rho^{\downarrow}, \rho^{\uparrow}] = \int \rho(\boldsymbol{r})[\epsilon_C^{UNIF}[\rho(\boldsymbol{r}), \xi(\boldsymbol{r})] + \beta t^2(r) + \cdots)]d\boldsymbol{r} \tag{3.49.a}$$

For slowly varying high densities $\beta = \beta_{GE} = 0.066725$. Since we are interested in weakly-varying valence-electron densities in densely packed solids, we wish to retain the excellent behaviour of LSDA. If

$$\mu = \pi^2\beta/3 \tag{3.49.b}$$

the LSDA response is recovered beyond LSDA. In PBE, the gradient expansion for correlation is respected, i.e., $\mu \approx 2\,\mu_{GE}$ and $\beta = \beta_{GE}$. But we have already argued that $\mu \approx 2\,\mu_{GE}$ is harmful for many condensed matter applications. Exact satisfaction of the previous equation for μ would yield $\beta = 0.0375$, but a compromise value will satisfy another, more relevant constraint for solid-state applications. In PBEsol, the value used for this parameter:

$$\beta = 0.046 \qquad (3.49.c)$$

(together with $\mu \approx \mu_{GE}$) provides the best fit to the results of the TPSS meta-GGA (Tao *et al.*, 2003; Constantin *et al.*, 2006) because it gives very good surface energies. Thus, the previous equation is violated in favour of good surface energies. But the value is considerably closer to that of the linear response requirement (0.0375) demanded by complete restoration of the gradient expansion.

PBEsol becomes exact for solids under intense compression, where real solids and their surfaces become truly slowly varying, and exchange dominates over correlation. PBEsol should improve most surface energies over LSDA, whereas PBE worsens them. To test our functional, a test set of 18 solids was used. The PBEsol greatly reduces the PBE overestimate of lattice constants by a factor of almost 4, except for semiconductors. PBEsol is much less accurate than PBE for atomization energies, but halves the error of LSDA.

3.2.2.3.4 Grimme Empirical Dispersion Correction

As previously mentioned, Density Functional Theory often fails to describe adequately long-range dispersive interactions. To overcome this problem, dispersive forces may be evaluated according to the semiempirical approach (DFT+D) suggested by Grimme (Grimme, 2006; Grimme *et al.*, 2010), which adds the following contribution to the calculated DFT energy:

$$E_{disp} = -s_6 \sum_{\boldsymbol{g}} \sum_{i \neq j} f_{dump}\,(R_{ij,g})\,\frac{C_6^i C_6^j}{R_{ij,g}^6} \qquad (3.50.a)$$

$$f_{dump} = \frac{1}{1 + e^{-d(R_{ij,g}/R_{vdw}-1)}} \qquad (3.50.b)$$

The summation is over all atom pairs ij and $\boldsymbol{g}$ lattice vectors, excluding the self- interaction contribution ($i \neq j$) for every $\boldsymbol{g}$. The parameter C_6^i is the dispersion coefficient for the atom i, s_6 is a scaling factor that depends on the adopted functional (0.75 and 1.05 for PBE and B3LYP, respectively) and $R_{ij,g}$ is the interatomic distance between atom i in the reference cell and atom i in the neighbouring cells at distance $|\boldsymbol{g}|$. f_{dump} is a dumping function used to avoid double counting of short-range contributions to the energy and depends on the sum of atomic van der Waals radii and on a steepness parameter (d = 20). In practice, pairwise dispersive contributions are damped out if the distance between atoms i and i is smaller than the sum of the respective Van der Waals radii. This approach has been widely used for both GGA and hybrid models and the correction was implemented in several codes as CASTEP (Clark *et al.*, 2005), CRYSTAL (Pascale *et al.*, 2004; Dovesi *et al.*, 2005; Tossoni et al., 2007; Civalleri et al., 2008) and VASP (Paier *et al.*, 2005, 2006).

3.2.3 Periodicity. Crystalline Solids

Since we are going to study solid state crystalline materials under an atomistic point of view, the mathematical microscopic description of these systems will be studied. In the first place, we will introduce the concepts of lattice and unit cell, making special emphasis in the symmetry characteristics of a periodic system.

The theoretical treatment of a crystal is most easily carried out in the so-called reciprocal space and it will be introduced in the second place. The periodicity conditions of a crystalline system

are enforced by using a fixed form of the electronic wavefunctions determined by Bloch theorem which will be studied in Section 3.2.3.3. These concepts are basic for understanding the theoretical treatment of these systems which is further developed in Section 3.2.3, with the introduction of plane wave basis sets and pseudopotentials.

3.2.3.1 Lattices, Unit Cells and Symmetry

Crystalline solids, as confirmed by experimental evidence, may be described as ordered repetitions of atoms or groups of atoms in three dimensions. In an ideal crystal, all repeating units are identical and are related by translational symmetry operations, corresponding to the set of vectors,

$$\boldsymbol{T} = u\boldsymbol{a} + v\boldsymbol{b} + w\boldsymbol{c} \tag{3.51}$$

where u, v and w are integers ranging from minus infinite to infinite and $\boldsymbol{a}$, $\boldsymbol{b}$, and $\boldsymbol{c}$ are three non-coplanar vectors defining a basis for the three-dimensional space.

Real crystals present more or less marked deviations from this ideal perfect order. The set of points at the end of the translational vectors forms a *three-dimensional lattice* and are called lattice nodes. The three integers u, v and w defining a given vector are the coordinates of the nodes in the reference system defined by the vectors $\boldsymbol{a}$, $\boldsymbol{b}$, and $\boldsymbol{c}$. The parallelepiped formed by these three vectors is called a *unit cell* and their directions define the *crystallographic axes* X, Y and Z. The *lattice constants* a, b, and c are the moduli or the three vectors $\boldsymbol{a}$, $\boldsymbol{b}$, and $\boldsymbol{c}$ and the *lattice angles* α, β, and γ are the angles between these three vectors (α between $\boldsymbol{b}$ and $\boldsymbol{c}$; β between $\boldsymbol{a}$ and $\boldsymbol{c}$; γ between $\boldsymbol{a}$ and $\boldsymbol{b}$). The choice of these vectors is rather arbitrary since in general there are several possible vectors yielding the same lattice. The *primitive unit cell* is defined as a unit cell described by the three vectors $\boldsymbol{a}$, $\boldsymbol{b}$, and $\boldsymbol{c}$ such that the cell has the smallest possible volume (see Fig. 3-17).

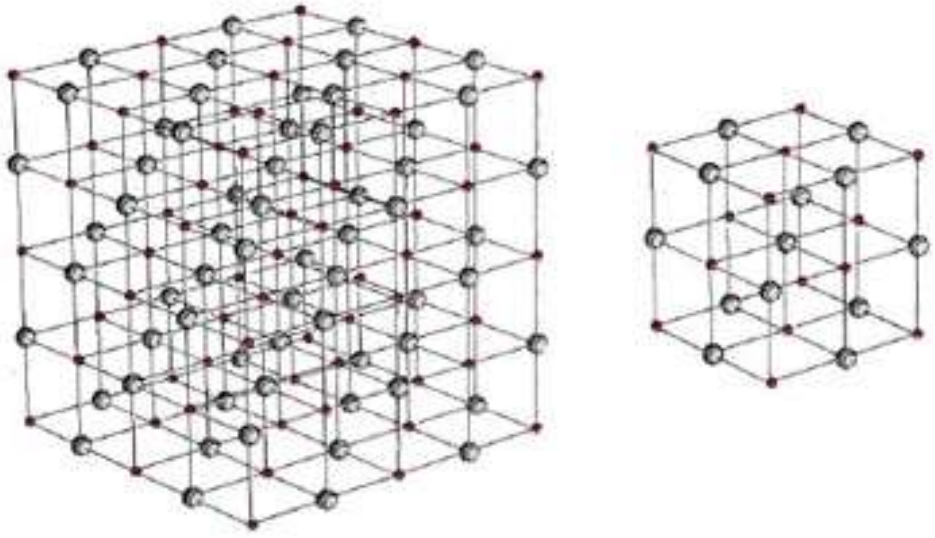

Figure 3-17. Crystal lattice and unit cell of NaCl.

The periodic repetition of the structural motif by the infinite set of vectors $\boldsymbol{T}$ (atoms, groups of atoms or molecules) yields the crystal structure which is completely determined once the lattice paramenters (constants and angles) and the coordinates x, y, and z of all the atoms in the unit cell are known. We can write the coordinate vectors linking the cell origin to the nucleus of j^{th} atom ($j = 1, 2, \dots, N$) as:

$$\boldsymbol{r_j} = x_j\boldsymbol{a} + y_j\boldsymbol{b} + z_j\boldsymbol{c} \tag{3.52.a}$$

For an atom inside the unit cell, the coordinate values will be within the interval 0 to 1. They are therefore called *fractional coordinates* and are given by:

$$x_j = \frac{X_j}{a};\ y_j = \frac{Y_j}{b};\ z_j = \frac{Z_j}{c} \qquad (3.52.b)$$

where X_j, Y_j and Z_j are the standard coordinates of the atom in the crystallographic reference system.

Just seven different arrangements of lattice vectors axes are needed in order to specify all three-dimensional structures and lattices (Table 3-1), these being identical to the seven *crystal systems* derived by studies of the morphology of crystals.

Table 3-1. The crystal systems (Tilley, 2004).

System	Unit cell parameters
Cubic (isometric)	$a = b = c;\ \alpha = 90°,\ \beta = 90°,\ \gamma = 90°$
Tetragonal	$a = b \neq c;\ \alpha = 90°,\ \beta = 90°,\ \gamma = 90°$
Orthorhombic	$a \neq b \neq c;\ \alpha = 90°,\ \beta = 90°,\ \gamma = 90°$
Monoclinic	$a \neq b \neq c;\ \alpha = 90°,\ \beta \neq 90°,\ \gamma = 90°$
Triclinic	$a \neq b \neq c;\ \alpha \neq 90°,\ \beta \neq 90°,\ \gamma \neq 90°$
Hexagonal	$a = b \neq c;\ \alpha = 90°,\ \beta = 90°,\ \gamma = 120°$
Rhombohedral	$a = b = c;\ \alpha = \beta = \gamma \neq 90°$
	$a' = b' \neq c';\ \alpha' = 90°,\ \beta' = 90°,$ $\gamma' = 120°$

A point group is the set of symmetry operations which when applied to a set of atoms leaves the set unchanged. The set of crystals having the same point group is called a *crystal class*, and its symbol is that of the point group. In three dimensions, there are only 32 possible *crystallographic point groups*. The crystallographic restriction theorem in its basic form is based on the observation that the rotational symmetry of a crystal are usually limited to 2-, 3-, 4- and 6-fold. In a crystal, the point group symmetry operations may coexist with more symmetry operations. In mathematics, physics and chemistry, a *space group* is the symmetry group of a configuration in space. The space group of a crystalline system is composed by the symmetry operations of the atoms within the unit cell (these symmetry operations are those which left the unit cell unchanged when applied to all the atoms of the unit cell). In three dimensions, there are 219 distinct space group types, or 230 if chiral copies (not identical to its mirror image) are considered distinct. The symmetry operations within the space groups are translational symmetry operations, point group symmetry operations as reflection, rotation and improper rotation (also called roto-inversion) and the screw axis (eje helicoidal in Spanish,) and glide plane (plano de deslizamiento in Spanish,) symmetry operations. A screw axis is a rotation about an axis, followed by a translation along the direction of the axis. A glide plane is a reflection in a plane, followed by a translation parallel with that plane. The combination of all these symmetry operations results in the 230 different space groups describing all possible crystal symmetries. A definitive source regarding three-dimensional space groups is *the International Tables for Crystallography.* A very complete description of crystal symmetry may be found in Viterbo (1996).

3.2.3.2 Reciprocal Lattice

Given the basis of a lattice ($\boldsymbol{a_1}$, $\boldsymbol{a_2}$, and $\boldsymbol{a_3}$ vectors), called here the direct lattice, we can associate to it a new lattice referred to as the *reciprocal lattice*. The reciprocal lattice is that having a basis of vectors $\boldsymbol{b_1}$, $\boldsymbol{b_2}$, and $\boldsymbol{b_3}$ vectors related to that of the direct lattice by the condition:

$$|\boldsymbol{a}><\boldsymbol{b}| = 2\pi\, \boldsymbol{I} \tag{3.53.a}$$

that is:

$$\begin{pmatrix} \boldsymbol{a_1}\cdot\boldsymbol{b_1} & \boldsymbol{a_1}\cdot\boldsymbol{b_2} & \boldsymbol{a_1}\cdot\boldsymbol{b_3} \\ \boldsymbol{b_2}\cdot\boldsymbol{a_1} & \boldsymbol{a_2}\cdot\boldsymbol{b_2} & \boldsymbol{a_2}\cdot\boldsymbol{b_3} \\ \boldsymbol{b_3}\cdot\boldsymbol{a_1} & \boldsymbol{b_3}\cdot\boldsymbol{a_2} & \boldsymbol{a_3}\cdot\boldsymbol{b_3} \end{pmatrix} = 2\pi \begin{pmatrix} \boldsymbol{1} & \boldsymbol{0} & \boldsymbol{0} \\ \boldsymbol{0} & \boldsymbol{1} & \boldsymbol{0} \\ \boldsymbol{0} & \boldsymbol{0} & \boldsymbol{1} \end{pmatrix} \tag{3.53.b}$$

or:

$$\boldsymbol{a_i}\cdot\boldsymbol{b_i} = 2\pi \tag{3.54.a}$$
$$\boldsymbol{a_i}\cdot\boldsymbol{b_j} = 0\ (i \neq j) \tag{3.54.b}$$
$$\boldsymbol{b_i}\cdot\boldsymbol{a_j} = 0\ (i \neq j) \tag{3.54.c}$$

The modulus and direction of the new vectors fixed by these equations. In particular, these equations show that $\boldsymbol{b_1}$ is normal to $\boldsymbol{a_2}$ and $\boldsymbol{a_3}$ and, therefore, to the plane defined by these two vectors. Similarly, $\boldsymbol{b_2}$ is normal to the $(\boldsymbol{a_1}, \boldsymbol{a_3})$ plane and $\boldsymbol{b_3}$ is normal to the plane $(\boldsymbol{a_1}, \boldsymbol{a_2})$. In fact, if we write:

$$\boldsymbol{b_1} = \frac{2\pi}{V}\boldsymbol{a_2}\times\boldsymbol{a_3} \tag{3.55.a}$$
$$\boldsymbol{b_2} = \frac{2\pi}{V}\boldsymbol{a_1}\times\boldsymbol{a_3} \tag{3.55.b}$$
$$\boldsymbol{b_3} = \frac{2\pi}{V}\boldsymbol{a_1}\times\boldsymbol{a_2} \tag{3.55.c}$$

where, V is the volume of the unit cell, all the above conditions are satisfied. That is, except for a constant, each reciprocal lattice vector is the vector product of vectors in the direct lattice. It may be shown that any reciprocal space vector,

$$\boldsymbol{K} = h\boldsymbol{b_1} + k\boldsymbol{b_2} + l\boldsymbol{b_3} \tag{3.56}$$

where h, k and l are integers is perpendicular to the family of direct lattice planes (hkl). An important property of the reciprocal lattice is that its reciprocal is again the direct lattice.

After having characterized mathematically the reciprocal lattice, let us now consider its physical meaning. Consider a set of points $\boldsymbol{T}$ constituting a direct lattice, and a plane wave, $e^{i\boldsymbol{k}\cdot\boldsymbol{r}}$. For general $\boldsymbol{k}$, such a plane wave will not, of course, have the periodicity of the lattice, but for certain special choices of wave vector it will. The set of all wave vectors $\boldsymbol{K}$ that yield plane waves with the periodicity of a given lattice is just the reciprocal lattice. Analytically, $\boldsymbol{K}$ belongs to the reciprocal lattice of the lattice points $\boldsymbol{T}$, if the relation:

$$e^{i\boldsymbol{k}\cdot(\boldsymbol{r}+\boldsymbol{T})} = e^{i\boldsymbol{k}\cdot\boldsymbol{r}} \tag{3.57.a}$$

holds for any $\boldsymbol{r}$ and for all $\boldsymbol{T}$. Factoring $e^{i\boldsymbol{k}\cdot(\boldsymbol{r}+\boldsymbol{T})}$ we can characterize the reciprocal lattice as the set of wave vectors $\boldsymbol{K}$ satisfying:

$$e^{i\boldsymbol{K}\cdot\boldsymbol{T}} = 1 \tag{3.57.b}$$

for all $\boldsymbol{T}$ in the direct lattice. Using the previous definitions of direct and reciprocal lattice vectors, we see that the product of $\boldsymbol{K}$ and $\boldsymbol{T}$ vectors is given by:

$$\boldsymbol{K}\cdot\boldsymbol{T} = (h\boldsymbol{b_1} + k\boldsymbol{b_2} + l\boldsymbol{b_3})\cdot(u\boldsymbol{a_1} + v\boldsymbol{b}\boldsymbol{a_2} + w\boldsymbol{a_3}) = hu\,\boldsymbol{b_1}\cdot\boldsymbol{a_1} + kv\,\boldsymbol{b_2}\cdot\boldsymbol{a_2} + lw\,\boldsymbol{b_3}\cdot\boldsymbol{a_3}$$
$$= 2\pi\,(hu + kv + lw) \tag{3.58}$$

And, therefore, the above condition ($e^{i\boldsymbol{K}\cdot\boldsymbol{T}} = 1$) is fulfilled.

In mathematics and solid state physics, the first *Brillouin zone* is a uniquely defined primitive cell in reciprocal space. The reciprocal lattice is broken up into Brillouin zones. The boundaries of this cell are given by planes related to points on the reciprocal lattice. The importance of the Brillouin zone stems from the Bloch wave description of waves in a periodic medium, in which it is found that the solutions can be completely characterized by their behavior in a single Brillouin zone. The first Brillouin zone is the locus of points in reciprocal space that are closer to the origin of the reciprocal lattice than they are to any other reciprocal lattice points. The first Brillouin zone

is often called simply the Brillouin zone. Using the definition of the reciprocal space vectors it is an easy mater to prove that if V is the volume of the direct primitive unit cell, the volume of the primitive unit cell of reciprocal lattice (that is the first Brillouin zone) is given by:

$$V_{BZ} = \boldsymbol{b_1} \cdot (\boldsymbol{b_2} \times \boldsymbol{b_3}) = \frac{(2\pi)^3}{V}. \tag{3.59}$$

From this relation, it follows that the volumes of the primitive unit cells in the direct and reciprocal lattices are inverse. Therefore, as the direct unit cell size increases the volume of the reciprocal one decreases and the system is more easily described in the reciprocal space.

3.2.3.3 The Bloch Theorem

To model an infinite system, either a significantly large number of atoms and electrons need to be calculated to avoid surface effects, or the problem can be bypassed by introducing the formalism of periodic boundary conditions. At the birth of DFT most of systems of interest were crystalline. Born-Von Karman periodic boundary conditions (Karman and Born 1913*a,b*; Ashcroft and Mermin, 1976) became the standard as they allowed the crystal structure to be reproduced by only considering the primitive unit cell. The study of solid state physics has moved away from systems with such high periodicity but even though periodic boundary conditions are no longer strictly necessary for many of the problems that we attempt to solve, they have not been abandoned and form an integral part of a majority of modern day DFT codes. In the case of crystalline solids, the periodicity conditions are enforced by using a fixed form of the electronic wavefunctions determined by Bloch theorem (Ashcroft and Mermin, 1976; Dovesi, 1996).

The introduction of periodic boundary conditions, forces periodicity onto the system. Many systems of interest do not have the full three-dimensional periodicity of a crystal. To study these systems, it is useful to make the supercell approximation, where an aperiodic system is approximated by creating a supercell. For a molecule, the size of the cell is increased until the interaction between molecules in neighbouring cells is negligible.

For a system of formally non-interacting particles in a static potential $v(r)$ like the potential in Kohn-Sham equations, the Schrödinger equation that governs the behaviour of the system is given by:

$$\left[-\frac{1}{2}\nabla^2 + v(\boldsymbol{r})\right] |\psi_n >= \varepsilon_n |\psi_n > \tag{3.60}$$

The periodicity of a crystal, requires that the potential must have the same periodicity as the crystal, such that:

$$v(\boldsymbol{r}) = v(\boldsymbol{r}) + v(\boldsymbol{r} + \boldsymbol{T}) \tag{3.61}$$

where $\boldsymbol{T}$ is the lattice translation vector. Bloch's theorem states that the wavefunction may be written as (Ashcroft and Mermin, 1976; Dovesi, 1996):

$$\psi_n(\boldsymbol{r}) = e^{i\boldsymbol{q}\cdot\boldsymbol{r}} u_n(\boldsymbol{r}) \tag{3.62.a}$$

where $u_n(\boldsymbol{r})$ is a function with the periodicity of the lattice such that:

$$u(\boldsymbol{r}) = u_n(\boldsymbol{r} + \boldsymbol{T}) \tag{3.62.b}$$

and $\boldsymbol{q}$ is a reciprocal lattice vector that spans the first Brillouin zone. We can now see that $\boldsymbol{q}$-vectors outside of the first Brillouin zone can be mapped back in by the operation $\boldsymbol{q'} = \boldsymbol{q} + \boldsymbol{G}$. Due to this mapping, we introduce a second suffix for the eigenstate which corresponds to the $\boldsymbol{q}$-vectors:

$$\psi_{n\boldsymbol{q}}(\boldsymbol{r}) = e^{i\boldsymbol{q}\cdot\boldsymbol{r}} u_{n\boldsymbol{q}}(\boldsymbol{r}) \tag{3.63}$$

For a periodic system, the infinite number of wavefunctions becomes represented by an infinite number of wavefunctions at each wave vector $\boldsymbol{q}$, where $\boldsymbol{q}$ is restricted to the first Brillouin zone.

If we replace the wavefunctions, using the Bloch theorem, in the Schrödinger equation

$$\left[-\frac{1}{2}\nabla^2 + v(\boldsymbol{r})\right]\psi_{n\boldsymbol{q}}(\boldsymbol{r}) = \varepsilon_n^{\boldsymbol{q}}\,\psi_{n\boldsymbol{q}}(\boldsymbol{r}) \qquad (3.64.a)$$

we obtain, by eliminating the exponential factor in both sides, that it becomes:

$$\left[-\frac{1}{2}(-i\nabla + q)^2 + v(\boldsymbol{r})\right]u_{n\boldsymbol{q}}(\boldsymbol{r}) = \varepsilon_n^{\boldsymbol{q}}\,u_{n\boldsymbol{q}}(\boldsymbol{r}) \qquad (3.64.b)$$

Bloch's theorem for a periodic system maps the problem of an infinite number of electron wavefunctions into an infinite set of wavefunctions sampled by a continuum of $\boldsymbol{q}$-points. In practise, it is not necessary to use a large number of $\boldsymbol{q}$-points. This is because the electronic wavefunctions at $\boldsymbol{q}$-points that are very close together will almost be identical. *It is therefore possible to represent the electronic wavefunctions over a region of reciprocal space with a single* $\boldsymbol{q}$*-point, and represent them over the entire reciprocal space with a finite set of* $\boldsymbol{q}$*-points*. This approximation allows the electronic potential to be calculated at an infinite number of $\boldsymbol{q}$-points and hence determine the total energy of the solid. The error incurred by this approximation can be made arbitrarily small by choosing a sufficiently dense set of $\boldsymbol{q}$-points. Methods have been devised for obtaining accurate approximations to the electronic potential from a called electronic band, by calculating the electronic wavefunctions at special sets of $\boldsymbol{q}$-points. The two most common methods for the generation of special sets of $\boldsymbol{q}$-points are those of Chadi and Cohen (1973) and Monkhorst and Pack (1976). The choice used in this work for the generation these sets, or *K meshes,* is that of Monkhorst and Pack (1976).

The energies in the Schrödinger equation become continuous functions in $\boldsymbol{q}$ and discrete functions in n. The set of energies for a given n are a continuous function in $\boldsymbol{q}$ which is referred to as an *electronic band*. An example of the band structure for Mg_2Si is given in Figure 3-18. The band energies in this case are calculated precisely only at the special $\boldsymbol{q}$-points **Γ**, **L**, **X**, **W**, **K**, and **G** (note that $\boldsymbol{\Gamma} = (0,0,0)$) and the energy values at $\boldsymbol{q}$ vectors between these points are obtained by numerical approximation.

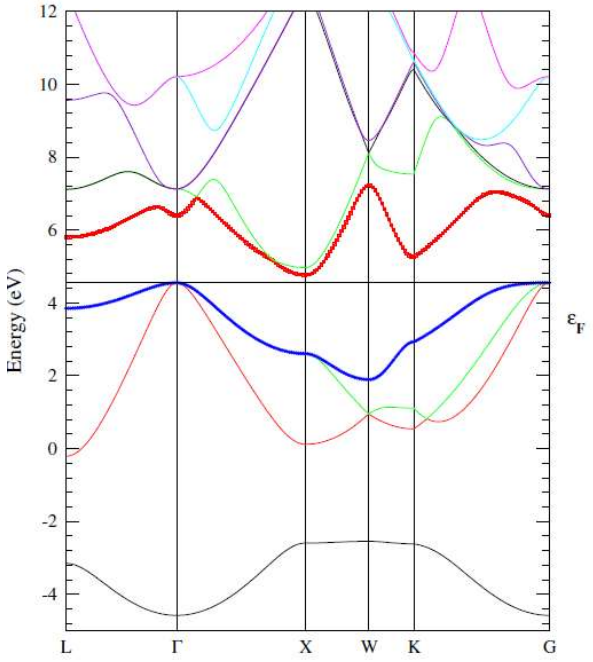

Figure 3-18. Band structure of Mg_2Si (Boulet *et al.*, 2011).

3.2.4 Plane Waves and Pseudopotentials

3.2.4.1 Plane Waves and Atomic Orbitals

In light of Bloch's theorem, the plane-wave basis is an obvious choice for periodic systems. The wavefunction can be represented by a linear combination of plane-waves:

$$u_{nq}(\boldsymbol{r}) = \sum_{G} C^{n}_{G,\boldsymbol{q}}\, e^{i\boldsymbol{G}\cdot\boldsymbol{r}} \tag{3.65}$$

where n is an integer and $\boldsymbol{G}\cdot\boldsymbol{L} = 2\pi\, n$, where $\boldsymbol{L}$ are the lattice vectors. The wavefunction can now be written as

$$\psi_{n\boldsymbol{q}}(\boldsymbol{r}) = \sum_{G} C^{n}_{G,\boldsymbol{q}}\, e^{i(\boldsymbol{G}+\boldsymbol{q})\cdot\boldsymbol{r}} \tag{3.66}$$

The electronic wavefunctions at each $\boldsymbol{q}$-point are expressed in terms of a discrete plane-wave basis set. In principle, this Fourier series is infinite. However, the plane-waves have a kinetic energy $1/2|\boldsymbol{G}+\boldsymbol{q}|^{2}$. Since the lower kinetic energy waves have a more important role in the inter-atomic interactions, a plane-wave *cut-off energy* brings the problem of modelling an infinite system back into the finite regime. In practise, the number of plane-wave basis functions needed to describe the system is very large. This is due to the rapid oscillations of the valence electrons in the region of the core due to the strong ionic potential. This basis set only becomes tractable when used in conjunction with the pseudopotential approximation. The plane-wave basis set, even with pseudopotentials, uses a large number of basis functions but the form of the basis has computational advantages as it works very efficiently with fast Fourier transforms (FFT). The accuracy of a calculation can be gauged by systematically increasing the energy cut-off of the plane-waves and the density of the $\boldsymbol{q}$-point sampling. This allows one to offset the computational cost with the desired accuracy of the calculation.

If we expand the wavefunctions in a finite basis set (as the plane wave one) for a given $\boldsymbol{q}$,

$$u_{nq}(\boldsymbol{r}) = \sum_{\mu} C^{n}_{\mu,\boldsymbol{q}}\, \phi_{\mu,\boldsymbol{q}}(r) \tag{3.67}$$

the coefficients in the expansion may be determined variationally by solving the set of standard coupled matrix equations (Dovesi *et al*, 1996):

$$\underline{H^{\boldsymbol{q}}}\,\underline{C^{\boldsymbol{q}}} = \underline{S^{\boldsymbol{q}}}\,\underline{C^{\boldsymbol{q}}}\,\underline{\varepsilon^{\boldsymbol{q}}} \tag{3.68.a}$$

$$\left(\underline{C^{\boldsymbol{q}}}\right)^{+}\underline{S^{\boldsymbol{q}}}\,\underline{C^{\boldsymbol{q}}} = \underline{I} \tag{3.68.b}$$

where $\underline{H^{\boldsymbol{q}}}$, $\underline{S^{\boldsymbol{q}}}$ and $\underline{C^{\boldsymbol{q}}}$ are the Hamiltonian, overlap and coefficient matrices represented in the basis set $\{\phi_{\mu,\boldsymbol{q}}\}_{\mu=1,\ldots,N_b}$, and $\underline{\varepsilon^{\boldsymbol{q}}}$ is the diagonal matrix containing the single-particle eigenvalues $\varepsilon^{\boldsymbol{q}}_{\mu}$.

Although the use of a plane-wave basis set is the natural choice, other basis function set have been used for the expansion of the wavefunctions. The localized functions, or atomic orbitals (AO), are the main alternative to the plane-wave basis set. They are generally expressed as linear combinations of atom centered gaussian functions by real, solid harmonics (Hehre *et al.*, 1986; Dovesi *et al*., 1996). Gaussian type functions are generally preferred to Slater type functions because their analytical properties. The AO basis set is the one used in popular solid-state computer programs as CRYSTAL (Pascale *et al.*, 2004) and SIESTA (Artacho *et al.,* 2008). In this work, we will use DFT methods based in plane-waves implemented in CASTEP code (Clark et al, 2005).

3.2.4.2 Pseudopotentials

When solving the Schrödinger equation for a system composed of atoms, calculating the total electronic wavefunction is an extremely hard task. The outer wavefunctions must be orthogonal to the inner ones due to the Pauli exclusion principle. This introduces nodes into the wavefunctions which, therefore, require a very high plane wave cutoff and a large number of basis set functions for expressing it accurately. In addition, most of the physical properties of a system depends on its valence electrons.

To introduce pseudopotential theory, we must consider three particle types. These particle types have very different properties and must be handled in a different way. These particles are the - nuclei, the inner electrons and the valence electrons. The valence electrons are the main responsible for the chemical bond and are localized in the outer external shells of the atom. However, inner electrons are almost unchanged when the isolated atom is included in the system because these electrons are located in the deeper shells of the atoms. Pseudopotential theory (Hamann *et al.*, 1979; Hamann, 1989; Troullier and Martins, 1991), makes use of these ideas and replaces the potential $V(\boldsymbol{r})$ describing the full atomic system by another in which the inner electrons states are removed and replaced by a pseudopotential $V_{ps}(\boldsymbol{r})$,which is much softer than the original potential in the core region surrounding the atomic nucleus and reproduces it in the external region (see figure 3-19). The valence electrons are described by pseudowavefunctions $\psi_{ps}(\boldsymbol{r})$ which, again, are softer than the original wavefunctions (see Figure 3-19). In the Figure 3-19 one observes that the valence wavefuncion oscillates rapidly in the core region due to the existence of a strong ionic potential.

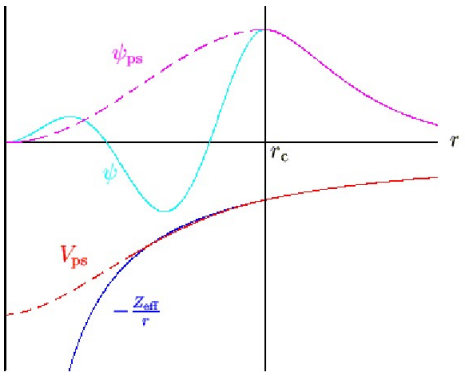

Figure 3-19. Potential of a real electron (continuous blue line) and of a pseudoelectron (discontinuous red line).

The pseudopotential must ideally be constructed in such a way that the valence electron scattering properties and the phase changes of the pseudowavefunction are identical to that of the original wavefunction. The pseudowavefunction should not present radial nodes in the core region, and this condition should be checked in the generated pseudopotential since in this case the calculation could introduce the so called non-physical of ghost states.

According to Hamann *et al.* (1979), the following conditions should be satisfied in the construction of the pseudopotentials:

(a) The eigenvalues of the pseudoelectrons must be equal to those of the valence electrons obtained in the original calculation of the atomic wavefunction.

(b) The pseudowavefunction and the real valence electron wavefunctions must coincide at any point beyond a cut-off ratio, r_c.

(c) The charge of the core electrons calculated from the pseudowavefunction must be the same as that calculated with original wavefunction. This property is known as *norm conservation*.

(d) The logarithmic derivative and first energetic derivatives of the pseudowavefunction and original wavefunction should coincide for $r > r_c$. The pseudowavefunctions and their first and second derivatives must be continuous within a region from $r = 0$ and $r = r_c$, and they must not oscillate in this region.

Properties (c) and (d) are crucial for an optimal transferability, that is in order to get a pseudopotential valid for the different solids in which this atom is present. Property (d) guarantee that the scattering properties of the pseudowavefunction can be reproduced with minimal differences with respect to those of the original wavefunction including the core and valence electrons. This property is different for each component of angular momentum of the original wavefunction and, therefore, the pseudopotential should be dependent on angular momentum. The pseudopotentials with angular momentum dependence are called *non-local* pseudopotentials.

For an atom with associated Hamiltonian H, we denote the core wavefunctions as $|\chi_n>$, its energy eigenvalues as ε_n, and the valence wavefunction as $|\psi>$. From the core states, we try to construct a soft pseudostate $|\varphi>$, as follows:

$$|\psi> = |\varphi> + \sum_{n}^{core} a_n \, |\chi_n> \tag{3.69}$$

Since the valence wavefunctions should be orthogonal to the core wavefunctions which, in turn, are orthogonal among themselves, it follows that:

$$<\chi_n|\psi> = 0 = <\chi_n|\varphi> + a_n \tag{3.70.a}$$

and

$$|\psi> = |\varphi> - \sum_{n}^{core} |\chi_n><\chi_n|\varphi> \tag{3.70.b}$$

Substituting this expression in the Schrödinger equation:

$$H\,|\psi> = \varepsilon\,|\psi> \tag{3.71}$$

we obtain:

$$\begin{aligned} H\,|\psi> &= H\,|\varphi> - \sum_{n}^{core} \varepsilon_n |\chi_n><\chi_n|\varphi> \\ &= \varepsilon\,|\psi> = \varepsilon\left(|\varphi> - \sum_{n}^{core} |\chi_n><\chi_n|\varphi>\right) \\ &= \varepsilon\,|\varphi> - \varepsilon \sum_{n}^{core} |\chi_n><\chi_n|\varphi> \end{aligned} \tag{3.72}$$

which may be rewritten as:

$$H\,|\varphi> + \sum_{n}^{core} (\varepsilon - \varepsilon_n)|\chi_n><\chi_n|\varphi> = \varepsilon\,|\varphi> \tag{3.73}$$

This is the Schrödinger equation which must be obeyed by the pseudowavefuntion:

$$H + V\,|\varphi> = \varepsilon\,|\varphi> \tag{3.74.a}$$

$$V = \sum_{n}^{core} (\varepsilon - \varepsilon_n)|\chi_n><\chi_n| \tag{3.74.b}$$

This expression may also be written in terms of the spherical harmonics $|ln>$ to emphasize that the core wavefunctions and the pseudopotentials are dependent in the angular momentum, l:

$$H + V\,|\varphi> = \varepsilon\,|\varphi> \tag{3.75.a}$$

$$V = \sum_{l} V_l \tag{3.75.b}$$

$$V_l = \sum_{n(l)}^{core} (\varepsilon - \varepsilon_n)|\, \chi_n >< \chi_n \,| = \sum_{n(l)}^{core} (\varepsilon - \varepsilon_{nl})|ln >< ln\,| \qquad (3.75.c)$$

This is the most general expression for a pseudopotential. The additional potential, V_l, whose effects are localized in the core region, is repulsive and partially cancels the coulombic potential in such a way that the result of the sum is a weak potential. Since in a system, the atoms interact between them, the atomic energy eigenvalues will change, but if the core states are reasonably far from the valence states ($\delta\varepsilon \ll \varepsilon - \varepsilon_n$), the use of V_l give us a fair approximation of the valence states. A detailed description of the conservation of the scattering properties was given by Hamann *et al.* (1979). A pseudopotential produces a phase change which is reduced to the change in form of the pseudowavefuntion in such a way that it has not radial nodes and therefore core states. Since the change in energy produced by phase changes is of first order, a good level of precision in energies and properties and correct transferability is only obtained if one equals these phase changes with those of the original problem. The satisfaction of condition (d) makes that the phase changes with respect to energy are the same to first order and improves transferability in a significant way.

The non-local nature of the pseudopotential is exhibited by the characterization of the different angular momentum states which are dispersed in a different way. A pseudopotential with the same form for all angular momentum components is known as a local potential. A local pseudopotential depends only in the electron-nucleus distance. The satisfaction of condition (b), implying the coincidence of the wavefunctions beyond the cut-off ratio, is possible by using non-local pseudopotentials which conserve the norm. This kind of potentials are the most transferable ones since are those which describe in a better way the scattering properties of the atoms in a wide variety of atomic environments.

3.2.4.2.1 Procedures of Pseudopotential Generation

The generation of pseudopotentials has been the object of a large number of studies due to its great utility (Hamann, 1989; Troullier and Martins, 1991; Fuchs and Scheffler, 1999). The usual method to generate a pseudopotential consists in first determining the wavefunction of all the electrons of an atom using the Schrödinger equation:

$$H\,\Psi = E\,\Psi \qquad (3.76)$$

yielding the one-electron states:

$$\mathcal{H}\,\psi_n = \varepsilon_n\,\psi_n \qquad (3.77)$$

where, Ψ is the total wavefunction of the system (*all-electron wavefunction* of an isolated atom) and ψ_n are the corresponding one-electron wavefunctions. The condition for that the pseudowavefunctions and all-electron wavefunctions be equal, out of the core region, may be written as:

$$\int_0^{r_c} \psi_n^*(r)\,\psi_n(r)dr = \int_0^{r_c} \varphi_n^{ps^*}(r)\varphi_n^{ps}(r)dr \qquad (3.78)$$

where, φ_n^{ps} are the pseudowavefunctions. The next step is to adjust the parameters for a pseudoatom calculation of the same type than the all-electron calculation. The all-electron eigenvalues of the valence electrons are introduced in the Schrödinger equation but with the wavefunction replaced with a pseudowavefunction parametrized in the form:

$$\varphi_n^{ps} = \sum_{i=1}^{n_b} \alpha_i^n\, J_i \qquad (3.79)$$

where, J_i are spherical Bessel functions. The solution of this equation, with the previous constrain, gives corresponding parameters, α_i^n, such that the wavefunctions and pseudowavefunctions are the same in the regions beyond the cut-off ratios and the eigenvalues are the same. In general, the pseudowavefunctions are developed in terms of three of four spherical Bessel functions. Since the wavefunctions are dependent one of another, an iterative solution of the pseudopotential equations must be used. A scheme of this iterative method is showed in Figure 3-20.

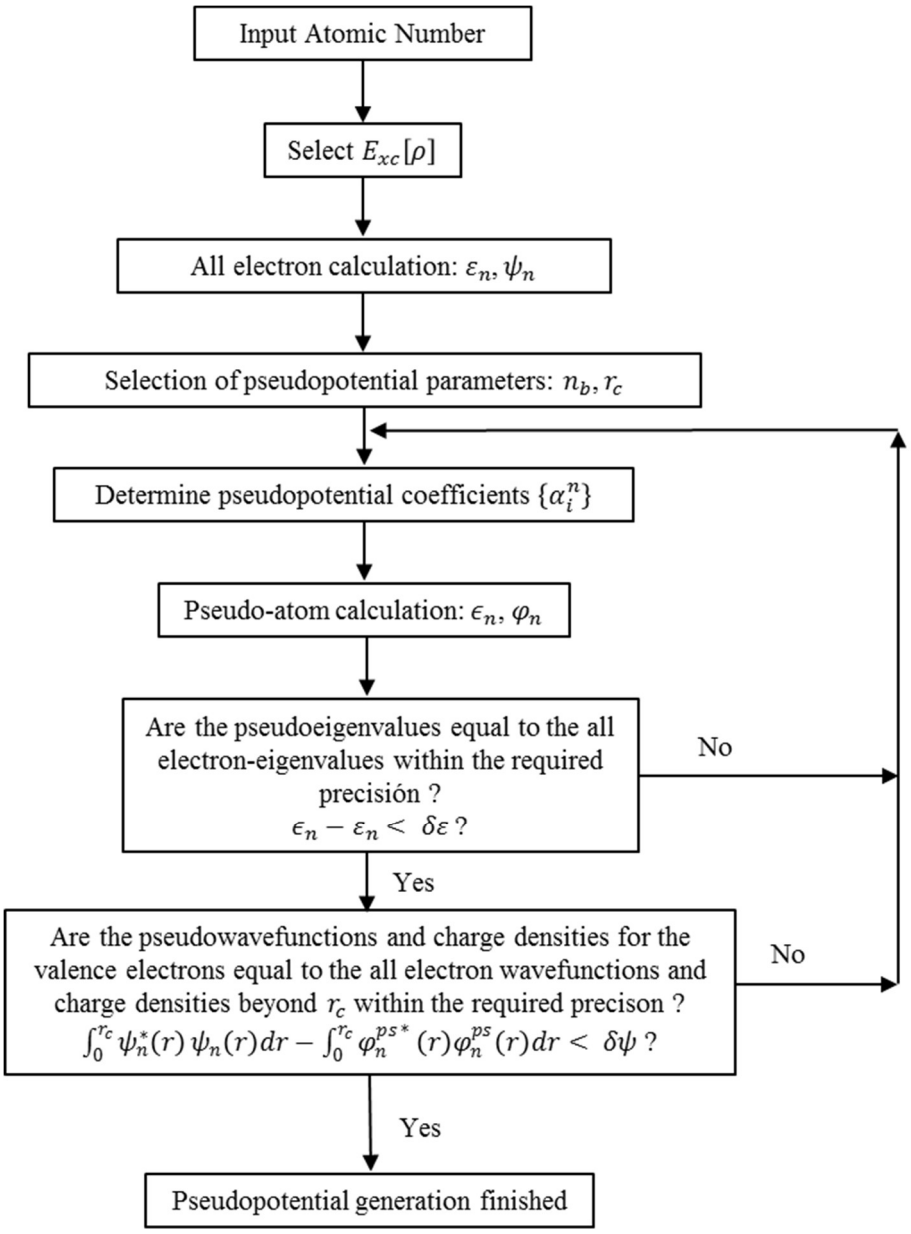

Figure 3-20. Flux diagram or the iterative procedure for the generation of a pseudopotential of an atom.

3.2.4.2.2 Relativistic Pseudopotential Generation in Density Functional Theory

Relativistic effects are important in the study of systems containing heavy atoms, because in those systems the electrons move very fast near the nuclei of heavy atoms and, therefore, the effects of special relativity must be taken into account. The use of a fully relativistic treatment for the systems considered in this work require an extremely large increase in computational power. Furthermore, these kinds of treatments are not included in any of the solid state computational packages available. At this moment, it is only possible to routinely perform relativistic calculations on actinide clusters (Schreckenbach and Shamov, 1999; Van Wezenbeek, 1992). All calculations in this thesis were done by using a norm-conserving relativistic pseudopotential for uranium atom, as this is necessary for a proper description of actinides. While the relativistic effects are not fully taken into account in the treatment of the systems studied in this work, the use of this kind of pseudopotential for uranium atom is required even if the calculations are made within a non-relativistic framework. Fortunately, the use of this kind of treatment yielded to significant results as it will be shown in next sections. In this section, the generation of a norm-conserving pseudopotential including relativistic effects appropriate to perform solid-state density functional theory calculations is described in detail (Fuchs and Scheffler, 1999).

Within the density-functional theory, the pseudopotentials are generated by assuming a spherical screening approximation and self-consistently solving the all-electron atomic Kohn-Sham equation. We have:

$$\left[-\frac{1}{2}\boldsymbol{\nabla}^2 + V^{ef}[\rho;\boldsymbol{r}]\right]\psi_k(\boldsymbol{r}) = \varepsilon_k\psi_k(\boldsymbol{r}) \tag{3.80}$$

where,

$$V^{ef}[\rho;\boldsymbol{r}] = V_H[\rho;\boldsymbol{r}] + V_{XC}[\rho;\boldsymbol{r}] + V_{ext}(\boldsymbol{r}) \tag{3.81.a}$$

In this equation, $V_H[\rho;r]$ and $V_{XC}[\rho;\boldsymbol{r}]$ are the Hartree and exchange correlation potentials:

$$V_H[\rho;\boldsymbol{r}] = \int \frac{\rho(\boldsymbol{r}')}{|\boldsymbol{r}-\boldsymbol{r}'|}d\boldsymbol{r}' \tag{3.81.b}$$

$$V_{XC}[\rho;\boldsymbol{r}] = \frac{\partial E_{XC}(\rho)}{\partial\rho(\boldsymbol{r})} \tag{3.81.c}$$

and $V_{ext}(\boldsymbol{r})$ is the external potential, which for an atomic system becomes $V_{ext}(\boldsymbol{r}) = -Z/r$, where Z is the atomic nuclear charge. The electron density is the sum of contributions from the occupied orbitals:

$$\rho(\boldsymbol{r}) = \sum_k f_k|\psi_k(\boldsymbol{r})|^2 \tag{3.82}$$

$$\int \rho(\boldsymbol{r})dr = N \tag{3.83}$$

where,

$$f_k = 1\ (\varepsilon_k < \varepsilon_N);\ f_k = 0\ (\varepsilon_k > \varepsilon_N) \tag{3.84}$$

The total energy of the system can be expressed as:

$$E_{TOT} = T[\rho] + E_H[\rho] + E_{XC}[\rho] + \int\left(-\frac{Z}{r}\right)\rho(\boldsymbol{r})d\boldsymbol{r} \tag{3.85}$$

where $T[\rho]$ is the kinetic energy; $E_H[\rho]$ is the Hartree energy:

$$E_H[\rho] = \int\frac{\rho(\boldsymbol{r}')\rho(\boldsymbol{r})}{|\boldsymbol{r}-\boldsymbol{r}'|}d\boldsymbol{r}d\boldsymbol{r}' \tag{3.86}$$

and $E_{XC}[\rho]$ is the exchange-correlation energy.

Due to the spherical atomic symmetry, the atomic Kohn-Sham wavefunctions may be written as:

$$\psi_k(\boldsymbol{r}) = \frac{R_{nl}(\varepsilon_k; r)}{r} \cdot Y_{lm}(\Omega) \tag{3.87}$$

where, $R_{nl}(\varepsilon_k; r)$ are the radial wavefunctions and $Y_{lm}(\Omega)$ are spherical harmonics. Relativistic effects, which in principle require a four-current and Dirac-spinor formulation of the previous equations, are treated by using a scalar-relativistic kinetic energy operator (Koellin and Harmon, 1977). This takes into account the kinematic relativistic terms (the mass-velocity and Darwin terms) needed to properly describe the core states and the relativistic shifts of the valence levels, in particular, for the heavier elements. The spin-orbit coupling terms are averaged over, as is commonly done in most applications (see for example, Hemstreet *et al*., 1993). The radial wavefunctions satisfy the radial atomic equation:

$$\left[\frac{1}{2M(r)}\left(-\frac{d^2}{dr^2} - \frac{1}{2M(r)c^2}\frac{d\mathcal{V}(r)}{dr} r \frac{d}{dr}\frac{1}{r} + \frac{l(l+1)}{r^2}\right) + \mathcal{V}(r)\right] R_{nl}(\varepsilon_{nl}; r)$$
$$= \varepsilon_k R_{nl}(\varepsilon_{nl}; r) \tag{3.88.a}$$

where, the relativistic electron mass is given by:

$$M(r) = 1 + (\varepsilon_k - \mathcal{V}(r))/2c^2 \tag{3.88.b}$$

and c is the velocity of light. The effective potential $\mathcal{V}(r)$ is given by:

$$\mathcal{V}(r) = -\frac{Z}{r} + V_H[\rho; r] + V_{XC}[\rho; r] \tag{3.88.c}$$

The Hartree potential can be written using only radial integrations as:

$$V_{\mathrm{H}}[\rho; r] = 4\pi \frac{1}{r}\int_0^r \rho(r')\, r'^2 dr' + 4\pi \int_r^\infty \rho(r')\, r' dr' \tag{3.88.d}$$

Due to the spherical symmetry, states with the same quantum numbers n and l but different m are energetically degenerate. For a given n, there are $(2l+1)$ states which are equally occupied and:

$$\rho(r) = \frac{1}{4\pi}\sum_n \sum_{l=0}^{n-1} f_{nl} \left|\frac{R_{nl}(\varepsilon_{nl}; r)}{r}\right|^2 \tag{3.89}$$

with $f_{nl} = 2 \cdot (2l+1)$ $(\varepsilon_{nl} < \varepsilon_N)$; $f_{nl} = 0$ $(\varepsilon_{nl} > \varepsilon_N)$, and:

$$\sum_{nl} f_{nl} = N \tag{3.90}$$

Having obtained the all-electron potential and valence states, we use either the scheme by Hamann (1989) or by Troullier and Martins (1991) to construct the intermediate, so-called *screened pseudopotential*. The latter acts as the effective potential on the (pseudo) valence states:

$$\varphi_l^{ps}(\boldsymbol{r}) = \frac{U_l^{ps}\left(\varepsilon_l^{ps}; r\right)}{r} \cdot Y_{lm}(\Omega) \tag{3.91}$$

where the radial part for the angular momentum, l, is the lowest eigenfunction of the nonrelativistic Schrodinger equation:

$$\left(-\frac{1}{2}\frac{d^2}{dr^2} + \frac{l(l+1)}{2r^2} + V_l^{ps-s}\quad(r)\right) U_l^{ps}\left(\varepsilon_l^{ps}; r\right) = \varepsilon_l^{ps} U_l^{ps}\left(\varepsilon_l^{ps}; r\right) \tag{3.92}$$

Initially, a radial pseudo wavefunction $U_l^{ps}\left(\varepsilon_l^{ps}; r\right)$ is derived from the all-electron valence level with angular momentum l such that the conditions are satisfied:

1) $\varepsilon_l^{ps} = \varepsilon_{nl}$ (3.93.a)
2) $\frac{d}{dr} l_n U_l^{ps}(\varepsilon_l^{ps}; r) \rightarrow \frac{d}{dr} l_n R_{nl}(\varepsilon_{nl}; r) \quad \text{for } r > r_c^l$ (3.93.b)
3) $U_l^{ps}(\varepsilon_l^{ps}; r) \rightarrow R_{nl}(\varepsilon_{nl}; r) \quad \text{for } r > r_c^l$ (3.93.c)
4) $\int_0^\infty \left|U_l^{ps}(\varepsilon_l^{ps}; r)\right|^2 dr = \int_0^\infty |R_{nl}(\varepsilon_{nl}; r)|^2 = 1$ (3.93.d)
5) The pseudo wavefunction is continuous, contains no radial nodes, and it is regular at the origin:

$$\lim_{r \to 0} U_l^{ps}(\varepsilon_l^{ps}; r) \propto r^{l+1} \tag{3.93.e}$$

Conditions 3) and 4), the equality of the wavefunctions beyond the cut-off ratio r_c^l and the normalization condition, imply the norm-conservation constraint:

$$\int_0^{r_c^l} \left|U_l^{ps}(\varepsilon_l^{ps}; r)\right|^2 dr = \int_0^{r_c^l} |R_{nl}(\varepsilon_{nl}; r)|^2 \tag{3.94}$$

The pseudopotential components are then constructed and correspond to an inversion of the Schrödinger equation for the respective pseudo wavefunctions:

$$V_l^{ps-scr}(r) = \varepsilon_l^{ps} - \frac{l(l+1)}{2r^2} + \frac{1}{2\, U_l^{ps}(r)} \frac{d^2}{dr^2}\, U_l^{ps}(r) \tag{3.95}$$

and become identical to the all-electron potential beyond $r > r_c^l$.

The formation of the spatial function, $U_l^{ps}(r)$, requires three free parameters to meet the constraints (1) to (4). The Hamann (1989) scheme is of this minimal type, while the Troullier-Martins (1991) scheme introduces additional constraints, namely that the curvature of the pseudopotentials vanish at the origin:

$$\frac{d^2}{dr^2}\, V_l^{ps-spr}(r)\Big|_{r=0} = 0 \tag{3.96}$$

and that all first four derivatives of the pseudo and the all-electron wavefunction agree at the core cut-off radius. Thereby it achieves softer pseudopotentials for the $2p$, and the $3,4,5d$ valence states of the first row and of the transition metal elements, respectively. For other elements, both schemes perform rather alike. The details about the construction procedures may be found in the corresponding references (Hamann, 1989; Troullier-Martins, 1991). It must be pointed that both schemes technically differ somewhat regarding the radii where the pseudo wavefunctions and pseudopotentials match their all-electron counterparts. The Hamann scheme accomplishes the matching exponentially beyond the core cutoff radius, while in the Troullier-Martins scheme this matching is exact at and beyond it. Although in the Hamann scheme the core cutoff radii are nominally smaller, the pseudo wavefunctions and pseudopotentials converge to the all-electron wavefunctions and potential, within a similar range as in the Troullier-Martins scheme. Default values for the core cut-off radii are provided by the program psgen in fhi98pp. Except for some fine-tuning, that might be necessary when the pseudopotentials are used in the Kleinman-Bylander form (Kleinman and Bylander, 1982), these default values should yield a reasonable compromise between pseudopotential transferability and efficiency.

In general, increasing r_c^l yields softer pseudopotentials, which converge more rapidly, e.g. in a plane wave basis. These will become less transferable however as the pseudo wavefunctions become less accurate at radii relevant to bonding. When decreasing r_c^l one must keep in mind that r_c^l has to be larger than the radius of the outermost radial node in the respective all-electron orbital. Taking r_c^l too close to such a node, results in poor pseudopotentials, as it is essentially at variance with requiring both a nodeless and at the same time norm-conserving pseudo wavefunction. A rugged or multiple-well structure seen in a plot of the screened pseudopotential and poor scattering properties can indicate such a breakdown.

The final *ionic pseudopotentials* are determined by subtracting from the screened pseudopotentials the electrostatic and the exchange-correlation screening contributions due to the valence electrons:

$$V_l^{ps}(r) = V_l^{ps-} \quad (r) - V_H[\rho_0^{ps}; r] - V_{XC}[\rho_0^{ps}; r] \tag{3.97}$$

where valence electron density is evaluated from the atomic pseudo wavefunctions, with the same occupancies f_{nl} as for the all-electron valence states given previously:

$$\rho_0^{ps}(r) = \frac{1}{4\pi} \sum_n \sum_{l=0}^{n-1} f_{nl} \left| \frac{U_{nl}(\varepsilon_{nl}; r)}{r} \right|^2 \tag{3.98}$$

with the pseudopotentials as defined by this equation the electronic total energy of an arbitrary system can be obtained from:

$$E_{TOT} = \sum_i f_i < \varphi_i | T + V^{ps} | \varphi_i > + E_H[\rho^{ps}] + E_{XC}[\rho^{ps}] \tag{3.99}$$

with:

$$\rho^{ps}(r) = \sum_i f_i \, |\varphi_i(\boldsymbol{r})|^2 \tag{3.100}$$

Here, E_{XC} refers to the exchange-correlation interaction between the valence electrons themselves. That between the valence and the core electrons is included in the pseudopotential energy, as a term which depends linearly on the valence density ρ^{ps}. Although E_{XC} is a nonlinear functional of the total electron density ρ, the above "linearization" of its core-valence contribution is a usual and mostly adequate approximation for calculations within both LDA and GGA. However, an explicit account of the core-valence nonlinearity of E_{XC} is sometimes required, for instance in studies involving alkali metal atoms or within spin-density functional theory. This is accomplished by restoring the dependence of E_{XC} (and V_{XC}) on the total electron density, i.e., adding the (atomic) core density to the valence density in the argument of E_{XC}. In turn, the ionic pseudopotentials are redefined. Rather than the full core density, it suffices to add a so-called partial core density $\tilde{\rho}_0^{core}$, as suggested by Louie *et al*. (1982). It reproduces the full core density ρ_0^{core} outside a chosen cut-off radius r^{nlc} but is a smoother function inside, which enables its later use together with plane waves.

3.2.4.2.3 The new Pseudopotential for Uranium Atom

Since the CASTEP (Clark *et al.*, 2005) code only allows determining vibrational properties using norm conserving pseudopotentials and there is no such pseudopotential for the uranium atom, we decided to construct a new one. First, we generated a Troullier-Martins (1991) type norm-conserving pseudopotential using the program fhi98PP (Fuchs and Scheffler, 1999) in cpi format. The pseudopotential included relativistic effects (scalar relativistic all electron calculations were used) and it was generated using the GGA-PBE (Perdew *et al*., 1996a) method. The electronic configuration of atomic uranium is $6s^2\ 6p^6\ 6\mathrm{d}^1\ 5f^3\ 7s^2$. The pseudopotential was obtained from an ionized electronic configuration $6s^2\ 6p^6\ 6\mathrm{d}^1\ 5f^3\ 7s^0$ with cutoff radii equal to 1.236, 2.447, 2.166 and 2.447 for s, p, d and f angular momenta, respectively. The s component of the pseudopotential was chosen as the local potential, and a Kleinman–Bylander (1982) form was used. Then, we transformed it into the recpot format used in CASTEP by using the tool cpi2recpot (Haynes and Refson, 2007). The use of this pseudopotential implies that the 14 valence electrons must be treated explicitly. In other works, 32 electrons were included in the valence shell (Schreckenbach and Shamov, 2010; Shamov *et al*., 2007; Odoh and Schreckenbach, 2013). This further increases the computational cost and only marginally improves the performance (Beridze and Kowalski, 2014; Iché-Tarrat and Marsden, 2008). This pseudopotential reproduces accurately the all-electron calculation in the reference configuration in which it was generated.

Further, checks of the smoothness of the nodeless pseudowavefunctions near the cutoff radii, and of the continuity of the logarithmic energy derivatives and transferability of the pseudopotential were performed. In order to probe the generated norm-conserving pseudopotential under different environments and to validate it, we computed the structures of a series of uranium containing minerals with small cutoffs and K meshes. The results are given in a table in Appendix A of Bonales *et al.* (2016a). As can be seen in Table A1 of this reference, the results are quite good for the lattice parameters of the species involved. Better results were obtained upon increasing the cutoff values and using larger *K* meshes (Bonales *et al.*, 2016a; Colmenero *et al.*, 2017a; Colmenero *et al.*, 2017b: Colmenero *et al.*, 2017c; Colmenero *et al.*, 2017d; Colmenero *et al.*, 2017e).

3.2.5 Structure Optimization Methods

Although many numerical techniques exist for function minimisation in multiple dimensions, no minimisation algorithm is guaranteed to find a global minimum. However, some are guaranteed to find a minimum, being either a global or only a local minimum (Payne *et al.*, 1992; Pfrommer *et al.*, 1997). The simplest routes use only the value of the energy at each step. The minimum can be found by dealing with one degree of freedom at a time. An initial guess of two points along the one-dimensional path are made so that the points lie either side of the energy minimum. Subsequent guesses are made within the bounding points so that the bounded region becomes smaller at each new guess. Once a tolerance has been reached the algorithm then switches to another degree of freedom. The variables are not independent, so several cycles will be required. This algorithm is not suitable for structural minimisation within DFT due to the number of energy evaluations required to find the energy minimum.

More efficient algorithms are possible if the first derivatives of the energy (the gradient vector) are employed and further improvements in algorithm efficiency can be gained by not only using the first derivatives of the energy but also using the second derivatives (the Hessian matrix). In principle, if the function is quadratic, algorithm will find the minimum in a single iteration. Close to the energy minimum, the energy function described by density functional theory is quadratic, so this technique would be highly efficient. However, the Hessian matrix is not directly available from the density functional framework, and calculating it is many times more expensive than a force evaluation step. A method of avoiding the direct evaluation of the Hessian matrix is to use an update scheme. The idea is to start off with an approximation to the Hessian matrix, maybe just a unit matrix. As the optimisation proceeds the gradients at the previous points are used to make a better approximation of the Hessian matrix for the actual system. Many updating schemes exist, including *Broyden-Fletcher-Goldfarb-Shanno* (BFGS) method (Pfrommer *et al*., 1997; Payne *et al*., 1992) which is used in this work.

Efficient use of these techniques relies on being able to generate accurate energies and forces from DFT. The choice of an optimisation scheme becomes a trade-off between the time for self consistency to be reached within DFT and the number of steps required to find the minimum in the forces. The increase the accuracy, augments the computational effort dramatically. For example, the computational time scales as the inverse cube of the real-space grid spacing.

In this work, geometry optimization was carried out in all the cases by using the Broyden–Fletcher–Goldfarb–Shanno optimization scheme with a convergence threshold on atomic forces of 0.01 eV/Å. The kinetic energy cut-off and k-point meshes were adopted to ensure good convergence for computed structures and energies. The structures were optimized in calculations with increasing complexity by increasing these parameters in order to find reasonable values of these parameters. Once the values of these parameters have been found, they are employed to determine the final results (structural, mechanical, thermodynamic and vibrational properties).

3.2.6 X-Ray Diffraction

The relative intensity of hkl reflection in the X-ray powder pattern is given by (Downs *et al.*, 1993; Brindley and Brown, 1980):

$$I_{hkl} = mI_oL_p|F_{hk}\ |^2 \tag{3.101}$$

where m is the multiplicity of hkl reflection, I_o is a factor that scales the highest relative intensity to 100 ($I_o = 100/I_{hk}^{maz}$); L_p is the Lorentz factor, which for X-ray radiation is given by $L_p = [1 + cos^2 2\theta]/cos^2\theta\ sin\theta$,and for neutron radiation is given by $L_p = 1/sin^2\theta\ cos\theta$; and F_{hkl} is the structure amplitude which is given by:

$$|F_{hkl}|^2 = {A_{hkl}}^2 + {B_{hkl}}^2 \tag{3.102}$$

where,

$$A_{hk}\ = \sum_{j=1}^{n} f_j \cos[2\pi(hx_j + ky_j + lz_j)] \tag{3.103.a}$$

$$B_{hkl} = \sum_{j=1}^{n} f_j \sin[2\pi(hx_j + ky_j + lz_j)] \tag{3.103.b}$$

In the last two expressions, the sum runs over all the atoms in the unit cell, f_j is the scattering factor of atom j modified for temperature and anomalous dispersion effects*, and x_j, y_j and z_j are the atomic fractional coordinates. From the atomic coordinates of the atoms in the unit cell and the scattering factors (whose value may be obtained from standard tables†) we can determine A_{hkl} and B_{hkl}. From these values, we can obtain $|F_{hkl}|^2$ and, therefore, the relative intensity of each reflection in the X-ray powder pattern. For each $h, k, l \leq 10$ (it may be proved that for higher values the intensities fall off rapidly), we may determine the corresponding intensity. From the intensity values, we can perform a plot against the corresponding values of 2θ (for a given hkl we obtain the distances between atomic planes d and obtain the 2θ value using Bragg's law). Thus, from the atomic fractional coordinates for the atoms in the unit cell we can obtain the corresponding X-ray powder diffractogram. Several programs have been coded that generate theoretical powder diffractometer patterns (Yvon *et al.*, 1977; Bish and Post, 1989; and references therein; Smrdok and Weiss, 1993; Downs *et al.*, 1993).

3.2.7 Vibrational Theory. Raman Spectroscopy

3.2.7.1 Phonons. Vibrational Normal Modes

We can then express the energy of a lattice as a Taylor-series expansion as a function of small atomic displacements around the equilibrium positions. If the series is truncated at the fourth order, we obtain the following expression for the energy:

* $f_j = f_j' O_j e^{-B_j s^2}$ where f_j' is the unmodified scattering factor, O_j is the occupancy factor, B_j is the isotropic temperature factor and $s = \sin(\theta/\lambda)$.

† See for example, International Tables for X-Ray Crystallography, Vol. 4, pp. 99-101.

$$E = E^0 + \sum_{am\alpha}\left(\frac{\partial E}{\partial \tau^a_{m\alpha}}\right)\tau^a_{m\alpha} + \sum_{am\alpha}\sum_{bn\beta}\left(\frac{\partial^2 E}{\partial \tau^a_{m\alpha}\partial \tau^b_{n\beta}}\right)\Delta\tau^a_{m\alpha}\Delta\tau^b_{n\beta} + \sum_{am\alpha}\sum_{bn\beta}\sum_{co\gamma}\left(\frac{\partial^3 E}{\partial \tau^a_{m\alpha}\partial \tau^b_{n\beta}\partial \tau^c_{o\gamma}}\right)\Delta\tau^a_{m\alpha}\Delta\tau^b_{n\beta}\,\Delta\tau^c_{o\gamma} + \sum_{am\alpha}\sum_{bn\beta}\sum_{co\gamma}\sum_{dp\delta}\left(\frac{\partial^4 E}{\partial \tau^a_{m\alpha}\partial \tau^b_{n\beta}\partial \tau^c_{o\gamma}\partial \tau^d_{p\delta}}\right) \quad (3.104)$$

where:

$$\tau^a_{m\alpha} = \Delta r^a_{m\alpha} = r^a_{m\alpha} - r^a_{m\alpha}(0) \quad (3.105)$$

is the displacement along direction α of the atom m in the unit cell a, from its equilibrium position $\mathrm{r}^a_{m\alpha}(0)$. In the above expression, the first term, E^0, corresponds to the static energy of the unperturbed lattice. The second term is the first derivative of the energy that yields the forces acting on the atoms:

$$F^a_{m\alpha} = -\frac{\partial E}{\partial \tau^a_{m\alpha}} \quad (3.106)$$

This term is zero for a structure at equilibrium. The third term is the second derivative of the energy with respect to two atomic displacements, which yields the curvature of the energy curve. This term is also called *harmonic* because of the parallel with an elastic resort. It is of central interest in our following discussion for determining the phonon frequencies and corresponding atomic displacement patterns. The truncation of the Taylor series immediately after the harmonic term is called the *harmonic approximation*. It describes the lattice as quasi-elastic where the interatomic forces and the phonons are not damped. In this case, the interactions between the atoms are elastic. The fourth and fifth terms are the first anharmonic term. If calculated they give the phonon lifetimes and Raman/infrared peak widths. In particular, the fourth-order derivatives are involved in the computation of the phonon-phonon interactions and of the lattice heat conductivity. Further higher terms in the series expansion give various better corrections for anharmonicities.

Therefore, in the harmonic approximation, the total energy E of a periodic system with small lattice distortions from the equilibrium positions, can be expressed as:

$$E = E^0 + \sum_{am\alpha}\sum_{bn\beta}\left(\frac{\partial^2 E}{\partial \tau^a_{m\alpha}\partial \tau^b_{n\beta}}\right)\Delta\tau^a_{m\alpha}\Delta\tau^b_{n\beta} \quad (3.107)$$

In the harmonic approximation, we can write the following relations to obtain the phonon frequencies. The force on the atom m, that arises because of the displacement of another atom n (which can also be itself) can be expressed as:

$$F^a_{m\alpha} = -\sum_{bn\beta}\left(\frac{\partial^2 E}{\partial \tau^a_{m\alpha}\partial \tau^b_{n\beta}}\right)\Delta\tau^b_{n\beta} \quad (3.108)$$

There is a one-to-one parallel to the case of an elastic lattice, where the elastic force (given by $F = -kx$, with k being the elastic constant and x the displacement around the equilibrium position) can be expressed as:

$$F^a_{m\alpha} = -\sum_{bn\beta} C_{m\alpha;n\beta}(a,b)\;\Delta\tau^b_{n\beta} \quad (3.109.a)$$

where the matrix C represents the matrix of interatomic force constants (IFC), containing the elastic-like constants of all interatomic interactions:

$$C_{m\alpha;n\beta}(a,b) = \left(\frac{\partial^2 E}{\partial \tau^a_{m\alpha} \partial \tau^b_{n\beta}}\right) \tag{3.109.b}$$

With the atoms under the influence of forces, the classical Newtonian formalism (the force is mass times acceleration, $F = m \cdot a$) can be applied in this case:

$$F^a_{m\alpha} = M_m \frac{\partial^2 \Delta\tau^a_{m\alpha}}{\partial t^2} \tag{3.110}$$

where M_m is the mass of atom m and t is the time. Then, the two expressions of the forces, elastic and Newtonian can be equated as:

$$-\sum_{bn\beta} C_{m\alpha;n\beta}(a,b)\ \Delta\tau^b_{n\beta} = M_m \frac{\partial^2 \Delta\tau^a_{m\alpha}(t)}{\partial t^2} \tag{3.111}$$

forming a system of differential equations, whose solution may be expressed as:

$$\Delta\tau^a_{m\alpha}(t) = \sum_{\sigma} A_\sigma U^a_\sigma(m,\alpha)\, e^{i\omega_\sigma t} + \mathsf{C} \tag{3.112}$$

where C is a constant and $U^a_\sigma(m,\alpha)$ satisfies:

$$\sum_{bn\beta} C_{m\alpha;n\beta}(a,b)\ U^b_\sigma(n,\beta) = M_m\, \omega^2_\sigma U^a_\sigma(m,\alpha) \tag{3.113}$$

The solution of this system of equations represents a set of periodic elastic waves that correspond to atomic vibrations around their positions of equilibrium with some specific frequencies. In these equations, σ labels the normal modes, A_σ their amplitude and ω_σ their normal mode angular frequency. The pattern of the atomic displacements is set by $U^a_\sigma(m,\alpha)$.

Let us now introduce the periodicity of the lattice. The Fourier transform if the IFC takes the form:

$$\tilde{C}_{m\alpha;n\beta}(\boldsymbol{q}) = \frac{1}{\mathcal{N}} \sum_{a,b} C_{m\alpha;n\beta}(a,b)\, e^{-i\boldsymbol{q}\cdot(\boldsymbol{R}_a - \boldsymbol{R}_b)} \tag{3.114.a}$$

where $\mathcal{N}$ is the number of unit cells in the system. Due to the periodicity of the system $C_{m\alpha;n\beta}(0,b) = C_{m\alpha;n\beta}(1,b) = \cdots = C_{m\alpha;n\beta}(N,b)$ and the Fourier transform may be rewritten:

$$\tilde{C}_{m\alpha;n\beta}(\boldsymbol{q}) = \sum_{b} C_{m\alpha;n\beta}(0,b)\, e^{-i\boldsymbol{q}\cdot\boldsymbol{R}_b} \tag{3.114.b}$$

The dynamical matrix or Hessian takes the form:

$$\widetilde{D}_{m\alpha;n\beta}(\boldsymbol{q}) = \frac{\tilde{C}_{m\alpha;n\beta}(\boldsymbol{q})}{\sqrt{M_m M_n}} \tag{3.115}$$

The normal modes of oscillation and the eigen-modes are available from the solution to the eigenvalue problem:

$$\sum_{n\beta} \widetilde{D}_{m\alpha;n\beta}(\boldsymbol{q})\, \chi_{\boldsymbol{q}\sigma}(n,\beta) = \omega^2_{\boldsymbol{q}\sigma} \chi_{\boldsymbol{q}\sigma}(m,\alpha) \tag{3.116}$$

where $\omega_{\boldsymbol{q}\sigma}$ is the phonon frequency of mode σ at a point in reciprocal space given by $\boldsymbol{q}$, and $\chi_{\boldsymbol{q}\sigma}(m,\alpha)$ are the normal modes of oscillation:

$$Q_\sigma = \sum_{m,\alpha} \chi_{\boldsymbol{q}\sigma}(m,\alpha)\, \tau_{m\alpha} \tag{3.117}$$

The dynamical matrix is square with dimension $3N \times 3N$, where N is the number of nuclei in the unit cell and 3 comes from the three directions of the space. Its diagonalization yields the eigenvalues, which are the square of the phonon frequencies, and the eigenvectors, which are the atomic displacements corresponding to the vibrations. Each eigenvector has $3N$ components, corresponding to the displacement of each of the N atoms along the three Cartesian directions. The phonons, also named phonon modes, can be degenerated. The full symmetry description of the phonons modes can be done using the irreducible representations (see next section).

The representation of the phonon frequencies as a function of wavevector $\boldsymbol{q}$ corresponds to the dispersion relations that form the phonon band structures (*phonon dispersion curves*). As for all waves propagating in a periodic medium, *e.g.* electronic wave, the wavevectors are restricted to the Brillouin zone, the smallest periodic cell of the reciprocal lattice delimited by Bragg planes. As for electrons, the phonon dispersion relations are represented for a selected set of high-symmetry points in the Brillouin zone.

From all the points of the Brillouin zone, the centre, $\boldsymbol{q} = (0,0,0)$, labelled the $\boldsymbol{\Gamma}$ point, is of particular interest. It is particularly useful to describe the phonon modes at $\boldsymbol{q} = \boldsymbol{0}$, as they are sampled using Raman and infrared spectroscopies. The phonons at $\boldsymbol{\Gamma}$ point have identical displacement patterns in all unit cells of the lattice. By contrast, all the other points in the Brillouin zone correspond to waves with a finite wavelength and a phase varying from cell to cell, *i.e.* propagating waves. There are three phonon branches, referred to as *acoustic*, which go to zero frequency when $\boldsymbol{q}$ approaches $\boldsymbol{0}$. For these modes, all atoms have identical displacements along each of three Cartesian directions. Due to the translational invariance, the structure is left invariant and the frequency of these modes is zero. The dispersion of these modes (measured for example in Brillouin spectroscopy) is related to the elastic constants tensor and eventually to the velocity of the acoustic waves travelling through the crystal.

In the harmonic approximation, because of the missing third- and higher-order derivatives, the potential wells are symmetrical around the atomic equilibrium positions. However, these wells are asymmetric, because the repulsion and attraction components of the interatomic interactions are not symmetrical. The effect of asymmetrization changes the curvature at zero and thus eventually affects the phonon frequency – one of the main reasons the computed phonon frequencies disagree with the measured ones. Considering high-order terms in the Taylor expansion increases the agreement between the two techniques. But for most of the physical applications and crystal structures, the quasiharmonic approximation gives already meaningful results.

3.2.7.2 Linear Response Phonon Calculation

The interatomic force constant matrix is a second order derivative of the energy. Linear response uses perturbation theory to calculate the second derivative without the need to resort to the finite-differences method. The basic tool for accomplishing this goal is the Hellmann-Feynman theorem (Hellmann, 1937; Feynman, 1939), which states that the first derivative of the eigenvalues of the Hamiltonian, H_λ, that depend on a parameter λ, is given by the expectation value of the derivative of the Hamiltonian:

$$\frac{\partial E_\lambda}{\partial \lambda} = \langle \Psi \left| \frac{\partial H_\lambda}{\partial \lambda} \right| \Psi \rangle \tag{3.118}$$

By applying the Hellmann-Feynman theorem to calculate the derivative of the energy with respect to the nuclear position, we obtain the forces on atom I as:

$$\frac{\partial E(\boldsymbol{R})}{\partial \boldsymbol{R_I}} = \langle \Psi \left| \frac{\partial H_0}{\partial \boldsymbol{R_I}} \right| \Psi \rangle \tag{3.119}$$

Since we have assumed the Born-Oppenheimer approximation, the Hamiltonian depends on $\boldsymbol{R}$, via the electron-ion interaction that couples to the electronic degrees of freedom only through the electron charge density, the forces can therefore be written as:

$$\frac{\partial E(\boldsymbol{R})}{\partial \boldsymbol{R_I}} = \int \rho^{\boldsymbol{R}}(\boldsymbol{r}) \frac{\partial V_{\boldsymbol{R}}(\boldsymbol{r})}{\partial \boldsymbol{R_I}} d\boldsymbol{r} - \frac{\partial E_N(\boldsymbol{R})}{\partial \boldsymbol{R_I}} \tag{3.120.a}$$

Where $\rho^{\boldsymbol{R}}$ is the ground state electron density corresponding to nuclear configuration $\boldsymbol{R}$, $V_{\boldsymbol{R}}$ is the electron nucleus interaction which is given by:

$$V_{\boldsymbol{R}}(r) = -\sum_J \frac{Z_J e^2}{|r - R_J|} \tag{3.120.b}$$

and E_N is the electrostatic nuclear repulsion energy:

$$E_N(\boldsymbol{R}) = -\sum_{I \neq J} \frac{Z_I Z_J e^2}{|R_I - R_J|} \tag{3.120.c}$$

The dynamical matrix can now be generated by differentiating this equation with respect to the nuclear coordinates (Baroni, 2001):

$$\frac{\partial^2 E(\boldsymbol{R})}{\partial \boldsymbol{R_I} \partial \boldsymbol{R_J}} = \int \frac{\partial \rho^{\boldsymbol{R}}(\boldsymbol{r})}{\partial \boldsymbol{R_J}} \frac{\partial V_{\boldsymbol{R}}(\boldsymbol{r})}{\partial \boldsymbol{R_I}} d\boldsymbol{r} + \int \rho^{\boldsymbol{R}}(\boldsymbol{r}) \frac{\partial^2 V_{\boldsymbol{R}}(\boldsymbol{r})}{\partial \boldsymbol{R_I} \partial \boldsymbol{R_J}} d\boldsymbol{r} - \frac{\partial^2 E_N(\boldsymbol{R})}{\partial \boldsymbol{R_I} \partial \boldsymbol{R_J}} \tag{3.121}$$

To calculate the dynamical matrix, it is therefore necessary to obtain both the electron density $\rho^{\boldsymbol{R}}$ and the linear response of the electron density $\partial \rho^{\boldsymbol{R}}(\boldsymbol{r}) / \partial \boldsymbol{R_J}$. The self consistent generation of the electron density is performed by means of a standard DFT calculation. The change in the electronic density is obtained by density functional perturbation theory (DFPT). Density functional perturbation allows the generation of the interatomic force constant matrix without the need to physically displace atoms from their equilibrium position. However, to simulate an atomic displacement it is still necessary to self consistently solve the perturbed Kohn-Sham energy functional. The increase in computational efficiency comes from the size of displacements needed. In finite displacements, small displacements are very sensitive to numerical errors, so it is necessary to use relatively large displacements. In DFPT the problem of numerical error is avoided, resulting in a reduced dependency on the size of the supercell and a smaller difference between ground-state and perturbed electron density, resulting in shorter times to reach self-consistency.

3.2.7.3 Density Functional Perturbation Theory (DFPT)

In order to simplify the notation and make the argument more general, we assume that the external potential acting on the electrons is a differentiable function of a set of parameters, $\lambda = \{\lambda_i\}$ ($\lambda_i = \boldsymbol{R_I}$, in the case of lattice dynamics). According to the Hellmann-Feynman theorem (Hellmann, 1937; Feynman, 1939), the first and second derivatives of the ground-state energy read:

$$\frac{\partial E}{\partial \lambda_i} = \int \frac{\partial V_\lambda(\boldsymbol{r})}{\partial \lambda_i} \rho_\lambda(\boldsymbol{r}) d\boldsymbol{r} \tag{3.122.a}$$

$$\frac{\partial^2 E}{\partial \lambda_i \partial \lambda_j} = \int \frac{\partial^2 V_\lambda(\boldsymbol{r})}{\partial \lambda_i \partial \lambda_j} \rho_\lambda(\boldsymbol{r}) d\boldsymbol{r} + \int \frac{\partial V_\lambda(\boldsymbol{r})}{\partial \lambda_i} \frac{\partial \rho_\lambda(\boldsymbol{r})}{\partial \lambda_j} d\boldsymbol{r} \tag{3.122.b}$$

The electron-density response, $\partial \rho_\lambda(\boldsymbol{r}) / \partial \lambda_i$, appearing in the last equation can be evaluated by linearizing the following equations with respect to the wavefunction, density and potential variations:

$$\left(-\frac{1}{2m}\frac{\partial^2}{\partial \boldsymbol{r}^2}+V_{SCF}(\boldsymbol{r})\right)\psi_n(\boldsymbol{r})=\epsilon_n\psi_n(\boldsymbol{r}) \qquad (3.123.a)$$

$$\rho(\boldsymbol{r})=2\sum_{n=1}^{N/2}|\psi_n(\boldsymbol{r})|^2 \qquad (3.123.b)$$

$$V_{SCF}(\boldsymbol{r})=V(\boldsymbol{r})+e^2\int\frac{\rho(\boldsymbol{r}')}{|\boldsymbol{r}-\boldsymbol{r}'|}d\boldsymbol{r}'+v_{XC}(\boldsymbol{r}) \qquad (3.123.c)$$

Linearization of the first equation, leads to:

$$\Delta\rho(\boldsymbol{r})=4\,Re\sum_{n=1}^{N/2}\psi_n^*(\boldsymbol{r})\Delta\psi_n(\boldsymbol{r}) \qquad (3.124.a)$$

where the finite-difference operator Δ^λ is defined as:

$$\Delta^\lambda F=\sum_{i=1}^{N/2}\frac{\partial F_\lambda}{\partial\lambda_i}\Delta\lambda_i \qquad (3.124.b)$$

The superscript λ has been omitted in the equation for $\Delta\rho(\boldsymbol{r})$, as well as in any subsequent formulas where such an omission does not give rise to ambiguities. Since the external potential (both unperturbed and perturbed) is real, each Kohn-Sham eigenfunction and its complex conjugate are degenerate. Therefore, the imaginary part of the sum appearing in the equation for $\Delta\rho(\boldsymbol{r})$ vanishes, so that the prescription to keep only the real part can be dropped.

The variation of the Kohn-Sham orbitals, $\Delta\psi_n(\boldsymbol{r})$, is obtained by standard first-order perturbation theory (Messiah, 1962):

$$H_{SCF}-\epsilon_n\mid\Delta\psi_n(\boldsymbol{r})>=-(\Delta V_{SCF}-\Delta\epsilon_n)\mid\psi_n(\boldsymbol{r})> \qquad (3.125.a)$$

where

$$H_{SCF}=-\frac{1}{2m}\frac{\partial^2}{\partial\boldsymbol{r}^2}+V_{SCF}(\boldsymbol{r}) \qquad (3.125.b)$$

is the unperturbed Kohn-Sham Hamiltonian:

$$\Delta V_{SCF}(\boldsymbol{r})=\Delta V(\boldsymbol{r})+e^2\int\frac{\Delta\rho(\boldsymbol{r}')}{|\boldsymbol{r}-\boldsymbol{r}'|}d\boldsymbol{r}'+\left.\frac{dv_{XC}(\boldsymbol{r})}{d\rho}\right|_{\rho=\rho(\boldsymbol{r})}\Delta\rho(\boldsymbol{r}) \qquad (3.125.c)$$

is the first-order correction to the self-consistent potential, and $\Delta\epsilon_n$ is the first-order variation of the Kohn-Sham eigenvalue ϵ_n.

In the atomic physics literature, an equation analogous to that of $H_{SCF}-\epsilon_n\mid\Delta\psi_n(\boldsymbol{r})>$ is known as the Sternheimer equation, after the work in which it was first used to calculate atomic polarizabilities (Sternheimer, 1954). A self-consistent version of the Sternheimer equation was introduced by Mahan (1980) to calculate atomic polarizabilities within density-functional theory in the LDA. Similar methods are known in the quantum chemistry literature under the generic name of analytic evaluation of second-order energy derivatives (Gerratt and Mills, 1968; Amos, 1987). In the specific context of the Hartree-Fock approximation, the resulting algorithm is called the coupled Hartree-Fock method (Gerratt and Mills, 1968).

The previous equations form a set of self-consistent equations for the perturbed system completely analogous to the Kohn-Sham equations in the unperturbed case with the Kohn-Sham eigenvalue equation being replaced by the solution of a linear system. In the present case, the self-consistency requirement manifests itself in the dependence of the right-hand side upon the solution of the linear system. As $\Delta V_{SCF}(\boldsymbol{r})$ is a linear functional of $\Delta\rho(\boldsymbol{r})$, which in turn depends linearly on the $\Delta\psi_n(\boldsymbol{r})'$s, the whole self-consistent calculation can be cast in terms of a generalized linear

problem. Note, however, that the right-hand side of the equation for $\Delta\psi_n(\boldsymbol{r})$, depends through $\Delta\rho$ on the solution of all the similar equations holding for the $\Delta\psi_m$ $(m \neq n)$. Hence all the N equations, for $\Delta\psi_n(\boldsymbol{r})$ are linearly coupled to each other, and the set of all the $\Delta\psi_n(\boldsymbol{r})$'s is the solution of a linear problem whose dimension is $(N\ M/2 \times N\ M/2)$, M being the size of the basis set used to describe the c's. The explicit form of this big linear equation can be worked out directly from present equations or it can equivalently be derived from a variational principle. Whether this large linear system is better solved directly by iterative methods or by the self-consistent solution of the smaller linear systems is a matter of computational strategy.

The first-order correction to a given eigenfunction of the Schrödinger equation, given by the previous equation, is often expressed in terms of a sum over the spectrum of the unperturbed Hamiltonian:

$$\Delta\psi_n(\boldsymbol{r}) = \sum_{m\neq n} \psi_m(\boldsymbol{r}) \frac{\langle\psi_m|\Delta V_{SCF}|\psi_n\rangle}{\epsilon_n - \epsilon_m} \qquad (3.126.a)$$

The sum runs over all the states of the system, occupied and empty, with the exception of the state being considered, for which the energy denominator would vanish. Using this equation, the electron charge-density response (the equation for $\Delta\rho(\boldsymbol{r})$), can be cast into the form:

$$\Delta\rho(\boldsymbol{r}) = 4\sum_{n=1}^{N/2}\sum_{m\neq n} \psi_m(\boldsymbol{r})\,\psi_n^*(\boldsymbol{r}) \frac{\langle\psi_m|\Delta V_{SCF}|\psi_n\rangle}{\epsilon_n - \epsilon_m} \qquad (3.126.b)$$

This equation shows that the contributions to the electron-density response coming from products of occupied states cancel each other, so that the m index can be thought of as attaching to conduction states only. This is equivalent to saying that the electron-density distribution does not respond to a perturbation, which acts only on the occupied-state manifold (or, more generally, to the component of any perturbation which couples occupied states among each other).

The explicit evaluation of $\Delta\psi_n(\boldsymbol{r})$ from its last expression would require a knowledge of the full spectrum of the Kohn-Sham Hamiltonian and extensive summations over conduction bands. In the prior equation, instead, only knowledge of the occupied states of the system is needed to construct the right-hand side of the equation, and efficient iterative algorithms—such as the conjugate gradient (Press *et al*., 1989; Stich *et al*., 1989; Payne *et al*., 1992) or minimal residual (Press *et al*. 1989; Saad and Schultz, 1986) methods—can be used for solution of the linear system. In this way, the computational cost of determining of the density response to a single perturbation is of the same order as that needed to calculate the unperturbed ground-state density.

The left-hand side of equation for $H_{SCF} - \epsilon_n \mid \Delta\psi_n(\boldsymbol{r}) >$ is singular because the linear operator appearing therein has a null eigenvalue. However, we saw above that the response of the system to an external perturbation depends only on the component of the perturbation that couples the occupied-state manifold with the empty-state one. The projection onto the empty-state manifold of the first-order correction to occupied orbitals can be obtained from this equation by replacing its right-hand side with $-P_c\,\Delta V_{SCF}(\boldsymbol{r})|\,\psi_n(\boldsymbol{r}) >$, where P_c is the projector onto the empty-state manifold, and by adding to the linear operator on its left-hand side $H_{SCF} - \epsilon_n$, a multiple of the projector onto the occupied-state manifold, P_v, so as to make it nonsingular:

$$H_{SCF} + \alpha P_v - \epsilon_n \mid \Delta\psi_n(\boldsymbol{r}) > = -P_c\,\Delta V_{SCF}(\boldsymbol{r})|\,\psi_n(\boldsymbol{r}) > \qquad (3.127)$$

In practice, if the linear system is solved by the conjugate-gradient or any other iterative method and the trial solution is chosen orthogonal to the occupied state manifold, orthogonality is maintained during iteration without regard for the extra P_v, term on the left-hand side of last equation. The above discussion applies to insulators in which the gap is finite. In metals, a finite density of states (DOS) occurs at the Fermi energy, and a change in the orbital occupation number may occur upon the application of an infinitesimal perturbation. The modifications of DFPT needed to treat the linear response of metals have been discussed by de Gironcoli (1995).

3.2.7.4 Electrostatics in Extended Systems. Born Charges

The standard picture of the polarisation of a material is that the material is composed of neutral polariseable units. The polarisation is the sum of the dipole moments per unit volume and each dipole moment is well defined. This is the model presented in Aschcroft and Mermin (1976) and Kittel (1996). However, in quantum mechanics all electrons are equivalent and an electron cannot be assigned to a given molecule or unit cell of a crystal. The charge density on the electrons is a continuous function of the positions and there is no definitive way to divide up the density to derive the dipole moment of a cell (Martin, 1974). It is, therefore, necessary to consider a finite system made of many unit cells. Unique, physically meaningful results can be derived in an extended material, only if one considers contributions to the polarisation, not only from the changes in the dipole moment in the cells in the interior but also from contributions of surface charges which do not vanish as the size of the sample goes to infinity (Martin, 1974). The change in the surface charge can however be related to integrals over currents flowing through the interior of the body. This relation to the current is the basis of the modern theory of polarisation, allowing the polarisation to be uniquely derived in terms of the wavefunction in the interior of the material (King-Smith and Vanderbilt, 1993).

Central to the modern theory of polarisation is the proposition of Resta (Resta, 1994) to write the electronic contribution to the change in polarisation due to a finite adiabatic change in the Kohn-Sham Hamiltonian as:

$$\Delta \boldsymbol{P} = \int_0^1 d\lambda \frac{\partial P}{\partial \lambda} \tag{3.128.a}$$

King-Smith and Vanderbilt (1993) showed that for an infinite periodic system the adiabatic expression can be cast as a Berry's phase approach (Berry, 1984) resulting in the expression:

$$\Delta \boldsymbol{P} = \boldsymbol{P^{(1)}} - \boldsymbol{P^{(0)}} \tag{3.128.b}$$

The α component of polarization vector $\boldsymbol{P}^{(\lambda)}$ is given by (King-Smith and Vanderbilt, 1993),

$$\boldsymbol{P}_{\alpha}^{(\lambda)} = -if\frac{2}{(2\pi)^3}\int_{BZ}\sum_{n}\langle u_{\boldsymbol{q}n}^{\lambda}\left|\frac{\partial}{\partial \boldsymbol{q}_{\alpha}}\right|u_{\boldsymbol{q}n}^{\lambda}\rangle\, d\boldsymbol{q} \tag{3.128.c}$$

The *static charge* is an intuitive concept based on partitioning the ground-state electronic density into contributions attributed to different atoms. It is however an ill-defined concept within quantum mechanics, where the electrons are delocalised and cannot be assigned to a particular state. Definitions can be introduced to divide up the charge between the atoms but the charge associated to an atom becomes dependent upon the convention chosen. On the other hand, it is possible to infer a *dynamical charge* using the theory of polarisation as described by King-Smith and Vanderbilt (1993). The dynamical or *Born charge* is directly related to the change in polarisation created by an atomic displacement and, hence, is a well-defined quantity and can in theory be measured by experiment. The dynamical charge is related to the polarisation upon atomic displacement, so unlike the static charge, the dynamical charge is a measurable quantity in principle. For a periodic solid, the Born effective charge of atom i is a tensor defined as the coefficient of proportionality under the conditions of zero macroscopic electric field, between the macroscopic polarisation per unit cell in direction α and to the displacement of atom i in direction β:

$$Z_{i,\alpha,\beta}^{*} = \frac{\Omega_0}{e}\left(\frac{\partial P_{\alpha}}{\partial u_{i,\beta}}\right)_{\boldsymbol{q}=\boldsymbol{0}} \tag{3.129}$$

where e is the charge of an electron and Ω_0 is the unit cell volume. The problem simply becomes the calculation of the change in polarisation for a given displacement, which we can calculate using the theory of polarisation for an extended quantum system. The direction of polarisation does not necessarily lie along the direction of displacement, thus leading to the Born effective charge being a tensor quantity.

3.2.7.5 Infrared Intensities

The infrared (IR) intensity of the vibrational modes are determined by how the electric dipole moment of the system changes with the atomic isolations. To the lowest order, the required properties are proportional to the derivatives of the dipole moment and polarizability with respect to the vibrational normal modes, evaluated at the equilibrium geometry. The IR intensity of the i-th vibrational mode is given by (Wilson, Decius, and Cross, 1955; Porezag and Pederson, 1996):

$$I_{\sigma}^{IR} = \frac{\mathcal{N}\pi}{3c}\left|\frac{d\boldsymbol{\mu}}{dQ_{\sigma}}\right|^{2} \tag{3.130}$$

where $\boldsymbol{\mu}$ is the dipole moment, $\mathcal{N}$ is the number of atoms per unit volume and Q_{σ} is the normal node coordinate corresponding to the σ^{th} mode:

$$Q_{\sigma} = \sum_{m,\alpha} \chi_{\sigma}(m,\alpha)\, r_{m\alpha} \tag{3.131}$$

We may write the last relation in matrix-vector form as:

$$\boldsymbol{Q} = \boldsymbol{\chi}\,\boldsymbol{r} \tag{3.132}$$

so that,

$$\boldsymbol{r} = \boldsymbol{\chi}^{-1}\boldsymbol{Q} = \boldsymbol{X}\boldsymbol{Q}\boldsymbol{r} \tag{3.133}$$

and, therefore,

$$r_{m\alpha} = \sum_{\sigma} X_{m,\alpha}^{\sigma}\, Q_{\sigma}\boldsymbol{r} \tag{3.134}$$

and

$$\frac{\partial r_{m\alpha}}{\partial Q_{\sigma}} = X_{m,\alpha}^{\sigma}\boldsymbol{r} \tag{3.135}$$

To obtain the IR intensity we must compute the dipole derivative with respect to the normal-mode coordinates. These can be viewed as directional derivatives in the space of $3N$ nuclear coordinates and expressed using the chain rule in terms of derivatives with respect to the atomic coordinates $r_{m\alpha}$ for an arbitrary function A:

$$\frac{dA}{dQ_{\sigma}} = \sum_{m,\alpha}\frac{\partial A}{\partial r_{m\alpha}}\frac{\partial r_{m\alpha}}{\partial Q_{\sigma}} = \sum_{m,\alpha}\frac{\partial A}{\partial r_{m\alpha}}X_{m,\alpha}^{\sigma} \tag{3.136}$$

Thus,

$$\frac{d\mu_{\beta}}{dQ_{\sigma}} = \sum_{m,\alpha}\frac{\partial \mu_{\beta}}{\partial r_{m\alpha}}X_{m,\alpha}^{\sigma} \tag{3.137}$$

The information required to calculate the IR intensity for a mode of oscillations can then be obtained from a full set of Born effective charges and the phonon normal modes:

$$\frac{\partial \mu_{\beta}}{\partial Q_{\sigma}} = \frac{\partial P_{\beta}}{\partial Q_{\sigma}} = \sum_{m,\alpha}\frac{\partial P_{\beta}}{\partial r_{m\alpha}}X_{m,\alpha}^{\sigma} = \Omega_{0}\sum_{m,\alpha} Z_{m,\beta,\alpha}^{*}X_{m,\alpha}^{\sigma} \tag{3.138.a}$$

$$I_{\sigma}^{IR} = \frac{N\pi}{3c\Omega_{0}}\sum_{\beta}\left|\frac{\partial P_{\beta}}{\partial Q_{\sigma}}\right|^{2} = \frac{N\pi\Omega_{0}}{3c}\sum_{\beta}\left[\sum_{m,\alpha} Z_{m,\beta,\alpha}^{*}\, X_{m,\alpha}^{\sigma}\right]^{2} \tag{3.138.b}$$

The IR spectrum obtained with this technique will only produce peaks at the point in the spectrum corresponding to the phonon frequency. In experimental IR data, broad peaks are observed resulting from thermal distortions or imperfections in the crystal. For example, water molecules produce very broad peaks due to local environment changes.

3.2.7.6 LO-TO Splitting

By imposing periodic boundary conditions on the unit cell, the electric field is forced to go to zero at the boundaries. The electrostatic interaction caused by the displacement of an atom is effectively damped. For insulators close to $\boldsymbol{q} = \boldsymbol{0}$, the behaviour of the dynamical matrix is strongly influenced by these long-range electrostatics with an average r^{-3} decay (r being the interatomic distance), corresponding to a dipole-dipole interaction (Gonze and Lee, 1997). Although other electrostatic interactions are possible, for example quadrupole-quadrupole interactions, which decays as r^{-5} , or octupole-octupole interactions, which decay as r^{-7}, the contribution of the dipole-dipole interaction is the strongest and has the longest range.

Therefore, the boundary conditions applied to the system prevent long range electrostatics. This becomes prominent when considering the phonon modes near the zone centre and is responsible for the longitudinal optic (LO) and transverse optic (TO) mode splitting. The largest contribution to the LO-TO splitting is from the dipole-dipole interaction. The dipole produced from a particular atomic displacement can be reproduced from the Born effective charges. A correction factor can be calculated for the dynamical matrix, which reintroduces the long-range dipole-dipole interaction from knowledge of the Born charges and the dielectric constant. The work of Archer (2004) may serve as an illustration of a form of introducing the LO-TO correction.

The LO and TO modes have interesting properties and reveal information on the structure and shape of the solid. The LO and TO modes always appear together with the frequency of the LO modes being always larger than that of TO modes. The separation of these modes depends on the intensity of the vibrational mode and on the shape of the particle being studied. The splitting of these modes for polycrystalline samples is given by (Kuo *et al*., 2002; Escribano, 2016):

$$\nu_{LO}^2 - \nu_{TO}^2 = \frac{4\pi}{\varepsilon_\infty \Omega_0} \left| \frac{\partial \boldsymbol{P}}{\partial Q_\sigma} \right|^2 \tag{3.139}$$

where Ω_0 is the volume of the unit cell, ε_∞ is the dielectric constant at frequencies far from the resonance and $\partial \boldsymbol{P} / \partial Q_\sigma$ is the polarization variation at the σ normal mode. Since the splitting is proportional to square of polarization variation, it may be determined from the observed value of the splitting.

3.2.7.7. Acoustic Sum Rule

Within the scheme proposed to generate the dynamical matrix, many numerical approximations have been made which result in errors in the dynamical matrix which break the translational invariance. The lack of translational invariance can be partially corrected by applying the acoustic sum rule to the dynamical matrix. The dynamical matrix at the zone centre should admit the homogeneous translations of the solid as eigenvectors with zero eigen frequency. The requirement is known as the *acoustic sum rule:*

$$\sum_n \tilde{C}_{m\alpha;n\beta}(\boldsymbol{q} = \boldsymbol{0}) = 0 \tag{3.140}$$

The condition can be restored by the following operation:

$$\tilde{C}_{m\alpha;n\beta}(\boldsymbol{q} = \boldsymbol{0}) = \tilde{C}_{m\alpha;n\beta}(\boldsymbol{q} = \boldsymbol{0}) - \delta_{mn} \sum_p \tilde{C}_{p\alpha;n\beta}(\boldsymbol{q} = \boldsymbol{0}) \tag{3.141.a}$$

By using this operation, the eigen-frequencies at $\boldsymbol{q} = \boldsymbol{0}$ will change and will no longer be the limit of the eigen-frequency obtained by making $\boldsymbol{q} \to \boldsymbol{0}$ unless the other dynamical matrices for $\boldsymbol{q} \neq \boldsymbol{0}$ are also corrected. The generalisation of the correction is

$$\tilde{C}_{m\alpha;n\beta}(\boldsymbol{q}) = \tilde{C}_{m\alpha;n\beta}(\boldsymbol{q}) - \delta_{mn} \sum_p \tilde{C}_{p\alpha;n\beta}(\boldsymbol{q} = \boldsymbol{0}) \tag{3.141.b}$$

3.2.7.8 Raman Intensities

The Raman intensity of a specific mode σ is determined by the specific Raman scattering efficiency (S) via a prefactor. The Raman scattering efficiency depends on the frequency of the incoming photon, ν_0, on the frequency of the phonon, ν_σ, on temperature, T, and on the Raman tensor $\boldsymbol{\alpha}^\sigma$ of a particular mode σ. Its full expression is (Cardona, 1982; Caracas and Bobocioiu, 2012; Placzek, 1934; Porezag and Pederson, 1996):

$$\frac{dS_\sigma}{d\Omega} = \frac{(\omega_0 - \omega_\sigma)^4}{c^4} |\boldsymbol{e_s} \cdot \boldsymbol{\alpha}^\sigma \cdot \boldsymbol{e_0}|^2 \frac{h}{2\omega_\sigma}(n_\sigma + 1) \tag{3.142}$$

where $\boldsymbol{e_s}$ and $\boldsymbol{e_0}$ are the orientations of the scattered and incident light (*i.e.* laser), respectively. The dependence on temperature is given by the boson factor:

$$n_\sigma = \frac{1}{e^{h\omega_\sigma/k_B T} - 1} \tag{3.143}$$

The Raman tensor is given by:

$$\alpha_{ij}^\sigma = \sqrt{\Omega_0} \sum_{n,\beta} \frac{\partial \alpha_{ij}}{\partial \tau_{n\beta}} X_{n,\beta}^\sigma = \sqrt{\Omega_0} \sum_{n,\beta} \frac{\partial \chi_{ij}^\infty}{\partial \tau_{n\beta}} X_{n,\beta}^\sigma = \sqrt{\Omega_0} \sum_{n,\beta} \frac{\partial}{\partial \tau_{n\beta}} \left(\frac{\partial^2 E}{\partial \varepsilon_i \partial \varepsilon_j} \right) \varepsilon_i \varepsilon_j X_{n,\beta}^\sigma$$
$$= \sum_{n,\beta} R_{ij}^{n\beta} X_{n,\beta}^\sigma \tag{3.144}$$

Therefore, it depends upon the polarizability tensor α derivatives, which in the case of solids become macroscopic dielectric tensor χ derivatives with respect to the set of atomic displacements that correspond to the phonon eigenvector (Baroni and Resta, 1986; Lazzeri and Mauri, 2003; Veithen *et al.*, 2005). The middle term in the above equation $|e_s \cdot \boldsymbol{\alpha}^m \cdot e_0|$ gives the coupling between the incoming phonon with polarization $\boldsymbol{e_0}$, the crystal, characterized by a Raman tensor $\boldsymbol{\alpha}^\sigma$ of phonon mode σ and the scattered phonon with polarization $\boldsymbol{e_s}$. The Raman tensors are the key ingredients needed to calculate the Raman spectra. They can be computed either from finite differences, as the change of the dielectric tensor due to infinitesimal atomic displacements, or from perturbation theory, as the derivative of the energy with respect to three perturbations: two electric fields and one atomic displacement.

Quite often experimental data are recorded using polarized or unpolarized lasers on powdered samples. If we ignore the surface effects on the Raman tensors, an approximation that is valid for anything but nanocrystals, the Raman spectra are averaged over all possible orientations of the crystals and sums over the parallel and perpendicular laser polarizations. The intensities of the two polarized components of the powder spectra, parallel and perpendicular, and the resulting total powder spectra are (Placzek, 1934; Prosandeev *et al.*, 2005):

$$I^{pdr} = I_\parallel^{pdr} + I_\perp^{pdr} = \sum_{n,\beta} R_{ij}^{n\beta} X_{n,\beta}^\sigma \tag{3.145}$$

$$I_\parallel^{pdr} = C(10\, G_0 + 4\, G_2) = \sum_{n,\beta} R_{ij}^{n\beta} X_{n,\beta}^\sigma \tag{3.146.a}$$

$$I_\perp^{pdr} = C(5\, G_1 + 3\, G_2) = \sum_{n,\beta} R_{ij}^{n\beta} X_{n,\beta}^\sigma \tag{3.146.b}$$

where,

$$G_0 = \frac{1}{3}(\, \alpha'_{xx} + \alpha'_{yy} + \alpha'_{zz}\,)^2 \tag{3.147.a}$$

$$G_1 = \left[\alpha'_{xy} - \alpha'_{yz}\right]^2 + [\alpha'_{yz} - \alpha'_{zx}]^2 + [\alpha'_{zx} - \alpha'_{xy}]^2 \tag{3.147.b}$$

$$G_2 = \left[\alpha'_{xy} + \alpha'_{yz}\right]^2 + \left[\alpha'_{yz} + \alpha'_{zx}\right]^2 + \left[\alpha'_{zx} + \alpha'_{xy}\right]^2 + \frac{1}{3}\left(\left[\alpha'_{xx} - \alpha'_{yy}\right]^2 + \left[\alpha'_{yy} - \alpha'_{zz}\right]^2 + \left[\alpha'_{zz} - \alpha'_{xx}\right]^2\right) \quad (3.147.c)$$

3.2.7.9 Vibrational Normal Modes and Symmetry

The methods which are used to classify the vibration modes in molecules by their symmetry properties can be extrapolated to crystals. The most important difference to consider in this case is that the symmetry operations of the group G are of type $(R, \boldsymbol{t_n} + \boldsymbol{\tau_R})$ where R represents the set of rotations, reflections, inversion, etc., leaving at least one point invariant (point group operations) and $\boldsymbol{t_n} + \boldsymbol{\tau_R}$ are the translations expressed in its most general form, *i.e.*:

$$\boldsymbol{t_n} = u\boldsymbol{a} + v\boldsymbol{b} + w\boldsymbol{c} \quad (3.148.a)$$

$$\boldsymbol{\tau_R} = x\boldsymbol{a} + y\boldsymbol{b} + z\boldsymbol{c} \quad (3.148.b)$$

where x, y, z are fractional and u, v, w are integers. In the approximation $\Delta\boldsymbol{q} = \boldsymbol{0}$ (where $\Delta\boldsymbol{q} = \boldsymbol{q} - \boldsymbol{q_0}$, is the wave vector difference between the scattered and the incident radiation), which is reasonably accurate for Raman scattering, all the atoms equivalent by lattice translations move in phase for a given vibration. Thus, the calculation of the number and types of vibration of the crystal can be reduced to the unit cell. The symmetry group to consider is the *factor group* $G_F = G_E/G_T$, the quotient of the G_E space group and the G_T crystal translation group. G_F is isomorphic to one of the 32 crystallographic point groups. Therefore, the analysis of the symmetry species can be done in the context of the symmetry group of the unit cell.

The symmetry operations which transforms the configuration of atoms in the unit cell into an equivalent configuration, are those of the 230 three-dimensional space groups (G_E). As it has been said, of these symmetry operations, the lattice translations ($\boldsymbol{t_n}$) do not concern us as the optically active crystal vibrations are unchanged by this translation (they are however important for the symmetry classification of phonon vibrations at $\boldsymbol{q}$ points which are not the $\boldsymbol{\Gamma} = (0,0,0)$ point because in this case the vibrations involve (Powel, 2010) atoms outside the unit cell). The remaining symmetry operations constitute a factor group and transform one atom into another that is not translationally equivalent. These elements include axes, planes and centers of symmetry (as for isolated molecules) and also screw axes and glide planes ($R + \boldsymbol{\tau_R}$), which are impossible for finite molecular systems. Crystal symmetries can however be classified as symmetric, antisymmetric or degenerate with respect to these symmetry operations just as for simple rotations and reflections. Disregarding translations and treating screw axes and glide planes as equivalent to rotation axes and or reflections, the 230 space groups reduce to the *32 crystallographic point groups*. Crystal vibrations can be classified in the symmetry species of the corresponding crystallographic point group for which the character tables and the IR and Raman activities are available. In order to check that the number and symmetry types obtained are correct, one may determine the site symmetries of each atom in the primitive unit cell and, using the tables of *site group to factor group correlation* (see for example Farmer, 1974), obtain the number of vibrations belonging to each symmetry species for our crystal system (Fateley *et al.*, 1971). Examples of the determination of Raman active vibrational modes of a crystal may be found in Fateley (1971) and Rull (2012).

3.2.8 Equations of State (EOS)

In physics and thermodynamics, an equation of state (EOS) is a thermodynamic equation relating state variables which describes the state of matter under a given set of physical conditions. It is a constitutive equation which provides a mathematical relationship between two or more state functions associated with the matter, such as its temperature, pressure, volume, or internal energy. Equations of state are useful in describing the properties of fluids, mixtures of fluids, solids, and

the interior of stars. The most prominent use of an equation of state is to correlate densities of gases, liquids and solids to temperatures and pressures. There are equations that model the interior of stars, including neutron stars, dense matter (quark–gluon plasmas) and radiation fields. A related concept is the perfect fluid equation of state used in cosmology. There are also equations of state describing solids, including the transition of solids from one crystalline state to another. Simple equations of state are generally used at low pressures and high temperatures but they become increasingly inaccurate at higher pressures and lower temperatures so that more complex equations are required. The most widely used EOS for solid systems are the Vinet, Murnahan, and Birch-Murnahan EOS, see below. However, there is a wide variety of EOS valid for specific extreme conditions as strong compression.

The EOS most commonly used for fitting isothermal data (i.e., constant temperature P-V datasets) for solid systems are listed briefly here. Further details of the derivations and limitations can be found in, for example, Anderson (1995) and Angel (2001).

Murnaghan. This EOS (Murnaghan, 1937) can be derived from the assumption that the *bulk modulus* varies linearly with pressure, $B = B_0 + B_0' \cdot P$; B_0', the bulk modulus derivative with respect to pressure, being independent of pressure. Integration yields the $P - V$ relationship:

$$V = V_0 \left[1 + \frac{B_0' P}{B_0}\right]^{-\frac{1}{B_0'}} \qquad (3.149.a)$$

This EOS both reproduces $P - V$ data and yields correct values of the room pressure bulk modulus for compressions up to about 10% (i.e. $V/V_0 > 0.9$), and has the advantage of algebraic simplicity over other formulations such as the Vinet or Birch- Murnaghan EOSs (*e.g.* Anderson, 1995; Angel, 2001) which should be used if the range of compression is greater than 10%. The Murnaghan EOS can also be re-arranged to provide a direct expression for pressure in terms of compression:

$$P = \frac{B_0}{B_0'}\left[\left(\frac{V_0}{V}\right)^{B_0'} - 1\right] \qquad (3.149.b)$$

Birch-Murnaghan. This is a "Finite strain EOS", and is based upon the assumption that the strain energy of a solid undergoing compression can be expressed as a Taylor series in the finite strain, f. The Birch-Murnaghan EOS (Birch, 1947) is based upon the Eulerian strain, $f_E = 1/2\left[(V_0/V)^{2/3} - 1\right]$. Expansion to fourth-order in the strain yields an EOS:

$$P = 3\,B_0\,f_E\,(1 + 2f_E)^{\frac{5}{2}}\left[1 + \frac{3}{2}(B' - 4)f_E + \frac{3}{2}\left\{B_0 B'' + (B' - 4)(B' - 3) + \frac{35}{9}\right\}{f_E}^2\right] \qquad (3.150)$$

If this EOS is truncated at second-order in the energy, then the coefficient of f_E must be identical to zero, which requires that B' has the fixed value of 4 (higher-order terms are ignored). The third-order truncation, in which the coefficient of ${f_E}^2$ is set to zero yields a three-parameter EOS (with V_0, B_0, and B') with an implied value of B'' given by (Anderson, 1995):

$$B'' = \frac{-1}{B_0}\left[(3 - B')(4 - B') + \frac{35}{9}\right] \qquad (3.151)$$

Natural strain. Poirier and Tarantola (1998) developed an EOS based upon the "natural" or "Hencky" measure of linear strain, $f_N = l_n(l/l_0)$ which, for hydrostatic compression, may be written as $f_N = 1/3\; l_n(V/V_0)$. This yields a pressure-volume relationship expanded to fourth-order in strain of:

$$P = 3\,B_0\left(\frac{V_0}{V}\right)\,f_N\,\left[1 + \frac{3}{2}(B' - 2)f_N + \frac{3}{2}\{1 + B_0\,B'' + (B' - 2) + (B' - 2)^2\}{f_N}^2\right] \qquad (3.152)$$

Examination of this equation shows that truncation of this "Natural strain" EOS at second-order in the strain implies a value of $B' = 2$, different from that of the second-order Birch-Murnaghan EOS. For truncation at third-order in the strain, the implied value of B'' is given by:

$$B'' = \frac{-1}{B_0}[1 + (B' - 2) + (B' - 2)^2] \tag{3.153}$$

Vinet. The finite-strain EOS do not accurately represent the volume variation of most solids under very high compression ($\eta < 0.6$), so Vinet *et al*. (1986, 1987) derived an EOS from a general inter-atomic potential. For simple solids under very high compressions the resulting Vinet EOS provides a more accurate representation of the volume variation with pressure:

$$P = 3\,B_0\left(\frac{1 - f_V}{f_V}\right) exp\left[\frac{3}{2}(B' - 1)(1 - f_V)\right] \tag{3.154}$$

where $f_V = (V/V_0)^{1/3}$. There is no theoretical basis for truncation of the EOS to lower order, although examination of this equation shows that such truncation yields an implied value for $B' = 1$. The value of B'' implied by this equation was given by Jeanloz (1988) as:

$$B'' = \frac{-1}{B_0}\left[\left(\frac{B'}{2}\right)^2 + \left(\frac{B'}{2}\right) - \frac{19}{36}\right] \tag{3.155}$$

Expansions of the Vinet EOS to include a refineable B'' have been proposed but are not required to fit most experimental $P - V$ data of simple solids. Despite being often called a "Universal EOS" (*e.g.* Vinet *et al.* 1986, 1987) it should be noted that the Vinet EOS is not intended for materials with significant degrees of internal structural freedom such as bond-bending (Jeanloz, 1988).

3.2.8.1 Determination of EOS

Bulk modulus and its pressure derivatives were calculated in this work by fitting the lattice volumes and pressures to an equation of state. In the present study, the lattice volumes around the equilibrium were computed by optimizing the structure at several different pressures between –1.0 and 12.0 GPa where negative pressure values mean traction or tension. The results were then fitted to a fourth-order Birch-Murnaghan equation of state (Birch, 1947) using the computed volume at 0 GPa as V_0 using EOSFIT 5.2 code (Angel, 1981)

3.2.9 Elasticity

The mechanical or elastic properties of a material constitute a very important group of properties determining the behavior of the material under an applied pressure. Clear expositions of the physical magnitudes involved, their significance and determination may by found in several sources (Nye, 1985; Ortega-Castro, 2007).

The mechanical stability of a given structure, its hardness and other related mechanical properties are determined by its elastic behavior and determine to a great extend the material durability and behavior under a large range of environmental conditions. For example, in terms of the elastic properties of minerals we can study the variation of their structures under different pressure conditions and to predict their behavior in the Earth's interior.

The determination of mechanical properties amounts to evaluate the deformation produced in the structure by a series of applied stresses. From these deformations the *elasticity tensor* may be determined and, from it, the mechanical stability of the corresponding structure may be studied and all the mechanical properties may be evaluated. Due to the complexity of their experimental

measurement and its great importance, theoretical methods aimed to their determination have been developed in the last decades.

Therefore, the elasticity tensor of a given compound provides a complete description of the response of the material to external stresses in the elastic limit (Nye, 1985). The analysis of this tensor, which is usually correlated with many mechanical properties, also helps to understand the nature of the bonding in the material.

3.2.9.1 Mechanical Properties and stability

At the optimized structures relaxed with respect to Hellmann-Feynman forces, elastic constants can be calculated at T = 0 K as the second derivatives of the energy with respect to the strain, *i.e.:*

$$C_{ij} = \frac{1}{V}\left(\frac{\partial^2 U}{\partial\varepsilon_i \partial\varepsilon_j}\right) \tag{3.156}$$

where V is the volume, U is the total energy of the system, and ε is the infinitesimal displacement (or infinitesimal strain). They can also be calculated from stress-strain relations. With this purpose, finite deformation technique is employed in CASTEP. In this technique, finite programmed symmetry-adapted strains (Nye, 1985) may be used to extract individual elastic constants from the stress tensor obtained as response of the system to the applied strains. For the calculation of elastic tensor, this stress-based method appears to be more efficient than the energy-based methods and the use of DFPT (Yu *et al.*, 2010).

The Voigt notation, which relates the elastic stiffness coefficients C_{ijkl} $(i,j,k,l = x,y,z)$ in the different directions in the crystal to the C_{ij} $(i,j = 1,..,6)$ elastic constants, was adopted in this study, *i.e.* $xx \rightarrow 1$, 1, $yy \rightarrow 2$, $zz \rightarrow 3$, $yz \rightarrow 4$, $zx \rightarrow 5$, $xy \rightarrow 6$.

The 6×6 elasticity tensor was determined by performing finite distortions of the equilibrium lattice and deriving the elastic constants from the strain-stress relationship (Le Page and Saxe, 2002). The elastic behaviour of the systems is determined to a great extent by the crystal symmetry of the system and, for example, for orthorhombic and monoclinic crystals the symmetric elasticity tensor is determined by 9 and 13 elastic constants, respectively (Nye, 1985; Weck *et al.*, 2015):

$$C^{ortho} = \begin{pmatrix} C_{11} & C_{12} & C_{13} & 0 & 0 & 0 \\ C_{12} & C_{22} & C_{23} & 0 & 0 & 0 \\ C_{13} & C_{23} & C_{33} & 0 & 0 & 0 \\ 0 & 0 & 0 & C_{44} & 0 & 0 \\ 0 & 0 & 0 & 0 & C_{55} & 0 \\ 0 & 0 & 0 & 0 & 0 & C_{66} \end{pmatrix} \tag{3.157.a}$$

and,

$$C^{mono} = \begin{pmatrix} C_{11} & C_{12} & C_{13} & 0 & C_{15} & 0 \\ C_{13} & C_{22} & C_{23} & 0 & C_{25} & 0 \\ C_{13} & C_{23} & C_{33} & 0 & C_{35} & 0 \\ 0 & 0 & 0 & C_{44} & 0 & C_{46} \\ C_{15} & C_{25} & C_{35} & 0 & C_{55} & 0 \\ 0 & 0 & 0 & C_{46} & 0 & C_{66} \end{pmatrix} \tag{3.157.b}$$

For low-symmetry monoclinic phases, a number of possible formulations of the generic Born elastic stability conditions (Born, 1940; Born and Huang, 1954) for an unstressed single crystal have been proposed. Popular criteria for mechanical stability are given by (Wu *et al.*, 2007; Weck *et al.*, 2015):

$$C_{ii} > 0 \ (i = 1, \ldots, 6) \tag{3.158.a}$$

$$C_{33}\,C_{55} - C_{35}\,C_{35} > 0 \tag{3.158.b}$$

$$C_{44}\,C_{66} - C_{46}\,C_{46} > 0 \tag{3.158.c}$$

$$C_{22}\,C_{33} - 2\,C_{23} > 0 \tag{3.158.d}$$

$$C_{11} + C_{22} + C_{33} + 2\,(C_{12} + C_{13} + C_{23}) > 0 \tag{3.158.e}$$

$$C_{22}\,(C_{33}\,C_{55} - C_{35}\,C_{35}) + 2\,C_{23}\,C_{25}\,C_{35} - C_{23}\,C_{23}\,C_{55} - C_{25}\,C_{25}\,C_{33} > 0 \tag{3.158.f}$$

$$2\,(h\text{-}i) + g\,C_{55} > 0 \tag{3.158.g}$$

with

$$g = C_{11}\,C_{22}\,C_{33} - C_{11}\,C_{23}\,C_{23} - C_{22}\,C_{13}\,C_{13} - C_{33}\,C_{12}\,C_{12} + 2\,C_{12}\,C_{13}\,C_{23}$$

$$h = C_{15}\,C_{25}\,(C_{33}\,C_{12} - C_{13}\,C_{23}) + C_{15}\,C_{35}\,(C_{22}\,C_{13} - C_{12}\,C_{23}) + C_{25}\,C_{35}\,(C_{11}\,C_{23} - C_{12}\,C_{13})$$

$$i = C_{15}\,C_{15}\,(C_{22}\,C_{33} - C_{23}\,C_{23}) + C_{25}\,C_{25}\,(C_{11}\,C_{33} - C_{13}\,C_{13}) + C_{35}\,C_{35}\,(C_{11}\,C_{22} - C_{12}\,C_{12})$$

(3.159)

While these are necessary (Watt, 1980), they are not sufficient criteria for mechanical stability, as recently noted by Mouhat and Coudert (2014). In particular, the generic necessary and sufficient Born criterion is that all eigenvalues of the C matrix be positive. The insatisfaction of the mechanical stability conditions for a given phase is a strong indication of phase metastability (Weck *et al*., 2015).

For the orthorhombic single crystals, the necessary and sufficient Born criteria for mechanical stability are (Mouhat and Coudert, 2014; Weck *et al.*, 2015):

$$C_{ii} > 0 \ (i = 1,4,5,6) \tag{3.160.a}$$

$$C_{11}\,C_{22} - C_{12} > 0 \tag{3.160.b}$$

$$C_{11}\,C_{22}\,C_{33} + 2\,C_{12}\,C_{13}\,C_{23} - C_{11}\,C_{23} - C_{22}\,C_{13} - C_{33}\,C_{12} > 0 \tag{3.160.c}$$

The bulk and shear moduli in the Voigt (Voigt, 1962) approximation, respectively, were calculated for both monoclinic and orthorhombic polycrystalline aggregates using the formulas:

$$B_V = \frac{1}{9}(C_{11} + C_{22} + C_{33} + 2\,[C_{12} + C_{13} + C_{23}]) \tag{3.161.a}$$

and,

$$G_V = \frac{1}{15}(C_{11} + C_{22} + C_{33} - C_{12} - C_{13} - C_{23} + 3[C_{44} + C_{55} + C_{66}]) \tag{3.161.b}$$

While the strain is assumed to be uniform throughout the aggregate of crystals in Voigt's method, the approximation formulated by Reuss (1929) considers the stress to be uniform and averaging of the relations expressing the strain is carried out. The Reuss methodology was also used to compute the isotropic elastic properties of and polycrystalline aggregates.

The bulk and shear moduli within the Reuss approximation were obtained for monoclinic phases using the expressions:

$$B_R = \Omega\,(a\,[\,C_{11} + C_{22} - 2\,C_{12}] + b\,[2\,C_{12} - 2\,C_{11} - C_{23}] + c\,[\,C_{15} - 2\,C_{25}] + d[2\,C_{12} + 2\,C_{23} - C_{13} - 2\,C_{22}] + 2\,e\,[\,C_{25} - C_{15}] + f)^{-1} \quad (3.162.a)$$

$$G_R = 15\,\{4\,(a\,[\,C_{11} + C_{22} + C_{12}] + b\,[C_{11} - C_{12} - C_{23}] + c\,[\,C_{15} + C_{25}] + d\,[\,C_{22} - C_{12} - C_{23} - C_{13}] + e\,[\,C_{15} - C_{25}] + f)/\Omega + 3\,(g/\Omega + [C_{44} + C_{66}]/[\,C_{44}\,C_{66} - C_{46}\,C_{46}])\}^{-1} \quad (3.162.b)$$

where,

$$\Omega = 2\,C_{15}C_{25}(\,C_{33}C_{12} - C_{13}C_{23}) + C_{15}C_{35}(\,C_{22}C_{13} - C_{12}C_{23}) + C_{25}C_{35}(\,C_{11}C_{23} - C_{12}C_{23}) - [C_{15}C_{15}(\,C_{22}C_{33} - C_{23}C_{23}) + C_{25}C_{25}(\,C_{11}C_{33} - C_{13}C_{13}) + C_{35}C_{35}(\,C_{11}C_{22} - C_{12}C_{12})] + gC_{55} \quad (3.163.a)$$

$$a = C_{33}C_{55} - C_{35}C_{35} \quad (3.163.b)$$

$$b = C_{23}C_{55} - C_{25}C_{35} \quad (3.163.c)$$

$$c = C_{13}C_{35} - C_{15}C_{33} \quad (3.163.d)$$

$$d = C_{13}C_{55} - C_{15}C_{35} \quad (3.163.e)$$

$$e = C_{13}C_{25} - C_{15}C_{23} \quad (3.163.f)$$

$$f = C_{11}(C_{22}C_{55} - C_{25}C_{25}) - C_{12}(C_{12}C_{55} - C_{15}C_{25}) + C_{15}(C_{12}C_{25} - C_{15}C_{22}) + C_{25}(C_{23}C_{35} - C_{25}C_{33}) \quad (3.163.g)$$

and g was defined previously.

For polycrystalline aggregates of orthorhombic symmetry, the Reuss bulk and shear moduli were calculated using the expressions:

$$B_R = \Delta\,(\,C_{11}\,[\,C_{22} + C_{33} - 2\,C_{23}] + C_{22}\,[\,C_{33} - 2\,C_{13}] - 2\,C_{33}\,C_{12} + C_{12}\,[2\,C_{23} - C_{12}] + C_{13}\,[2\,C_{12} - C_{13}] + C_{23}\,[\,2\,C_{13} - C_{23}])^{-1} \quad (3.164.a)$$

and

$$G_R = 15\,\{4\,(C_{11}[\,C_{22} + C_{33} + C_{23}] + C_{22}\,[C_{33} + C_{13}] + C_{33}\,C_{12} - C_{12}\,[\,C_{23} + C_{12}] - C_{13}\,[\,C_{12} + C_{13}] - C_{23}\,[\,C_{13} + C_{23}])/\Delta + 3\,(C_{44}^{-1} + C_{55}^{-1} + C_{66}^{-1})\}^{-1} \quad (3.164.b)$$

where,

$$\Delta = C_{13}(\,C_{12}C_{23} - C_{13}C_{22}) + C_{23}(\,C_{12}C_{13} - C_{23}C_{11}) + C_{33}(\,C_{11}C_{22} - C_{12}C_{12}) \quad (3.165)$$

The Voigt and Reuss methods employed above for bulk and shear modulus calculations yield differences which are generally small. However, they may lead to differences seem larger than usually obtained for crystalline systems with strong anisotropy, such as studtite, metastudtite and rutherfordine (Weck *et al*., 2015; Colmenero *et al*., 2017a) with structures featuring large differences between elastic constants along different directions.

As shown by Hill (Hill, 1952). the Reuss and Voigt approximations result in lower and upper limits, respectively, of polycrystalline constants and practical estimates of the polycrystalline bulk and shear moduli in the Hill approximation were computed using the formulas:

$$B_H = 1/2(B_R + B_V) \tag{3.166.a}$$

$$G_H = 1/2(G_R + G_V) \tag{3.166.b}$$

In an effort to assess the uncertainty of the elastic parameters and the derived elastic properties, the bulk modulus may be calculated using fits to an equation of state and comparing the resulting value with the bulk modulus calculated from the elastic constants in the Voigt, Reuss, and Hill approximations.

The ratio $D = B/G$ of the bulk modulus divided by the shear modulus was proposed by Pugh (1954) as a simple indicator of the correlation between the ductile/brittle properties of crystals and their elastic constants. A material is considered ductile if $D > 1.75$, otherwise it is brittle.

As discussed by Pugh (1954) and Frantsevich *et al*. (1983), the Poisson's ratio, ν, can also be utilized to measure the malleability of crystalline compounds and is related to the Pugh's ratio given above by the relation $D = (3 - 6\nu)/(8 + 2\nu)$. The Poisson's ratio is close to $1/3$ for ductile materials, while it is generally much less than $1/3$ for brittle materials. Using the bulk and shear moduli, Poisson's ratio, ν, can be obtained using the expression:

$$\nu = (3B - 2G)/[2(2B + G)] \tag{3.167}$$

The hardness of these systems is computed according to a recently introduced empirical scheme (Niu *et al.*, 2011; Chen *et al.*, 2011) that correlates the Vickers hardness and Pugh ratio ($D = B/G$). The Vickers hardness, H, for systems characterized by large D ratios, have smaller values.

Young's modulus, corresponding to the ratio of the stress to strain ($E = \sigma/\varepsilon$), was computed using the formula:

$$E = 9BG/(3B + G) \tag{3.168}$$

Alternatively, the axial components of Young's modulus, were derived from the elastic compliances, with its components along the a, b, c directions expressed as $E_a = S_{11}^{-1}$, $E_b = S_{22}^{-1}$ and $E_c = S_{33}^{-1}$. The elastic compliances, S_{ij}, can be readily obtained by inverting the elastic constant tensor, *i.e.* $S = C^{-1}$.

In order to assess the elastic anisotropy, the shear anisotropic factors for the $\{100\}$ (A_1), $\{010\}$ (A_2) and $\{001\}$ (A_3) crystallographic planes may be computed using the formulas:

$$A_1 = \frac{4C_{44}}{C_{11} + C_{33} - 2C_{13}} \tag{3.169.a}$$

$$A_2 = \frac{4C_{55}}{C_{22} + C_{33} - 2C_{23}} \tag{3.169.b}$$

$$A_1 = \frac{4C_{66}}{C_{11} + C_{22} - 2C_{12}} \tag{3.169.c}$$

Alternatively, the percentage of anisotropy in compression and shear was obtained using:

$$A_{comp} = \frac{B_V - B_R}{B_V + B_R} \times 100 \tag{3.170.a}$$

$$A_{shear} = \frac{G_V - G_R}{G_V + G_R} \times 100 \tag{3.170.b}$$

In terms of the recently introduced universal anisotropy index (Ranganathan and Ostoja-Starzewski, 2008):

$$A^U = 5\left(\frac{G_V}{G_R}\right) + \left(\frac{B_V}{B_R}\right) - 6 \tag{3.171}$$

The acoustic transverse wave velocity, v_t, and longitudinal wave velocity, v_l, can also be derived from the bulk and shear moduli using the formulas:

$$v_t = \sqrt{\frac{G}{\rho}} \tag{3.172.a}$$

and

$$v_l = \sqrt{\frac{3B + 4G}{3\rho}} \tag{3.172.b}$$

Using the computed acoustic transverse and longitudinal wave velocities, the mean sound velocity, v_m, can be obtained using the expression:

$$v_m = \left[\frac{1}{3}\left(\frac{2}{v_t^3} + \frac{1}{v_l^3}\right)\right]^{-\frac{1}{3}} \tag{3.173}$$

and the Debye temperature from:

$$\theta_D = \frac{h}{k_B}\left[\frac{3n}{4\pi}\left(\frac{N_A\rho}{M}\right)\right]^{\frac{1}{3}} v_m \tag{3.174}$$

where h is Planck's constant, k_B is Boltzmann's constant, N_A is Avogadro's number, n and M are the number of atoms and molar mass per formula unit, and ρ is the crystal density. The Debye temperature is related to important properties such as the specific heat or melting temperature of crystalline structures; in particular, at relatively low temperature, θ_D calculated from elastic constants or obtained from calorimetric measurements are similar.

3.2.10 Thermodynamics

Computational thermodynamics is the use of computers in the solving and simulation of thermodynamic problems specific to materials science. One example is the construction of phase diagrams. Nowadays, there are several open and commercial programs to perform these operations. The concept of the technique is minimization of Gibbs free energy of the system; the success of the method is not only due to properly measuring thermodynamic properties, such as free-energies, enthalpies, entropies and specific heats, but the extrapolation of the properties of metastable phases. Currently, Computational Thermodynamics may be considered as a part of Materials Informatics. However, these simulation codes require the collection of an extensive thermodynamic database including most of the interesting materials in order to resolve the thermodynamic equations involved in the simulations.

There is still a gap between *ab initio* methods and operative computational thermodynamics databases. The challenge is to make the two communities related to Solid State Physics and Materials Science talk and work together. Promising results from *ab initio* quantum mechanics simulation package CASTEP, are given in this work which extend previous good thermodynamic data results for systems involving lighter atoms.

3.2.10.1 Thermodynamic properties

The phonon spectrum at different points in the Brillouin zone can also be determined by DFPT as second-order derivatives of the total energy (Baroni *et al.*, 2001). The knowledge of the entire phonon spectrum allows the phonon dispersion curves and density of states to be calculated and, from them, the evaluation of several important thermodynamic quantities in the quasiharmonic approximation, such as *free energies, enthalpies, entropies, specific heats,* and *Debye temperatures* (Baroni *et al.*, 2001; Lee and Gonze, 1995).

The above-mentioned thermodynamic functions require summations over phonon eigenstates labelled by the phonon wave vector $\boldsymbol{q}$ and the phonon mode l. However, the expressions to be evaluated, say f, at each $\boldsymbol{q}$ and l often depend on $\boldsymbol{q}$ and l only through the frequency $\omega = \omega(\boldsymbol{q}, l)$. We can then turn $\sum_{\boldsymbol{q},l} f(\omega(\boldsymbol{q}, l))$ into a one-dimensional integral $\int_0^{\omega_l} f(\omega)\, g(\omega) d\omega$ where ω_l is the largest phonon frequency and $g(\omega)\, d\omega$ is defined to be the fractional number of phonon frequencies in the range between ω and $\omega + d\omega$. The *phonon density of states*, also known as *vibrational density of states* (VDOS), $g(\omega)$, is normalized so that $\int_0^{\omega_l} g(\omega) d\omega = 3nN$, where n is the number of atoms within the unit cell and N is the number of unit cells, namely:

$$g(\omega) = \sum_{\boldsymbol{q},l} \delta(\omega - \omega(\boldsymbol{q}, l)) \tag{3.175}$$

Specifically, we may obtain a large number of expressions for several thermodynamic properties as a function of temperature (Maradudin *et al.*, 1971, Lee and Gonze, 1995; Baroni *et al.*, 2001) within the quasi-harmonic approximation. The temperature dependence of the energy is given by:

$$E(T) = E_{TOT} + E_{zp} + \int \frac{\hbar\omega}{\exp\left(\frac{\hbar\omega}{kT}\right) - 1}\, g(\omega) d\omega \tag{3.176}$$

where E_{zp} if the zero-point vibrational energy, k is Boltzmann's constant, ħ is Planck's constant and $g(\omega)$ is the phonon density of states. E_{zp} can be evaluated as:

$$E_{zp} = \frac{1}{2} \int \hbar\omega\, g(\omega) d\omega \tag{3.177}$$

The vibrational contribution to the free energy, F, is given by:

$$G(T) = E_{TOT} + E_{zp} + kT \int L_n \left[1 - \exp\left(\frac{\hbar\omega}{kT}\right)\right] g(\omega) d\omega \tag{3.178}$$

The vibrational contribution to the entropy, S, can be obtained using:

$$S(T) = k \left\{ \int \frac{\frac{\hbar\omega}{kT}}{\exp\left(\frac{\hbar\omega}{kT}\right) - 1}\, g(\omega) d\omega - \int L_n \left[1 - \exp\left(\frac{\hbar\omega}{kT}\right)\right] g(\omega) \right\} \tag{3.179}$$

The lattice contribution to the heat capacity at constant volume C_v, is:

$$C_v(T) = k \int \frac{\left(\frac{\hbar\omega}{kT}\right)^2 \exp\left(\frac{\hbar\omega}{kT}\right)}{\left[\exp\left(\frac{\hbar\omega}{kT}\right) - 1\right]}\, g(\omega) d\omega \tag{3.180}$$

Debye temperature, Θ_D, is an important quantity which gives a relative idea for a temperature scale above which the vibrations within a solid behave classically and the heat capacity follows the Dulong-Petit law (Ascroft and Mermin, 1976). Below the Debye temperature the quantum effects are important. Debye temperature may be estimated in terms of the mean sound velocity of a crystal or elasticity constants (Anderson, 1963; see previous section). Thus, its temperature dependence comes from that of elasticity constants and it is very slight.

A popular representation of the experimental data on heat capacity is based on the comparison of the actual heat capacity to that predicted by the Debye model. This leads to the concept of the temperature dependent Debye temperature, $\Theta_D(T)$. Heat capacity in Debye model is given by (Ashcroft and Mermin, 1976):

$$C_v(T) = 9Nk\frac{T}{\Theta_D}\int_0^{\Theta_D/T}\frac{x^4 e^x}{(e^x-1)^2}dx \tag{3.181}$$

where N is the number of atoms per unit cell. Thus, the value of the Debye temperature, Θ_D, at a given temperature, T, is obtained by calculating the actual heat capacity and then inverting the previous equation to obtain Θ_D.

Other thermodynamic properties of interest are the enthalpies and the specific heats at constant pressures. They may be obtained in terms of the free energies and entropies using the standard thermodynamic expressions:

$$H = G + TS \tag{3.182}$$

and

$$C_p(T) = \left(\frac{\partial H}{\partial T}\right)_p \tag{3.183}$$

Part II. Results and Discusion

Chapter 4. Rutherfordine: Structure and Raman Spectroscopy

This chapter is based on the published article "*Spectroscopic Raman characterization of Rutherfordine: a combined DFT and experimental study"*, by L. J. Bonales, F. Colmenero, J. Cobos and V. Timón, Phys. Chem. Chem. Phys. 18, 16575–16584 (2016).

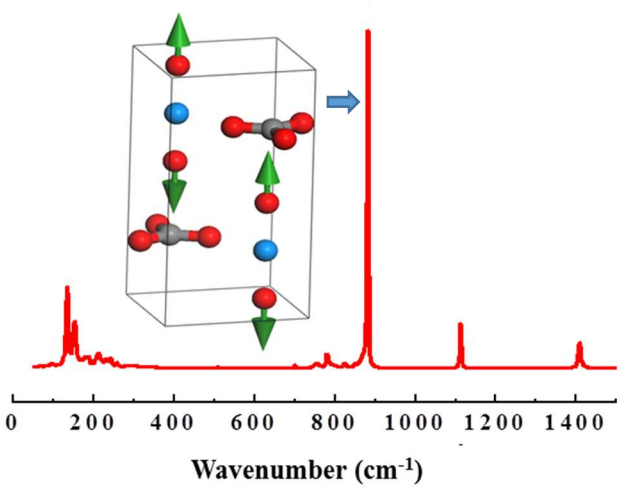

Abstract

A rutherfordine mineral was studied by means of Raman spectroscopy combined with first principle calculations based on the density functional theory (DFT) method. The pseudopotential of a uranium atom was generated and its performance was evaluated for a series of uranium-containing minerals. The structure of rutherfordine was determined for two symmetries (Pmmn and Imm2) and the resulting lattice parameters, bond lengths, bond angles, and X-ray powder diffractogram were found to be in very good agreement with experimental values. The Raman spectrum was experimentally determined in the range 0–1700 cm^{-1} and calculated using density functional perturbation theory. The non-scaled theoretical wavenumbers also agreed with the experimental values, and therefore a detailed interpretation of the theoretical spectra allowed us to assign the Raman bands found in the experimental spectrum.

4.1 Introduction

One of the most interesting uranyl minerals is rutherfordine, UO_2CO_3. Rutherfordine is the only known uranyl mineral phase of interest in the research of spent nuclear fuel (SNF) that contains only uranyl and carbonate. There are other uranyl carbonate hydrated phases such as blatonite, $UO_2CO_3 \cdot H_2O$ (Vochten and Deliens, 1998) and joliotite, $UO_2CO_3 \cdot 2H_2O$ (Walenta, 1998), but the structures of these minerals are unknown. Uranium carbonate compounds and their importance in actinide environmental chemistry have been reviewed by Clark *et al.* (1995) Carbonate and bicarbonate, present in significant concentrations in many natural waters, are exceptionally strong complexing agents for actinide ions and, therefore, carbonate complexes of actinide ions play an important role in migration from nuclear waste repositories or in accidental site contamination. This is reflected by the formation of many naturally occurring uranyl carbonate minerals such as rutherfordine, liebigite, and andersonite among others (Clark *et al.*, 1995). Uranium carbonates may precipitate where evaporation is significant or where the partial pressure of CO_2 is large, rutherfordine becoming a more stable uranium phase with respect to schoepite. Rutherfordine would be expected to replace schoepite in environments where the CO_2 pressure is high, possibly in a repository environment or in saturated soils. Replacement of schoepite by rutherfordine has been observed at the Shinkolobwe U-deposit (Finch and Ewing, 1992; Grenthe *et al.*, 2006). The study of the structural and thermodynamic stabilities of uranium carbonates is thus particularly relevant to nuclear waste disposal.

Rutherfordine was discovered by Marckwald (1906) and described as a mineral species by Frondel and Meyrowitz (1956). Its solid-state structure has been determined from crystals of both the natural mineral and synthetic samples. Rutherfordine forms green–yellow crystals with an orthorhombic structure. The structure of rutherfordine was provided by Christ and Clark (1955, 1956). The structure was later refined by Finch *et al.* (1999). Christ *et al.* (1956) presented two structures: (1) structure A, which is consistent with Pmmn symmetry, and adjacent layers have the CO_3^{2-} groups pointing in opposite directions; and (2) structure B, which is consistent with Imm2 symmetry, and adjacent layers have the CO_3^{2-} groups pointing in the same direction. They suggested that structures A and B are energetically equivalent, and that crystals can contain domains of each structure, separated by stacking faults. Finch *et al.* (1999) suggested that structure B should be favored. Pmmn and Imm2 structures are considered in the present theoretical calculations, and the results indicate that both may be simultaneously present in nature in accordance with the suggestion of Christ *et al.* (1956). In this paper, we present a detailed study of the rutherfordine mineral using Raman spectroscopy and DFT calculations. This section work is structured as follows: in subsection 2, the materials and methods used in this work are described for the experimental and theoretical parts of this study. Density functional theory calculations are described, as well as the generation of the pseudopotential used for uranium atom. Then, in subection 3, experimental results are presented and compared with theoretical data for the Pmmn and Imm2 symmetries and the assignment of the main fundamental band wavenumbers is carried

out. Moreover, the effect of water addition to the rutherfordine structure is studied by further calculations.

4.2 Materials and Methods

4.2.1 Experimental

The analyzed sample is a ‘‘uraninite + gummite’’ mineral from Sierra Albarrana (Córdoba, Spain), collected during the uranium extractive activity in 1960. The sample structure corresponds to ideal gummite occurrence (central core black and a yellow surrounding zone, formed by several minerals (Frondel, 1956)). A detailed description of the mineral setting and other structural characteristics is described elsewhere (Bonales *et al.*, 2015). The sample was cut using a diamond saw and polished. A polished section of the sample was analyzed via Raman spectroscopy by using a Horiba LabRam HR evolution spectrometer (Jobin Yvon Technology). A HeNe laser with a wavelength of 632.81 nm and an operation power of 20 mW was used as the excitation source. The laser was focused onto the sample using the 100× objective of a confocal microscope (BX4 with confocal 800mm); the scattered light was collected with the same objective and then dispersed with a Jobin-Yvon spectrometer (600 grooves per mm), and detected with a Peltier cooled CCD detector (256×1024 pix.). The spectral resolution was about 1 cm^{-1} per pixel.

4.2.2 Theoretical

The rutherfordine unit cell has been modeled using the CASTEP Code (Clark *et al.*, 2005), a module of the Materials Studio package (Materials Studio, 2017). The generalized gradient approximation (GGA) with several different energy functionals was employed. The main one was the PBESOL functional (Perdew *et al.*, 1996, 2008). Also, since the rutherfordine structure is composed of sheets held together by van der Waals forces, we used the PBE functional (Perdew *et al.*, 1996) with the Grimme empirical dispersion correction, the DFT-D2 approach (Grimme, 2006), to evaluate the importance of this kind of interaction.

Geometry optimization was carried out using the Broyden–Fletcher–Goldfarb–Shanno optimization scheme (Pfrommer *et al.*, 1997; Payne *et al.*, 1992) with a convergence threshold on atomic forces of 0.01 eV A^{-1}. The different kinetic energy cutoffs and K-point meshes (Monkhorst and Pack, 1976) adopted are indicated in each case. They were selected to ensure good convergence for the computed structures and energies. For the calculations of the vibrational properties, linear response density functional perturbation theory (DFPT) (Refson *et al.*, 2006; Baroni *et al.*, 2001; Gonze *et al.*, 1997) implemented in the CASTEP code was used, where the phonon wavenumbers at the gamma point of the Brillouin zone were computed using atomic displacement perturbations. Raman intensities are the third-order derivatives of the total energy with respect to the vibrational mode (atomic position) and laser field (electric field, twice). These are calculated in CASTEP (Milman *et al.*, 2010) using a combination of perturbation theory (second derivative with respect to field) and finite differences (third derivative with respect to atomic displacement). The wavenumbers presented in this work have not been scaled to correct for anharmonicity and correspond to the harmonic approximation of the force field.

Since the CASTEP code only allows determining vibrational properties using norm conserving pseudopotentials and as there is no such pseudopotential for the uranium atom, we decided to construct a new one. First, we generated a Troullier–Martins type norm-conserving pseudopotential (Troullier and Martins, 1991) using the program fhi98PP (Fuchs and Schefler, 1999) in cpi format. The pseudopotential included relativistic effects (scalar relativistic all

electron calculations are used) and it was generated using the GGA-PBE (Perdew *et al.*, 1996) method. The electronic configuration of atomic uranium is $6s^2\ 6p^6\ 6d^1\ 5f^3\ 7s^2$. The pseudopotential was obtained from an ionized electronic configuration $6s^2\ 6p^6\ 6d^1\ 5f^3\ 7s^0$ with cutoff radii equal to 1.236, 2.447, 2.166 and 2.447 for s, p, d and f angular momenta, respectively. The s component of the pseudopotential was chosen as the local potential, and a Kleinman–Bylander form (Kleinman and Bylander, 1982) was used. Then, we transformed it into the recpot format used in CASTEP by using the tool cpi2recpot (Haynes and Refson, 2007). The use of this pseudopotential implies that the 14 valence electrons must be treated explicitly. In other works, 32 electrons were included in the valence shell (Schreckenbach *et al.*, 2010; Shamov *et al.*, 2007; Odoh *et al.*, 2013). This further increases the computational cost and only marginally improves the performance (Beridze *et al.*, 2014; Iche-Tarrat *et al.*, 2008). This pseudopotential reproduces accurately the all-electron calculation in the reference configuration in which it was generated. Further, checks of the smoothness of the nodeless pseudowavefunctions near the cutoff radii, of the continuity of the logarithmic energy derivatives and of the transferability of the pseudopotential were performed. In order to probe the generated normconserving pseudopotential under different environments and to validate it, we computed the structures of a series of uranium containing minerals with small cutoffs and K meshes. The results are given in a table in Appendix 4.A. As can be seen in Table 4.A.1 the results are quite good for the lattice parameters of the species involved. Better results are expected upon increasing the cutoff values and using larger K meshes.

4.3 Results and Discusion

4.3.1 Structure

A determination of the best geometrical structure was first carried out searching for a minimum in the potential energy surface. From the optimized structure, we have obtained both the structural parameters and the X-ray powder pattern.

We have considered both orthorhombic structures in rutherfordine, Pmmn and Imm2. The results are nearly the same and the energy difference for the optimized structures is less than 0.001 eV, the Pmmn structure being the lowest one.

The structure of rutherfordine contains approximately linear UO_2^{2-} uranyl ions that are coordinated by six O atoms arranged at the equatorial vertices of uranyl hexagonal bipyramids. These O atoms belong to four carbonate ligands and U is bonded with two carbonate ions in a bidentate manner and two in a monodentate manner. Each uranyl polyhedron is linked to two other uranyl polyhedra in a trans arrangement by edge sharing, resulting in chains of polyhedra. Adjacent chains are linked by the sharing of equatorial vertices between uranyl polyhedra, which results in a sheet structure that contains triangular voids. Carbonate triangles occupy one half of the voids, such that they share the equatorial edges of two adjacent uranyl hexagonal bipyramids and single vertices of two additional uranyl polyhedra (see Figure 4.1). The resulting sheets or layers are electroneutral, and adjacent sheets in rutherfordine are bonded together by van der Waals forces. The UO_2CO_3 layers are staggered with respect to the layer above or below, such that uranyl units lie above and below a carbonate carbon atom in adjacent layers. Layers are separated by a distance of about 4.6 Å. The computed structure is shown in Figure 4.1. Fig. 4.1.A and B show two contiguous sheets (Pmmn and Imm2 symmetry structures). In Fig. 4.1.C a view from the (010) axis is observed (similar for the two symmetry structures), showing the relative disposition of the uranyl polyhedra and carbonate triangles in the plane. As can be seen, for the Pmmn structure the carbonate triangles in contiguous sheets point in opposite directions while in the Imm2 structure they point in the same direction.

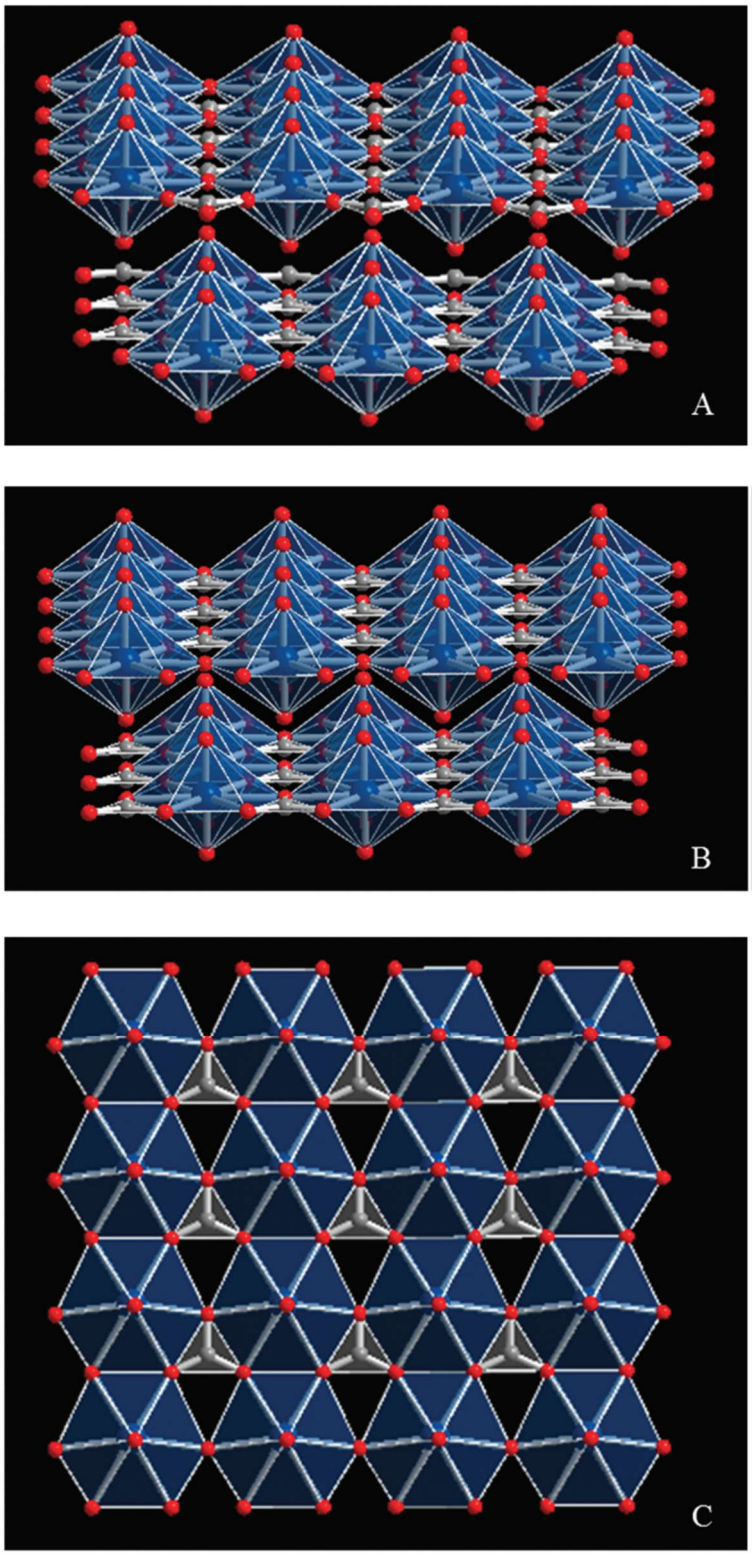

Figure 4.1 (A) Two contiguous sheets in the structure of rutherfordine for the Pmmn structure; (B) as figure A for the Imm2 structure; (C) upper (010) view of a sheet in the structure of rutherfordine. Color code: U – blue, O – red, C – carbon.

The lattice parameters of rutherfordine, as well as the volumes and densities, were determined in calculations of increasing complexity by increasing the different parameters (larger kinetic energy cutoffs and K meshes). The optimizations performed with a cutoff of 1000 eV and a K mesh of 5×3×6 (18 K points) gave well converged structures and were considered sufficient to determine the final material properties. Table 4.1 gives the final lattice parameters, volumes and densities obtained for the Pmmn and Imm2 structures, respectively. Tables 2 and 3 of the article (Bonales *et al.*, 2016a) give the corresponding bond distances and angles.

Table 4.1 Lattice parameters. Experimental values are from Finch *et al.* (1999).

Calculation	*a* (Å)	*b* (Å)	*c* (Å)	α	β	γ	Vol. (Å^3)	Dens. (g cc^{-1})
Pmmn	4.8257	9.3321	4.2720	90	90	90	192.4	5.697
Imm2	4.8267	9.3639	4.2727	90	90	90	193.1	5.675
Exp.	4.840	9.273	4.298	90	90	90	192.9	5.682

The powder X-ray pattern of rutherfordine was computed (Downs *et al.,* 1993) from the experimental (Finch *et al.*, 1999) and computed structures using CuKa radiation (l = 1.540598 A). The most intense lines (I > 10%) are compared in Figures 4.2.b–d, and, as can be seen, the line positions and intensities are in good agreement. The use of spectra derived directly from the experimental and computed structures allows for a fair comparison of the results free of interferences, such as the experimental conditions or possible artifacts from the presence of sample impurities, since both are determined under identical conditions. Nevertheless, the use of an experimental pattern also leads to an excellent agreement. Computer program XPowder (Martin, 2012) using the PDF-2 database (ICDD, 2003) directly recognizes the computed spectrum as that of the rutherfordine mineral (pattern 89-6527; Finch *et al.*, 1999). The experimental X-ray spectrum can be seen in Figure 4.2.a where it is compared with the previously described spectra. The precise values of the main reflections for the Imm2 and Pmmn computed structures and the experimental ones are given in Table 4 of the article (Bonales *et al.*, 2016a).

4.3.2 Raman Spectra and Band Assignment

In this section, we analyze the experimental profile of the rutherfordine Raman spectra obtaining the wavenumber of the main characteristic bands. Also, the theoretical spectrum is presented and the assignment of the vibrational bands is performed. The results are compared with some published data of this mineral phase.

In order to calculate the number of contributions of a given band from the experimental spectrum we carry out the analysis by the second derivative method (del Corro Garcia, 2011). The first derivative gives us an idea of the number of contributions involved but, as usual in spectroscopy, it is the second derivative which enables us to determine the number of contributions, since each one leads to a minimum.

The Raman spectra for the Pmmn and Imm2 structures were computed at T = 298 K, λ = 532 nm, FWHM = 5 cm^{-1}. The atomic motions associated with some vibrational normal modes are shown in Appendices 4.B and 4.C. Figure 4.3 shows the experimental Raman spectrum of rutherfordine, together with the calculated ones. A summary of the measured and calculated spectra is shown in Table 4.2 (Pmmn symmetry) as well as the approximate assignments of the vibrational modes, derived from the calculations. The corresponding summary for Imm2 symmetry is given in Table 6 of the article (Bonales *al.*, 2016a). As can be seen in Figure 3, the general aspect of the computed spectrum is very similar to that of the experimental spectrum up to 1550 cm^{-1}. The band observed at higher wavenumber (~1603 cm^{-1}) in the experimental spectrum does not appear in the

computed ones, as expected, due to the fact that this band corresponds to the water bending vibration, and the calculations do not include water within the structure. A more detailed comparison will be given below. Note that when the symmetry of a certain vibration is cited, we refer to that of the Pmmn structure. To find the corresponding symmetry for the Imm2 structure, see Table 6 of the article (Bonales *et al.*, 2016a).

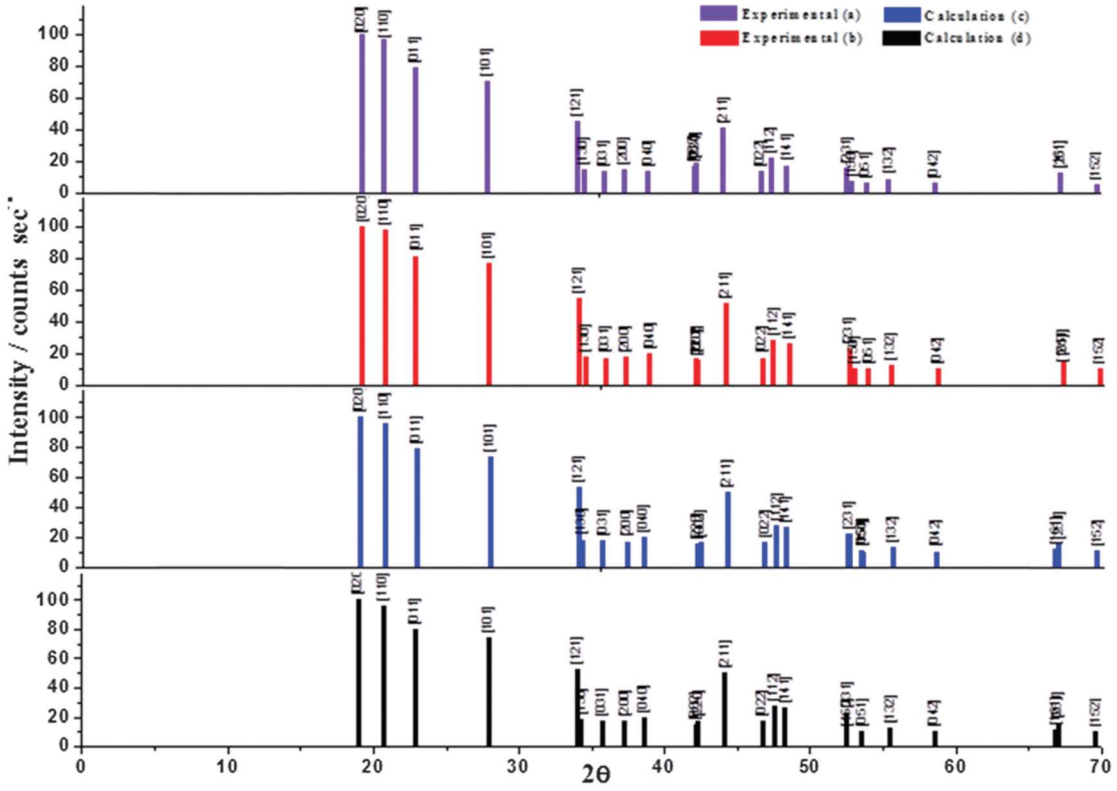

Figure 4.2 X-ray powder spectrum of rutherfordine using CuKa radiation: (a) experimental spectrum (pattern 89-6527 in the PDF-2 database); (b) X-ray powder spectrum computed form experimental geometry; (c) X-ray powder spectrum computed from calculated geometry (Pmmn); (d) X-ray powder spectrum computed from calculated geometry (Imm2).

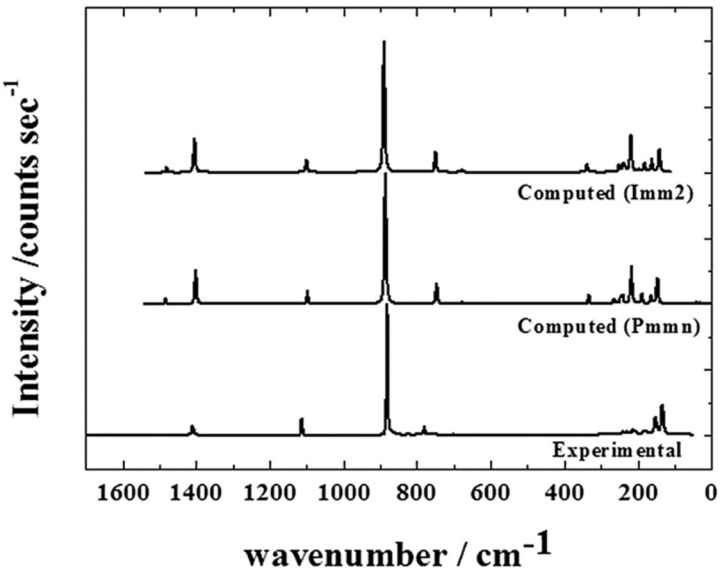

Figure 4.3 Calculated and experimental Raman spectra.

The Raman spectra of the regions 1200–850 cm^{-1} and 1700–1200 cm^{-1} are shown in Fig. 4.4.A and B, respectively, together with the computed spectra. Fig. 4.4.A shows the region of the uranyl stretching vibration. In this region, there is a main band at 882 cm^{-1}, which corresponds to the uranyl symmetric stretching vibration ν_1, which is commonly used as a fingerprint of this mineral (Bonales *et al.*, 2015). The value was very well reproduced by the theoretical calculations (886 cm^{-1} and 900 cm^{-1}, for Pmmn and Imm2, respectively, Ag symmetry), and it is in agreement with previous published data (886 cm^{-1}; Frost *et al.*, 2009a). At higher wavenumbers (around 1113 cm^{-1}) we found a band which is assigned to the CO_3^{2-} symmetric stretching vibration ν_1 (free CO_3^{2-} ion value of 1060 cm^{-1}), which is also in good agreement with both the calculated value (1098 cm^{-1} and 1100 cm^{-1}, Ag symmetry) and the experimental value of Frost *et al.* (2009) (1115 cm^{-1}).

Figure 4.4.B shows the spectrum in region 1700–1200 cm^{-1}. The band at 1409 cm^{-1} is assigned to the asymmetric stretching vibrations of CO_3^{2-} ion ν_3 and this value is very close to the computed wavenumbers (1401 cm^{-1} and 1403 cm^{-1}). Frost *et al.* (2009a) observed this band at 1412 cm^{-1}. The existence of a less intense band at about 1499 cm^{-1} can be explained as a result of the splitting of the ν_3 band. In the free undistorted ion, it is degenerate, symmetry E', and located at about 1415 cm^{-1}. The band is split into two components when the ion symmetry is lowered from D_{3h} to C_{2v}, whose computed values are 1401 and 1483 cm^{-1} with symmetries Ag and B2g, respectively, for the Pmmn structure and 1403 and 1481 cm^{-1} for Imm2 structure. The experimental value of the splitting is $\Delta = 1499–1409 = 90$ cm^{-1} while the computed values are 82 and 78 cm^{-1}. The values are also comparable to the IR spectrum bands at 1414 and 1505 cm^{-1} (Cejka and Urbanec, 1988) or 1433 and 1520 cm^{-1} (Cejka, 1999).

Table 4.2 Experimental and calculated Raman shifts, calculated intensities and assignments (Pmmn symmetry).

Exp. Raman shift (cm^{-1})	Calc. Raman shift (cm^{-1})	Irr. rep. (D_{2h})	Intensity ($Å^4$)	Assignment
78.63	32.743	A_g	0.051	$T(UO_2^{2+} + CO_3^{2-})$
95.34	43.405	B_{3g}	0.129	$T(UO_2^{2+} + CO_3^{2-})$
133.77	147.179	B_{1g}	11.632	$\delta^{a}(UO_2^{2+}) + \delta^{op}(CO_3^{2-})$
152.91	149.758	B_{3g}	2.860	$\delta^{op}(CO_3^{2-})$
168.187	164.700	B_{3g}	4.693	$T(CO_3^{2-})$
187.24	189.777	B_{3g}	8.011	$\delta^{a}(UO_2^{2+})$
212.98	217.417	A_g	35.316	$T(CO_3^{2-})$
241.59	241.484	B_{2g}	7.366	$\delta^{s}(UO_2^{2+}) + \delta^{ip}(CO_3^{2-})$
256.68	264.646	B_{2g}	7.636	$\delta^{s}(UO_2^{2+}) + \delta^{ip}(CO_3^{2-})$
339.15	332.824	B_{2g}	16.935	$\delta^{ip}(CO_3^{2-})$
700.29	677.803	A_g	15.199	$\delta^{ip}(CO_3^{2-})$
754.448	752.046	B_{3g}	0.432	$\delta^{op}(CO_3^{2-})$
780.203	746.833	B_{2g}	110.074	$\delta^{ip}(CO_3^{2-})$
793.045	—	—	—	—
803.534	—	—	—	—
823.306	—	—	—	—
882.288	886.469	A_g	879.905	$\nu^{s}(UO_2^{2+})$
1113.33	1097.712	A_g	120.246	$\nu^{s}(CO_3^{2-})$
1408.98	1401.211	A_g	407.713	$\nu^{a}(CO_3^{2-})$
1498.92	1482.837	B_{2g}	76.985	$\nu^{a}(CO_3^{2-})$

The Raman spectra of the regions 500–0 cm^{-1} and 850–500 cm^{-1} are shown in Fig. 4.5.A and B, respectively, together with the computed spectra.

The low wavenumber region 500–0 cm^{-1} is shown in Fig. 4.5A. The bands located at 339, 257, 242, 213, 187, 168, 153, and 134 cm^{-1} have theoretical counterparts of 332, 265, 242, 217, 190, 165, 150, and 147 cm^{-1} for Pmmn and 338, 251, 240, 219, 182, 162 and 142 cm^{-1}, for the Imm2

symmetry. The first one, at 339 cm^{-1}, is assigned to a carbonate in plane bending vibration (B2g), and that located at 153 cm^{-1} to a carbonate out of plane vibration (B3g). While the 257 and 242 cm^{-1} bands are assigned mainly to uranyl symmetric bending vibrations (B2g), the 187 and 134 cm^{-1} bands are assigned to uranyl antisymmetric bending vibrations (B3g and B1g). Finally, the 213 and 168 cm^{-1} bands are assigned to carbonate group translations (Ag and B3g). The final bands found at 95 and 79 cm^{-1} are not as well reproduced theoretically and may be described as overall carbonate and uranyl group translations.

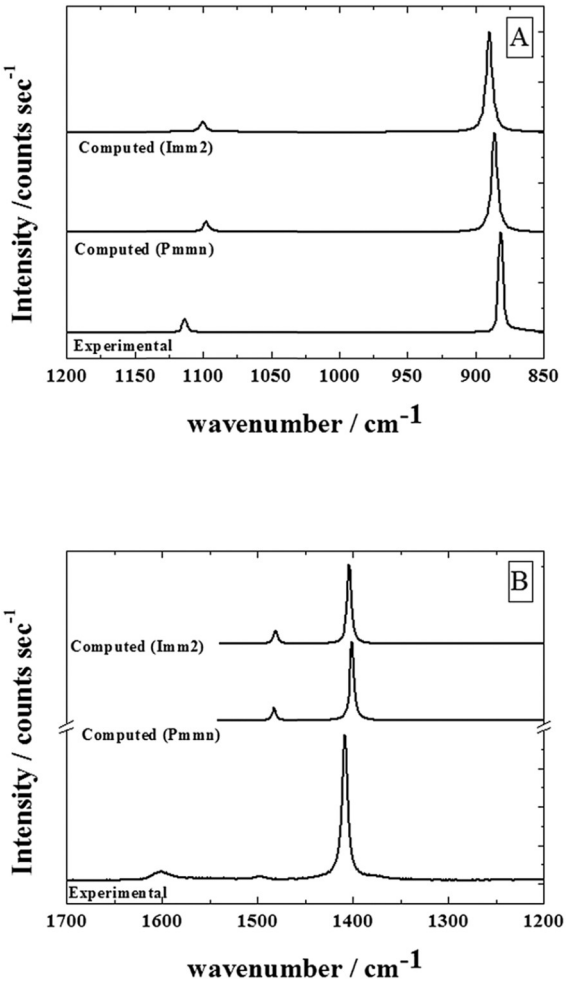

Figure 4.4 A) Raman spectrum of the region 850–1200 cm^{-1}; (B) Raman spectrum of the region 1200–1700 cm^{-1}.

Among the low wavenumber bands of the published data (Frost *et al.,* 2009a) a band is found at 343 cm^{-1} which seems to split into two components at 336 and 330 cm^{-1}. These bands were attributed to the $\nu(U-O)$ vibrations (Hoekstra and Siegel, 1973). As can be seen in the vibrational mode picture, the calculated band at 333 cm^{-1} (associated with the experimental value of 339 cm^{-1}), actually represents a carbonate in plane vibration. Bands were also observed at 279, 263, 252 and 241 cm^{-1} (bands at 257 and 242 cm^{-1} appear in our spectrum) and were ascribed without specification to the ν_2 bending modes of the UO_2^{2+} units and lattice vibrations. We believe that they correspond to uranyl symmetric bending vibrations, the antisymmetric ones and lattice vibrations falling somewhat lower in wavenumber.

Figure 4.5.B shows the region 850–500 cm^{-1}. The bands at 700 and 780 cm^{-1} are attributed to the CO_3^{2-} in plane bending vibrations ν_4 and are calculated at 678, and 747 cm^{-1} for Pmmn and 678 and 750 cm^{-1} for Imm2. The free ion wavenumber value is 680 cm^{-1}. This vibration (E''

symmetry) splits, as the ν_3 one, into two components of symmetries Ag and B2g. In this case, the second one has the largest intensity. The splitting is Δ = 69 cm^{-1} for Pmmn and 72 cm^{-1} for Imm2 while the experimental value is 80 cm^{-1}. The CO_3^{2-} out of plane deformation vibration ν_2 is believed to fall at 754 cm^{-1} while the theoretical value is 752 cm^{-1} for Pmmn and 750 cm^{-1} for Imm2 as can be seen in the vibrational mode pictures (see Fig. 4.B.1 in Appendix 4.B and Fig. 4.C.1 in Appendix 4.C). The free ion value is however 880 cm^{-1}. It is very weak in the theoretical Raman spectra as expected from an inactive Raman vibration for the free carbonate ion.

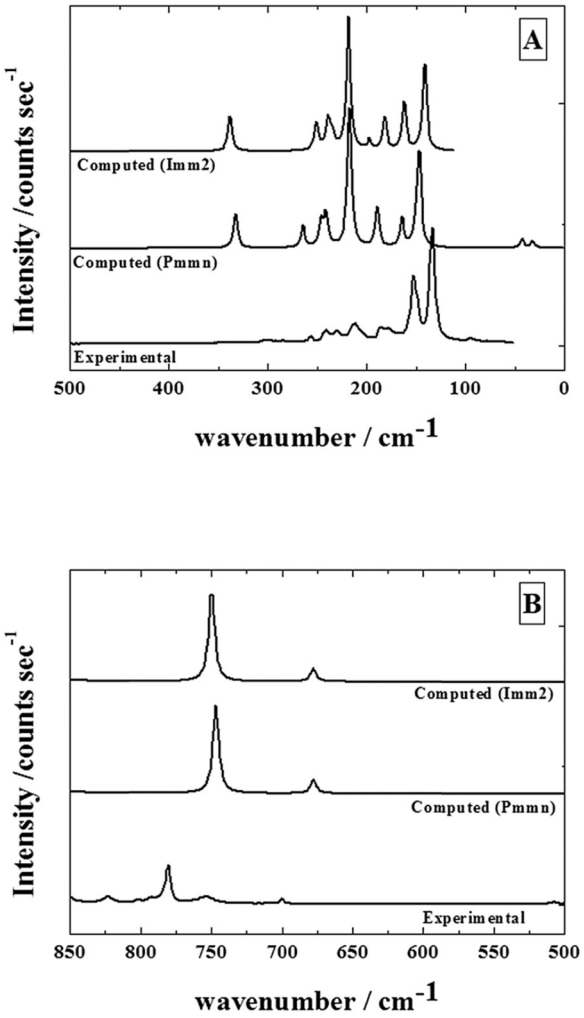

Figure 4.5 (A) Raman spectrum of the region 0–500 cm^{-1}; (B) Raman spectrum of the region 500–850 cm^{-1}.

It should be noted that weak bands at 793, 803, and 823 cm^{-1} do not have counterparts in the theoretical spectra; these bands must correspond to other species of carbonate anions in the rutherfordine structure (Frost *et al.,* 2009a; Cejka, 1999) or another different mineral phases present in the natural sample being studied.

The Raman spectra of schoepite (Frost *et al.,* 2007b) shows bands at 897, 886, 870, 855, 839, 826, 817, 802, 554, 545, 507, 460, 458, 402, 351, 330, 305, 274, 248, 216, 194 and 168 cm^{-1}. The bands at 803 and 823 cm^{-1} are close to those schoepite bands at 802 and 826 cm^{-1}. Thus, they may be relics of schoepite bands. They were attributed (Frost *et al*., 2007b) to the splitting of $\nu^s(UO_2^{2+})$ symmetric stretching vibration in schoepite (different U–O bond lengths in uranyl) or to $\nu(U-OH)$ bending vibrations. This correspondence is in accordance with the solid solution suggestion, which implies that solid solutions with limited solubility may exist in the system

$UO_2(CO_3)/UO_2(OH)_2 \cdot yH_2O$ (rutherfordine/schoepite, metaschoepite, and dehydrated schoepite), thus forming $UO_2(CO_3)_{1-x} \cdot yH_2O$ (Frost *et al.,* 2007a; Finch *et al.*, 1999; Cejka and Urbanek, 1988; Catalano and Brown, 2004).

The band at 793 cm^{-1} can also be related to the uranophane alpha band found (Bonales *et al.*, 2015; Frost *et al.,* 2006a) at about 797 cm^{-1}. From the analysis described above, it can be concluded that both theoretical spectra corresponding to the Pmmn and Imm2 symmetries are similar to the experimental one. However, in the Raman spectra associated with the Pmmn structure we note the presence of three additional active translation modes, absent in the calculated Raman spectrum associated with the Imm2 structure. Nonetheless, both structures may be simultaneously present in nature, as suggested by Christ *et al.* (1956).

4.3.3 Effects of the Introduction of Dispersion Corrections and Water Molecules in the Structure of Rutherfordine

Additional calculations were carried out with the aim of: (a) analyzing the influence of dispersion corrections in the theoretical results and (b) studying the influence of the introduction of water molecules inside the structure of rutherfordine in the band wavenumbers, particularly in the out of plane deformation wavenumber for the carbonate groups. A comparison of this wavenumber was also carried out with values reported in the literature.

Since the sheets in the structure of rutherfordine are bonded together by van der Waals forces, we carried out calculations using the PBE functional (Perdew *et al*., 1996) including the empirical dispersion correction of Grimme (Grimme, 2006). The kinetic energy cutoff used was 1200 eV and the K mesh 5×3×6 (18 K points). The computed lattice parameters were *a* = 4.8647 Å, *b* = 9.5435 Å, *c* = 4.3295 Å (α = β = γ = 90 deg). The main effect is, therefore, the increase of the intersheet distance (*b* parameter). The agreement with experimental structure is worse than in the calculations obtained in previous sections and thus, the PBESOL (Perdew *et al.*, 2008) functional works better in this case, at least for the structural determination. The vibrational Raman spectrum is however quite similar to the PBESOL one. Dispersion corrections, therefore, do not seem to modify significantly the calculated spectra.

As mentioned before, the computed spectra do not include water molecules in the rutherfordine structure and since the presence of water might cause significant shifts in the bands associated with both UO_2^{2+} and CO_3^{2-} units, additional calculations were carried out. Particularly, the carbonate out of plane deformation wavenumber was shown to be much lower than the free ion value. The main displacements in this mode arise from the carbon atoms of the carbonate groups. Due to the presence of uranyl groups placed just above and below them, the out of plane motion may be hindered and water molecules placed in the intersheet space could modify the corresponding wavenumber. Two water molecules were introduced in the space between the sheets of the unit cell of rutherfordine. The calculation was performed again with the dispersion corrected PBE functional, a kinetic energy cutoff of 900 eV and a 3×1×3 K mesh (5 K points). The intersheet space was greatly increased, but the carbonate main bands were only slightly modified: $\nu^a(CO_3^{2-})$=473, 1378 cm^{-1}; $\nu^s(CO_3^{2-})$=1091 cm^{-1}; $\delta^{op}(CO_3^{2-})$=761 cm^{-1}; $\delta^{ip}(CO_3^{2-})$ =750, 680 cm^{-1}.

Majumdar *et al.* (2002, 2003) and Chaudhuri *et al* (2004) carried out molecular calculations (gas phase) of $UO_2(CO_3)$, $PuO_2(CO_3)$, and related clusters including hydrated species using DFT (B3LYP functional), second-order Moller–Plesset (MP2) perturbation and multireference configuration interaction methods and large gaussian basis sets. The calculated ν_2 and ν_4 vibrational wavenumbers of the carbonate group were given only for the isostructural $PuO_2(CO_3)$ gas phase species. The values obtained at the MP2 level for the anhydrous system $PuO_2(CO_3)$ are ν_2=629, 719 cm^{-1} and ν_4=754 cm^{-1}. The ν_4 value obtained for the anhydrous species, 754 cm^{-1}, is thus consistent with our calculated wavenumber of 752 cm^{-1} and present experimental value of 754 cm^{-1}.

APPENDIX 4.A. Calculated Structures of Uranium Containing Minerals Using the New Pseudopotential.

Lattice parameters calculated for a selected series of uranium containing minerals with small cutoffs and K meshes. All calculations were carried out using the PBESOL functional (Perdew *et al.,* 2008). Note that for solids as uranium dioxide (uraninite) the calculations predict them to be metals. This is a well known deffect of simple DFT calculations (Crocombette *et al.,* 2001; Beridze *et al.,* 2014; Dudarev *et al.,* 2007; Nerikar *et al.,* 2009; Andersson *et al.,* 2013; Wen *et al.,* 2012, 2013). Hybrid functionals or DFT simple modifications such as the inclusión of the Mott-Hubbard correction improving the description of strongly correlated uranium 5f electrons (DFT+U) may restore this deffect predicting the insulating state for these solids (Dudarev *et al.,* 2007; Nerikar *et al.,* 2009; Andersson *et al.,* 2013; Wen *et al.,* 2012, 2013; Beridze *et al.,* 2014). However, these methods cannot be used currently to determine the vibrational spectra within CASTEP, and they were not used in the calculations.

Table 4.A.1. Calculated structures of uranium containing minerals compared with experimental values.

Mineral (N. of atoms per unit cell / N. of valence electrons) Symmetry	**Experimental/ Calculated values**	**Lattice parameters and Cell volume a,b,c (Å) α,β,γ (deg) V (Å^3)**	**E cut (eV) K mesh**
Uraninite (12/204) Fm-3m	UO_2[a]	5.468, 5.468, 5.468 90, 90, 90 163.5	-
	Calculated	5.2915, 5.2915, 5.2915 90, 90, 90 148.16	830 5 x 5 x 5
U_3O_8 (22/108) (Amm2)	U_3O_8[b]	4.145, 11.95, 6.722 90, 90, 90 332.96	-
	Calculated	4.1142, 11.6899, 6.7298 90, 90, 90 323.66	750 6 x 2 x 4
α-$UO_2(OH)_2$ (28/160) Cmce	$UO_2(OH)_2$[c]	4.242, 10.302, 6.868 90, 90, 90 300.1	-
	Calculated	4.1841, 10.1017, 6.7969 90.00, 90.00, 90.00 287.28	830 3 x 1 x 2
β-$UO_2(OH)_2$ (28/160) Pbca	$UO_2(OH)_2$[d]	5.6438, 6.2867, 9.9372 90, 90, 90 352.6	-
	Calculated	5.7850, 6.0844, 9.6516 89.98, 90.00, 89.93 339.72	830 3 x 2 x 1

Mineral (N. of atoms per unit cell / N. of valence electrons) Symmetry	Experimental/ Calculated values	Lattice parameters and Cell volume a,b,c (Å) α,β,γ (deg) V (Å^3)	E cut (eV) K mesh
γ-$UO_2(OH)_2$ (14/80) P121/c1	$UO_2(OH)_2$[e]	5.56, 5.522, 6.416 90, 112.71, 90 181.7	-
	Calculated	5.3691, 5.6474, 6.3017 89.97, 111.55, 90.10 177.72	830 3 x 2 x 1
Brannerite (18/148) C12/m1	UTi_2O_6[f]	9.87, 3.76, 6.95 90, 119.5, 90 224.5	-
	Calculated	9.95, 3.71, 6.79 90, 121.82, 90 213.26	830 2 x 4 x 2
Rutherfordine (14/96) Pmmn O_2	$[UO_2][CO_3]$[g]	4.85, 9.22, 4.3 90, 90, 90 192.3	-
	Calculated	4.8285, 9.3370, 4.2731 90, 90, 90 192.65	830 3 x 2 x 3
Grimselite (44/272) P-62c	$K_3Na[UO_2][CO_3]_3[H_2O]$[h]	9.302, 9.302, 8.260 90, 90, 120 619.0	900 2 x 2 x 2
	Calculated	9.3857, 9.38570, 8.3946 90.01, 90.01, 121.29 627.64	-
Coffinite (16/168) I41/amd	$USiO_4$[i]	6.995, 6.995, 6.263, 90, 90, 90, 306.449	-
	Calculated	6.9192, 6.9192, 6.2353 90, 90, 90 298.52	830 2 x 2 x 2
Vanderbrandeite (24/130) P-1	$Cu[UO_2][OH]_4$[j]	5.449, 6.089, 7.855 78.1, 89.2, 88.56 254.9	-
	Calculated	5.2352, 6.3528, 8.5518 85.52, 86.89, 92.26 282.88	880 5 x 4 x 3
Becquerelite (236/1184) Pna21	$Ca[UO_2]_6O_4[OH]_6[H2O]_8$[k]	13.838, 14.924, 12.378 90, 90, 90 2500.88	-
	Calculated	13.785, 14.630, 12.201 90, 90, 90 2460.73	800 1 x 1 x 1
Uranophane-alpha (68/320) P1211	$CaH_2[H_2O]_5[SiO_4]_2[UO_2]_2$[l]	6.665, 7.002, 15.909 90, 97.27, 90 736.5	-

Mineral (N. of atoms per unit cell / N. of valence electrons) Symmetry	**Experimental/ Calculated values**	**Lattice parameters and Cell volume a,b,c (Å) α,β,γ (deg) V (Å^3)**	**E cut (eV) K mesh**
	Calculated	6.6276, 6.9614, 15.7299 90, 98.17, 90 718.37	880 2 x 2 x 1
Uranophane-beta (136/640) P121/c1	$Ca[H_2O]_5O_6[OH]_2Si_2[UO_2]$[m]	6.632, 15.443, 13.966 90, 91.38, 90 1429.95	-
	Calculated	6.6084, 15.3807, 13.887 90, 89.875, 90 1411.51	800 2 x 1 x 1
Schoepite (meta) (320/1536) Pbcn	$[UO_2]_4O[OH]_6.[H_2O]_5$[n]	14.686, 13.980, 16.706 90, 90, 90 3430	-
	Calculated	14.484, 13.826, 16.373 90.00, 90.00, 90.00 3378.63	830 1 x 1 x 1
Soddyite (136/768) Fddd O2	$[UO_2]_2[SiO_4][H_2O]_2$[o]	8.334, 11.212, 18.668 90, 90, 90 1744.4	-
	Calculated	7.902, 11.476, 18.686 90, 90, 90 1694.48	830 2 x 1 x 1
Studtite (68/280) C12/c1	$[UO_2][O_2][H_2O]_4$[p]	14.068, 6.721, 8.428 90, 123.356, 90 665.6	-
	Calculated	13.6114, 6.6938, 8.3936 90.00, 122.88, 90.00 642.27	830 1 x 2 x 1
Kasolite (36/272) P21/c	$[UO_2]Pb[SiO_4][H_2O]$[q]	6.704, 6.932, 13.252 90, 104.22, 90 596.98	-
	Calculated	6.7035, 6.8325, 13.1795 90, 101.92, 90 590.63	820 2 x 2 x 1
Boltwoodite (26/144) P1211	$K[H_3O][UO_2][SiO_4]$[r]	6.638, 7.064, 7.073 90, 105.75, 90 319.2	-
	Calculated	6.6229, 7.0252, 7.0239 90, 104.57, 90 316.29	830 2 x 2 x 2

a) L. Desgranges, G. Baldinozzi, G. Rousseau, J.-C. Nièpce and G. Calvarin, *Inorganic Chemistry*, 2009, **48**, 7585-7592.

b) J. B. Ainscough and I. F. Ferguson, *Journal of Inorganic and Nuclear Chemistry*, 1974, **36**, 193-194.

c) J. Taylor, *Acta Crystallographica Section B*, 1971, **27**, 1088-1091.

d) J. C. Taylor and H. J. Hurst, *Acta Crystallographica Section B*, 1971, **27**, 2018-2022.

e) S. Siegel, H. R. Hoekstra and E. Gebert, *Acta Crystallographica Section B*, 1972, **28**, 3469-3473.

f) A. M. Lejus and D. Goldberg, *C. R. Seances Acad. Sci. (Ser. C)*, 1966, **263**, 1223-1226.
g) R. J. Finch, M. A. Cooper, F. C. Hawthorne and R. C. Ewing, *The Canadian Mineralogist*, 1999, **37**, 929-938.
h) L. H. Fuchs and E. Gebert, *American Mineralogist*, 1958, **43**, 243-248.
i) Y. Li and P. C. Burns, *The Canadian Mineralogist*, 2001, **39**, 1147-1151.
j) A. Rosenzweig and R. R. Ryan, *Cryst. Struct. Commun.*, 1977, **6**, 53-56.
k) M. K. Pagoaga, D. E. Appleman and J. M. Stewart, *American Mineralogist*, 1987, **72**, 1230-1238.
l) D. Ginderow, *Acta Crystallographica Section C*, 1988, **44**, 421-424.
m) K. Viswanathan and O. Harneit, *American Mineralogist*, 1986, **71**, 1489-1493.
n) M. T. Weller, M. E. Light and T. Gelbrich, *Acta Crystallographica Section B*, 2000, **56**, 577-583.
o) F. Demartin, C. M. Gramaccioli and T. Pilati, *Acta Crystallographica Section C*, 1992, **48**, 1-4.
p) P. C. Burns and K.-A. Hughes, *American Mineralogist*, 2003, **88**, 1165-1168.
q) V. I. Mokeeva, *Sov. Phys. Crystallogr. (Engl. Transl.) - Kristallografiya*, 1965, **9**, 621-622.
r) F. V. Stohl and D. K. Smith, *American Mineralogist*, 1981, **66**, 610-625.

APPENDIX 4.B. Normal Modes of Rutherfordine (Pmmn Symmetry)

Figure 4.B.1. Atomic motions associated to some Raman active vibrational normal modes of Rutherfordine (Pmmn symmetry).

Mode v=1483 cm^{-1}. Asymmetric CO_3^{2-} stretching (B2g).

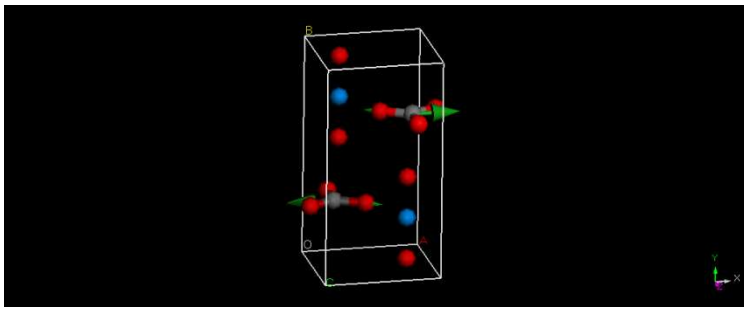

Mode v=1402 cm^{-1}. Asymmetric CO_3^{2-} stretching (Ag).

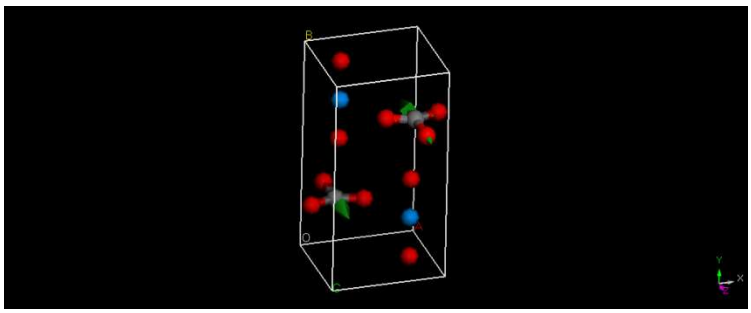

Mode v=1097 cm^{-1}. Symmetric CO_3^{2-} stretching (Ag).

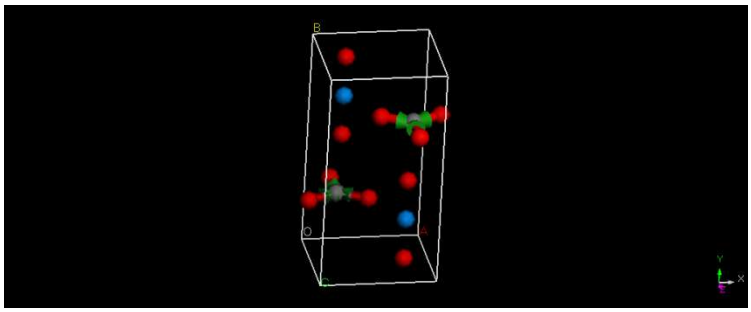

Mode v=979 cm^{-1}. Antisymmetric UO_2^{2+} stretching (B3g).

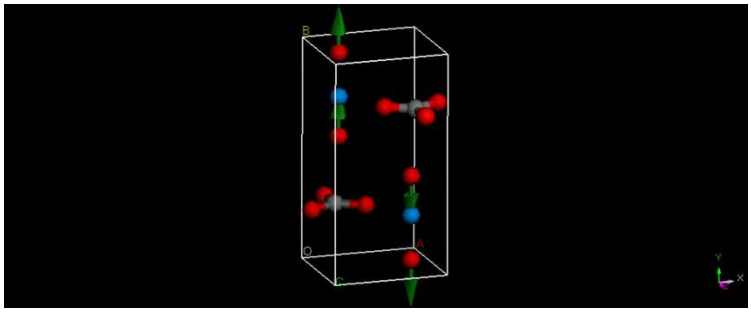

Mode v=886 cm^{-1}. Symmetric UO_2^{2+} stretching (Ag).

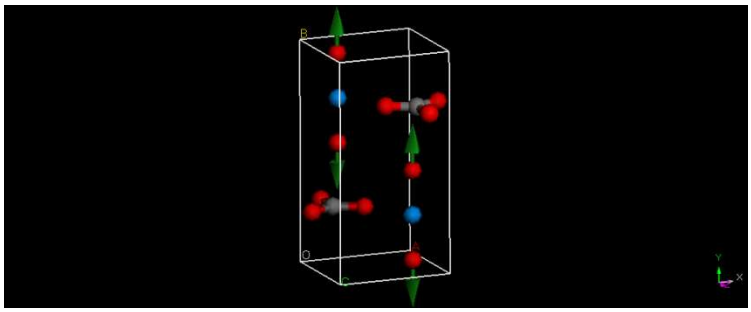

Mode v=752 cm^{-1}. Out of plane CO_3^{2-} bending (B3g).

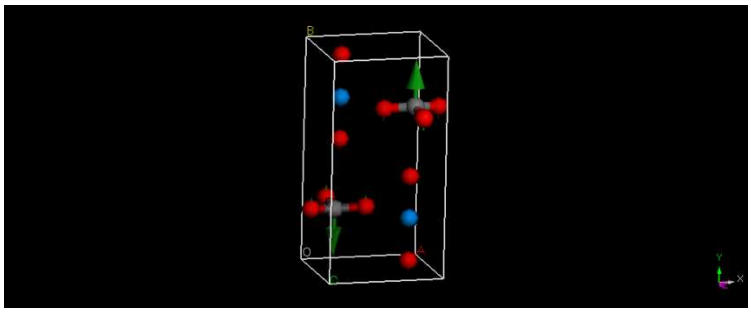

Mode v=746 cm^{-1}. In plane CO_3^{2-} bending (B2g).

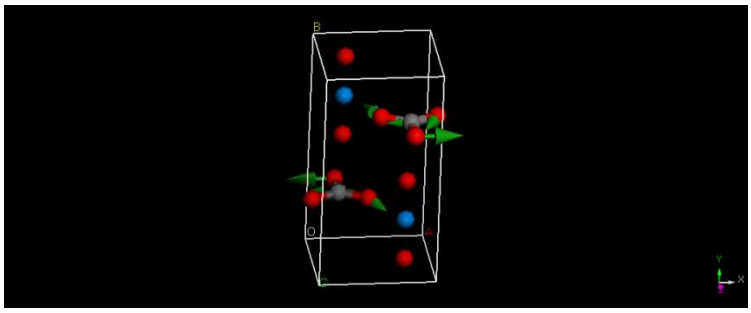

Mode v=678 cm^{-1}. In plane CO_3^{2-} bending (Ag).

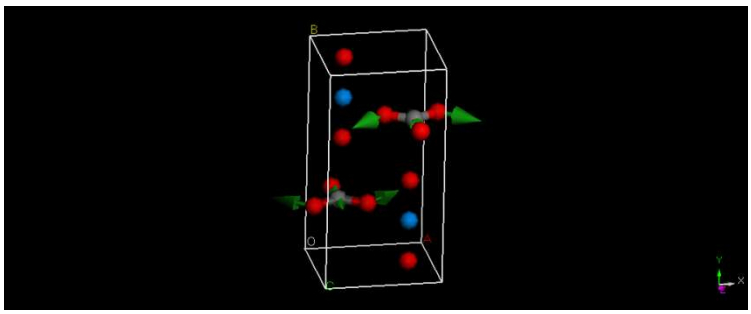

APPENDIX 4.C. Normal Modes of Rutherfordine (Imm2 Symmetry)

Figure 4.C.1. Atomic motions associated to some Raman active vibrational normal modes of Rutherfordine (Imm2 symmetry).

Mode ν=1481 cm^{-1}. Asymmetric CO_3^{2-} stretching (B2).

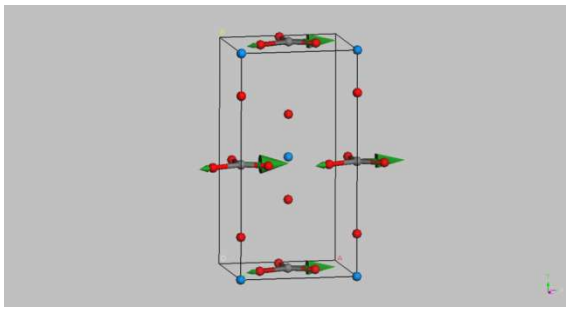

Mode ν=1403 cm^{-1}. Asymmetric CO_3^{2-} stretching (A1).

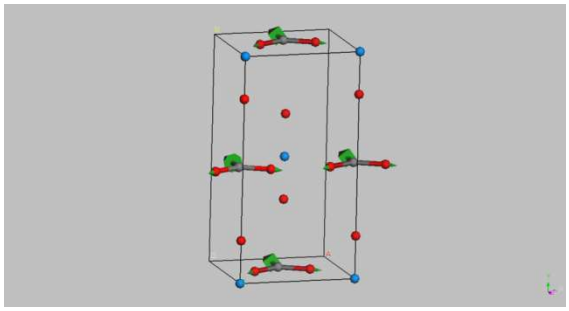

Mode ν=1100 cm^{-1}. Symmetric CO_3^{2-} stretching (A1).

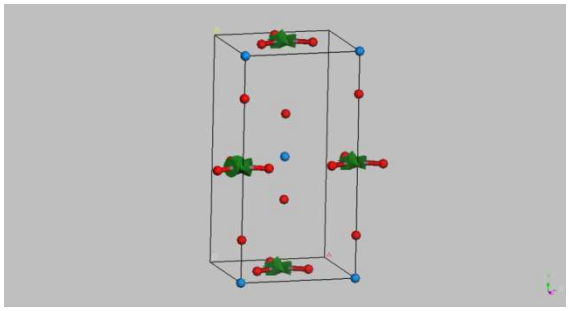

Mode ν=890 cm^{-1}. Symmetric UO_2^{2+} stretching (A1).

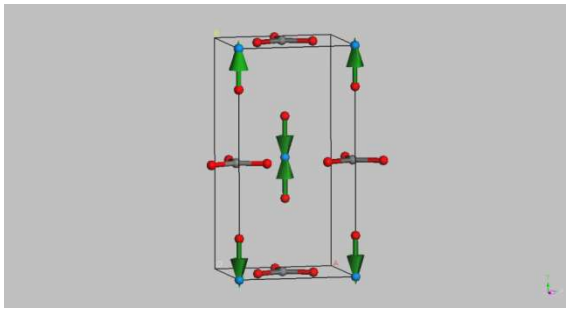

Mode v=750 cm^{-1}. Out of plane CO_3^{2-} bending (B1).

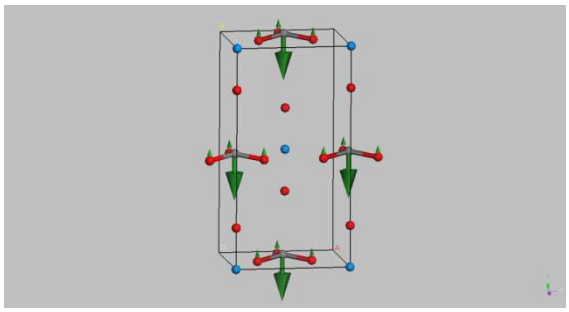

Mode v=750 cm^{-1}. In plane CO_3^{2-} bending (B2).

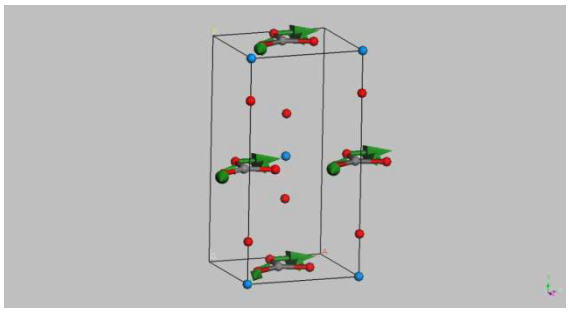

Mode v=678 cm^{-1}. In plane CO_3^{2-} bending (A1).

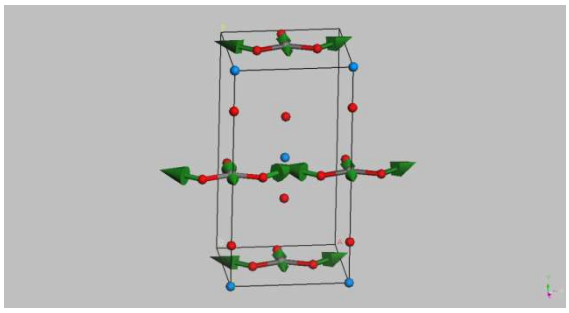

Chapter 5. Rutherfordine: Thermodynamic and Mechanical Properties

This chapter is based on the published article *"Thermodynamic and mechanical properties of rutherfordine mineral based on density functional theory"*, by F. Colmenero, L. J. Bonales J. Cobos and V. Timón, J. Phys. Chem. C 121, 5994–6001 (2017).

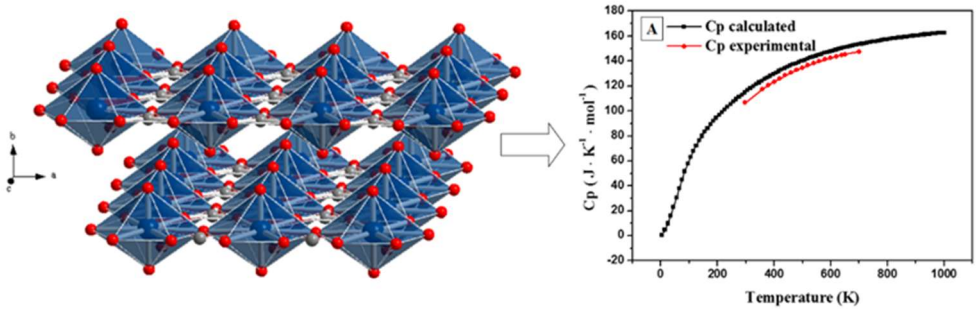

Abstract

The thermodynamic and mechanical properties of rutherfordine, a uranyl carbonate mineral, were studied by means of first principles calculations based on density functional theory. Thermodynamic properties, including enthalpy, free energy, entropy, heat capacity, and Debye temperature, were evaluated as a function of temperature and compared with experimental data in the 300−700 K range. Our calculations show very good agreement with experimental data, and based on them, the knowledge of these properties is extended to the temperature range from 0 to 1000 K, including the full range of thermal stability (0-700 K). The computed values of the heat capacity, entropy, and free energy at 298 K deviate from the experimental values by about 8, 0.3 and 0.3%, respectively. At 700 K, the corresponding differences remain very small, 3.9, 2.3 and 1.3%, respectively. The equation of state and mechanical properties were also computed. The crystalline structure is seen to be mechanically and dynamically stable. Rutherfordine is shown to be a highly anisotropic and brittle material with a very large compressibility along the direction perpendicular to the sheets characterizing its structure. The computed bulk modulus is very small, B ≈ 20 GPa, in comparison to the values obtained in previous calculations.

5.1 Introduction

Uranium carbonate compounds and their importance in actinide environmental chemistry have been reviewed by Clark *et al.* (1995). Because carbonate and bicarbonate, present in significant concentrations in many natural waters, are exceptionally strong complexing agents for actinide ions, the carbonate complexes of actinide ions play an important role in the migration from nuclear waste repositories or in accidental site contamination. *Therefore, the study of the structural and thermodynamic stabilities of uranium carbonates is particularly relevant to nuclear waste disposal*. Because of the great relevance of uranyl carbonates, the rutherfordine mineral was studied using experimental and theoretical methods in our previous work (Bonales *et al*., 2016a). As far as we are concerned, there is only a previous study (Matar, 2010) of this mineral by means of solid-state theoretical methods. However, the analysis of the results of this work reveals that the computed structure is not very precise. Therefore, the bulk modulus extracted from the equation of state of the rutherfordine mineral reported in that work may not be accurate because of structural deficiencies, and it deviates largely from the value reported in this work.

In this section, we study the thermodynamic and mechanical properties of mineral rutherfordine by means of computational density functional theory (DFT) calculations. In this way, we extend the previous study of this mineral (Bonales *et al.*, 2016a) in which the structure, X-ray powder pattern, and Raman spectra were determined using a new norm-conserving relativistic pseudopotential for the uranium atom. All of the thermodynamic properties are evaluated as a function of temperature in the 0−1000 K range and are compared with experimental data in the 300−700 K range. This section is organized as follows. In subsection 5.2, the methods used are described. In subsection 5.3, the main results of our calculations of thermodynamic properties are given and compared to experimental data. Finally, the computed equation of state and mechanical properties are also reported.

5.2 Methods

The rutherfordine unit cell has been modeled using the CASTEP code (Clark *et al*, 2005), a module of the Materials Studio package (Materials Studio, 2017). The generalized gradient approximation (GGA) with the PBESOL functional (Perdew *et al*., 1996, 2008) was used. Geometry optimization was carried out using the Broyden-Fletcher-Goldfarb-Shanno optimization scheme (Pfromer *et al.* 1997; Payne *et al.* 1992) with a convergence threshold on

atomic forces of 0.01 eV/Å. The kinetic energy cutoff employed was 1000 eV, and the corresponding k-point mesh (Monkhorst and Pack, 1976) adopted was 5 × 3 × 6 (18 K points). They were selected in our previous work (Bonales *et al*., 2016a) by performing calculations of increasing complexity. The above calculation parameters gave well converged structures and were considered sufficient to determine the final material properties. The X-ray powder pattern was determined from the optimized structure. Also, in that work we used the linear response density functional perturbation theory (DFPT) (Baroni *et al.,* 1987; Baroni *et al.,* 2001; Gonze *et al.*, 1992; Gonze *et al.,* 1997; Refson *et al.,* 2006) implemented in the CASTEP code in order to determine the Raman spectra of the rutherfordine mineral. All of these properties were evaluated for two different rutherfordine structures with symmetries Imm2 and Pmmn. For these structures, we obtained very close results for the energies and properties; therefore, we concluded that both could be simultaneously present in nature (Bonales *et al.,* 2016a). In present work, we have chosen the structure with Imm2 symmetry among these two nearly degenerate structures in order to determine the thermodynamic and mechanical properties. The phonon spectrum at different points in the Brillouin zone can also be determined by DFPT as second-order derivatives of the total energy (Baroni *et al.,* 2001). The knowledge of the entire phonon spectrum allows the phonon dispersion curves and density of states to be calculated and, from them, the evaluation of several important thermodynamic quantities in the quasiharmonic approximation, such as free energies, enthalpies, entropies, specific heats, and Debye temperatures (Baroni *et al.,* 2001; Lee and Gonze, 1991).

The bulk modulus and its pressure derivative were calculated by fitting the lattice volumes and pressures to an equation of state. In the present study, the lattice volumes around the equilibrium were computed by optimizing the structure at several different pressures between -0.75 and 12 GPa, where negative pressure values mean traction or tension. The results were then fitted to a fourth-order Birch-Murnaghan equation of state (Birch, 1947) using the computed volume at 0 GPa as V_0 using EOSFIT 5.2 code (Angel, 2001).

Elastic constants, needed for the calculation of mechanical properties and for the study of the mechanical stability of rutherfordine crystal structure, were calculated from stress-strain relations. For this purpose, the finite deformation technique is employed in CASTEP. In this technique, finite programmed symmetry-adapted strains (Nye, 1985) may be used to extract individual elastic constants from the stress tensor obtained as the response of the system to the applied strains. For the calculation of the elastic tensor, this stress-based method appears to be more efficient than the energy-based methods and the use of DFPT (Yu *et al.,* 2010).

The norm-conserving relativistic pseudopotential (Troullier and Martins, 1991) for the uranium atom employed in the computations was generated in our previous work (Bonales *et al.*, 2016a) This paper and other publications (Colmenero *et al.,* 2017b-f) may be consulted to find the details of its construction and behaviour for many different uranyl minerals. The pseudopotentials used for C and O atoms in the unit cell of the rutherfordine mineral were standard norm-conserving pseudopotentials given in the CASTEP code (00PBE-OP type).

5.3 Results and Discusion

5.3.1 Thermodynamic Properties

A phonon calculation was performed for the optimized rutherfordine structure (Imm2 symmetry) and with the same calculation parameters as in our previous work (Bonales *et al.,* 2016a). From it, the thermodynamic properties were evaluated. Figure 5.1 (A−D) shows the isobaric heat capacity, entropy, enthalpy, and free-energy functions, respectively, compared to the experimental data of Hemingway (1982). Finally, Figure 5.1.E shows the calculated Debye temperature function. More details about the Debye temperature function calculated in this work are given in Appendix B of the Supporting Information of the article (Colmenero *et al.*, 2017a).

Note that all enthalpy and free-energy values have been divided by the temperature to express these properties in the same units as entropy and heat capacity (J/(K·mol)).

The value obtained for the isobaric specific heat at zero pressure and 298 K is Cp = 115.0 J/(K·mol), which may be compared to the experimental value of Gurevich *et al.* (Gurevich *et al.*, 1987; Grenthe *et al.*, 2004) of 120.1 ± 0.1 J/(K·mol) and that of Hemingway1 of 106.5 J/(K·mol). The agreement is quite good, with our value being between both experimental values and the deviations being about 4 and 8%, respectively. The heat capacity function is compared with that of Hemingway (1982) in Figure 5.1.A in the temperature range of 298-700 K. As can be appreciated, the calculated and experimental curves are closely parallel. The computed value at 700 K, near the limit of thermal stability (Hemingway, 1982), Cp=153.3 J/(K·mol), differs from the experimental value of 147.6 J/(K·mol) by only 3.9%. A precise comparison of the specific heat values at selected temperatures is given in Table 5.1.

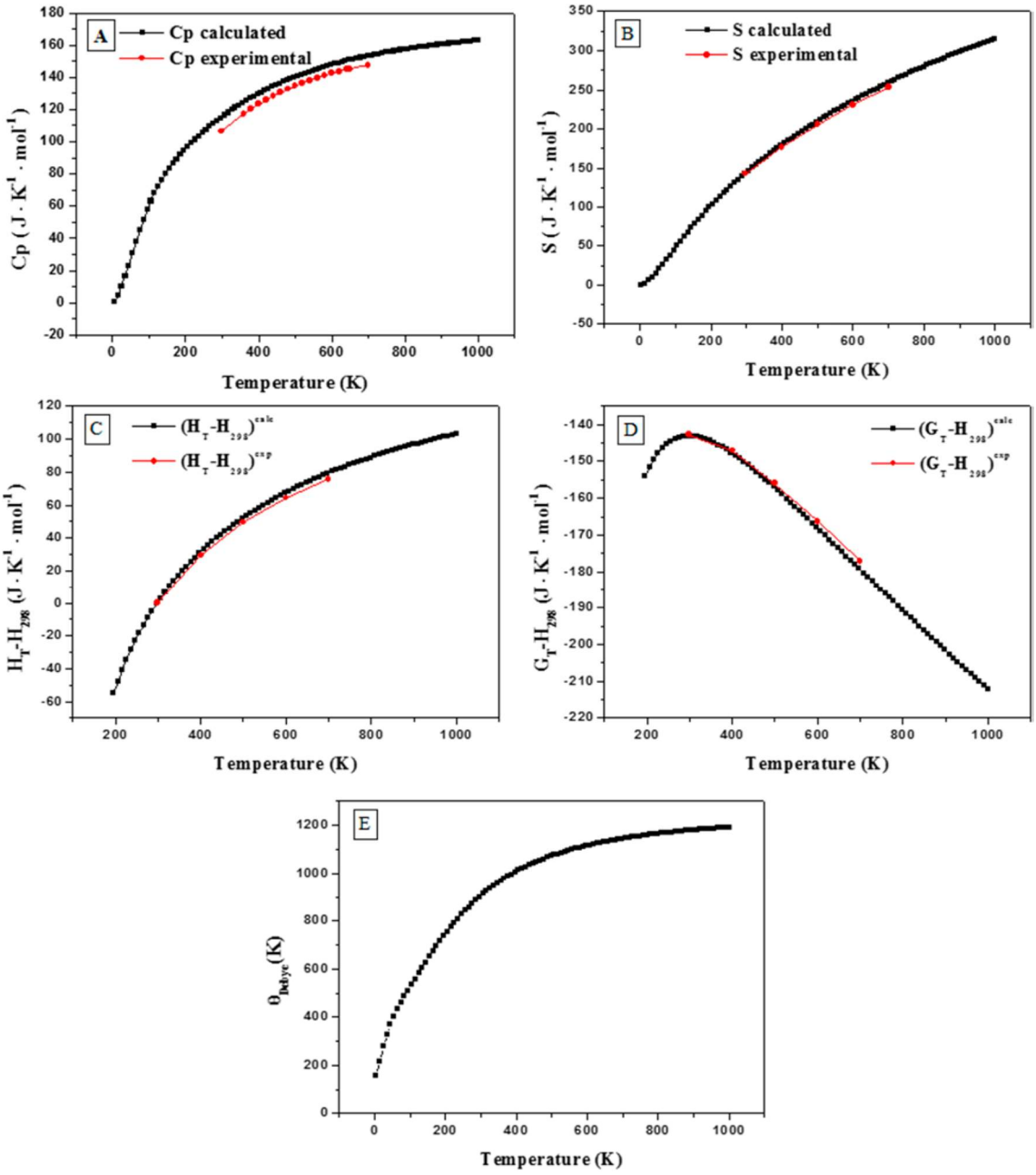

Figure 5.1. (A) Isobaric specific heat, (B) entropy, (C) enthalpy, (D) Gibbs free energy, and (E) Debye temperature. All functions are given as a function of temperature.

Table 5.1. Comparison of Calculated and Experimental Isobaric Heat Capacity Functions[a].

T(K)	C_p^{exp}	C_p^{calc}
298.15	106.5	115.02
360	117.4	124.55
380	120.5	127.25
400	123.3	129.78
420	125.9	132.15
440	128.4	134.38
460	130.6	136.46
480	132.7	138.41
500	134.68	140.24
520	136.5	141.96
540	138.2	143.56
560	139.7	145.07
580	141.2	146.48
600	142.48	147.81
620	143.7	149.05
640	144.8	150.22
650	145.3	150.78
700	147.57	153.32

[a]All values are given in units of J/(K·mol). The experimental data are from Hemingway.[1]

To facilitate the use of the calculated heat capacity function, we have fitted it to a fifth-order polynomial, and the results are given in Table 5.2. The fit was carried out with 52 points, and it should be valid over a large range of temperature of 250-750 K. It has a very small sum of squared deviations (SSD) and a very good correlation factor (R). The calculated data may also be fitted, as usual, to a Haas-Fisher (HF) polynomial, Cp(T) =a + bT + cT^{-2}+ dT−0.5+ eT^2, yielding coefficients a = 259.03119 J/(K·mol), b = −0.00101 J/(K^2·mol), c = 1.06343 × 10^6 J/(K^{-1}·mol), d = −2668.47225 J/($K^{0.5}$·mol), and e = −1.28601 ×10^5 J/(K^3·mol). However, we prefer the polynomial fit because the SSD associated with the HF fit is 2 orders of magnitude larger (0.01091). The calculated heat capacity function over the temperature range of 0-1000 K is given in Appendix A of the Supporting Information of the article (Colmenero *et al.*, 2017a). The last value of Cp calculated at a temperature of 1000 K, Cp = 162.8 J/(K·mol), is still well below the Dulong-Petit asymptotic value, Cp = 3nR = 174.6 J/(K·mol).

Table 5.2. Fifth-Order Polynomial Fit of the Calculated Heat Capacity, Entropy, Enthalpy, and Free-Energy Functions[a].

	C_p^{calc}	S^{calc}	$(H_T - H_{298})^{calc}$	$(G_T - H_{298})^{calc}$
A_0	32.31873	−20.33277	−299.5316	279.1873
A_1	0.4175506	0.7833474	2.078814	1.295351
$A_2 \times 10^3$	−0.5960663	−1.101300	−5.651087	−4.549320
$A_3 \times 10^6$	0.4846092	1.303643	8.807384	7.502775
$A_4 \times 10^9$	−0.2220333	−0.9440572	−7.225174	−6.280124
$A_5 \times 10^{12}$	0.04688578	0.2968067	2.418783	2.121575
SSD	0.00024	0.00051	0.05419	0.04450
R	1.00000	1.00000	1.00000	1.00000

[a]$F(T) = A_0 + A_1T + A_2T^2 + A_3T^3 + A_4T^4 + A_5T^5$). The A_i coefficients are given in J/(K^{1+i}·mol) units.

The computed entropy value at zero pressure and a temperature of 298 K is S = 143.1 J/(K·mol). The agreement with the experimental value of Hemingway (1982), 142.7 J/(K·mol), is excellent. The value of entropy at 298 K given by Langmuir (1978) was also 142.7 J/(K·mol). The estimate of Lemire and Tremaine (1980) of 194 J/(K·mol) is ruled out because it is too large in comparison to the experimental values and the calculated one. Cordfunke and O'Hare (1978) gave an estimation of 139 J/(K·mol). Although the errors are slightly larger at higher temperatures (Table

5.3), the entropy variation with temperature is very good. The calculated entropy function compared to the experimental one is displayed in Figure 5.1.B. The differences with respect to Hemingway's experimental values range from 0.3% at 298 K to 2.3% at 700 K. The results of a fifth-order polynomial fit to the calculated entropy, valid from 250 to 750 K, are given in Table 5.2. The calculated entropy function over the full range of temperature, 0-1000 K, is given in Appendix A of the Supporting Information of the article (Colmenero *et al.*, 2017a).

Table 5.3. Comparison of Calculated and Experimental Entropy Functions[a].

T(K)	S^{exp}	S^{calc}
298.15	142.70	143.11
400	176.50	179.10
500	205.32	209.24
600	230.61	235.52
700	252.99	258.74

[a]All values are given in units of J/(K·mol). The experimental data are from Hemingway.[1]

Table 5.4. Comparison of Calculated and Experimental Enthalpy Functions, H_T-H_{298}[a].

T(K)	$(H_T - H_{298})^{exp}$	$(H_T - H_{298})^{calc}$
298.15	0.00	0.0
400	29.400	31.3
500	49.382	52.0
600	64.292	67.5
700	75.854	79.3

[a]All values are given in units of J/(K·mol). The experimental data are from Hemingway.[1]

Table 5.5. Comparison of Calculated and Experimental Free-Energy Functions, G_T-H_{298}[a].

T(K)	$(G_T - H_{298})^{exp}$	$(G_T - H_{298})^{calc}$
298.15	−142.70	−143.11
400	−147.10	−147.81
500	−155.94	−157.20
600	−166.32	−168.06
700	−177.14	−179.44

[a]All values are given in units of J/(K·mol). The experimental data are from Hemingway.[1]

The calculated enthalpy value at zero pressure and temperature of 298.15 K is H_{298} = 70.95 J/(K·mol). The enthalpy variation with temperature is very good, as can be seen in Table 5.4, where the values of enthalpy relative to its value at 298.15 K (H_T-H_{298}) are compared to their experimental counterparts at 400, 500, 600, and 700 K. The calculated enthalpy function compared to the experimental one is displayed in Figure 5.1.C. The computed value at 700 K, (H_T-H_{298}) = 79.3 J/(K·mol), deviates from experiment, (H_T-H_{298}) = 75.8 J/(K·mol), by 4.6%. The results of a fifth-order polynomial fit to the calculated enthalpy, valid from 250 to 750 K, are given in Table 5.2. The computed enthalpy function over the temperature range of 0-1000 K is given in Appendix A of the Supporting Information.

The variation of the free energy with temperature is also good, as can be seen in Table 5.5, where the calculated values relative to the enthalpy at 298 K (G_T-H_{298}) are compared with the corresponding experimental data at 298, 400, 500, 600, and 700 K. Computed values differ from experiment by 0.3 and 1.3% at 298 and 700 K, respectively. The calculated free-energy function compared to the experimental one is displayed in Figure 5.1.D, and the results of a fifth-order polynomial fit to the calculated free energy, valid from 250 to 750 K, are given in Table 5.2. The calculated free-energy function over the temperature range of 0-1000 K is given in Appendix A of the Supporting Information.

5.3.2 Equation of State

Lattice volumes around equilibrium were calculated by optimizing the structure at 17 different applied pressures. The results are displayed in Figure 5.2.

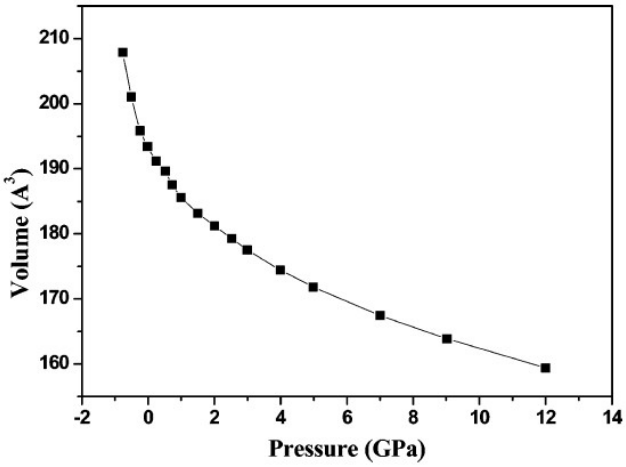

Figure 5.2. Rutherfordine unit cell volume versus applied pressure.

The calculated data were then fitted to a fourth-order Birch-Murnaghan equation of state (EOS, see equation (3.150)) using the computed volume at 0 GPa (193.7 Å^3) as V_0 using the EOSFIT 5.2 code (Angel, 2001). The values found for the bulk modulus and its first and second derivatives at the temperature of 0 K, were B = 19.03 (±0.36) GPa, B'= 15.34 (±0.72), and B'' = −7.43 (±1.32) GPa^{-1} ($\chi 2$ = 0.003). The value obtained for the bulk modulus is very different to that computed previously by Matar (2010). Because our previous structural and spectroscopic results (Bonales *et al*, 2016a) and the thermodynamic properties computed in this work are in very good agreement with experimental data, we believe that the present value of B is much more accurate.

5.3.3 Mechanical Properties and Stability

The elastic tensor, needed for the calculation of mechanical properties and to study the mechanical stability of the rutherfordine crystal structure, was calculated, at the optimized equilibrium structure, from stress−strain relations using the finite deformation technique implemented in CASTEP. Crystals with orthorhombic symmetry have nine nondegenerate elastic constants in the symmetric stiffness matrix (Nye, 1985; Weck *et al.*, 2015) which may be written as in equation (3.157.a). The precise values of these constants obtained in our computations are given in Table 5.6.

Table 5.6. Nine Independent Elastic Constants in the Stiffness Matrix for the Orthorhombic Lattice Structure of Rutherfordine[a].

C_{11}	C_{22}	C_{33}	C_{44}	C_{55}	C_{66}	C_{12}	C_{13}	C_{23}
259.88	23.03	165.27	9.85	65.88	15.06	−8.33	72.39	−5.18

[a]All values are in GPa.

For orthorhombic crystals, the necessary and sufficient Born criteria for mechanical stability were given in equations (3.160.$a-c$). Because the above conditions are fulfilled by the elastic constants of rutherfordine reported in Table 5.6, its mechanical stability can be inferred. To analyze the stability of the material in a complete form, we must also study the dynamic stability.

A structure is dynamically stable if and only if all of its phonon modes have positive frequencies for all wave vectors (Mouhat and Coudert, 2014). The satisfaction of this condition has also been verified from the phonon calculation utilized to determine the thermodynamic properties of rutherfordine.

The fact that C_{22}, the diagonal component of the C matrix along the b direction, is much smaller than either C_{11} or C_{33} suggests that the thermal expansion of the material will occur predominantly along this direction (perpendicular to rutherfordine sheets). Diagonal component C_{11} is the largest (along the a direction). A simple view of the elastic constants given in Table 5.6 shows that the mechanical properties are very different along the different directions. Therefore, the rutherfordine crystal structure is highly anisotropic. This anisotropy may be understood from the analysis of the structure, as illustrated in Figure 5.3. Although rutherfordine sheets, perpendicular to the b direction, are held together with weak van der Waals forces, the atoms within the sheets are linked with strong UO and CO bonds.

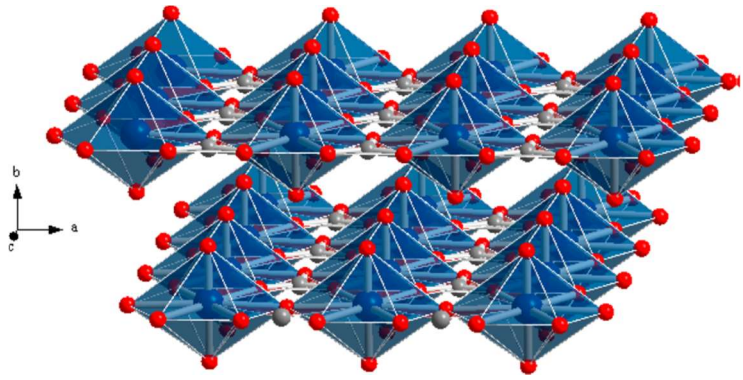

Figure 5.3. Crystal structure of rutherfordine (Bonales *et al*., 2016). Color code: U, blue; O, red; and C, gray.

Bulk and shear moduli (B and G) of polycrystalline aggregates of rutherfordine crystals were determined from the elastic tensor according to Voigt, Reuss, and Hill schemes (Voight, 1962; Reuss, 1929; Hill, 1952). Relevant formulas for these approximations may be found in Section 3.2.9. Large differences between these approximations are expected for crystalline systems with strong anisotropy, featuring large differences between elastic constants along different directions (Weck *et al*., 2015). The Reuss scheme gave the best comparison of the computed bulk modulus with that determined from the equation of state, given in the previous section. The bulk and shear moduli calculated in this approximation together with the values obtained for other mechanical properties are given in Table 5.7. The numerical estimate of the error in the computed bulk modulus given by the CASTEP code is 0.94 GPa. Our value of the bulk modulus, B = 17.97 ± 0.94 GPa, agrees reasonably well with that obtained from the EOS, B = 19.03 ± 0.36 GPa.

Table 5.7. Bulk, Modulus, Shear Modulus, Young Modulus, Poisson Ratio, Pugh's Ratio, and Vickers Hardness (B, G, E, ν, D and H) calculated in the Reuss Approximation[a].

property	value
B	17.97
G	19.47
E	42.92
ν	0.10
D	0.92
H	9.47

[a]Values of *B*, *G*, and *E* are given in GPa.

In general, a large value of the shear modulus is an indication of the more pronounced directional bonding between atoms. The shear modulus represents the resistance to plastic deformation whereas the bulk modulus represents the resistance to fracture. The individual components of the bulk and Young's moduli were obtained from the elastic compliance matrix components as explained in Section 3.2.9. The corresponding values are given in Table 5.8. As can be seen, B_b is much smaller than either B_a or B_c. Also, component E_b is much smaller than E_a or E_c. Thus, the b direction, perpendicular to rutherfordine sheets, is the most compressible and least stiff, in agreement with the results of the components of the elastic C matrix.

Table 5.8. Bulk and Young Moduli Components along the Crystallographic Axes[a].

	a axis	*b* axis	*c* axis
B	271.19	21.70	170.06
E	226.57	22.71	144.75

[a]All values are given in GPa.

Pugh and Poisson (Pugh, 1954) ratios were also determined to measure the ductility and malleability of rutherfordine (see Section 3.2.9). As it can be seen in Table 5.7, for rutherfordine we find small ratios D and ν corresponding to a *brittle material*. For comparison, both studtite and metastudtite were found to be ductile (Weck *et al*, 2015).

The hardness of this system was also computed according to the empirical scheme (Niu *et al*., 2011) that correlates the Vickers hardness and Pugh ratio. The Vickers hardness, H, of polycrystalline rutherfordine is given in Table 5.7. Its value, about 9.5, corresponds to material of *intermediate hardness*. For comparison, we can compute the hardness of studtite and metastudtite using the elasticity data of Weck *et al.* (2015). These systems, characterized by much larger D ratios, have a much smaller hardness (smaller than 1).

To assess the elastic anisotropy of rutherfordine, shear anisotropic factors were obtained. These factors provide a measure of the degree of anisotropy in the bonding between atoms in different planes and are very important in the study of material durability. Shear anisotropic factors for the {100} (A1), {010} (A2), and {001} (A3) crystallographic planes were computed as explained in Section 3.2.9. The computed values were 0.14, 1.33, and 0.20. Thus, the anisotropies are very large in the {100} and {001} planes. The {010} plane, containing rutherfordine sheets, is the least anisotropic.

In the recently introduced universal anisotropy index (Ranganathan and Ostoja-Starzewski, 2008) the departure of A^U from zero defines the extent of single-crystal anisotropy and accounts for both the shear and the bulk contributions unlike all other existing anisotropy measures. It must also be noted that A^U is independent of the scheme used to determine the polycrystalline elastic properties because it is defined in terms of the bulk and shear moduli in both Voigt and Reuss approximations. Thus, A^U represents a universal measure to quantify the single-crystal elastic anisotropy. Rutherfordine is characterized by a computed anisotropy index of 8.82, which is a rather large value ($A^U = 0$ corresponds to a perfectly isotropic crystal). For comparison, studtite and metastudtite exhibit anisotropy values of 2.17 and 1.44, respectively (Weck *et al.*, 2015).

Chapter 6. Soddyite: Structure, Mechanical Properties, Equation of State, and Raman Spectroscopy

This chapter is based on the published article "*Structural, mechanical and vibrational study of uranyl silicate mineral soddyite by DFT calculations*", by F. Colmenero, L. J. Bonales, J. Cobos and V. Timón, J. Solid. State. Chem. 253, 249–257 (2017).

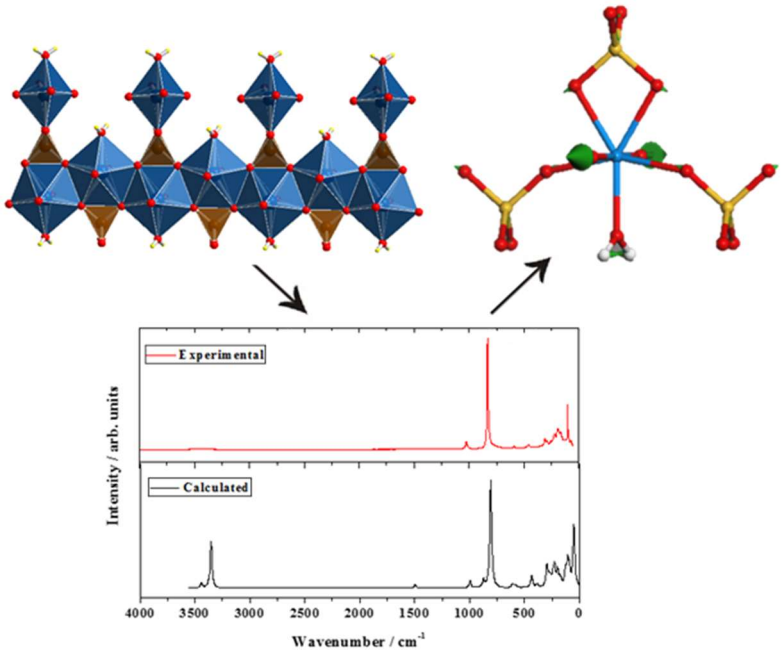

Abstract

Uranyl silicate mineral soddyite, $(UO_2)_2(SiO_4)\cdot 2(H_2O)$, is a fundamental component of the paragenetic sequence of secondary phases that arises from the weathering of uraninite ore deposits and corrosion of spent nuclear fuel. In this work, soddyite was studied by first principle calculations based on the density functional theory. As far as we know, this is the first time that soddyite structure is determined theoretically. The computed structure of soddyite reproduces the one determined experimentally by X-Ray diffraction (orthorhombic symmetry, spatial group *Fddd O2*; lattice parameters *a*=8.334 Å, *b*=11.212 Å; *c*=18.668 Å). Lattice parameters, bond lengths, bond angles and X-Ray powder pattern were found to be in very good agreement with their experimental counterparts. Furthermore, mechanical properties were obtained and the satisfaction of the Born conditions for mechanical stability of the structure was demonstrated by means of calculations of the elasticity tensor. Equation of state of soddyite was obtained by fitting lattice volumes and pressures to a fourth order Birch-Murnahan equation of state. Raman spectrum was also computed by means of density functional perturbation theory and compared with the experimental spectrum obtained from a natural soddyite sample. The results were also found in agreement with the experimental data. A normal mode analysis of the theoretical spectra was carried out and used in order to assign the main bands of the Raman spectrum.

6.1 Introduction

One of the minerals found very often in nature as alteration product of uraninite is soddyite. Mineral soddyite is a hydrated uranyl nesosilicate which was found in Shinkolobwe Mine (Kasolo Mine), Shinkolobwe, Katanga Cooper Crescent, Katanga (Shaba), Democratic Republic of Congo (Zaire), and it was first described by Schoep in 1922 (Schoep, 1922). In nature, soddyite occurs as fine grained pale-yellow aggregates or flat crystals or fibers having a color from greenish to canary yellow (Gorman, 1952). Soddyite, $(UO_2)_2(SiO_4)\cdot 2(H_2O)$, is the unique uranyl silicate mineral known characterized by a uranium to silicon ratio of 2:1 (Stohl and Smith, 1982). Most uranyl silicate minerals have uranium to silicon ratio of 1:1 and contain sheets (Grenthe *et al.*, 2006; Burns, 2005; Stohl and Smith, 1982) except soddyite (Demartin *et al.*, 1992) and weeksite (Jackson and Burns, 2001) which have framework crystal structures (Burns, 1999a, 2005; Demartin *et al.*, 1992). Soddyite is isostructural to a uranyl germanate mineral (Stohl and Smith, 1982; Demartin *et al.*, 1992) studied by Legros and Jeanin (1975). The crystal structure of $Na_2(UO_2)_2SiO_4F_2$ (Blaton *et al.*, 1999) is structurally related to soddyite. Its structure is very complex and includes 136 atoms in the unit cell, as well as 768 valence electrons. In oxidizing waters that contain uranyl and silicate ions, the solid uranyl orthosilicate may form as a solubility-controlling solid (Moll *et al.*, 1995). It has been synthetized in the laboratory, for example, by Legros *et al.* (1972), Kuznetsov *et al.* (1981), Nozik *et al.* (1990) and Moll *et al.* (1995). The latter synthesized the uranyl orthosilicate with reproducible yields of about 81 %, and phase purity.

Despite the structure of soddyite have been determined by experimental X-ray diffraction techniques, it has never been confirmed by means of theoretical solid state calculations. In this paper, we perform a complete structural characterization of soddyite by theoretical solid state methods that allow us to confirm the structure obtained experimentally. From the obtained structure, we had studied the mechanical properties and stability of soddyite structure, based on the elastic constants computed in this study. Soddyite equation of state is also reported. The elastic constant tensor of an inorganic compound provides a complete description of the response of the material to external stresses in the elastic limit (Nye, 1985). The analysis of this tensor is important to understand the nature of the bonding in the material, and usually correlate with many mechanical properties. Also, although the Raman spectrum of this mineral has been determined by experimental methods (Giamar, 2001; Giamar and Herring, 2002; Biwer *et al.*, 1990; Amme *et al.*, 2002; Frost *et al.*, 2006b), a precise assignation of the main bands in the spectra is lacking, since they have been characterized incompletely and by using empirical arguments. The theoretical Raman spectrum of soddyite is reported here, including the computation of intensities

and the assignment of the vibrational bands. We have performed the assignment of the experimental vibrational Raman bands since theoretical methods provide detailed microscopic scale views of the atomic vibrational motions in the corresponding normal modes. Computations were carried out by means of Density Functional Theory (Hohenberg and Kohn, 1964; Kohn and Sham, 1965; Parr and Yang, 1989) (DFT) based on plane waves and pseudopotentials (Payne *et al.*, 1992). A norm conserving relativistic pseudopotential for uranium atom (Troullier and Martins, 1991) developed in a previous paper (Bonales *et al.*, 2016a) was used.

6.2 Materials and Methods

6.2.1 Experimental

The mineral sample studied in this work (Bonales *et al.*, 2015) is a natural mineral from Sierra Albarrana (Córdoba, Spain) whose structure corresponds to the ideal gummite occurrence (Frondel, 1956) (central core black and a yellow surrounding zone, formed by several minerals). The sample contains a mixture of alteration phases of natural uraninite: rutherfordine, soddyite, uranophane and kasolite. Soddyite prevails in the inner part of the sample.

A polished section of the sample was analysed by Raman using a Horiba LabRam HR evolution spectrometer (Jobin Yvon Technology). A red laser of HeNe with a wavelength of 632.81 nm and an operation power of 20 mW was used as excitation source. The laser was focused onto the sample by using 100x objective at the confocal microscope BX4 with confocal 800 mm; the scatter light was collected with the same objective and then dispersed with a Jobin-Yvon spectrometer (600 grooves/mm), and detected with a Peltier cooled CCD detector (256 x 1024 pixel). The spectral resolution was about 1 cm^{-1} per pixel.

6.2.2 Theoretical DFT Calculations

CASTEP code (Clark *et al.*, 2005; Milman *et al.*, 2010), a module of the Materials Studio package (Materials Studio, 2017), was employed to model soddyite structure. The generalized gradient approximation (GGA) together with PBE functional (Perdew *et al.*, 1996) and Grimme empirical dispersion correction, the DFT-D2 approach (Grimme, 2006) were used. The Grimme dispersion correction was included to describe correctly the hydrogen bonds present in the soddyite structure. The pseudopotentials used for H, O and Si atoms in the unit cell of soddyite mineral were standard norm-conserving pseudopotentials (Troullier and Martins, 1991) given in CASTEP code (00PBE-OP type). The norm-conserving relativistic pseudopotential for U atom was generated from first principles and is shown in a previous work (Bonales *et al.*, 2016a).

Geometry optimization was carried out by using the Broyden–Fletcher–Goldfarb–Shanno optimization scheme (Pfromer *et al.*, 1997; Payne *et al.*, 1992) with a convergence threshold on atomic forces of 0.01 eV/Å. The kinetic energy cut-off and k-point mesh (Monkhorst and Pack, 1976) must be adopted to ensure good convergence for computed structures and energies. Soddyite structure was optimized in calculations with increasing complexity by increasing these parameters. The optimization performed with a cut-off of 930 eV and a K mesh of 3×2×1 gave a well converged structure and it was used to determine the final results.

Elastic constants, used for the calculation of mechanical properties and to study the mechanical stability of soddyite crystal structure, were calculated from stress-strain methodology. With this purpose, finite deformation technique is employed in CASTEP. In this technique, finite programmed symmetry-adapted strains (Nye, 1985) are applied to the equilibrium conformation generating a set of distorted structures. The individual elastic constants are then extracted from the stress tensor obtained as response of the system to the applied strains. For the calculation of

elastic tensor, this stress-based method appears to be more efficient than the energy-based methods and the use of DFPT (Yu *et al.*, 2010).

Bulk modulus and its pressure derivatives were also calculated by fitting the lattice volumes and pressures to an equation of state. In the present study, the lattice volumes around the equilibrium were calculated by optimizing the structure at several different pressures -1.0, -0.75, -0.50, -0.25, 0.0, 0.25, 0.50, 0.75, 1.0, 1.5, 2.0, 3.0, 4.0, 5.0, 7.0, and 9.0 GPa, where negative pressure values mean traction or tension. The results were then fitted to a fourth-order Birch-Murnaghan equation of state (Birch, 1947) using EOSFIT 5.2 code (Angel, 2001).

For the calculations of vibrational properties, the linear response density functional perturbation theory (DFPT) (Baroni *et al.*, 1987, 2001; Gonze *et al.*, 1992, 1997; Refson *et al.*, 2006) implemented in the CASTEP code was used in the same way as in previous works (Bonales *et al.* 2016a; Colmenero *et al.*, 2017a-b).

6.3 Results and Discussion

The unit cell parameters and internal atomic positions were first optimized using an initial atomistic model based in the atomic coordinates given by Demartin *et al.* (1992). From the optimized structure, we have obtained both the structural parameters as well as the X-Ray powder pattern. Elastic tensor was calculated, at the optimized equilibrium structure, from stress-strain relations using the finite deformation technique implemented in CASTEP. From elastic tensor, mechanical properties such as elastic modulus, shear modulus, Vickers hardness and anisotropy index were then computed. Besides, soddyite equation of state is obtained by fitting lattice volumes and pressures to a fourth order Birch-Murnahan equation of state. Finally, the vibrational Raman spectrum was predicted as a list of wavenumber and intensity values for each normal mode (Refson *et al.*, 2006). Experimental Raman spectrum was then compared with the computed one and the assignment of main fundamental band frequencies was carried out.

6.3.1 Structure

Stohl and Smith (1981) categorized naturally occurring uranyl silicates according to the uranium to silicon ratio which in part determines the structures of these minerals. Most uranyl silicate minerals, as uranophane and boltwoodite, have uranium to silicon ratios of 1:1 and are sheet silicates (Grenthe *et al.*, 2006; Burns, 2005; Stohl and Smith, 1981). The sheets are composed of $[(UO_2)_2(SiO_4)_2]^{4-}$ units bound at the equatorial edges. Charge compensating cations, as calcium in uranophane and potassium in boltwoodite, lie in the interlayer space between the sheets. Soddyite (Demartin *et al.*, 1992) and weeksite (Jackson and Burns, 2001) have uranium to silicon ratios of 2:1 and 2:5, respectively, and their structure involve frameworks of U^{6+} polyhedra (Burns, 1999a, 2005; Stohl and Smith, 1981). In soddyite, charge compensation for the uranyl silicate groups is not required as the basic building unit is neutral $[(UO_2)_2(SiO_4)]$ (Belokoneva *et al.*, 1979).

The computed structure is shown in Figure 6.1. Figure 6.1.A, shows a view of the unit cell from [001]. Figure 6.1.B is a view of a 2 x 2 x 2 supercell along [110]. Fig 6.1.C is a view of the latter cell where only a subset of atoms is retained in order to show a clearer view of the soddyite structure. As can be seen, U atoms display pentagonal bipyramid coordination, $UO_6(H_2O)$, and Si atoms present tetrahedral coordination, SiO_4. The U bipyramids are connected by sharing two non-adjacent edges of the equatorial plane to form zigzag chains (see Figure 6.1.C). The single unshared equatorial vertex of the bipyramid is occupied by H_2O. The chains are parallel to [110] plane and are cross bonded through two opposite edges of the SiO_4 tetrahedra; i.e. adjacent uranyl silicate chains are directly linked as each tetrahedron shares two edges with bipyramids from two different chains. Moreover, the cohesion of the structure is enhanced by a pattern of hydrogen bonds involving the water molecules and the uranyl O atoms.

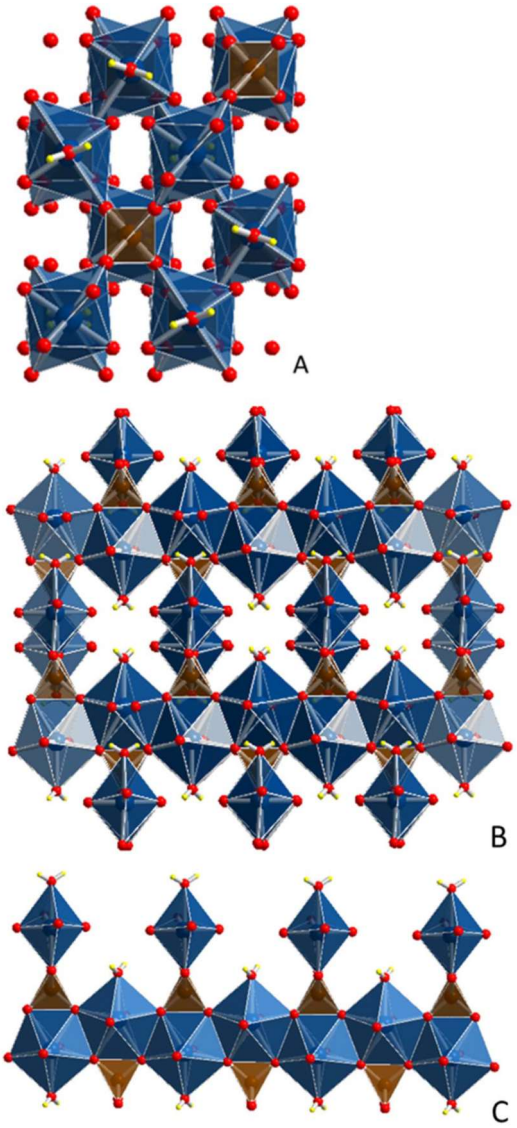

Figure 6.1. Structure of soddyite mineral: A) View of the unit cell from [001]; B) View of a 2 x 2 x 2 supercell from [110]; C) View of a 2 x 2 x 2 supercell from [110], retaining only a subset of atoms in order to show more clearly the structure. Colour code: U-Blue, Si-Brown, O-Red, H-White.

As it has been mentioned, the structure of soddyite was determined in calculations with increasing complexity. Table 6.1 gives the final lattice parameters, volumes and densities obtained compared with the experimental ones from Demartin *et al.* (1992). As it can be seen, theoretical and experimental results are in good agreement.

Table 6.1. Lattice parameters. The experimental data is from Demartin *et al.* (1992).

	a **(Å)**	***b*** **(Å)**	***c*** **(Å)**	**α**	**β**	**γ**	**Vol. (Å^3)**	**Dens. (g/cc)**
Calc.	8.0780	11.4253	18.8380	90	90	90	1738.6	5.104
Exp.	8.334	11.212	18.668	90	90	90	1744.4	5.088

Tables 2 and 3 of the article (Colmenero *et al.*, 2017c) give a comparison of the more important geometric parameters (bond distances and angles) obtained with the corresponding experimental data of Demartin *et al.* (1992). Soddyite has only one structurally (symmetrically) identical U^{6+} ion and one structurally (symmetrically) identical Si^{4+} ion in its crystal structure. The two O atoms in the uranyl group, UO_2^{2+} (O1 and its symmetry related companion), are in apical positions of the pentagonal bipyramids at a distance of 1.781 Å. The calculated value is 1.801 Å. The remaining five O atoms (four O2 and OW) lie in the equatorial plane which U-O distances which range from 2.313 to 2.424 Å (calculated 2.312 to 2.436 Å). The distances between adjacent O atoms range from 2.462 to 3.126 Å (calculated 2.467 to 3.166 Å), the shortest values corresponding to the shared edges with other U centered bipyramids and SiO_4 groups. The SiO_4 tetrahedron is markedly irregular, the O-Si-O angles ranging from 98.0 to 119.0 degrees (calculated 98.1 and 119.6 degrees). The O-O distances range from 2.462 to 2.811 Å (calculated 2.487 and 2.846 Å). The Si-O distances, 1.631 Å, are within the normal range (calculated value is 1.647 Å). The geometry and orientation of the plane of water molecule is mainly determined by the hydrogen bond interaction, directed towards O1. The OW-H-O1 angle determined experimentally is 156 degrees which is satisfactorily reproduced in our calculations, 149 degrees.

The X-Ray powder diffractogram of soddyite was computed from the experimental (Demartin *et al.*, 1992) and computed structures (Downs *et al.*, 1993) using CuKα radiation (λ=1.540598 Å). The most intense lines (I > 10%) are compared in Figure 6.2, and as it can be seen, the agreement in line positions and intensities is very good. The use of spectra derived directly from the experimental and computed structures allows for a fair comparison of the results free of interferences as the experimental conditions or possible artefacts as the presence of sample impurities since both are determined under the identical conditions. Nevertheless, the use of an experimental pattern also leads to an excellent agreement. Computer program XPowder (Martin, 2012) using the PDF-2 database (ICDD, 2003) recognizes the computed spectrum as that of soddyite (pattern 77-0604 which corresponds to synthetic soddyite sample, see Nozik and Kuznetsov (1990)). The values of the main reflections are given in Table 4 of the article (Colmenero *et al.*, 2017c).

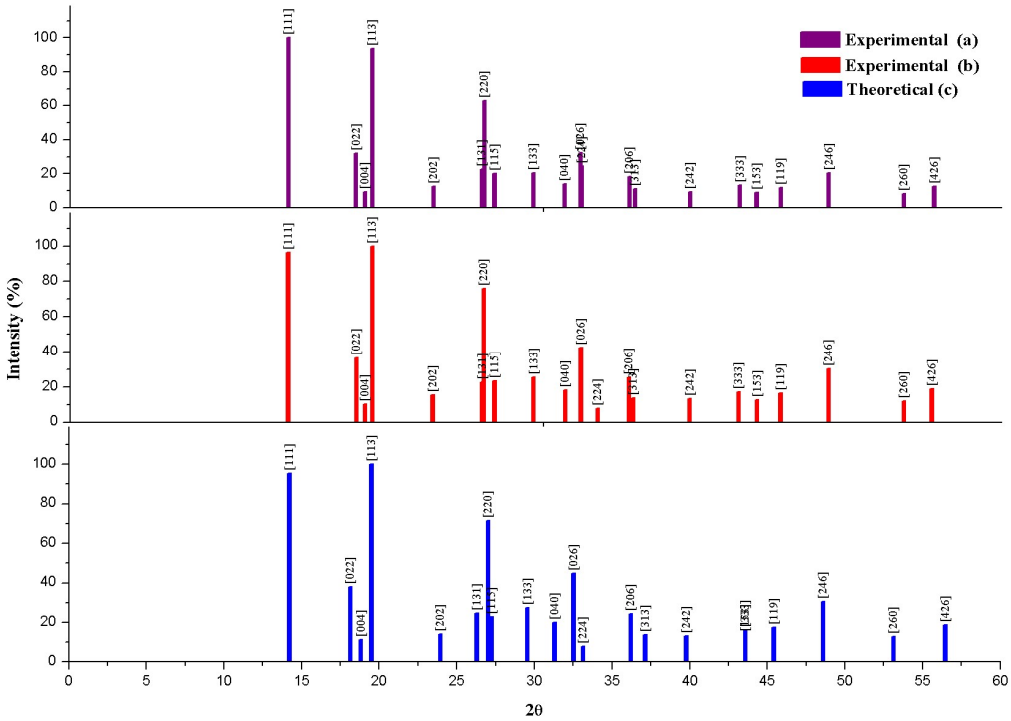

Figure 6.2. X-Ray powder pattern of soddyite using CuKα radiation: a) Experimental pattern (pattern 77-0604 in the PDF-2 database); b) X-Ray powder pattern computed from experimental geometry (Demartin *et al.*, 1992); c) X-Ray powder pattern computed from calculated geometry. The results for the main reflections are given in Table 4 of Colmenero *et al.* (2017c).

6.3.2 Mechanical Properties and Stability

Elastic tensor, used for the calculation of mechanical properties and for studying the mechanical stability of soddyite crystal structure, was calculated, at the optimized equilibrium structure, from stress-strain relations using the finite deformation technique implemented in CASTEP. Crystals with orthorhombic symmetry have nine non-degenerate elastic constants in the symmetric stiffness matrix (Nye, 1985; Weck *et al.*, 2015), which may be written as in equation $(3.157.a)$. The precise values of these constants obtained in our computations are given in Table 6.2.

Table 6.2. The nine independent elastic constants in the stiffness matrix for the orthorhombic lattice structure of soddyite. All values are given in GPa.

C_{11}	C_{22}	C_{33}	C_{44}	C_{55}	C_{66}	C_{12}	C_{13}	C_{23}
81.65	120.92	161.54	40.99	25.93	42.14	35.61	22.59	49.84

For orthorhombic crystals, the necessary and sufficient Born criteria for mechanical stability were given in equations $(3.160.a-c)$. Since the above conditions are fulfilled by the elastic constants of soddyite reported in Table 6.2, its mechanical stability can be inferred. The generic necessary and sufficient Born criterion that all eigenvalues of the C matrix be positive (Mouhat and Coudert, 2014) was also checked. The C matrix was diagonalized numerically and all eigenvalues were found to be positive, as expected. The lowest eigenvalue was about 0.026, so that soddyite structure is far from instability.

The fact that C_{11}, the diagonal component of C matrix along a direction, is much smaller than either C_{22} or C_{33} suggest that thermal expansion of the material will occur predominantly along this direction (contained in the plane of soddyite chains). The diagonal component C_{33} is the largest (along direction perpendicular to soddyite chains).

If single crystal samples are not available, the measurement of the individual elastic constants cannot be possible. Instead, the polycrystalline bulk modulus (B) and shear modulus (G) may be determined experimentally. The Voigt and Reuss (Nye, 1985) schemes were used to compute the isotropic elastic properties of soddyite polycrystalline aggregates. As shown by Hill (1952), the Reuss and Voigt approximations result in lower and upper limits, respectively, of polycrystalline constants and practical estimates of the polycrystalline bulk and shear moduli in the Hill approximation can be computed using average formulas. Relevant formulae for these approximations may be found in Section 3.2.9. The bulk and shear moduli and other mechanical properties computed in these approximations are given in Table 6.3.

Table 6.3. Bulk, modulus, shear modulus, Young modulus, Poisson ratio, Pugh's ratio, and Vickers hardness (B, G, E, ν, D, and H) calculated in the Voigt, Reuss, and Hill approximations. Values of B, G and E are given in GPa.

Property	Voigt	Reuss	Hill
B	64.4615	58.4136	61.4375
G	38.8807	36.0015	37.4411
E	97.1164	89.5976	93.3586
ν	0.2489	0.2444	0.2467
D	1.6579	1.6225	1.6409
H	6.4217	6.2374	6.3280

The numerical estimate of the error in the computed bulk modulus given by the CASTEP code is 2.312 GPa, quite similar to the difference of the values in the Hill and Voigt/Reuss schemes, 3.024 GPa. Voigt and Reuss methods yield quite small differences for soddyite. Larger differences are expected for crystalline systems with strong anisotropy, featuring large differences between elastic constants along different directions (Weck *et al.*, 2015). The values of the bulk modulus computed by Weck *et al.* (2015) for studtite and metastudtite (about 30 and 42 GPa, respectively) are smaller than the value obtained here for soddyite.

In general, a large value of shear moduli is an indication of the more pronounced directional bonding between atoms. Shear modulus G represents the resistance to plastic deformation while the bulk modulus represents the resistance to fracture (Ravindran *et al.*, 1998; Bouhadda *et al.*, 2012). Young modulus defines the relationship between stress (force per unit area) and strain (proportional deformation) in a material, that is, $E = \sigma/\varepsilon$. The individual components of the bulk and Young's moduli were obtained from the elastic compliance matrix components as explained in Section 3.2.9. The corresponding values are given in Table 6.4. As can be seen, B_c is larger than either B_a or B_b. Also, component E_c is larger than E_a or E_b. Thus, the c direction, perpendicular to the plane containing the chains, is the least compressible and stiffest one, in agreement with the results of the components of the elastic C matrix.

Table 6.4. Bulk and Young moduli components along the crystallographic axes. All values are given in GPa.

Property	*a* axis	*b* axis	*c* axis
B	105.10	251.92	275.08
E	70.68	95.09	140.12

Pugh and Poisson (Pugh, 1954) ratios were also determined to measure the ductility and malleability of soddyite (see Section 3.2.9). As it can be seen in Table 6.3, for soddyite we find ratios D and ν about 1.65 and 0.25, respectively. These values are only slightly smaller than 1.75 and 1/3, respectively, corresponding to a *brittle material*. For comparison, both studtite and metastudtite were found to be ductile (Weck *et al*, 2015).

The hardness of soddyite was also computed according to an empirical scheme of Niu *et al.* (2011) that correlates the Vickers hardness and Pugh ratio. The Vickers hardness, H, of polycrystalline soddyite is given in Table 6.3. Its value, about 6.3, corresponds to material of *intermediate hardness*. For comparison, we can compute the hardness of studtite and metastudtite using the elasticity data of Weck *et al.* (2015). These systems, characterized by much larger D ratios, have a much smaller hardness (smaller than 1).

In order to assess the elastic anisotropy of soddyite, shear anisotropic factors were obtained. These factors provide a measure of the degree of anisotropy in the bonding between atoms in different planes and are very important to study material durability. Shear anisotropic factors for the $\{100\}$ (A_1), $\{010\}$ (A_2), and $\{001\}$ (A_3) crystallographic planes and percentages of anisotropy in compression and shear (A_{comp} and A_{shear}) were computed using the formulae given by Ravindran *et al.* (1998). For an isotropic crystal, the factors A_1, A_2, and A_3 must be one, while any value smaller or greater than unity is a measure of the degree of elastic anisotropy possessed by the crystal. For percentage anisotropies, a value of 0% represents a perfectly isotropic crystal. For soddyite (see Table 6.5), the anisotropies grow in the planes $\{100\}$, $\{001\}$, and $\{010\}$ ($A_1 < A_3 < A_2$). The $\{010\}$ plane is shown to be the most anisotropic one. Percentage anisotropies in compression and shear are about 5 and 4 %, respectively.

In the recently introduced universal anisotropy index (Ranganathan and Ostoja-Starzewski, 2008), the departure of A^U from zero defines the extent of single crystal anisotropy and accounts for both the shear and the bulk contributions unlike all other existing anisotropy measures. Thus, A^U represents a universal measure to quantify the single crystal elastic anisotropy. Soddyite is

characterized by an anisotropy index is 0.50, which is a rather small value ($A^U = 0$ corresponds to a perfectly isotropic crystal). For comparison, studtite and metastudtite exhibit much larger anisotropies. The values computed by Weck *et al.* (2015) are 2.17 and 1.44, respectively.

Table 6.5. Shear anisotropy factors (A_1, A_2 and A_3), percentages of anisotropy in compression and shear (A_{comp} and A_{shear}), and universal anisotropy index (A^U).

A_1	A_2	A_3	A_{comp} (%)	A_{shear} (%)	A^U
0.8282	0.5674	1.2836	4.9220	3.8449	0.5034

A set of fundamental physical properties may be estimated using the calculated elastic constants. For example, V_L and V_T, the transverse and longitudinal elastic wave velocities of the polycrystalline materials may be determined in terms of the bulk and shear moduli (Weck *et al.*, 2015). The values obtained are 2.708 and 4.671 km/s, respectively, using the calculated crystal density of 5.104 g/cc (see Table 1).

6.3.3 Equation of State

Lattice volumes around equilibrium were calculated by optimizing the structure at 17 different applied pressures. The results are displayed in Figure 6.3.

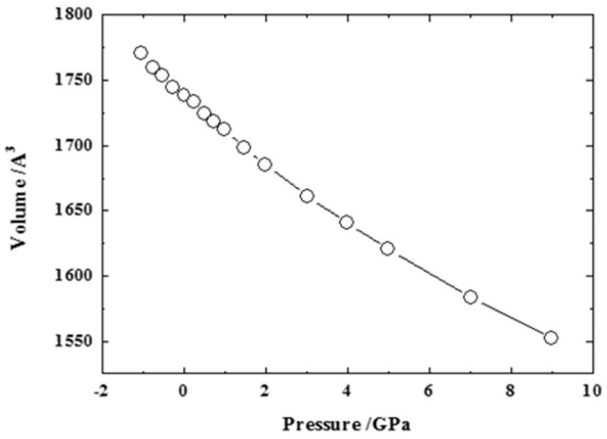

Figure 6.3. Soddyite unit cell volume vs. applied pressure.

The calculated data were then fitted to a fourth-order Birch-Murnaghan equation of state (EOS, see equation (3.150)) using the computed volume at 0 GPa (1738.6 Å^3) as V_0 using the EOSFIT 5.2 code (Angel, 2001). The values found for the bulk modulus and its first and second derivatives at the temperature of 0 K, were $B = 60.07\ (\pm 0.67)$ GPa, $B' = 4.19\ (\pm 0.60)'$ and $B'' = 0.25\ (\pm 0.20)$ GPa^{-1} ($\chi 2 = 0.001$). The bulk modulus found agrees very well with those determined from calculated elastic constants given in Table 6.3. As in other works (Ulian *et al.*, 2014), the agreement is better with the bulk modulus obtained in the Reuss approximation ($B = 58.41 \pm 2.31$ GPa). This is due to the fact that values of B obtained from the EOS are generally smaller than those obtained from elastic tensor because relaxations of cell shapes are also performed while the cell shapes are fixed in the determinations of elastic constants (Shang *et al.*, 2007).

6.3.4 Raman Spectra and Band Assignment

The theoretical Raman spectrum in the wavenumber range of 3600-0 cm^{-1} is compared with the one obtained experimentally in Fig. 6.4. As can be seen in this figure, the calculated spectrum is quite similar to the experimental one. The theoretical spectrum was computed at T=298 K, λ=532 nm, FWHM=20 cm^{-1}. Pictures of the atomic motions in the Raman active vibrational modes are given in Appendix 6.A. (Figure 6.A.1).

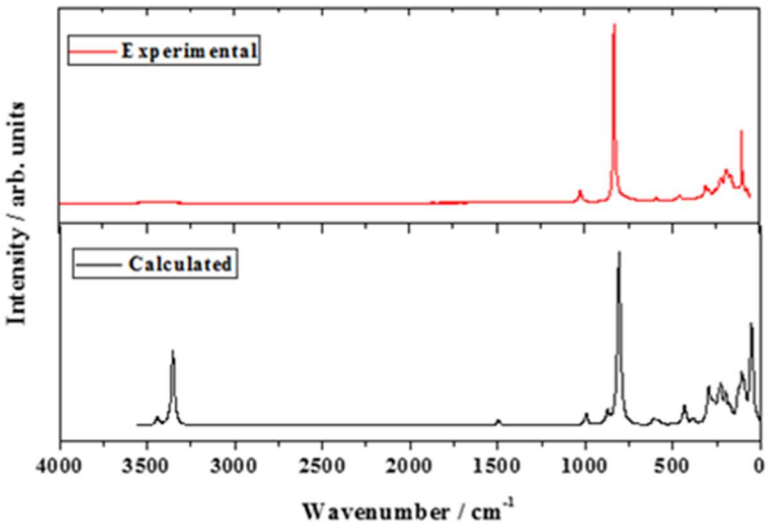

Figure 6.4. Experimental and calculated Raman spectra of soddyite mineral.

In order to calculate the number of contributions of a given band in the experimental spectrum we carry out the analysis by the second derivative method (del Corro Garcia, 2011; Bonales *et al.*, 2016a). In Fig. 6.5, we show the experimental and theoretical Raman spectra divided in four regions: (A) OH stretching vibration region from 3800 to 3000 cm^{-1} (Fig. 6.5.A); (B) H_2O bending region 1800-1300 cm^{-1} (Fig. 6.5.B); (C) uranyl UO_2^{2+} and silicate SiO_4^{4-} fundamental vibrations region from 1400 to 700 cm^{-1} (Fig. 6.5.C); and (D) low wavenumber region from 700 to 0 cm^{-1} (Fig. 6.5.D). The wavenumber of both spectra along with the corresponding calculated intensities and assignments are given in Table 6.6. The Raman shifts and assignments performed by Frost *et al.* (2006b) are also given in this table with the aim of comparison. The results obtained in each region will now be discussed.

(A) *OH stretching vibrations region*

In the hydroxyl stretching region we found one broad band with two contributions at about 3488 cm^{-1} and 3398 cm^{-1}. The corresponding computed Raman shifts are 3443 and 3353 cm^{-1}. These bands are assigned to antisymmetric and symmetric water stretching vibrations, ν^a(OH) and ν^s(OH), respectively. Although the difference of computed and experimental shifts is quite large, it must be noted that the infrared OH stretching frequencies calculated for uranyl silicate clusters have much larger differences with respect to experiment (Wheaton *et al.*, 2003). Note that the low intensity contribution band at wavenumber 3147 cm^{-1} is not found in the calculated spectrum. This band is also found by Frost *et al.* (2006b) at 3158 cm^{-1}.

(B) *H_2O bending vibration region*

The Raman shift associated to the water bending vibration, δ(H_2O), was found to be placed at about 1584 cm^{-1} comparable to the calculated shift at 1495 cm^{-1}. Note that Frost *et al.* (2006b) found a shoulder at 1596 cm^{-1}. This was attributed to water absorbed on the sample surface (Moll *et al.*, 1995).

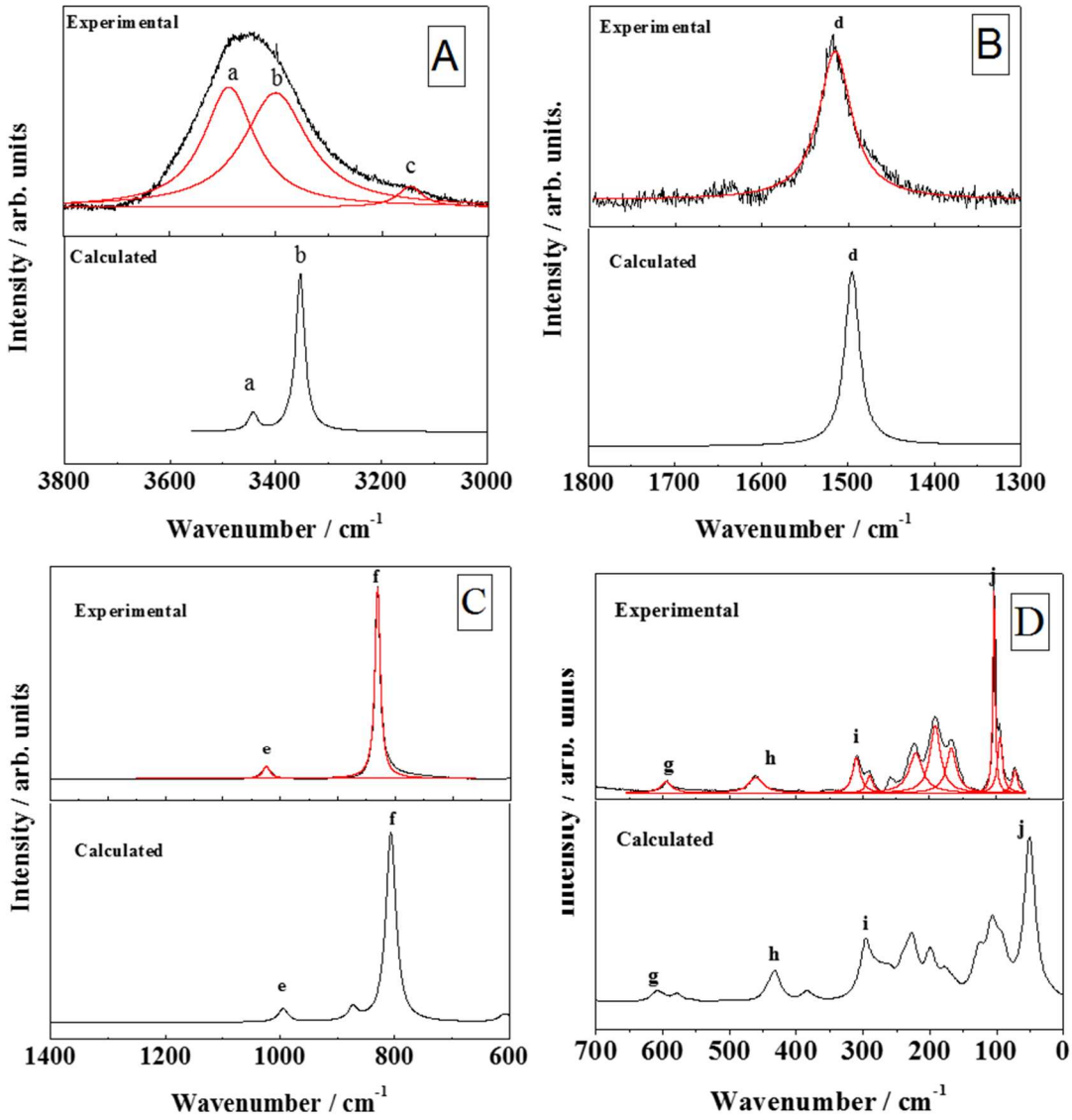

Figure 6.5. Experimental and theoretical Raman spectra of soddyite mineral. (A) Region: 3800-3000 cm^{-1}; (B) Region: 1800-1300 cm^{-1}; (C) Region: 1400-700 cm^{-1}; (D) Region: 700-0 cm^{-1}.

(C) *Uranyl UO_2^{2+} and silicate SiO_4^{4-} fundamental vibrations region*

The experimental band at 1024 cm^{-1}, corresponds to the band calculated at 995 cm^{-1} which is assigned to SiO_4^{4-} asymmetric stretching vibration, $\nu^a(SiO_4)^{4-}$ (see vibrational mode picture in Appendix 6.A). Similar wavenumbers were found by Frost *et al.* (2006b) and Biwer *et al.* (1990) (1025 and 1018 cm^{-1}, respectively).

The most intense band in the Raman spectrum is found experimentally at about 830 cm^{-1}, and calculated at 807 cm^{-1}. This band was found to be placed at 824, 830, and 828 cm^{-1} by Biwer *et al.* (1990), Amme *et al.* (2002) and Frost *et al.* (2006b). As it can be observed in the vibrational mode picture in Appendix 6.A, it is assigned to UO_2^{2+} symmetric stretching vibration, $\nu^s(UO_2)^{2+}$.

It should be noted that in the computed spectrum appear two very close bands at 874 and 873 cm^{-1}. Frost *et al.* (2006b) also found two bands in this region at 909 and 897 cm^{-1} whose were attributed to the $\nu^a(UO_2)^{2+}$. Based in our computed results we think that the band at 909 cm^{-1} correspond to the calculated vibration at 873 cm-1 which is attributed to the symmetric stretching SiO_4^{4-} vibration. Additionally, Frost *et al.* (2006b) found a band at 791 cm^{-1} and assigned it to

water librational vibrations. This band is close to the computed one at 799 cm^{-1}, assigned to $\nu^{s}(UO_2)^{2+}$.

(D) *Low wavenumber region*

The bands computed at 610 and 579 cm^{-1} are comparable to the experimental value of 592 cm^{-1} and assigned to water librational vibrations (twisting and rocking, respectively). In the experimental work of Frost *et al.* (2006b), the 591 cm^{-1} band is assigned to a silicate bending vibration, $\delta(SiO_4)^{4-}$. This kind of vibration appear in the theoretical spectrum at 431 cm^{-1} which is comparable to the experimental band at 460 cm^{-1}. The corresponding values found by Biwer *et al.* (1990), Amme *et al.* (2002) and Frost *et al.* (2006b), are 457, 455 and 459 cm^{-1}, respectively. While Biwer *et al.* (1990), attribute this band to an equatorial UO stretching vibration, Frost *et al.* (2006b), assign this band to $\delta(SiO_4)^{4-}$ in agreement with the data shown in this work. The free ion value for this vibration is 527 cm^{-1} (Nakamoto, 1986; Cejka, 1999).

The bands calculated at 299, 296 and 295 cm^{-1} are assigned mainly to a silicate translation the first, and the others to different silicate deformation vibrations, $t(SiO_4)^{4-}$ and $\rho(SiO_4)^{4-}$ (twisting and rocking). They are comparable to the experimental band at about 289 cm^{-1}.

Finally, the band calculated at 50 cm^{-1} can be approximately mapped to the experimental shift of 103 cm^{-1}.

Table 6.6. Experimental and calculated Raman band wavenumbers, calculated intensities and assignations. Raman shifts and assignments performed by Frost *et al.* (2006b) are also given in this table with the aim of comparison.

Band Name	Exp. Raman shift (cm^{-1}) (This work)	Exp. Raman shift (cm^{-1}) (Frost *et al.*, 2006b) shift/assignation	Calc. Raman shift (cm^{-1})	Irr. Rep. (D_{2h})	Int. (Å^4)	Assignation
OH stretching region						
a	3488	3516/ν(OH)	3443	B_{2g}	3229.1	$\nu^{a}(OH)$
b	3398	3414/ν(OH)	3353	A_g	27818.8	$\nu^{s}(OH)$
c	3147	3158/ν(OH)	-	-	-	-
H_2O bending region						
d	1584	1584,1596/$\delta(H_2O)$	1495	A_g	433.8	$\delta(H_2O)$
UO_2^{2+} and SiO_4^{4-} fundamental vibrations region						
e	1024	1025/$\nu^{a}(SiO_4)^{4-}$	995	B_{1g}	750.1	$\nu^{a}(SiO_4)^{4-}$
	-	909,897/$\nu^{a}(UO_2)^{2+}$	874	B_{2g}	53.5	$\nu^{a}(UO_2)^{2+}$+$\rho(H_2O)$
			873	A_g	583.7	$\nu^{s}(SiO_4)^{4-}$
f	830	838,828,820/$\nu^{s}(UO_2)^{2+}$	807	A_g	8054.0	$\nu^{s}(UO_2)^{2+}$
	-	791/l(H_2O)	799	B_{1g}	387.3	$\nu^{s}(UO_2)^{2+}$
Low wavenumber region						
g	592	591/$\delta(SiO_4)^{4-}$	610	A_g	168.6	$t(H_2O)$
			579	B_{2g}	138.4	$\rho(H_2O)$
h	460	459/$\delta(SiO_4)^{4-}$	431	A_g	323.3	$\delta(SiO_4)^{4-}$
i	289	310	299	B_{1g}	54.8	$T(SiO_4)^{4-}$
			296	A_g	39.6	$t(SiO_4)^{4}$
			295	B_{3g}	308.3	$\rho(SiO_4)^{4-}$
j	103	111,102	50	B_{2g}	54.5	$\delta^{op}(U\text{-}OH_2)$

APPENDIX 6.A. Raman Active Normal Modes of Soddyite.

Figure 6.A.1 The atomic motions associated to some Raman active vibrational normal modes of soddyite.

Mode ν=3442 cm^{-1} – ν(OH) – Antisymmetric OH stretching.

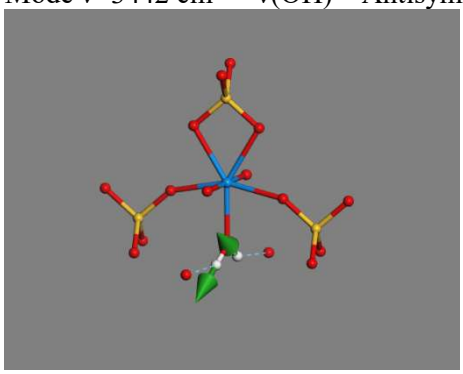

Mode ν=3353 cm^{-1} – ν(OH) - Symmetric OH stretching.

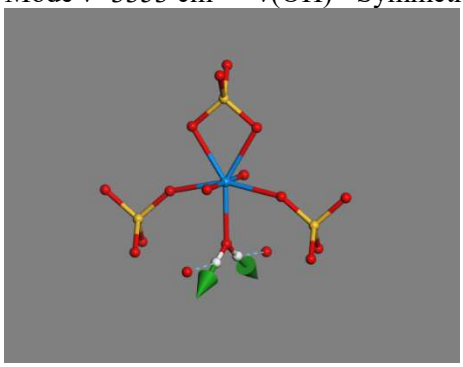

Mode ν=1495 cm^{-1} – δ(H_2O) – H_2O bending.

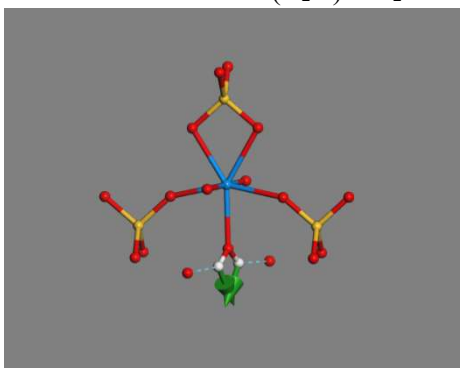

Mode ν=995 cm^{-1} – $\nu^{a}(SiO_4)^{4-}$ – Asymmetric $(SiO_4)^{4-}$ stretching.

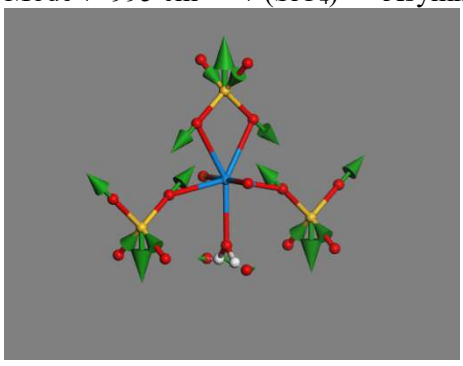

Mode ν=874 cm^{-1} – $\nu^{a}(UO_2)^{2+}+\rho(H_2O)$ – Asymmetric $(UO_2)^{2+}$ stretching plus H_2O rocking vibration.

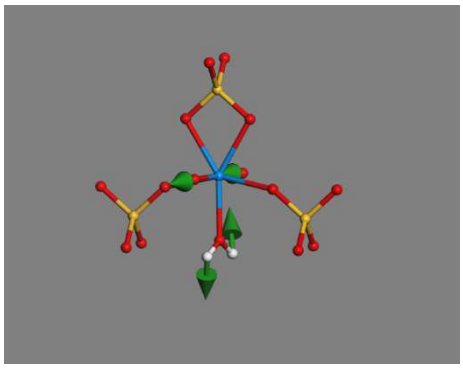

Mode ν=873 cm^{-1} – $\nu^{s}(SiO_4)^{4-}$ – Symmetric $(SiO_4)^{4-}$ stretching.

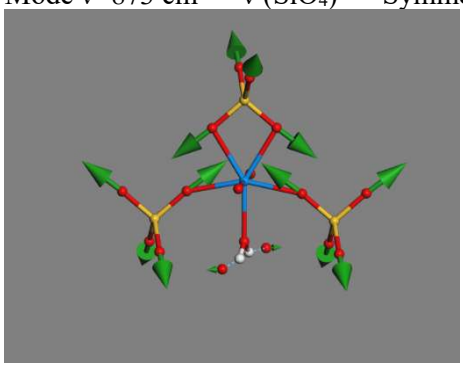

Mode ν=807 cm^{-1} – $\nu^{s}(UO_2)^{2+}$– Symmetric $(UO_2)^{2+}$ stretching.

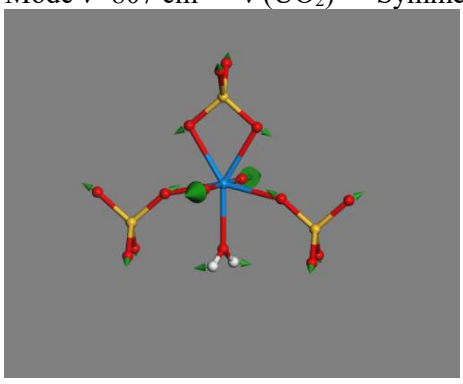

Mode ν=799 cm^{-1} – $\nu^{s}(UO_2)^{2+}$ – Symmetric $(UO_2)^{2+}$ stretching.

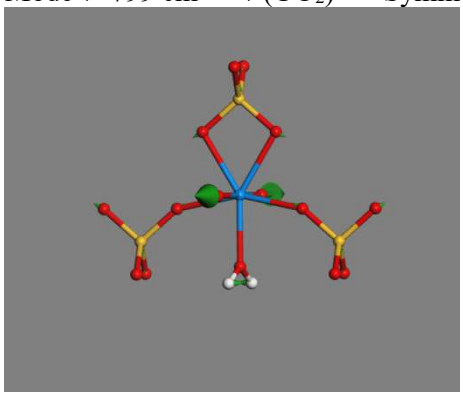

Mode ν=610 cm^{-1} – t(H_2O) – H_2O twisting.

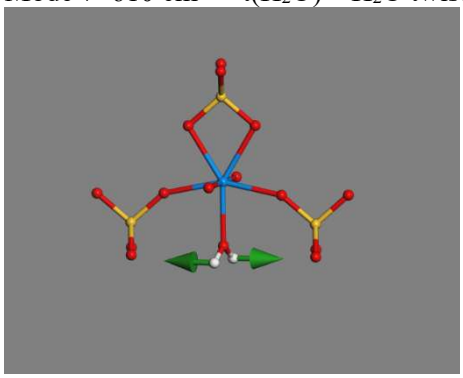

Mode ν=579 cm^{-1} – ρ(H_2O) – H_2O rocking.

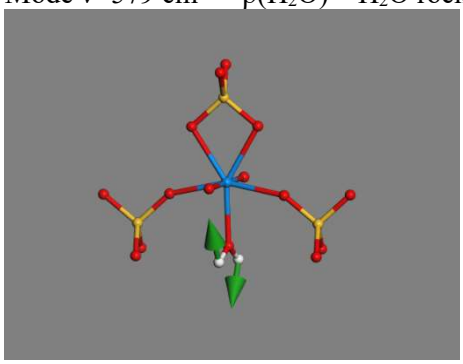

Mode ν=431 cm^{-1} – δ$(SiO_4)^{4-}$ – Silicate $(SiO_4)^{4-}$ symmetric bending.

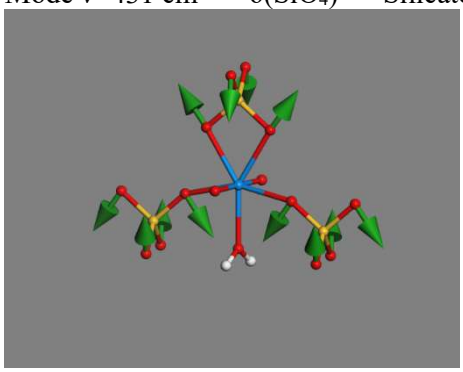

Chapter 7. Studtite: Structure, Raman Spectroscopy and Thermal Stability

This chapter is based on the published article *"Study of the thermal stability of studtite by in situ Raman spectroscopy and DFT calculations"*, by F. Colmenero, L. J. Bonales, J. Cobos and V. Timón, Spectrochim. Acta A 174, 245–253 (2017).

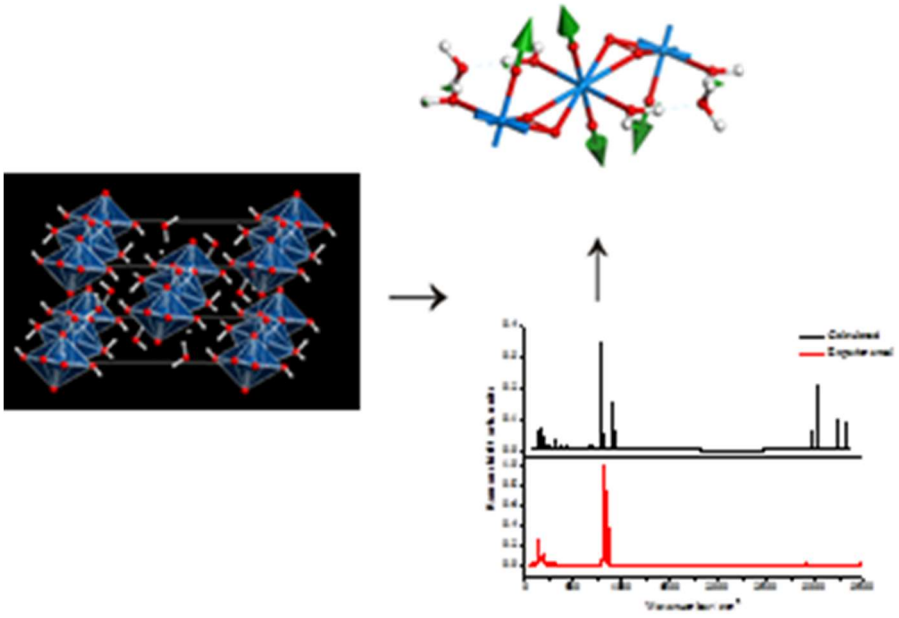

Abstract

The design of a safe spent nuclear fuel repository requires the knowledge of the stability of the secondary phases which precipitate when water reaches the fuel surface. Studtite is recognized as one of the secondary phases that play a key-role in the mobilization of the radionuclides contained in the spent fuel. Thereby, it has been identified as a product formed under oxidation conditions at the surface of the fuel, and recently found as a corrosion product in the Fukushima-Daiichi nuclear plant accident. Thermal stability is one of the properties that should be determined due to the high temperature of the fuel.

In this work, we report a detailed analysis of the structure and thermal stability of studtite. The structure has been studied both by experimental techniques (SEM, TGA, XRD and Raman spectroscopy) and theoretical DFT electronic structure and spectroscopic calculations. The comparison of the results allows us to perform for the first time the Raman bands assignment of the whole spectrum. The thermal stability of studtite has been analyzed by in situ Raman spectroscopy, with the aim of studying the effect of the heating rate and the presence of water. For this purpose, a new cell has been designed. The results show that studtite is stable under dry conditions only at temperatures below 30 ºC, in contrast with the higher temperatures published up to date (~ 130 ºC). Opposite behaviour has been found when studtite is in contact with water; under these conditions studtite is stable up to 90 ºC, what is consistent with the encounter of this phase after the Fukushima-Daiichi accident.

7.1 Introduction

Nuclear fuel, commonly composed of UO_2 pellets enriched from 0.7 to 3–5 % of ^{235}U (Choppin and Liljenzin, 1995), is obtained from natural minerals found in the rocks of the Earth´s crust. After its irradiation (one or more irradiation cycles) the fuel is considered as spent nuclear fuel (SNF) and must be managed as waste. The SNF is composed of a UO_2 matrix (> 95 %) and other radioactive elements. The latter are very hazardous, making the waste management difficult. Their hazard progressively decreases by natural processes (radioactive decay) leading, after several millions of years, to a total radioactivity that equals the radioactivity of natural uranium (Hedin, 1997). Therefore, it has been proposed that the most appropriate and natural way of managing this waste is to return it to the Earth's crust. For this aim, the generally agreed solution is the burial of the SNF in the so called deep geological disposal of radioactive wastes for a period, at least, as long as the radioactive decay time.

The design of a deep geological repository must avoid the reach of these radionuclides to the biosphere for such a long time, and the best recognized option for this purpose is the use of a multi-barrier system which, in general, involves containing the radioactive waste inside canisters, then a buffer that protects the canisters and, finally the whole system is surrounded by geological natural barriers. Despite the barriers, it is well-known that, at such a long time, water could be the vehicle that interacts with the barriers and could mobilize radionuclides. Therefore, the studies about the reaction between SNF and groundwater under the possible repository conditions are of great interest (SKB-91, 1992).

Although the groundwater conditions in a repository are generally reducing, in a layer near the fuel surface, i.e. within < 50 µm of the fuel surface, an oxidative environment has been postulated (Christensen and Sunder, 1996). This ambient is produced by the radiolysis of water due to the ionizing radiation associated with the fuel (Shoesmith, 2000; Sunder, 1998; Allen, 1961). The radiolysis of groundwater results in the production of oxidants as H_2O_2 among others (Wang and Katayama, 1982), which in contact with UO_2, leads to the formation of uranyl peroxides (Sattonnay *et al.*, 2001; Amme *et al.*, 2002; Clarens *et al.*, 2004; McNamara *et al.*, 2004, 2005; Hanson *et al.*, 2005). Studtite: $(UO_2)(O_2)\cdot 4H_2O$, and its dehydration product metastudtite:

$(UO_2)(O_2)\cdot 2H_2O$, are the only known uranyl peroxides (Kubatko *et al.*, 2003; Kubatko, 2005; Burns and Hughes, 2003) and both were found as corrosion products of SNF (McNamara *et al.*, 2004, 2005; Hanson *et al.*, 2005) in two-year experiments with deionized water.

From this foundings, different essays have been performed highlighting that studtite plays an important role in the SNF corrosion process. For example, Amme (2002) showed the precipitation of studtite by direct leaching of UO_2 with H_2O_2, and Kubatko *et al.* (2003) showed that studtite may be formed even at very low peroxide concentrations ($1.1\cdot 10^{-14}$ M H_2O_2), created by the alpha flux of natural uranium ores. Forbes *et al.* (2011) found that studtite could be the alteration product of other uranyl hydrates as schoepite and soddyite, recognized as the fundamental secondary phases of SNF. Furthermore, studtite has been recently proposed as a corrosion product in sea water after the Fukushima-Daiichi nuclear plant accident (Armstrong *et al.*, 2012; Burns *et al.*, 2012; Giménez *et al.*, 2014). Despite the importance of this uranyl mineral, there is still some doubt concerning its formation process and crystal structure (Burns and Hughes, 2003).

The structures of uranyl peroxide hydrates have been investigated by means of theoretical methods in several previous works. The first study was that of Ostanin and Zeller (2007a) in which the structures of studtite and metastudtite were determined by means of density functional theory (DFT) methods using ultrasoft pseudopotentials. Studtite and the incorporation of neptunium into its structure were later investigated by Shuller (2010b) using the same kind of techniques and pseudopotentials. These calculations were refined by Weck *et al.* (2012, 2015) by using DFT techniques and the projector augmented wave (PAW) method to describe the interaction between valence electrons and ionic cores. These authors also researched the mechanical stablility of uranyl peroxide hydrates. Walshe *et al.* (2014) have studied the local electronic structure of the hydrated uranium peroxides by means of ab initio quantum chemical calculations based on the real space Green function calculations. Studies of atomic clusters closely related to these systems have been reported by Odoh *et al.* (2013, 2016).

In this work, we study the structure of synthetic studtite by both experimental techniques (SEM, TGA, XRD and Raman spectroscopy) and computational density functional theory calculations. The DFT results were obtained by using a norm-conserving relativistic pseudopotential for uranium atom reported and validated for this kind of materials in a previous work (Bonales *et al.*, 2016a). As far as we know, there is not any published theoretical study on the vibrational spectra of these materials. Comparison of the experimental and computed Raman spectra allows us to assign the different Raman bands that form the whole spectra. The thermal stability of studtite has been analyzed at different conditions by in situ Raman spectroscopy. Specifically, we have studied the effect of the heating rate and the presence of liquid water on the studtite irreversible dehydration of studtite.

7.2 Materials and Methods

7.2.1 Experimental

Synthetic studtite, $(UO_2)(O_2)\cdot 4H_2O$, was precipitated at room temperature by adding dropwise a solution of 1M H_2O_2 (Sigma-Aldrich) over a solution of 10-4 M uranyl nitrate hexahydrate $UO_2(NO_3)_2.6H_2O$ (Sigma-Aldrich). This reaction yields yellow crystals, which were rinsed with cold water and dried before experiments. The precipitate was characterized by thermogravimetry (TG), scanning electron microscopy (SEM), X-ray diffraction (XRD) and Raman spectroscopy (RS).

A Q50 thermo-balance (TA Instruments, Spain) was used in synthetic air for the TG analysis. Texture of the sample was analyzed with a Jeol 5600-LV scanning electron microscope (SEM) equipped with an Oxford Industries INCA X-sight energy dispersive X-ray spectrometer. XRD was conducted using a Philips PANalytical X'Pert MPD diffractometer using Cu K_{α_1} radiation (λ=1.54056 Å) and operating at 45 kV and 40 mA. A Bragg–Brentano configuration geometry

was used. The 2θ range covered was from 20° to 120°, with a scanning step of 0.02° and an overall exposure time of 18 hours. Horiba LabRam HR evolution spectrometer (Jobin Yvon Technology) was used in order to acquire the Raman spectra. A red laser of HeNe with a wavelength of 632.81 nm and a nominal power of 20 mW was used as excitation source. The grating used has 600 grooves/mm leading to a resolution better than 1 cm-1/pixel. The details of this equipment are described elsewhere (Bonales *et al.*, 2015).

In situ Raman characterization of the dehydration of studtite was carried out by using a Linkam temperature controlled pressure stage, THMS-600, coupled with the BX4 Olympus microscope of the Raman spectrometer. The mechanical design and electronics of the Linkam stage provided precise control and temperature stability better than 0.2 K. Spectra were collected with a 50× long-range objective through a silica window (used in place of the standard quartz optical window) on the top of the stage.

A very simple home cell had been specifically used to perform the *in situ* Raman measurements of studtite in contact with liquid water. This cell was mainly composed by two borosilicate glass cover slides separated by an O-ring. Therefore, the sample with water was housed between the two cover slides, separated by the O-ring. A detailled description of this cell and its set up can be found in Section 3.1.1.1.

7.2.2 Theoretical DFT Calculations

Studtite models of unit cells have been calculated using the CASTEP code (Clark *et al.*, 2005), a module of the Materials Studio package (Materials Studio, 2017). The generalized gradient approximation (GGA) together with PBE functional (Perdew *et al.*, 1996) was used. Grimme empirical dispersion correction, the DFT-D2 approach (Grimme, 2006) was used in order to describe properly the hydrogen bonding present in the system studied in this work. Geometry optimization was carried out using the Broyden–Fletcher–Goldfarb–Shanno optimization scheme (Pfrommer *et al.*, 1997; Payne *et al.*, 1992) with a convergence threshold on atomic forces of 0.01 eV/Å. The different kinetic energy cutoffs and k-point meshes (Monkhorst and Pack, 1976), must be adopted to ensure good convergence for computed structures and energies. Studtite structure was optimized in calculations with increasing complexity by increasing these parameters. The optimization performed with a cutoff of 1000 eV and a K mesh of 2×4×4 (8 K points) gave a well converged structure and was used to determine the final results.

For the calculations of vibrational properties, the linear response density functional perturbation theory (DFPT) (Baroni *et al.*, 2001; Gonze *et al.*, 1997; Refson *et al.*, 2006) implemented in the CASTEP code was used, where the phonon frequencies at the gamma point of the Brillouin zone were computed using atomic displacement perturbations. Raman intensities are third-order derivatives of total energy with respect to vibrational mode (atomic position) and laser field (electric field, twice). These are calculated in CASTEP (Milman *et al.*, 2010) by using a combination of perturbation theory (second derivative with respect to field) and finite differences (third derivative with respect to atomic displacement). The frequencies presented in this work have not been scaled to correct for anharmonicity and remaining errors of the theoretical treatment employed, such as incomplete treatment of electron correlation and basis set truncation (Hehre *et al.*, 1986). They correspond to the harmonic approximation of the force field. Since the effects of these defects tend to cancel out, the scale factor should be near to unity.

The pseudopotential for uranium atom used is a scalar relativistic GGA-PBE Troullier-Martins (Troullier and Martins, 1991) type norm-conserving pseudopotential. Its generation was described in a previous work (Bonales *et al.*, 2016a).

7.3 Results and Discusion

7.3.1 Experimental Characterization

The synthesized studtite was analyzed by different techniques: scanning electron microscopy (SEM), TGA, X-Ray diffraction (XRD) and Raman spectroscopy (RS). Results are shown in Figure 7.1.

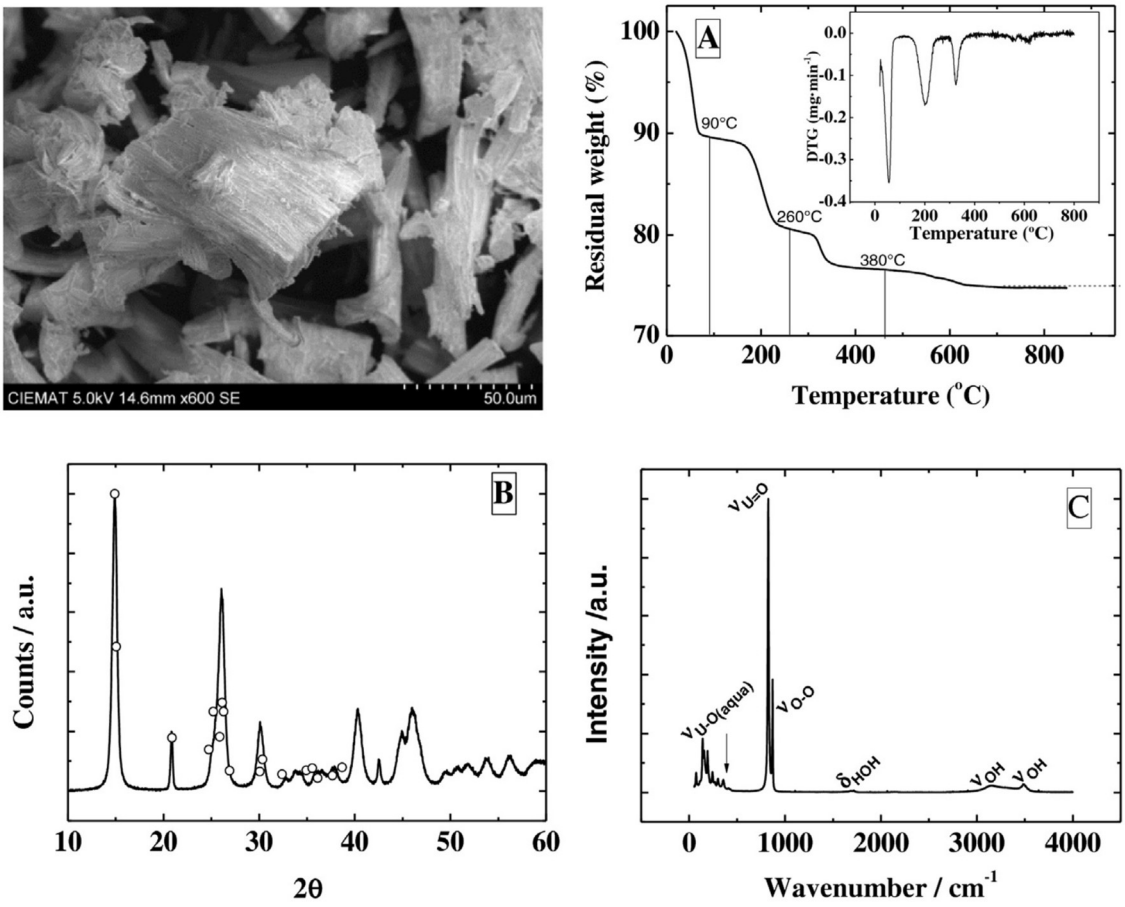

Figure 7.1. Synthetic studtite characterization: SEMimage of the precipitated crystals, and graphics corresponding to: (A) TGA curve and DTG (thermogravimetric derivative curve), (B) X-ray powder diffraction pattern and (C) Raman spectrum.

SEM micrographs reveal the high crystallinity of the rod-shaped sample, as the general morphology of studtite.

The curve shown in Fig. 7.1.A was obtained by placing a few milligrams (~ 8 mg) of the sample in the platinum TGA balance, and increasing the temperature up to 850 oC at a rate of 5 ºC/min, in a synthetic air flow of 60 mL/min. The TGA results, (see the DTG curve in the inset of Fig. 7.1.A) show a reasonable agreement with the literature data (Rey *et al.*, 2009a), i.e. the initial studtite loses two molecules of water from 22 to 90 ºC (Eq. 7.1). Between 90 and 260 ºC the decrease in weight can be associated with a loss of one oxygen and two molecules of water forming UO_3 (Eq. 7.2), which is not stable and forms U_3O_8 (Eq. 7.3) at temperatures higher than 570 ºC.

$$UO_2(O_2)\cdot 4H_2O \rightarrow UO_2(O_2)\cdot 4H_2O \quad (-2H_2O;\ 22-90ºC) \tag{7.1}$$

$$UO_2(O_2)\cdot 2H_2O \rightarrow UO_3 \quad (-O;\ 90-260ºC) \tag{7.2}$$

$$UO_3 \rightarrow U_3O_8 \tag{7.3}$$

The XRD pattern showed in Fig. 7.1.B can be identified as that of studtite (Debets, 1963; Walenta, 1974), $(UO_2)(O_2)\cdot 4H_2O$, in agreement with the data published by the International Center of Diffraction Data (ICDD, 2003). Open symbols in Fig. 7.1.B correspond to the ICDD 98-016-7992 studtite pattern.

The Raman spectrum of the sample, shown in Fig. 7.1.C, corresponds to the typical spectrum of studtite in agreement with the published ones (Walshe *et al*., 2014; Bastians *et al.*, 2004; Labs, 2015). The only band assignment so far, was performed by Bastians *et al.* (2004) and therefore, in the following discussion we have used the band assignment given in this reference. Four regions can be distinguished in the spectrum. From 3000 to 3600 cm^{-1} two broad bands are assigned to the OH stretching vibrations of water. Around 1600 cm^{-1} the two small bands are assigned to the water bending vibrations. The strongest bands appear in the intermediate region, from 700 to 900 cm^{-1}. The one at 819 cm^{-1} corresponds to the symmetric uranyl stretch, $\nu^s(UO_2^{2+})$, and the one at 865 cm^{-1} to the peroxo stretch, ν(OO), of the bridging peroxo ligands. The band at about 348 cm^{-1} was assigned to a symmetric stretching, $\nu^s(UO_{aqua})$.

In Figure 7.2 the experimental analysis of the spectrum is presented. The fit, shown in this figure (dashed line), was obtained as follows: first, determining the number of contributions of a given band from the experimental spectrum by the second derivate method; and second, performing a Lorentzian fit. Results are summarized in Table 1 of the printed article (Colmenero *et al*., 2017b), in which they are compared with some published data of this mineral phase (Bastians *et al.*, 2004). As can be seen in this table, the data obtained are in good agreement with those previously published, except for the bands at 433, 815 and 840 cm^{-1}. It should be noted that these bands could be due to the presence of impurities, since the bands at 433 and 815 cm^{-1} appear only in the spectrum of the synthetic sample, and they are not present in the natural one. Besides, these bands are very weak. The band at 840 cm^{-1} can be related to metastudtite, and therefore it is probably associated to the partial dehydration of studtite by natural processes or due to heating of the Raman excitation laser.

7.3.2 DFT Calculations

7.3.2.1 Structure

The optimized studtite structure is displayed in Fig. 7.3. As can be observed, uranium atom displays hexagonal bipyramid coordination. Two oxygen atoms are in apical positions and the six equatorial oxygen atoms are two peroxo groups (four oxygen atoms) forming opposite edges of the hexagon and two water molecule oxygen atoms. The different bipyramids are linked by sharing the peroxo equatorial edges and form zig-zag chains. The studtite structure has two kinds of water molecules in the structure, one half being the structural ones and the other crystallization water molecules; thus, the structure is more correctly formulated as $[UO_2)(O_2)\cdot 2H_2O]\cdot 2H_2O$. The chains are held together by means of a network of hydrogen bonds between these water molecules. Each water molecule forming part of the uranyl polyhedra (structural water, also called terminal aqua groups) donates two hydrogen bonds with other water molecules which do form part of the bipyramids (crystallization water).

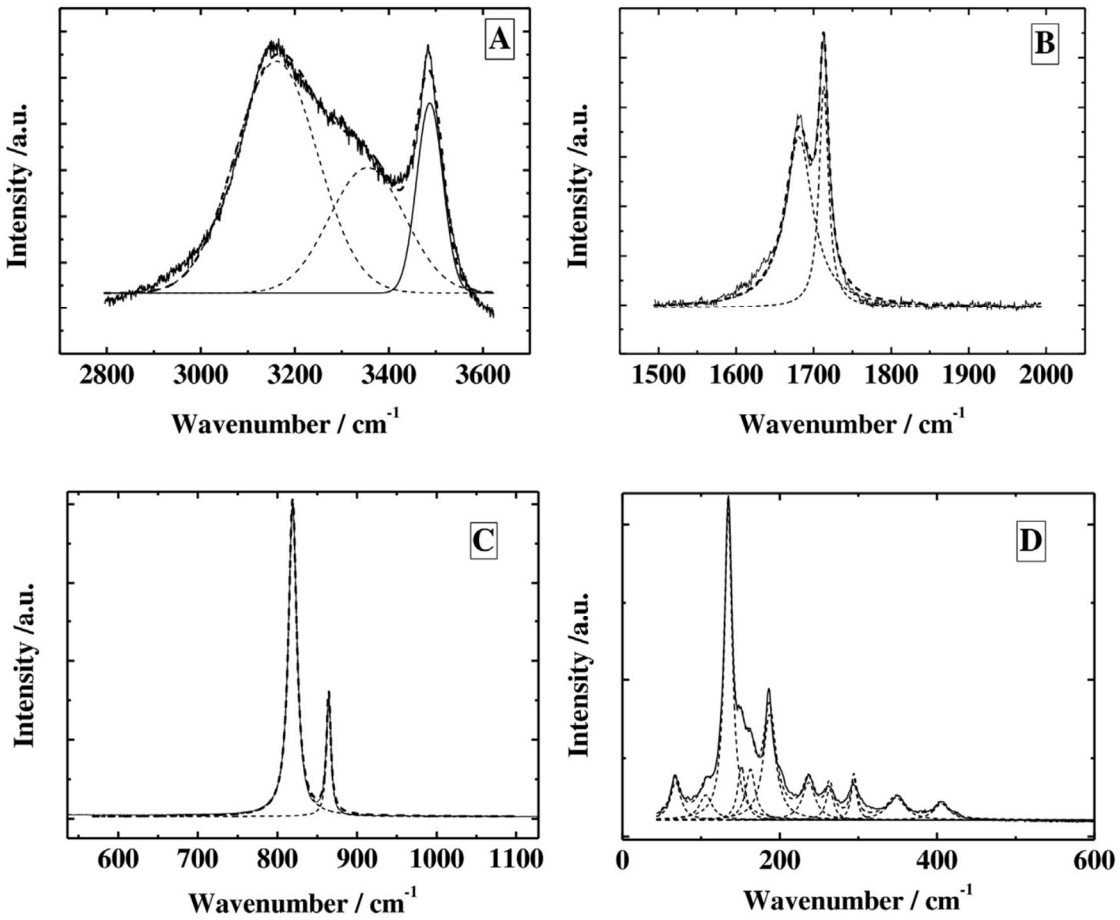

Figure 7.2. Experimental Raman spectra obtained for studtite at STP conditions: A) OH stretching region: 2800–3600 cm^{-1}, B) OH bending region: 1500–2000 cm^{-1}, C) Uranyl and peroxo stretching region: 600–1100 cm^{-1}, and D) low frequency region: 50–600 cm^{-1}.

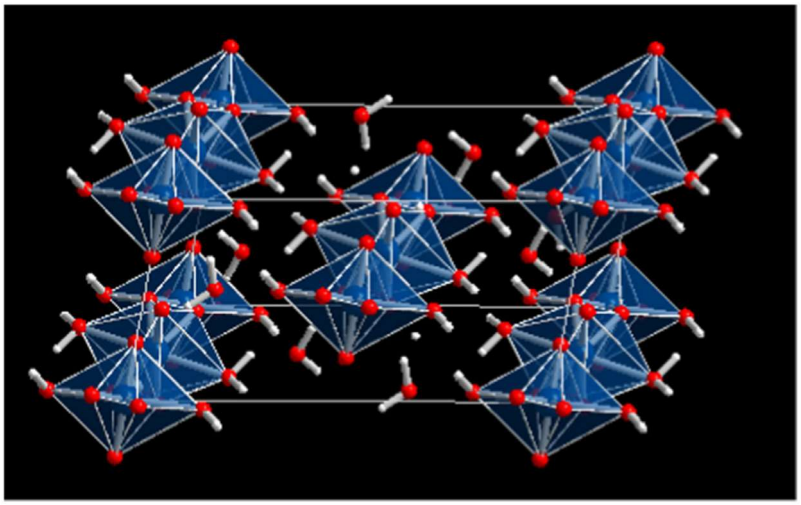

Figure 7.3. General view of the studtite structure (UO2)(O2)·4H2O: Color code: U-Blue, O-Red, H-Grey.

The X-ray pattern of studtite was computed from the calculated structure using program REFLEX, a module of Materials Studio Package (Materials Studio, 2017) and compared with an experimental one in Figure 7.4. As can be seen, the agreement in line positions and intensities is quite satisfactory.

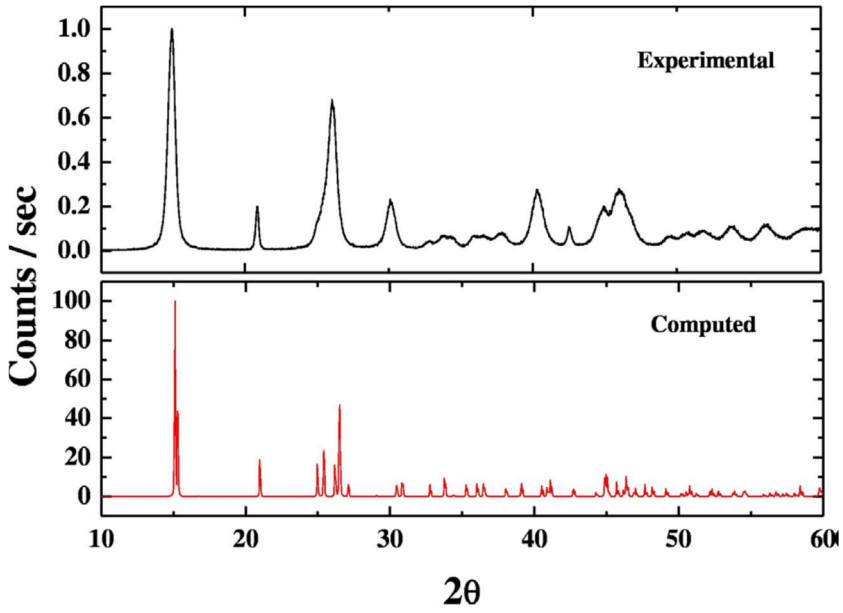

Figure 7.4. Comparison of experimental and computed XRD patterns.

Studtite optimized lattice parameters, volumes and densities compared with those obtained in previous theoretical studies (Ostanin and Zeller, 2007a; Shuller, 2010b; Weck *et al.*, 2012, 2015) and experimental results (Burns and Hughes, 2003) are shown in Table 7.1. As it can be seen, the agreement is excellent. The computed volume is larger than experimental value by only about 0.7 %. Overstimation of volume and bond distances (see Appendix B of the Supplementary Information of the article (Colmenero *et al.*, 2017b)) is a general trend in DFT calculations (Grinberg *et al.*, 2001; Kohn *et al*., 1998).

A more complete description and additional data about the calculated studtite structure and its X-ray powder spectra is given in Appendix 7.A.

Table 7.1. Studtite lattice parameters.

Parameters	a (Å)	b (Å)	c (Å)	α	β	γ	Vol. (Å^3)	Density (g/cm^3)
This work	13.813	6.804	8.496	90.0	122.951	90.0	669.98	3.708
DFT [a]	13.93	6.84	8.55	90.0	122.7	90.0	685.6	-
DFT [b]	13.96	6.88	8.53	90.0	122.55	90.0	689.9	-
Exp. [c]	14.068	6.721	8.428	90	123.356	90	665.6	3.733

[a] Weck *et al.* (2012); [b] Shuller (2010b): [c] Burns and Hughes (2003).

7.3.2.2 Raman Spectrum and Band Assignment

The Raman spectrum of studtite was calculated at T=298 K, λ=532 nm, FWHM=5 cm^{-1} and compared with the experimental one in Figure 7.5. The experimental and calculated wavenumbers, the calculated intensities and the assignments derived from the calculations are

shown in Table 7.2. The atomic motions associated to some vibrational normal mode are shown in the Appendix 7.B.

Table 7.2. Studtite experimental and calculated Raman shifts, calculated intensities and assignations.

Exp. Wavenumber (cm^{-1})	Calc. Wavenumber (cm^{-1})	Irr. Rep. (C_{2h})	Intensity ($Å^4$)	Assignation
(a)67.7 (0.3)	(a)101	Ag	2.39	$\rho(OUO_{aqua})+\rho(UO_2^{2+})+T(H_2O\text{-cr.})$
(b)106 (1)	(b)135	Ag	9.16	$\rho(OUO_{aqua})+\rho(UO_2^{2+})+T(H_2O\text{-cr.})$
(c)134.61 (0.04)	(c)154	Ag	43.42	$\rho(OUO_{aqua})+\rho(UO_2^{2+})+\rho(OUO_{perox})+T(H_2O\text{-cr.})$
(d)151.3 (0.4)	(d)163	Bg	29.06	$T(H_2O\text{-cr})$
(e)162.8 (0.6)	(e)179	Bg	10.48	$\rho(UO_2^{2+})$
(f)186.9 (0.2)	(f)185	Ag	34.17	$\rho(UO_2^{2+})+\rho(OUO_{aqua})+\rho(OUO_{perox})+T(H_2O\text{-cr.})$
(g) 236.8 (0.4)	(g1)213	Ag	5.66	$\rho(UO_2^{2+})+\rho(OUO_{aqua})+T(H_2O\text{-cr.})$
	(g2)223	Bg	9.864	$\rho(OUO_{aqua})+\rho(UO_2^{2+})+\rho(OUO_{perox})$
(h)263.4 (0.4)	(h_1)247	Ag	21.54	$\rho(UO_2^{2+})+\rho(OUO_{aqua})+T(H_2O\text{-cr.})$
	(h_2)257	Bg	12.76	$\rho(UO_2^{2+})+\rho(OUO_{aqua})+\rho(OUO_{perox})+T(H_2O\text{-cr.})$
(i)294.3 (0.2)	(i_1)308	Ag	40.90	$\rho(OUO_{perox})$
	(i_2)309	Ag	32.93	$\rho(OUO_{aqua})+T(H_2O\text{-cr.})$
(j)348.11 (0.8)	(j)373	Bg	30.48	$\rho(OUO_{perox})$
(k)405.6 (0.9)	(k)402	Ag	17.42	$\rho(OUO_{perox})$
(l)819.05 (0.01)	(l)798	Ag	2537.86	$\nu^s(UO_2^{2+})$
(m)864.40 (0.03)	(m)917	Ag	1344.38	$\nu(OO)$
(n)1681.1 (0.2)	(n)1638	Ag	142.66	$\delta(H_2O)$
(o)1713.04 (0.07)	(o)1679	Ag	139.50	$\delta(H_2O)$
(p) --	(p)2970	Ag	2993.29	$\nu(OH)$
(q)3161 (2)	(q)3033	Ag	10233.49	$\nu(OH)$
(r)3354 (3)	(r)3238	Ag	4734.37	$\nu(OH)$
(s)3487.1 (0.8)	(s)3319	Ag	5109.120	$\nu(OH)$

The two bands at the highest wavenumbers are mainly attributed to OH stretching vibrations for the crystallization water molecules and the ones at the lowest wavenumbers to the structural water molecules (see vibrational mode pictures of the Appendix 7.B). The two bands placed at about 1650 cm^{-1} represent water bending vibrations, $\delta(H_2O)$. The band at lower wavenumber corresponds mainly to the bending of crystallization water molecules whereas the band at higher wavenumber should be associated to the structural water molecules.

The experimental band at about 864 cm^{-1} is shifted in the computed spectra by nearly 53 cm^{-1} (calculated value is 917 cm^{-1}). It is assigned to peroxo group O-O stretching, $\nu(OO)$. The most intense band in the Raman spectrum appears at 819 cm^{-1} and the calculated wavenumber is 798 cm^{-1}. It is attributed to the uranyl symmetric stretching vibration $\nu^s(UO_2^{2+})$.

The bands placed at 405 and 348 cm^{-1} have theoretical counterparts of 402 and 373 cm^{-1} and are assigned to a $\rho(OUO_{perox})$ vibration. With the symbol ρ we denote an antisymmetric motion of O atoms belonging to equatorial peroxo groups at opposite sides of U atom. Since the O-U-O atoms form an angle of nearly 180 degrees and the central U atom does not move during the motion, the result can be described as a planar rotation similar to a rocking vibration, usually denoted with symbol ρ (see the corresponding vibrational mode pictures in Appendix 7.B). However, the last band was assigned to an asymmetric U-O_{aqua} stretching, $\nu^{as}(UO_{aqua})$ in the experimental work performed by Bastians *et al.* (2004). In this work, the symmetric U-O_{aqua} stretching band appears at a higher wavenumber, at 446 cm^{-1} (see Appendix 7.B).

The band located at 294 cm^{-1} is associated with two nearly coincident theoretical bands at 308 and 309 cm^{-1}. The first is assigned to $\rho(OUO_{perox})$. Since in this case the two O atoms of the

peroxide group of each side of U atom perform the same vibrations, the peroxide group motion is nearly a translation. The second band is mainly assigned to $\rho(OUO_{aqua})$, that is, now, the O atoms involved are those belonging to equatorial aqua groups. It must be noted that the H atoms in the aqua groups performs similar motions as O atom. Crystallization water molecules nearly translate in this mode.

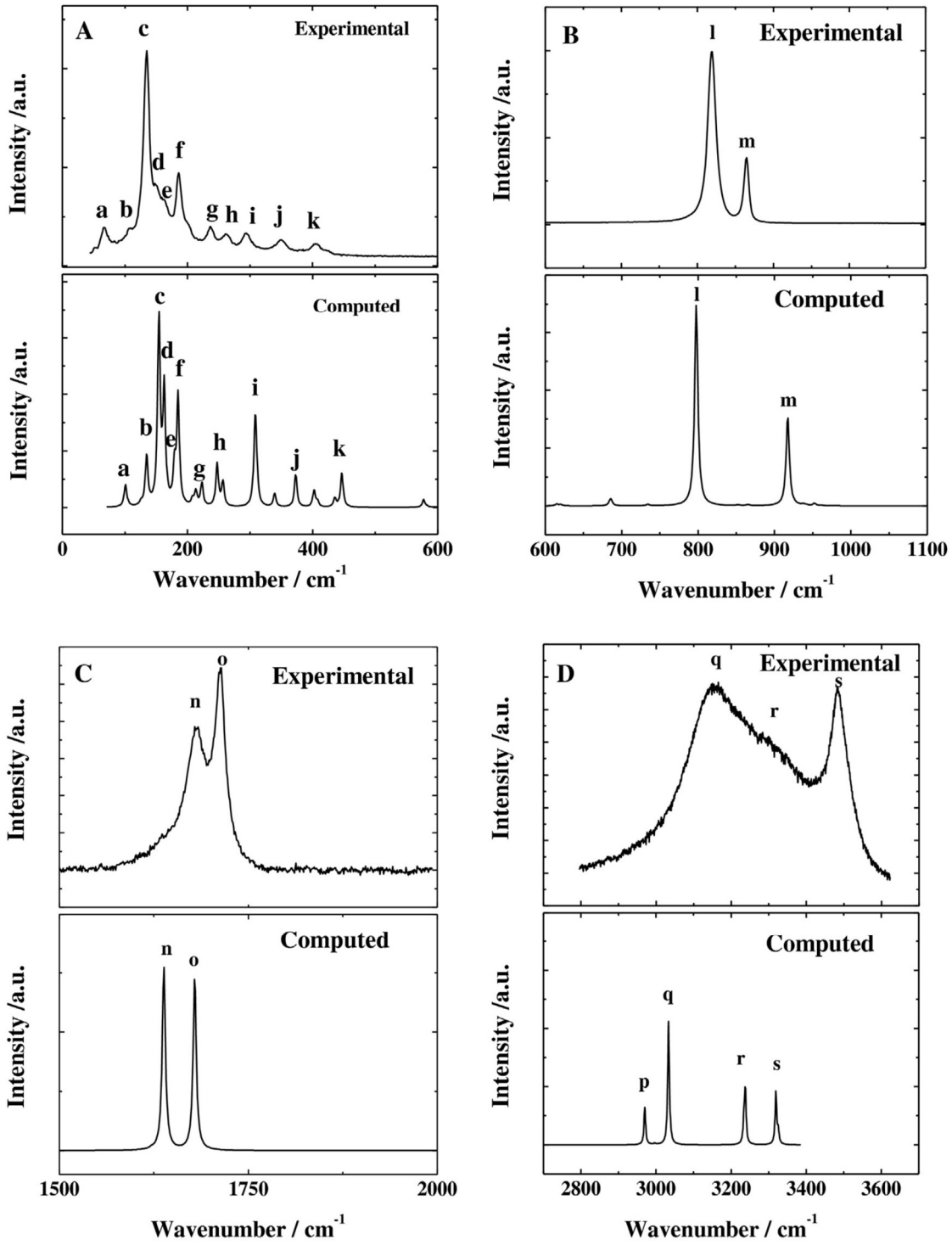

Figure 7.5. Experimental and computed Raman spectra obtained for studtite at STP conditions: (A) low frequency region: 50–600 cm^{-1}, (B) uranyl and peroxo stretching region: 600-1100 cm^{-1}, (C) HOH bending region: 1500 - 2000 cm^{-1}, and (D) OH stretching region: 2800-3600 cm^{-1}.

Bands placed at 263, 184 and 135 cm^{-1} are determined at 257, 185, and 154 cm^{-1}, and attributed to a combination of ρ(O-U-O) vibrations, axial ρ(UO_2^{2+}) and equatorial ρ(OUO_{perox}) and ρ(OUO_{aqua}), and crystallization water molecules translations. For the bands at 237, 203, 107 and 67 cm^{-1} we obtained theoretical values of 247, 223, 135, and 101 cm^{-1}, associated with uranyl axial ρ(UO_2^{2+}) and equatorial ρ(OUO_{aqua}) vibrations and crystallization water molecules translations. Finally, the ones at 164 and 150 cm^{-1} are calculated at 179 and 163 cm^{-1}. The first is assigned to uranyl axial ρ(UO_2^{2+}) vibration and the second one to crystallization water molecules translations.

7.3.3 Thermal Stability of Studtite

It is well-known that studtite loses two water molecules forming metastudtite with the rise of temperature (see TGA results in Figure 7.1.A). In this section, the stability of studtite is studied with the aim of knowing the effect of: 1) the heating rate, and 2) the presence of water in the dehydration process.

7.3.3.1 Heating Rate Effect

In order to study the heating rate effect on the stability of studtite, different dehydration processes at three different heating rates in dry air were performed in the Linkam stage. The processes were analyzed by in situ Raman spectroscopy. Figure 7.6 shows, as an example, some of the Raman spectra obtained at different temperatures when a small amount of studtite is heated at 1 ºC/min. Fig. 7.6.A shows the spectra from 27.1 ºC to 29.6 ºC, Fig. B from 30.2 ºC to 32.6 ºC, Fig. C from 33.2 ºC to 35.6 ºC and Fig. D from 36.2 ºC to 38.7 ºC.

As can be appreciated, a new band appears as a shoulder at ~830 cm^{-1} (see asterisk in Fig. 7.6.B) when the temperature reaches 32.6 ºC. From this temperature on, the intensity of such new band, previously attributed to the metastudtite symmetric uranyl stretch ($\nu^S_{O=U=O}$) (Bastians *et al.*, 2004), increases. Opposite behaviour is shown for the band corresponding to $\nu^S_{O=U=O}$ of studtite at ~819 cm^{-1}. At 33.9 ºC the intensities of both bands are very similar, leading to a symmetric broad band centered at ~ 827 cm^{-1}. The intensity of the $\nu^S_{O=U=O}$ band corresponding to studtite vanishes at temperatures above 35.6 ºC. In Fig. 7.6, a shift to higher frequencies of the peroxo stretch ν_{O-O} of the bridging peroxo ligands can also be observed at ~ 865 cm^{-1}. This behaviour reflects a phase transition from studtite to metastudtite.

Figure 7.7 shows the analysis of the Raman spectra obtained at three temperatures in the phase transition region.

As can be seen, the band at around ~ 827 cm^{-1} can be understood as the direct sum of the symmetric uranyl stretch ($\nu^S_{O=U=O}$) of studtite (819 cm^{-1}) and metastudtite (830 cm^{-1}).

From this analysis, it becomes clear that it is possible to analyze the phase transition by analyzing the intensities of the mentioned bands. Therefore, the relative intensity IS/ IMS, (where I_S and I_{MS} corresponds to the symmetric uranyl stretch ($\nu^S_{O=U=O}$) intensity band for studtite and metastudtite, respectively) are shown in Figure 7.8 as a function of temperature for heating rates of 0.2, 1 and 5 ºC/min.

By considering the temperature at which $I_S/I_{MS} \sim 0$, the transition temperatures, T_t, are 50, 35 and 35 ºC for the rate studies; i.e., at low heating rates (0.2 ºC/min) the transition temperature is around 35 ºC, whereas at a high rate (5 ºC/min) the T_t is higher. This increase in T_t could be due to the fact that the system is out of equilibrium at such a high heating rate and, therefore, T_t at equilibrium should be obtained in experiments at heating rates below 1 ºC/min.

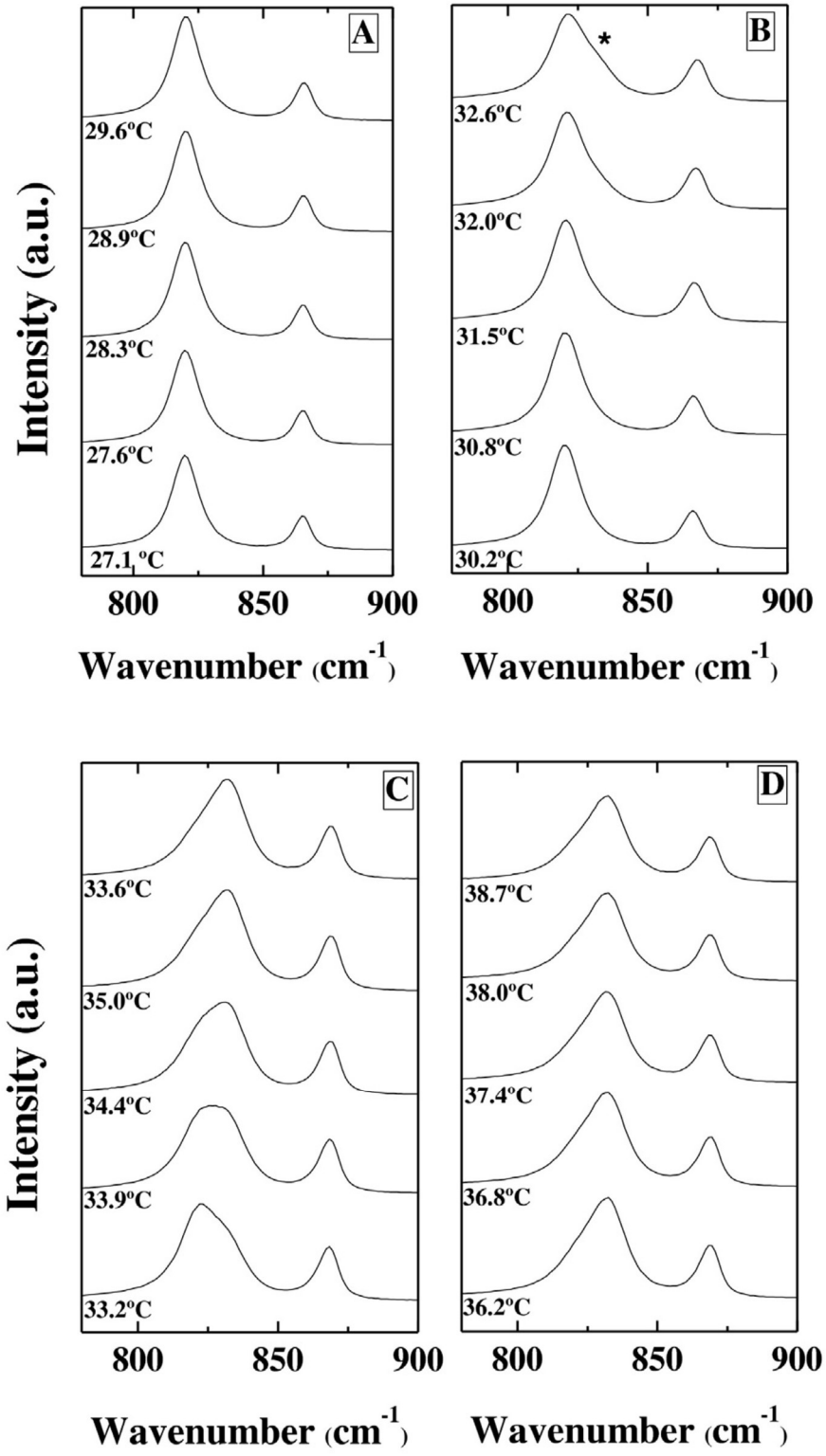

Figure 7.6. Evolution of the Raman spectrum along a 1 ºC/min heating process, obtained by the use of Raman microscopy in conjunction with a Linkam thermal stage. Fig. 6.A corresponds to spectra from 27.1 ºC to 29.6 ºC, Fig. B from 30.2 ºC to 32.6 ºC, Fig. C from 33.2 ºC to 35.6 ºC and Fig. D from 36.2 ºC to 38.7 ºC.

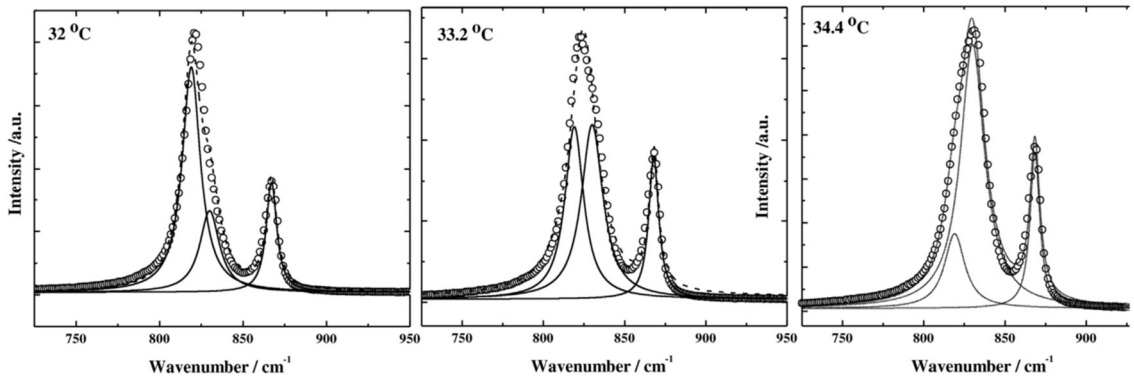

Figure 7.7. Lorentzian fit of the Raman spectra obtained at three temperatures in the phase transition region.

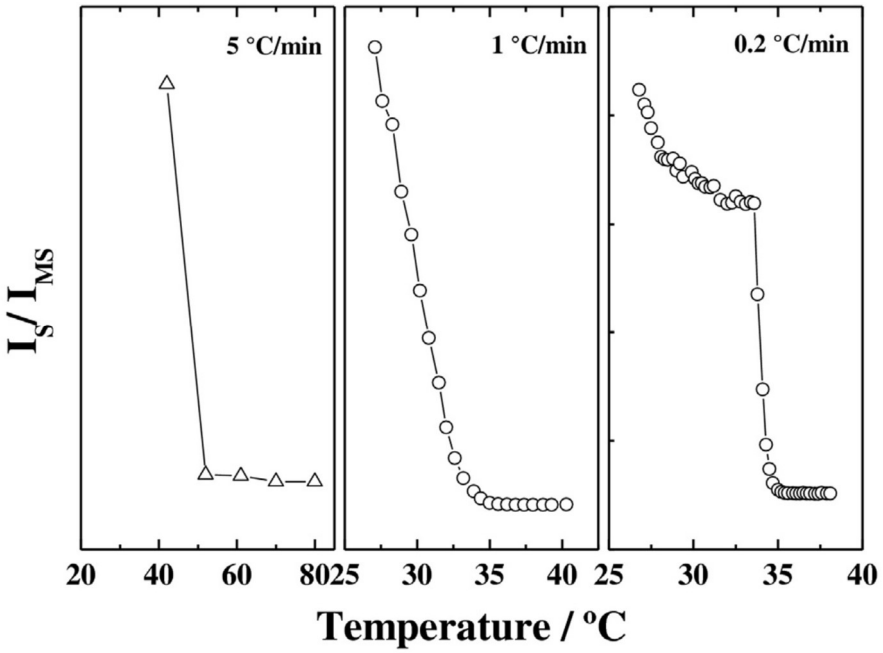

Figured 7.8. I_S/I_{MS} ratio as a function of temperature for three different heating rates. I_S and I_{MS} correspond to the symmetric uranyl stretch ($v^S_{O=U=O}$) intensity band for studtite and metastudtite, respectively.

7.3.3.2 Presence of Liquid Water

The effect of water molecules in contact with the mineral on the studtite thermal stability was studied by placing a few mg of studtite covered with liquid water in the designed cell. The cell was housed in the Linkam stage in which the temperature of the system was increased at 0.2 ºC/min. Figure 7.9 shows some of the Raman spectra obtained in the *in situ* analysis of these experiments.

As can be observed, all spectra correspond to the studtite structure, *i.e.*, in presence of liquid water the dehydration of the molecule does not take place in the temperature range studied. This behavior (higher thermal stability against dehydration than that in air) has been shown in other systems (Chou *et al.*, 2002).

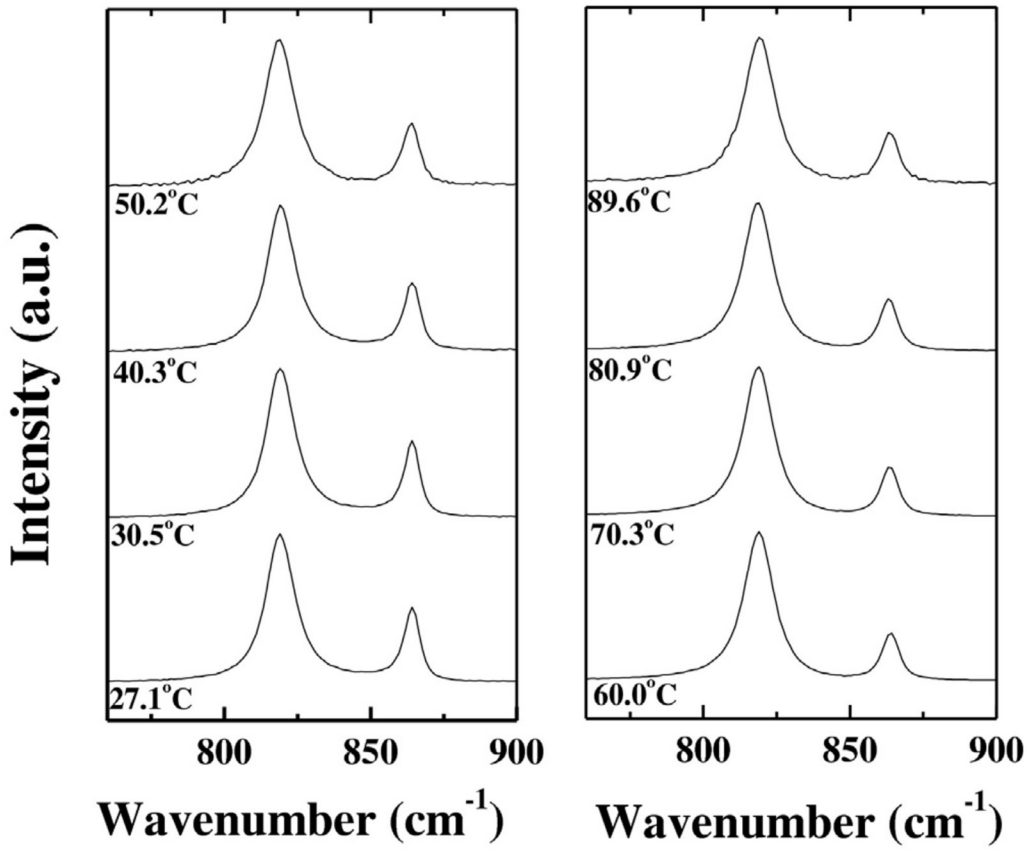

Figure 7.9. Evolution of the Raman spectrum of studtite in contact with liquid water during heating experiments in the designed cell with a Linkam thermal stage.

APPENDIX 7.A. Studtite DFT Calculations.

The mineral studtite was originally described in 1947 by Vaes (1947) as a hydrated carbonate of uranium from a qualitative chemical analysis. Subsequent chemical and powder XRD investigations by Walenta (1974) demonstrated that mineral studtite is identical to synthetic $(UO_2)O_2{\cdot}4H_2O$ (Sato, 1961a,b, 1963; Debets, 1963). Subsequent analyses of studtite from the type locality (Shinkolobwe) by Cejka *et al.* (1996) confirmed Walenta's unit-cell determination. The structure of studtite was finally reported in 2003 by Burns and Hughes (2003) which showed that its unit cell is approximately twice the size of the previously accepted unit-cell. The structure is displayed in Figure 7.A.1. Equilibrium structure is monoclinic and crystallizes in the space group *C2/c (Z=4)*. Kubatko *et al.* (2003), also reported the thermodynamic stability of the peroxide-containing uranyl minerals.

In studtite, uranium atom displays hexagonal bipyramid coordination. Two oxygen atoms are in apical positions forming with uranium atom nearly linear uranyl UO_2^{2+} uranyl ions. The six equatorial oxygen atoms are two peroxo groups (four oxygen atoms) forming opposite edges of the hexagon and two water molecule oxygen atoms. The different bipyramids are linked by sharing the peroxo equatorial edges and form zig-zag chains along [001] direction.

Most uranyl minerals including uranium as the only high-valence cation invariably contain sheets. However, some minerals as studtite are not based upon sheet of uranyl polyhedra, but contain polymerized uranyl polyhedra in only one dimension. The occurrence of chains rather sheets in U(VI) minerals is usually due to distortions in the polyhedra (Grenthe *et al.*, 2006). The presence of peroxide at the equatorial positions of the uranyl polyhedra results in distorted hexagonal bipyramids, with the peroxide O–O edge length (about 1.46 Å) being much shorter than the typical O–O edge length in uranyl hexagonal bipyramid (about 2.4 Å) This distortion may prevent the formation of two-dimensional layer structures.

The chains are held together by means of a network of hydrogen bonds. The hydrogen bond structure is show in detail in Figure 7.A.2. Each water molecule forming part of the uranyl polyhedra (structural water, also called terminal aqua groups) donate two hydrogen bonds with other water molecules which do form part of the bipyramids (crystallization water). The last two molecules participate in four hydrogen bonds. They are acceptors of two hydrogen bonds donated by structural water molecules of two subsequent bipyramids of a chain and are donors of two hydrogen bonds, one with a uranyl oxygen atom and one with a peroxide oxygen atom. These oxygen atoms belong to upper and lower chains. The uranyl oxygen atom is acceptor of one hydrogen bond and the two oxygen atoms in a peroxide group are each one also acceptors of one hydrogen bond. Thus, the network of hydrogen bonds enforces the structure by linking the chains at the same height and upper and lower chains. In studtite two subsequent bipyramids are linked not only by sharing a peroxo O-O edge but also through hydrogen bonds with an intermediate molecule outer of the bypiramids. The outer molecule receives these hydrogen bonds and donates hydrogen bonds to upper and lower chains.

Since there are two kinds of water molecules in the structure, one half being the structural ones and the other crystallization water molecules, the structure is more correctly formulated as $[(UO_2)O_2(H_2O)_2]{\cdot}2H_2O$. Due to the fact that peroxo groups are side-bonded (η^2) to the uranium atoms, the structure is commonly referred to as $[(UO_2)(\eta^2\text{-}O_2)(H_2O)_2]{\cdot}2H_2O$. However, the notation $[(UO_2)(\mu^2\text{-}O_2)(H_2O)_2]{\cdot}2H_2O$ may also be used, indicating that peroxo atoms are μ^2-bridging between symmetry related uranium metal centers.

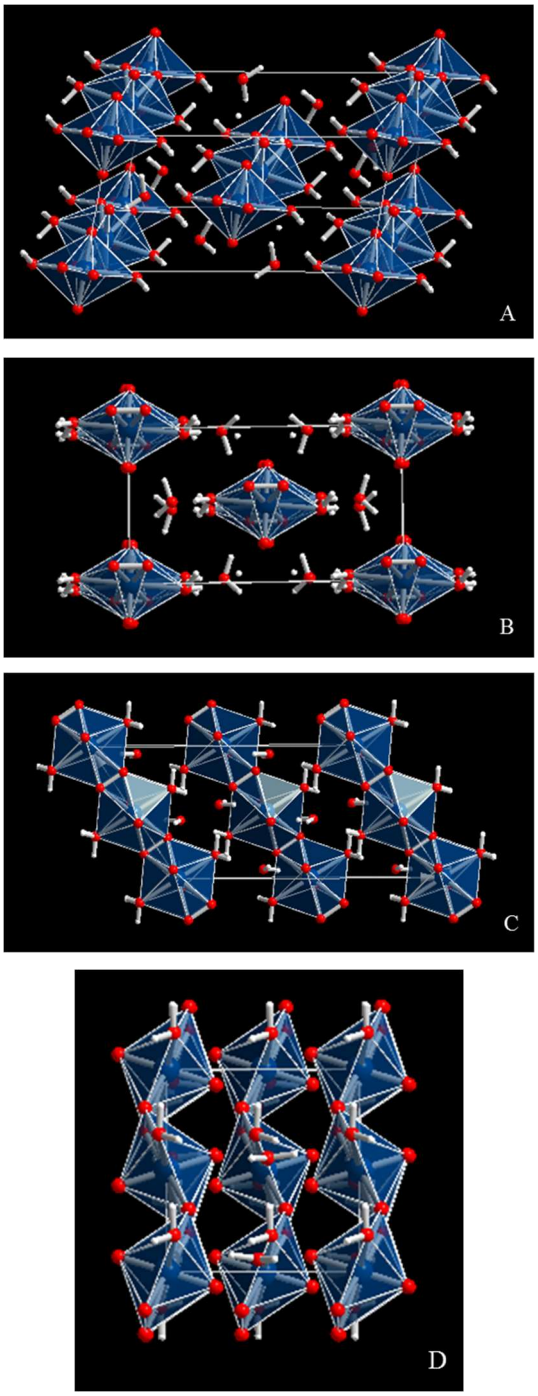

Figure 7.A.1. Structure of studtite, $(UO_2)(O_2)\cdot 4H_2O$: a) General view of the studtite structure; b) view from [001]; c) view from [010]; d) view from [100]. Color code: U-Blue, O-Red, C-Carbon.

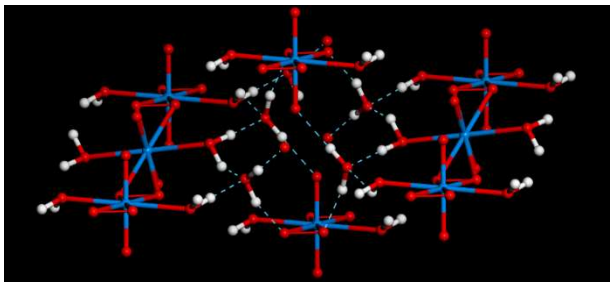

Figure 7.A.2. Detailed view of the hydrogen bond structure of studtite.

In this work, studtite structure was optimized in the calculations by increasing the different parameters (larger kinetic energy cutoffs and K meshes), i.e., increasing complexity. The optimization performed with a cutoff of 1000 eV and a K mesh of 2×4×4 (8 K points) gave a well converged structure and was used to determine the final material properties. Calculated lattice parameters, volumes and densities compared with the results of other calculations and the experimental results are given in table 7.1. The corresponding bond distances and angles are given in Tables B.1 and B.2 of the Supplementary Information of the article (Colmenero *et al.*, 2017b). Present results are comparable in accuracy with those of Weck *et al.* (2012, 2015).

The powder X-ray powder spectrum of studtite was computed from the experimental and computed structures (Downs *et al.*, 1993). The most intense lines are compared in Figure 7.A.3 and, as can be seen, the agreement in line positions and intensities is very good. The use of spectra derived directly from the experimental and computed structures allows for a fair comparison of the results free of interferences as the experimental conditions or possible artifacts as the presence of sample impurities since both are determined under the identical conditions. Nevertheless, agreement with the experimental pattern of Debets (1963) (see also Walenta, 1974) is also good. The main results are given in Table B.3 of the Supplementary Information of the article (Colmenero *et al.*, 2017b). The pattern computed with program REFLEX, a module of Materials Studio package (Materials Studio, 2017), is given in Figure 7.4.

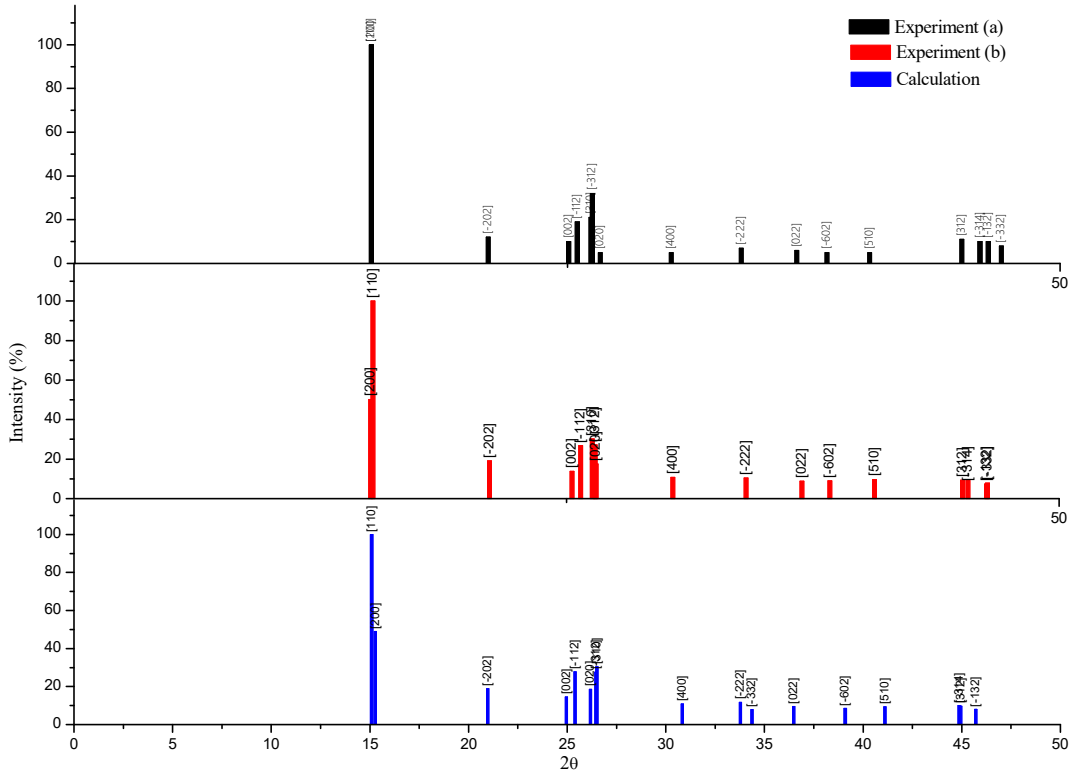

Figure 7.A.3. X-ray powder spectrum of studtite using CuKα radiation: a) Experimental spectrum (Debets, 1963); b) X-ray powder spectrum computed form experimental geometry (Burns and Hughes, 2003); c) X-ray powder spectrum computed from calculated geometry.

APPENDIX 7.B. Raman Modes of Studtite.

Figure 7.B.1. The atomic motions associated to some Raman active vibrational normal modes of studtite.

Mode 3319 cm^{-1} – ν(OH) – OH stretching for crystallization H_2O molecules.

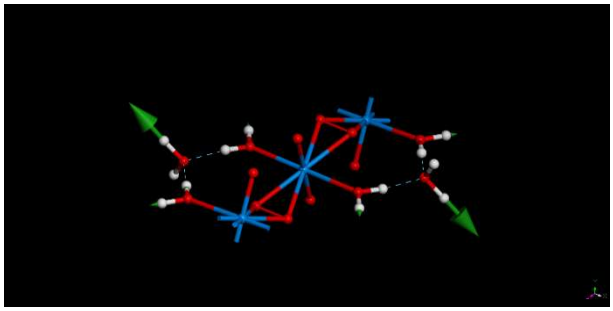

Mode 3033 cm^{-1} – ν(OH) – OH stretching for structural H_2O molecules.

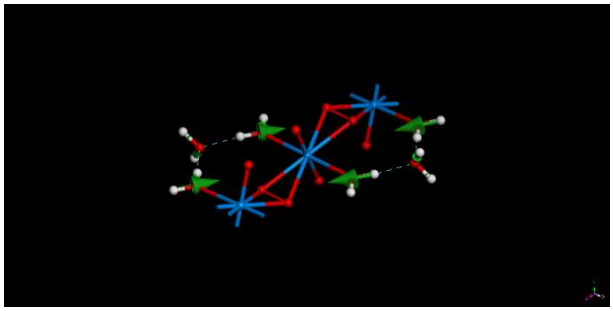

Mode 1679 cm^{-1} – δ(H_2O) – H_2O bending for structural H_2O molecules.

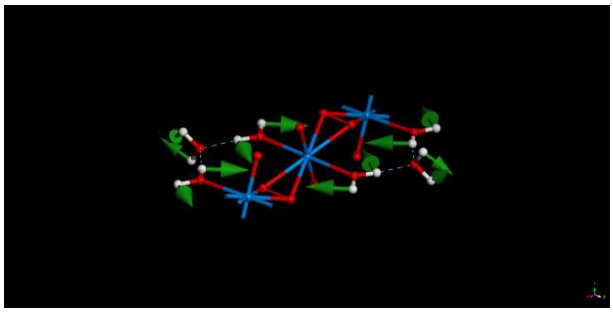

Mode 1638 cm^{-1} – δ(H_2O) – H_2O bending for crystallization H_2O molecules.

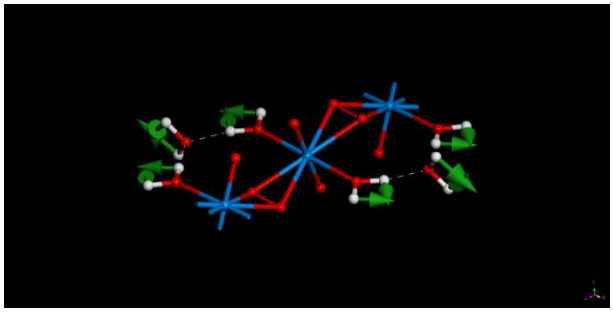

Mode 917 cm^{-1} – ν(OO) – Peroxo O-O stretching.

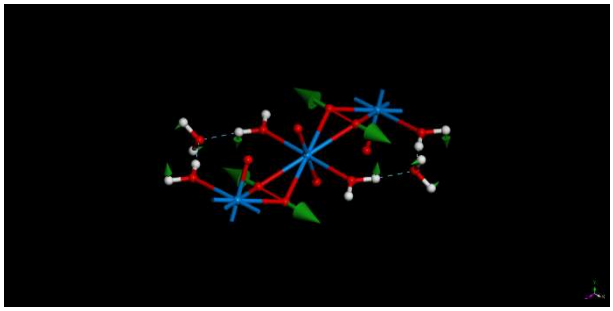

Mode 798 cm^{-1} – $\nu^{s}(UO_2^{2+})$ – Symmetric UO_2^{2+} stretching.

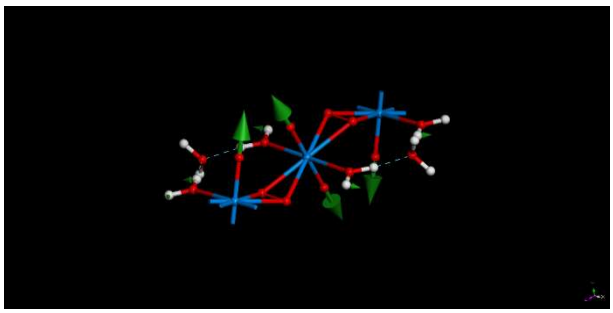

Mode 446 cm^{-1} – $\nu^{s}(UO_{aqua})$ – Symmetric UO_{aqua} stretching (H_2O-str. translation).

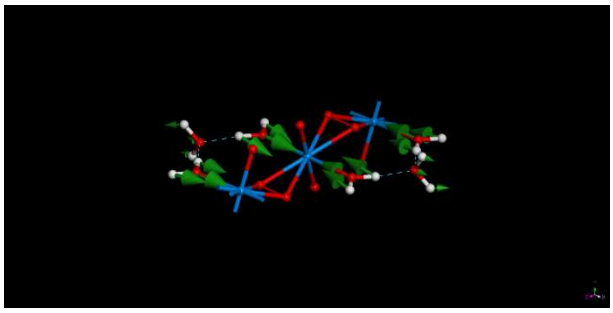

Mode 402 cm^{-1} – $\rho(OUO_{perox})$ – OUO_{perox} rocking.

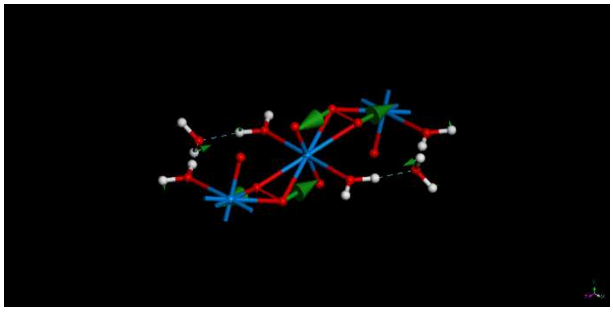

Mode 373 cm^{-1} – $\rho(OUO_{perox})$ – OUO_{perox} rocking.

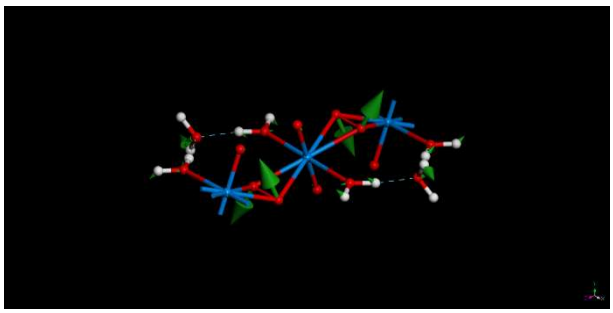

Mode 309 cm^{-1} – $\rho(OUO_{aqua})+T(H_2O\text{-cr.})$ – OUO_{aqua} rocking plus crystallization H_2O translation.

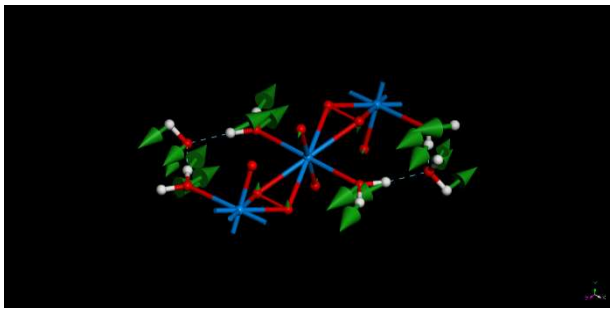

Mode 307 cm^{-1} – $\rho(OUO_{perox})$ – OUO_{perox} rocking.

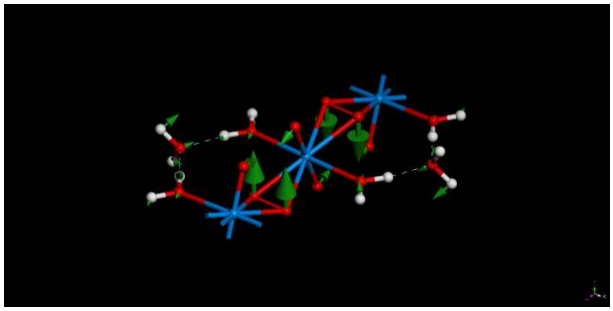

Chapter 8. Structural, Mechanical and Raman Spectroscopic Characterization of Layered Uranyl Silicate Mineral Uranophane-α by DFT Methods

This chapter is based on the published article "*Structural, Mechanical and Raman Spectroscopic Characterization of Layered Uranyl Silicate Mineral Uranophane-α by DFT Methods*" by F. Colmenero, V. Timón, L. J. Bonales, and J. Cobos, Clay Minerals XX, XXXX–XXXX (2017, submitted).

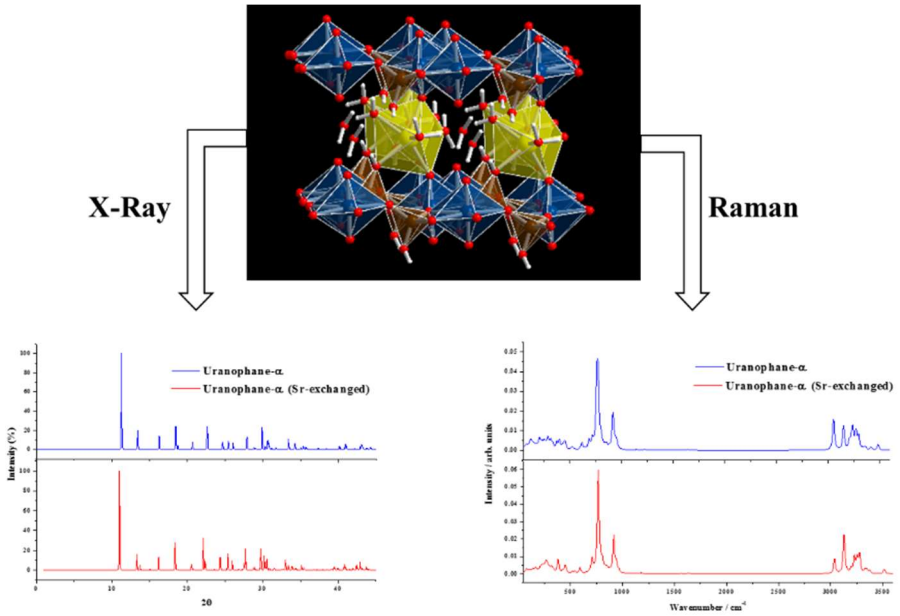

Abstract

Layered uranyl silicate clay-like mineral uranophane-α, $Ca(UO_2)_2(SiO_3OH)_2 \cdot 5H_2O$, was studied by first principle calculations based on density functional theory method. Its structure, present in nature in a wide variety of compounds having the uranophane sheet anion-topology is confirmed here for the first time by means of rigorous theoretical solid state calculations. The computed lattice parameters, bond lengths, and bond angles were in very good agreement with their experimental counterparts and the calculated X-ray powder pattern reproduced accurately the experimental one. The mechanical properties of this mineral for which there are no experimental data to compare with were determined and the satisfaction of the mechanical stability Born conditions of the structure was demonstrated by means of calculations of the elasticity tensor. The Raman spectrum was computed by means of density functional perturbation theory and compared with the experimental spectrum were. The vibrational properties of this mineral were very well characterized, showing a good performance in all the spectral calculated range. Theoretical methods allowed us to assign the Raman spectrum bands to vibrations localized in different fragments within the crystal unit cell. Finally, the possibility of incorporation of strontium in uranophane was studied. According to the experimental results, the computed structure, X-Ray powder pattern and Raman spectrum of Sr-exchanged uranophane were found to be very close to those of normal uranophane.

8.1 Introduction

Uranyl silicates are very important materials because they form as alteration phases during hydration-oxidation weathering of uraninite (Frondel, 1956; Finch and Ewing, 1992) and spent nuclear fuel (SNF) (Wronkiewicz *et al*., 1992, 1996; Pearcy *et al*., 1994; Plasil, 2014) which is mainly composed of uranium dioxide, UO_2. The contact of groundwaters containing dissolved silicate with dissolved uranyl, is expected to result in the formation of uranyl silicate minerals (Wronkiewicz *et al.*, 1992, 1996; Pearcy *et al*., 1994; Plasil, 2014). These minerals play a major role in the long-term dosage of nuclear waste repositories. Ubiquity of uranophane-α suggests that the uranyl silicates are among the most important phases controlling uranium concentrations in groundwater (Finch and Ewing, 1992; Plasil, 2014).

Mineral uranophane-α, $Ca(UO_2)_2(SiO_3OH)_2 \cdot 5H_2O$, is one of the earliest known uranyl minerals. It is a hydrated uranyl nesosilicate which was first described by Websky (1953, 1959). Since then, it has been identified in nearly all major and most of the minor uranium deposits in the world. Its β polymorph, also monoclinic, is much more infrequent and was observed for the first time by Novacek (1935). In nature, uranophane, when well crystallized, is always fibrous and, usually, the fibers consist of several crystals in parallel growth (Gorman, 1955; Smith *et al*., 1957). A cluster of single crystals rarely is found. Where uranophane occurs as radiating fibers, it is yellow and has a vitreous luster, but more commonly it occurs as massive crusts which are pale yellow to yellow-orange and have a waxy luster. Uranophane-α has been synthetized in the laboratory, for example, by Nguyen *et al.* (1992), Cesbron *et al.* (1993), Vochten *et al.* (1997) and Wall *et al.* (2010). Wall *et al.* (2010) presented a detailed, optimized technique to synthesize this layered uranyl silicate using aqueous solutions of uranyl acetate, calcium acetate, and sodium metasilicate as starting materials. So far, nobody has succeeded in preparing β-uranophane. Other uranyl silicates, as boltwoodite, can be synthesized only if calcium is virtually absent.

Uranophane-α is characterized by a 1:1 uranium to silicon ratio (Stohl and Smith, 1981). Its structure is very complex and includes 68 atoms in the unit cell, as well as 320 valence electrons. Uranyl silicate minerals having this ratio contain sheets (Stohl and Smith, 1981; Burns, 2005; Grenthe *et al.*, 2006). Nine uranyl silicate minerals (uranophane-α and β, sklodowskite, cuprosklodowskite, boltwoodite, sodium boltwoodite, kasolite, oursinite and swamboite) have been classified as members of the uranophane group on the basis of the uranium to silicon ratio and a similar uranophane anion sheet topology (Burns, 1998, 1999a, 2005; Burns *et al.*, 1996;

1997b; Grenthe *et al.*, 2006). Structural connectivities of uranophane-β polymorph differ substantially from those of uranophane-α (Viswanathan and Harneit, 1986; Burns, 1999a). Soddyite has 2:1 uranium to silicon ratio and framework crystal structure (Demartin *et al*., 1992; Stohl and Smith, 1981; Burns, 2005). The ratio 2:5 was found in the crystal structures of weeksite (Jackson and Burns, 2001), haiweeite (Burns, 2001) and coutinhoite (Attencio *et al.*, 2004), and probably also in some uranyl silicate minerals from Russia that are not approved (Sidorenko *et al.*, 1975, 2001). Some synthetic framework uranyl silicates have also been described (Burns and Hill, 2000; Huang *et al.*, 2003).

Uranyl silicate minerals are mostly layered uranyl silicates that behave much like clay minerals. The layers are composed of sheets having a net negative charge which stack up with cations in the interlayer spaces to provide charge balance within the structure (Burns, 1999b, 2005; Burns and Li, 2002; Douglas *et al.*, 2002; Grenthe *et al.*, 2006). Uranyl cation in the sheet could be replaced by other non-uranyl cations, similar to cation substitution in the sheets of clay minerals, providing a mechanism for incorporation of transuranic elements into these phases (Burns, 1998; 1999b; Burns *et al.*, 1996; 1997a,b, 2004; Douglas *et al.*, 2005a,b; Murphy and Grambow, 2008; Burns and Klingensmith, 2006; Klingensmith and Burns, 2007; Shuller *et al*., 2010a-b, 2013, 2014). Also, other cations can be substituted into the interlayer spaces via ion exchange, providing a mechanism of incorporation of fission products as cesium or strontium (Burns, 1998, 1999b; Burns and Li, 2002; Burns *et al.*, 1996, 1997a, Douglas *et al.*, 2002). Thus, these mineral phases formed at the SNF surface may potentially act as an additional barrier to radionuclide migration through the accessible environment via mineral sorption reactions. The incorporation mechanisms seem to be more favorable in structures with charged sheets and cations in the interlayer than in structures with electroneutral sheets since coupled substitutions involving the interlayer may be a charge-balancing mechanism that permits the substitution (Burns and Klingensmith, 2006; Klingensmith and Burns, 2007). The incorporation of fission products as ^{137}Cs and ^{90}Sr into the structure of uranophane was studied by Douglas *et al*. (2002). Incorporation of Cs into the structure of the closely related mineral boltwoodite was previously reported by Burns (1999b). Also, the substitution of uranium by neptunium in uranophane sheets was studied by Douglas *et al.* (2005b), Murphy and Grambow (2008), Burns and Klingensmith (2006). Finally, the sorption of Eu (III) into the surface of uranophane was studied by Kuta *et al.* (2013).

While the structure of uranophane has been determined by experimental X-Ray diffraction techniques (Ginderow, 1988), it has never been confirmed by means of theoretical solid state calculations. Although classical molecular dynamics methods based in empirical force fields have been employed to study the uranophane-water interface as well as the interfacial reactivity of this uranyl silicate (Kuta *et al.*, 2013), rigorous first principles methods have only been used by Kuta *et al.* (2013) and Wheaton *et al.* (2003) to study uranyl silicate clusters.

As far as we know, no experimental or computational studies have been reported of the mechanical properties of uranophane, and the conditions of mechanical stability of its structure have not been studied. The confirmation of the structure and stability of the uranophane structure by means of first principles methods is also relevant because this structure represents one of the most fundamental anion topologies in the U(VI) minerals, referred to as the uranophane sheet anion-topology in the literature (Grenthe *et al.*, 2006; Burns, 1998, 1999a, 2005; Burns *et al.*, 1996, 1997b). This topology is also at the basis of the structure of a large series of phosphates, arsenates, vanadates and molybdates (Grenthe *et al.*, 2006; Jouffret *et al.*, 2007a,b,c; Forbes and Burns, 2006: Jin *et al*., 2011; Mer *et al.*, 2012).

Radiotoxicity of these substances complicates its handling under security conditions and, therefore, its characterization. The proper characterization techniques to analyze these materials must be non-destructive, should not require any special sample preparation, and must allow the analysis of very small amount of sample. A technique satisfying these requirements is Raman spectroscopy (Dubessy *et al.*, 2012). Raman spectra of uranyl silicate minerals have been given by Frost *et al*. (2006a-c), Amme *et al.* (2002), Bonales *et al.* (2016) and Driscoll *et al.* (2014). A very complete characterization study of uranophane including scanning electron microscopy (SEM), X-Ray diffraction (XRD), thermogravimetric analysis (TGA), surface area and charge

determination, and Raman spectroscopy, was carried out by Wall *et al.* (2012). Although the Raman spectra of this mineral has been determined experimentally a precise assignation of the main bands in the spectra is lacking. Theoretical methods allow for a complete characterization of these materials free of all the difficulties associated to the experimental techniques associated to its radiotoxicity. The assignment of the experimental vibrational bands is possible since these methods provide detailed microscopic scale views of the atomic vibrational motions in the corresponding normal modes. However, the application of theoretical methods to uranium containing solids is very complicated and computationally demanding, not only due to the great size of the corresponding unit cells but also to the high level of theory required to describe correctly these systems In our previous paper (Bonales *et al.*, 2016a) a norm conserving relativistic pseudopotential (Troullier and Martins, 1991) for uranium atom was generated. Studies of uranyl containing materials carried out with this pseudopotential are the theoretical studies of rutherfordine (Bonales *et al*., 2016a; Colmenero *et al*., 2017a) studtite (Colmenero *et al.*, 2017b) and soddyite (Colmenero *et al*., 2017c) minerals.

8.1 Methods: Theoretical DFT calculations.

CASTEP code (Clark *et al*., 2005), a module of the Materials Studio package (Materials Studio, 2017), was employed to model uranophane-α structure as in our previous papers (Bonales et al., 2016a; Colmenero *et al.*, 2017a,b,c). Also, the generalized gradient approximation (GGA) together with PBE functional (Perdew *et al.*, 1996) and Grimme empirical dispersion correction, the DFT-D2 approach (Grimme, 2006), were employed. The introduction of dispersion corrections produces a remarkable improvement of the results for systems in which the accurate description of non-bonded interactions is important (Tunega *et al*., 2012). The methods employed for geometry optimization and calculation of vibrational Raman spectra, mechanical properties and equation of state were the same as in our previous works (Bonales *et al*., 2016a; Colmenero *et al*., 2017a,b,c) and their description will be not repeated here. However, present uranophane computations required larger kinetic energy cutoffs and K-point meshes to ensure good convergence for computed structures and energies. A kinetic energy cutoff of 1000 eV and a K mesh of 3×3×1 (4 K points) were selected to determine the final results.

8.3 Results and Discussion

8.3.1 Structure

The unit cell of uranophane-α, $Ca(UO_2)_2(SiO_3OH)_2{\cdot}5H_2O$, has monoclinic symmetry, spatial group $P2_1$ *(Z=4)*. It contains 68 atoms: 4 U, 4 Si, 2 Ca, 34 O and 24 H. In our computations, 320 valence electrons should be described explicitly.

Stohl and Smith (1981) categorized naturally occurring uranyl silicates according to the uranium to silicon ratio, which in part determines the structures of these minerals. Most uranyl silicate minerals have 1:1 uranium to silicon ratio and are sheet silicates (Stohl and Smith, 1981, Burns, 2005; Grenthe *et al*., 2006). The uranyl silicate sheets are composed of $[(UO_2)_2(SiO_4)_2]^{-4}$ units bound at the equatorial edges (see Figs. 8.1.A and 8.1.B). A sheet, $[(UO_2)(SiO_4)]_n^{-2n}$, contains UO_7 pentagonal bipyramids and SiO_3OH tetrahedra. Charge compensating cations, calcium in uranophane, lie in the interlayer space between the sheets (see Fig. 8.1.C). Two uranyl silicate sheets are connected by $CaO_2(OH)(H_2O)_4$ polyhedra (distorted pentagonal bipyramid). The Ca atom ligands are four water molecules, two uranyl oxygen atoms belonging to the upper and the lower sheets, and one OH group of a SiO_3OH tetrahedra. One water molecule is out of the Ca polyhedra. While this water molecule is described as free or crystallization water, the four water

molecules belonging to Ca atom coordination sphere are referred to as structural water. Hydrogen bonds reinforce the bonding between the uranyl silicate sheets, the Ca atom, and the free water. As it can be seen in Fig. 8.1.C, the upper sheet SiO_3OH tetrahedra have free OH groups pointing downwards and the lower sheet tetrahedra have OH groups pointing upwards which belong to the Ca atom coordination sphere.

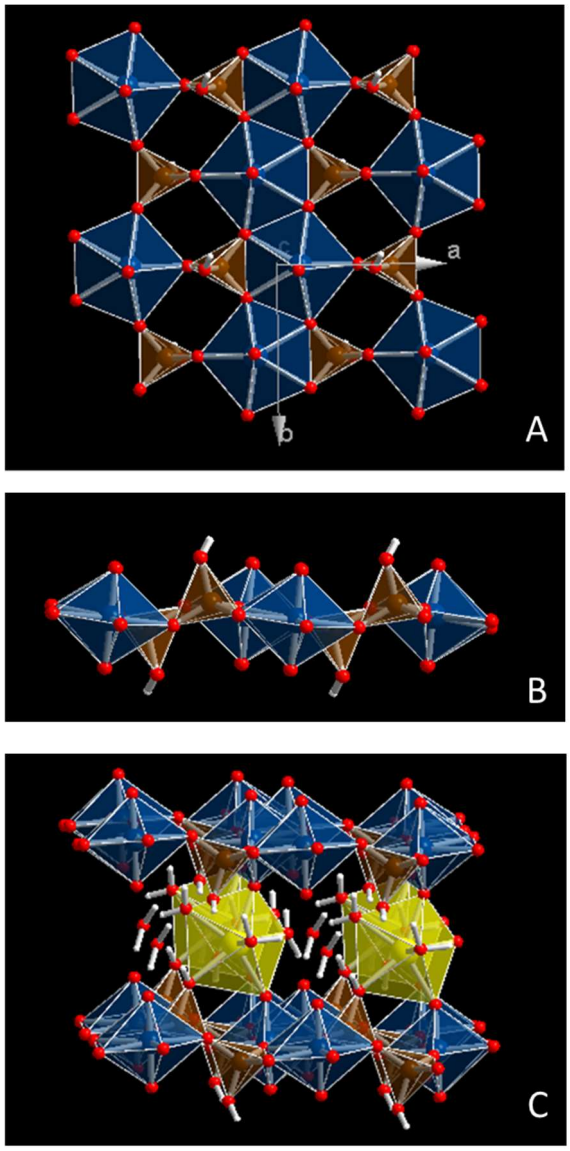

Figure 8.1. Structure of uranophane-α mineral: a) View of a 2×2×2 supercell from [001] showing a uranyl silicate sheet $[(UO_2)(SiO_4)]_n^{-2n}$ composed of UO_7 pentagonal bipyramids and SiO_3OH tetrahedra; b) The same view as in a) from [010]; c) View of a 2×2×2 supercell from [010] showing two uranyl silicate sheets connected by $CaO_2(OH)(H_2O)_4$ polyhedra (distorted pentagonal bipyramid). One water molecule is out of the Ca polyhedra (free water). Color code: U-Blue, Si-Brown, O-Red, H-White, Ca-Yellow.

The structure of uranophane-α was determined in calculations with increasing complexity in order to obtain a set of calculation parameters yielding good convergence for computed structures and energies. Table 8.1 gives the final lattice parameters, volumes and densities obtained compared with the corresponding experimental values of Ginderow (1988).

Table 8.1. Lattice parameters. The experimental data are from Ginderow (1988).

Parameter	*a* (Å)	*b* (Å)	*c* (Å)	α	β	γ	Vol. (Å^3)	Dens. (g/cm^3)
Calculated	6.6689	7.0022	15.8684	90.0	98.0748	90.0	733.6520	3.8766
Exp.	6.665	7.002	15.909	90.0	97.27	90.0	736.478	3.8618

Table 2 of the article (Colmenero *et al*., 2017e) give a comparison of the more important geometric parameters (bond distances) obtained with the corresponding experimental data of Ginderow (1988). Uranophane-α has two structurally (symmetrically) identical U^{6+} ions and two structurally (symmetrically) identical Si^{4+} ions in its crystal structure. However, the two non-symmetrically related uranyl and silicate polyhedra are nearly the same. The two O atoms in the uranyl group, UO_2^{2+}, are in apical positions of the pentagonal bipyramids at distances of 1.801 and 1808 Å for both U1 and U2. The calculated values are 1.828 and 1.843 Å for U1 and 1.825 and 1.829 Å for U2, respectively. The remaining five O atoms lie in the equatorial plane which U-O distances which range from 2.241 to 2.463 Å (calculated 2.214 to 2.457 for U1 and 2.236 to 2.462 Å for U2, respectively). The Si-O distances, ranging from 1.601 to 1.638 Å, are within the normal range (calculated 1.621 to 1.663 Å for Si1 and 1.620 to 1.666 for Si2, respectively). Ca-O distances in the distorted pentagonal bipyramid are satisfactorily reproduced and range from 2.371 to 2.445 Å (calculated 2.372 to 2.509 Å). Thus, the solvation structure around the interlayer Ca atom is satisfactorily described.

We conclude that the experimental geometrical parameters and our theoretical values agree quite well in spite of the complexity of the uranophane-α structure.

The X-Ray powder pattern of uranophane-α was computed from the experimental (Ginderow *et al*., 1988) and computed structures (Downs *et al*., 1993) using CuKα radiation (λ=1.540598 Å). The most intense lines (I > 10%) are compared in Figures 8.2.b and 8.2.c, and, as can be seen, the agreement in line positions and intensities is very good. The use of spectra derived directly from the experimental and computed structures allows for a fair comparison of the results free of interferences as the experimental conditions or possible artifacts as the presence of sample impurities since both are determined under the identical conditions. Nevertheless, the use of an experimental pattern also leads to an excellent agreement. Computer program XPowder (Martin, 2012) using the PDF-2 database (ICDD, 2003) recognizes the computed pattern as that of uranophane-α (pattern 78-1840, from Ginderow (1988)). The experimental X-Ray powder pattern can be seen in Figure 8.2.a where it is compared with the previously described spectra. The precise values of the main reflections for are given in Table 3 of the article (Colmenero *et al*., 2017e).

8.3.2 Mechanical Properties and Stability

The elastic tensor, needed for the calculation of mechanical properties and to study the mechanical stability of the uranophane crystal structure, was calculated, at the optimized equilibrium structure, from stress−strain relations using the finite deformation technique implemented in CASTEP. Crystals with monoclinic symmetry have 13 nondegenerate elastic constants in the symmetric stiffness matrix (Nye, 1985; Weck *et al.*, 2015) which may be written as in equation (3.157. *b*). The precise values of these constants obtained in our computations are (all values are given in GPa):

$$C = \begin{pmatrix} 156.59 & 44.77 & 17.85 & 0 & -6.84 & 0 \\ 44.77 & 152.19 & 14.46 & 0 & 0.60 & 0 \\ 17.85 & 14.46 & 94.34 & 0 & 2.46 & 0 \\ 0 & 0 & 0 & 23.93 & 0 & 2.27 \\ -6.84 & 0.60 & 2.46 & 0 & 27.71 & 0 \\ 0 & 0 & 0 & 2.27 & 0 & 34.54 \end{pmatrix}$$

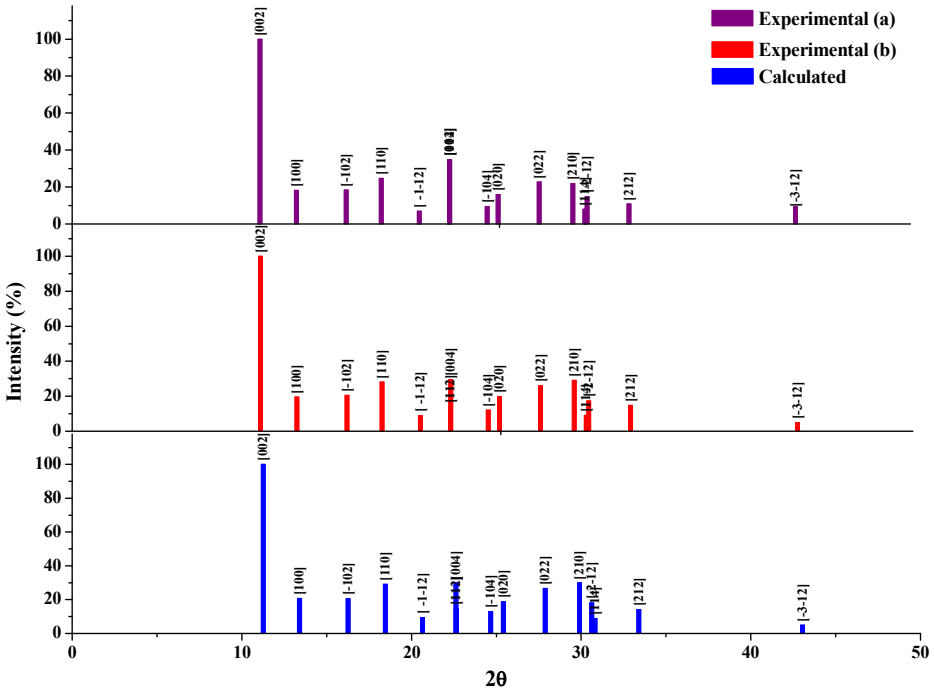

Figure 8.2. X-Ray powder spectrum of uranophane-α using CuKα radiation: a) Experimental spectrum (pattern 78-1840 in the PDF-2 database); b) X-Ray powder spectrum computed from experimental geometry (Ginderow, 1988); c) X-Ray powder spectrum computed from calculated geometry.

For monoclinic crystals, a set of necessary (but not sufficient) Born criteria for mechanical stability were given in Section 3.2.9. These conditions are fully satisfied. The generic necessary and sufficient Born criterion is that all eigenvalues of the C matrix be positive (Mouhat and Coudert, 2014). The C matrix was diagonalized numerically and all eigenvalues were found to be positive. Since the above condition is satisfied, uranophane-α mechanical stability can be inferred.

The fact that C_{33}, the diagonal component of C matrix along c direction, is much smaller than either C_{11} or C_{22} suggest that thermal expansion of the material will occur predominantly along direction perpendicular to the uranyl silicate sheets. This is consistent with the fact that intersheet space containing the hydrated Ca ions and free water molecules will increase as temperature increases. The diagonal component C_{11} (a direction contained in the plane of the uranyl silicate sheets, see Fig. 8.1.A) is the largest.

If single crystal samples are not available, the measure of the individual elastic constants cannot be possible. Instead, the polycrystalline bulk modulus (B) and shear modulus (G) may be determined experimentally. The Voigt (1962) and Reuss (1929) schemes were used to compute the isotropic elastic properties of uranophane polycrystalline aggregates as in our previous studies of rutherfordine and soddyite minerals (Colmenero *et al*., 2017a,c). As shown by Hill (1952), the Reuss and Voigt approximations result in lower and upper limits, respectively, of polycrystalline constants and practical estimates of the polycrystalline bulk and shear moduli in the Hill approximation can be computed using average formulas. Relevant formulae for these approximations may be found in Section 3.2.9. The bulk and shear moduli and other mechanical properties computed in the Voigt, Reuss and Hill approximations are given in Table 8.2.

The numerical estimate of the error in the computed bulk modulus given by the CASTEP code is 2.455 GPa, is reasonable and very similar to the the difference of the values in the Hill and Voigt/Reuss schemes, 2.721 GPa. Thus, we estimate the error to be about 5%. Voigt and Reuss methods yield quite small differences for uranophane-α. Larger differences are expected for

crystalline systems with strong anisotropy, featuring large differences between elastic constants along different directions (Weck *et al*., 2015; Colmenero *et al*., 2017a).

Table 8.2. Bulk, modulus, shear modulus, Young modulus, Poisson ratio, Pugh's ratio, and Vickers hardness (B, G, E, ν, D, and H) calculated ind the Voigt, Reuss, and Hill approximations. Values of B, G and E, are given in GPa.

Property	Voigt	Reuss	Hill
$\boldsymbol{B}$	61.9215	56.4799	59.2007
$\boldsymbol{G}$	38.9723	34.0691	36.5207
$\boldsymbol{E}$	96.6419	85.0969	90.8752
$\boldsymbol{\nu}$	0.2399	0.2489	0.2442
$\boldsymbol{D}$	1.5889	1.6578	1.6210
$\boldsymbol{H}$	6.9163	5.7218	6.3253

In general, a large value of shear moduli is an indication of the more pronounced directional bonding between atoms (Ravindran *et al.*, 1998). Shear modulus represents the resistance to plastic deformation while the bulk modulus represents the resistance to fracture (Bouhadda *et al.,* 2012; Ravindran *et al*., 1998). Young modulus defines the relationship between stress (force per unit area) and strain (proportional deformation) in a material, that is, $E = \sigma/\varepsilon$. It is possible to get the individual components of of Bulk and Young's moduli from the elastic compliance matrix components (Weck *et al*., 2015; Bouhadda *et al*., 2012; Ravindran *et al*., 1998). Compliance matrix is the inverse of stiffness C matrix. The corresponding values for our structure are given in Table 8.3. As it can be seen, B_c is much smaller than either B_a or B_b. Thus, c direction is the most compressible one. Also, the component E_c is much smaller (less stiff) than E_a and E_b. Thus, direction perpendicular to the plane containing the uranyl silicate sheets is the most compressible and least stiff in agreement with results of elasticity C matrix.

Table 8.3. Bulk and Young moduli components along the crystallographic axes. All values are given in GPa.

Property	*a* axis	*b* axis	*c* axis
$\boldsymbol{B}$	246.35	221.84	109.43
$\boldsymbol{E}$	139.47	138.26	91.33

Pugh (1954) introduced the proportion of bulk to shear modulus of polycrystalline phases ($D = B/G$) as a measure of ductility by considering the interpretation of the shear and bulk modulus given above. A higher D value is usually associated with higher ductility and the critical value which separates ductile and brittle materials is 1.75, i.e., if $B/G > 1.75$, the material behaves in a ductile manner, otherwise the material behaves in a brittle manner (Bouhadda *et al*., 2012). The Poisson's ratio, ν, can also be utilized to measure the malleability of crystalline compounds and is related to the Pugh's ratio given above by the relation $D = (3 - 6\nu) / (8 + 2\nu)$. The Poisson's ratio is close to 0.33 (1/3) for ductile materials, while it is generally much less than 0.33 for brittle materials. As it can be seen in Table 8.2, for uranophane we find ratios D and ν about 1.62 and 0.24, respectively. These values are only slightly smaller than 1.75 and 0.33, respectively, corresponding to a brittle material. For comparison, both studtite and metastudtite were found to be ductile (Weck *et al*., 2015).

Hardness of these systems is computed according to a recently introduced empirical scheme (Niu *et al.*, 2011; Chen *et al.*, 2011) which correlates the Vickers hardness and the Pugh's ratio ($D = B/G$). Vickers hardness, H, of polycrystalline uranophane is given in Table 8.2. Its value, about

6.3, corresponds to material of intermediate hardness. For comparison, we can compute the hardness of studtite and metastudtite using the elasticity data of Weck *et al.* (2015). These systems, characterized by much larger D ratios, have much smaller hardnesses (smaller than one). Uranophane has a hardness close to that of soddyite uranyl silicate mineral for which we have computed a hardness value about 6.3 (Colmenero *et al.*, 2017c).

In order to assess the elastic anisotropy of uranophane, shear anisotropic factors were obtained. These factors provide a measure of the degree of anisotropy in the bonding between atoms in different planes and are very important to study material durability (Bouhadda *et al.*, 2012; Ravindran *et al.*, 1998). Shear anisotropic factors for the $\{100\}$ (A_1), $\{010\}$ (A_2), and $\{001\}$ (A_3), crystallographic planes and percentages of anisotropy in compression and shear (A_{comp} and A_{shea}) were computed using the formulae given by Ravindran *et al.* (1998). For an isotropic crystal, the factors A_1, A_2, and A_3 must be one, while any value smaller or greater than unity is a measure of the degree of elastic anisotropy possessed by the crystal. For percentage anisotropies, a value of 0% represents a perfectly isotropic crystal. For uranophane (see Table 8.4), the anisotropies grow in the planes $\{100\}$, $\{010\}$, and $\{001\}$ ($A_1 < A_2 < A_3$). The $\{100\}$ plane is shown to be the most anisotropic one. Percentage anisotropies in compression and shear are about 5 and 7 %, respectively.

In the recently introduced universal anisotropy index (Ranganathan and Ostoja-Starzewski, 2008), the departure of A^U from zero defines the extent of single crystal anisotropy and accounts for both the shear and the bulk contributions unlike all other existing anisotropy measures. Thus, A^U represents a universal measure to quantify the single crystal elastic anisotropy. Uranophane is characterized by an anisotropy index of 0.81, which is a rather small value ($A^U = 0$ corresponds to a perfectly isotropic crystal). For comparison, studtite and metastudtite exhibit much larger anisotropies. The values computed by Weck *et al.* (2015) are 2.17 and 1.44, respectively. Soddyite mineral calculations result in a value of A^U of 0.50 (Colmenero *et al.*, 2015c). Therefore, soddyite and uranophane uranyl silicate minerals are characterized by small anisotropies.

Table 8.4. Shear anisotropy factors (A_1, A_2, and A_3), percentages of anisotropy in compression and shear (Acomp and Ashear), and universal anisotropy index (A^U).

A_1	A_2	A_3	A_{comp} (%)	A_{shear} (%)	A^U
0.4448	0.5094	0.6301	4.5959	6.7129	0.8159

A set of fundamental physical properties may be estimated using the calculated elastic constants. For example, V_L and V_T, the transverse and longitudinal elastic wave velocities of the polycrystalline materials may be determined in terms of the bulk and shear moduli (Weck *et al.*, 2015). The values obtained are 3.069 and 5.276 km/s, respectively, using the calculated crystal density of 3.877 gr/cc (see Table 8.1).

8.3.3 Equation of State

Lattice volumes around the equilibrium were calculated by optimizing the structure at seventeen different applied pressures between -1.0 and 12.0 GPa. The calculated data were then fitted to a fourth-order Birch-Murnaghan equation of state (EOS, see equation (3.150)) using the computed volume at 0 GPa (733.6 Å^3) as V_0 using the EOSFIT 5.2 code (Angel, 2001). The values found for the bulk modulus and its first and second derivatives at the temperature of 0 K, were $B = 59.96$ (± 2.1) GPa, $B' = 2.29$ (± 1.11), and $B'' = -0.25$ (± 0.19) $(\chi 2 = 0.014)$. The value obtained for the bulk modulus agrees very well with that determined from elastic constants. For comparison, the bulk modulus obtained in the Hill approximation is $B = 59.20 \pm 2.45$ GPa.

8.3.4 Raman Spectra and Band Assignment

In this section, we analyze the theoretically determined Raman spectrum and compare the main band wavenumbers obtained with the corresponding values found experimentally in the literature (Frost *et al*., 2006a,c) for this mineral phase. Additional information about the Raman spectrum of uranophane can be found in Amme *et al.* (2002), Bonales *et al.* (2015), Driscoll *et al.* (2014) and Wall *et al.* (2010). The experimental band wavenumbers of Frost *et al.* (2006a,c) are given in Table 7 of the article (Colmenero *et al.,* 2017e) being their assignments also given in this Table. Experimental and calculated Raman shifts, calculated intensities and assignations are given in Table 8.5. For the purpose of visual comparison, the spectrum computed at T=298 K, λ=532 nm, FWHM=20 cm-1 is shown in Figure 8.3, where it is compared with an experimental spectrum of RRUFF database (Downs, 2006; record RRUFF-050380). As can be seen in Figure 8.3, the calculated spectrum is very similar to the experimental one. Pictures of the atomic motions in some of the Raman active vibrational modes are given in Appendix 8.A (Figure 8.A.1).

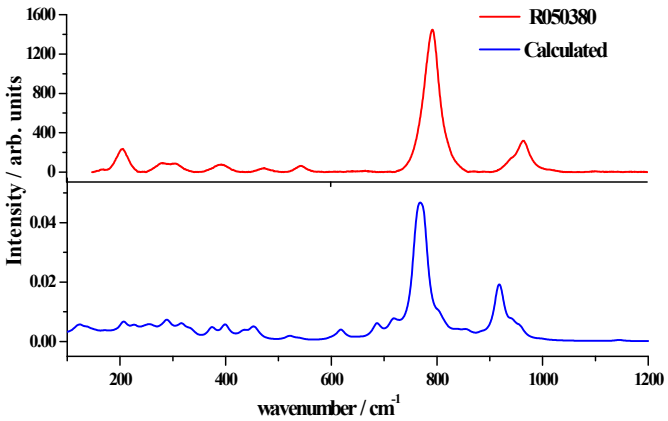

Figure 8.3. Raman spectra of uranophane-α mineral. a) RRUFF-050380 (Downs, 2006); b) Calculated.

Although the bands in the OH stretching region seems to be quite variable from one sample to another, most bands are well reproduced theoretically. Wavenumbers of these bands observed in the experimental samples are generally comparable but not identical (Frost *et al*., 2006a,c). This supports the presence of mobile protons that may be exchanged between the uranyl silicate sheets and the interlayer and influence the hydrogen-bonding networks in their crystal structures (Cejka, 1999; Frost *et al.*, 2006c). We find experimental bands centered at about 3492, 3463, 3358, 3326, 3310, 3216 and 3142, cm^{-1}, which can be compared with the calculated wavenumbers of 3485, 3478, 3357, 3295, 3272, 3238, and 3149 cm^{-1}. It should be underlined that theoretical methods allow to distinguish the origin of these bands which may be assigned to specific stretching vibrations. The first two ones are attributed to OH stretching vibrations of crystallization water molecules (labelled as *cr* in Table 8.5). The next three bands are instead due to vibrations localized on structural (coordinated) water molecules (labelled as *st* in Table 8.5). The next one is ascribed to vibrations in crystallization and structural water molecules and OH stretching vibrations in SiO_3OH fragments including OH groups which do not form part of the Ca atom coordination sphere (referred to as *fr* in Table 8.5). Finally, the last band is assigned to vibrations in structural water molecules and SiO_3OH fragments including OH groups which are not coordinated with interlayer Ca atoms. In previous experimental works, all these bands were attributed without specification to OH stretching vibrations in the water molecules. As it can be seen, the bands at lower wavenumbers contain also contributions from OH stretching vibrations in the free SiO_3OH fragments. Frost *et al*. (2006a), placed these vibrations at wavenumbers higher than 3600 cm^{-1}.

Table 8.5 Experimental and calculated Raman band frequencies, calculated intensities and assignations.

Exp. Raman shift (cm^{-1})	Calc. Raman shift (cm^{-1})	Irr. Rep. (C_{2v})	Intensity ($Å^4$)	Assignation
3492 (a)	3485	B	543.453	ν(OH) [*cr*-H_2O]
3463 (a)	3478	A	234.841	
3358 (a)	3359	B	206.215	ν(OH) [*st*-H_2O]
	3357	A	241.922	
3326 (b)	3295	B	1298.612	
3310 (b)	3272	B	1627.297	
3216 (a)	3238	B	2003.074	ν(OH) [*cr*- and *st*-H_2O and *fr*-SiOH]
	3222	B	638.256	
3142 (b)	3149	B	2468.104	ν(OH) [*st*-H_2O and *fr*-SiOH]
1272 (b)	1222	B	22.349	δ(*co*-SiOH)
1169 (b)	1146	B	13.621	δ(*fr*-SiOH)
964, 960 (a)	958	B	102.979	δ(*co*-SiOH)+l(H_2O)
950 (a)	942	B	126.692	
886 (a)	884	B	25.099	δ(SiOH)+l(H_2O)
839 (a)	857	A	23.425	ν(*fr*-SiO)+l(H_2O)
	837	B	25.221	δ(SiOH)+l(H_2O)
	813	B	29.204	δ(SiOH)+l(H_2O)+ν(UO_2)
797, 793 (a)	804	B	113.942	δ(SiOH)+l(H_2O)+ν(UO_2)
	776	B	767.503	δ(*fr*-SiOH)+l(H_2O)+ν(UO_2)
786 (a)	766	B	504.625	δ(*fr*-SiOH)+l(H_2O)+ν(UO_2)
	760	B	521.123	
711 (a)	717	B	103.711	δ(*fr*-SiOH)+l(H_2O)
	686	B	104.691	
627 (b)	618	B	72.848	δ(*co*-SiOH)+l(H_2O)
545 (a)	539	B	8.337	l(H_2O)
525 (b)	524	B	9.467	δ(*co*-SiO_3OH)+l(H_2O)
	519	B	15.642	δ(*fr*-SiO_3OH)+l(H_2O)
469 (a)	459	B	21.980	δ(*co*-SiO_3OH)+l(H_2O)
	452	B	48.164	δ(*fr*-SiO_3OH)+l(H_2O)
444 (b)	434	B	29.965	δ(*co*-SiO_3OH)+l(H_2O)
399 (a)	399	B	61.655	δ(*co*-SiO_3OH)+l(H_2O)
376 (a)	374	B	44.165	δ(*fr*-SiO_3OH)+δ(UO_2)+l(H_2O)
347 (a)	333	A	11.578	δ(*fr*-SiO_3OH)+δ(UO_2)+l(H_2O)
325 (a)	317	B	12.801	δ(SiO_3OH)+ δ(UO_2)+l(H_2O)
306 (a)	316	A	23.824	δ(*co*-SiO_3OH)+δ(UO_2)+l(H_2O)
289 (a)	289	A	18.128	δ(*co*-SiO_3OH)+δ(UO_2)+l(H_2O)
	288	B	9.997	δ(SiO_3OH)+δ(UO_2)+l(H_2O)
280 (a)	276	A	11.180	δ(*fr*-SiO_3OH)+δ(UO_2)+l(H_2O)
250 (a)	256	B	13.132	δ(SiO_3OH)+δ(UO_2)+l(H_2O)
214 (a)	226	A	17.045	δ(SiO_3OH)+δ(UO_2)+l(H_2O)
205 (a)	206	B	18.514	δ(SiO_3OH)+δ(UO_2)+l(H_2O)
167 (a)	186	A	4.163	δ(SiO_3OH)+δ(UO_2)+l(H_2O)
	175	B	3.374	δ(SiO_3OH)+δ(UO_2)+l(H_2O)
139 (a)	138	B	4.891	δ(*co*-SiO_3OH)+δ(UO_2)+l(H_2O)
137 (a)	135	A	1.229	δ(*co*-SiOH)+l(H_2O)
122 (a)	126	B	7.777	δ(SiO_3OH)+δ(UO_2)+l(H_2O)
112 (a)	119	B	4.741	δ(SiO_3OH)+δ(UO_2)+l(H_2O)

(a) R.L. Frost, *et al.*, 2006a.
(b) R.L. Frost, *et al.*, 2006c.

However, in other works (see Frost *et al*., 2006a,c), OH stretching vibrations at SiO_3OH groups at about 3200 cm^{-1} were reported on the basis of the infrared spectra.

The water bending vibration is not observed in the experimental Raman spectra and, accordingly, the corresponding computed band, at 1639 cm^{-1}, has a very small intensity (see vibrational mode picture in Appendix 8.A).

Experimental bands located at 1272 and 1156 cm^{-1} are placed at 1222 and 1146 cm^{-1} in the computed spectrum. These are assigned, respectively, to SiOH bending vibrations localized in SiO_3OH fragments including OH groups which are coordinated with interlayer Ca atoms (referred to as *co*, in Table 8.5), and in free SiO_3OH fragments (referred to as *fr* in Table 8.5, as it has already been mentioned), respectively.

The experimental bands at 960 and 950 cm^{-1} are close the theoretical ones located at wavenumbers 958 and 942 cm^{-1}, respectively. These bands are ascribed to SiOH bending vibrations localized in SiO_3OH fragments including coordinated OH groups, δ(*co*-SiOH), and water librations. These bands were however assigned to silicate stretching vibrations, $\nu^s(SiO_4^{4-})$ (ν_1) in most experimental works (Frost *et al*., 2006a,c; Amme *et al.*, 2002; Bonales *et al.*, 2015; Driscoll *et al.*, 2014; Wall *et al*., 2010). This assignment seems therefore not to be correct. It must also be noted that the correspondence with symmetric vibrations of the free silicate group are lost for uranophane (monoclinic symmetry) as it can be seen in the vibrational mode pictures given in Appendix 8.A. The contribution of SiO_3OH group vibrations to these modes is very small. A band appears in the calculated spectrum at 915 cm^{-1} which is assigned to SiO stretching vibrations of the SiO_3OH fragments with coordinated OH groups (see vibrational mode picture in Appendix 8.A). Thus, silicate stretching vibrations appears at smaller wavenumbers than those reported in the experimental works.

The band placed at 886 cm^{-1} is obtained theoretically at 884 cm^{-1} and that at 839 cm^{-1} is calculated to be at 837 cm^{-1}. Both bands are assigned to SiOH bending vibrations (localized in *fr* and *co* SiO_3OH fragments) and water librations.

The band placed at 797 cm^{-1} is the most intense of the Raman spectrum and it is calculated to be at 776 cm^{-1}. This band is assigned in the experimental works (Frost *et al*., 2006a,c; Amme *et al*., 2002; Bonales *et al*., 2015; Driscoll *et al.*, 2014; Wall *et al*., 2010), to symmetric uranyl stretching vibrations $\nu^s(UO_2^{2+})$. However, our calculations show that it is the result of a combination of vibrations including SiOH vibrations localized in *fr*-SiO_3OH fragments, uranyl stretching vibrations, and water librations. The uranyl vibrations make one a small contribution to this mode. As it has already been mentioned the symmetry of this vibration is lost and therefore the term symmetric should not be used. A weak band at 786 cm^{-1} is also observed and it is comparable to calculated bands at 760 and 766 cm^{-1} having the same assignation that the intense band at 798 cm^{-1}.

For the bands at 711, 627, 544, 525, 469, 444, and 399 cm^{-1} we obtain the theoretical counterparts 717, 618, 539, 519, 452, 434, and 399 cm^{-1} which correspond to different *fr* and *co* SiOH bending vibrations. The band placed at 544 cm^{-1} and found at 539 cm^{-1} it is attributed to water librational vibrations only.

Uranyl bending vibrations begin to appear at about 376 cm^{-1}. Bands at wavenumbers 376, 347, 325, 306, 289, 280, 250, 214, 205, 167, 139, 137, 122 and 112 cm^{-1} are close to the calculated bands at 374, 333, 317, 316, 289, 276, 256, 226, 206, 186, 137, 135, 126, and 119 cm^{-1}. Most of them are assigned to a combination of silicate, SiO_3OH, deformations (localized in *fr* or *co* groups), uranyl bending vibrations and water librations. The bands in this region were assigned by Frost *et al.* (2006a) to uranyl bending vibrations. However, it must be pointed out that uranyl bending vibration is only a contribution, generally small, to these modes and is accompanied by silicate deformation vibrations and water librations. The precise assignations are given in Table 8.5.

It must be emphasized that band assignment is a very difficult task in the case of complex systems having low symmetry. While the assignations made by correlating the bands with those of free fragments (Nakamoto, 1986; Cejka, 1999) are generally very useful to understand the origin of the bands which are experimentally found, these correspondences cannot always be made, especially for many systems with low symmetry (monoclinic in this case). For example, as it is shown here, vibrations with specific motions similar to those of free silicate fragment ($\nu_3(SiO_4^{4-})$, $\nu_1(SiO_4^{4-})$, $\nu_4(SiO_4^{4-})$ and $\nu_2(SiO_4^{4-})$) and free uranyl fragment ($\nu_3(UO_2^{2+})$, $\nu_1(UO_2^{2+})$ and $\nu_2(UO_2^{2+})$) are not found for uranophane-α.

8.3.5 Sr-Exchanged Uranophane-α

The possibility of incorporation of Strontium in the structure of uranophane-α was investigated by Douglas *et al.* (2002). This research was made in order to analyze if this 1:1 uranyl silicate may serve as a host for the incorporation of fission products by substitution of Ca^{2+} in the interlayer spaces in the solid. Uranophane-α was synthetized by these authors and Ca^{2+} was exchanged completely or partially in the structure. The resulting solid was then characterized by X-Ray diffraction, scanning electron microscopy (SEM) and elemental analysis. The Sr^{2+} analog of uranophane yielded a diffractogram that resembles the XRD pattern obtained for synthetic uranophane, although the morphology of the solid is different from that of normal uranophane.

Theoretical methods allow to study this incorporation in a simple way free of the difficulties associated to the radiotoxicity of these materials. We have studied the Sr-exchanged uranophane material by replacing the Ca^{2+} ion by Sr^{2+} in the structure of uranophane and performing a structural reoptimization under the same theoretical conditions as for normal uranophane. According to the table 8.6, the crystal structure experimented very small variations upon exchange. The interlayer cation solvation sphere was very similar to that of normal uranophane. The same structure was obtained when the calculations were made from different initial forms of the hydrogen bond structure in the interlayer space. The corresponding lattice parameters are given in Table 8.6. As it can be seen, the main variation is the increase of the interlayer space, corresponding to an increase of 0.35 Å of the *c* lattice parameter. The change of *a* and *b* lattice parameters was only of about 0.02 Å. The volume is increased approximately 3%. These results may be compared with those of Berghout *et al.* (2010) for the Ca- and Sr-exchanged two layer montmorillonites. In this case, the computed increase in the *c* lattice parameter was of 0.21 Å and the unit cell volume increased by 2.4%.

Table 8.6. Lattice parameters of normal and Sr-exchanged uranophane-α.

Parameter	*a* (Å)	*b* (Å)	*c* (Å)	α	β	γ	Vol. (Å^3)	Dens. (g/cm^3)
Calculated (Ca)	6.6689	7.0022	15.8684	90.0	98.0748	90.0	733.65	3.877
Calculated (Sr)	6.6959	7.0233	16.2127	90.0	97.3650	90.0	756.15	3.970

The X-Ray powder diffractograms of normal and Sr-exchanged uranophane were obtained from the optimized atomistic positions using program REFLEX included in Materials Studio package (Materials Studio, 2017). As expected from the study of Douglas *et al.* (2002), the diffractograms of both forms is very similar and are given in Figure 8.4.

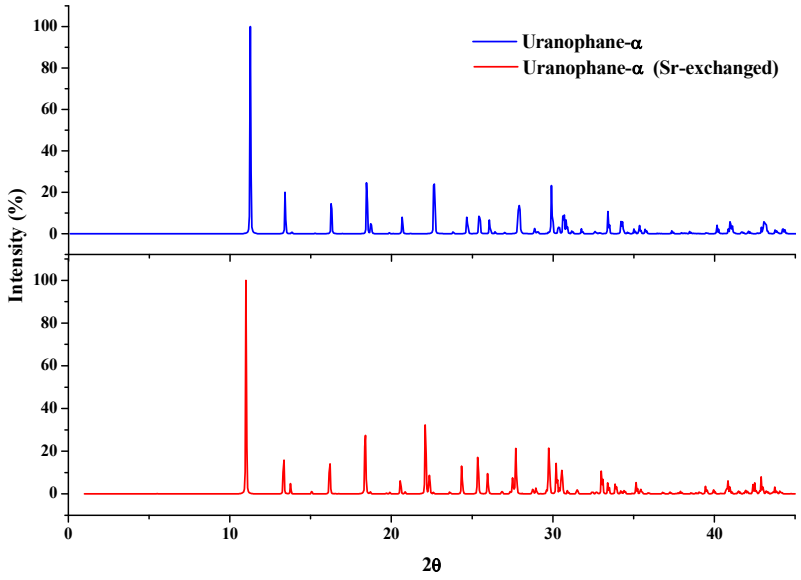

Figure 8.4. Computed X-Ray powder diffractograms of normal and Sr-exchanged uranophane.

In order to know whether we can differentiate these materials by Raman spectroscopy we computed the corresponding spectra of Sr-exchanged uranophane using Density Functional Perturbation Theory. The corresponding spectra, were again very similar and are given in Figure 8.5.

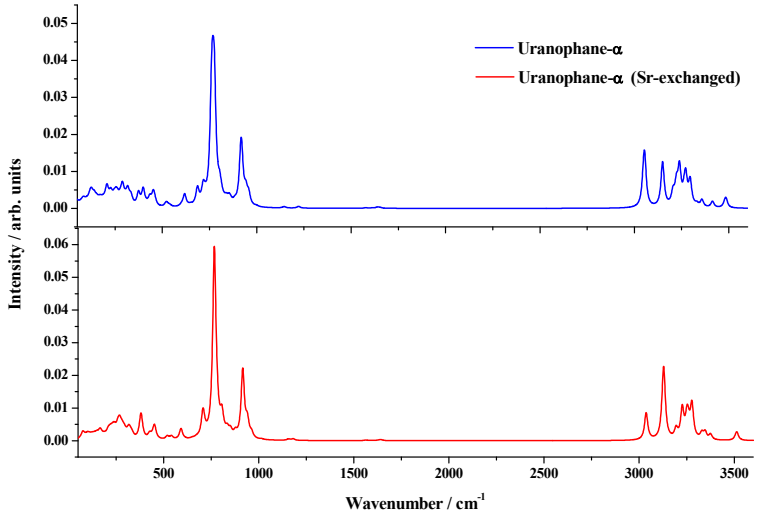

Figure 8.5. Computed Raman spectra of normal and Sr-exchanged uranophane.

Since the motion of the interlayer cation do not appears in any of the main bands in the Raman spectrum (see vibrational mode pictures in Figure 8.A.1 of Appendix 8.A) and the solvation structure of the interlayer cation remain almost unchanged, the Raman spectra of normal and Sr-exchanged uranophane are very close. In summary, we have found that the incorporation of Sr^{2+} in the structure of uranophane by cation exchange is possible in accordance with the experimental results of Douglas *et al.* (2002) and that the identification of the exchanged solid cannot be made neither by X-ray diffraction nor Raman spectroscopy.

APPENDIX 8.A. Raman Active Normal Modes of Uranophane-α.

Figure 8.A.1 The atomic motions associated to some Raman active vibrational normal modes of Uranophane-α.

Note that the abbreviations *cr* and *st* will be used to distinguish crystallization and structural water molecules. Note also that the labels *fr* and *co* will be employed to denote SiO_3OH fragments with free and coordinated OH groups. If none of these labels is given both kinds of fragments are involved.

Mode ν=3485 cm^{-1} – ν(OH) [*cr*-H_2O] – OH stretching.

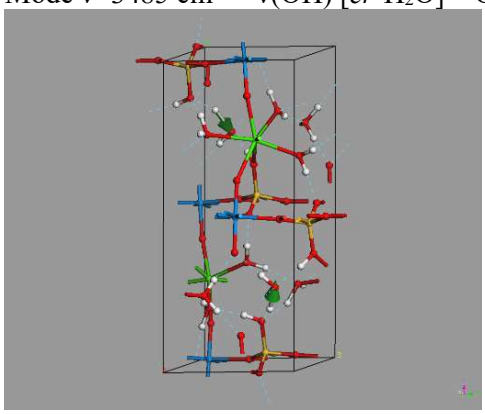

Mode ν=3357 cm^{-1} – ν(OH) [*st*-H_2O] – OH stretching.

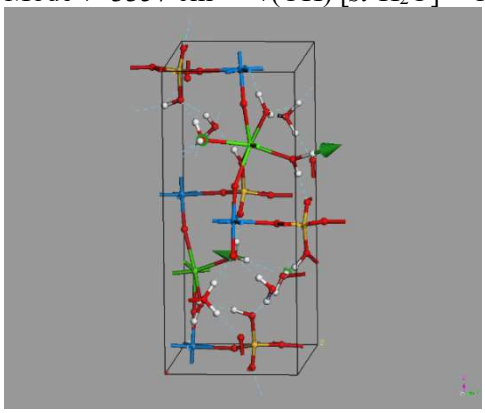

Mode ν=3238 cm^{-1} – ν(OH) [*cr*- and *st*-H_2O and *fr*-SiOH] – OH stretching.

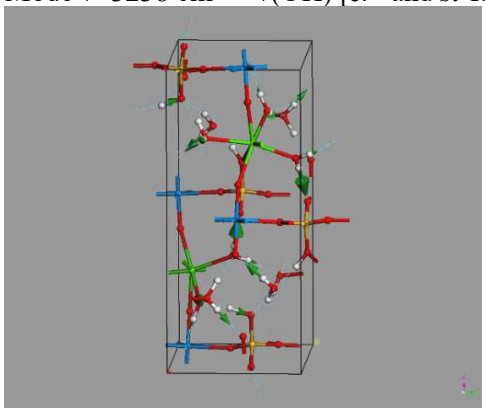

Mode ν=3149 cm^{-1} – ν(OH) [*st*-H_2O and *fr*-SiOH] – OH stretching.

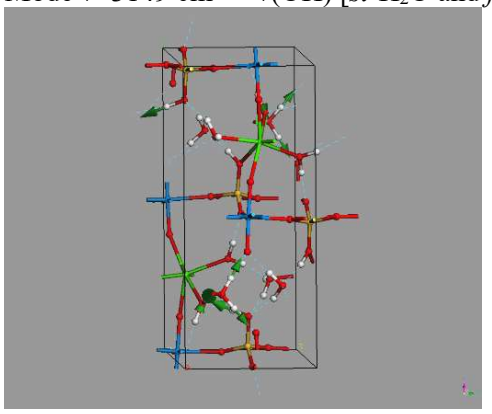

Mode ν=1639 cm^{-1} – δ(H_2O) – H_2O bending.

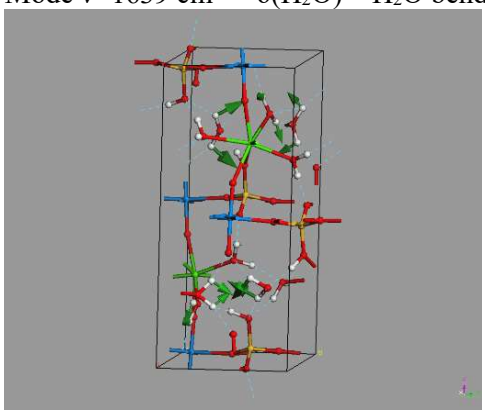

Mode ν=1222 cm^{-1} – δ(*co*-SiOH) – SiOH bending.

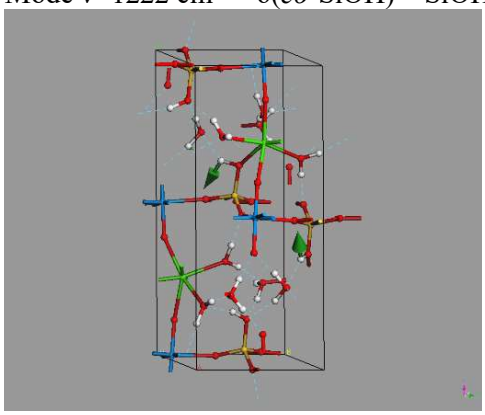

Mode ν=1146 cm^{-1} – δ(*fr*-SiOH) – SiOH bending.

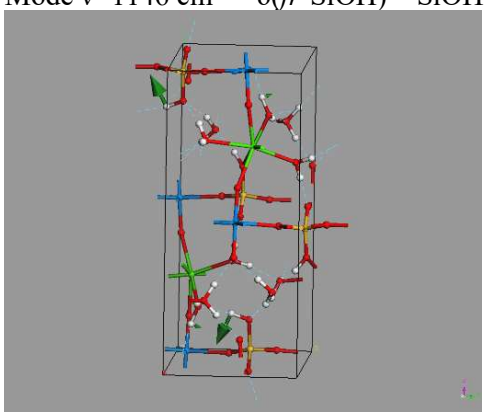

Mode ν=942 cm^{-1} – δ(*co*-SiOH)+l(H_2O) – SiOH bending plus water librations.

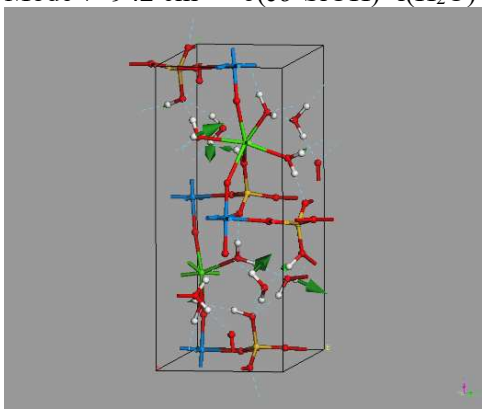

Mode ν=915 cm^{-1} – ν(*co*-SiO)+l(H_2O) – SiO stretching plus water librations.

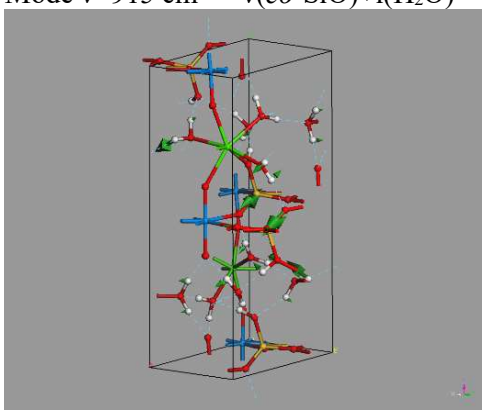

Mode ν=837 cm^{-1} – δ(SiOH)+l(H_2O) – SiOH bending plus water librations.

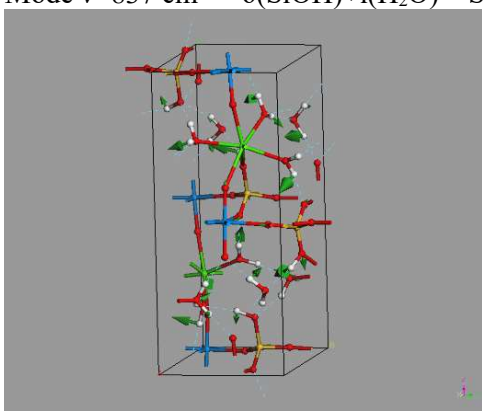

Mode ν=776 cm^{-1} – δ(*fr*-SiOH)+l(H_2O)+ν(UO_2) – SiOH bending + water librations + uranyl UO stretching.

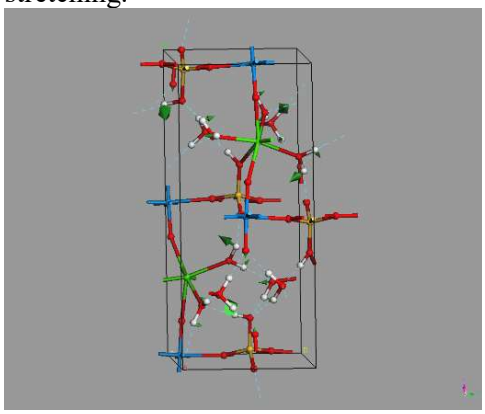

Mode ν=686 cm^{-1} – δ(*fr*-SiOH)+l(H_2O) – SiOH bending plus water librations.

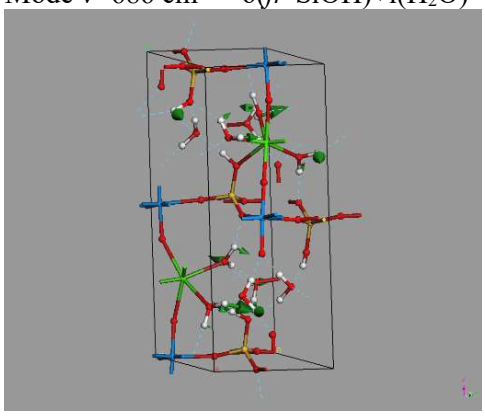

Mode ν=618 cm^{-1} – δ(*co*-SiOH)+l(H_2O) – SiOH bending plus water librations.

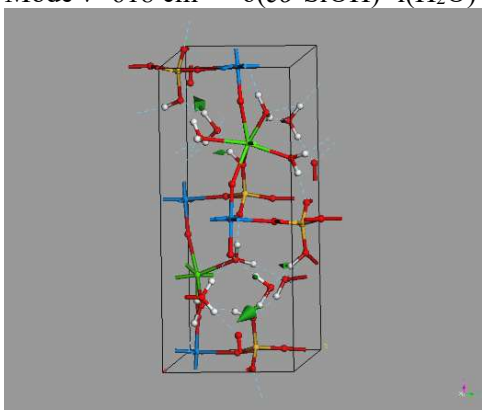

Mode ν=539 cm^{-1} – l(H_2O) – water librations.

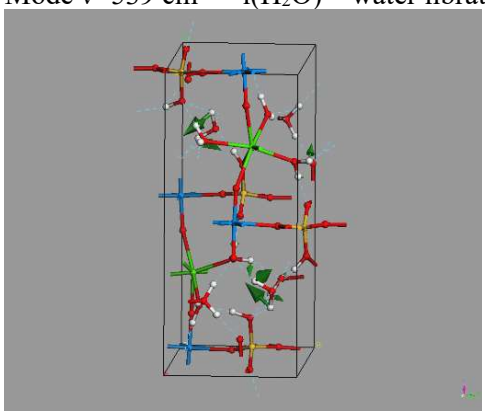

Mode ν=524 cm^{-1} – δ(*co*-SiO_3OH)+l(H_2O) – SiO_3OH deformation + water librations.

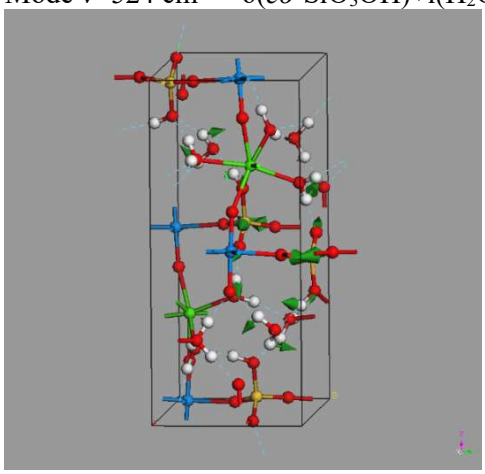

Chapter 9. Uranium-Oxygen Bond-Length to Uranyl Symmetric Stretching Raman Shift relationship.

This chapter is based on the published article "*Relation of uranium-oxygen bond length and uranyl symmetric stretching Raman shift obtained from theoretical DFT calculations*", by F. Colmenero, L. J. Bonales, J. Cobos and V. Timón, J. Mol. Struct. (to be submitted)

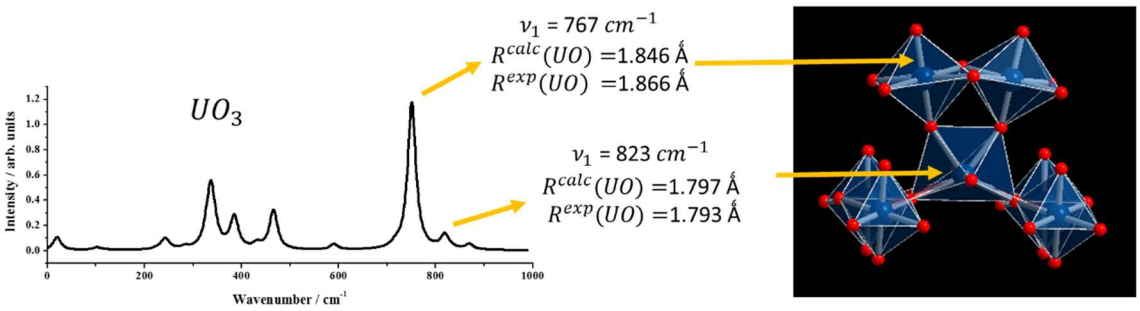

Abstract

An expression for the uranium-oxygen bond length in terms of the uranyl symmetric stretching Raman shift was obtained by means of a least-squares fit of data from theoretical solid state Density Functional Theory calculations of a small set of uranyl containing materials. The resulting expression provides bond-lengths with an accuracy comparable to that obtained previously from a large set of experimental results. The average deviation of calculated bond-length values with respect to experimental ones for a large set of materials is 3.5 pm.

9.1 Introduction

Based in Badger's relation (Badger, 1935), approximate expressions relating the uranium-oxygen bond length with spectroscopy data have been derived (Jones, 1958, 1959; McGlynn *et al.*, 1961; Carnall *et al.*, 1965; Bullock, 1969; Veal *et al.*, 1975; Bartlett and Cooney, 1989) and used extensively in the research of uranyl containing systems (Frost *et al.*, 2005-2011; Plasil *et al.*, 2013; Hoekstra and Siegel, 1961; Faulques *et al.*, 2015b; Ohwada, 1980; Gal *et al.*, 1984; Zhang *et al.*, 2014: Shepherd *et al.*, 2016; Biswas *et al.*, 2016; Servaes *et al.*, 2007; Ramirez *et al.*, 2017; Falaise *et al.*, 2017; Martin *et al.*, 2016; Henry *et al.*, 2011; Hao *et al.*, 2016). The most widely used of these expressions is that of Bartlett and Cooney (1989) relating the uranium-oxygen bond length with the uranyl symmetric stretching Raman shift. These relations have been employed by many research groups (Frost *et al.*, 2005-2011; Plasil *et al.*, 2013; Hoekstra and Siegel, 1961; Faulques *et al.*, 2015b) in order to rationalize the results of Raman and Infrared spectroscopy of solid materials by correlating them with the uranyl group geometries obtained from X-Ray diffraction. However, these expressions are particularly useful to investigate solid materials in which crystallographic methods are difficult to apply and in the study of uranyl complexes in solution (Ohwada, 1980; Gal *et al.*, 1984). They may also be used, for example, to follow the changes in UO bond upon variations of the experimental conditions, *i.e.* temperature and pressure (for instance in dehydration experiments), or along the course of chemical reactions (Zhang *et al.*, 2014: Shepherd *et al.*, 2016; Biswas *et al.*, 2016; Servaes *et al.*, 2007; Ramirez *et al.*, 2017; Falaise *et al.*, 2017; Martin *et al.*, 2016; Henry *et al.*, 2011; Hao *et al.*, 2016) using *in situ* spectroscopic measurements.

In this communication, we report an expression relating uranium-oxygen bond length and the uranyl symmetric stretching Raman shift similar to that of Bartlett and Cooney (1989), deduced from a least squares fit to a set of data obtained from theoretical density functional theory (DFT) (Hohenberg and Kohn, 1964; Kohn and Sham, 1965; Parr and Yang, 1994) calculations on uranyl containing materials (Bonales *et al.*, 2016a; Colmenero *et al.*, 2017a-e). These calculations were carried out employing plane waves and pseudopotentials (Payne *et al.*, 1992). A new norm conserving relativistic pseudopotential (Troullier and Martins, 1991) for uranium atom generated from first principles in our previous work (Bonales *et al.*, 2016a) was employed opening the possibility of performing complete theoretical solid-state calculations of the Raman spectra of uranyl containing materials. The methods used are presented in Section 2. In Section 3, our relation is reported and discussed.

9.2 Methods

We use a UO bond length to wavenumber relation of the form:

$$R_{UO} = a \cdot {\nu_1}^{-b} + c$$

where $b = \frac{2}{3}$. In order to obtain approximate values of the remaining parameters a and c, we use a least squares analysis of the data presented in Table 9.1. The values given in this table were

obtained from ab initio theoretical solid state DFT calculations (Bonales *et al.*, 2016a; Colmenero *et al.*, 2017a-e).

Table 9.1. UO bond lengths and UO symmetric stretching uranyl symmetric stretching Raman shifts used in the least squares analysis.

System	$\nu_1\ (cm^{-1})$	$R_{UO}(pm)$
Rutherfordine	886.5	176.4
Studtite	797.6	180.7
Soddyite	806.8	180.1
Uranophane-α	775.6	183.1
α-$UO_2(OH)_2$	819.3	179.2
ϒ-UO_3	751.9	188.6
ϒ-UO_3	818.0	179.4

The calculations include six different uranyl containing materials: the uranyl carbonate rutherfordine, UO_2CO_3 (Bonales *et al.*, 2016a; Colmenero *et al.*, 2017a), the uranyl peroxide studtite, $(UO_2)(O_2)\cdot 4H_2O$ (Colmenero *et al.*, 2017b), the uranyl silicates soddyite, $(UO_2)_2(SiO_4)\cdot 2(H_2O)$ (Colmenero *et al.*, 2017c), and uranophane-α, $Ca(UO_2)_2(SiO_3OH)_2\cdot 5H_2O$ (Colmenero *et al.*, 2017e), the uranyl hydroxide dehydrated schoepite, α-$UO_2(OH)_2$ (Colmenero *et al*., 2017g), and the uranyl oxide, ϒ-UO_3 (Colmenero *et al.*, 2017d). The unit cells of these materials were modelled with the help of CASTEP code (Clark *et al*., 2005), a module of Materials Studio package (Materials Studio, 2017).

The generalized gradient approximation (GGA) together with two different functionals were employed (Perdew *et al.*, 1996). In the case of rutherfordine and uranium trioxide, the PBESOL functional (Perdew *et al.*, 2008) was utilized. For the remaining four materials, the PBE functional (Perdew *et al.*, 1996), together with the Grimme empirical dispersion correction, the DFT-D2 approach (Grimme, 2006) was used in order to describe properly the hydrogen bonding present in the systems. Geometry optimization was carried out using the Broyden–Fletcher–Goldfarb–Shanno optimization scheme (Pfrommer *et al.*, 1997; Payne *et al.*, 1992) with a convergence threshold on atomic forces of 0.01 eV/Å. The different kinetic energy cutoffs and k-point meshes (Monkhorst and Pack, 1976) adopted were selected to ensure good convergence for computed structures and energies.

For the calculations of vibrational properties, the linear response density functional perturbation theory (DFPT) (Baroni *et al.*, 2001) implemented in the CASTEP code was used, where the phonon frequencies at the gamma point of the Brillouin zone were computed by using atomic displacement perturbations. These are calculated in CASTEP (Milman *et al.*, 2010) using a combination of perturbation theory (second derivative with respect to field) and finite differences (third derivative with respect to atomic displacement). The wavenumbers presented in this work have not been scaled to correct for anharmonicity and remaining errors of the theoretical treatment employed, such as incomplete treatment of electron correlation and basis set truncation (Hehre *et al.*, 1986). They correspond to the harmonic approximation of the force field. Since the effects of these defects tend to cancel out, the scale factor should be near to unity.

The pseudopotentials used for H, C, O, Si, and Ca atoms in the unit cells of these materials were standard norm-conserving pseudopotentials (Troullier and Martins, 1991) given in CASTEP code (00PBE-OP type). The norm-conserving relativistic pseudopotential for U atom was generated from first principles in our previous work (Bonales *et al.*, 2016a) and the reader may consult this

reference for more details about its construction and performance. The pseudopotential must be norm conserving; otherwise vibrational spectra cannot be determined with CASTEP software.

9.3 Results and Discussion

The least squares fit to the data given in Table 9.1 is showed if Figure 9.1, and the resulting parameters are given in Table 9.2, compared with those of Bartlett and Cooney (1989).

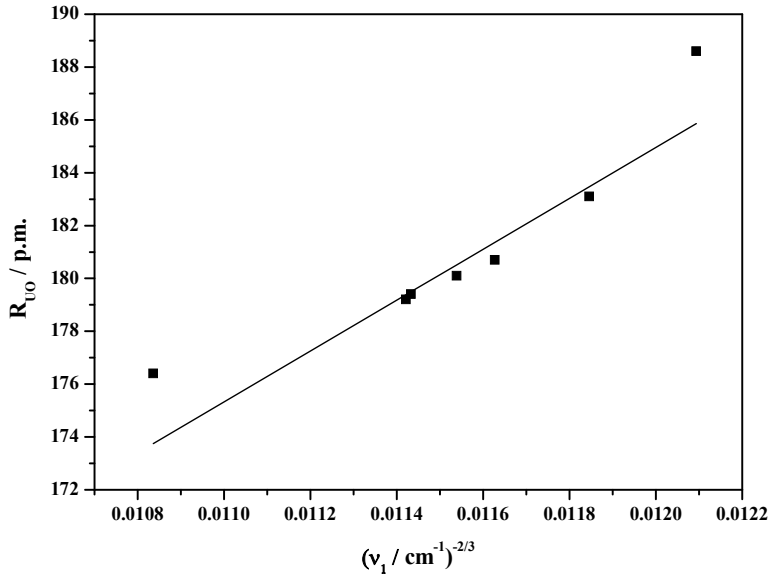

Fig. 9.1. Least squares fit to $(R_{UO}, {\nu_1}^{-2/3})$ data points. The data used in the fit is given in Table 9.1.

Table 9.2. Least squares fit results. The a and c parameters obtained in this work are compared with those of Bartlett and Cooney (1989).

Reference	a	c
This work	9096.149	76.081
Bartlett and Cooney (1989)	10650	57.5

By using these parameters and those of Bartlett and Cooney (1989), we can obtain the values of the uranium-oxygen bond distance for the same set of experimental uranyl symmetric stretching frequencies as in the work of these authors (Bartlett and Cooney, 1989). The resulting bond lengths are given in Table 9.3, compared with the experimental values. The averaged deviation of the calculated values (the sum of the absolute values of the errors divided by the number of systems considered) is 3.5 pm for both the relation obtained in this work and that of Bartlett and Cooney (1989). This fact is quite surprising since while this is the set used by these authors to derive the relation we have used only a small set of data derived from ab initio DFT theoretical calculations. It must be noted that the errors obtained by using the parameters obtained in this work seems to be smaller when the UO bond length is large and greater when the UO bond is short.

Table 9.3. Bond lengths obtained for a series of uranyl ion containing systems. Raman shifts and bond-lengths are given in units of cm^{-1} and pm respectively. The references for the experimental data may be found in the work of Bartlett and Cooney (1989).

System	ν_1^{Exp}	R_{UO}			Errors	
		This work	Bartlett and Cooney	Exp.	This work	Bartlett-Cooney
$UO_2Cl_2 \cdot 3H_2O$	879	175.2	173.6	165	-10.2	-8.6
UO_2CO_3	870	175.9	174.4	169	-6.9	-5.4
α-$UO_2(OH)_2$	848	177.6	176.4	170	-7.6	-6.4
$Na[UO_2(Ac)_3]$	856	177.0	175.6	171	-6.0	-4.6
$(Ph_3AsO)_2(UO_2)(NO_3)_2$	818	180.1	179.3	171	-9.1	-8.3
UO_2F_2	872	175.7	174.2	174	-1.7	-0.2
UO_2Cl_2	852	177.3	176.0	174	-3.3	-2.0
$[Et_4N][UO_2(S_2PMe_2)]Cl$	861	176.6	175.2	175	-1.6	-0.2
$UO_2(NO_3)_2 \cdot 6H_2O$	869	176.0	174.5	176	0.0	1.5
$K_3[UO_2F_5]$	803	181.4	180.8	176	-5.4	-4.8
$(Ph_3PO)_2UO_2(NO_3)_2$	848	177.6	176.4	176	-1.6	-0.4
$[(UO_2)_2(NO_3)_4(H_2O)_2] \cdot [C_3H_4N_2]_2$	856	177.0	175.6	177	0.0	1.4
$Rb(UO_2)(NO_3)_2$	879	175.2	173.6	178	2.8	4.4
$Na_3[UO_2)_2F_7] \cdot 6H_2O$	840	178.3	177.1	178	-0.3	0.9
$[(UO_2)_4O_2Cl_8(H_2O)_2]^{4-}$	833	178.8	177.8	178	-0.8	0.2
ϒ-UO_3	829	179.2	178.2	179	-0.2	0.8
$K_5(UO_2)_2F_9$	807	181.0	180.4	179	-2.0	-1.4
$(UO_2)_2(OH)_2Cl_2(H_2O)_4$	848	177.6	176.4	179	1.4	2.6
$UO_2(S_2PPh_2)_2 \cdot EtOH$	868	176.0	174.5	180	4.0	5.5
$Cs_3[UO_2F_5]$	784	183.1	182.8	180	-3.1	-2.8
β-$UO_2(OH)_2$	821	179.8	179.0	181	1.2	2.0
ϒ-$UO_2(OH)_2$	821	179.8	179.0	181	1.2	2.0
$[UO_2(NH_2O)_2(H_2O)_2] \cdot H_2O$	783	183.2	182.9	181	-2.2	-1.9
$Cs_2[UO_2Cl_4]$	831	179.0	178.0	181	2.0	3.0
UO_2Cl_2	766	184.7	184.7	181	-3.7	-3.7
$(NH_4)_2UO_2(SO_4)_2 \cdot 2H_2O$	836	178.6	177.5	182	3.4	4.5
$[Cs_4[(UO_2)_2F_8] \cdot 2H_2O$	814	180.4	179.7	184	3.6	4.3
$[Rb_4[(UO_2)_2F_8] \cdot 2H_2O$	813	180.5	179.8	184	3.5	4.2
Li_2UO_4	725	188.8	189.5	189	0.2	-0.5
α-Na_2UO_4	737	187.6	188.0	190	2.4	2.0
$(NH_4)_3UO_2F_5$	819	180.0	179.2	190	10.0	10.8

Larger order fits were also carried out in order to adjust the initial data in a more accurate way. However, the resulting fits gave distance-wavenumber relations providing similar averaged deviations with respect to experiment.

Since we are interested in the secondary phases appearing as products of alteration (hydration-oxidation weathering) of spent nuclear fuel (SNF), we have made a comparison of the bond-lengths obtained from these relations for some of the most important secondary phases. The results are given in Table 9.4. In these cases, we have several band wavenumbers assigned to uranyl symmetric stretching vibrations. For each of these bands, the corresponding UO distances are obtained and compared with the experimental average UO length determined from the distances obtained from X-ray single-crystal structure analyses. The averaged deviation of the calculated values is 1.3 pm for the relation obtained in this work and 1.4 pm for that of Bartlett and Cooney (1989).

Table 9.4. Bond lengths obtained for a series of uranyl ion containing systems. Raman shifts and bond-lengths are given in units of cm^{-1} and pm respectively. The references for the experimental data (Raman shifts and average UO distances) may be found in the first column of the table.

System	ν_1^{Exp}	R_{UO}		Exp.	Errors	
		This work	Bartlett and Cooney (1989)		This work	Bartlett and Cooney (1989)
Rutherfordine [a,b]	882.3	174.96	173.27	174.4	-0.56	1.13
Studtite [c,d]	819.05	179.99	179.16	176.9	-3.09	-2.26
Soddyite [e,f]	830.0	179.07	178.09	178.1	-0.97	0.01
Uranophane-α [g,h]	798.3	181.78	181.26	180.45	-1.33	-0.81
Becquerelite [i,j]	838.3	178.39	177.29	179.39	1.00	2.10
	831.1	178.98	177.98		0.41	1.41
	813.7	180.44	179.69		-1.05	-0.31
Schoepite [i,k]	838.7	178.36	177.25	177.9	-0.46	0.65
	826.2	179.39	178.46		-1.49	-0.55
	817.1	180.15	179.35		-2.25	-1.45
	802.3	181.43	180.85		-3.53	-2.95
Billietite [i,l]	830.7	179.02	178.02	180.14	1.12	2.12
	830.3	179.05	178.06		1.09	2.08
	810.0	180.76	180.06		-0.62	0.08
	794.6	182.11	181.64		-1.97	-1.50
Curite [i,m]	803.0	181.37	180.77	182.50	1.13	1.73
	791.0	182.43	182.02		0.07	0.48
Vandendriesscheite [i,n]	852.3	177.27	175.97	179.55	2.28	3.58
	840.6	178.21	177.07		1.34	2.48
	831.9	178.92	177.90		0.63	1.65
	819.4	179.96	179.12		-0.41	0.43

[a] Bonales *et al*., 2016; [b] Finch *et al.*, 1999; [c] Colmenero *et al.*, 2017b; [d] Burns and Hughes, 2003; [e] Colmenero *et al.,* 2017c; [f] Demartin *et al*., 1992; [g] Colmenero *et al*., 2017e; [h] Ginderow, 1988; [i] Frost *et al.,* 2007b; [j] Burns and Li, 2002; Pagoaga *et al.*, 1987; [k] Finch *et al.*, 1996; [l] Finch *et al*., 2006; [m] Li and Burns, 2000; [n] Burns, 1997.

Part III. Conclusions

Chapter 10. Conclusions

Because of uranyl compounds, containing UO_2^{2+}, will appear as secondary phases at the surface of spent nuclear fuel in the final geological disposal conditions, its characterization and the determination of its properties are extraordinarily important. However, due to the radiotoxicity of these materials, the experimental study of these substances requires an extremely careful handling of the samples. The theoretical methods, based in the laws of quantum physics and chemistry studying these systems at the atomic level, are free of these difficulties and were used in this work as an interpretative tool of the experimental results and as a predictive tool for the properties of these substances inaccessible through their experimental measurement.

In this PhD Thesis, the uranyl minerals rutherfordine, studtite, soddyite and uranophane, which have been widely recognized to be fundamental components of the paragenetic sequence of secondary phases that arises from the weathering of uraninite ore deposits and corrosion of SNF, have been studied by means of X-Ray powder diffraction and Raman spectroscopy combined with first principle (*ab initio*) calculations based on density functional theory (DFT) methods.

The conclusions of this work are presented in this section. The conclusions specific from each one of the studies of the different mineral phases, described in the Chapters 4 to 9, are presented separately in the Sections 10.1.1, 10.1.2, 10.2, 10.3, 10.4 and 10.5, respectively. Then, the final conclusions and perspectives are provided in Sections 10.6 and 10.7, respectively.

10.1 Rutherfordine

10.1.1 Structure and Raman Spectra

A natural rutherfordine mineral was characterized by means of Raman spectroscopy combined with theoretical calculations based on density functional theory (DFT) methods. The structural parameters and X-ray powder spectrum obtained indicates that rutherfordine mineral is accurately described by our theoretical computations. Pmmn and Imm2 structures were considered in this work. Since these structures are nearly degenerate and the properties computed from them are very similar, we conclude that both may simultaneously be present in nature in accordance with the suggestion of Christ *et al.* (1955).

The Raman spectrum obtained experimentally was also fairly well reproduced. The main vibrations used as a fingerprint to identify rutherfordine were the two ν_1 symmetric stretching bands of the UO_2^{2+} and CO_3^{2-} groups placed at 882 and 1113 cm^{-1}, respectively. These bands are very well reproduced theoretically at 886 and 1098 cm^{-1}, respectively. Next bands, obtained by Raman spectroscopy, located at 1409 and 780 cm^{-1}, are attributable to the CO_3^{2-} group asymmetric stretching and in plane bending modes ν_3 and ν_2, the calculated ones being located at 1401 and 747 cm^{-1}. In the low wavenumber region, we found three main bands at 134, 153 and 213 cm^{-1}, which are well reproduced by theoretical calculations with wavenumbers located at 147, 150 and 217 cm^{-1}.

For most of the bands in the experimental spectrum we found a correspondence to bands in the theoretical one and, therefore, they were assigned to specific vibrational motions. The band wavenumbers which are not reproduced in our theoretical calculations were attributed to the presence of other uranyl minerals as uranophane.

The introduction of dispersion corrections and the introduction of water molecules into the space between the sheets of the unit cell of rutherfordine did not modify the computed Raman spectrum significantly.

11.1.2 Thermodynamic and Mechanical Properties

The thermodynamic and mechanical properties of the rutherfordine mineral were studied by means of first principles calculations based on density functional theory. These calculations extend the knowledge and interpretation of the structure and properties of this uranyl carbonate mineral reported in the previous study of this mineral (Bonales *et al.*, 2016) and illustrate the power of theoretical methods as a predictive tool in the research of uranium-containing materials.

All the thermodynamic properties, including the enthalpy, free energy, entropy, heat capacity and Debye temperature, were evaluated as a function of temperature and compared to experimental data in the range of 300−700 K. Our calculations show very good agreement with experimental data. These thermodynamic properties were obtained in the extended range of 0−1000 K, including the full range of thermal stability, up to 700 K (Hemingway *et al*, 1982). The computed values of the heat capacity, entropy, and free energy at 298 K deviate from experimental values by about 8, 0.2 and 0.5%, respectively. At 700 K, the corresponding differences remain very small, 3.9, 2.3 and 1.3%, respectively.

The equation of state and mechanical properties were also computed. The crystalline structure was shown to be mechanically and dynamically stable. Rutherfordine is shown to be a highly anisotropic and brittle material with very large compressibility along the direction perpendicular to the sheets characterizing its structure. The computed bulk modulus is very small, B ≈ 20 GPa, in comparison to the values obtained in previous calculations (Matar, 2010). This emphasizes the need for very high levels of theory in the computational treatment of uranium containing materials because inaccuracies in the calculations may lead to imprecise results for material properties. A large amount of relevant mechanical data of the rutherfordine mineral is reported here, including bulk modulus and its derivatives, elastic coefficients, shear and Young moduli, Poisson ratios, ductility and hardness indices and elastic anisotropy measures.

10.2 Soddyite. Structure, Mechanical Properties, Equation of State and Raman Spectra

In this work, soddyite structure was determined theoretically for the first time. The calculations have been performed by using the CASTEP module of Materials Studio software. The pseudopotentials used for H, O and Si atoms in the unit cell of soddyite mineral were standard norm-conserving pseudopotentials whereas pseudopotential for U atom was generated from first principles in a previous paper (Bonales *et al*., 2016).

These calculations, based on density functional theory, show the role of water in the structural and vibrational properties of uranyl silicate mineral soddyite. Water molecules enter in the structure of soddyite as structural water forming part of the coordination structure of uranium atom, that is within the pentagonal bipyramids, $UO_6(H_2O)$. Structural optimization performed using the GGA-PBE exchange-correlation functional taking into account a dispersion correction scheme has produced unit cell lattice parameters and atomic bond distances and angles in excellent agreement with experimental data. The computed X-Ray powder spectrum is also in very good according with experimental data.

Elastic tensor was calculated from stress-strain relations using the finite deformation technique implemented in CASTEP at the optimized equilibrium structure. The analysis of the calculated elasticity stiffness tensor has revealed that the soddyite structure satisfies properly the mechanical

stability conditions. Furthermore, mechanical properties of this mineral, for which there are not experimental data to compare with, are predicted.

Soddyite equation of state was obtained by fitting lattice volumes and pressures to a fourth order Birch-Murnahan equation of state.

Raman spectrum was also computed and compared with its experimental counterpart. The normal mode analysis of the theoretical spectra was carried out and used to assign the main bands of the Raman spectra. It also should be noted that some spectral bands, as that placed at 3147 cm^{-1}, were not found in the theoretical spectrum. Thus, they may correspond to other phases present in the natural mineral under study.

This work verifies that the DFT method is a reliable tool to analyse the structure, mechanical properties and vibrational spectra of uranyl silicate minerals.

10.3 Studtite. Structure, Raman Spectra and Thermal Stability

In this work studtite was synthetized and characterized by scanning electron microscopy (SEM), TGA, X-Ray diffraction (XRD) and Raman spectroscopy. The structure was besides analyzed by computed DFT calculations. The computed X-ray diffractogram, in agreement with the experimental one, indicates that the optimized structure of studtite describes accurately the experimental studtite structure. Moreover, the computed Raman spectrum shows a correspondence to the experimental bands and, therefore, they could be assigned to specific vibrational motions. The OH stretching and bending bands were found to be associated to specific types of water molecules (crystallization and structural).

The thermal stability of studtite was studied by *in situ* Raman spectroscopy, performing the dehydration of studtite at different heating rates (5, 1 and 0.2 °C/min) and in presence of water. For this work, a new cell was designed. The results show how the temperature of the dehydration process at low heating rates takes place around 33–34 °C. However, when the experiments were performed at a higher heating rate (5 °C/min) the temperature increased at 50 °C. This discrepancy may be due to the fact that the system is out of equilibrium at such a high heating rate, which would explain the TGA results, and the previous published ones (Rey *et al.*, 2009a), which shows a high loss of water at low temperatures (< 90 °C), and points out the importance of applying low heating rates in this kind of studies.

From the experiments performed in presence of water, the studtite is stable up to 90 °C, what is consistent with the founding of this phase after the Fukushima-Daiichi accident (Armstrong *et al.*, 2012; Burns *et al.*, 2013; Giménez *et al.*, 2014). More studies are needed to be done in order to clarify the moisture effect on the thermal stability of this mineral phase.

10.4 Uranophane-α. Structure, Mechanical Properties, Equation of State and Raman Spectra

The DFT results show the important role of water in the structural and vibrational properties of uranyl silicate mineral uranophane-α. Water molecules enter in the structure of uranophane-α as structural and crystallization water. Structural water molecules form part of the coordination structure of calcium ion present in the interlayer space between the uranyl silicate sheets, that is, within the distorted pentagonal bipyramids, $CaO_2(OH)(H_2O)_4$. Crystallization water molecules are also localized in the interlayer space but are free, that is, they do not coordinate the calcium ions. Structural optimization performed using the GGA-PBE exchange-correlation functional taking into account a dispersion correction scheme has produced unit cell lattice parameters and

atomic bond distances in excellent agreement with experimental data. The computed X-Ray powder spectrum is also in very good agreement with experiment.

An analysis of the calculated elasticity stiffness tensor has revealed that uranophane-α structure satisfies properly the mechanical stability conditions. Furthermore, mechanical properties of this mineral, for which there are not experimental data to compare with, are predicted. Uranophane-α is brittle and is characterized by small anisotropy and large hardness in comparison with those of other uranyl containing materials. The equation of state of uranophane-α was obtained by fitting lattice volumes and pressures to a fourth order Birch-Murnahan equation of state.

Raman spectrum was also computed by means of density functional perturbation theory and compared with its experimental counterpart. The results were also found to be in good agreement well the experimental data. A normal mode analysis of the theoretical spectrum was carried out and used in order to assign the main bands of the Raman spectra. Theoretical methods allowed us to assign the bands to vibrations localized in different fragments within the crystal unit cell.

Main band used as fingerprints to identify uranophane-α are those placed at wavenumbers 797 and 960 cm^{-1}. The corresponding values resulting from our computations are quite close to the experimental values, 776 and 958 cm^{-1}. The first band is assigned to a combination of SiOH bending vibrations localized in *fr* SiO_3OH fragments, uranyl UO stretching vibrations, and water librations. The second one is assigned to a combination of SiOH bending vibrations localized in *co* SiO_3OH fragments and water librations. In the experimental works, these bands were attributed to uranyl symmetric stretching, $\nu^s(UO_2)^{2+}$, and silicate symmetric stretching, $\nu^s(SiO_4)^{4-}$, vibrations. As indicated by our theoretical calculations, these assignations are incorrect or incomplete since they do not include several contributions, as those coming from vibrations arising from the ubiquitous water molecules and SiOH fragments. These contributions underline the role of the hydrogen bond structure in uranophane-α and its impact in the vibrational spectra. Further, the correlation of these bands with those of free fragments is lost due to the low crystal symmetry.

The bands situated at wavenumbers 545, 469, and 399 cm^{-1} are also satisfactorily reproduced theoretically, the corresponding values being 539, 459 and 399 cm^{-1}. The first band is ascribed to water librational vibrations only and the other ones represent SiOH bending vibrations localized in SiO_3OH fragments with coordinated OH groups and water librational vibrations. Previous assignments of these bands are not correct since involve silicate group deformations, $\nu_4(SiO_4^{4-})$ and $\nu_2(SiO_4^{4-})$. Further, as it has already been said, the correspondence with free silicate group vibrations cannot be performed for uranophane.

In the low wavenumber region, we have four main bands located at wavenumbers 289, 250, 205 and 167 cm^{-1}, which are determined theoretically to be placed at 289, 256, 206 and 186 cm^{-1}, respectively. These were mainly attributed to uranyl bending vibrations. Theoretical calculations indicate that these bands correspond to a combination of silicate (SiO_3OH) deformations, uranyl bending vibrations and water librations. The uranyl bending vibration appears to be only a small contribution.

In the OH stretching region most bands are well reproduced theoretically, in spite of the fact that the bands in this region are quite variable from one sample to another. The theoretical analysis allows to assign these bands to vibrations localized in different fragments of the unit cell. The bands at higher wavenumber are attributed to OH stretching vibrations in crystallization water molecules. The bands at medium wavenumbers are due to OH stretching vibrations localized in structural water molecules. Finally, the bands with lowest wavenumbers contain contributions from OH stretching vibrations localized in the SiOH fragments containing OH groups out of the coordination sphere of interlayer calcium ions.

For the bands placed at 1272 and 1156 cm^{-1} (comparable to the theoretical bands located at 1222 and 1146 cm^{-1}, respectively) the band assignment reveals that while both are attributable to SiOH bending vibrations, these vibrations are localized in different SiO_3OH fragments (the higher wavenumber one in coordinated SiO_3OH fragments and the lower one in free fragments).

Finally, the possibility of incorporation of strontium into the structure of uranophane-α was investigated. The structure of Sr-exchanged uranophane and the structure of the solvation sphere of the interlayer cation are showed to be very similar to that of normal uranophane, the main difference being, as in the case of montmorillonite clay mineral (Berghout *et al*., 2010), the increase of in the interlayer space (the *c* parameter increased by about 0.35 Å). The X-Ray powder pattern and Raman spectrum of Sr-exchanged uranophane are also showed to be extremely close to those of normal uranophane. These findings agree with the results of the experimental study of Douglas *et al.* (2002).

10.5 Uranium-Oxygen Bond-Length to Uranyl Symmetric Stretching Raman Shift Relation.

The purpose of this work was to derive the parameters of the expression relating the uranium-oxygen bond-length and symmetric stretching Raman shift, from a small set of results derived from first principle calculations, that is without using any experimental information. The resulting parameters gave an expression with essentially the same accuracy as that derived by Bartlett and Cooney (1989) employing a large set of experimental results.

Similar relations could be obtained for bonds involving different elements using data obtained from first principles methods. However, it should be noted that, although the number of theoretical calculations required may be small, the corresponding calculations are computationally time-consuming if one desires to reach a good level of accuracy in the computed vibrational spectra.

The present study suggests that when the relation given in this work and that given by Bartlett and Cooney (1989) are used to determine bond-lengths in terms of experimental Raman shifts, bond-lengths are obtained, whose accuracy is limited only by the approximate character of the distance-wavenumber relation. Relations deduced from larger sets of data or from expressions of larger order aiming to adjust the initial data in a more accurate way do not provide better averaged deviations with respect to the corresponding experimental data.

10.6 Final conclusions: Implications for the Characterization of Secondary Phases of Spent Nuclear Fuel in Definitive Disposal Conditions

(1) The results obtained in the published papers reported in this PhD Thesis suggest that the theoretical computations are an extremely powerful tool in the research of uranium containing compounds. Once the proper *relativistic norm-conserving pseudopotential* has been generated, the structural information (lattice parameters, bond lengths, bond angles and X-ray powder patterns), the vibrational Raman spectra and mechanical and thermodynamic properties of these substances may be obtained. This result is very significant because, if we have access to the adequate computational resources, very accurate resuls can be obtained in spite of the large size of the systems and the fact that the level of theory required to describe them is very high (Crocombette *et al*., 2001; Beridze *et al*., 2014). The use of these methods is free of the difficulties of the experimental methods associated to the radiotoxicity of these compounds requiring a careful management of the samples. Thus, the *theoretical calculations allow the safe study of secondary phases of spent nuclear fuel (SNF) in definitive disposal conditions.* The natural samples used in the experimental studies are generally mixtures of several minerals and *the theoretical treatment allows to study pure substances*. Furthermore, the synthesis of these compounds is very complex and generally produce samples with low crystallinity.

(2) The theoretical results may be used, in conjunction with experimental techniques, as an *interpretative tool* of the experimental structural and vibrational data or as a *predictive tool* to

determine the structural, vibrational, mechanical and thermodynamic properties of these substances. The understanding of the structures of these compounds is very important itself to characterize them and to evaluate the possible incorporation of transuranic elements and fission products in to the structures of uranyl minerals (Burns *et al.*, 1997a; Burns, 2005). X-Ray diffraction and Raman spectroscopy (Baker, 2014) are the most widely used techniques used for the identification of these substances because they are non-destructive techniques, which do not require any special preparation of the samples and allow for the analysis of very small amounts of sample. *The corresponding theoretical X-Ray powder patterns and Raman spectra are in a very good agreement with their experimental counterparts when they are available for comparison.* The assignation of the main bands in the vibrational spectra of these compounds, performed usually by the experimentalist in an empirical way, can be made in a rigorous form since the theoretical methods produce microscopic scale views of the motion of the atoms in the corresponding normal vibrational states. In the systems studied the *theoretical calculations has permitted the correct assignment of the bands of the full Raman spectrum for the first time*. The main bands used to fingerprint these minerals were put into correspondence with specific structural data. The correspondence of the vibrational information with the structure was used in order to determine a very useful equation relating the uranyl symmetric stretching Raman shift and the UO bond length, by employing solely the information derived from the theoretical calculations.

(3) One of the most relevant issues in nuclear and energetic sciences is the protection of the environment. The prediction of the behaviour of hazardous materials under diverse environmental conditions is extremely important. *Fundamental thermodynamic data are the indispensable basis for a dynamic modelling of the chemical behaviour of contaminant waste components*. They are needed in order to evaluate the origin and evolution of uranium ore bodies, in developing programs for the solution mining of uranium deposits or mine dumps, in the study of spent nuclear fuel (SNF) radioactive waste and in the containment of such waste, and may also be of importance in reactions within breeder reactors (Hemingway *et al*., 1982; Langmuir, 1997; Casas *et al*., 1994; Navrotsky *et al*., 2013). The knowledge of precise thermodynamic data is basic in the development of geochemical and used fuel degradation models (Sassani *et al*., 2013)

The enormous importance of the thermodynamic information in the assessment of the safety of nuclear waste repositories is reflected by the large number of recent experimental works on this topic culminating in large reviews and updates of thermodynamic properties of uranium bearing species (Wanner and Forest, 1992; Murphy and Pabalan, 1995; Grenthe *et al*., 2004; Shvareva *et al*., 2012) and other systems containing related elements (Guillaumont, 2003). While the thermodynamic information database of uranium-bearing species is very advanced, there are many secondary phases for which the corresponding data is inaccurate due to large experimental uncertainties (Langmuir, 1997) Additionally, the range of conditions (*i.e.*, temperature and pressure) for which these properties are known is quite limited. *The theoretical calculations of these thermodynamic properties of rutherfordine mineral (Colmenero et al., 2017a) have allowed us to evaluate the quality of the calculated properties, and the range of temperature in which these properties are known has extended to 0-700 K. Further, the recent calculations of these properties for γ-UO_3 (Colmenero et al., 2017d), have demonstrated their high quality even at very low temperatures.*

(4) As noted by Weck *et al*. (2015), the availability of a great amount of information on the formation, thermodynamic stability and phase transformations of alteration phases formed at the SNF surface contrasts with the paucity of data regarding the mechanical stability and mechanical properties of these phases. This appears particularly surprising since the underlying atomistic deformation modes and interactions determine to a large extent the thermodynamic phase stability and transformation. In fact, saving the theoretical study of the uranyl peroxide hydrates, studtite and metastudtite, by Weck *et al*. (2015), no experimental or computational studies reporting data of this kind have been carried up to date. *The results of the calculations reported in this PhD. Thesis about rutherfordine, soddyite and uranophane minerals have demonstrated the mechanical stability of their structures. Besides, a large amount of relevant mechanical data of*

these minerals were reported here, including bulk modulus and its derivatives, elastic coefficients, shear and Young moduli, Poisson ratios, ductility and hardness indices, and elastic anisotropy measures. Their equations of state where also determined by fitting lattice volumes and pressures to a fourth order Birch-Murnahan equation of state.

10.7 Perspectives. Lessons learned from this research

In the first contact with the persons forming the Unidad de Residuos Radiactivos de Alta Actividad of CIEMAT, I learned that they were working in two main lines of research. The first one was the study of the oxidation of uranium oxides in dry conditions and the second one the research involving the oxidation-hydration process of uranium dioxide leading to the study of the formation of secondary phases at the surface of spent-nuclear fuel. Both lines were being studied with experimental methods, mainly X-ray diffraction and Raman spectroscopy, and I was invited to apply the theoretical methodology to the research in these lines. I left CIEMAT with some notions about the oxidation processes of spent nuclear fuel and with a simple list of uranium atom containing minerals of interest for the disposal of radioactive nuclear waste. At first sight, I thought that these fields of research should be quite developed and that my contribution could be a simple application of theoretical methods, mainly in the determination of Raman spectra of uranium-bearing minerals. However, my surprise was enormous when, in the first search of literature, I found that there were only a very few studies of the vibrational spectra of these materials. In fact, none of these studies included a complete determination of these spectra since only the phonon frequencies at gamma point were calculated and band intensities were not reported. The reasons for the very limited amount of theoretical treatments was very clear once I revised the bibliography: 1) The high level of theory required to describe the uranium atom containing systems; 2) The large number of atoms in the unit cells of these materials; 3) The large number of valence electrons which must be described explicitly in the calculations; and 4) The absence of good norm-conserving pseudopotentials needed for the computation of the theoretical vibrational spectra.

Having in mind these problems, I tried to characterize the corresponding materials by X-Ray diffraction. This was accomplished by computing the crystal structures of all the materials in which I was interested by using ultrasoft (US) pseudopotentials, which are not norm-conserving. While the results were quite good, the most interesting part of the study cannot be accomplished with this methodology. For this reason, the possibility of generating a new norm-conserving pseudopotential from first principles was considered. Several different strategies and computer programs were studied and after several months of intense work, I succeeded in the generation of a norm-conserving GGA-PBE relativistic pseudopotential, using program fhi98PP and the conversion tool cpi2recpot, valid for determining the vibrational spectra of the materials considered within program CASTEP. The pseudopotential was validated by calculating the structures of a large number of secondary phases and the Raman spectra of uranyl carbonate mineral Rutherfordine (Bonales *et al.,* 2016). The results were excellent and they were published in the journal *Physical Chemistry Chemical Physics*.

The study of rutherfordine mineral was quite complicated due to several reasons. In the first place, I found that two different quasi-degenerate orthorhombic structures could be simultaneously present in nature. This feature duplicated the computational work, which showed that the X-Ray powder diffraction patterns and Raman spectra associated to both structures were extraordinarily similar. In the second place, the layered structure of rutherfordine mineral demanded the study of the influence of Van der Waals interactions in the computations. In the third place, the presence of bands corresponding to water molecules in the Raman spectrum required the study of the introduction of water in the structure. The second problem was studied by means of the use of density functionals with dispersion corrections (Grimme empirical dispersion correction), and the third one by means of the introduction of water molecules in the interlaminar space from the unit cell of rutherfordine. Finally, it was observed that there were some bands in the experimental Raman spectrum that were absent in the spectrum calculated theoretically. These bands, therefore,

should be due to the fact that the natural mineral sample studied was a mineral mixture. It was verified that these extra bands were due to the presence of traces of schoepite and uranophane minerals.

The first published work after the initial study of rutherfordine mineral was that of the uranyl peroxide studtite (Colmenero *et al.*, 2017b). This material was synthetized at CIEMAT, where its thermal stability was being studied by means of *in situ* Raman spectroscopy. A large set of computations for studtite mineral were carried out with increasing computer time and complexity corresponding to increasingly stringent calculation parameters. The presence of water in the unit cell of studtite demanded a correct description of the hydrogen bonds present in the structure and, therefore, the PBE functional with Grimme empirical dispersion correction was used. The last computations resulted in structures very well converged with respect to the calculation parameters, which showed a very good agreement with the experimental geometry and X-Ray powder pattern. For this reason, the theoretical determination of the Raman spectrum was carried out and all the bands in the experimental spectrum were assigned for the first time. The assignation of the band corresponding to the UO bond symmetric stretching and the experimental analysis of its displacement with temperature allowed the study of the thermal stability of studtite in presence and absence of water. One of the main conclusions of this study was that this material in humid conditions is stable up to temperatures much higher than in dry conditions (larger than 90ºC), and this justified its encounter after the Fukushima-Daiichi nuclear accident (instead of its dehydration product, metastudtite). The combined theoretical-experimental study was published in the journal *Spectrochimica Acta A* (Colmenero *et al.*, 2017b).

Further intensive computations gave very good results not only of the structural and vibrational properties of these kind of materials but also permitted to carry out computations of mechanical and thermodynamic properties (Colmenero *et al.*, 2017a; Colmenero *et al.,* 2017c; Colmenero *et al.*, 2017d; Colmenero *et al.*, 2017e). The results of the thermodynamic and mechanical properties of the uranyl carbonate mineral rutherfordine were published in the *Journal of Physical Chemistry C* (Colmenero *et al.*, 2017a). These computations enhanced the range in which the thermodynamic properties of this mineral were known to 0-700 K. In this work, we demonstrated that rutherfordine structure was mechanically and dynamically stable, and predictions were made for a large number of mechanical properties for which there were not experimental measurements. The study of the structural and mechanical properties, the equation of state and the Raman spectrum of the uranyl silicate mineral soddyite has been submitted for its publication in the *Journal of Solid State Chemistry* (Colmenero *et al.*, 2017c). In this work, its structure determined experimentally by means of X-Ray diffraction techniques has been confirmed by our theoretical calculations. We are now considering the publication of a work with an analogous content for the uranyl silicate mineral uranophane which has a structure completely different to that of soddyite (Colmenero *et al.*, 2017e). A great predictive power of these theoretical methods in the research of uranium containing materials was found. This happened not only for secondary phases resulting of the oxidation-hydration of uranium dioxide by also for dry uranium oxides such as UO_3 (Colmenero *et al.,* 2017d). The results obtained for the structural and thermodynamic properties, equation of state, and Raman spectrum of the γ polymorph of uranium trioxide have been accepted for its publication in the *Journal of Physical Chemistry C* (Colmenero *et al.*, 2017d). The structural and spectroscopic results were in excellent agreement with the experimental information. In this way, we have solved the uncertainties in the assignation of the bands in the Raman spectrum, since all the bands in this spectrum have been assigned. Finally, we have found an excellent agreement with the thermodynamic properties obtained experimentally both at low and high temperatures, and we have predicted the values of the bulk modulus and its derivatives.

In view of the work performed along the last three years, we are in position to study a large number of additional very interesting secondary phases as uranyl oxyhydroxides (schoepite, becquerelite, curite, etc.), uranyl silicates (boltwoodite, weeksite, kasolite, etc.), uranyl carbonates (grimselite, etc.), uranyl phosphates (autunite, torbenite, saleeite, etc.), and uranyl vanadates (carnotite, etc.). The study of uranyl oxyhydroxide schoepite has already being initiated. The

results for the dehydrated schoepite were found to be very good in comparison with available experimental data, and those of the hydrated schoepite mineral are being now analysed. This last material is very complex and the calculations were extremely expensive. For these materials, many interesting properties may be determined with the current methodology, and additional properties not studied so far (for example the optical properties) could also be studied. The experimental measurement of these properties from synthetic and/or natural samples can also be considered.

The line of research involving the oxidation of uranium dioxide in dry conditions could also be expanded. We have already studied the γ-UO_3 system, the results being in very good agreement with experimental data. Additional polymorphic forms of this system could equally be studied. However, the study of materials such as UO_2, U_3O_8, coffinite, etc., that is, oxides and minerals in which the oxidation state of some of the uranium atoms involved is IV, requires the use of more advanced theoretical treatments because standard DFT fails in these cases. This is due to the presence of unpaired electrons in high angular momenta states (*f* states). The description of these systems is usually accomplished by the addition of Hubbard correction to standard DFT functionals (Beridze *et al.*, 2014, and references therein), but in this case the calculation of vibrational spectra and other interesting properties is still not implemented. The use of hybrid or meta-GGA functionals could also be tried, but its use is very expensive and they are not implemented with full functionality in most computer codes. Other programs such as CRYSTAL or VASP or future versions of CASTEP could allow the complete study of these systems with advanced functionals. This line of research should be considered in a greater detail. *The experience gained in these years show that most problems involved can be solved with only a high dose of patience, dedication, effort and interest.*

Capítulo 10. Conclusiones

Debido a que los compuestos uranílicos, que contienen UO_2^{2+}, aparecerán como fases secundarias en la superficie del SNF en condiciones de almacenamiento geológico final, su caracterización y la determinación de sus propiedades es extraordinariamente importante. Sin embargo, debido a la radiotoxicidad de estos materiales, el estudio experimental de estas sustancias requiere una manipulación extremadamente cuidadosa de las muestras. Los métodos teóricos, basados en las leyes de la física y química cúantica que estudian estos sistemas a nivel atomístico, están libres de estas dificultades y se han utilizado en este trabajo tanto como herramienta interpretativa de los resultados de las técnicas experimentales, como herramienta predictiva para las propiedades de estas sustancias que son inaccesibles a su medida experimental.

En este trabajo de Tesis Doctoral, los minerales uranílicos ruderfordina, studtita, soddyita y uranofana, que han sido ampliamente reconocidos como componentes fundamentales de la secuencia paragenética de las fases secundarias que surgen de la alteración de la uraninita y la corrosión del SNF, han sido estudiados por medio de difracción de Rayos X en polvo y espectroscopia Raman combinados con cálculos de primeros principios basados en los métodos de la teoría del funcional de la densidad (DFT).

Las conclusiones de este trabajo se presentan en esta sección. Las conclusiones específicas de cada uno de estudios de las diferentes fases minerales, descritos en los Capítulos 4 a 9, se presentan separadamente en las Secciones 10.1.1, 10.1.2, 10.2, 10.3, 10.4 and 10.5, respectivamente. Por último, las conclusiones finales y perspectivas de este estudio se detallan en las Secciones 10.6 and 10.7, respectivamente.

10.1 Ruderfordina

10.1.1 Estructura y Espectro Raman

En este artículo se caracterizó una muestra natural de ruderfordina por medio de espectroscopia Raman combinada con cálculos teóricos basados en los métodos de la teoría del funcional de la densidad (DFT). Los parámetros estructurales y el espectro de Rayos X en polvo obtenidos indicaron que el mineral ruderfordina fue descrito con mucha precisión mediante cálculos teóricos. En este trabajo se consideraron dos estructuras cristalinas diferentes asociadas a las simetrías espaciales Pmmn e Imm2. Ya que se encontró que estás dos estructuras eran muy próximas en energía y las propiedades computadas a partir de ellas eran muy similares, concluimos que ambas podrían estar presentes simultáneamente en la naturaleza de acuerdo a la sugerencia de Christ *et al.* (1955).

El espectro Raman obtenido experimentalmente también fue muy bien reproducido. Las vibraciones principales que se usan como huella dactilar para identificar a la ruderfordina son las dos bandas asociadas al estrechamiento simétrico, ν_1, de los grupos UO_2^{2+} y CO_3^{2-} situadas en los números de onda 882 and 1113 cm^{-1}, respectivamente. Estas bandas fueron muy bien reproducidas teóricamente en 886 and 1098 cm^{-1}, respectivamente. Las siguientes bandas, obtenidas por espectroscopia Raman, localizadas en 1409 and 780 cm^{-1}, fueron encontradas teóricamente en 1401 and 747 cm^{-1} y son atribuibles a los modos de estrechamiento asimétrico y doblamiento en el plano, ν_3 and ν_2, del grupo CO_3^{2-}. En la región de números de onda bajos se encontraron tres bandas principales localizadas en 134, 153 y 213 cm^{-1}, que fueron bien reproducidas por los cálculos teóricos con números de onda de 147, 150 y 217 cm^{-1}.

Para la mayor parte de las bandas en el espectro experimental se encontró una correspondencia con las bandas en espectro teórico y, por tanto, se pudieron asignar a movimientos vibracionales específicos. Los números de onda de las bandas que no se reprodujeron en nuestros cálculos teóricos fueron atribuidos a la presencia de otros minerales que contienen el ion uranilo, como la uranofana.

La introducción de correcciones de dispersión y la introducción de moléculas de agua en el espacio situado entre las láminas de la celda unidad de la ruderfordina no modificaron significativamente el espectro Raman computado.

11.1.2 Propiedades Termodinámicas y Mecánicas

Las propiedades termodinámicas y mecánicas del mineral ruderfordina fueron estudiadas por medio de cálculos de primeros principios basados en la teoría del funcional de la densidad. Estos cálculos ampliaron el conocimiento e interpretación de la estructura y propiedades de este mineral carbonato de uranilo obtenidos en un estudio previo de este mineral (Bonales *et al.*, 2016), e ilustran la gran potencia de los métodos teóricos como herramienta predictiva en la investigación de materiales que contienen uranio.

Todas las propiedades termodinámicas, incluyendo la entalpía, energía libre, entropía, capacidad calorífica y temperatura de Debye fueron evaluadas en función de la temperatura y comparadas con datos experimentales en el rango 300−700 K. Nuestros cálculos, muestran muy buen acuerdo con los datos experimentales. Estas propiedades termodinámicas fueron obtenidas en el rango extendido 0−1000 K, que incluye el rango completo de estabilidad térmica de la ruderfordina, hasta 700 K (Hemingway *et al*, 1982). Los valores calculados de la capacidad calorífica, entropía y energía libre a 298 K, se desvían de los valores experimentales un 8, 0.2 and 0.5%, respectivamente. A 700 K, las correspondientes diferencias siguen siendo muy pequeñas, 3.9, 2.3 and 1.3%, respectivamente.

La ecuación de estado y propiedades mecánicas de este mineral también fueron computadas. Se demostró que la estructura cristalina de la ruderfordina satisface las condiciones de estabilidad mecánica y dinámica. Se mostró que la ruderfordina es un material altamente anisotrópico y quebradizo con una compresibilidad muy grande a lo largo de la dirección perpendicular a las láminas que caracterizan la estructura. El módulo de la elasticidad calculado es muy pequeño, B ≈ 20 GPa, en comparación con los valores obtenidos en cálculos previos (Matar, 2010). Esto enfatiza la necesidad de altos niveles de la teoría en el tratamiento computacional de los materiales que contienen el átomo de uranio ya que pequeñas imprecisiones en los cálculos pueden llevar a resultados erráticos para las propiedades materiales. En este trabajo se detallan una gran cantidad de datos mecánicos relevantes del mineral ruderfordina incluyendo el módulo elástico y sus derivadas, coeficientes de elasticidad, módulos de Young y cizalladura, radios de Poisson, índices de ductilidad y dureza y medidas de anisotropía elástica.

10.2 Soddyita. Estructura, Propiedades Mecánicas, Ecuación de Estado y Espectro Raman

En este trabajo se determinó teóricamente por primera vez la estructura de mineral soddyita. Los cálculos se realizaron usando el módulo CASTEP incluido en el paquete de programas Materials Studio. Los pseudopotenciales usados para los átomos de H, O and Si en la celda unidad del mineral soddyita fueron pseudopotenciales estándar conservadores de la norma, mientras que el pseudopotencial de átomo de uranio fue generado desde los primeros principios en un artículo previo (Bonales *et al*., 2016).

Estos cálculos, basados en la teoría del funcional de la densidad, muestran el papel que juega el agua en las propiedades estructurales y vibracionales de mineral silicato de uranilo soddyita. Las moléculas de agua entran en la estructura del mineral soddyita como agua estructural que forma parte de la estructura de coordinación del átomo de uranio, esto es dentro de las bipirámides pentagonales, $UO_6(H_2O)$. La optimización estructural realizada con el funcional de intercambio-correlación GGA-PBE teniendo en cuenta un esquema empírico de Grimme para la corrección de las interacciones de dispersión produce parámetros de la celda unidad y distancias y ángulos de enlace en un acuerdo excelente con los datos experimentales. El patrón de Rayos X en polvo calculado está también en muy buen acuerdo con el patrón experimental.

El tensor elástico fue calculado a partir de las relaciones tensión-deformación usando la técnica de deformaciones finitas implementada en CASTEP para la geometría de equilibrio optimizada. El análisis del tensor de elasticidad ha revelado que la estructura de la soddyita satisface apropiadamente las condiciones de Born de estabilidad mecánica. Además, se predice el valor de gran cantidad de propiedades mecánicas de este mineral, para el que no existe información experimental con la que comparar.

La ecuación de estado del mineral soddyita fue obtenida ajustando los volúmenes optimizados de la celda unidad sometida a presión y las presiones correspondientes a una ecuación de estado de tipo Birch-Murnahan de cuarto orden.

El espectro Raman también fue calculado y comparado con el espectro experimental. El análisis de modos normales del espectro teórico fue llevado a cabo y usado para asignar el espectro Raman. Además, debe notarse que algunas de las bandas experimentales, como la situada en 3147 cm^{-1}, no fueron encontradas en el espectro teórico. Por tanto, deben corresponder a otras fases presentes en el mineral natural que se está estudiando.

Este trabajo verifica que el método DFT es una herramienta fiable para analizar la estructura, propiedades mecánicas y espectros vibracionales de minerales silicato de uranilo.

10.3 Studtita. Estructura, Espectro Raman y Estabilidad Térmica

En este trabajo, se sintetizaron cristales de studtita y se caracterizaron por microscopía electrónica de barrido (SEM), análisis termogravimétrico (TGA), difracción de Rayos X (XRD) y espectroscopia Raman (RS). La estructura fue además estudiada por medio de cálculos computacionales basados en la teoría del funcional de la densidad (DFT). El difractograma de Rayos X en polvo computado, en buen acuerdo con el patrón experimental, indica que la estructura optimizada de la studtita describe con precisión la estructura experimental. Adicionalmente, el espectro Raman computado muestra buena correspondencia con las bandas experimentales y, por tanto, estas bandas fueron asignadas a movimientos vibracionales específicos. Se encontró que las bandas de estrechamiento de los enlaces OH y de doblamiento de las moléculas de agua estaban asociadas a tipos específicos de moléculas de agua (de cristalización y estructurales).

La estabilidad térmica de la studtita fue estudiada por espectroscopia Raman *in situ*, realizando la deshidratación de la studtita a diferentes velocidades de calentamiento (5, 1 y 0.2 °C/min) y en presencia de agua. Para este trabajo, se diseñó una nueva celda experimental. Los resultados muestran como la temperatura del proceso de deshidratación a velocidades bajas de calentamiento tiene lugar en torno a 33–34 °C. Sin embargo, cuando los experimentos fueron realizados a una velocidad de calentamiento más alta (5 °C/min) la temperatura de deshidratación aumentó a 50 °C. Esta discrepancia puede deberse a que el sistema está fuera de equilibrio a altas velocidades de deshidratación, lo que podría explicar por qué los resultados TGA y los publicados previamente (Rey *et al.*, 2009a) muestran una gran pérdida de agua a temperaturas bajas (< 90 °C) pero mayores que las obtenidas en este trabajo. Además, este trabajo enfatiza la importancia de aplicar bajas velocidades de calentamiento en esta clase de estudios.

A partir de los experimentos realizados en presencia de agua, se concluye que la studtita es estable hasta 90 °C, lo cual es consistente con el encuentro de esta fase después del accidente de Fukushima-Daiichi (Armstrong *et al*., 2012; Burns *et al*., 2013; Giménez *et al*., 2014). Es necesario hacer más estudios para clarificar el efecto de la humedad en la estabilidad térmica de esta fase mineral.

10.4 Uranofana-α. Estructura, Propiedades Mecánicas, Ecuación de Estado y Espectro Raman

Los resultados DFT muestran el importante papel del agua en las propiedades estructurales y vibracionales del mineral silicato de uranilo uranofana-α. Las moléculas de agua entran en la estructura de la uranofana-α como agua estructural y de cristalización. Las moléculas de agua estructurales forman parte de la estructura de coordinación de los iones de calcio presentes en el espacio interlaminar entre las hojas de silicato de uranilo, esto es, dentro de las bipirámides pentagonales distorsionadas $CaO_2(OH)(H_2O)_4$. Las moléculas de agua de cristalización están también localizadas en el espacio interlaminar, pero están libres, es decir, no coordinan a los iones calcio. La optimización estructural realizada usando el funcional de intercambio-correlación GGA-PBE e introduciendo correcciones de dispersión ha producido parámetros de red de la celda unidad y longitudes y ángulos de enlace en un acuerdo excelente con los datos experimentales. El patrón de Rayos X en polvo está también en muy buen acuerdo con el patrón experimental.

Un análisis del tensor de la elasticidad calculado ha revelado que la estructura de la uranofana-α satisface apropiadamente las condiciones de la estabilidad mecánica. Además, se predicen los valores de las propiedades mecánicas de este mineral para el que no existen datos experimentales con los que comparar. El mineral uranofana-α es quebradizo y está caracterizado por una anisotropía baja y dureza alta en comparación con otros materiales que contienen el ion uranilo. La ecuación de estado del mineral uranofana fue obtenida ajustando los volúmenes optimizados de la celda unidad sometida a presión y las presiones correspondientes a una ecuación de estado de tipo Birch-Murnahan de cuarto orden.

El espectro Raman fue también computado usando teoría de perturbaciones del funcional de la densidad y comparado con el espectro experimental. Ya que se encontró que los resultados estaban en buen acuerdo con los datos experimentales, se realizó un análisis de los modos normales del espectro teórico que fue usado para asignar las bandas principales del espectro Raman. Los métodos teóricos, nos permitieron asignar las bandas a vibraciones localizadas en diferentes fragmentos dentro de la celda unidad del cristal.

Las bandas principales usadas como huella dactilar para identificar la uranofana-α son las situadas a números de onda 797 and 960 cm^{-1}. Los valores correspondientes resultantes de nuestros cálculos son bastante próximos a los valores experimentales, 776 and 958 cm^{-1}. La primera banda la asignamos a una combinación de vibraciones de doblamiento en unidades SiOH localizadas en fragmentos *fr*-SiO_3OH, vibraciones de estrechamiento UO y libraciones del agua. La segunda banda se asigna a una combinación de vibraciones de doblamiento en unidades SiOH localizadas en fragmentos *co*-SiO_3OH y libraciones del agua. En los trabajos experimentales, estas bandas fueron atribuidas a vibraciones de estrechamiento simétrico UO en fragmentos uranilo, $\nu^s(UO_2)^{2+}$, y a vibraciones de estrechamiento simétrico en fragmentos silicato, $\nu^s(SiO_4)^{4-}$. Como indican los cálculos teóricos, estas asignaciones son incorrectas o incompletas ya que no incluyen varias contribuciones como las que provienen de vibraciones en las ubicuas moléculas de agua y en los fragmentos SiOH. Estas contribuciones ponen de manifiesto el papel de la estructura de enlaces de hidrógeno en el mineral uranofana-α y su impacto en los espectros vibracionales. Además, la correlación de estas bandas con las bandas de los fragmentos libres no se puede establecer debido a la baja simetría cristalina.

Las bandas situadas en números de onda 545, 469 y 399 cm^{-1} también se reprodujeron satisfactoriamente en los cálculos teóricos siendo los correspondientes desplazamientos Raman

539, 459 y 399 cm^{-1}. La primera banda se adscribe a libraciones del agua solamente y las otras dos representan vibraciones de doblamiento en unidades SiOH localizadas en fragmentos *co*-SiO_3OH y libraciones del agua. Las asignaciones previas de estas bandas no son correctas ya que involucran deformaciones del grupo silicato, $\nu_4(SiO_4^{4-})$ and $\nu_2(SiO_4^{4-})$. Además, como ya hemos dicho, la correspondencia con las vibraciones del grupo silicato libre no se puede establecer en la uranofana.

En la zona de bajos números de onda, encontramos cuatro bandas principales localizadas en los números de onda 289, 250, 205 and 167 cm^{-1} que se obtienen teóricamente en 289, 256, 206 and 186 cm^{-1}, respectivamente. Estas fueron atribuidas principalmente a vibraciones de doblamiento de ion uranilo. Los cálculos teóricos indican que estas bandas se corresponden con una combinación de deformaciones de los fragmentos silicato (SiO_3OH), vibraciones de doblamiento del ion uranilo y libraciones del agua. La vibración de doblamiento del ion uranilo parece ser solo una pequeña contribución a los modos vibracionales correspondientes.

En la región de las vibraciones de estrechamiento de los enlaces OH, la mayor parte de las bandas se reproducen bien teóricamente, a pesar de que las bandas en esta región son bastante variables de una muestra a otra. El análisis teórico permite asignar estas bandas a vibraciones localizadas en diferentes fragmentos de la celda unidad. Las bandas situadas a mayores números de onda se atribuyen a vibraciones de estrechamiento OH en las moléculas de agua de cristalización y las bandas a números de media se corresponden con vibraciones localizadas en las moléculas de agua estructurales. Finalmente, las bandas con números de onda más bajos contienen contribuciones provenientes de vibraciones de estrechamiento localizadas en fragmentos SiOH que contienen grupos OH grupos que están fuera de la esfera de coordinación de los iones calcio interlaminares.

Para las bandas situadas en 1272 and 1156 cm^{-1} (comparables con las bandas teóricas situadas a números de onda 1222 and 1146 cm^{-1}, respectivamente), la asignación revela que, aunque ambas son atribuibles a vibraciones de doblamiento SiOH, estas vibraciones están localizadas en diferentes tipos de fragmentos SiO_3OH (la de mayor número de onda en fragmentos SiO_3OH coordinados y la de menor número de onda en fragmentos SiO_3OH libres).

Finalmente, se investigó la posibilidad de incorporación de estroncio en la estructura de la uranofana-α. Se demostró que la estructura obtenida por intercambio catiónico de Ca^{2+} por Sr^{2+} (Sr-uranofana) y la estructura de la esfera de solvatación del nuevo catión interlaminar eran muy similares a las de la uranofana normal. La principal diferencia que se encontró entre la Sr-uranofana y la uranofana normal fue, como en caso del mineral arcilloso montmorillonita (Berghout *et al.*, 2010), el aumento del espacio interlaminar (el parámetro de red *c* aumento aproximadamente 0.35 Å). El patrón de Rayos X y el espectro Raman de la Sr-uranofana también fueron extremadamente similares a los de la uranofana normal. Estos resultados están de acuerdo con el estudio experimental de Douglas *et al*. (2002)

10.5 Relación entre la Longitud de Enlace Uranio-Oxígeno y el Desplazamiento Raman Asociado a la Vibración de Estrechamiento Simétrica en el Ion Uranilo.

El propósito de este trabajo fue la derivación de los parámetros de la expresión que relaciona la longitud de enlace uranio-oxígeno y el desplazamiento Raman asociado a la vibración de estrechamiento simétrica del ion uranilo a partir de un pequeño conjunto de datos derivados de cálculos de primeros principios, es decir, sin utilizar ninguna información experimental. Los parámetros resultantes proporcionaron una expresión con esencialmente la misma precisión que la derivada por Barlett and Cooney (1989) a partir de un gran conjunto de datos experimentales.

Sería posible obtener relaciones similares para enlaces que involucran diferentes elementos químicos usando datos obtenidos a partir de cálculos de primeros principios. Sin embargo, debe mencionarse que, aunque el número de cálculos teóricos requeridos es pequeño, las

computaciones correspondientes consumen mucho tiempo y recursos si se desear alcanzar un buen nivel de precisión en el espectro vibracional calculado.

Nuestro estudio sugiere que la relación dada en este trabajo y la de Bartlett y Cooney (1989), cuando se emplean para obtener las longitudes de enlace en términos de los desplazamientos Raman experimentales, proveen distancias cuya precisión está limitada solamente por el carácter aproximado de la relación entre la distancia de enlace y el número de onda. Las relaciones deducidas a partir de mayores conjuntos de datos o a partir de expresiones de mayor orden que ajustan los datos iniciales en una forma más precisa no proporcional mejores desviaciones promediadas con respecto a los correspondientes datos experimentales.

10.6 Conclusiones Finales: Implicaciones para la Caracterización de Fases Secundarias del Combustible Nuclear Gastado en Condiciones de Almacenamiento Definitivo

(1) Los resultados obtenidos en los artículos incluidos en esta tesis sugieren que las computaciones teóricas son una herramienta extremadamente potente para la investigación de materiales que contienen el átomo de uranio. Una vez que se ha generado el correspondiente *pseudopotencial relativista conservador de la norma,* se pueden obtener las propiedades estructurales (parámetros de red, longitudes de enlace, ángulos de enlace y patrones de Rayos X en polvo), los espectros vibracionales Raman y las propiedades termodinámicas y mecánicas de estas sustancias. Este resultado es muy significativo ya que, si tenemos acceso a los recursos computacionales adecuados, se pueden obtener resultados muy precisos a pesar del gran tamaño de estos sistemas y de que el nivel de la teoría requerido para describirlos es muy alto (Crocombette *et al*., 2001; Beridze *et al*., 2014). El uso de estos métodos está libre de las dificultades de los métodos experimentales asociadas a la radiotoxicidad de estos compuestos que requiere un manejo cuidadoso de las muestras. Por tanto, *los cálculos teóricos permiten el estudio seguro de las fases secundarias del combustible nuclear gastado (SNF) en condiciones de almacenamiento definitivo*. Las muestras naturales usadas en los estudios experimentales son generalmente mezclas de varios minerales y *el tratamiento teórico permite el estudio de sustancias puras*. Además, la síntesis de estos compuestos es muy compleja y produce muestras con bajos índices de cristalinidad.

(2) Los resultados teóricos pueden ser usados, junto con los datos experimentales, como una *herramienta interpretativa* de los datos estructurales y vibracionales o como una *herramienta predictiva* para la determinación de propiedades estructurales, vibracionales, termodinámicas y mecánicas de estas sustancias. El entendimiento de las estructuras de estos compuestos es muy importante en sí mismo para caracterizarlos y para evaluar la posible incorporación de elementos transuránicos y productos de fisión en las estructuras de los minerales uranílicos (Burns *et al.*, 1997a; Burns, 2005). La difracción de Rayos X y la espectroscopia Raman (Baker, 2014) están entre las técnicas más ampliamente utilizadas para la identificación de estas sustancias porque son técnicas no-destructivas, no requieren ninguna preparación especial de las muestras y permiten el análisis de cantidades muy pequeñas del material. *Los correspondientes patrones de Rayos X en polvo y espectros Raman calculados teóricamente están en muy buen acuerdo con los obtenidos experimentalmente cuando están disponibles para su comparación.* La asignación de las principales bandas de los espectros vibracionales de estos compuestos, realizada usualmente por el experimentalista en una forma empírica, puede hacerse de una manera rigurosa ya que los métodos teóricos producen vistas a escala microscópica del movimiento de los átomos en los correspondientes estados vibracionales. En los sistemas estudiados, *los cálculos teóricos han permitido la correcta asignación de las bandas del espectro Raman completo por primera vez*. Las principales bandas usadas como huellas para identificar estos minerales se pusieron en correspondencia con datos estructurales específicos. Esta correspondencia entre la información vibracional con la estructura fue usada para la derivación de una expresión muy útil que relaciona

la longitud de enlace uranio-oxígeno y el desplazamiento Raman asociado a la vibración de estrechamiento simétrica del ion uranilo, usando solamente la información derivada de los cálculos teóricos.

(3) Uno de los problemas más relevantes en las ciencias nucleares y energéticas es la protección del medio ambiente. La predicción del comportamiento de materiales contaminantes bajo condiciones medioambientales diversas es extremadamente importante. *Los datos termodinámicos fundamentales son la base indispensable para la modelización dinámica del comportamiento químico de los componentes de los residuos contaminantes*. Estos datos son necesarios para evaluar el origen y evolución de las menas de uranio, para desarrollar programas para el tratamiento de depósitos de uranio o vertederos resultantes de su minería, para el estudio del combustible nuclear gastado (SNF) y el almacenamiento de estos residuos radioactivos, y también, pueden ser de importancia para el estudio de las reacciones que suceden en los reactores de alimentación rápida (Hemingway *et al*., 1982; Langmuir, 1997; Casas *et al*., 1994; Navrotsky *et al*., 2013). Además, el conocimiento de datos termodinámicos precisos es básico para el desarrollo de modelos geoquímicos y modelos de degradación del combustible nuclear usado (Sassani *et al*., 2013).

La enorme importancia de la información termodinámica en la evaluación de la seguridad de los repositorios de residuos nucleares se refleja en el gran número de trabajos experimentales recientes sobre este tema que han culminado en la realización de grandes revisiones y actualizaciones de las propiedades termodinámicas de especies que contienen uranio (Wanner and Forest, 1992; Murphy and Pabalan, 1995; Grenthe *et al*., 2004; Shvareva *et al*., 2012) y otros sistemas que contienen elementos relacionados (Guillaumont, 2003). Aunque la base de datos de información termodinámica de especies que contienen uranio está muy avanzada, existen muchas fases secundarias para las que los datos correspondientes son imprecisos debido a grandes incertidumbres experimentales (Langmuir, 1997). Además, el rango de condiciones (temperatura y presión) para el que se conocen estas propiedades es bastante limitado. *Los cálculos teóricos de estas propiedades termodinámicas para el mineral ruderfordina (Colmenero et al., 2017a) han permitido evaluar la calidad de las propiedades calculadas y han permitido extender el rango de temperatura en el que se conocen estas propiedades a 0-700 K. Además, cálculos recientes de estas propiedades para el trióxido de uranio, γ-UO_3 (Colmenero et al., 2017d), han demostrado su alta calidad incluso a temperaturas muy bajas.*

(4) Como fue notado por Weck *et al*. (2015), la disponibilidad de una gran cantidad de información sobre la formación, estabilidad termodinámica y trasformaciones de fase de las fases de alteración formadas en la superficie del SNF, contrasta con la pobreza en datos relativos a la estabilidad y propiedades mecánicas de estas fases. Esto es particularmente sorprendente ya que los modos de deformación atómica subyacentes e interacciones determinan en gran medida la estabilidad termodinámica de las fases y su transformación. En realidad, exceptuando el trabajo teórico de los peróxidos hidratados de uranilo, studtita y metastudtita, realizado por Weck *et al*. (2015), no existe hasta la fecha ningún estudio, ni teórico ni experimental, en el que se hayan obtenido datos de este tipo. *Los resultados de los cálculos dados en este trabajo sobre los minerales ruderfordina, soddyita y uranofana han demostrado la estabilidad mecánica de sus estructuras. Además, se han generado una gran cantidad de datos mecánicos relevantes de estos minerales incluyendo el módulo elástico y sus derivadas, coeficientes de elasticidad, módulos de Young y cizalladura, radios de Poisson, índices de ductilidad y dureza y medidas de anisotropía elástica. También se obtuvieron sus ecuaciones de estado, ajustando los volúmenes optimizados de la celda unidad sometida a presión y las presiones correspondientes a una ecuación de estado de tipo Birch-Murnahan de cuarto orden.*

10.7 Perspectivas. Lecciones aprendidas durante esta investigación

En el primer contacto con las personas que forman la Unidad de Residuos Radiactivos de Alta Actividad del CIEMAT, aprendí que ellos estaban trabajando principalmente en dos líneas de investigación. La primera, era el estudio de la oxidación de los óxidos de uranio en condiciones secas, y la segunda, la investigación que involucra el proceso de oxidación-hidratación del dióxido de uranio y lleva al estudio de la formación de fases secundarias en la superficie del combustible nuclear gastado. Ambas líneas de investigación estaban siendo analizadas mediante métodos experimentales, principalmente difracción de Rayos X y espectroscopia Raman, y fui invitado a aplicar la metodología teórica a la investigación en estas líneas. Abandoné CIEMAT con algunas nociones sobre el proceso de oxidación del combustible nuclear gastado y con una simple lista de minerales que contienen el átomo de uranio de interés en el almacenamiento del combustible nuclear gastado. A primera vista, pensé que estos campos de investigación deberían estar bastante desarrollados y que mi contribución a estas líneas sería una simple aplicación de los métodos teóricos, principalmente en la determinación de espectros Raman de minerales que contienen el átomo de uranio. Sin embargo, mi sorpresa fue enorme cuando, en la primera búsqueda bibliográfica, encontré que solo existían muy pocos estudios del espectro vibracional de estos materiales. En realidad, ninguno de estos estudios incluía una determinación completa de estos espectros, ya que solo se calculaban las frecuencias de los fonones en el punto gamma y las intensidades de las bandas no se obtenían. Las razones de esta limitada cantidad de tratamientos teóricos se revelaron muy claras una vez que revise la bibliografía: 1) El alto nivel de teoría requerido para describir correctamente los sistemas que contienen el átomo de uranio; 2) El gran número de átomos en las celdas unidad de estos materiales; 3) El gran número de electrones de valencia que es preciso describir explícitamente en los cálculos; y 4) La ausencia de buenos pseudopotenciales conservadores de la norma necesarios para la computación de los espectros vibracionales teóricos.

Siendo consciente de estas dificultades, intenté caracterizar los materiales correspondientes por difracción de Rayos X. Esto fue abordado mediante la computación de las estructuras cristalinas de los materiales en los que estaba interesado usando pseudopotenciales ultrasoft (US), que no son conservadores de la norma. Aunque los resultados eran bastante buenos, la parte más interesante del estudio no podía llevarse a cabo con esta metodología. Por esta razón, consideré la posibilidad de generar desde el inicio un nuevo pseudopotencial conservador de la norma. Estudié varias posibles estrategias y paquetes de programas y después de varios meses de trabajo, tuve éxito en la generación de un pseudopotencial GGA-PBE relativista conservador de la norma, usando el programa fhi98PP y la herramienta de conversión cpi2recpot, válido para la determinación de espectros vibracionales dentro del programa CASTEP. El pseudopotencial fue validado mediante el cálculo de las estructuras de una gran cantidad de fases secundarias y el espectro Raman del mineral carbonato de uranilo ruderfordina (Bonales *et al.,* 2016a). Los resultados fueron excelentes y fueron publicados en la revista *Physical Chemistry Chemical Physics*.

El estudio de la ruderfordina fue bastante complicado por varias razones. En primer lugar, por que se encontró que dos estructuras ortorrómbicas cuasi-degeneradas podían estar presentes simultáneamente en la naturaleza. Esto duplicó el trabajo computacional, que mostró que los patrones de Rayos X y espectros Raman asociados a ambas estructuras eran extraordinariamente similares. En segundo lugar, la estructura en capas de la ruderfordina demandaba el estudio de la influencia de las interacciones de Van der Waals en las computaciones. En tercer lugar, la presencia de bandas correspondientes a moléculas de agua en el espectro Raman requería el estudio de la introducción de agua en la estructura. El segundo problema fue estudiado mediante el uso de funcionales de la densidad con correcciones de dispersión (corrección empírica de Grimme) y el tercero mediante la introducción de moléculas de agua en el espacio interlaminar en la celda unidad de la ruderfordina. Finalmente, se observó que existían algunas bandas en el espectro Raman experimental que no aparecían en el espectro calculado teóricamente. Estas bandas, por tanto, debían ser debidas a que la muestra natural estudiada era una mezcla de

minerales. Se verificó que estas bandas *extra* eran debidas a la presencia de trazas de schoepita y uranofana.

El primer trabajo publicado después del estudio inicial de la ruderfordina fue el del peróxido de uranilo studtita (Colmenero *et al.*, 2017b). Este material fue sintetizado en CIEMAT, en donde se estaba estudiando su estabilidad térmica mediante espectroscopia Raman *in situ.* Se realizaron una larga serie de computaciones de la studtita cada vez más largos y complicados, correspondientes a parámetros de cálculo cada vez más exigentes. La presencia de agua en la celda unidad de la studtita demandaba además la correcta descripción de los puentes de hidrógeno presentes en la estructura, por lo que se utilizó el funcional PBE junto con la corrección empírica de Grimme. Las últimas computaciones resultaron en estructuras muy bien convergidas con respecto a los parámetros de cálculo y con muy buen acuerdo con la geometría y patrón de Rayos X experimentales. Por ello, se abordó la determinación teórica del espectro Raman y se asignaron todas las bandas del espectro experimental por primera vez. La asignación de la banda correspondiente a la vibración de estrechamiento simétrica UO y el análisis experimental de su desplazamiento con la temperatura permitieron estudiar la estabilidad térmica de la studtita en presencia y ausencia de agua. Una de las principales conclusiones de este estudio fue que este material en condiciones húmedas es estable hasta temperaturas mucho mayores que en ausencia de agua (mayores que 90ºC) lo que justificaba su encuentro después del accidente nuclear de Fukushima-Daiichi (en lugar de su producto de deshidratación, la metastudtita). El estudio combinado teórico-experimental fue publicado en la revista *Spectrochimica Acta A* (Colmenero *et al.*, 2017b)

Computaciones intensivas realizadas con posterioridad dieron muy buenos resultados no solo para las propiedades vibracionales de esta clase de materiales sino también permitieron llevar a cabo computaciones de las propiedades termodinámicas y mecánicas (Colmenero *et al.*, 2017a; Colmenero *et al.,* 2017c; Colmenero *et al.*, 2017d; Colmenero *et al.*, 2017e). Los resultados de las propiedades termodinámicas y mecánicas y la ecuación de estado del mineral carbonato de uranilo ruderfordina fueron publicadas en *Journal of Physical Chemistry C* (Colmenero *et al.*, 2017a). Estas computaciones ampliaron el rango en que las propiedades termodinámicas de este mineral eran conocidas al rango 0-700 K. Se demostró que la estructura cristalina de la ruderfordina era mecánica y dinámicamente estable, y se hicieron predicciones de un largo número de propiedades mecánicas para las que no existían mediciones experimentales. El estudio de las propiedades estructurales, mecánicas, ecuación de estado, y el espectro Raman del mineral silicato de uranilo soddyita ha sido enviado para su publicación en *Journal of Solid State Chemistry* (Colmenero *et al.*, 2017c). En este trabajo, su estructura determinada experimentalmente por medio de técnicas de difracción de Rayos X, ha sido confirmada por los cálculos teóricos. Se está considerando en la actualidad la publicación de un trabajo de contenido análogo sobre el mineral silicato de uranilo uranofana que tiene una estructura completamente distinta a la de la soddyita (Colmenero *et al.*, 2017e). Se ha encontrado que los métodos teóricos tienen una gran potencia predictiva en la investigación de materiales que contienen el átomo de uranio. Esto se ha encontrado no solo para las fases secundarias resultantes de la oxidación-hidratación del combustible nuclear gastado, sino también para óxidos de uranio anhidros como el UO_3 (Colmenero *et al.,* 2017d). Los resultados obtenidos para las propiedades estructurales, termodinámicas, la ecuación de estado y el espectro Raman del polimorfo γ del trióxido de uranio han sido enviadas para su publicación en el *Journal of Physical Chemistry C* (Colmenero *et al.*, 2017d). Los resultados estructurales y espectroscópicos están en un acuerdo excelente con la información experimental. De esta manera se ha resuelto la incertidumbre casi total en la asignación del espectro Raman ya que se han asignado todas las bandas de este espectro. Finalmente se ha encontrado un excelente acuerdo con las propiedades termodinámicas obtenidas experimentalmente tanto a baja como a alta temperatura, y se han predicho los valores del módulo de elasticidad y sus derivadas.

En vista del trabajo realizado en los últimos tres años, vemos que estamos en posición de estudiar un gran número de fases secundarias adicionales muy interesantes como oxi-hidróxidos de uranilo (schoepita, bequerelita, curita, etc.), silicatos de uranilo (boltwoodita, weeksita, kasolita, etc.),

carbonatos de uranilo (grimselita, etc.), fosfatos de uranilo (autunita, torbenita, saleeita, etc.) y vanadados de uranilo (carnotita, etc.). El estudio del oxi-hidróxido schoepita ya se ha iniciado. Los resultados para la schoepita deshidratada están en muy buen acuerdo en comparación con la información experimental disponible, y los resultados del mineral schoepita están siendo analizados. Este último material es muy complejo y los cálculos son extremadamente caros. Para estos materiales es posible obtener un gran número de propiedades interesantes con la metodología actual, pudiéndose analizar otras no estudiadas hasta ahora, como por ejemplo, las propiedades ópticas. La medida experimental de estas propiedades a partir de muestras sintéticas y naturales puede ser también considerada.

La línea de investigación que involucra la oxidación del dióxido de uranio en condiciones secas podría también ser extendida. Ya hemos estudiado el sistema γ-UO_3, estando los resultados en excelente acuerdo con los datos experimentales. Las otras formas polimórficas del UO_3 podrían ser igualmente estudiadas. Sin embargo, el estudio de materiales como el UO_2, U_3O_8, cofinita, etc., es decir, óxidos y minerales en los que el estado de oxidación de los átomos involucrados es IV, requiere del uso de tratamientos teóricos más avanzados, ya que los métodos DFT standard fallan en este caso. Esto es debido a la presencia de electrones desapareados en orbitales de alto momento angular (estados *f*). La descripción de estos sistemas se realiza normalmente añadiendo la corrección de Hubbard a los funcionales DFT standard (Beridze *et al*., 2014, y otras referencias dadas aquí), pero en este caso el cálculo de los espectros vibracionales y otras propiedades interesantes no está implementado todavía. También podríamos intentar usar funcionales híbridos o meta-GGA pero su uso es muy costoso en tiempo, y además, no están implementados con funcionalidad completa en la mayoría de los códigos computacionales. Otros códigos como CRYSTAL o VASP o versiones futuras de CASTEP podrían permitir el estudio completo de estos sistemas con funcionales avanzados. Esta línea de investigación debe ser abordada en mayor detalle. *La experiencia ganada en estos años muestra que la mayor parte de estos problemas pueden ser resueltos con una gran dosis de paciencia, dedicación, esfuerzo e interés.*

Part IV. References

References

Ahn, T. M.; Mohanty, S. *Dissolution kinetics of commercial spent nuclear fuels in the potential Yucca mountain repository environment*; U.S. Nuclear Regulatory Commission: Washington, **2007**.

Allen, A. O. *The Radiation Chemistry of Water and Aqueous Solutions*; D. Van Nostrand Co. Inc.: Princeton, **1961**.

Amme, M. Contrary effects of the water radiolysis product H_2O_2 upon the dissolution of nuclear fuel in natural ground water and deionized water. Radiochim. Acta **2002**, *90*, 399–406.

Amme, M.; Renker, B.; Schmid, B.; Feth, M. P.; Bertagnolli, H.; Döbelin, W. Raman microspectrometric identification of corrosion products formed on UO_2 nuclear fuel during leaching experiments. J. Nucl. Mater. **2002**, *306*, 202–212.

Amme, M.; Wiss, T.; Thiele, H.; Boulet, P.; Lang, H. Uranium secondary phase formation during anoxic hydrothermal leaching processes of UO_2 nuclear fuel. J. Nucl. Mater. **2005**, *341*, 209–223.

Amos, R. D. *Ab Initio Methods in Quantum Chemistry–I*; Lawley, K. P. (ed.); Wiley: New York, **1987**; p. 99.

Anderson, H. L.; Booth, E. T.; Dunning, J. R.; Fermi, E.; Glasoe, G. N.; Slack, F. G. The Fission of Uranium. Phys. Rev. **1939**, *55*, 511.

Anderson, O. L. A Simplified Method for Calculating the Debye Temperature from Elastic Constants. J. Phys. Chem. Solids **1963**, *24*, 909–917.

Anderson, O. L. *Equations of State of Solids for Geophysics and Ceramic Science*; Oxford University Press: Oxford, **1995**.

Andersson, D. A.; Baldinozzi G.; Desgranges, L.; Conradson, D. R.; Conradson, S. D. Density Functional Theory Calculations of UO_2 Oxidation: Evolution of UO_{2+x}, U_4O_{9-y}, U_3O_7, and U_3O_8. Inorg. Chem. **2013**, *52*, 2769–2778.

Angel, R. J. Equations of State. Rev. Mineral. Geochem. **2001**, *41*, 35–60. EOSFIT 5.2 software, http://www.ccp14.ac.uk/ccp/webmirrors/ross-angel/rja /soft/.

Antoniewicz, P. R.; Kleinman, L. Kohn-Sham exchange potential exact to first order in ρ. Phys. Rev. B **1985**, *31*, 6779.

Archer, T. D. *Computer Simulations of Calcite*; Ph.D. Thesis; University of Cambridge: **2004**.

Armstrong, C. R.; Nyman, M.; Shvareva, T. Y.; Sigmon, G. E.; Burns, P. C.; Navrotsky, A. Uranyl Peroxide Enhanced Nuclear Fuel Corrosion in Seawater. Proc. Natl. Acad. Sci. U.S.A. **2012**, *109*, 1874–1877.

Artacho, E.; Anglada, E.; Diéguez, O.; Gale, J. D.; García A.; Junquera, J.; Martin, R. M.; Ordejón, P.; Pruneda, J. M.; Sánchez-Portal, D.; Soler, J. M. The SIESTA Method; Developments and Applicability. J. Phys. Condens. Matter **2008**, *20*, 064208.

Ashcroft, N. W.; Mermin, N. D. *Solid State Physics*; Harcourt College Publishers: New York, **1976**.

Astudillo Pastor, J. *El almacenamiento geológico profundo de los residuos de alta actividad. Principios básicos y tecnología*; ENRESA: **2001**.

Atencio, D.; Carvalho, F. M. S.; Matioli, P. A. Coutinhoite, a new thorium uranyl silicate hydrate, from Urucum mine, Galiléia, Minas Gerais, Brazil. Am. Mineral. **2004**, *89*, 721–724.

Bader, R. F. W. *Atoms and Molecules. A Quantum Theory*; Clarendon Press: Oxford, **1990**.

Badger, R. M. The Relation Between the Internuclear Distances and Force Constants of Molecules and Its Application to Polyatomic Molecules. J. Chem. Phys. **1935**, *3*, 710–714.

Baker, R. J. Uranium minerals and their relevance to long term storage of nuclear fuels. Coord. Chem. Rev. **2014**, *266–267*, 123–136.

Baroni, S.; Resta, R. Ab initio calculation of the low-frequency Raman cross section in silicon. Phys. Rev. B **1986**, *33*, 5969–5971.

Baroni, S.; Giannozzi, P.; Testa, A. Green's-Function Approach to Linear Response in Solids. Phys. Rev. Lett. **1987**, *58*, 1861–1864.

Baroni S.; de Gironcoli, S.; Dal Corso, A. Phonons and Related Crystal Properties from Density-Functional Perturbation Theory. Rev. Mod. Phys. **2001**, *73*, 515–562.

Bartlett, J. R.; Cooney, R. P. On the determination of uranium-oxygen bond lengths in dioxouranium(VI) compounds by Raman spectroscopy. J. Mol. Struct. **1989**, *193*, 1989.

Bastians, S.; Crump, G.; Griffith, W. P.; Withnall, R. Raspite and studtite: Raman spectra of two unique minerals. J. Raman Spectrosc. **2004**, *35*, 726–731.

Becke, A. D. Density functional calculations of molecular bond energies. J. Chem. Phys. **1986**, *84*, 4524.

Becke, A. D. Density-functional exchange-energy approximation with correct asymptotic behavior. Phys. Rev. A **1988**, *38*, 3098.

Becquerel, A. H. Sur les radiations invisibles émises par les corps phosphorescents. Comptes. Rendus Acad. Sci. **1896**, *122*, 501–502.

Becquerel, A. H. *On radioactivity, a new property of matter*; Nobel Lecture: December 11, **1903**.

Belokoneva, E. L.; Mokeeva, V. I.; Kuznetsov, L. M.; Simonov, M. A.; Makarov, E. S.; Belov, N. V. Crystal structure of synthetic soddyite $(UO_2)_2[SiO_4](H_2O)_2$. Doklady Akademii Nauk SSSR **1979**, *246*, 93–96.

Beridze, G.; Kowalski, P. M. Benchmarking the DFT+U Method for Thermochemical Calculations of Uranium Molecular Compounds and Solids. J. Phys. Chem. A **2014**, *118*, 11797–11810.

Berry, M. V. Quantal Phase Factors Accompanying Adiabatic Changes. Proc. Roy. Soc. London A **1984**, *392*, 45–57.

Birch, F. Finite Elastic Strain of Cubic Crystal. Phys. Rev. **1947**, *71*, 809–824.

Bish, D. L.; Post, J. E. Modern Powder Diffraction. Rev. Mineral. Geochem. **1989**, *20*, 369 pp.

Biswas, S.: Steudtner, R.; Schmidt, M.; McKenna, C.; Vintro, L. L.; Twamley, B.; Baker, R. J. An investigation of the interactions of Eu^{3+} and Am^{3+} with uranyl minerals: implications for the storage of spent nuclear fuel. Dalton Trans. **2016**, *45*, 6383–6393.

Biwer, D. M.; Ebert, W. L.; Bates, J. K. The Raman spectra of several uranyl-containing minerals using a microprobe. J. Nucl. Mater. **1990**, *175*, 188–193.

Blaton, N.; Vochten, R.; Peeters, O. M.; van Springel, K. The crystal structure of $Na_2(UO_2)_2SiO_4F_2$, a compound structurally related to soddyite, and formed during uranyl silicate synthesis in Teflon-linedbombs. Neues Jahrbuch fuer Mineralogie, Monatshefte **1999**, *6*, 253–264.

Bleam, W. F. Atomic theories of phyllosilicates: quantum chemistry, statistical mechanics, electrostatic theory, and crystal chemistry. Rev. Geophys. **1993**, *31*, 51–73.

Bocharov, D.; Gryaznov, D.; Zhukovskii, Yu. F.; Kotomin, E. A. DFT calculations of point defects on UN (001) surface. Surf. Sci. **2011**, *605*, 396–400.

Bonales, L. J.; Menor-Salvan, C.; Cobos, J. Study of the alteration products of a natural uraninite by Raman spectroscopy. J. Nucl. Mater. **2015**, *462*, 296–303.

Bonales, L. J.; Colmenero, F.; Cobos, J.; Timón, V. Spectroscopic Raman Characterization of Rutherfordine: A Combined DFT and Experimental Study. Phys. Chem. Chem. Phys. **2016a**, *18*, 16575–16584.

Bonales, L. J.; Elorrieta, J. M.; Lobato, A.; Cobos, J. *Raman Spectroscopy, a Useful Tool to Study Nuclear Materials*; In Applications of Molecular Spectroscopy to Current Research in the Chemical and Biological Sciences; Stauffer, M. T. (ed.); Intech: **2016b**.

Born, M. On the Stability of Crystal Lattices. I. Math. Proc. Cambridge Philos. Soc. **1940**, *36*, 160–172.

Born, M.; Oppenheimer, J. R. Zur Quantentheorie der Molekeln (On the Quantum Theory of Molecules). Ann. Phys. **1927**, *389* 457–484.

Born, M., Huang, K. *Dynamics Theory of Crystal Lattices*, Oxford University Press: Oxford, **1954**.

Bouhadda, Y.; Djella, S.; Bououdina, M.; Fenineche, N.; Boudouma, Y. Structural and elastic properties of $LiBH_4$ for hydrogen storage applications. J. Alloy. Compd. **2012**, *534*, 20–24.

Boulet, P.; Verstraete, M. J.; Crocombette, J.-P.; Briki, M., Record, M.-C. Electronic Properties of the Mg2Si Thermoelectric Material Investigated by Linear-Response Density-Functional Theory. Comput. Mater. Sci. **2011**, *50*, 847–851.

Brandenburg, K.; Putz, H. Endeavour versión 1.6, agosto **2008**, © 2000–2008 Crystal Impact GbR.

Brindley, G. W.; Brown, G. (eds.). *Crystal Structures of Clay Minerals and their X-Ray Identification*; Mineralogical Society Monographs No. 5; Mineralogical Society: London, **1980**.

Bruno, J.; Ewing, R. C. Spent Nuclear Fuel. Elements **2006**, *2*, 343–349.

Bruno, J.; Casas, I.; Sandino, A. Static and Dynamic SIMFUEL dissolution studies under oxic conditions. J. Nucl. Mater. **1992**, *190*, 61–69.

Buck, E. C.; Finch, R. J.; Finn; P. A.; Bates, J. K. Retention of Neptunium in Uranyl Alteration Phases Formed During Spent Fuel Corrosion. MRS Online Proceedings Library **1997**, *506.*

Bullock, J. I. Raman and infrared spectroscopic studies of the uranyl ion: the symmetric stretching frequency, force constants, and bond lengths. J. Chem. Soc. A **1969**, 781-784.

Burns, P. C. The structure of boltwoodite and implications of solid solution towards sodium boltwoodite. Can. Mineral. **1998**, *36*, 1069–1075.

Burns, P. C. The crystal chemistry of uranium. Rev. Mineral. **1999a**, *38*, 23–90.

Burns, P. C. Cs boltwoodite obtained by ion exchange from single crystals: Implications for radionuclide release in a nuclear repository. J. Nucl. Mater. **1999b**, *265*, 218–223.

Burns, P. C. A new uranyl silicate sheet in the structure of haiweeite and comparison to other uranyl silicates. Can. Mineral. **2001**, *39*, 1153–1160.

Burns, P. C. U^{6+} minerals and inorganic compounds: insights into an expanded structural hierarchy of crystal structures. Can. Mineral. **2005**, *43*, 1839–1894.

Burns, P. C.; Hill, F. C. A new uranyl sheet in $K_5[(UO_2)_{10}O_8(OH)_9](H_2O)$: New insight into sheet anion-topologies. Can. Mineral. **2000**, *38*, 163–173.

Burns, P. C.; Li, Y. The structures of becquerelite and Sr-exchanged becquerelite. Am. Mineral. **2002**, *87*, 550–557.

Burns, P. C.; Hughes, K.-A. Studtite, $[(UO_2)(O_2)(H_2O)_2](H_2O)_2$: the first structure of a peroxide mineral. Am. Mineral. **2003**, *88*, 1165–1168.

Burns, P. C.; Klingensmith, A. L. Uranium Mineralogy and Neptunium Mobility. Elements **2006**, *2*, 351–356.

Burns, P. C.; Miller, M. L.; Ewing, R. C. U^{6+} Minerals and inorganic phases: A comparison and hierarchy of crystal structures, Can. Mineral. **1996**, *34*, 845–880.

Burns, P. C.; Ewing, R. C.; Miller, M. L. Incorporation mechanisms of actinide elements in to the structures of U^{6+} phases formed during the oxidation of spent nuclear fuel. J. Nucl. Mater. **1997a**, *245*, 1–9.

Burns, P. C., Ewing, R. C.; Hawthorne, F. C. The crystal chemistry of hexavalent uranium: Polyhedron geometries, bond-valence parameters, and polymerization of polyhedral. Can. Mineral. **1997b**, *35*, 1551–1570.

Burns, P. C., Deely, K. M.; Skanthakumar, S. Neptunium incorporation into uranyl compounds that form as alteration products of spent nuclear fuel: Implications for geologic repository performance. Radiochim. Acta **2004**, *92*, 151–159.

Burns, P. C.; Ewing, R. C.; Navrotsky, A. Nuclear Fuel in a Reactor Accident. Science **2012**, *335*, 1184–1188.

Caracas, R.; Bobociou, E. Theoretical modelling of Raman spectra. EMU Notes in Mineralogy **2012**, *12*, 175–194.

Carbol, P.; Cobos, J.; Glatz, J.-P.; Ronchi, C.; Rondinella, V.; Wegen, D. H.; Wiss, T.; Loida, A.; Metz, V.; Kienzler, B.; *et al. The effect of dissolved hydrogen on the dissolution of ^{233}U doped UO_2(s), high burn-up spent fuel and MOX fuel*, Technical Report TR-05-09, SKB: Stockholm, **2005**.

Cardona, M. *Light Scattering in Solids II: Basic Concepts and Instrumentation*; Topics in Applied Physics Vol. 50; M. Cardona, M, Guntherodt, G. (eds.); Springer: New York, **1982**.

Carnall, W. T.; Neufeldt, S. J.; Walker, A. Reactions in Molten Salt Solutions. I. Uranate and Neptunate Formation in Molten Lithium Nitrate-Sodium Nitrate. Inorg. Chem. **1965**, *4*, 1808-1813.

Casas, I.; Bruno, J.; Cera, E.; Finch, R. J.; Ewing, R. C. *Kinetic and Thermodynamic Studies of Uranium Minerals Assessment of the Long-Term Evolution of Spent Nuclear Fuel*; SKB Technical Report 94-16; Swedish Nuclear Fuel and Waste Management Co.: Stockholm, Sweden, **1994**.

Castro, L.; Yahia, A.; Maron, L. Are 5f Electrons Really Active in Organoactinide Reactivity? Some Insights from DFT Studies. Chem. Phys. Chem. **2010**, *11*, 990–994.

Catalano, J. G.; Brown, G. E. Analysis of uranyl-bearing phases by EXAFS spectroscopy: Interferences, multiple scattering, accuracy of structural parameters and spectral differences. Am. Mineral. **2004**, *89*, 1004–1021.

Cejka, J. Infrared spectroscopy and thermal analysis of the uranyl minerals. Rev. Mineral. **1999**, 38, 521–622.

Cejka, J.; Urbanec, Z. Contribution to the hydrothermal origin of rutherfordine, UO_2CO_3. Casopis Narodniho Muzeo **1988**, *157*, 1–10.

Cejka, J.; Sejkora, J.; Deliens, M. New data on studtite, $UO_4 \cdot 4H_2O$, from Shinkolobwe, Shaba, Zaire. Neues Jahrbuch fuer Mineralogie, Monatshefte **1996**, *3*, 125–134.

Ceperley, D. M.; Alder, B. J. Ground State of the Electron Gas by a Stochastic Method. Phys. Rev. Lett. **1980**, *45*, 566.

Cera, E. *Estudis termodinàmics i cinètics de disolució de fases naturals d'urani representatives d'un procés d'alteració oxidativa de l'oxid d'urani (IV). Analogia amb el comportament i amb l'evolució a llarg terme d'un repositori de residus radioactius*. Ph.D. Thesis. Universidad Autonoma de Barcelona: **1996**.

Cesbron, F.; Ildefonse, P.; Sichere, M. C. New mineralogical data on uranophane and β-uranophane; synthesis of uranophane. Mineral. Mag. **1993**, *57*, 301–308.

Civalleri, B.; Zicovich-Wilson, C. M.; Valenzano, L.; Ugliengo, P. B3LYP augmented with an empirical dispersion term (B3LYP-D*) as applied to molecular crystals. Crystengcomm **2008**, *10*, 405–410.

Clarens, F.; de Pablo, J.; Díez-Perez, I.; Casas, I.; Gimenez, J.; Rovira, M. Formation of studtite during the oxidative dissolution of UO_2 by hydrogen peroxide: A SFM study. Environ. Sci. Technol. **2004**, *38*, 6656–6661.

Clarens, F.; de Pablo, J.; Casas, I.; Giménez, J.; Rovira, M.; Merino, J.; Cera, E.; Bruno, J.; Quiñones, J.; Martínez-Esparza, A. The oxidative dissolution of unirradiated UO_2 by hydrogen peroxide as a function of pH. J. Nucl. Mater. **2005**, *345*, 225–231.

Clark, D. L.; Hobart, D. E.; Neu, M. P. Actinide carbonate complexes and their importance in actinide environmental chemistry. Chem. Rev. **1996**, *95*, 25–48.

Clark, S. J.; Segall, M. D.; Pickard, C. J.; Hasnip, P. J.; Probert, M. I. J.; Refson, K.; Payne, M. C. First Principles Methods Using CASTEP. Z. Kristallogr. - Cryst. Mater. **2005**, *220*, 567–570.

Cobos, J.; Rondinella, V. V.; Glatz, J. P.; Wiss, T.; Quiñones, J.; Martínez Esparza, A. *Quantification of radiolytically enhanced fuel dissolution. Alpha radiolysis enhanced fuel dissolution. Review and conclusions of the experimental work performed under ITU / ENRESA - CIEMAT Special contract 1 into framework agreement 15983*. In J.R. Centre, Ed. Technical Report, p. 38; Institute for Transuranium Elements: **2006**.

Colmenero, F.; Perez del Valle, C.; Valdemoro, C. Approximating q-order reduced density matrices in terms of the lower-order ones. I. General relations. Phys. Rev. A **1993a**, *47*, 971–978.

Colmenero, F.; Valdemoro, C. Approximating q-order reduced density matrices in terms of the lower-order ones. II. Applications. Phys. Rev. A **1993b**, *47*, 979–985.

Colmenero, F.; Valdemoro, C. Self-Consistent Approximate Solution of the Second-Order Schrödinger Equation, Int. J. Quant. Chem. **1994**, *51*, 369-388.

Colmenero, F.; Bonales, L. J.; Cobos, J. Timón, V. Thermodynamic and Mechanical Properties of the Rutherfordine Mineral Based on Density Functional Theory. J. Phys. Chem. C **2017a**, *121*, 5994–6001.

Colmenero, F.; Bonales, L. J.; Cobos, J.; Timón, V. Study of the Thermal Stability of Studtite by In Situ Raman Spectroscopy and DFT Calculations. Spectrochim. Acta. A **2017b**, *174*, 245–253.

Colmenero, F.; Bonales, L. J.; Cobos, J.; Timón, V. Structural, mechanical and vibrational study of uranyl silicate mineral soddyite by DFT calculations. J. Solid. State Chem **2017c**, *253*, 249–257.

Colmenero, F.; Bonales, L. J.; Cobos, J.; Timón, V. Density Functional Theory Study of the Structural, Thermodynamic and Vibrational Properties of γ-UO3 Polymorph. J. Phys. Chem. C, **2017d**, in press.

Colmenero, F.; Bonales, L. J.; Cobos, J.; Timón, V. Structural, mechanical and Raman spectroscopic characterization of uranyl silicate mineral Uranophane-α by DFT and experimental methods. Clay Minerals, **2017e**, submitted.

Colmenero, F.; Bonales, L. J.; Cobos, J.; Timón, V. Relation of uranium-oxygen bond length and uranyl symmetric stretching Raman shift obtained from theoretical DFT calculations. J. Mol. Struct. **2017f,** to be submitted.

Colmenero, F.; Bonales, L. J.; Cobos, J.; Timón, V. **2017g,** in preparation.

Constantin, L. A; Perdew, J. P.; Tao, J. Meta-generalized gradient approximation for the exchange-correlation hole with an application to the jellium surface energy. Phys. Rev. B **2006**, *73*, 205104.

Corbel, C.; Sattonnay, G.; Guilbert, S.; Garrido, F.; Barthe, M. F.; Jégou, C. Addition versus radiolytic production effects of hydrogen peroxide on aqueous corrosion of UO_2. J. Nucl. Mater. **2006**, *348*, 1–17.

Cordfunke, E. H. P.; O'Hare, P. A. G. *The Chemical Thermodynamics of Actinide Elements and Compounds. Part 3. Miscellaneous Actinide Compounds*; International Atomic Energy Agency: Vienna, Austria, **1978**.

Cowan, G. A. A Natural Fission Reactor. Sci. Am. **1976**, *235,* 36.

Craig, B. D.; Lane, R. A.; Rose, D. H. *Handbook of corrosion and prevention control: A program management guide for selecting materials*; Advanced Materials, Manufacturing, and Testing Information Analysis Center (AMMTIAC); Alion Science & Technology: New York, 2nd edition, **2006**, 276 p.

Cramer, J.; Smellie, J. (eds.) *Final report of the AECL/SKB Cigar Lake analogue study*. SKB TR94-04; SKB: **1994**.

Craw, J. S.; Vincent, M. A.; Hillier, I. H.; Wallwork, A. L. Ab initio quantum chemical calculations on uranyl UO_2^{2+}, plutonyl PuO_2^{2+}, and their nitrates and sulfates. J. Phys. Chem. **1995**, *99*, 10181-10185.

Crocombette, J. P.; Jollet, F.; Thien Nga, L.; Petit, T. Plane-wave pseudopotential study of point defects in uranium dioxide. Phys. Rev. B **2001**, *64*, 104107.

CSN, Consejo de Seguridad Nuclear. https://www.csn.es/documents/10182/932121/ retrieved **2017**.

Čuba, V.; Múčka, V.; Pospíšil, M. *Radiation Induced Corrosion of Nuclear Fuel and Materials;* in Advances in Nuclear Fuel*,* Revankar, S. T. (ed.); InTech: **2012**; Chapter 2.

Curie, P. Radioactive substances, especially radium. Nobel Lecture: June 6, **1905.**

Curie, P; Curie, M. Sur une substance nouvelle radio-active contenue dans la pechblende. Comptes Rendus Acad. Sci. **1898a**, *127*, 175–178.

Curie, P; Curie, M.; Bémont, G. Sur une nouvelle substance fortement radio-active contenue dans la pechblende. Comptes Rendus Acad. Sci. **1898b,** *127*:1215–1218.

Chadi, D. J.; Cohen, M. L. Special Points in the Brillouin Zone. Phys. Rev. B **1973**, *8*, 5747.

Chadwick., J. Possible Existence of a Neutron. Nature **1932**, *129*, 312

Chaudhuri, D.; Balasubramanian, K. Electronic structure and spectra of plutonyl complexes and their hydrated forms: PuO_2CO_3 and $PuO_2CO_2 \cdot nH_2O$ (n = 1,2). Chem. Phys. Lett. **2004**, *399*, 67–72.

Chen, X.-Q.: Niu, H; Li, D.; Li, Y. Modeling hardness of polycrystalline materials and bulk metallic glasses. Intermetallics **2011**, *19*, 1275–1281.

Choppin, G.; Liljenzin, J. O.; Rydberg, J. *Radiochemistry and Nuclear Chemistry*, Reed Educational and Professional Publishing Ltd: Oxford, **1995**.

Chou, I.-M.; Seal, R. R.; Hemingway, B. S. Determination of melanterite-rozenite and chalcanthite-bonattite equilibria by humidity measurements at 0.1MPa. Am. Mineral. **2002**, *87*, 108–114.

Christ, C. L.; Clark, J. R. Some observations on rutherfordine. Am. Mineral. **1956**, *41*, 844-850.

Christ, C. L.; Clark, J. R.; Evans, H. T. Crystal Structure of Rutherfordine, UO_2CO_3. Science **1955**, *121*, 472–473.

Christensen, H. Radiation induced dissolution of UO_2. Mat. Res. Soc. Symp. Proc. **1991**, *212*, 213–220.

Christensen, H. Calculations simulating spent-fuel leaching experiments. Nucl. Technol. **1998**, *124*, 165–174.

Christensen, H.; Sunder, S.; Shoesmith, D. W. Oxidation of nuclear fuel (UO_2) by the products of water radiolysis: development of a kinetic model. J. Alloys Comp. **1994**, *213-214*, 93–99.

Christensen, H.; Sunder, S. An evaluation of layer water thickness effective in the oxidation of UO_2 fuel due to radiolysis of water. J. Nucl. Mater. **1996**, *238*, 70–77.

Christensen, H.; Sunder, S. Current state of knowledge of water radiolysis effects on spent nuclear fuel corrosion. Nucl. Technol. **2000**, *131*, 102–123.

Chroneos, A.; Rushton, M. J. D.; Jiang, C.; Tsoukalas, L. H. Nuclear wasteform materials: Atomistic simulation case studies. J. Nucl. Mater. **2013**, *441*, 29–39.

Davis, J. R. *Corrosion: Understanding the basics*; ASM International: **2000**, 563 p.

Debets, P. C. X-ray diffraction data on hydrated uranium peroxide. J. Inorg. Nucl. Chem. **1963**, *25*, 727–730.

Deditius, A. P.; Utsunomiya, S.; Wall, M. A.; Pointeau, V. R; Ewing, R. C. Crystal chemistry and radiation-induced amorphization of P-coffinite from the natural fission reactor at Bangombé, Gabon. Am. Mineral. **2009**, *94*, 827–837.

De Gironcoli, S. Lattice dynamics of metals from density-functional perturbation theory. Phys. Rev. B **1995**, *51*, 6773.

Del Corro García, E. Ph.D. Thesis; Universidad Complutense de Madrid: **2011**.

Demartin, F.; Gramaccioli, C. M.; Pilati, T. The Importance of Accurate Crystal Structure Determination of Uranium Minerals. II. Soddyite $(UO_2)_2(SiO_4)\cdot 2H_2O$. Acta Crystallogr. C **1992**, *48*, 1–4.

De Pablo, J.; Casas, I.; Clarens, F.; Giménez, J.; Rovira, M. *Contribución experimental y modelización de procesos básicos para el desarrollo del modelo de alteración de la matriz del combustible irradiado*; Publicaciones técnicas 01/2003; ENRESA: Madrid, SPAIN, **2003a**.

De Pablo, J.; Casas, I.; Giménez, J.; Clarens, F.; Rovira, M.; Dies, X.; Serrano, D.; Glatz, J. P.; Martínez Esparza, A.; Gago, J. A.; Cera, E.; Merino, J.; Bruno, J.; Quiñones, J.; Díaz Arocas, P. P.; Cobos, J.; González de la Huebra, A. *Contribución experimental al estudio de la matriz de combustible*; In ENRESA, Ed. V Jornadas de investigación, desarrollo tecnológico y demostración para la gestión de residuos radiactivos. Sinopsis de pósteres, 07/2003, p. 42; ENRESA: Madrid, **2003b**.

Desgranges, L.; Baldinozzi, G.; Simon, P.; Guimbretière, G.; Canizares, A. Raman spectrum of U_4O_9: a new interpretation of damage lines in UO_2. J. Raman Spectrosc. **2012**, *43*, 455–458.

Dirac, P. A. M. Quantum Mechanics of Many-Electron Systems. Proc. Roy. Soc. A **1929**, *123*, 714–733.

Dirac, P. A. M. Note on exchange phenomena in the Thomas atom. Proc. Cambridge Phil. Soc. **1930**, *26*, 376–385.

DOE. *DOE Fundamentals Handbook: Nuclear Physics and Reactor Theory, Volume 1*. U.S. Department of Energy: **1993a.**

DOE. *DOE Fundamentals Handbook: Nuclear Physics and Reactor Theory, Volume 2*. U.S. Department of Energy, **1993b**.

Douglas, M.; Clark, S. B.; Utsunomiya, S.; Ewing, R. C. Cesium and Strontium Incorporation into Uranophane, $Ca[(UO_2)(SiO_3OH)]_2 \cdot 5H_2O$. J. Nucl. Sci. Technol. Suppl. **2002**, 3, 504–507.

Douglas, M.: Clark, S. B.; Friese, J. I.; Arey, B. W.; Buck, E. C.; Hanson, B. D. Neptunium(V) Partitioning to Uranium(VI) Oxide and Peroxide Solids. Environ. Sci. Technol. **2005a**, *39*, 4117–4124.

Douglas, M.; Clark, S. B.; Friese, J. I.; Arey, B. W.; Buck, E. C.; Hanson, B. D.; Utsunomiya, S.; Ewing, R. C. Microscale characterization of uranium(VI) silicate solids and associated neptunium(V). Radiochim. Acta **2005b**, *93*, 265–272.

Dovesi, R. *Crystal Lattices and Crystal Symmetry*, in Quantum Mechanical Ab Initio Calculation of the Properties of Crystalline Materials; Pisani, C. (ed.); Lecture Notes in Chemistry Vol. 67; Springer: Berlin, **1996**; pp. 31–46.

Dovesi, R.; Civalleri, B.; Orlando, R.; Roetti, C.; Saunders, V. R. *Ab initio quantum simulation in solid state chemistry*; In Lipkowitz, K. B, Larter, R., Cundari, T. R. (eds.); Reviews in Computational Chemistry, Vol. 21, p. 1–125; Wiley: New York, **2005**.

Downs, R. T. The RRUFF Project: an integrated study of the chemistry, crystallography, Raman and infrared spectroscopy of minerals, Program and Abstracts of the 19th General Meeting of the International Mineralogical Association in Kobe, Japan, **2006**. O03-13; RRUFF database, http://rruff.info/uranophane. Record RRUFF-050380 corresponds to a natural mineral sample from Grafton County, New Hampshire, USA.

Downs, R. T.; Bartelmehs, K. L.; Gibbs, G. V.; Boisen, M. B. Interactive Software for Calculating and Displaying X-Ray or Neutron Powder Diffractometer Patterns of Crystalline Materials. Am. Mineral. **1993**, *78*, 1104–1107.

Downs; R. T.; Bartelmehs, K.; Sinnaswamy, K. XtalDraw, Versión Agosto **2003**.

Driscoll, R. J. P.; Wolverson, D.; Mitchels, J. M.; Skelton, J. M.; Parker, S. C.; Molinari, M.; Khan, I.; Geeson, D.; Allen, G. C. A Raman spectroscopic study of uranyl minerals from Cornwall, UK. RSC Adv. **2014**, *4*, 59137–59149.

Dubessy, J.; Caumon, M. C.; Rull, F. (eds.) *Raman Spectroscopy Applied to Earth Sciences and Cultural Heritage*; European Mineralogical Union Notes in Mineralogy Series, Vol. 12; European Mineralogical Union and The Mineralogical Society of Great Britain & Ireland: **2012**. ISBN 9780903056311.

Dudarev, S. L.; Nguyen Manh, D.; Sutton, A. P. Effect of Mott-Hubbard correlations on the electronic structure and structural stability of uranium dioxide. Phil. Mag. B **1997**, *75*, 613–628.

Eisenhower, D. D. https://www.eisenhower.archives.gov/research/online_documents/atoms_for_peace.htm. November 28, **1953**.

Engelkemeir, D. W.; Flynn, K. F.; Glendenin, L. E. Positron Emission in the Decay of ^{40}K. Phys. Rev. **1962**, *126*, 1818.

ENRESA. *Tercer Plan de Investigación y Desarrollo*. ENRESA: Madrid, **1995**.

ENRESA. *Evaluación del comportamiento y de la seguridad de un almacenamiento geológico profundo en granito;* Publicación técnica ENRESA, 06-97; ENRESA: Madrid., **1997a.**

ENRESA. *Terceras Jornadas de I+D y Tecnologías de Gestión de Residuos Radiactivos*. ENRESA: Madrid, **1997b**.

ENRESA. *Evaluación del comportamiento y de la seguridad de un almacenamiento de combustible gastado en una formación granítica, 49-1PP-M-15-01 Rev. 0,* ENRESA: Madrid, **2001**.

ENRESA. *Evaluación del comportamiento y de la seguridad de un almacén geológico profundo de residuos radiactivos de alta actividad en arcilla. Proceso de selección del elemento combustible de referencia.* ENRESA: Madrid, **2003**.

Eriksen, T. E.; Eklund, U. B.; Werme, L. O.; Bruno, J. Dissolution of irradiated fuel: a radiolytic mass balance study. J. Nucl. Mater. **1995**, *227*, 76–82.

Eriksen, T. E.; Shoesmith, D. W.; Jonsson, L. Radiation induced dissolution of UO_2 based nuclear fuel - A critical review of predictive modelling approaches. J. Nucl. Mater. **2012**, *420*, 409–423.

Escribano, R. *Introduction to Spectroscopy*; in A Laboratory Spectroscopy Workshop for Astrophysics, ALABASTRO-2016; Jaca, Spain, June **2016**; Chapter 3, p. 27.

Esteban, J. A.; Martínez Esparza, A.: de Pablo, J.; Casas, I.; Díaz Arocas, P. P.; Serrano, J. A.; Rodríguez Almazán, J. L.; Quiñones, J. *Descripción y características quimicofísicas de los combustibles nucleares irradiados*. DFN/RA-03/OP-98, p. 100. CIEMAT: Madrid, **1998**.

Evans, H. T. Uranyl ion coordination. Science, **1963**, *141*, 154–158.

Ewing, R. C. The Nuclear Fuel Cycle: A Role for Mineralogy and Geochemistry. Elements **2006**, *2*, 331–334.

Ewing, R. C. Long-term storage of spent nuclear fuel. Nature Mater. **2015**, *14*, 252–256.

Ewing, R. C.; Meldrum, A.; Wang, L.; Wang, S. Radiation-Induced Amorphization. Rev. Mineral. Geochem. **2000**, *39*, 319–361.

Ewing, R. C.: Weber, W. J.; Lian, J. Nuclear Waste Disposal—Pyrochlore ($A_2B_2O_7$): Nuclear Waste Form for the Immobilization of Plutonium and "Minor" Actinides. J. Appl. Phys. **2004**, *95*, 5949–5971.

Falaise, C.; Delille, J.; Volkringer, C.; Vezin, H.; Rabu, P.; Loiseau, T. Series of Hydrated Heterometallic Uranyl-Cobalt(II) Coordination Polymers with Aromatic Polycarboxylate Ligands: Formation of U=O-Co Bonding upon Dehydration Process. Inorg. Chem. **2016**, *55*, 10453–10466.

Farmer, V. C. *The Infrared Spectra of Minerals*; Mineralogical Society Monographs No. 4, Mineralogical Society: London, **1974**; Appendix, p. 515.

Fateley, G. W.; McDevitt, N. T.; Bentley, F. F. Infrared and Raman Selection Rules for Lattice Vibrations: The Correlation Method. Appl. Spectrosc. **1971**, *25*, 155–173.

Faulkes, E.; Russo, R. E.; Perry, D. L. Raman spectral studies of uranyl sulfate and its urea complex structural isomers. Spectrochim. Acta A **1993**, *49*, 975–983.

Faulkes, E.; Russo, R. E.; Perry, D. L. Raman studies of uranyl nitrate and its hydroxy bridged dimer. Spectrochim. Acta A **1994**, *50*, 757–763.

Faulkes, E.; Massuyeau, F.; Kalashnyk, N.; Perry, D. L. Application of Raman and photoluminiscence spectroscopy for identification of uranium minerals in the environment. Spectroscopy Europe **2015a**, *27*, 14–17.

Faulques, E.; Kalashnyk, N.; Massuyeau, F.; Perry, D. L. Spectroscopic markers for uranium(VI) phosphates: A vibronic study. RSC Adv. **2015b**, *5*, 71219–71227.

Fermi, E. Eine statistische Methode zur Bestimmung einiger Eigenschaften des Atoms und ihre Anwendung auf die Theorie des periodischen Systems der Elemente. Z. Phys. **1928**, *48*, 73-79.

Fermi, E.; Szilard, L. Neutronic Reactor. U.S. Patent 2,708, (issued 17 May **1955**); Fermi and Szilard applied for a patent on reactors on 19 December **1944**. Its issuance was delayed for 10 years because of wartime secrecy.

Fermi, E.; Amaldi, E.; d'Agostino, O.; Rasetti, F.; Segré, E. Artificial Radioactivity Produced by Neutron Bombardment. Proc. Roy. Soc. (London) A, **1934a**, *146*, 483–500.

Fermi, E.; Amaldi, E.; d'Agostino, O.; Rasetti, F.; Segrè. E. Radioattività provocata da bombardamento di neutroni III. La Ricerca Scientifica, **1934b**, *5*, 452–453.

Feynman, R. P. Forces in Molecules. Phys. Rev. **1939**, *56*, 340.

Finch, R. J.; Ewing, R. C. *Alteration of natural UO_2 under oxidizing conditions from Shinkolobwe, Katanga, Zaire: A natural analogue for the corrosion of spent fuel*. SKB TR 89-37: SKB: **1989**.

Finch, R. J.; Ewing, R. C. The corrosion of uraninite under oxidizing conditions, J. Nucl. Mater. **1992**, *190*, 133–156.

Finch, R. J.; Ewing, R. C. *Uraninite alteration in an oxidizing environment and its relevance to the disposal of spent nuclear fuel*; SKB Technical Report, TR 91-15. SKB: **2003**.

Finch, R.; Murakami, T. Systematic and paragenesis of uranium minerals. Rev. Mineral. **1999**, *38*, 91–179.

Finch, R. J.; Miller, M. L.; Ewing, R. C., Weathering of natural uranyl oxide hydrates: schoepite polytypes and dehydration effects. Radiochim. Acta **1992**, *58*, 433–443.

Finch, R. J.; Cooper, M.; Hawthorne, F. Refinement of the crystal structure of rutherfordine. Can. Mineral. **1999**, *37*, 929-938.

Flerov, G. N.; Petrzhak, K. A. Spontaneous fission of uranium. Phys. Rev. **1940**, *58*, 89.

Forbes, T. Z.; Burns, P. C. $Ba(NpO_2)(PO_4)(H_2O)$, its relationship to the uranophane group, and implications for Np incorporation in uranyl minerals. Am. Mineral. **2006**, *91*, 1089–1093.

Forbes, T. Z.; Horan, P.; Devine, T.; McInnis, D.; Burns, P. C. Alteration of dehydrated schoepite and soddyite to studtite, $[(UO_2)(O_2)(H_2O)_2](H_2O)_2$. Am. Mineral. **2011**, *96*, 202–206.

Forsyth, R. S. *Spent nuclear fuel: a review of properties of possible relevance to corrosion process*; SKB Technical report, 95:23; SKB: Stockholmo, **1995**.

Forsyth, R. S.; Werme, L. O.; Bruno, J. The corrosion of spent UO_2 fuel in synthetic groundwater, J. Nucl. Mater. **1986**, *138*, 1–5.

Frantsevich, I. N.; Voronov, F. F.; Bokuta. S. A. *Elastic Constants and Elastic Moduli of Metals and Insulators Handbook*; Frantsevich, I. N. (ed.); Naukova Dumka: Kiev, **1983**, pp. 60–180.

Freyss, M.; Petit, T.; Crocombette, J. P. Point defects in uranium dioxide: Ab initio pseudopotential approach in the generalized gradient approximation, J. Nucl. Mat. **2005**, *347*, 44–51.

Freyss, M.; Vergnet, N.; Petit, T. Ab initio modeling of the behavior of helium and xenon in actinide dioxide nuclear fuels. J. Nucl. Mater. **2006**, *352*, 144–150.

Friese, J. I.; Douglas, M.; McNamara, B. K.; Clark, S. B.; and Hanson, B. D. Np Behavior in Synthesized Uranyl Phases: Results of Initial Test. **2004**.

Frisch, O. R. Physical Evidence for the Division of Heavy Nuclei under Neutron Bombardment. Nature **1939**, *143*, 276.

Frondel, C. Mineral composition of gummite. Am. Mineral. **1956**, *41*, 539–568.

Frondel, C. Systematic mineralogy of uranium and thorium. U.S. Geol. Surv. Bull. **1958**, *1064*.

Frondel, C.; Meyrowitz, R. Studies of uranium minerals (XIX): Rutherfordine, diderichite, and clarkeite. Am. Mineral. **1956**, *41*,127-133.

Frost, R. L.; Carmody, O.; Erickson, K. L.: Weier, M. L.; Henry, D. O.; Cejka, J. Molecular structure of the uranyl mineral uranopilite - A Raman spectroscopic study. J. Mol. Struct. **2005a**, *733*, 203–210.

Frost, R. L.; Weier, M. L.; Bostrom, T.; Cejka, J. Molecular structure of the uranyl mineral zippeite - an XRD, SEM and Raman spectroscopic study. Neues Jahrbuch fuer Mineralogie **2005b**, *181*, 271–279.

Frost, R. L.; Cejka, J.; Weier, M. L.; Martens, W. Molecular structure of the uranyl silicates – a Raman spectroscopic study. J. Raman Spectrosc. **2006a,** *37*, 538–551.

Frost, R. L.; Weier, M. L.; Martens, W.; Kloprogge, T.; Cejka, J. A Raman and infrared spectroscopic study of the uranyl silicates –weeksite, soddyite and haiweeite. Spectrochim. Acta **2006b**, *63*, 305–312.

Frost, R. L.; Cejka, J.; Weier, M. L.; Martens, W. Raman spectroscopy study of selected uranophanes. J. Mol. Struct. **2006c**, *788*, 115–125.

Frost, R. L.; Cejka, J.; Dickfos, M. J. Raman and infrared spectroscopic study of the molybdate containing uranyl mineral calcurmolite. J. Raman Spectrosc. **2006d**, *39*, 779–785.

Frost, R. L.; Weier, M. L.; Martens, W. N.; Kloprogge, J. T.; Kristof, J. Thermo-Raman spectroscopic study of the uranium mineral sabugalite. J. Raman Spectrosc. **2006e**, *36*, 797–805.

Frost, R. L.; Cejka, J. A Raman spectroscopic study of the uranyl mineral rutherfordine. J. Raman Spectrosc. **2007a**, *38*, 1488–1493.

Frost, R. L.; Cejka, J.; Weier, M. L. Raman spectroscopic study of the uranyl oxyhydroxide hydrates: becquerelite, billietite, curite, schoepite and vandendriesscheite. J. Raman Spectrosc. **2007b**, *38*, 460–466.

Frost, R. L.; Cejka, J.; Weier, M. L.; Martens, W.; Ayoko, G. A. Raman spectroscopy of uranopilite of different origins – implications for molecular structure. J. Raman Spectrosc. **2007c**, *38*, 398–409.

Frost, R. L.; Cejka, J.; Ayoko, G.; Dickfos, M. Raman spectroscopic study of the multi-anion uranyl mineral schroeckingerite. J. Raman Spectrosc. **2007d**, *38*, 1609–1614

Frost, R. L.; Dickfos, M. J; Cejka, J. Raman spectroscopic study of the uranyl carbonate mineral zellerite. J. Raman Spectrosc. **2008a**, *39*, 582–586.

Frost, R. L.; Cejka, J.; Ayoko, G. Raman spectroscopic study of the uranyl phosphate minerals phosphuranylite and yingjiangite. J. Raman Spectrosc. **2008b**, *39*, 495-502.

Frost, R. L.; Cejka, J. A Raman spectroscopic study of the uranyl mineral rutherfordine – revisited. J. Raman Spectrosc. **2009a**, *40*, 1096–1103.

Frost, R. L.; Cejka, J.; Dickfos, M. J. Raman spectroscopic study of the uranyl minerals vanmeersscheite $U(OH)_4[(UO_2)_3(PO_4)_2(OH)_2]\cdot 4H_2O$ and arsenouranylite $Ca(UO_2)[(UO_2)_3(AsO_4)_2(OH)_2].(OH)_2\cdot 6H_2O$. Spectrochim. Acta **2009b**, *71*, 1799-1803.

Frost, R. L.; Reddy, B. J. Raman spectroscopic study of the uranyl titanate mineral brannerite (U, Ca, Y, Ce)$_2$(Ti,Fe)$_2$O$_6$: effect of metamictisation, J. Raman Spectrosc. **2011**, *42*, 691–695.

Fuchs, M.; Scheffler, M. Ab initio Pseudopotentials for Electronic Structure Calculations of Poly-Atomic Systems Using Density-Functional Theory. Comput. Phys. Commun. **1999**, *119*, 67–98.

Fyfe, W. F.; Babuska, V.; Price, N. J.; Schmidt, E.; Tsang, C. F.; Uyeda, S.; Velde, B. The geology of nuclear waste disposal. Nature **1984**, *310*, 537–540.

Gal, M.; Goggin P. L.; Mink, J. Mid-, far-infrared and Raman spectra of uranyl complexes in aqueous solutions. J. Mol. Struct. **1984**, *114*, 459–462.

Garisto, F.; Barber, D. H.; Chen, E.; Inglot, A.; Morrison, C. A. *Alpha, Beta and Gamma Dose Rates in Water in contact with Used CANDU Fuel*. Nuclear Waste Management Organization: **2009**.

Geipel, G.; Thieme, M. Determination of inorganic species in seepage water of uranium mining rockpiles and in related media. J. Radional. Inorg. Nucl. Chem. **1994**, *183*, 139–145.

Gerratt, J.; Mills, I. M. Force Constants and Dipole-Moment Derivatives of Molecules from Perturbed Hartree–Fock Calculations. I. J. Chem. Phys. **1968**, *49*, 1719.

Giammar, D. E. *Geochemistry of uranium at mineral-water interfaces: rates of sorption-desorption and dissolution-precipitation reactions*. Ph.D. Thesis. California Institute of Technology: Pasadena, California, **2001**.

Giammar, D. E.; Hering, J. G. Equilibrium and kinetic aspects of soddyite dissolution and secondary phase precipitation in aqueous suspension. Geochim. Cosmochim. Acta **2002**, *66*, 3235–3245.

Giannozzi, P.; Baroni, S.; Bonini, N.; Calandra, M.; Car, R.; Cavazzoni, C.: *et al*. QUANTUM ESPRESSO: a modular and open-source software project for quantum simulations of materials. J. Phys.: Condens. Matter **2009**, *21*, 395502 (19 pp).

Gilbert, T. L. Hohenberg-Kohn theorem for nonlocal external potentials. Phys. Rev. B **1975**, *12*, 2111.

Giménez, J.; Casas, I.; De Pablo, J.; Martínez-Esparza, A. *Secondary phase formation on UO_2 fuel*. In E. Commission, Ed. NF-PRO: **2005a**, p. 43.

Giménez, J.; Clarens, F.; Casas, I.; Rovira, M.; de Pablo, J.; Bruno, J. Oxidation and dissolution of UO2 in bicarbonate media: Implications for the spent nuclear fuel oxidative dissolution mechanism. J. Nucl. Mater. **2005b**, *345*, 232–238.

Giménez, J.; Sureda, R.; De Pablo, J.; Casas, I.; Martinez-Llado, X.; Rovira, M.; Martinez-Esparza, A. The role of uranium peroxide studtite on the retention of Cs, Sr and Se(VI). MRS Online Proceedings Library **2009**, *1193*.

Giménez, J.; Martínez-Lladó, X.; Rovira, M.; de Pablo, J.; Casas, I.; Sureda, R.; Martínez-Esparza, A. Cesium sorption on studtite ($UO_2O_2{\cdot}4H_2O$). Radiochim. Acta **2010**, *98*, 479–483.

Giménez, J.; de Pablo, J.; Casas, I.; Martínez-Lladó, X.; Rovira, M.; Martínez Torrents, A. Solubility study and point of zero charge of studtite ($UO_2O_2{\cdot}4H_2O$), Appl. Geochem. **2014**, *49*, 42–45.

Ginderow, D. Structure de l'Uranophane Alpha, $Ca(UO_2)_2(SiO_3OH)_2.5H_2O$, Acta Crystallogr. **1988**, *44*, 421–424.

Gonze, X.; Allan, D. C.; Teter, M. P. Dielectric tensor, effective charges and phonon in α-quartz by variational density-functional perturbation theory. Phys. Rev. Lett. **1992**, *68*, 3603–3606.

Gonze, X.; Lee, C. Dynamical Matrices, Born Effective Charges, Dielectric Permittivity Tensors, and Interatomic Force Constants from Density-Functional Perturbation Theory. Phys. Rev. B **1997**, *55*, 10355–10368.

Gonze, X.; Rignanese, G.-M.; Verstraete, M.; Beuken, J.-M.; Pouillon, Y.; Caracas, R.; *et al*. A brief introduction to the ABINIT software package. Z. Kristallogr. **2005**, *220*, 558–562.

Gonze, X.; Amadon, B.; Anglade, P.-M.; Beuken, J.-M.; Bottin, F.; Boulanger. P.; *et al*. ABINIT: First-principles approach to material and nanosystem properties. Comput. Phys. Commun. **2009**, *180*, 2582–2615.

Gorman, D. H. Studies of radioactive compounds: V-soddyite. Am. Mineral. **1952**, *37*, 386–393

Gorman, D. H.; Nuffield, E. W. Studies of Radioactive Compounds: VIII-Uranophane, Am. Mineral. **1955**, *40*, 634–645

Gorman-Lewis, D.; Mazeina, L.; Fein, J. B.; Szymanowski, J. E. S.; Burns, P. C.; Navrotsky, A. Thermodynamic Properties of Soddyite from Solubility and Calorimetry Measurements. J. Chem. Thermodyn. **2007**, *39*, 568–575.

Gorman-Lewis, D.; Burns, P. C.; Fein, J. B. Review of uranyl mineral solubility measurements. J. Chem. Thermodyn. **2008a,** *40*, 335–352.

Gorman-Lewis, D.; Fein, J. B.; Burns, P. C.; Szymanowski, J. E. S.; Jenalee, C. Solubility measurements of the uranyl oxide hydrate phases metaschoepite, compreignacite, Na-compreignacite, becquerelite and clarkeite. J. Chem. Thermodyn. **2008b**, 40, 980–990.

Gorman-Lewis, D.; Shvareva, T. Y.; Kubatko, K.-A.; Burns, P. C.; Wellman, D. M.; McNamara, B.; Szymanowsky, J. E. S; Navrotsky, A.; Fein, J. B. Thermodynamic Properties of Autunite, Uranyl Hydrogen Phosphate, and Uranyl Orthophosphate from Solubility and Calorimetric Measurements. Environ. Sci. Technol. **2009**, *43*, 7416–7422.

Grambow, B.; Ferry, C.; Casas, I.; Bruno, J.; Quiñones, J.; Johnson, L. Spent Fuel Waste Disposal: Analyses of Model Uncertainty in the MICADO Project. Energy Procedia **2010**, *7*, 487–494.

Grauer, R. *The chemical behaviour of montmorillonite in a repository backfill: selected aspects*. NAGRA technical report 88-24E. NAGRA, **1990**.

Gray, W. J., Leider, H. R.; Stewart, S. A. Parametric study of the LWR spent fuel dissolution kinetics. J. Nucl. Mater. **1992,** *190*, 46–52.

Greathouse, J. A.; Cygan, R. T. Water Structure and Aqueous Uranyl(VI) Adsorption Equilibria onto External Surfaces of Beidellite, Montmorillonite, and Pyrophyllite: Results from Molecular Simulations. Environ. Sci. Technol. **2006**, *40*, 3865–3871.

Grenthe, I., Stumm, W.; Laalsuharju, M.; Nilson, A. C.; Wikberg, P. Redox potentials and redox reactions in deep groundwater systems. Chem. Geol. **1992**, *98*, 131–150.

Grenthe, I; Fuger, J.; Konings, R. J. M.; Lemire, R. J.; Muller, A. B.; Nguyen-Trung, C.; Wanner, H. *Chemical Thermodynamics of Uranium*; Nuclear Energy Agency Organisation for Economic Co-Operation and Development, OECD: Issy-les-Moulineaux, France, **2004**.

Grenthe, I.; Drozdzynski, J.; Fujino, T.; Buck, E. C.; Albrecht-Schmitt, T. E.; Wolf, S.F. *Uranium*; in "The Chemisty of Actinide and Transactinide Elements"; Chapter V, Vol. I; Morss, L. R.; Edelstein, N. M., Fuger, J. (eds.); Springer Science and Business Media: Berlin, **2006**; pp. 253–638.

Grimme, S. Semiempirical GGA-type density functional constructed with a long-range dispersion correction. J. Comput. Chem. **2006**, *27*, 1787-1799.

Grimme, S.; Anthony, J.; Ehrlich, S.; Krieg, H. A consistent and accurate *ab initio* parametrization of density functional dispersion correction (DFT-D) for the 94 elements H-Pu. J. Chem. Phys. **2010,** *132*, 154104.

Grinberg, I.; Ramer, N. J.; Rappe, A. M. Quantitative criteria for transferable pseudopotentials in density functional theory. Phys. Rev. B **2001**, *63*, 201102.

Guillaumont, N. Y. R.; Fanghänel, T.; Neck, V.; Fuger, J.; Palmer, D. A.; Grenthe, I.; Rand, M. H. *Update on the Chemical Thermodynamics of Uranium, Neptunium, Plutonium, Americium, and Technetium*; Mompean, F. J., Illemassene, M., Domenech-Orti, C., Ben Said, K., Eds.; OECD Nuclear Energy Agency, Data Bank: Issy-les-Moulineaux, France, **2003**.

Guo, X.; Ushakova S. V.; Labs, S.; Curtius, H.; Bosbach, D.; Navrotsky, A. Energetics of Metastudtite and Implications for Nuclear Waste Alteration. Proc. Natl. Acad. Sci. U.S.A. **2014a**, 111, 17737–17742.

Guo, X.; Szenknect, S.; Mesbah, A.; Labs, S.; Clavier, N.; Poinssote; C.; Ushakova, S. V.; Curtius, H.; Bosbach, D.; Ewing, R. C.; Burns, P. C.; Dacheux, N.; Navrotsky, A. Thermodynamics of Formation of Coffinite, $USiO_4$. Proc. Natl. Acad. Sci. U.S.A. **2014b**, *112*, 6551–6555.

Gurevich, V. M.; Sergeyeva, E. I.; Gavrichev, K. S.; Gorbunov, V. E.; Khodakovsky, I. L. Low-Temperature Specific Heat of UO_2CO_3. Russ. J. Phys. Chem. **1987**, *61*, 856−857.

Hahn, O. From the natural transmutations of uranium to its artificial fission. Nobel Lecture: December 13, **1946**.

Hahn, O.; Strassmann, F. On the detection and characteristics of the alkaline earth metals formed by irradiation of uranium with neutrons. Naturwissenschaften **1939**, *27*, 11–15.

Hamann, D. R. Generalized Norm-Conserving Pseudopotentials. Phys. Rev. B **1989**, *40*, 2989–2989.

Hamann, D. R.; Schlüter, M.; Chiang, C. Norm-Conserving Pseudopotentials. Phys. Rev. Lett. **1979**, *43*, 1494–1497.

Hanson, B. D.; McNamara, B.; Buck, E. C.; Friese, J. I.; Jenson, E.; Krupka, K.; Arey, B. W. Corrosion of commercial spent nuclear fuel. 1. Formation of studtite and metastudtite. Radiochim. Acta **2005**, *93*, 159–168.

Hao, Y.; Klepov, V. V.; Murphy, G. L.; Modolo, G.; Bosbach, D.; Albrecht-Schmitt, T.E.; Kennedy, B. J.; Wang, S.; Alekseev, E. V. Influence of Synthetic Conditions on Chemistry and Structural Properties of Alkaline Earth Uranyl Borates. Cryst. Growth Des. **2016**, *16*, 5923–5931.

Hay, P. J.; Martin, R. L. Theoretical studies of the structures and vibrational frequencies of actinide compounds using relativistic effective core potentials with Hartree–Fock and density functional methods: UF_6, NpF_6, and PuF_6. J. Chem. Phys. **1998**, *109*, 3875–3885.

Hay, P. J.; Martin, R. L.; Schreckenbach, G. Theoretical Studies of the Properties and Solution Chemistry of $AnO_2(2+)$ and $AnO_2(+)$ Aquo Complexes for An=U, Np, and Pu, J. Phys. Chem. A **2000**, *104*, 6259–6270.

Haynes, P.; Refson, K. cpi2recpot: Converts from cpi Format Generated by fhi98PP to the recpot Format Used by CASTEP and ONETEP, **2007**.

He, H.; Shoesmith, D. W. Raman spectroscopic studies of defect structures and phase transition in hyper-stoichiometric UO_{2+x}. Phys. Chem. Chem. Phys. **2010**, *12*, 8108–8117.

Hedin, A. *Spent nuclear fuel - how dangerous is it?* A report from the project "Description of risk", p. 60; Swedish Nuclear Fuel and Waste Management Co.:**1997**.

Hehre, W. J.; Radom, L.; Schleyer, P. V. R.; Pople, J. A. *Ab Initio Molecular Orbital Theory*; Wiley: New York, **1986**.

Hellmann, H. *Einführung in die Quantenchemie*; Franz Deuticke: Leipzig, **1937**.

Hemingway, B. S. *Thermodynamic Properties of Selected Uranium Compounds and Aqueous Species at 298.15 K and 1 Bar and at Higher Temperatures - Preliminary Models for the Origin of Coffinite Deposits*; USGS Open-File Report 82–619: **1982**.

Hemstreet, L. A.; Fang, C. Y.; Nelson, J. S. First-principles calculations of spin-orbit splittings in solids using nonlocal separable pseudopotentials, Phys. Rev. B **1993**, *47*, 4238.

Henry, N.; Lagrenee, M.; Loiseau, T.; Clavier, N.; Dacheux, N.; Abraham, F. Tetrameric entity resulting from two distinct dinuclear uranyl-centered motifs bridged through μ^2-OH and pyridazine-3,6-dicarboxylate. Inorg. Chem. Commun. **2011**, *14*, 429-432.

Hill, R. The Elastic Behaviour of a Crystalline Aggregate. Proc. Phys. Soc. London **1952**, *65*, 349–354.

Hoekstra, H. R.; Siegel, S. The uranium-oxygen system U_3O_8-UO_3. J. Inorg. Nucl. Chem. **1961**, *18*, 154-165.

Hoekstra, H. R.; Siegel, S. The uranium trioxide – water system. J. Inorg. Nucl. Chem. **1973**, *35*, 761-779.

Hohenberg, P.; Kohn, W. Inhomogeneous electron gas. Phys. Rev. **1964**, *136*, B864–B871.

Hollister, C. D.; Nadis, S. Burial of Radioactive Waste under the Seabed. Sci. Am. **1998**, *278*, 60–65.

Huang, J.; Wang, X.; Jacobson, A. J. Hydrothermal Synthesis and Structures of the New Open-Framework Uranyl Silicates $Rb_4(UO_2)_2(Si_8O_{20})$ (USH-2Rb), $Rb_2(UO_2)(Si_2O_6)\cdot H_2O$ (USH-4Rb) and $A_2(UO_2)(Si_2O_6)\cdot 0.5H_2O$ (USH-5A, A=Rb,Cs), J. Mater. Chem. **2003**, *13*, 191–196.

IAEA. *Minimization of Waste from Uranium Purification, Enrichment and Fuel Fabrication;* IAEA-TECDOC-1115; International Atomic Energy Agency: Vienna, **1999**.

IAEA. *Radioactive Waste Management Glossary. 2003 Edition*. International Atomic Energy Agency (IAEA): Vienna, Austria, **2003**.

IAEA. *Classification of Radioactive waste. General Safety Guide*. International Atomic Energy Agency (IAEA): Vienna, Austria, **2009**.

ICDD, The international center for diffraction data, PDF-2 Database, © **2003**.

Iché-Tarrat, N.; Marsden, C. J. Examining the Performance of DFT Methods in Uranium Chemistry: Does Core Size Matter for a Pseudopotential? J. Phys. Chem. A **2008**, *112*, 7632–7642.

IEA. *World Energy Outlook*; International Energy Agency: **2009**. p. 160.

Ikonen, K. Thermal Analyses of Spent Nuclear Fuel Repository; Report POSIVA 2003-04; Posiva: Olkiluoko, **2003**.

IPCC, https://www.ipcc.ch/pdf/assessment-report/ar5/wg3/ipcc_wg3_ar5_full.pdf, **2014**.

Isobe, H.; Murakami, T.; Ewing, R. C. Alteration of uranium minerals in the Koongarra deposit, Australia: unweathered zone. J. Nucl. Mater. **1992**, *190*, 174–190.

Jackson, J. M.; Burns, P. C. The re-evaluation of the structure of weeksite: a uranyl silicate framework mineral. Can. Mineral. **2001**, *39*, 187–195.

Janeczek, J.; Ewing, R. C. Dissolution and alteration of uraninite under reducing conditions. J. Nucl. Mater. **1992**, *190*, 157–173.

Janeczek, J.; Ewing, R. C.; Oversby, V. M.; Werme, L. O. Uraninite and UO_2 in spent nuclear fuel: a comparison. J. Nucl. Mater. **1996**, *238,* 121–130.

Jeanloz, R. Universal Equation of State. Phys Rev B **1988**, *38*, 805–807.

Jégou, C.; Muzeau, B.; Broudic, V.; Peuget, S.; Poulesquen, A.; Roudil, D.; Corbel, C. Effect of external gamma irradiation on dissolution of the spent UO_2 fuel matrix. J. Nucl. Mater. **2005a**, *341*, 62–82.

Jégou, C.; Muzeau, B.; Broudic, V.; Poulesquen, A.; Roudil, D.; Jorion, F.; Corbel, C. Effect of alpha irradiation on UO_2 surface reactivity in aqueous media. Radiochim. Acta **2005b**, *93*, 35–42.

Jégou, C.; Muzeau, B.; Broudic, V.; Roudil, D.; Deschanels, X. Spent fuel UO_2 matrix alteration in aqueous media under oxidizing conditions. Radiochim. Acta, **2007**, *95*, 513–522.

Jin, G. B.; Skanthakumar, S.; Soderholm, L. Two New Neptunyl(V) Selenites: A Novel Cation-Cation Interaction Framework in $(NpO_2)_3(OH)(SeO_3)(H_2O)_2\cdot H_2O$ and a Uranophane-Type Sheet in $Na(NpO_2)(SeO_3)(H_2O)$, Inorg. Chem. **2011**, *50*, 6297–6303.

Joliot, F., Joliot-Curie, I. Artificial Production of Radioactive Elements. The Nobel Prize in Chemistry 1935. Nobel Lecture: December 12, **1935**.

Jones, L. H. Systematics in the vibrational spectra of uranyl complexes. Spectrochim. Acta **1958**, *10*, 395–403.

Jones, L. H. Determination of U-O bond distance in uranyl complexes from their infrared spectra. Spectrochim. Acta **1959**, *15*, 409–411.

Jones, R. O.; Gunnarson, O. The density functional formalism, its applications and prospects. Rev. Mod. Phys. **1989**, *61*, 689.

Jouffret, L.; Rivenet, M.; Abraham, F. U(VI) oxygen polyhedra as pillars for building frameworks from uranophane-type layers. IOP Conf. Series: Mat. Sci. Eng. **2010**, *9*, 012028.

Jouffret, L.; Shao, Z.; Rivenet, M.; Abraham, F. New three-dimensional inorganic frameworks based on the uranophane-type sheet in monoamine templated uranyl-vanadates. J. Solid State Chem. **2010**, *183*, 2290–2297.

Jouffret, L.; Rivenet, M.; Abraham, F. A new series of pillared uranyl-vanadates based on uranophane-type sheets in the uranium-vanadium-linear alkyl diamine systems, J. Solid State Chem. **2010**, *183*, 84–92.

Kármán, Th. von; Born, M. Zur Theorie der spezifischen Wärme (On the theory of the specific heat). Phys. Z. **1913a**, *14*, 15-19

Kármán, Th. von; Born, M. Über die Verteilung der Eigenschwingungen von Punktgittern (The distribution of the natural vibrations of point lattices). Phys. Z. **1913b**, *14*, 65-71.

Kienzler, B.; Altmaier, M.; Bube, C.; Metz, V., Radionuclide Source Term for HLW Glass, Spent Nuclear Fuel, and Compacted Hulls and End Pieces (CSD-C Waste); KIT Scientific Reports 7624; KIT Scientific Publishing: Karlsruhe, **2012**.

King-Smith, R. D.; Vanderbilt, D. Theory of polarization of crystalline solids. Phys. Rev. B **1993**, *47*, 1651–1654.

Kittel, C. *Introduction to Solid State Physics*. John Wiley and Sons: New York, **1996**.

Kleinman, L.; Bylander, D. M. Efficacious Form for Model Pseudopotentials. Phys. Rev. Lett. **1982**, *48*, 1425–1428.

Klingensmith, A. L.; Burns, P. C. Neptunium substitution in synthetic uranophane and soddyite. Am. Mineral. **2007a**, *92*, 1946–1951.

Klingensmith, A. L.; Deely, K. M.; Kinman, W. S.; Kelly, V.; Burns, P. C. Neptunium incorporation in sodium-substituted metaschoepite. Am. Mineral. **2007b**, *92*, 662–669.

Koelling, D. D.; Harmon, B. N. A technique for relativistic spin-polarised calculations. *J. Phys. C* **1977**, *10*, 3107.

Kohn, W.; Sham, L. J. Self-Consistent Equations Including Exchange and Correlation Effects. Phys. Rev. **1965**, *140*, A1133–A1138.

Kohn, W.; Meir, Y.; Makarov, D. E. van der Waals energies in density functional theory. Phys. Rev. Lett. **1998**, *80*, 4153–4156.

Kotomin, E. A.; Grimes, R. W.; Mastrikov, Yu. A.; Ashley, N. J. Atomic scale DFT simulations of point defects in uranium nitride, J. Phys.: Condens. Matter **2007**, *19*, 106208.

Kotomin, E. A.; Mastrikov, Yu. A.; Rashkeev, S., van Uffelen, P. Implementing first principles calculations of defect migration in a fuel performance code for UN simulations. J. Nucl. Mat. **2009**, *393*, 292.

Krauskopf, K. B. Aqueous Geochemistry of Radioactive Waste Disposal. Appl. Geochem. **1986**, *1*, 15–23.

Kubatko, K.-A. Crystallography, Hyerarchy of Crystal Structures, and Chemical Thermodynamics of Selected Uranyl Phases. Ph.D. Thesis, Graduate School of the University of Notre Dame, Illinois, **2005a**.

Kubatko, K.-A.; Helean, K. B.; Navrotsky, A.; Burns, P. C. Stability of Peroxide-Containing Uranyl Minerals. Science **2003**, *302*, 1191–1193.

Kubatko, K.-A., Helean, K. B., Navrotsky, A., Burns, P. C. Thermodynamics of Uranyl Minerals: Enthalpies of Formation of Rutherfordine, UO_2CO_3, Andersonite, $Na_2CaUO_2(CO_3)_3(H_2O)_5$, and Grimselite, $K_3NaUO_2(CO_3)\cdot 3H_2O$. Am. Mineral. **2005b**, *90*, 1284–1290.

Kuo, S.-Y.; Li, C.-T.; Hsieh, W.-F. Decreasing giant splitting of longitudinal and transverse optical phonons in $Pb_xSr_{1-x}TiO_3$ due to Pb covalency. Appl. Phys. Lett. **2002**, *81*, 3019–3021.

Kuta, J.: Wang, Z.; Wisuri, K.; Wander, M. C. F.; Wall, N. A.; Clark, A. E. The surface structure of α-uranophane and its interaction with Eu(III) – An integrated computational and fluorescence spectroscopy study. Geochim. Cosmochim. Acta **2013**, *103*, 184–196.

Kuroda, P. K. On the Nuclear Physical Stability of the Uranium Minerals. J. Chem. Phys. **1956**, *25*, 781.

Kuznetsov, L. M.; Tsvigunov, A. N.; Makarov, E. S. Hydrothermal synthesis and physics-chemical study of the synthetic analog of soddyite. Geochimiya **1981**, *10*, 1493.

Labs, S. Secondary Uranium Phases of Spent Nuclear Fuel - Coffinite, $USiO_4$, and Studtite, $UO_4\cdot 4H_2O$ - Synthesis, Characterization, and Investigations Regarding Phase Stability, Forschungszentrum Jülich GmbH Verlag Zentralbibliothek: **2015**.

Langmuir, D. Uranium Solution-Mineral Equilibria at Low Temperatures with Applications to Sedimentary Ore Deposits. Geochim. Cosmochim. Acta **1978**, *42*, 547−570.

Langmuir, D. *Aqueous Environmental Geochemistry*; Prentice-Hall: New Jersey, **1997**; pp 486–557.

Langreth, D. C.; Mehl, M. J. Beyond the local-density approximation in calculations of ground-state electronic properties. Phys. Rev. B **1983**, *28*, 1809.

L'Annunziata, M. F. *Radioactivity: Introduction and History*; Elsevier Science: Amsterdam, **2007**. ISBN 9780080548883.

Lazzeri, M.; Mauri, F. First-Principles Calculation of Vibrational Raman Spectra in Large Systems: Signature of Small Rings in Crystalline SiO_2. Phys. Rev. Lett. **2003**, *90*, 036401.

Le Caër, S. Water Radiolysis: Influence of Oxide Surfaces on H_2 Production under Ionizing Radiation. Water **2011**, *3*, 235–253.

Lee, C.; Gonze, X. Ab Initio Calculation of the Thermodynamic Properties and Atomic Temperature Factors of SiO_2 α-Quartz and Stishovite. Phys. Rev. B **1995**, *51*, 8610–8613.

Legros, J. P.; Legros, R.; Masdupuy, E. Sur un silicate d'uranyle, isomorphe du germanated'uranyle, et sur les solutions solides conespondantes. Application a l'etudestructurale du germanated'uranyle. Bull. Chim. France **1972**, *8*, 3051.

Legros, J. P.; Jeannin, Y. Coordination de l'uranium par l'ion germanate. II. Structure du germanate d'uranyle dihydrate $(UO_2)_2GeO_4(H_2O)_2$. Acta Crystallogr. B **1975**, *31*, 1140–1143.

Lemire, R. J., *Effects of high ionic strength groundwaters on calculated equilibrium concentrations in the uranium-water system*; Atomic Energy of Canada Limited Report, AECL-9545, **1988**.

Lemire, R. J.; Tremaine, P. R. Uranium and Plutonium Equilibria in Aqueous Solutions to 200°C. J. Chem. Eng. Data **1980**, *25*, 361−370.

Le Page, Y.; Saxe, P. Symmetry-General Least-Squares Extraction of Elastic Data for Strained Materials from *Ab Initio* Calculations of Stress. Phys. Rev. B **2002**, *65*, 104104.

Levy, M. Universal variational functionals of electron densities, first-order density matrices, and natural spin-orbitals and solution of the v-representability problem. Proc. Natl. Acad. Sci. USA **1979**, 76, 6062-6065.

Levy, M. Electron densities in search of Hamiltonians. Phys. Rev. A **1982**, 26, 1200.

Lewis, I. R.: Edwards, H. Handbook of Raman Spectroscopy: From the Research Laboratory to the Process Line; CRC Press: New York, **2001**.

Li, Y.; Geckeis, H.; Lutzenkirchen, J. L.; Polly, R.; Rabung, T.; Schmidt, M. Mineral-Water Interface Reactions of Actinides, Chem. Rev. **2013**, *113*, 1016–1062.

Lian, J.; Zhang, J. M.; Pointeau, V.; Zhang, E. X.; Lang, M.; Lu, F. Y.; Poinssot, C.; Ewing, R. C. Response of synthetic coffinite to energetic ion beam irradiation. J. Nucl. Mater. **2009**, *393*, 481–486.

Lian, J.; Wang, S. X.; Wang, L. M.; Ewing, R. C. Radiation damage and nanocrystal formation in uranium-niobium titanates. J. Nucl. Mater. **2011**, *297*, 89–96.

Lillard, J. A.; Hanrahan, R. J. *Corrosion of uranium and uranium alloys*; in ASM Handbook, Volume 13B: Corrosion Materials; ASM International: **2005**; pp. 370–384.

Lipscy, P.; Kushida, K.; Incerti, T. The Fukushima Disaster and Japan's Nuclear Plant Vulnerability in Comparative Perspective. Environ. Sci. Technol. **2013**, *47*, 6082–6088.

Louie, S. G.; Froyen, S.; Cohen, M. L. Nonlinear Ionic Pseudopotentials in Spin-Density-Functional Calculations. Phys. Rev. B **1982**, *26*, 1738–1742.

Lousada, C. M.; Trummer, M.; Jonsson, M. Reactivity of H_2O_2 towards different UO_2-based materials: The relative impact of radiolysis products revised, J. Nucl. Mater. **2013**, *434*, 434–439.

Ludeña, E. V.; Illas, F.; Ramirez-Solis, A. On the N-representability and universality of $F[\rho]$ in the Hohenberg-Kohn-Sham version of density functional Theory. Int. J. Mod. Phys. B **2008**, *22*, 4642-4654

MacKenzie, A. B.; Linsalata, P.; Miekeley, N.; Osmond, J. K.; Curtis, D. B. *Natural radionuclide and stable element studies of rock samples from the Osamu Utsumi mine and Morro do Ferro analogue study sites, Poços de Caldas, Brasil*; SKB Technical Report TR90-16; SKB: **1990**.

Mahan, G. D. Modified Sternheimer equation for polarizability. Phys. Rev. A **1980**, *22*, 1780.

Majumdar, D.; Balasubramanian, K.; Nitsche, H. A comparative theoretical study of bonding in UO_2^{++}, UO_2^{+}, UO_2, UO_2^{-}, OUCO, $O_2U(CO_2)$ and UO_2CO_3. Chem. Phys. Lett. **2002**, *361*, 143–151.

Majumdar, D.; Roszak, S.; Balasubramanian, K., Nitsche, H. Theoretical study of aqueous uranyl carbonate (UO_2CO_3) and its hydrated complexes: $UO_2CO_3 \cdot nH_2O$ (n=1–3). Chem. Phys. Lett. **2003**, *372*, 232–241.

Manara, D.; Renker, B. Raman spectra of stoichiometric and hyperstoichiometric uranium dioxide. J. Nucl. Mater. **2003**, *321*, 233-237.

Maradudin, A. A.; Montroll, E. M.; Weiss, G. H.; Ivatova, I. P. *Solid State Physics*; second edition, Ehrenreich, E.H., Seitz, F. and Turnbull, D. (eds.). Academic: New York, **1971**, Chap 4.

Marckwald, W. Über Uranerze aus Deutsh-Ostafrika, Centralblatt Mineralogy **1906**, 763.

Martin, R. M. Comment on Calculations of Electric Polarization in Crystals. Phys. Rev. B **1974**, *9*, 1998.

Martin, J. D. XPowder12, Ver. 04.13, © **2012.**

Martin, N. P.; Falaise, C.; Volkringer, C.; Henry, N.; Fargen, P.; Falk, C.; Delahaye, E.; Rabu, P.; Loiseau, T. Hydrothermal Crystallization of Uranyl Coordination Polymers Involving an Imidazolium Dicarboxylate Ligand: Effect of pH on the Nuclearity of Uranyl-Centered Subunits. Inorg. Chem. **2016**, *55*, 8697–8705.

Martínez Esparza, A.: Gago, J. A.; Quiñones, J.; Iglesias, E.; Peréz de Andés, S. *D.1.4.1. Review on influence of burnup and irradiation history on spent fuel instant realease.* In E. Commission, Ed., **2004**.

Matar, S. F. Lattice Anisotropy, Electronic and Chemical Structures of Uranyl Carbonate, UO_2CO_3, from First Principles. Chem. Phys. **2010**, *372*, 46–50.

Materials Studio, http://accelrys.com/products/collaborativescience/biovia-materials-studio/, accessed Jan 20, **2017**.

Maya, L.; Begun, G. M. A Raman spectroscopy study of hydroxo and carbonate species of the uranyl (VI) ion. J. Inorg. Nucl. Chem. **1981**, *43*, 2827–2832.

McGlynn, S. P.; Smith, J. K.; Neely, W. C. Electronic Structure, Spectra, and Magnetic Properties of Oxycations. III. Ligation Effects on the Infrared Spectrum of the Uranyl Ion. J. Chem. Phys. **1961**, *35*, 105-116.

McMenamin, T. (ed.) *Management and Disposal of Radioactive Waste*; Fourth European Conference on Management and Disposal of Radioactive Waste; EUR 17543 EN, **1997**.

McNamara, B.; Hanson, B.; Buck, E.; Soderquist, C. *Observation of studtite and metastudtite on spent fuel*; Finch, R. J., Bullen, D.B (eds.); Scientific Basis for Nuclear Waste Management XXVI, 757. Material Research Society: **2004**.

McNamara, B.; Hanson, B.; Buck, E.; and Soderquist, C. Corrosion of comercial spent nuclear fuel. 2. Radiochemical analyses of metastudtite and leachates. Radiochimica Acta **2005**, *93*, 169–175.

Mei, Z.-G.; Stan, M.; Pichler, B. First-principles study of structural, elastic, electronic, vibrational and thermodynamic properties of UN. J. Nucl. Mater. **2013**, *440*, 63–69.

Mei, Z.-G.; Stan, M.; Yang, J. First-principles study of thermophysical properties of uranium dioxide. J. Alloys Comp. **2014**, *603*, 282–286.

Meitner, L.; Frisch, O. R. Disintegration of Uranium by Neutrons: A New Type of Nuclear Reaction. Nature. **1939**, *143,* 239–240.

Mer, A.; Obbade, S.; Rivenet, M.; Renard, C.; Abraham, F. $[La(UO_2)V_2O_7][(UO_2)(VO_4)]$ the first lanthanum uranyl-vanadate with structure built from two types of sheets based upon the uranophane anion-topology. J. Solid State Chem. **2012**, *185*, 180–186.

Merino Rodríguez, I. *Sistema de simulación de escenarios de ciclos avanzados de combustible nuclear en transición (Simulation system for advanced fuel cycle transition scenarios)*. Ph.D. Thesis, Universidad Politécnica de Madrid: **2014.**

Messiah, A. *Quantum Mechanics*; North-Holland: Amsterdam, **1962**.

Michal, R. Fifty years ago in December: Atomic reactor EBR-I produced first electricity. Nuclear News, November **2001**, p. 28.

Miller, W.; Alexander R.; Chapman, N.; McKinley, L.; Smellie, J. *Natural Analogue studies in the geological disposal of radioactive wastes*; Studies in Environmental Sciences 57; Elsevier: Amsterdam, **1994**.

Milman, V.; Refson, K.; Clark, S. J.; Pickard, C. J.; Yates, J. R.; Gao, S.-P., Hasnip, P. J.; Probert, M. I. J.; Perlov, A., Segall, M. D. Electron and vibrational spectroscopies using DFT, plane waves and pseudopotentials: CASTEP implementation. J. Mol. Struct. THEOCHEM **2010**, *954*, 22–35.

MITYC. Sexto plan general de residuos radiactivos. Ministerio de industria, turismo y comercio. Gobierno de España: Madrid, **2006**.

Moll, H.; Matz, W.; Schuster, G.; Brendler, E.; Bernhard, G.; Nitsche, H. Synthesis and characterization of uranyl orthosilicate $(UO_2)_2SiO_4 \cdot 2H_2O$. J. Nucl. Mater. **1995**, *227*, 40–49.

Monkhorst, H. J.; Pack, J. D. Special Points for Brillonin-Zone Integration. Phys. Rev. B **1976**, *13*, 5188–5192.

Mouhat, F.; Coudert, F.-X. Necessary and Sufficient Elastic Stability Conditions in Various Crystal Systems. Phys. Rev. B **2014**, *90*, 224104.

Murnaghan, F. D. Finite Deformations of an Elastic Solid. Am. J. Math. **1937**, *49*, 235–260.

Murphy, A. W. (ed.) *The Nuclear Power Controversy*; Prentice Hall: New Jersey, **1976**.

Murphy, W. M.; Grambow, B. Thermodynamic interpretation of neptunium coprecipitation in uranophane for application to the Yucca Mountain repository. Radiochim. Acta **2008**, *96*, 563–567.

Murphy, W. M.; Pabalan, R. T. *Review of Empirical Thermodynamic Data for Uranyl Silicate Minerals and Experimental Plan*; Nuclear Regulatory Commission Contract NRC-02-93-005; Center for Nuclear Waste Regulatory Analyses: San Antonio, Texas, June **1995**.

Muzeau, B.; Jégou, C.; Delaunay, F.; Broudic, V.; Brevet, A.; Catalette, H.; Simoni, E.; Corbel, C. Radiolytic oxidation of UO_2 pellets doped with alpha-emitters ($^{238/239}Pu$). J. Alloys Comp. **2009**, *467*, 578–589.

Nakamoto, K. *Infrared and Raman Spectra of Inorganic and Coordination Compounds*. J. Wiley and Sons: New York, **1986.**

Navrotsky, A.; Shvareva, T. Y.; Guo, X.; Rock, P. A. Chapter 4: *Thermodynamics of Uranium Minerals and Related Materials*; Mineralogical Association of Canada Short Course 43: Winnipeg, MB, May **2013**.

Naylor, A.; Wilson, D. D. *Recovery of Uranium and Plutonium from Irradiated Nuclear Fuel*; Handbook of Solvent Extration. John Wiley and Sons: New York, **1983**.

NEA. *Geological Disposal of Radioactive Waste- Review of Developments in the Last Decade.* OCDE: Paris, **2000**.

Nerikar, P.; Watanabe, T.; Tulenko, J. S.; Phillpot, S. R.; Sinnott, S. B. Energetics of intrinsic point defects in uranium dioxide from electronic-structure calculations. J. Nucl. Mater. **2009**, *384*, 61–69.

Nguyen, S. N.; Silva, R. J.; Weed, H. C.; Andrews, L. E. Standard Gibbs Free Energies of Formation at the Temperature 303.15 K of Four Uranyl Silicates: Soddyite, Uranophane, Sodium Boltwoodite, and Sodium Weeksite. J. Chem. Thermodyn. **1992**, *24*, 259–276.

Nielsen, F.; Lundahl, K.; Jonsson, M. Simulations of H_2O_2 concentration profiles in the water surrounding spent nuclear fuel. J. Nucl. Mater. **2008**, *372*, 32–35.

Niu, H.; Wei, P.; Sun, Y.; Chen, C.-X.; Franchini, C.; Li, D.; Li, Y. Electronic, Optical, and Mechanical Properties of Superhard Cold-Compressed Phases of Carbon. Appl. Phys. Lett. **2011**, *99*, 031901.

Novacek, R. Study of some secondary uranium minerals, Vesnik Kral. Ceske. Spol. Nauk II, **1935**, No. 7, 36 pp., 2 pls.

Nozik, Y. Z.; Kuznetsov, L. M. Neutron diffraction study of synthetic soddyite by the full-profile analysis technique. Kristallografiya **1990**, *35*, 1563–1564.

Nye, J. F. *The Physical Properties of Crystals: Their Representation by Tensors and Matrices*; Oxford University Press: New York, **1985**.

Odoh, S. O.; Schreckenbach, G. DFT Study of Uranyl Peroxo Complexes with H_2O, F^-, OH^-, CO_3^{2-} and NO_3^-. Inorg. Chem. **2013**, *52*, 5590–5602.

Odoh, S. O.; Shamblin, J.; Colla, C. A.; Hickam, S.; Lobeck, H. L.; Lopez, R. A. K.; Olds, T.; Szymanowski, J. E. S.; Sigmon, G. E.; Neuefeind, J.; Casey, W. H.; Lang, M.; Gagliardi, L.; Burns, P. C. Structure and reactivity of X-ray amorphous uranyl peroxide, U_2O_7. Inorg. Chem. **2016**, *55*, 3541–3546.

Ohwada, K. Laser Raman Spectra and Normal Coordinate Analysis of Some Uranyl Tetrachloride Complexes. Appl. Spectrosc. **1980**, *34*, 327-331.

Oliphant, M. L. E.; Kinsey, B. B.: Rutherford, E. The transmutation of Lithium by Protons and by Ions of Heavy Isotope of Hydrogen. Proc. Roy. Soc. (London) A **1933**, *141*, 722–733.

Ollila, K. Dissolution studies of UO_2 pellets and powdered UO_2. In SKB, Ed. Technical Report, 90-06; SKB, **1990.**

Opium package, http://opium.sourceforge.net, Version 3.8, April 4, **2014.**

Ordejon, P., Artacho, E., Soler, J. M. Self-consistent order N density functional calculations for very large systems. Phys. Rev. B **1996**, *53*, 1044.

Orlando, R.; Delle Piane, M.; Bush, I. J.; Ugliengo, P.; Ferrabone, M.; R. Dovesi, R. A New Massively Parallel Version of CRYSTAL for Large Systems on High Performance Computing Architectures. J. Comput. Chem. **2012**, *33*, 2276–2284.

Ortega-Castro, J. *Investigación mecano-cuántica del orden/desorden catiónico y propiedades elásticas de filosilicatos 2:1 dioctaédricos.* Ph.D. Thesis, Universidad de Granada: 2007.

Ortiz, G.; Ballone, P. Correlation energy, structure factor, radial distribution function, and momentum distribution of the spin-polarized uniform electron gas. Phys. Rev. B **1994**, *50*, 1391–1405; *56*, 9970(E).

Ostanin, S.; Zeller, P. Ab initio study of uranyl peroxides: Electronic factors behind the phase stability. Phys. Rev. B **2007a**, 75, 073101.

Ostanin, S.; Zeller, P. Ab initio study of the uranyl oxide hydrates: a proton transfer mediated by water. J. Phys.: Condens. Matter **2007b**, 19, 246108.

Oversby, V. M. *Uranium dioxide, SIMFUEL, and spent fuel dissolution rates - a review of published data*; SKB Technical Reports, TR-99-22; SKB: **1999**.

Paier, J.; Hirschl, R.; Marsman, M., Kresse, G. The Perdew–Burke–Ernzerhof exchange-correlation functional applied to the G2-1 test set using a plane-wave basis set. J. Chem. Phys. **2005**, *122*, 234102.

Paier, J.; Marsman, M.; Hummer, K.; Kresse, G.; Gerber, I. C.; Angyan, J. G. Screened hybrid density functionals applied to solids. J. Chem. Phys. **2006**, *124*, 154709.

Palomo, C. *Incorporación de actínidos en las fases secundarias del combustible generadas en condiciones de almacén*. Ph.D. Thesis. Universidad Complutense de Madrid: **2014.**

Paquete, J.; Lemire, R. A description of the chemistry of aqueous solutions of uranium and plutonium at 200 ºC using potential-ph diagram. Nucl. Sci. Eng. **1981**, *79*, 26–48.

Parr, R. G.; Yang, W. *Density-Functional Theory of Atoms and Molecules*; Oxford University Press: New York, **1989**.

Pascale, F.; Zicovich-Wilson, C. M.; López Gejo F.; Civalleri, B., Orlando, R; Dovesi, R. The Calculation of the Vibrational Frequencies of Crystalline Compounds and its Implementation in the CRYSTAL Code. J. Comput. Chem. **2004**, *25*, 888–897.

Payne, M. C.; Teter, M. P.; Allan, D. C.; Arias, A.; Joannopoulos, J. D. Iterative Minimization Techniques for Ab Initio Total-Energy Calculations: Molecular Dynamics and Conjugate Gradients. Rev. Mod. Phys. **1992**, *64*, 1045–1097.

Pearcy, E. C.; Prikryl, J. D.; Murphy, W. M.; Leslie, B. W. Alteration of Uraninite from the Nopal I Deposit, Peña Blanca District, Chihuahua, Mexico, Compared to Degradation of Spent Nuclear Fuel in the Proposed US High-Level Nuclear Waste Repository at Yucca Mountain, Nevada. Appl. Geochem. **1994**, *9*, 713–732.

Pehrman, R. *Oxidative dissolution of spent nuclear fuel under the influence of ionizing radiation*. Ph.D. Thesis. University of Helsinki: **2012**.

Perdew, J. P. Unified Theory of Exchange and Correlation Beyond the Local Density Approximation, in Electronic Structure of Solids '91; Ziesche, P. and Eschrig, H. (eds.); Akademie Verlag: Berlin, **1991**; p. 11.

Perdew, J. P.; Zunger, A. Self-Interaction Correction to Density Functional Approximations for Many-Electron Systems. Phys. Rev. B **1981**, *23*, 5048–5079.

Perdew, J. P.; Chevary, J. A.; Vosko, S. H.; Jackson, K. A.; Pederson, M. A.; Singh, D. J.; Fiolhais, C. Atoms, Molecules, Solids, and Surfaces: Applications of the Generalized Gradient Approximation for Exchange and Correlation. Phys. Rev. B **1992**, *46*, 6671–6687; ibid. **1993**, *48*, 4978 (E).

Perdew, J. P.; Burke, K.; Ernzerhof, M. Generalized Gradient Approximation Made Simple. Phys. Rev. Lett. **1996a**, *77*, 3865–3868; ibid. **1997**, *78*, 1396 (E).

Perdew, J. P.; Burke, K.; Wang, Y. Generalized Gradient Approximation for the Exchange-Correlation Hole of a Many-Electron System. Phys. Rev. B **1996b**, *54*, 16533–16539; *ibid.* **1998**, *57*, 14999 (E).

Perdew, J. P.; Kurth, S.; Zupan, A.; Blaha. P. Accurate Density Functional with Correct Formal Properties: A Step Beyond the Generalized Gradient Approximation. Phys. Rev. Lett. **1999**, *82*, 2544–2547; *ibid.* **1999**, *82*, 5179.

Perdew; J. P.; Ruzsinszky, A.; Csonka, G. I.; Constantin, L. A.; Zhou, X.; Vydrov, O. A.; Scuseria, G. E.; Burke, K. Restoring the Gradient Expansion for Exchange in Solids and Surfaces. Phys. Rev. Lett. **2008**, *100*, 136406: *ibid.* **2009**, *102*, 039902 (E).

Petit, T.; Lemaignan, C.; Jollet, F.; Bigot, B.; Pasturel, A. Point defects in uranium dioxide. Phil. Mag. B **1998**, *77*, 779–786.

Pfrommer, B. G.; Cote, M.; Louie, S. G.; Cohen, M. L. Relaxation of Crystals with the Quasi-Newton Method. J. Comput. Phys. **1997**, *131*, 233–240.

Placzek, G. *Rayleigh-Streung und Raman-Effekt*; In Handbuch der Radiologie, Vol. 6; Marx, G. (ed.); Akademische: Frankfurt-Main, Germany, **1934**; pp. 205–374.

Plasil, J. Oxidation-hydration weathering of uraninite: the current state-of knowledge. J. Geosci. **2014**, *59*, 99–114.

Plasil, J.; Veselovsky, F.; Hlousek, J.; Skoda, R.; Novak, M.; Sejkora, J.; Cejka, J.; Skacha, P.; Kasatkin, A. V. Mathesiusite, $K_5(UO_2)_4(SO_4)_4(VO_5)(H_2O)_4$, a new uranyl vanadate-sulfate from Jachymov, Czech Republic. Am. Mineral. **2013**, *99*, 625–632.

Poinssot, C.; Kelm, M.; Grambow, B.; Martinez, A.; Johnson, L.; Andriambololona, Z.; Bruno, J.; Cachoir, C.; Cavedon, J. M.; Christensen, H.; Corbel, C.; Ferry, C.; Jegou, C.; Lemmens, K.; Loida, A.; Lovera, P.: Miserque, F.; de Pablo, J.; Poulesquen, A.; Quinones, J.; Spahiu, K.;

Wegen, D. *Spent fuel stability under repository conditions;* Spent Fuel Stability SFS final report; Poinsot, C.; Ferry, C. (eds.); European Comission: **2004**.

Poirier, J.-P.; Tarantola, A. A Logarithmic Equation of State. Phys. Earth. Planet. Int. **1998**, *109*, 1–8.

Porezag, D.; Pederson, M. R. Infrared intensities and Raman-scattering activities within density-functional theory. Phys. Rev. B **1996**, *54*, 7830–7836.

Powell, R.C. *Symmetry, Group Theory, and the Physical Properties of Crystals*; Springer: New York, **2010**.

Press, W. H.; Teukolsky, S. A.; Vetterling, W. T.; Flannery, B. P. *Numerical Recipes: The Art of Scientific Computing*; Cambridge University Press: Cambridge, U.K., **1989**.

Prosandeev, S. A.; Waghmare, U.; Levin, I.; Maslar, J. First-order Raman spectra of $AB'_{1/2}B''_{1/2}O_3$ double perovskites. Phys. Rev. B **2005**, *71*, 214307.

Pugh, S. F. XCII. Relations Between the Elastic Moduli and the Plastic Properties of Polycrystalline Pure Metals. Philos. Mag. **1954**, *45*, 823–843.

Quiñones, J.; García Serrano, J.; Serrano, J. A.; Díaz Arocas, P. P.; Rodríguez Almazán, J. L. *SIMFUEL and UO_2 solubility and leaching behaviour under anoxic conditions*. In I.G. McKinley, and C. McCombie, Eds. Scientific Basis for Nuclear Waste Management XXI, 506, p. 247-252; Materials Research Society: Warrendale, Pennsylvania, **1998**.

Quiñones, J.; Serrano, J. A.; Díaz Arocas, P. P.; Rodríguez Almazán, J. L.; Esteban, J. A.; Martínez Esparza, A. *Modelación de la generación de productos radiolíticos en agua por la radiación a originada por un combustible gastado en un almacén subterráneo profundo,* DFN/RA-03/SP-99. CIEMAT: Madrid, **1999**.

Quiñones, J.; Serrano, J. A. *Studies of the influence of water radiolysis to the spent fuel matrix dissolution process*. In J.L. Díaz-Díaz, J. Quiñones, Eds.; Hot Laboratories and Remote Handling; Ciemat: Madrid, **2002**.

Quiñones, J.; Cobos, J. *Modelación de los resultados de lixiviación de pastillas de UO_2 dopadas con ^{238}Pu*, DFN/RA-04/SP-02, **2002**.

Quiñones, J.; Cobos, J.; Díaz Arocas, P.; De Pablo, J.; Casas, I.; Giménez, J.; Rovira, M.; Clarens, F.; Cera, E.; Merino, J.; Bruno, J. *Descripción del residuo (Combustible Nuclear Gastado) - ENRESA 2003*. AGP arcilla DFN/RA-02/SP-03. CIEMAT, **2003**.

Quiñones, J.; Cobos, J.; Díaz Arocas, P. P.; Rondinella, V. V. *Modelling of the (U-^{238}Pu)O_{2+x} leaching behaviour in deionised water under anoxic conditions*. In: Oversby, V. M., Werme, L. O. (eds.) Scientific Basis for Nuclear Waste Management XXVII, 807, p. 409-414. Materials Research Society: **2004a**.

Quiñones, J.; González de la Huebra, A.; Martínez-Esparza, A. Effect of corroded engeniering barrier on the alteration process of the spent fuel matrix under repository conditions. Geochim. Cosmochim. Acta **2004b**, 68, 113.

Quiñones, J.; Cobos, J.; Iglesias, E.; Martínez Esparza, A.; Gago, J. A.; Glatz, J. P.; Wegen, D.; Rondinella, V. V. *Leaching studies performed with alpha doped pellet under repository conditions. Review and conclusions of the experimental work performed under ITU-ENRESA-Ciemat special contract 1 into framework agreement 15983*; Informe técnico, DFN/RR-10/SP-04; Ciemat: Madrid, **2005**.

Quiñones, J.; Cobos, J.; Iglesias, E.; Martínez Esparza, A.; van Winckel, S.; Glatz, J. P. *Preliminary approach obtained from Spent Fuel Leaching Experiments performed by ITU - ENRESA/CIEMAT*; In CIEMAT, Ed. Informe CIEMAT, p. 27; CIEMAT: Madrid, **2006**.

Quiñones, J.; Iglesias, E.; Rodriguez Villagra, N. *Final activity report - CIEMAT*. In E. Union, Ed. NF-PROF. Contract number I6W-CT-2003-0238, **2007**.

Raman, C. V. The molecular scattering of light. Nobel Lecture: December 11, **1930**.

Raman, C. V.; Krishnan, K. S. Polarisation of Scattered Light-Quanta. Nature **1928**, *122*, 169.

Ramirez, F. D. M.; Palomares-Castillo, K.; Ocampo-Garcia, B.; Morales-Avila, E.; Varbanov, S. Physicochemical behaviour of a dinuclear uranyl complex formed with an octaphosphinoylated para-tert-butylcalix[8]arene. Spectroscopic studies in solution and in the solid state. Polyhedron **2017**, *123*, 75–89.

Ranganathan, S. I.; Ostoja-Starzewski, M. Universal Elastic Anisotropy Index. Phys. Rev. Lett. **2008**, *101*, 055504.

Ravindran, P.; Fast, L.; Korzhavyi, P. A.; Johansson, B.; Wills, J.; Eriksson, O. Density functional theory for calculation of elastic properties of orthorhombic crystals: application to $TiSi_2$, J. Appl. Phys. **1998**, *84*, 4891–4904.

Refson, K.; Tulip, P. R.; Clark, S. J. Variational density-functional perturbation theory for dielectrics and lattice dynamics. Phys. Rev. B **2006**, *73*, 155114.

Resta, R. Macroscopic Polarization in Crystalline Dielectrics: The Geometric Phase Approach. Rev. Mod. Phys. **1994**, *66*, 899–915.

Reuss, A. Berechnung der Fliessgrenze von Mischkristallen auf Grund der Plastizitatsbedingung fur Einkristalle. Z. Angew. Math. Mech. **1929**, *9*, 49–58.

Rey, A.; Giménez, J.; Casas, I.; Clarens, F.; de Pablo, J. Secondary phase formation on UO_2 in phosphate media. Appl. Geochem. **2008**, *23*, 2249–2255.

Rey, A.; Casas, I.; Giménez, J.; Quiñones, J.; de Pablo, J. Effect of temperature on studtite stability: Thermogravimetry and differential scanning calorimetry investigations. J. Nucl. Mater. **2009a**, *385*, 467–473.

Rey, A.; Utsunomiya, S.; Giménez, J.; Casas, I.; de Pablo, J.; Ewing, R. C. Stability of uranium (VI) peroxide hydrates under ionizing radiation. Am. Mineral. **2009b**, *94*, 229–235.

Rhodes, R. *The Making of the Atomic Bomb*; Simon and Schuster: New York, **1986**. ISBN 0671441337.

Rodríguez Almazán, J. L. *Evolución de la dosis gamma generada por el combustible gastado en diversas zonas de un almacén subterráneo profundo*; p. 22. Ciemat. DFN/RA-02/SP-00; CIEMAT: Madrid, **2000**.

Roth, O.; Jonsson, M. Oxidation of UO_2 (s) in aqueous solution. Cent. Eur. J. Chem. **2008**, *6*, 1–14.

Royuela, S. *Caracterization of UO_2 y sus fases secundarias por espectroscopía Raman*. Master Thesis. Universidad Complutense: Madrid, **2014**.

Rull, F. The Raman Effect and the Vibrational Dynamics of Molecules and Crystalline Solids. EMU Notes in Mineralogy **2012**, *12,* 1–60.

Rutherford, E. Uranium radiation and the electrical conduction produced by it. Phil. Mag. **1899**, *47*, 116.

Rutherford, E. *The Chemical Nature of the Alpha Particles from Radioactive Substances*. Nobel Lecture: December 11, **1908**.

Rutherford, E; Soddy, F. Radioactive Change. Phil. Mag. **1903**, *5*, 576–591.

Saad, Y.; Schultz, M. H. GMRES: A Generalized Minimal Residual Algorithm for Solving Nonsymmetric Linear Systems. SIAM J. Sci. Stat. Comput. **1986**, *7*, 856–869.

Samuel, W. J. *Three Mile Island: a nuclear crisis in historical perspective.* University of California Press: Berkeley, Calif., **2004**.

Shang, S.; Wang, Y.; Liu, Z. K. First-principles elastic constants of α-and θ-Al_2O_3. Appl. Phys. Lett. **2007**, *90*, 101909.

Sassani, D. C.; Jové-Colón, C. F.; Weck, P. F.; Jerden, J. L.; Frey, K. E.; Cruse, T.; Ebert, W. L.; Buck, E. C.; Wittman, R. S. *Used Fuel Degradation: Experimental and Modeling Report, Fuel Cycle Research and Development Report FCRD-UFD-2013-000404*; Sandia National Laboratories: Albuquerque, New Mexico, October 17, **2013**.

Sato, T. Thermal decomposition of uranium peroxide hydrate. Naturwissenschaften **1961a**, *48*, 693-693.

Sato, T. Uranium peroxide hydrates. Naturwissenschaften **1961b**, *48*, 668-668.

Sato, T. Preparation of uranium peroxide hydrates. J. Appl. Chem. **1963**, *13*, 361-365.

Sattonnay, G.; Ardois, C.; Corbel, C.; Lucchini, J. F.; Barthe, M. F.; Garrido, F.; Gosset, D. Alpha-radiolysis effects on UO_2 alteration in water. J. Nucl. Mater. **2001**, *288*, 11–19.

Savage, D. (ed.) *The Scientific and Regulatory Basis for the Geological Disposal of Radioactive Waste*; Wiley and Sons: New York, **1995**.

Schoep, A. La soddite, nouveau minéral radioactif. Comptes Rendus Acad. Sci. **1922**, *174*, 1066–1067.

Schreckenbach, G.; Shamov, G. A. Theoretical Actinide Molecular Science. Acc. Chem. Res. **2010**, *43*, 19–29.

Schulz, W. W. *Uranium Processing*; in Encyclopedia Britannica, https:// global.britannica.com/technology/uranium-processing. Accesed: February **2017**.

Servaes, K.; Hennig, C.; Billard, I.; Gaillard, C.; Binnemans, K.; Gorller-Walrand, C.; Van Deun, R. Speciation of Uranyl Nitrato Complexes in Acetonitrile and in the Ionic Liquid 1-Butyl-3-methylimidazolium Bis(trifluoromethylsulfonyl)imide. Eur. J. Inorg. Chem. **2007**, *32*, 5120–5126.

Shamov, G. A.; Schreckenbach, G.; Vo, T. N. A Comparative Relativistic DFT and Ab Initio Study on the Structure and Thermodynamics of the Oxofluorides of Uranium(IV), (V) and (VI). Chem. Eur. J. **2007**, *13*, 4932–4947.

Shepherd, N. D.; Zhang, Y.; Karatchevtseva, I.; Price, J. R.; Kong, L.; Scales, N.; Lumpkin, G. R. One-dimensional uranium(VI) coordination polymers with pyridinecarboxylate ligands. Polyhedron **2016**, *113*, 88–95.

Shoesmith, D. W. Fuel corrosion processes under waste disposal conditions. J. Nucl. Mater. **2000**, *282*, 1–31.

Shoesmith, D. W.; Sunder, S. The prediction of nuclear fuel (UO_2) dissolution rates under waste disposal conditions. J. Nucl. Mater. **1992**, *190*, 20–35.

Shuller, L. C. *Atomistic modeling of the solid - state chemistry of actinide minerals*; Ph.D. Thesis; Materials Science and Engineering University of Michigan: Ann Arbor, **2010b**.

Shuller, L. C.; Ewing, R. C.; Becker, U. Quantum-mechanical evaluation of Np-incorporation into studtite. Am. Mineral. **2010a**, *95*, 1151–1160.

Shuller, L. C.; Ewing, R. C.; Becker, U. Np-incorporation into uranyl phases: A quantum–mechanical evaluation. J. Nucl. Mater. **2013**, *434*, 440–450.

Shuller, L. C.; Bender, W. M.; Walker, S. M.; Becker, U. Quantum-Mechanical Methods for Quantifying Incorporation of Contaminants in Proximal Minerals. Minerals **2014**, *4*, 690–715.

Shvareva, T. Y.; Mazeina, L.; Gorman-Lewis, D.; Burns, P. C.; Szymanowski, J. E. S.; Fein, J. B.; Navrotsky, A. Thermodynamic Characterization of Boltwoodite and Uranophane: Enthalpy of Formation and Aqueous Solubility. Geochim. Cosmochim. Acta **2011**, *75*, 5269–5282.

Shvareva, T. Y.; Fein, J. B.; Navrotsky, A. Thermodynamic Properties of Uranyl Minerals: Constraints from Calorimetry and Solubility Measurements. Ind. Eng. Chem. Res. **2012**, *51*, 607–613.

Sidorenko, G. A.; Moroz, I. K.; Zhiltsova, I. G. Zapiski Vsesoyuznogo Mineralogicheskogo Obshchestva **1975**, *104*, 559.

Sidorenko, G. A.: Chukanov, N. V.; Naumova, I. S. Mineral. Z. **2001**, *23*, 55.

SKB-91. *Final Disposal of spent nuclear fuel. Importance of the bedrock for safety*; SKB Report 92-20, May **1992**.

SKB. http://www.skb.com/future-projects/the-spent-fuel-repository/our-methodology/ retrieved **2017**.

Slater, J. C. *Quantum Theory of Molecules and Solids, Vol. 4, The Self-consistent field for molecules and solids*; McGraw-Hill: New York, **1974**.

Smekal, A. Zur Quantentheorie der Dispersion. Naturwissenschaften **1923**, *11*, 873–875.

Smith, D. K.; Gruner, J. W.; Lipscomb, W. N. The crystal structure of Uranophane, $[Ca(H_3O)_2](UO_2)_2(SiO_4)_2{\cdot}3H_2O$, Am. Mineral**. 1957**, *42*, 594–618.

Smrcok, L.; Weiss, Z. DIFK91: A Program for the Modelling of Powder Diffraction Patterns on a PC. J. Appl. Cryst, **1993**, *26*,140–141.

Sobry, R. Etude des uranate hydrates –II, Exame des propietes vibrationelles des urinate hydrates de cations vibralents. J. Inorg. Nucl. Chem. **1973**, *35*, 2753–2768.

Sternheimer, R. M. Electronic Polarizabilities of Ions from the Hartree-Fock Wave Functions. Phys. Rev. **1954**, *96*, 951.

Stich, I.; Car, R.; Parrinello, M.; Baroni, S. Conjugate gradient minimization of the energy functional: A new method for electronic structure calculation. Phys. Rev. B **1989**, *39*, 4997.

Stohl, F. V.; Smit, D. K. The crystal chemistry of the uranyl silicate minerals. Am. Mineral. **1981**, *66* 610-624.

Stroes-Gascoyne, S.; Johnson, L. H.; Beeley, P. A.; Sellinger, D. M.; Dissolution of used CANDU fuel at various temperatures and redox conditions. Mat. Res. Soc. Symp. Proc. **1985**, *50*, 317–326.

Strutt, J. (Lord Rayleigh). On the transmission of light through an atmosphere containing small particles in suspension, and on the origin of the blue of the sky. Phil. Mag. **1899**, *47*, 375–394.

Sunder, S. Calculation of Radiation Dose Rates in a Water Layer in Contact with Used CANDU UO_2 Fuel. Nucl. Tech. **1998**, *122*, 211–221.

Sunder, S.; Shoesmith, D. W.; Christensen, H.; Miller, N. H. Oxidation of UO_2 fuel by the products of gamma radiolysis of water. J. Nucl. Mater. **1992**, *190*, 78–86.

Sunder, S.; Shoesmith, D. W.; Miller, N. H. Oxidation and dissolution of nuclear fuel (UO_2) by the products of the alpha radiolysis of water. J. Nucl. Mater. **1997**, *244*, 66–74.

Sundin, S.; Dahlgren, B.; Roth, O.; Jonsson, M. H_2O_2 and radiation induced dissolution of UO_2 and SIMFUEL in deficient aqueous solution. J. Nucl. Mater. **2013**, *443*, 291–297.

Sureda, R.; Martínez-Lladó, X.; Rovira, M.; de Pablo, J.; Casas, I.; Giménez, J. Sorption of strontium on uranyl peroxide: Implications for a high-level nuclear waste repository. J. Hazard. Mater. **2010**, *181*, 881–885.

Sureda, R.; Casas, I.; Giménez, J.; de Pablo, J.; Quiñones, J.; Zhang, J.; Ewing, R. C. Effects of Ionizing Radiation and Temperature on Uranyl Silicates: Soddyite $(UO_2)_2(SiO_4)(H_2O)_2$ and Uranophane $Ca(UO_2)_2(SiO_3OH)_2{\cdot}5H_2O$. Environ. Sci. Technol. **2011**, *45*, 2510–2515.

Suutarinen, R.; Blomqvist, R.; Halonen, S.; Jaakkola T. Uranium in groundwater of Palmottu analogue study site in Finland. Radiochim. Acta **1991**, *52/53*, 373–380.

Szilard, L. Improvements in or relating to the transmutation of chemical elements. British patent number: GB630726 (filed: 28 June **1934**).

Tao, J.; Perdew, J. P.; Staroverov, V. N.; Scuseria, G. E. Climbing the Density Functional Ladder: Nonempirical Meta–Generalized Gradient Approximation Designed for Molecules and Solids. Phys. Rev. Lett. **2003**, *91*, 146401.

Thomas, L. H. The calculation of atomic fields. Proc. Camb. Phil. Soc. **1926**, *23*, 542-548

Tilley, R. J. D. *Understanding Solids. The Science of Materials*; John Wiley and Sons: Chichester, **2004**.

Tosoni, S.; Tuma, C.; Sauer, J.; Civalleri, B.; and Ugliengo, P. A comparison between plane wave and Gaussian-type orbital basis sets for hydrogen bonded systems: Formic acid as a test case. J. Chem. Phys. **2007**, *127*, 154102.

Troullier, N.; Martins, J. L. Efficient Pseudopotentials for Plane-Wave Calculations. Phys. Rev. B **1991**, *43*, 1993–2006.

Ulian, G.; Tosoni, S.; Valdre, G. The compressional behaviour and the mechanical properties of talc [$Mg_3Si_4O_{10}(OH)_2$]: a density functional theory investigation. Phys. Chem. Miner. **2014**, *41*, 639–650.

US-DOE. *Environmental Impact Statement, Operation of PUREX and Uranium Oxide Plant Facilities*; DOE/EIS-0089D; Department of Energy: Hanford Site Richland, Washington, U.S., **1982**.

Utsunomiya, S.; Wang, L.-M.; Douglas, M.; Clark, S. B.; Ewing, R. C. The effect of ionizing radiation on uranophane. Am. Mineral. **2003a**, *88*, 159–166.

Utsunomiya, S.; Yudintsev, S.; Wang, L.M.; Ewing, R. C. Ion-beam and electron-beam irradiation of synthetic britholite. J. Nucl. Mater. **2003b**, *322*, 180–188.

Utsunomiya, S.; Ewing, R. C. Radiation-induced decomposition of U(VI) alteration phases of UO_2. MRS Proceedings **2006**, *932*.

Vaes, J.F. Six nouveaux mineraux d'urane provenant de Shinkolobwe (Katanga). Ann. Soc. Geol. Belg. **1947**, *70*, B212–B229.

Van Wezenbeek, E. M. *Relativistic effects in atoms and in uranium compounds*, Ph.D. Thesis. Vrije university. **1992**.

Veal, B. W.; Lam, D. J.; Carnall, W. T.; Hoekstra, H. R. X-ray photoemission spectroscopy study of hexavalent uranium compounds. Phys. Rev. B **1975**, *12*, 5651-5663.

Veithen, M.; Gonze, X.; Ghosez, Ph. Non-linear optical susceptibilities, Raman efficiencies and electro-optic tensors from first-principles density functional perturbation theory. Phys. Rev. B **2005**, *71*, 125107.

Villard, P. Sur la réflexion et la réfraction des rayons cathodiques et des rayons déviables du radium. Comptes rendus Acad. Sci. **1900a**, *130*, 1010–1012

Villard, P. Sur le rayonnement du radium. Comptes rendus Acad. Sci. **1900b**, *130*, 1178–1179.

Vinet, P.; Ferrante, J.; Smith, J. R.: Rose, J. H. A Universal Equation of State for Solids. J. Phys. C **1986**, 19, L467–L473.

Vinet P.; Ferrante, J.; Rose, J. H.; Smith, J. R. Compressibility of Solids. J. Geophys. Res. **1987**, 92, 9319–9325.

Viswanathan, K.: Harneit, O. Refined crystal structure of beta-uranophane, $Ca(UO_2)_2(SiO_3OH)_2{\cdot}5H_2O$. Am. Mineral. **1986**, *71*, 1489–1493.

Viterbo, D., *Crystal Lattices and Crystal Symmetry*, in Quantum Mechanical Ab Initio Calculation of the Properties of Crystalline Materials; Pisani, C. (ed.); Lecture Notes in Chemistry Vol. 67; Springer: Berlin, **1996**; pp. 1–30.

Vochten, R.; Blaton, N.; Peeters, O.; van Springel, K.; van Haverbeke, L. A new method of synthesis of boltwoodite and of formation of sodium boltwoodite, uranophane, sklodowskite and kasolite from boltwoodite. Can. Mineral. **1997**, *35*, 735–741.

Vochten, R.; Deliens, M. Blatonite, $UO_2CO_3(H_2O)$, a new uranyl carbonate monohydrate from San Juan County, Utah. Can. Mineral. **1998**, *36*, 1077–1081.

Voigt W. Lehrbuch der Kristallphysik; Teubner: Leipzig, **1962**.

Von Barth, U.; Hedin, L. A local exchange-correlation potential for the spin polarized case. I. J. Phys. C **1972**, *5*, 1629.

Von Halban, H.; Joliot, F.; Kowarski, L. Number of Neutrons Liberated in the Nuclear Fission of Uranium. Nature. **1939**, *143,* 680–680.

Walenta, K. On studtite and lts composition. Am. Mineral. **1974**, *59*, 166–171.

Walenta, K. Widenmannit und Joliotit, zwei neue uranylkarbonatmineralien aus den Schwartzw atd. Schweiz. MineraL. Petrogr. Mitt. **1998**, *56*, 167–185.

Wall, N. A.; Clark, S. B.; McHale, J. L. Synthesis and characterization of 1:1 layered uranyl silicate mineral phases. Chem. Geol. **2010**, *274*, 149–157.

Walshe, A.; Pru, T.; Vitova, T.; Baker, R. J. An EXAFS and HR-XANES study of the uranyl peroxides $[UO_2(\eta^2\text{-}O_2)(H_2O)_2]\cdot nH_2O$ (n = 0, 2) and uranyl (oxy)hydroxide $[(UO_2)_4O(OH)_6]\cdot 6H_2O$, Dalton Trans. **2014**, *43*, 4400–4407.

Wang, R.; Katayama, Y. B. Dissolution mechanisms for UO_2 and spent fuel. Nucl. Chem. Waste Manag. **1982**, *3*, 83–90.

Wang, B. T.; Zhang, P.; Lizarraga, R.; Di Marco, I., Eriksson, O. Phonon spectrum, thermodynamic properties, and pressure-temperature phase diagram of uranium dioxide. Phys. Rev. B **2013**, *88*, 104107.

Wanner, H.; Forest, I., Eds. *Chemical Thermodynamics of Uranium*; Elsevier Science Publishers B.V.: Amsterdam, North-Holland, **1992**.

Watt, J. P. Hashin-Shtrikman Bounds on the Effective Elastic Moduli of Polycrystals with Monoclinic Symmetry. J. Appl. Phys. **1980**, *51*, 1520–1524.

Weber, W. H.: Merlin, R. (eds.). *Raman Scattering in Materials Science*; Springer: Berlin, **2000**.

Websky, M. Über die geognostichen Verhaltnisse der Erzlagerstäten von Kupferberg u. Rudelstadt in Schlesien. Zs. d. Deutsch. Geol. Ges. **1853**, *V*, 391

Websky, M. Ueber Uranophan. Zs. d. Deutsch. Geol. Ges. **1859**, *XI*, 384.

Weck, P. F.; Kim, E.; Balakrishnan, N.; Poineau, F.; Yeamans, C. B.; Czerwinski, K. R. First-principles study of single-crystal uranium mono- and dinitride. Chem. Phys. Lett. **2007**, *443*, 82–86.

Weck, P. F.; Kim, E.; Jove-Colon, C. F.; Sassani, D. Structures of uranyl peroxide hydrates: a first-principles study of studtite and metastudtite. Dalton Trans. **2012**, *41*, 9748–9752.

Weck, P. F.; Kim, E. Layered uranium(VI) hydroxides: structural and thermodynamic properties of dehydrated schoepite $\alpha\text{-}UO_2(OH)_2$. Dalton Trans. **2014**, *43*, 17191–17199.

Weck, P. F.; Kim, E.; Buck, E. C. On the Mechanical Stability of Uranyl Peroxide Hydrates: Implications for Nuclear Fuel Degradation. RSC Adv. **2015**, *5*, 79090–79097.

Weck, P. F.; Kim, E. Uncloaking the Thermodynamics of the Studtite to Metastudtite Shear-Induced Transformation. J. Phys. Chem. C **2016,** *120*, 16553–16560.

Wen, X.-D., Martin, R. L.; Roy, L. E.; Scuseria, G. E.; Rudin, S. P.; Batista, E. R., McCleskey, T.M.; Scott, B.L.; Bauer, E.; Joyce, J. J.; Durakiewicz, T. Effect of spin-orbit coupling on the actinide dioxides AnO_2 (An=Th, Pa, U, Np, Pu, and Am): A screened hybrid density functional study. J. Chem. Phys. **2012**, *137*, 154707.

Wen, X.-D.; Martin, R. L.; Scuseria, G. E.; Rudin, S. P.; Batista, E. R.; Burrell, A. K. Screened hybrid and DFT+U studies of the structural, electronic, and optical properties of U_3O_8, J. Phys.: Condens. Matter **2013**, *25*, 025501.

Wheaton, V.; Majumdar, D.; Balasubramanian, K.; Chauffe, L.; Allen, P. G. A. Comparative theoretical study of uranyl silicate complexes. Chem. Phys. Lett. **2003**, *371*, 349–359.

Wikberg, P. *The chemistry of deep groundwaters in crystalline rocks*. Ph.D. Thesis. Royal Institute of Technology (KTH): **1987**.

Wilson, C. N. *Summary of results from the series 2 and series 3 NWSI bare fuel dissolution test*; In: Apted, M. J.; Westerman, R. E. (eds.), Scientific Basic for Nuclear Waste Management XI, 112, p. 473–483; Material Research Society: Boston, Massachusetts, **1987**.

Wilson, P. D. *The nuclear fuel cycle from ore to waste*. Oxford University Press: Oxford. **1996**.

Wilson, E. B.; Decius, J. C., Cross, P. C. *Molecular Vibrations*; McGraw-Hill: New York, **1955**.

WNA, World Nuclear Association. http://www.world-nuclear.org/info/Country-Profiles/Countries-O-S/Spain/ retrieved **2017a**.

WNA, World Nuclear Association. http://www.world-nuclear.org/information-library/nuclear-fuel-cycle/nuclear-power-reactors/nuclear-power-reactors.asp retrieved **2017b**.

Wronkiewicz, D. J.; Bates, J. K.; Gerding, T. J.; Veleckis, E.; Tani, B. S. Uranium release and secondary phase formation during unsaturated testing of UO_2 at 90°C. J. Nucl. Mater. **1992**, *190*, 107–127.

Wronkiewicz, D. J.; Bates, J. K.; Wolf, S. F.; Buck, E. C. Ten-year results from unsaturated drip tests with UO_2 at 90°C: implications for the corrosion of spent nuclear fuel. J. Nucl. Mater. **1996**, *238*, 78–95.

Wu, Z.; Cohen R. E. More accurate generalized gradient approximation for solids. Phys. Rev. B **2006**, *73*, 235116.

Wu, Z. J.; Zhao, E. J.; Xiang, H. P.; Hao, X. F.; Liu X. J., Meng, J. Crystal Structures and Elastic Properties of Superhard IrN_2 and IrN_3 from First Principles. Phys. Rev. B **2007**, *76*, 054115.

Yablokov, A. V.; Nesterenko, V. B.; Nesterenko, A. *Chernobyl: Consequences of the Catastrophe for People and the Environment.* Blackwell Publishing for the Annals of the New York Academy of Sciences: Boston, **2009**.

Yin, Q.; Savrasov, S. Y. Origin of Low Thermal Conductivity in Nuclear Fuels. Phys. Rev. Lett. **2008**, *100*, 225504.

Yu, R.; Zhu, J.; Ye, H. Q. Calculations of Single-Crystal Elastic Constants Made Simple. Comput. Phys. Commun. **2010**, *181*, 671–675.

Yun, Y.; Legut, D.; Oppeneer, P.M. Phonon spectrum, thermal expansion, and heat capacities of UO_2 from first principles. J. Nucl. Mater. **2012**, *423*, 109–114.

Yvon, K.; Jeitschko, W.; Parthe, E. LAZYPULVERIX: A Computer Program for Calculating X-ray and Neutron Diffraction Powder Patterns. J. Appl. Cryst. **1977**, *10*, 73–74.

Zhang, Y.; Bhadbhade, M.; Price, J. R.; Karatchevtseva, I.; Collison, D.; Lumpkin, G. R. Kinetics vs thermodynamics: A unique crystal transformation from a uranyl peroxo- nanocluster to a nanoclustered uranyl polyborate. RSC Adv. **2014**, *4*, 34244–34247.

Part V. Appendix: Publications

Rutherfordine: Structure and Raman Spectroscopy

Article: "*Spectroscopic Raman characterization of Rutherfordine: a combined DFT and experimental study"*, by L. J. Bonales, F. Colmenero, J. Cobos and V. Timón, Phys. Chem. Chem. Phys. 18, 16575–16584 (2016).

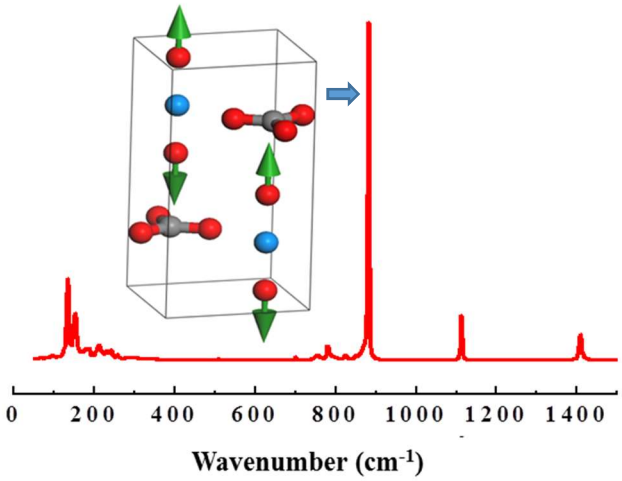

PCCP

PAPER

View Article Online
View Journal | View Issue

Cite this: Phys. Chem. Chem. Phys., 2016, 18, 16575

Spectroscopic Raman characterization of rutherfordine: a combined DFT and experimental study†

L. J. Bonales,*[a] F. Colmenero,[b] J. Cobos[a] and V. Timón[b]

Received 4th March 2016,
Accepted 19th May 2016

DOI: 10.1039/c6cp01510g

www.rsc.org/pccp

A rutherfordine mineral was studied by means of Raman spectroscopy combined with first principle calculations based on the density functional theory (DFT) method. The pseudopotential of a uranium atom was generated and its performance was evaluated for a series of uranium-containing minerals. The structure of rutherfordine was determined for two symmetries (*Pmmn* and *Imm*2) and the resulting lattice parameters, bond lengths, bond angles, and X-ray powder diffractogram were found to be in very good agreement with experimental values. The Raman spectrum was experimentally determined in the range 0–1700 cm^{-1} and calculated using density functional perturbation theory. The non-scaled theoretical wavenumbers also agreed with the experimental values, and therefore a detailed interpretation of the theoretical spectra allowed us to assign the Raman bands found in the experimental spectrum.

1 Introduction

Evaluation of the performance of the final repository for spent nuclear fuel (SNF) as a deep geological repository requires knowledge of the behavior of the waste after storage times on the order of thousands of years.[1] It is widely accepted that after such a long time the barriers that protect the waste will be breached and SNF will be in contact with water.[2] The matrix of the spent nuclear fuel composed of uranium dioxide, UO_2, could dissolve in water and then release into the biosphere of fission products, and heavier actinide contents in the SNF, could occur.[3–5]

This corrosion process is described primarily *via* the oxidation of U(IV) to U(VI), and then by the formation of alteration products, usually containing UO_2^{2+} in their crystal structures:[6]

$$U(IV) \rightarrow U(VI) \quad (1)$$

$$U(VI) \rightarrow UO_2^{2+}(s) \quad (2)$$

Great efforts have been spent studying the reaction mechanism and establishing the key parameter that controls corrosion of the SNF, such as leaching/dissolution experiments,[7–9] and studies of uraninite[10,11] as a natural analogue of the spent nuclear fuel matrix. These stability studies require characterization of the products of the SNF and its reaction products, which is a great challenge not only because these materials are very complicated (containing almost the entire periodic table), but also due to their radiotoxicity.[12] The last feature complicates the handling of these substances under security conditions and, therefore, its characterization. The proper characterization technique to analyze these materials should meet several requirements, such as: (1) the samples should not require any special preparation; (2) the technique must allow the analysis of a very small amount of sample and, (3) it must be a non destructive technique.

One technique that meets all the above criteria is Raman spectroscopy.[13] This technique has proven useful in the study of several systems in extreme conditions, such as very high[14] or very low temperatures,[15] high pressures,[16] and also radioactivity.[17] Raman spectroscopy can give information on both the molecular structure and the surrounding environment. However, in order to obtain this information, it is necessary to have a precise assignment of the bands in the Raman spectrum and models to interpret the values of the band wavenumbers and their changes. Beside the fact that the Raman technique has already been used to analyze SNF and its alteration products, the database with good assignment of the different bands is still rather limited, apart from some works[7,18–23] and the efforts of Frost *et al.*[24–29] who studied a high number of secondary phases. A few research groups[30–32] have focused their studies on the characterization of uranium oxides.

The difficulties in the assignment of the different vibrational bands can be overcome by using theoretical calculations.

[a] Centro de Investigaciones Energéticas, Medioambientales y Tecnológicas (CIEMAT), Avda/Complutense, 40, 28040 Madrid, Spain. E-mail: laura.jimenez@ciemat.es
[b] Instituto de Estructura de la Materia (CSIC), C/Serrano, 113, 28006 Madrid, Spain

† Electronic supplementary information (ESI) available: Calculated structures of uranium containing minerals using a new pseudopotential; normal modes of rutherfordine (*Pmmn* and *Imm*2 symmetries). See DOI: 10.1039/c6cp01510g

Solid state codes run on modern large computers are nowadays capable of optimizing the structures of complex systems, and then performing theoretical predictions of many observable quantities comparable with experiment.[33–35] *Ab initio* lattice dynamics provide theoretical vibrational spectra as well as detailed microscopic scale views of the atomic vibrational motion (normal modes), thus allowing a reliable assignment of experimental Raman bands.[36] One of the methods for which this kind of calculation is feasible is DFT (Density Functional Theory),[37] based on plane waves and employing pseudopotentials.[38] The use of DFPT (Density Functional Perturbation Theory)[36,39,40] has permitted the theoretical prediction of IR and Raman spectra with a good level of accuracy and cost/performance ratios. However, its application to minerals containing rare earth elements presents difficulties not only due to the great number of atoms and valence electrons involved, but also to the high level of theory required to describe these elements.[41,42] Uranium is a complex atom showing four oxidation states (+3, +4, +5, and +6) with a very large size of its ions, forming complicated compounds with large coordination numbers. The number of valence electrons in the outer shells, which should be explicitly described, is high and includes orbitals of high angular quantum number (5f shell). The good relativistic pseudopotentials needed to describe the inner electrons of these elements as required for vibrational studies of solids are difficult to find or generate. As a matter of fact, there are very few published works on the theoretical vibrational spectra of uranium containing solids.[43–46] These studies are limited to uranium oxides and nitrides and the unique spectral features considered are the vibrational band wavenumbers. For example, Yun *et al.*[43] determined the phonon spectrum of UO_2 at the gamma point and compared their calculated wavenumbers with the experimental ones. Nevertheless, some studies on other properties of these materials[41,42,47–53] and of related gas-phase molecular clusters have been reported.[54–58]

One of the uranyl minerals of interest is rutherfordine, UO_2CO_3. Rutherfordine is the only known uranyl mineral phase of interest in the SNF that contains only uranyl and carbonate. There are other uranyl carbonate hydrated phases such as blatonite, $UO_2CO_3{\cdot}H_2O$,[59] and joliotite, $UO_2CO_3{\cdot}2H_2O$,[60] but the structures of these minerals are unknown. Uranium carbonate compounds and their importance in actinide environmental chemistry have been reviewed by Clark *et al.*[61] Carbonate and bicarbonate, present in significant concentrations in many natural waters, are exceptionally strong complexing agents for actinide ions and, therefore, carbonate complexes of actinide ions play an important role in migration from nuclear waste repositories or in accidental site contamination. This is reflected by the formation of many naturally occurring uranyl carbonate minerals such as rutherfordine, liebigite, and andersonite among others.[61] Uranium carbonates may precipitate where evaporation is significant or where the partial pressure of CO_2 is large, rutherfordine becoming a more stable uranium phase with respect to schoepite. Rutherfordine would be expected to replace schoepite in environments where the CO_2 pressure is high, possibly in a repository environment or in saturated soils. Replacement of schoepite by rutherfordine has been observed at the Shinkolobwe U-deposit.[62,63] The study of the structural and thermodynamic stabilities of uranium carbonates is thus particularly relevant to nuclear-waste disposal.

Rutherfordine was discovered by Marckwald[64] and described as a mineral species by Frondel and Meyrowitz.[65] Its solid state structure has been determined from crystals of both the natural mineral and synthetic samples. Rutherfordine forms green–yellow crystals with an orthorhombic structure. The structure of rutherfordine was provided by Christ and Clark.[66,67] The structure was later refined by Finch *et al.*[68] Christ *et al.*[66] presented two structures: (1) structure A, which is consistent with *Pmmn* symmetry, and adjacent layers have the CO_3^{2-} groups pointing in opposite directions; and (2) structure B, which is consistent with *Imm*2 symmetry, and adjacent layers have the CO_3^{2-} groups pointing in the same direction. They suggested that structures A and B are energetically equivalent, and that crystals can contain domains of each structure, separated by stacking faults. Finch *et al.*[68] suggested that structure B should be favored. *Pmmn* and *Imm*2 structures are considered in the present theoretical calculations, and the results indicate that both may be simultaneously present in nature in accordance with the suggestion of Christ *et al.*[66]

In this paper we present a detailed study of the rutherfordine mineral using Raman spectroscopy and DFT calculations. The work is structured as follows: in Section 2, the materials and methods used in this work are described for the experimental and theoretical parts of this study. Density functional theory calculations are described, as well as the generation of the pseudopotential used for uranium atom. Then, in Section 3, experimental results are presented and compared with theoretical data for the *Pmmn* and *Imm*2 symmetries and the assignment of the main fundamental band wavenumbers is carried out. Moreover, the effect of water addition to the rutherfordine structure is studied by further calculations. The conclusions of this work are presented in Section 4.

2 Materials and methods

2.1 Experimental

The analyzed sample is a "uraninite + gummite" mineral from Sierra Albarrana (Córdoba, Spain), collected during the uranium extractive activity in 1960. The sample structure corresponds to ideal gummite occurrence (central core black and a yellow surrounding zone, formed by several minerals).[10] A detailed description of the mineral setting and other structural characteristics is described elsewhere.[69]

The sample was cut using a diamond saw and polished. A polished section of the sample was analyzed *via* Raman spectroscopy by using a Horiba LabRam HR evolution spectrometer (Jobin Yvon Technology). A HeNe laser with a wavelength of 632.81 nm and an operation power of 20 mW was used as the excitation source. The laser was focused onto the sample using the 100× objective of a confocal microscope (BX4 with confocal 800 mm); the scattered light was collected with the same objective and then dispersed with a Jobin-Yvon spectrometer

(600 grooves per mm), and detected with a Peltier cooled CCD detector (256 × 1024 pix.). The spectral resolution was about 1 cm^{-1} per pixel.

2.2 Theoretical

The rutherfordine unit cell has been modeled using the CASTEP code,[33] a module of the Materials Studio package.[70] The generalized gradient approximation (GGA) with several different energy functionals was employed. The main one was the PBESOL functional.[71,72] Also, since the rutherfordine structure is composed of sheets held together by van der Waals forces, we used the PBE functional[71] with the Grimme empirical dispersion correction, the DFT-D2 approach,[73] to evaluate the importance of this kind of interaction.

Geometry optimization was carried out using the Broyden–Fletcher–Goldfarb–Shanno optimization scheme[74] with a convergence threshold on atomic forces of 0.01 eV $Å^{-1}$. The different kinetic energy cutoffs and *K*-point meshes[75] adopted are indicated in each case. They were selected to ensure good convergence for the computed structures and energies.

For the calculations of the vibrational properties, linear response density functional perturbation theory (DFPT)[36,39,40] implemented in the CASTEP code was used, where the phonon wavenumbers at the gamma point of the Brillouin zone were computed using atomic displacement perturbations. Raman intensities are the third-order derivatives of the total energy with respect to the vibrational mode (atomic position) and laser field (electric field, twice). These are calculated in CASTEP[34] using a combination of perturbation theory (second derivative with respect to field) and finite differences (third derivative with respect to atomic displacement). The wavenumbers presented in this work have not been scaled to correct for anharmonicity and correspond to the harmonic approximation of the force field.

Since the CASTEP code only allows determining vibrational properties using norm conserving pseudopotentials and as there is no such pseudopotential for the uranium atom, we decided to construct a new one. First, we generated a Troullier–Martins type norm-conserving pseudopotential[76] using the program fhi98PP[77] in cpi format. The pseudopotential included relativistic effects (scalar relativistic all electron calculations are used) and it was generated using the GGA-PBE[71] method. The electronic configuration of atomic uranium is $6s^2 6p^6 6d^1 5f^3 7s^2$. The pseudopotential was obtained from an ionized electronic configuration $6s^2 6p^6 6d^1 5f^3 7s^0$ with cutoff radii equal to 1.236, 2.447, 2.166 and 2.447 for s, p, d, and f angular momenta, respectively. The s component of the pseudopotential was chosen as the local potential, and a Kleinman–Bylander form[78] was used. Then, we transformed it into the recpot format used in CASTEP by using the tool cpi2recpot.[79] The use of this pseudopotential implies that the 14 valence electrons must be treated explicitly. In other works, 32 electrons were included in the valence shell.[56] This further increases the computational cost and only marginally improves the performance.[42,57]

This pseudopotential reproduces accurately the all-electron calculation in the reference configuration in which it was generated. Further, checks of the smoothness of the nodeless pseudo-wavefunctions near the cutoff radii, and of the continuity of the logarithmic energy derivatives and transferability of the pseudopotential were performed. In order to probe the generated norm-conserving pseudopotential under different environments and to validate it, we computed the structures of a series of uranium containing minerals with small cutoffs and K meshes. The results are given in a table in Appendix A of ESI.† As can be seen in Table A1 (ESI†) the results are quite good for the lattice parameters of the species involved. Better results are expected upon increasing the cutoff values and using larger K meshes.

3 Results and discussion

3.1 Structure

A determination of the best geometrical structure was first carried out searching for a minimum in the potential energy surface. From the optimized structure we have obtained both the structural parameters and the X-ray powder pattern.

We have considered both orthorhombic ($Z = 2$) structures in rutherfordine, *Pmmn* and *Imm*2. The results are nearly the same and the energy difference for the optimized structures is less than 0.001 eV, the *Pmmn* structure being the lowest one.

The structure of rutherfordine contains approximately linear UO_2^{2+} uranyl ions that are coordinated by six O atoms arranged at the equatorial vertices of uranyl hexagonal bipyramids. These O atoms belong to four carbonate ligands and U is bonded with two carbonate ions in a bidentate manner and two in a monodentate manner. Each uranyl polyhedron is linked to two other uranyl polyhedra in a *trans* arrangement by edge sharing, resulting in chains of polyhedra. Adjacent chains are linked by the sharing of equatorial vertices between uranyl polyhedra, which results in a sheet structure that contains triangular voids. Carbonate triangles occupy one half of the voids, such that they share the equatorial edges of two adjacent uranyl hexagonal bipyramids and single vertices of two additional uranyl polyhedra (see Fig. 1). The resulting sheets or layers are electroneutral, and adjacent sheets in rutherfordine are bonded together by van der Waals forces. The UO_2CO_3 layers are staggered with respect to the layer above or below, such that uranyl units lie above and below a carbonate carbon atom in adjacent layers. Layers are separated by a distance of about 4.6 Å. The structure is shown in Fig. 1. Fig. 1A and B show two contiguous sheets (*Pmmn* and *Imm*2 symmetry structures). In Fig. 1C a view from the (010) axis is observed (similar for the two symmetry structures), showing the relative disposition of the uranyl polyhedra and carbonate triangles in the plane. As can be seen, for the *Pmmn* structure the carbonate triangles in contiguous sheets point in opposite directions while in the *Imm*2 structure they point in the same direction.

The lattice parameters of rutherfordine, as well as the volumes and densities, were determined in calculations of increasing complexity by increasing the different parameters (larger kinetic energy cutoffs and K meshes). The optimizations performed with a cutoff of 1000 eV and a K mesh of 5 × 3 × 6 (18 *K* points) gave

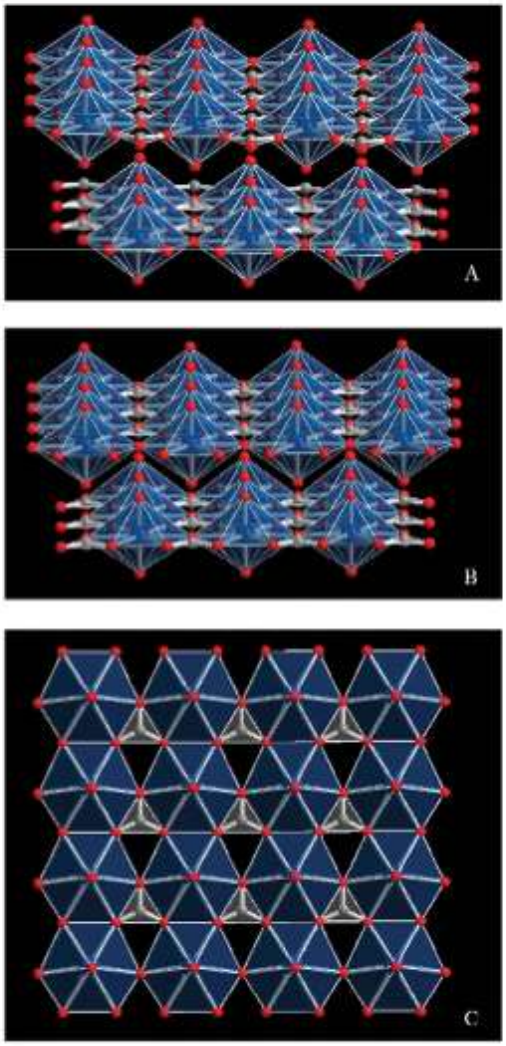

Fig. 1 (A) Two contiguous sheets in the structure of rutherfordine for the *Pmmn* structure; (B) as figure A for the *Imm*2 structure; (C) upper (010) view of a sheet in the structure of rutherfordine. Color code: U – blue, O – red, C – carbon.

Table 1 Lattice parameters

Calculation	a (Å)	b (Å)	c (Å)	α	β	γ	Vol. (Å^3)	Dens. (g cc^{-1})
Pmmn	4.8257	9.3321	4.2720	90	90	90	192.4	5.697
*Imm*2	4.8267	9.3639	4.2727	90	90	90	193.1	5.675
Exp.[68]	4.840	9.273	4.298	90	90	90	192.9	5.682

well converged structures and were considered sufficient to determine the final material properties. Table 1 gives the final lattice parameters, volumes and densities obtained for the *Pmmn* and *Imm*2 structures, respectively. Tables 2 and 3 give the corresponding bond distances and angles.

The powder X-ray pattern of rutherfordine was computed[80] from the experimental[68] and computed structures using CuK_α radiation (λ = 1.540598 Å). The most intense lines ($I > 10\%$) are

Table 2 Bond distances (in Å)

Bond	Exp.[68]	*Pmmn*	*Imm*2
U–O3	2.444	2.435	2.428
U–O2	2.48	2.436	2.437
U–O2′	2.52	2.525	2.535
U–O1	1.744	1.764	1.764
U–C	2.94	2.912	2.918
C–O3	1.32	1.301	1.301
C–O2	1.26	1.280	1.280
⟨CO⟩	1.28	1.287	1.287
C–O1	2.93	2.946	2.960

Table 3 Bond angles (in deg)

Bond angle	Exp.[68]	*Pmmn*	*Imm*2
O1a–U–O1	179	178.61	179.92
O1–U–O2 × 4	91	90.59	90.03
O1–U–O2b × 4	89	89.40	89.97
O1–U–O3 × 4	90.1	89.91	89.99
O2–U–O2c	60.8	59.89	58.70
O2b–U–O2d	62.1	62.32	62.61
O3–U–O2b × 2	67.0	66.62	66.72
O3–U–O2 × 2	51.6	52.27	52.13
O2–C–O2e	131	128.42	128.33
O2–C–O3 × 2	114	115.79	115.83
⟨O–C–O⟩	120	120	120

compared in Fig. 2b–d, and, as can be seen, the line positions and intensities are in good agreement. The use of spectra derived directly from the experimental and computed structures allows for a fair comparison of the results free of interferences, such as the experimental conditions or possible artifacts from the presence of sample impurities, since both are determined under identical conditions. Nevertheless, the use of an experimental pattern also leads to an excellent agreement. Computer program XPowder[81] using the PDF-2 database[82] directly recognizes the computed spectrum as that of the rutherfordine mineral (pattern 89-6527).[68] The experimental X-ray spectrum can be seen in Fig. 2a where it is compared with the previously described spectra. The precise values of the main reflections for the *Imm*2 and *Pmmn* computed structures and the experimental ones are given in Table 4.

3.2 Raman spectra and band assignment

In this section we analyze the experimental profile of the rutherfordine Raman spectra obtaining the wavenumber of the main characteristic bands. Also the theoretical spectrum is presented and the assignment of the vibrational bands is performed. The results are compared with some published data of this mineral phase.

In order to calculate the number of contributions of a given band from the experimental spectrum we carry out the analysis by the second derivative method.[83] The first derivative gives us an idea of the number of contributions involved but, as usual in spectroscopy, it is the second derivative which enables us to determine the number of contributions, since each one leads to a minimum.

The Raman spectra for the *Pmmn* and *Imm*2 structures were computed at T = 298 K, λ = 532 nm, FWHM = 5 cm^{-1}.

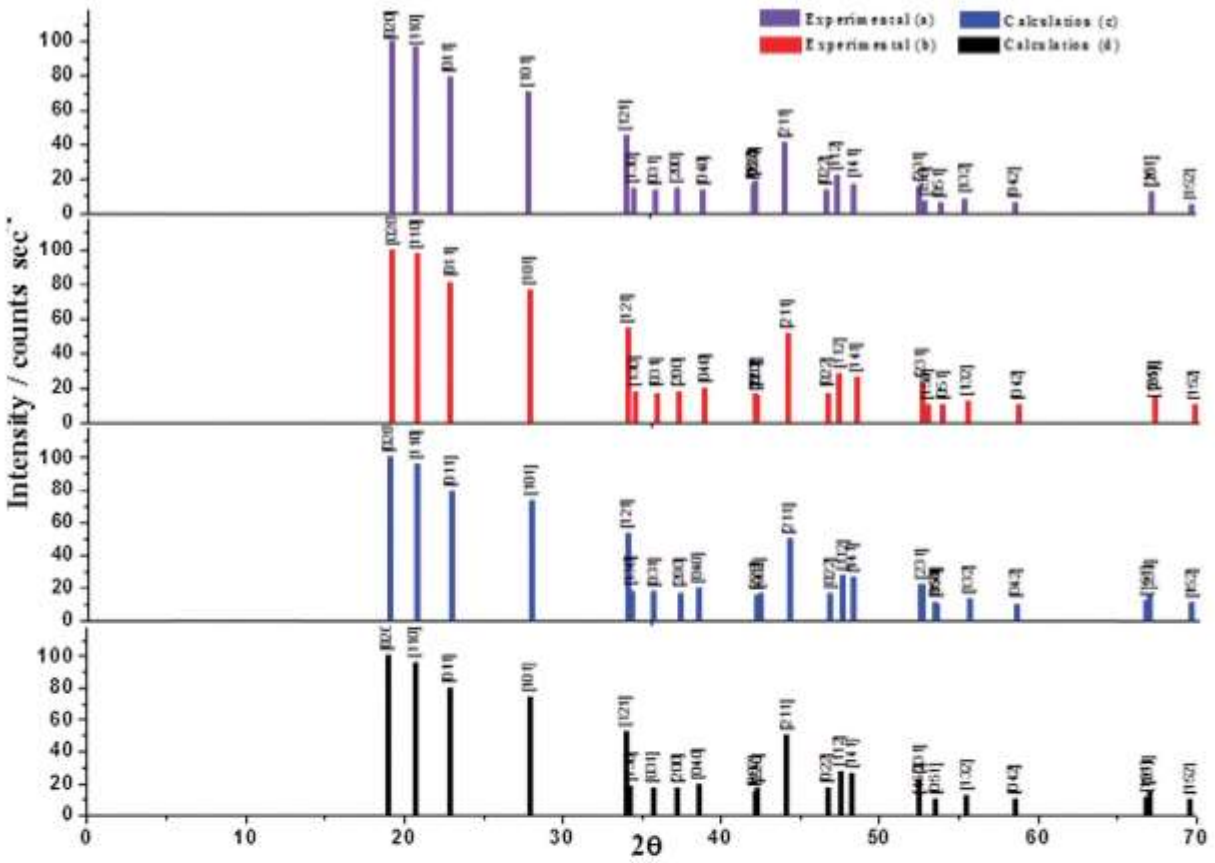

Fig. 2 X-ray powder spectrum of rutherfordine using CuK_α radiation: (a) experimental spectrum (pattern 89-6527 in the PDF-2 database[68]); (b) X-ray powder spectrum computed form experimental geometry; (c) X-ray powder spectrum computed from calculated geometry (*Pmmn*); (d) X-ray powder spectrum computed from calculated geometry (*Imm*2).

Table 4 Main reflections in the X-ray powder spectrum of rutherfordine. The experimental data are from the pattern 89-6527 in the PDF-2 database[68]

Experimental reflections				Calculated reflections *Pmmn*			Calculated reflections *Imm*2		
2θ	d (Å)	I (%)	hkl	2θ	d (Å)	I (%)	2θ	d (Å)	I (%)
19.127	4.636	100.0	020	19.004	4.6660	100.0	18.939	4.682	100.0
20.684	4.290	97.397	110	20.705	4.2865	96.227	20.687	4.290	95.591
22.786	3.899	78.679	011	22.876	3.8846	79.564	22.859	3.887	79.089
27.736	3.214	70.771	101	27.870	3.1987	73.600	27.864	3.199	73.535
33.912	2.641	45.445	121	33.952	2.6383	52.598	33.909	2.641	52.942
34.398	2.605	14.514	130	34.269	2.6146	18.163	34.182	2.621	18.049
35.752	2.509	12.913	031	35.675	2.5147	17.219	35.591	2.520	17.129
37.121	2.420	14.615	200	37.235	2.4128	17.005	37.227	2.413	16.853
38.814	2.318	13.213	040	38.558	2.3330	19.736	38.422	2.341	19.670
42.010	2.149	16.216	002	42.128	2.1433	14.949	42.269	2.136	16.452
42.084	2.145	18.218	220	42.277	2.1360	16.627	42.089	2.145	14.870
44.001	2.056	40.741	211	44.151	2.0496	50.157	44.134	2.050	49.782
46.541	1.950	12.913	022	46.734	1.9422	16.829	46.697	1.944	16.699
47.268	1.921	21.521	112	47.522	1.9118	27.663	47.505	1.912	27.535
48.373	1.880	17.017	141	48.242	1.8849	25.788	48.125	1.889	25.791
52.489	1.742	15.315	231	52.519	1.7410	22.368	52.451	1.743	22.219

The atomic motions associated with each vibrational normal mode are shown in the ESI† (Appendices B and C). Fig. 3 shows the experimental Raman spectrum of rutherfordine, together with the calculated ones. A summary of the measured and calculated spectra is shown in Tables 5 and 6 for *Pmmn* and *Imm*2, respectively, as well as the approximate assignments of the vibrational modes, derived from the calculations. As can be seen in Fig. 3, the general aspect of the computed spectrum is

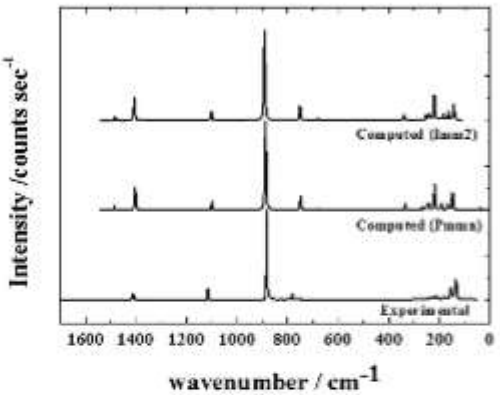

Fig. 3 Calculated and experimental Raman spectra.

Table 5 Experimental and calculated Raman shifts, calculated intensities and assignments (*Pmnn* symmetry)

Exp. Raman shift (cm^{-1})	Calc. Raman shift (cm^{-1})	Irr. rep. (D_{2h})	Intensity (Å^4)	Assignment
78.63	32.743	A_g	0.051	$T(UO_2^{2+} + CO_3^{2-})$
95.34	43.405	B_{3g}	0.129	$T(UO_2^{2+} + CO_3^{2-})$
133.77	147.179	B_{1g}	11.632	$\delta^a(UO_2^{2+}) + \delta^{op}(CO_3^{2-})$
152.91	149.758	B_{3g}	2.860	$\delta^{op}(CO_3^{2-})$
168.187	164.700	B_{3g}	4.693	$T(CO_3^{2-})$
187.24	189.777	B_{3g}	8.011	$\delta^a(UO_2^{2+})$
212.98	217.417	A_g	35.316	$T(CO_3^{2-})$
241.59	241.484	B_{2g}	7.366	$\delta^a(UO_2^{2+}) + \delta^{ip}(CO_3^{2-})$
256.68	264.646	B_{2g}	7.636	$\delta^a(UO_2^{2+}) + \delta^{ip}(CO_3^{2-})$
339.15	332.824	B_{2g}	16.935	$\delta^{ip}(CO_3^{2-})$
700.29	677.803	A_g	15.199	$\delta^{ip}(CO_3^{2-})$
754.448	752.046	B_{1g}	0.432	$\delta^{op}(CO_3^{2-})$
780.203	746.833	B_{2g}	110.074	$\delta^{ip}(CO_3^{2-})$
793.045	—	—	—	—
803.534	—	—	—	—
823.306	—	—	—	—
882.288	886.469	A_g	879.905	$\nu^s(UO_2^{2+})$
1113.33	1097.712	A_g	120.246	$\nu^s(CO_3^{2-})$
1408.98	1401.211	A_g	407.713	$\nu^s(CO_3^{2-})$
1498.92	1482.837	B_{2g}	76.985	$\nu^a(CO_3^{2-})$

Table 6 Experimental and calculated Raman shifts, calculated intensities and assignment (*Imm2* symmetry)

Exp. Raman shift (cm^{-1})	Calc. Raman shift (cm^{-1})	Irr. rep. (D_{2h})	Intensity (Å^4)	Assignation
78.63	—	—	—	—
95.34	—	—	—	—
133.77	141.673	A_2	10.780	$\delta^a(UO_2^{2+}) + \delta^{op}(CO_3^{2-})$
152.91	—	—	—	—
168.187	162.271	B_1	7.754	$\delta^a(UO_2^{2+}) + \delta^{op}(CO_3^{2-})$
187.24	182.062	B_1	6.165	$\delta^a(UO_2^{2+}) + \delta^{op}(CO_3^{2-})$
212.98	218.675	A_1	34.726	$\delta^s(UO_2^{2+}) + T(CO_3^{2-})$
241.59	239.638	B_2	6.546	$\delta^s(UO_2^{2+}) + \delta^{ip}(CO_3^{2-})$
256.68	250.776	B_2	8.407	$\delta^s(UO_2^{2+}) + \delta^{ip}(CO_3^{2-})$
339.15	338.196	B_2	17.723	$\delta^{ip}(CO_3^{2-})$
700.29	677.882	A_1	16.450	$\delta^{ip}(CO_3^{2-})$
754.448	750.148	B_1	0.542	$\delta^{op}(CO_3^{2-})$
780.203	749.753	B_2	112.461	$\delta^{ip}(CO_3^{2-})$
793.045	—	—	—	—
803.534	—	—	—	—
823.306	—	—	—	—
882.288	889.836	A_1	872.824	$\nu^s(UO_2^{2+})$
1113.33	1099.867	A_1	117.486	$\nu^s(CO_3^{2-})$
1408.98	1403.178	A_1	407.867	$\nu^s(CO_3^{2-})$
1498.92	1480.873	B_2	75.720	$\nu^a(CO_3^{2-})$

very similar to that of the experimental spectrum up to 1550 cm^{-1}. The band observed at higher wavenumber (~1603 cm^{-1}) in the experimental spectrum does not appear in the computed ones, as expected, due to the fact that this band corresponds to the water bending vibration, and the calculations do not include water within the structure. A more detailed comparison will be given below. Note that when the symmetry of a certain vibration is cited, we refer to that of the *Pmnn* structure. To find the corresponding symmetry for the *Imm*2 structure, see Table 6 given below.

The Raman spectra of the regions 1200–850 cm^{-1} and 1700–1200 cm^{-1} are shown in Fig. 4A and B, respectively, together with the computed spectra. Fig. 4A shows the region of the uranyl stretching vibration. In this region there is a main band at 882 cm^{-1}, which corresponds to the uranyl symmetric stretching vibration ν_1, which is commonly used as a fingerprint of this mineral.[69] The value was very well reproduced by the theoretical calculations (886 cm^{-1} and 900 cm^{-1}, for *Pmnn* and *Imm*2, respectively, A_g symmetry), and it is in agreement with previous published data (886 cm^{-1}).[25] At higher wavenumbers (around 1113 cm^{-1}) we found a band which is assigned to the CO_3^{2-} symmetric stretching vibration ν_1 (free CO_3^{2-} ion value of 1060 cm^{-1}), which is also in good agreement with both the calculated value (1098 cm^{-1} and 1100 cm^{-1}, A_g symmetry) and the experimental value of ref. 25 (1115 cm^{-1}).

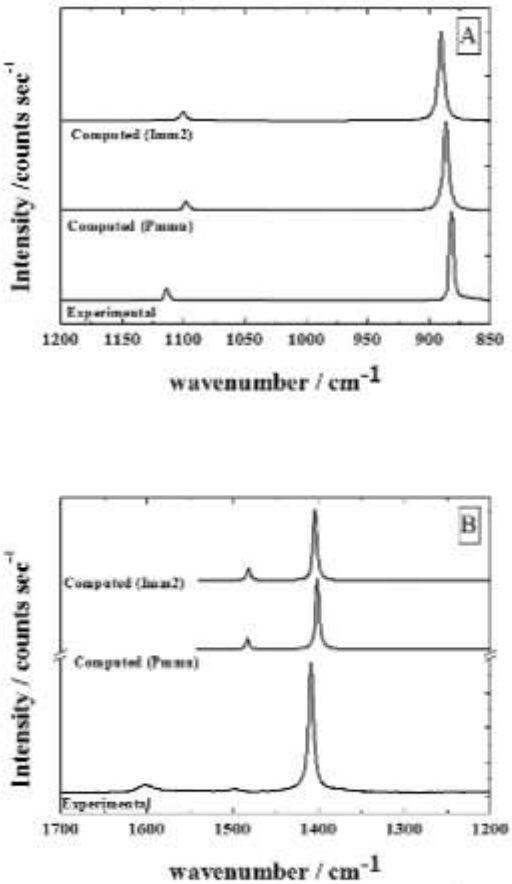

Fig. 4 (A) Raman spectrum of the region 850–1200 cm^{-1}; (B) Raman spectrum of the region 1200–1700 cm^{-1}.

Fig. 4B shows the spectrum in region 1700–1200 cm^{-1}. The band at 1409 cm^{-1} is assigned to the asymmetric stretching vibrations of CO_3^{2-} ion ν_3 and this value is very close to the computed wavenumbers (1401 cm^{-1} and 1403 cm^{-1}). Frost *et al.*[25] observed this band at 1412 cm^{-1}.

The existence of a less intense band at about 1499 cm^{-1} can be explained as a result of the splitting of the ν_3 band. In the free undistorted ion it is degenerate, symmetry E', and located at about 1415 cm^{-1}. The band is split into two components when the ion symmetry is lowered from D_{3h} to C_{2v}, whose computed values are 1401 and 1483 cm^{-1} with symmetries A_g and B_{2g}, respectively, for the *Pmmn* structure and 1403 and 1481 cm^{-1} for *Imm*2 structure. The experimental value of the splitting is Δ = 1499–1409 = 90 cm^{-1} while the computed values are 82 and 78 cm^{-1}. The values are also comparable to the IR spectrum bands at[84] 1414 and 1505 cm^{-1} or[85] 1433 and 1520 cm^{-1}.

The Raman spectra of the regions 500–0 cm^{-1} and 850–500 cm^{-1} are shown in Fig. 5A and B, respectively, together with the computed spectra.

The low wavenumber region 500–0 cm^{-1} is shown in Fig. 5A. The bands located at 339, 257, 242, 213, 187, 168, 153, and 134 cm^{-1} have theoretical counterparts of 332, 265, 242, 217, 190, 165, 150, and 147 cm^{-1} for *Pmmn* and 338, 251, 240, 219, 182, 162 and 142 cm^{-1}, for the *Imm*2 symmetry. The first one, at 339 cm^{-1}, is assigned to a carbonate in plane bending vibration (B_{2g}), and that located at 153 cm^{-1} to a carbonate out of plane vibration (B_{3g}). While the 257 and 242 cm^{-1} bands are assigned mainly to uranyl symmetric bending vibrations (B_{2g}), the 187 and 134 cm^{-1} bands are assigned to uranyl antisymmetric bending vibrations (B_{3g} and B_{1g}). Finally, the 213 and 168 cm^{-1} bands are assigned to carbonate group translations (A_g and B_{3g}). The final bands found at 95 and 79 cm^{-1} are not as well reproduced theoretically and may be described as overall carbonate and uranyl group translations.

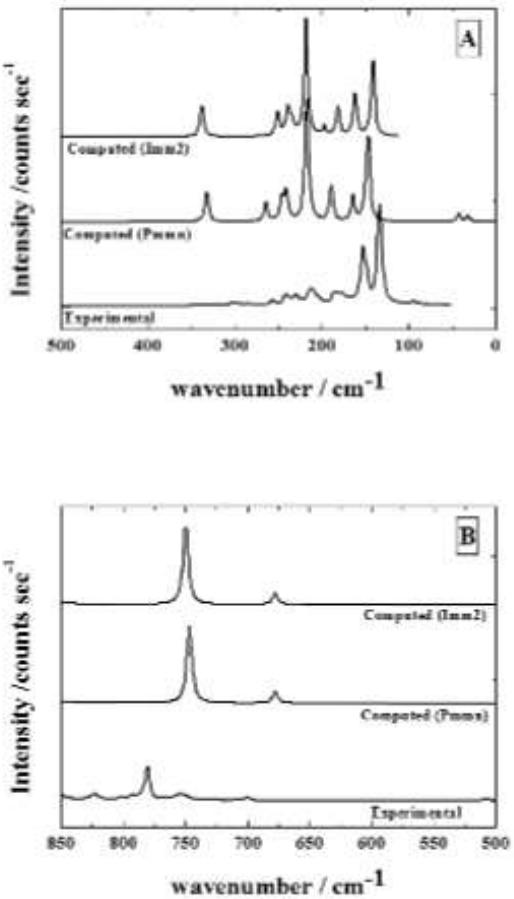

Fig. 5 (A) Raman spectrum of the region 0–500 cm^{-1}; (B) Raman spectrum of the region 500–850 cm^{-1}.

Among the low wavenumber bands of the published data[25] a band is found at 343 cm^{-1} which seems to split into two components at 336 and 330 cm^{-1}. These bands were attributed to the ν(U–O equatorial) vibrations.[86] As can be seen in the vibrational mode picture, the calculated band at 333 cm^{-1} (associated with the experimental value of 339 cm^{-1}), actually represents a carbonate in plane vibration. Bands were also observed at 279, 263, 252 and 241 cm^{-1} (bands at 257 and 242 cm^{-1} appear in our spectrum) and were ascribed without specification to the ν_2 bending modes of the $(UO_2)^{2+}$ units and lattice vibrations. We believe that they correspond to uranyl symmetric bending vibrations, the antisymmetric ones and lattice vibrations falling somewhat lower in wavenumber.

Fig. 5B shows the region 850–500 cm^{-1}. The bands at 700 and 780 cm^{-1} are attributed to the CO_3^{2-} in plane bending vibrations ν_4 and are calculated at 678, and 747 cm^{-1}, for *Pmmn* and 678 and 750 cm^{-1} for *Imm*2. The free ion wavenumber value is 680 cm^{-1}. This vibration (E'' symmetry) splits, as the ν_3 one, into two components of symmetries A_g and B_{2g}. In this case the second one has the largest intensity. The splitting is Δ = 69 cm^{-1} for *Pmmn* and 72 cm^{-1} for *Imm*2 while the experimental value is 80 cm^{-1}. The CO_3^{2-} out of plane deformation vibration ν_2 is believed to fall at 754 cm^{-1} while the theoretical value is 752 cm^{-1} for *Pmmn* and 750 cm^{-1} for *Imm*2 as can be seen in the vibrational mode pictures (see Fig. B1 in Appendix B and Fig. C1 in Appendix C of ESI†). The free ion value is however 880 cm^{-1}. It is very weak in the theoretical Raman spectra as expected from an inactive Raman vibration for the free carbonate ion.

It should be noted that weak bands at 793, 803, and 823 cm^{-1} do not have counterparts in the theoretical spectra; these bands must correspond to other species of carbonate anions in the rutherfordine structure[25,85] or other different mineral phases present in the natural sample being studied.

The Raman spectra of schoepite,[28] shows bands at 897, 886, 870, 855, 839, 826, 817, 802, 554, 545, 507, 460, 458, 402, 351, 330, 305, 274, 248, 216, 194 and 168 cm^{-1}. The bands at 803 and 823 cm^{-1} are close to those schoepite bands at 802 and 826 cm^{-1}. Thus, they may be relics of schoepite bands. They were attributed[28] to the splitting of $\nu^s(UO_2^{2+})$ symmetric stretching vibration in schoepite (different U–O bond lengths in uranyl) or to ν(U–OH) bending vibrations. This correspondence is in accordance with the solid solution suggestion, which implies that solid solutions with limited solubility may exist in the system $UO_2(CO_3)/UO_2(OH)_2{\cdot}yH_2O$ (rutherfordine/schoepite, metaschoepite, and dehydrated schoepite), thus forming $UO_2(CO_3)_{1-x}(OH)_{2x}{\cdot}yH_2O$.[25,68,84,87]

The band at 793 cm^{-1} can also be related to the uranophane alpha band found[26,69] at about 797 cm^{-1}.

From the analysis described above, it can be concluded that both theoretical spectra corresponding to the *Pmmn* and *Imm*2 symmetries are similar to the experimental one. However, in the Raman spectra associated with the *Pmmn* structure we note the presence of three additional active translation modes, absent in the calculated Raman spectrum associated with the *Imm*2 structure. Nonetheless, both structures may be simultaneously present in nature, as suggested by Christ *et al.*[66]

3.3 Effects of the introduction of dispersion corrections and water molecules in the structure of rutherfordine

Additional calculations were carried out with the aim of: (a) analyzing the influence of dispersion corrections in the theoretical results and, (b) studying the influence of the introduction of water molecules inside the structure of rutherfordine in the band wavenumbers, particularly in the out of plane deformation wavenumber for the carbonate groups. A comparison of this wavenumber was also carried out with values reported in the literature.

Since the sheets in the structure of rutherfordine are bonded together by van der Waals forces, we carried out calculations using the PBE functional[71] including the empirical dispersion correction of Grimme.[73] The kinetic energy cutoff used was 1200 eV and the K mesh 5 × 3 × 6 (18 *K* points). The computed lattice parameters were a = 4.8647 Å, b = 9.5435 Å, c = 4.3295 Å ($\alpha = \beta = \gamma = 90$ deg). The main effect is, therefore, the increase of the intersheet distance (b parameter). The agreement with experimental structure is worse than in the calculations obtained in previous sections and thus, the PBESOL[72] functional works better in this case, at least for the structural determination. The vibrational Raman spectrum is however quite similar to the PBESOL one. Dispersion corrections, therefore, do not seem to modify significantly the calculated spectra.

As mentioned before, the computed spectra do not include water molecules in the rutherfordine structure and since the presence of water might cause significant shifts in the bands associated with both UO_2^{2+} and CO_3^{2-} units, additional calculations were carried out. Particularly, the carbonate out of plane deformation wavenumber was shown to be much lower than the free ion value. The main displacements in this mode arise from the carbon atoms of the carbonate groups. Due to the presence of uranyl groups placed just above and below them, the out of plane motion may be hindered and water molecules placed in the intersheet space could modify the corresponding wavenumber. Two water molecules were introduced in the space between the sheets of the unit cell of rutherfordine. The calculation was performed again with the dispersion corrected PBE functional, a kinetic energy cutoff of 900 eV and a 3 × 1 × 3 K mesh (5 *K* points). The intersheet space was greatly increased, but the carbonate main bands were only slightly modified: $\nu^{a}(CO_3^{2-})$ = 1473, 1378; $\nu^{s}(CO_3^{2})$ = 1091; $\delta^{op}(CO_3^{2-})$ = 761; $\delta^{ip}(CO_3^{2-})$ = 750, 680.

Majumdar *et al.*[58] carried out molecular calculations (gas phase) of UO_2CO_3, PuO_2CO_3, and related clusters including hydrated species using DFT (B3LYP functional), second-order Moller–Plesset (MP2) perturbation and multireference configuration interaction methods and large gaussian basis sets. The calculated ν_2 and ν_4 vibrational wavenumbers of the carbonate group were given only for the isostructural PuO_2CO_3 gas phase species. The values obtained at the MP2 level for the anhydrous system PuO_2CO_3 are ν_2 = (629, 719) cm^{-1} and ν_4 = 754 cm^{-1}. The ν_4 value obtained for the anhydrous species, 754 cm^{-1}, is thus consistent with our calculated wavenumber of 752 cm^{-1} and present experimental value of 754 cm^{-1}.

4 Conclusions

A natural rutherfordine mineral was characterized by means of Raman spectroscopy combined with theoretical calculations based on DFT methods. The structural parameters and X-ray powder spectrum obtained indicates that the rutherfordine mineral is accurately described by our theoretical computations. *Pmmn* and *Imm*2 structures were considered in this work. Since these structures are nearly degenerate and the properties computed from them are very similar, we conclude that both may simultaneously be present in nature in accordance with the suggestion of Christ *et al.*[66]

The Raman spectrum obtained experimentally is also fairly well reproduced. The main vibrations used as a fingerprint to identify rutherfordine were the two ν_1 symmetric stretching bands of the UO_2^{2+} and CO_3^{2-} groups placed at 882 and 1113 cm^{-1}, respectively. These bands are very well reproduced theoretically at 886 and 1098 cm^{-1}, respectively. Next bands, obtained by Raman spectroscopy, located at 1409 and 780 cm^{-1}, are attributable to the CO_3^{2-} group asymmetric stretching and in plane bending modes ν_3 and ν_2, the calculated ones being located at 1401 and 747 cm^{-1}. In the low wavenumber region, we found three main bands at 134, 153 and 213 cm^{-1}, which are well reproduced by theoretical calculations with wavenumbers located at 147, 150 and 217 cm^{-1}.

For most of the bands in the experimental spectrum we found a correspondence to bands in the theoretical one and, therefore, they were assigned to specific vibrational motions. The band wavenumbers which are not reproduced in our theoretical calculations were attributed to the presence of other uranyl minerals as uranophane.

The introduction of dispersion corrections and the introduction of water molecules into the space between the sheets of the unit cell of rutherfordine did not modify the computed Raman spectrum significantly.

Acknowledgements

This work was supported by ENRESA in the project: No. 079000189 "Aplicación de técnicas de caracterización en el estudio de la estabilidad del combustible nuclear irradiado en condiciones de almacenamiento" (ACESCO) and project FIS2013-48087-C2-1-P. Supercomputer time from the CETA-CIEMAT and CESGA centers is also acknowledged. This work has been carried out in

the context of a CSIC–CIEMAT collaboration agreement: "Caracterización experimental y teórica de fases secundarias y óxidos de uranio formados en condiciones de almacenamiento de combustible nuclear".

References

1 SKB-91, Final Disposal of spent nuclear fuel, Importance of the bedrock for safety, Report 92-20, May, 1992.
2 R. C. Ewing, *Nat. Mater.*, 2015, **14**, 252.
3 D. W. Shoesmith, *J. Nucl. Mater.*, 2000, **282**, 1.
4 S. Sunder, *Nucl. Technol.*, 1998, **122**(2), 211.
5 H. Christensen and S. Sunder, *J. Nucl. Mater.*, 1996, **238**(1), 70.
6 O. Roth and M. Jonsson, *Cent. Eur. J. Chem.*, 2008, **6**(1), 1.
7 M. Amme, B. Renker, B. Schmid, M. P. Feth, H. Bertagnolli and W. Döbelin, *J. Nucl. Mater.*, 2002, **306**(2–3), 202.
8 A. Rey, J. Giménez, I. Casas, F. Clarens and J. de Pablo, *Appl. Geochem.*, 2008, **23**(8), 2249.
9 C. M. Lousada, M. Trummer and M. Jonsson, *J. Nucl. Mater.*, 2013, **434**(1–3), 434.
10 C. Frondel, *Am. Mineral.*, 1956, **41**, 539.
11 J. Plášil, *J. Geosci.*, 2014, **59**, 99.
12 J. Bruno and R. C. Ewing, *Elements*, 2006, **2**(6), 343.
13 *Raman spectroscopy applied to Earth sciences and cultural heritage*, ed. J. Dubessy, M. C. Caumon and F. Rull, European Mineralogical Union, 2011.
14 *Handbook of Vibrational Spectroscopy: Vibrational Raman Spectroscopy of High-temperature Superconductors*, ed. J. M. Chalmers and P. R. Griffiths, John Wiley & Sons Ltd., 2002.
15 V. Muñoz-Iglesias, O. Prieto-Ballesteros and L. J. Bonales, *Geochim. Cosmochim. Acta*, 2014, **125**, 466.
16 A. Arencibia, M. Taravillo, F. J. Pérez, J. Núñez and V. G. Baonza, *Phys. Rev. Lett.*, 2002, **89**(19), 195504.
17 G. Guimbretiere, L. Desgranges, C. Jegou, A. Canizares, P. Simon, R. Caraballo, N. Raimboux, M. F. Barthe, M. R. Ammar, O. A. Maslova, F. Duval and R. Omnee, *IEEE Trans. Nucl. Sci.*, 2014, **61**, 2045.
18 R. Sobry, *J. Inorg. Nucl. Chem.*, 1973, **35**(8), 2753.
19 L. Maya and G. M. Begun, *J. Inorg. Nucl. Chem.*, 1981, **43**(11), 2827.
20 B. M. Biwer, W. L. Ebert and J. K. Bates, *J. Nucl. Mater.*, 1990, **175**(3), 188.
21 (*a*) E. Faulques, R. E. Russo and D. L. Perry, *Spectrochim. Acta, Part A*, 1993, **49**(7), 975; (*b*) E. Faulques, R. E. Russo and D. L. Perry, *Spectrochim. Acta, Part A*, 1994, **50**(4), 757; (*c*) E. Faulkes, F. Massuyeau, N. Kalashnyk and D. L. Perry, *Spectrosc. Eur.*, 2015, **27**, 14.
22 S. Bastians, G. Crump, W. P. Griffith and R. Withnall, *J. Raman Spectrosc.*, 2004, **35**(8–9), 726.
23 R. J. P. Driscoll, D. Wolverson, J. M. Mitchels, J. M. Skelton, S. C. Parker, M. Molinari, I. Khan, D. Geeson and G. C. Allen, *RSC Adv.*, 2014, **4**, 59137.
24 R. L. Frost and J. Čejka, *J. Raman Spectrosc.*, 2007, **38**(11), 1488.
25 R. L. Frost and J. Čejka, *J. Raman Spectrosc.*, 2009, **40**(9), 1096.
26 R. L. Frost, J. Čejka, M. L. Weier and W. Martens, *J. Raman Spectrosc.*, 2006, **37**(4), 538.
27 R. L. Frost, J. Čejka, M. L. Weier and W. Martens, *Spectrochim. Acta, Part A*, 2006, **63**, 305.
28 R. L. Frost, J. Čejka and M. L. Weier, *J. Raman Spectrosc.*, 2007, **38**(4), 460.
29 R. L. Frost, M. J. Dickfos and J. Čejka, *J. Raman Spectrosc.*, 2008, **39**(5), 582.
30 H. He and D. Shoesmith, *Phys. Chem. Chem. Phys.*, 2010, **12**, 8109.
31 L. Desgranges, G. Baldinozzi, P. Simon, G. Guimbretière and A. Canizares, *J. Raman Spectrosc.*, 2012, **43**(3), 455.
32 D. Manara and B. Renker, *J. Nucl. Mater.*, 2003, **321**(2–3), 233.
33 S. J. Clark, M. D. Segall, C. J. Pickard, P. J. Hasnip, M. I. J. Probert, K. Refson and M. C. Payne, *Z. Kristallogr.*, 2005, **220**, 567.
34 V. Milman, K. Refson, S. J. Clark, C. J. Pickard, J. R. Yates, S. P. Gao, P. J. Hasnip, M. I. J. Probert, A. Perlov and M. D. Segall, *THEOCHEM*, 2010, **954**(1–3), 22.
35 (*a*) X. Gonze, G.-M. Rignanese, M. Verstraetre, J.-M. Beuken, R. Pouillon and R. Caracas, *Z. Kristallogr.*, 2005, **220**, 558; (*b*) P. Giannozzi, S. Baroni, N. Bonini, M. Calandra, R. Car and C. Cavazzoni, *et al.*, *J. Phys.: Condens. Matter*, 2009, **21**(39), 395502; (*c*) F. Pascale, C. M. Zicovich-Wilson, F. López Gejo, B. Civalleri, R. Orlando and R. Dovesi, *J. Comput. Chem.*, 2004, **25**(6), 888; (*d*) E. Artacho, E. Anglada, O. Diéguez, J. D. Gale, A. García, J. Junquera, R. M. Martin, P. Ordejón, J. M. Pruneda, D. Sánchez-Portal and J. M. Soler, *J. Phys.: Condens. Matter*, 2008, **20**(6), 064208.
36 K. Refson, P. R. Tulip and S. J. Clark, *Phys. Rev. B: Condens. Matter Mater. Phys.*, 2006, **73**(15), 155114.
37 (*a*) P. Hohenberg and W. Kohn, *Phys. Rev.*, 1964, **136**, B864; (*b*) W. Kohn and L. J. Sham, *Phys. Rev.*, 1965, **140**, A1133.
38 M. C. Payne, M. P. Teter, D. C. Allan, T. A. Arias and J. D. Joannopoulos, *Rev. Mod. Phys.*, 1992, **64**(4), 1045.
39 S. Baroni, S. de Gironcoli, A. Dal Corso and P. Giannozzi, *Rev. Mod. Phys.*, 2001, **73**(2), 515.
40 X. Gonze and C. Lee, *Phys. Rev. B: Condens. Matter Mater. Phys.*, 1997, **55**(16), 10355.
41 (*a*) J. P. Crocombette, F. Jollet, L. T. Nga and T. Petit, *Phys. Rev. B: Condens. Matter Mater. Phys.*, 2001, **64**(2), 104107; (*b*) M. Freyss, T. Petit and J.-P. Crocombette, *J. Nucl. Mater.*, 2005, **347**(1–2), 44.
42 G. Beridze and P. M. Kowalski, *J. Phys. Chem. A*, 2014, **118**(50), 11797.
43 Y. Yun, D. Legut and P. M. Oppeneer, *J. Nucl. Mater.*, 2012, **426**(1–3), 109.
44 Q. Yin and S. Y. Savrasov, *Phys. Rev. Lett.*, 2008, **100**(22), 225504.
45 B. T. Wang, P. Zhang, R. Lizárraga, I. Di Marco and O. Eriksson, *Phys. Rev. B: Condens. Matter Mater. Phys.*, 2013, **88**(10), 104107.
46 (*a*) Z.-G. Mei, M. Stan and J. Yang, *J. Alloys Compd.*, 2014, **603**, 282; (*b*) Z.-G. Mei, M. Stan and B. Pichler, *J. Nucl. Mater.*, 2013, **440**(1–3), 63.

47 S. L. Dudarev, D. N. Manh and A. P. Sutton, *Philos. Mag. B*, 1997, **75**(5), 613.
48 D. A. Andersson, G. Baldinozzi, L. Desgranges, D. R. Conradson and S. D. Conradson, *Inorg. Chem.*, 2013, **52**(5), 2769.
49 P. Nerikar, T. Watanabe, J. S. Tulenko, S. R. Phillpot and S. B. Sinnott, *J. Nucl. Mater.*, 2009, **384**(1), 61.
50 (*a*) X.-D. Wen, R. L. Martin, L. E. Roy, G. E. Scuseria, S. P. Rudin, E. R. Batista, T. M. McCleskey, B. L. Scott, E. Bauer, J. J. Joyce and T. Durakiewicz, *J. Chem. Phys.*, 2012, **137**, 154707; (*b*) X.-D. Wen, R. L. Martin, G. E. Scuseria, S. P. Rudin, E. R. Batista and A. K. Burrell, *J. Phys.: Condens. Matter*, 2013, **25**(2), 025501.
51 (*a*) P. F. Weck, E. Kim, N. Balakrishnan, F. Poineau, C. B. Yeamans and K. R. Czerwinski, *Chem. Phys. Lett.*, 2007, **443**(1–3), 82; (*b*) P. F. Weck, E. Kim, C. F. Jove-Colon and D. C. Sassani, *Dalton Trans.*, 2012, **41**, 9748; (*c*) P. F. Weck and E. Kim, *Dalton Trans.*, 2014, **43**, 17191.
52 (*a*) S. Ostanin and P. Zeller, *J. Phys.: Condens. Matter*, 2007, **19**(24), 246108; (*b*) S. Ostanin and P. Zeller, *Phys. Rev. B: Condens. Matter Mater. Phys.*, 2007, **75**(7), 073101.
53 (*a*) L. C. Shuller, R. C. Ewing and U. Becker, *J. Nucl. Mater.*, 2013, **434**(1–3), 440; (*b*) L. C. Shuller, M. W. Bender, M. S. Walker and U. Becker, *Minerals*, 2014, **4**, 690; (*c*) L. C. Shuller, R. C. Ewing and U. Becker, *Am. Mineral.*, 2010, **95**, 1151.
54 (*a*) P. J. Hay and R. L. Martin, *J. Chem. Phys.*, 1998, **109**, 3875; (*b*) P. J. Hay, R. L. Martin and G. Schreckenbach, *J. Phys. Chem. A*, 2000, **104**(26), 6259.
55 L. Castro, A. Yahia and L. Maron, *ChemPhysChem*, 2010, **11**(5), 990.
56 (*a*) G. Schreckenbach and G. A. Shamov, *Acc. Chem. Res.*, 2010, **43**(1), 19; (*b*) G. A. Shamov, G. Schreckenbach and T. N. Vo, *Chem. – Eur. J.*, 2007, **13**(17), 4932; (*c*) S. O. Odoh and G. Schreckenbach, *Inorg. Chem.*, 2013, **52**(9), 5590.
57 N. Iché-Tarrat and C. J. Marsden, *J. Phys. Chem. A*, 2008, **112**(33), 7632.
58 (*a*) D. Majumdar, K. Balasubramanian and H. Nitsche, *Chem. Phys. Lett.*, 2002, **361**(1–2), 143; (*b*) D. Majumdar, S. Roszak, K. Balasubramanian and H. Nitsche, *Chem. Phys. Lett.*, 2003, **372**(1–2), 232; (*c*) D. Chaudhuri and K. Balasubramanian, *Chem. Phys. Lett.*, 2004, **399**(1–3), 67.
59 R. Vochten and M. Deliens, *Can. Mineral.*, 1998, **36**, 1077.
60 K. Walenta, *Mineral. Petrogr. Mitt.*, 1998, **56**, 167.
61 D. L. Clark, D. E. Hobart and M. P. Neu, *Chem. Rev.*, 1995, **95**(1), 25.
62 R. J. Finch and R. C. Ewing, *J. Nucl. Mater.*, 1992, **190**, 133.
63 I. Grenthe, J. Drożdżyński, T. Fujino, E. C. Buck, T. E. Albrecht-Schmitt and S. F. Wolf, *The chemistry of the actinide and transactinide elements*, Springer Netherlands, 2008, pp. 253–698.
64 W. Marckwald, *Zentralbl. Mineral., Geol. Palaeontol.*, 1906, 761.
65 C. Frondel and R. Meyrowitz, *Am. Mineral.*, 1956, **41**, 127.
66 C. L. Christ, J. R. Clark and H. T. Evans, *Science*, 1955, **121**, 472.
67 C. L. Christ and J. R. Clark, *Am. Mineral.*, 1956, **41**, 844.
68 R. J. Finch, M. A. Cooper, F. C. Hawthorne and R. C. Ewing, *Can. Mineral.*, 1999, **37**(4), 929.
69 L. J. Bonales, C. Menor-Salván and J. Cobos, *J. Nucl. Mater.*, 2015, **462**, 296.
70 MaterialsStudio, http://accelrys.com/products/materials-studio, 2014.
71 J. P. Perdew, K. Burke and M. Ernzerhof, *Phys. Rev. Lett.*, 1996, **77**, 3865.
72 J. P. Perdew, A. Ruzsinszky, G. I. Csonka, O. A. Vydrov, G. E. Scuseria, L. A. Constantin, X. Zhou and K. Burke, *Phys. Rev. Lett.*, 2008, **100**, 136406.
73 S. Grimme, *J. Comput. Chem.*, 2006, **27**(15), 1787.
74 B. G. Pfrommer, M. Côté, S. G. Louie and M. L. Cohen, *J. Comput. Phys.*, 1997, **131**(1), 233.
75 H. J. Monkhorst and J. D. Pack, *Phys. Rev. B: Condens. Matter Mater. Phys.*, 1976, **13**(12), 5188.
76 N. Troullier and J. L. Martins, *Phys. Rev. B: Condens. Matter Mater. Phys.*, 1991, **43**(3), 1993.
77 M. Fuchs and M. Scheffler, *Comput. Phys. Commun.*, 1999, **119**(1), 67.
78 L. Kleinman and D. M. Bylander, *Phys. Rev. Lett.*, 1982, **48**(20), 1425.
79 P. Haynes and K. Refson, *cpi2recpot: Converts from .cpi format generated by fhi98PP to the recpot format used by CASTEP and ONETEP*, 2007.
80 R. T. Downs, K. L. Bartelmehs, G. V. Gibbs and M. B. Boisen, *Am. Mineral.*, 1993, **78**, 1104.
81 J. D. Martin, *XPowder12, Ver. 04.13*, 2012.
82 ICDD, The international center for diffraction data, PDF-2 database, 2003.
83 E. del Corro Garcia, PhD thesis, Universidad Complutense de Madrid, CC. Químicas Departamento de Química Física I, 2011.
84 J. Cejka and Z. Urbanec, *Casopis Narodniho Muzeo*, 1988, **157**, 1–10.
85 J. Cejka, *Rev. Mineral. Geochem.*, 1999, **38**, 521.
86 H. R. Hoekstra and S. Siegel, *J. Inorg. Nucl. Chem.*, 1973, **35**(3), 761.
87 J. G. Catalano and G. E. Brown, *Am. Mineral.*, 2004, **89**, 1004.

Electronic Supplementary Material (ESI) for Physical Chemistry Chemical Physics.

APPENDIX A. Calculated structrures of uranium containing minerals using the new pseudopotential.

Lattice parameters calculated for a selected series of uranium containing minerals with small cutoffs and K meshes. All calculations were carried out using the PBESOL functional.[1] Note that for solids as uranium dioxide (uraninite) the calculations predict them to be metals. This is a well known deffect of simple DFT calculations.[2-4] Hybrid functionals or DFT simple modifications such as the inclusión of the Mott-Hubbard correction improving the description of strongly correlated uranium 5f electrons (DFT+U) may restore this deffect predicting the insulating state for these solids.[4] However these methods cannot be used currently to determine the vibrational spectra within CASTEP, and they were not used in the calculations.

Table A.1. Calculated structures of uranium containing minerals compared with experimental values.

Mineral **N. of atoms per unit cell / N. of valence electrons** **Symmetry**	**Experimental/ Calculated values**	**Lattice parameters and Cell volume** **a,b,c (Å)** **α,β,γ (deg)** **V (Å³)**	**E cut (eV)** **K mesh**
Uraninite (12/204) Fm-3m	UO_2[a]	5.468, 5.468, 5.468 90, 90, 90 163.5	-
	Calculated	5.2915, 5.2915, 5.2915 90, 90, 90 148.16	830 5 x 5 x 5
U_3O_8 (22/108) (Amm2)	U_3O_8[b]	4.145, 11.95, 6.722 90, 90, 90 332.96	-
	Calculated	4.1142, 11.6899, 6.7298 90, 90, 90 323.66 8.64	750 6 x 2 x 4
α-$UO_2(OH)_2$ (28/160) Cmce	$UO_2(OH)_2$[c]	4.242, 10.302, 6.868 90, 90, 90 300.1	-

	Calculated	4.1841, 10.1017, 6.7969 90.00, 90.00, 90.00 287.28	830 3 x 1 x 2
β-$UO_2(OH)_2$ (28/160) Pbca	$UO_2(OH)_2$[d]	5.6438, 6.2867, 9.9372 90, 90, 90 352.6	-
	Calculated	5.7850, 6.0844, 9.6516 89.98, 90.00, 89.93 339.72	830 3 x 2 x 1
γ-$UO_2(OH)_2$ (14/80) P121/c1	$UO_2(OH)_2$[e]	5.56, 5.522, 6.416 90, 112.71, 90 181.7	-
	Calculated	5.3691, 5.6474, 6.3017 89.97, 111.55, 90.10 177.72	830 3 x 2 x 1
Brannerite (18/148) C12/m1	UTi_2O_6[f]	9.87, 3.76, 6.95 90, 119.5, 90 6.36 224.5	-
	Calculated	9.95, 3.71, 6.79 90, 121.82, 90 213.26 6.69	830 2 x 4 x 2
Rutherfordine (14/96) Pmmn O_2	$[UO_2][CO_3]$[g]	4.85, 9.22, 4.3 90, 90, 90 192.3	-
	Calculated	4.8285, 9.3370, 4.2731 90, 90, 90 192.65	830 3 x 2 x 3
Grimselite (44/272) P-62c	$K_3Na[UO_2][CO_3]_3[H_2O]$[h]	9.302, 9.302, 8.260 90, 90, 120 619.0	900 2 x 2 x 2
	Calculated	9.3857, 9.38570, 8.3946 90.01, 90.01, 121.29 627.64	-

Coffinite (16/168) I41/amd	$USiO_4$[i]	6.995, 6.995, 6.263, 90, 90, 90, 306.449	-
	Calculated	6.9192, 6.9192, 6.2353 90, 90, 90 298.52	830 2 x 2 x 2
Vanderbrandeite (24/130) P-1	$Cu[UO_2][OH]_4$[j]	5.449, 6.089, 7.855 78.1, 89.2, 88.56 254.9	-
	Calculated	5.2352, 6.3528, 8.5518 85.52, 86.89, 92.26 282.88	880 5 x 4 x 3
Becquerelite (236/1184) Pna21	$Ca[UO_2]_6O_4[OH]_6$ $[H2O]_8$[k]	13.8378, 14.9238, 12.3781 90, 90, 90 2500.88	-
	Calculated	13.7854, 14.6297, 12.2014 90, 90, 90 2460.73	800 1 x 1 x 1
Uranophane-alpha (68/320) P1211	$CaH_2[H_2O]_5[SiO_4]_2$ $[UO_2]_2$[l]	6.665, 7.002, 15.909 90, 97.27, 90 736.5	-
	Calculated	6.6276, 6.9614, 15.7299 90, 98.17, 90 718.37	880 2 x 2 x 1
Uranophane-beta (136/640) P121/c1	$Ca[H_2O]_5O_6[OH]_2$ $Si_2[UO_2]$[m]	6.632, 15.443, 13.966 90, 91.38, 90 1429.95	-
	Calculated	6.6084, 15.3807, 13.8872 90, 89.875, 90 1411.51	800 2 x 1 x 1
Schoepite (meta) (320/1536) Pbcn	$[UO_2]_4O[OH]_6$. $[H_2O]_5$[n]	14.6861, 13.9799, 16.7063 90, 90, 90 3430	-

	Calculated	14.4837, 13.8257, 16.3729 90.00 , 90.00, 90.00 3378.63	830 1 x 1 x 1
Soddyite (136/768) Fddd O2	$[UO_2]_2[SiO_4][H_2O]_2$[o]	8.334, 11.212, 18.668 90, 90, 90 1744.4	-
	Calculated	7.9018, 11.4763, 18.6857, 90, 90, 90 1694.48	830 2 x 1 x 1
Studtite (68/280) C12/c1	$[UO_2][O_2][H_2O]_4$[p]	14.068, 6.721, 8.428 90, 123.356, 90 665.6	-
	Calculated	13.6114, 6.6938, 8.3936 90.00, 122.88, 90.00 642.27	830 1 x 2 x 1
Kasolite (36/272) P21/c	$[UO_2]Pb[SiO_4][H_2O]$[q]	6.704, 6.932, 13.252 90, 104.22, 90 596.98	-
	Calculated	6.7035, 6.8325, 13.1795 90, 101.92, 90 590.63	820 2 x 2 x 1
Boltwoodite (26/144) P1211	$K[H_3O][UO_2][SiO_4]$[r]	6.638, 7.064, 7.073 90, 105.75, 90 319.2	-
	Calculated	6.6229, 7.0252, 7.0239 90, 104.57, 90 316.29	830 2 x 2 x 2

a) L. Desgranges, G. Baldinozzi, G. Rousseau, J.-C. Nièpce and G. Calvarin, *Inorg. Chem*, 2009, **48**, 7585-7592.

b) J. B. Ainscough and I. F. Ferguson, *J. Inorg. Nucl. Chem.*, 1974, **36**, 193-194.

c) J. Taylor, *Acta Crystallogr., Sect. B: Struct. Crystallogr. Cryst. Chem.*, 1971, **27**, 1088-1091.

d) J. C. Taylor and H. J. Hurst, *Acta Crystallogr., Sect. B: Struct. Crystallogr. Cryst. Chem.*, 1971, **27**, 2018-2022.

e) S. Siegel, H. R. Hoekstra and E. Gebert, *Acta Crystallogr., Sect. B: Struct. Crystallogr. Cryst. Chem.*, 1972, **28**, 3469-3473.

f) A. M. Lejus and D. Goldberg, *C. R. Seances Acad. Sci. (Ser. C)*, 1966, **263**, 1223-1226.

g) R. J. Finch, M. A. Cooper, F. C. Hawthorne and R. C. Ewing, *Can. Mineral.*, 1999, **37**, 929-938.

h) L. H. Fuchs and E. Gebert, *Am. Mineral.*, 1958, **43**, 243-248.

i) Y. Li and P. C. Burns, *Can. Mineral.*, 2001, **39**, 1147-1151.

j) A. Rosenzweig and R. R. Ryan, *Cryst. Struct. Commun.*, 1977, **6**, 53-56.

k) M. K. Pagoaga, D. E. Appleman and J. M. Stewart, Can. Mineral., 1987, **72**, 1230-1238.

l) D. Ginderow, *Acta Crystallogr., Sect. C: Struct. Chem.*, 1988, **44**, 421-424.

m) K. Viswanathan and O. Harneit, Am. Mineral., 1986, **71**, 1489-1493.

n) M. T. Weller, M. E. Light and T. Gelbrich, , *Acta Crystallogr., Sect. B: Struct. Crystallogr. Cryst. Chem.*, 2000, **56**, 577-583.

o) F. Demartin, C. M. Gramaccioli and T. Pilati, *Acta Crystallogr., Sect. C: Struct. Chem.*, 1992, **48**, 1-4.

p) P. C. Burns and K.-A. Hughes, , *Am. Mineral.*, 2003, **88**, 1165-1168.

q) V. I. Mokeeva, *Sov. Phys. Crystallogr. (Engl. Transl.) - Kristallografiya*, 1965, **9**, 621-622.

r) F. V. Stohl and D. K. Smith, , *Am. Mineral.*, 1981, **66**, 610-625.

APPENDIX B. Normal modes of rutherfordine (Pmmn symmetry)

Figure B.1. The atomic motions associated to each Raman active vibrational normal mode of Rutherfordine (Pmmn symmetry).

Mode ν=1483 cm^{-1}. Asymmetric CO_3^{2-} stretching (B_{2g}).

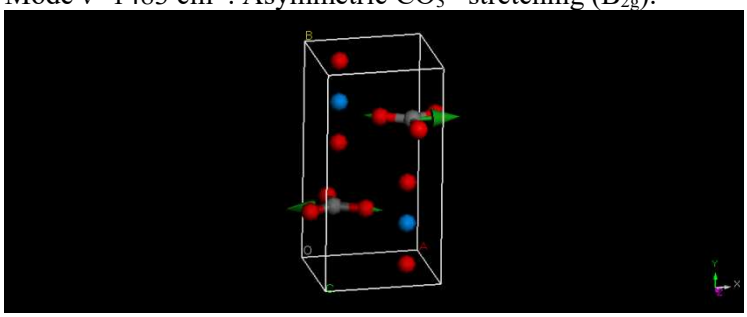

Mode ν=1402 cm^{-1}. Asymmetric CO_3^{2-} stretching (A_g).

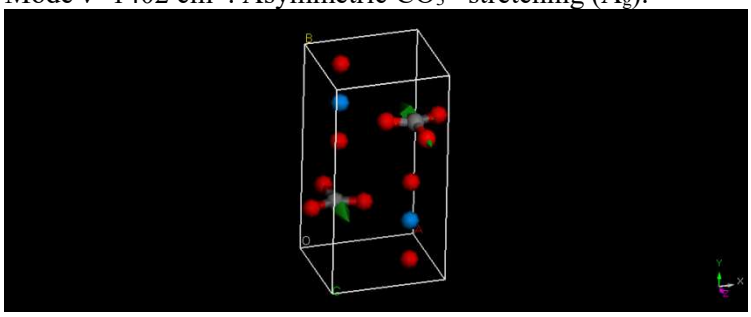

Mode ν=1097 cm^{-1}. Symmetric CO_3^{2-} stretching (A_g).

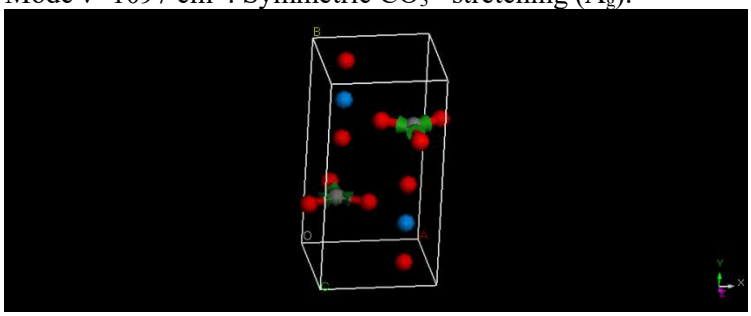

Mode ν=979 cm^{-1}. Antisymmetric UO_2^{2+} stretching (B_{3g}).

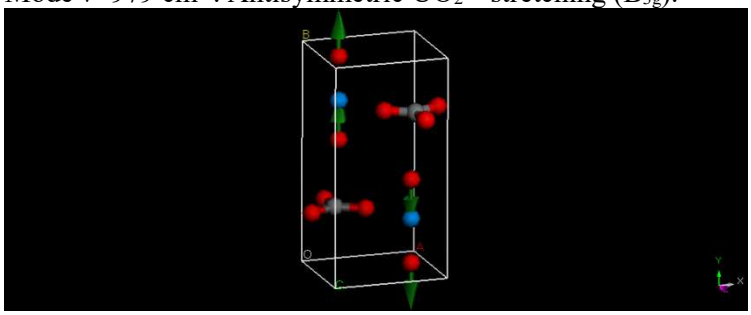

Mode ν=886 cm^{-1}. Symmetric UO_2^{2+} stretching (A_g).

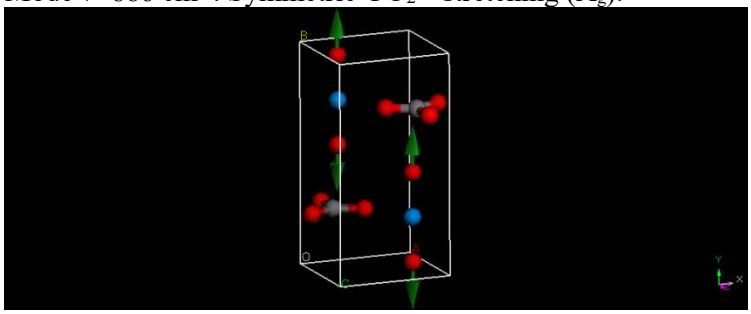

Mode ν=752 cm^{-1}. Out of plane CO_3^{2-} bending (B_{3g}).

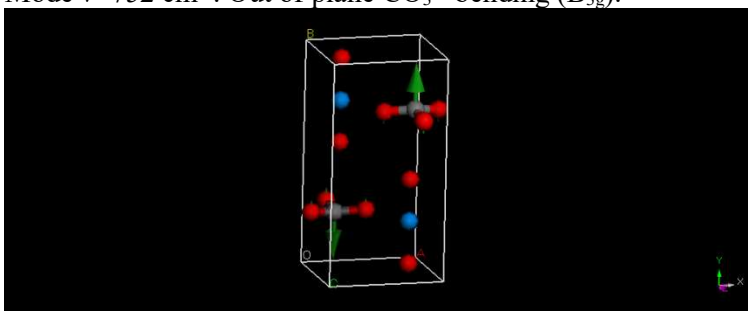

Mode ν=746 cm^{-1}. In plane CO_3^{2-} bending (B_{2g}).

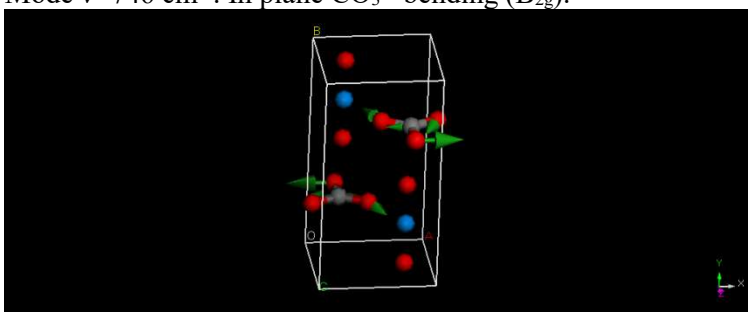

Mode ν=678 cm^{-1}. In plane CO_3^{2-} bending (A_g).

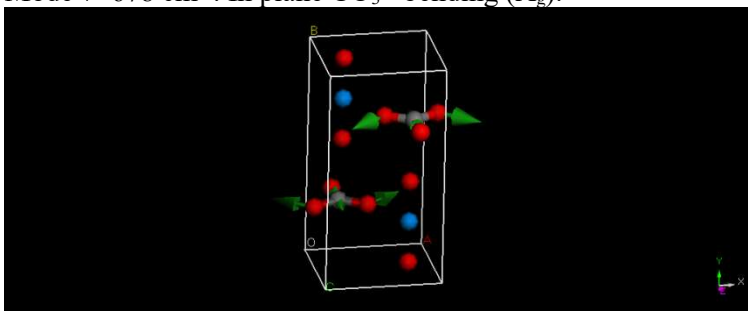

Mode ν=333 cm^{-1}. In plane CO_3^{2-} bending (B_{2g}).

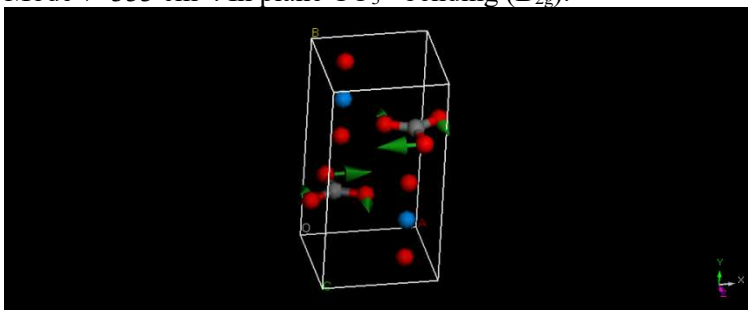

Mode ν=265 cm^{-1}. Symmetric UO_2^{2+} bending plus in plane CO_3^{2-} bending (B_{2g}).

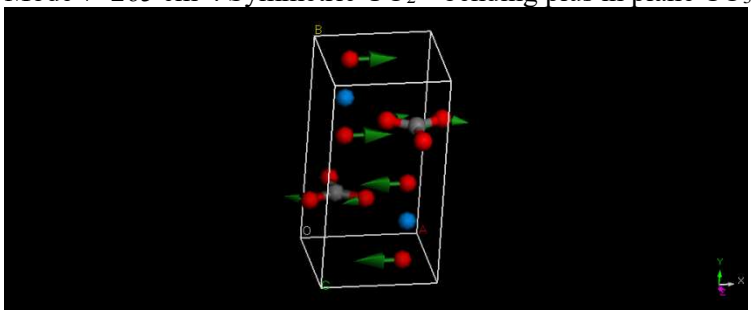

Mode ν=246 cm^{-1}. Symmetric UO_2^{2+} bending (A_g).

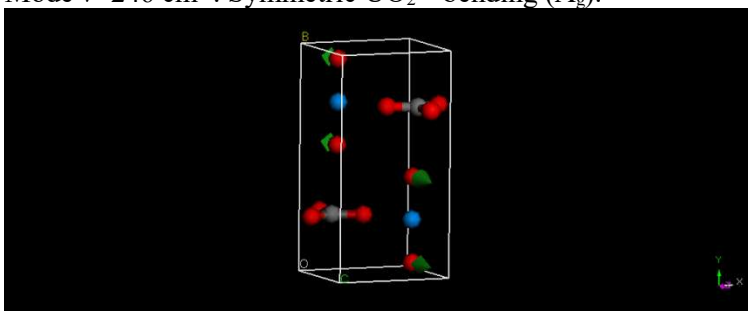

Mode ν=241 cm^{-1}. Symmetric UO_2^{2+} bending plus in plane CO_3^{2-} bending. (B_{2g}).

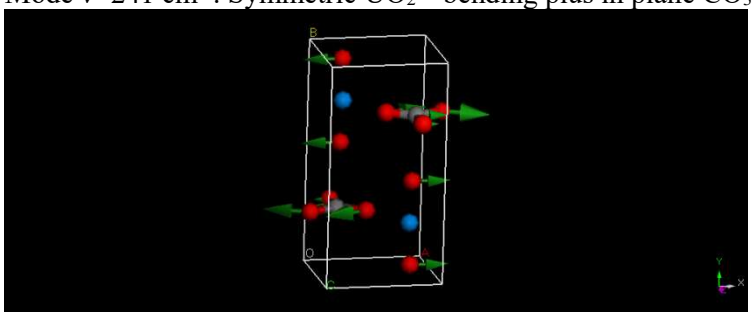

Mode ν=240 cm^{-1}. Antisymmetric UO_2^{2+} bending plus out of plane CO_3^{2-} bending (B_{1g}).

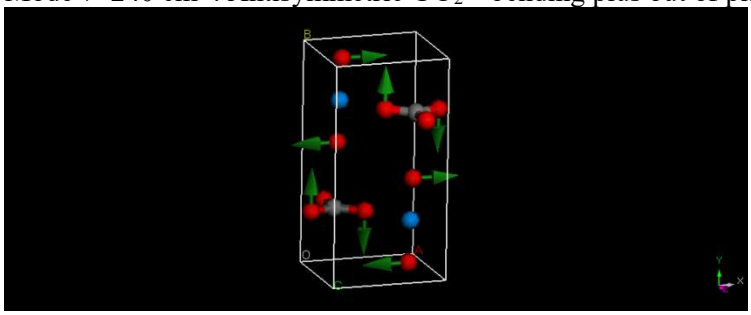

Mode ν=217 cm^{-1}. CO_3^{2-} translation (A_g).

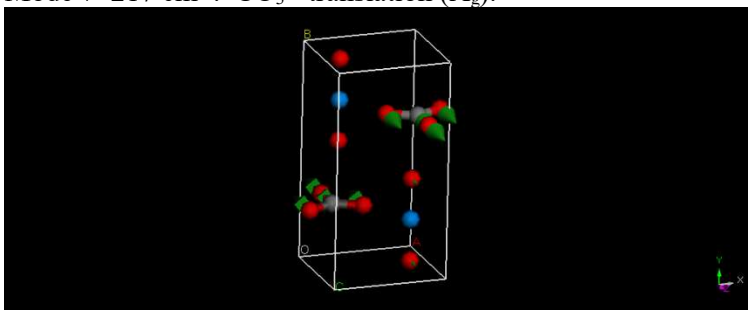

Mode v=190 cm^{-1}. Antisymmetric UO_2^{2+} bending (B_{3g}).

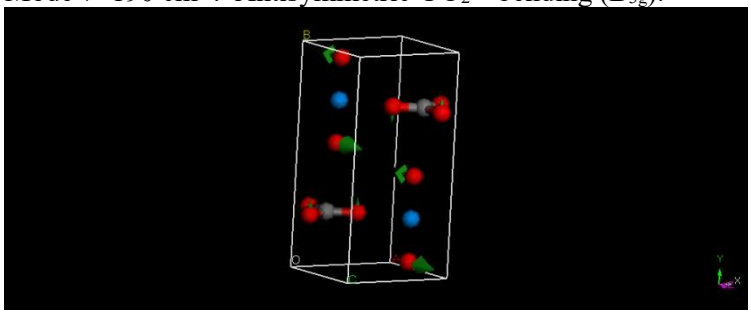

Mode v=165 cm^{-1}. CO_3^{2-} translation (B_{3g}).

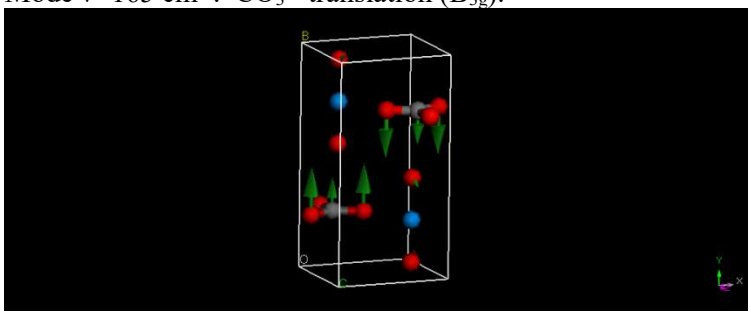

Mode v=150 cm^{-1}. Out of plane CO_3^{2-} bending (B_{3g}).

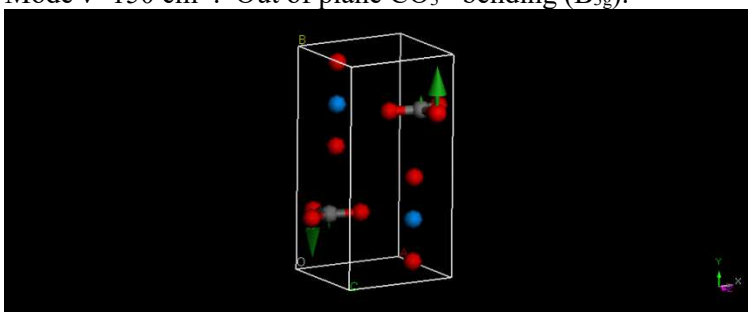

Mode v=147 cm^{-1}. Antisymmetric UO_2^{2+} bending plus out of plane CO_3^{2-} bending (B_{1g}).

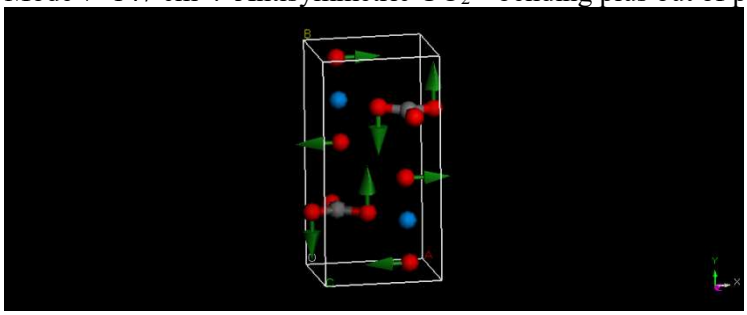

Mode v=43 cm^{-1}. UO_2^{2+} and CO_3^{2-} translation (B_{3g}).

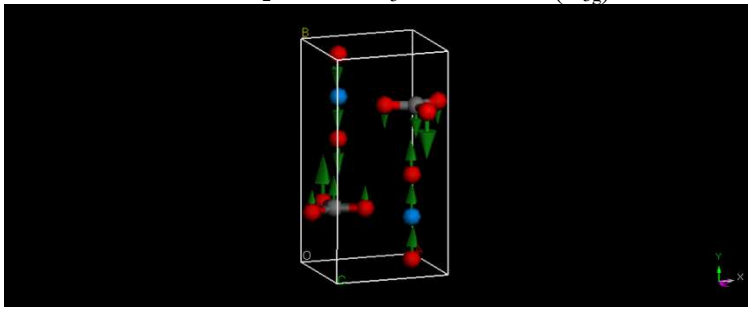

Mode ν=32 cm^{-1}. UO_2^{2+} and CO_3^{2-} translation (A_g).

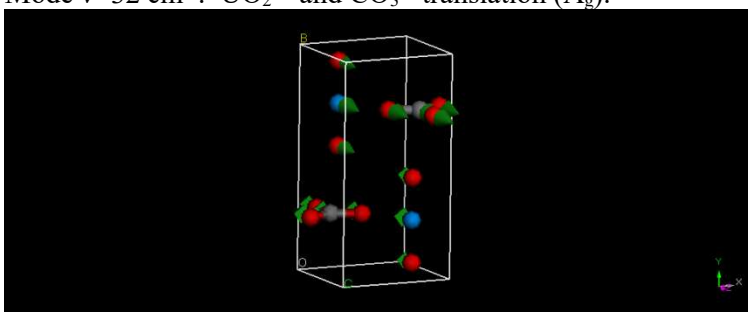

Mode ν=31 cm^{-1}. UO_2^{2+} and CO_3^{2-} translation (B_{2g}).

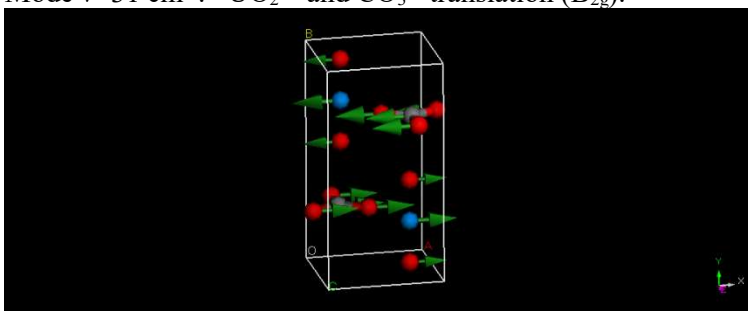

APPENDIX C. Normal modes of rutherfordine (Imm2 symmetry)

Figure C.2. The atomic motions associated to each Raman active vibrational normal mode of Rutherfordine (Imm2 symmetry)

Mode ν=1481 cm^{-1}. Asymmetric CO_3^{2-} stretching (B_2).

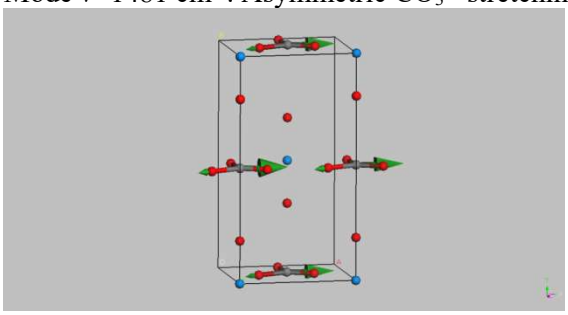

Mode ν=1403 cm^{-1}. Asymmetric CO_3^{2-} stretching (A_1).

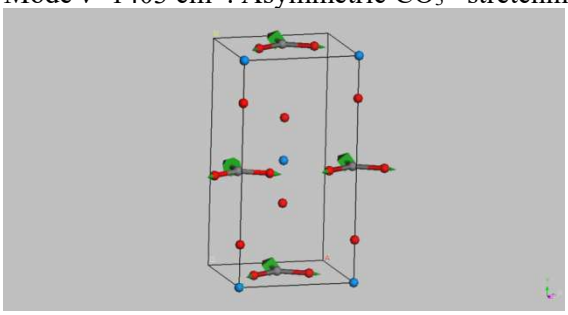

Mode ν=1100 cm^{-1}. Symmetric CO_3^{2-} stretching (A_1).

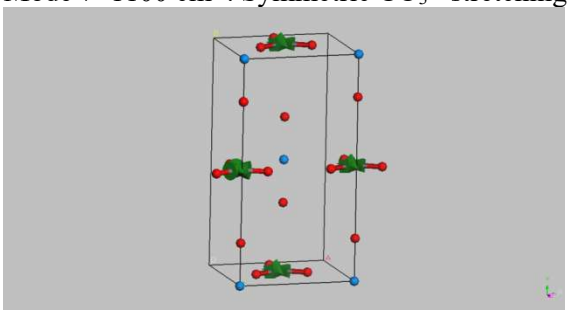

Mode ν=890 cm^{-1}. Symmetric UO_2^{2+} stretching (A_1).

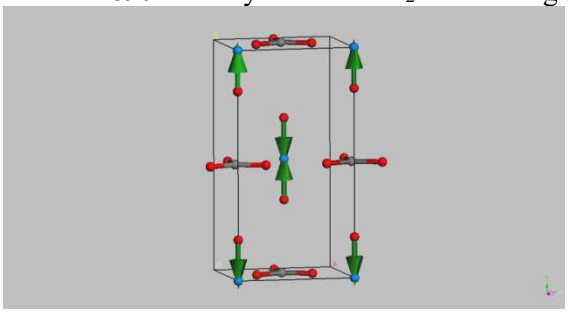

Mode ν=750 cm^{-1}. Out of plane CO_3^{2-} bending (B_1).

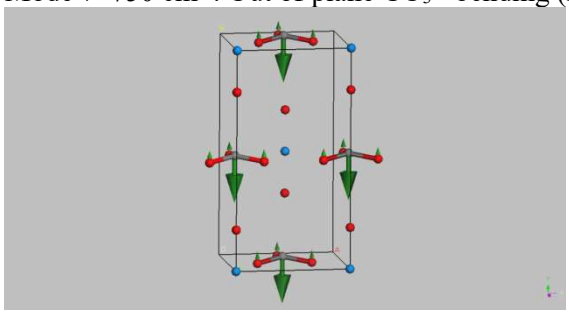

Mode ν=750 cm^{-1}. In plane CO_3^{2-} bending (B_2).

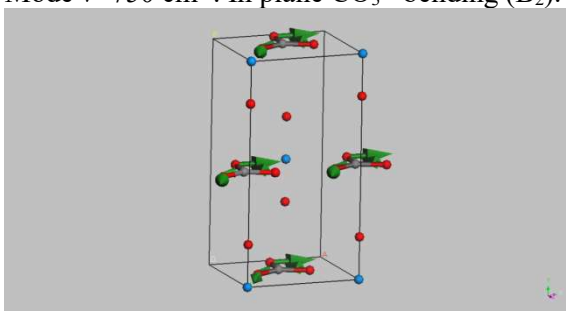

Mode ν=678 cm^{-1}. In plane CO_3^{2-} bending (A_1).

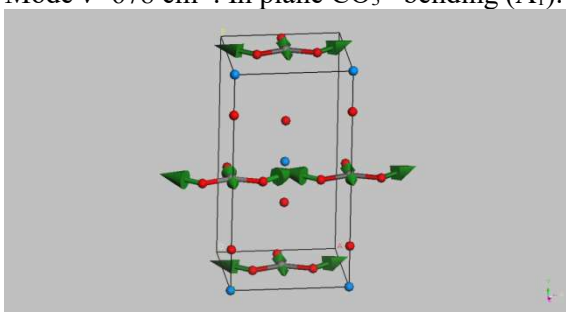

Mode ν=338 cm^{-1}. In plane CO_3^{2-} bending (B_2).

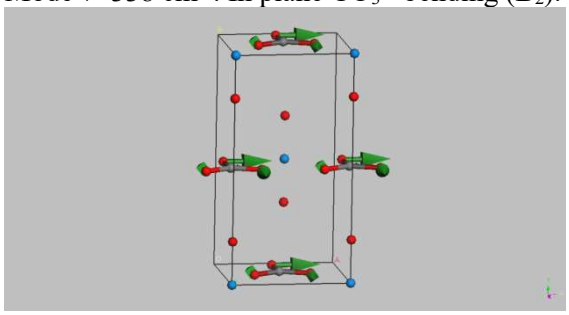

Mode ν=251 cm^{-1}. Symmetric UO_2^{2+} bending plus in plane CO_3^{2-} bending (B_2).

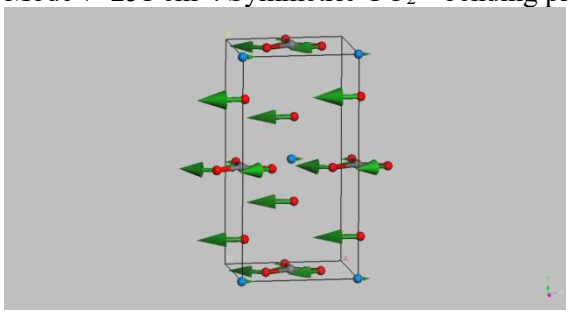

Mode ν=240 cm^{-1}. Symmetric UO_2^{2+} bending plus in plane CO_3^{2-} bending (B_2).

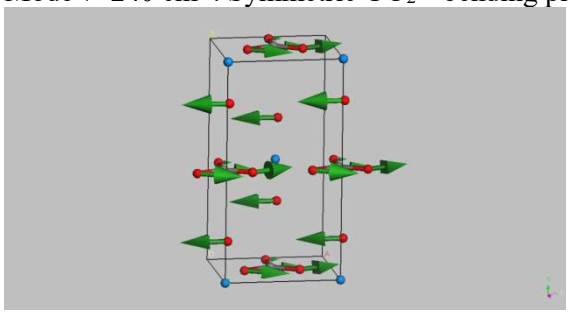

Mode ν=237 cm^{-1}. Antisymmetric UO_2^{2+} bending plus out of plane CO_3^{2-} bending (A_2).

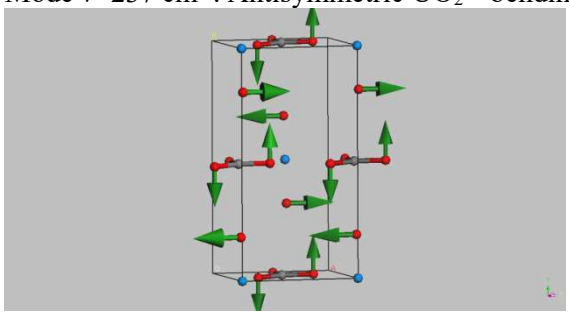

Mode ν=234 cm^{-1}. Symmetric UO_2^{2+} bending (A_1).

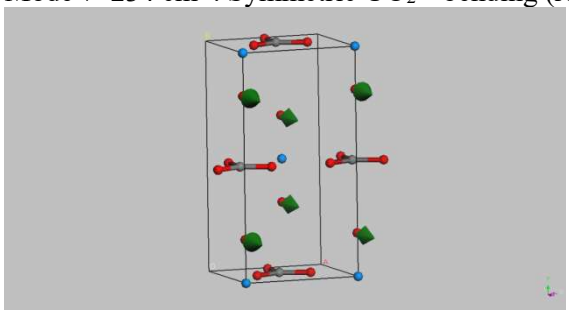

Mode ν=219 cm^{-1}. Symmetric UO_2^{2+} bending plus CO_3^{2-} translation (A_1).

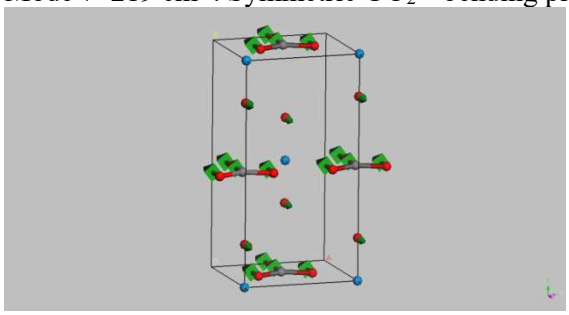

Mode ν=197 cm^{-1}. Antisymmetric UO_2^{2+} bending plus out of plane CO_3^{2-} bending (B_1).

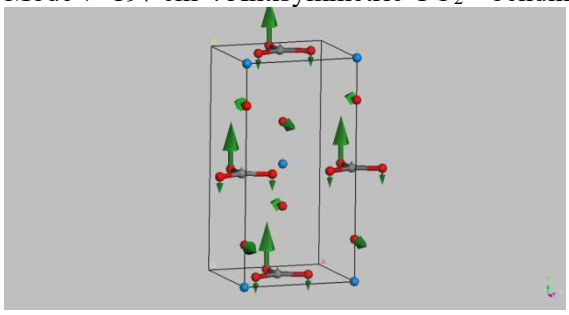

Mode ν=182 cm^{-1}. Antisymmetric UO_2^{2+} bending plus out of plane CO_3^{2-} bending (B_1).

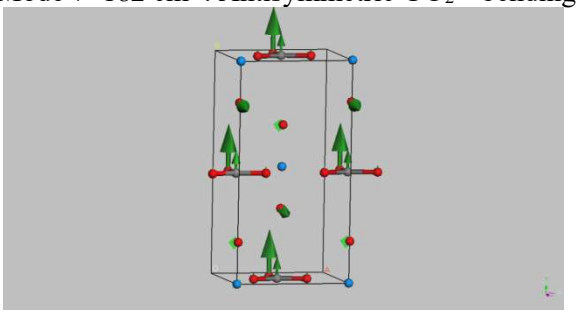

Mode ν=162 cm^{-1}. Antisymmetric UO_2^{2+} bending plus out of plane CO_3^{2-} bending (B_1).

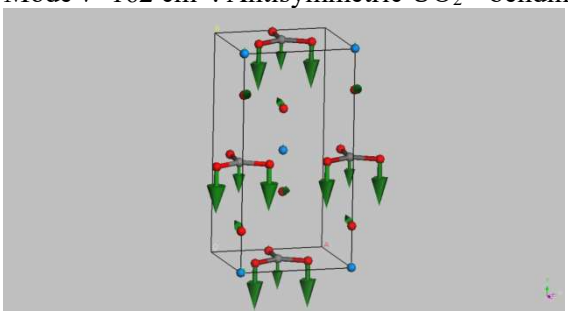

Mode ν=142 cm^{-1}. Antisymmetric UO_2^{2+} bending plus out of plane CO_3^{2-} bending (A_2).

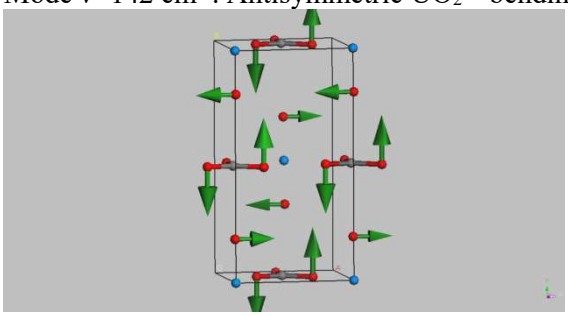

REFERENCIAS

1. J. P. Perdew, A. Ruzsinszky, G. I. Csonka, O. A. Vydrov, G. E. Scuseria, L. A. Constantin, X. Zhou and K. Burke, *Physical Review Letters*, 2008, **100**, 136406.
2. J. P. Crocombette, F. Jollet, L. T. Nga and T. Petit, *Physical Review B*, 2001, **64**, 104107.
3. G. Beridze and P. M. Kowalski, *The Journal of Physical Chemistry A*, 2014, **118**, 11797-11810.
4. a) S. L. Dudarev, D. N. Manh and A. P. Sutton, *Philosophical Magazine Part B*, 1997, **75**, 613-628; b) D. A. Andersson, G. Baldinozzi, L. Desgranges, D. R. Conradson and S. D. Conradson, *Inorganic Chemistry*, 2013, **52**, 2769-2778; c) P. Nerikar, T. Watanabe, J. S. Tulenko, S. R. Phillpot and S. B. Sinnott, *Journal of Nuclear Materials*, 2009, **384**, 61-69; d) X.-D. Wen, R. L. Martin, L. E. Roy, G. E. Scuseria, S. P. Rudin, E. R. Batista, T. M. McCleskey, B. L. Scott, E. Bauer, J. J. Joyce and T. Durakiewicz, *The Journal of Chemical Physics*, 2012, **137**, 154707; e) X.-D. Wen, R. L. Martin, G. E. Scuseria, S. P. Rudin, E. R. Batista and A. K. Burrell, *Journal of Physics: Condensed Matter*, 2013, **25**, 025501.

Rutherfordine: Thermodynamic and Mechanical Properties

Article: *"Thermodynamic and mechanical properties of rutherfordine mineral based on density functional theory"*, by F. Colmenero, L. J. Bonales J. Cobos and V. Timón, J. Phys. Chem. C 121, 5994–6001 (2017).

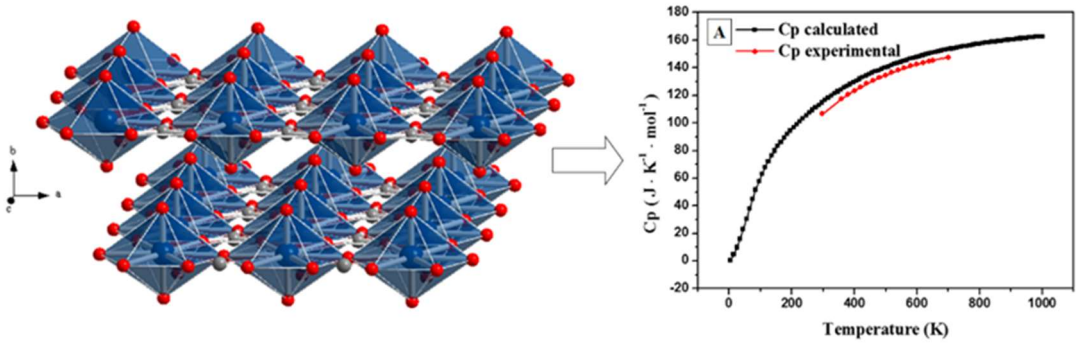

THE JOURNAL OF PHYSICAL CHEMISTRY C

Article

pubs.acs.org/JPCC

Thermodynamic and Mechanical Properties of the Rutherfordine Mineral Based on Density Functional Theory

Francisco Colmenero,[†] Laura. J. Bonales,[‡] Joaquín Cobos,[‡] and Vicente Timón*[,†]

[†]Instituto de Estructura de la Materia (CSIC), C/Serrano 113, 28006 − Madrid, Spain

[‡]Centro de Investigaciones Energéticas, Medioambientales y Tecnológicas (CIEMAT), Avda/Complutense 40, 28040 − Madrid, Spain

Supporting Information

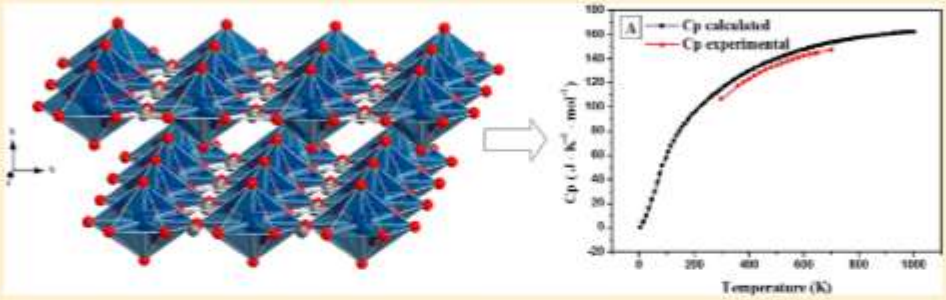

ABSTRACT: The thermodynamic and mechanical properties of rutherfordine, a uranyl carbonate mineral, were studied by means of first principles calculations based on density functional theory. Thermodynamic properties, including enthalpy, free energy, entropy, heat capacity, and Debye temperature, were evaluated as a function of temperature and compared with experimental data in the 300−700 K range. Our calculations show very good agreement with experimental data, and based on them, the knowledge of these properties is extended to the temperature range from 0 to 1000 K, including the full range of thermal stability (0−700 K). The computed values of the heat capacity, entropy, and free energy at 298 K deviate from the experimental values by about 8, 0.3, and 0.3%, respectively. At 700 K, the corresponding differences remain very small, 3.9, 2.3, and 1.3%, respectively. The equation of state and mechanical properties were also computed. The crystalline structure is seen to be mechanically and dynamically stable. Rutherfordine is shown to be a highly anisotropic and brittle material with a very large compressibility along the direction perpendicular to the sheets characterizing its structure. The computed bulk modulus is very small, $B \approx 20$ GPa, in comparison to the values obtained in previous calculations.

I. INTRODUCTION

One of the most relevant issues in nuclear and energy sciences is the protection of the environment. The prediction of the behavior of hazardous materials under diverse environmental conditions is extremely important. Fundamental thermodynamic data are the indispensable basis for a dynamic modeling of the chemical behavior of contaminant waste components. They are needed in order to evaluate the origin and evolution of uranium ore bodies, in developing programs for the solution mining of uranium deposits or mine dumps, in the study of spent nuclear fuel (SNF) radioactive waste and in the containment of such waste, and may also be of importance in reactions within breeder reactors.[1−4] The knowledge of precise thermodynamic data is basic in the development of geochemical and used fuel degradation models.[5]

The enormous importance of the thermodynamic information in the assessment of the safety of nuclear waste repositories is reflected by the large number of recent experimental works on this topic culminating in large reviews and updates of the thermodynamic properties of uranium-bearing species[6−9] and other systems containing related elements.[10] Recent studies include, among others, the important experimental determinations by means of solubility and calorimetry measurements of the thermodynamic properties of uranyl peroxide hydrates,[11−14] uranyl carbonate minerals,[15] uranyl phosphate and orthophosphate minerals,[16] and uranyl silicates.[17−20] Whereas the thermodynamic information database of uranium-bearing species is very advanced, there are many secondary phases for which the corresponding data is inaccurate due to large experimental uncertainties.[2] Additionally, the range of conditions (i.e., temperature and pressure) for which these properties are known is quite limited.

As noted by Weck et al.,[21] the availability of a great amount of information on the formation, thermodynamic stability, and phase transformations of alteration phases formed at the SNF surface contrasts with the paucity of data regarding the mechanical stability and properties of these phases. In fact, except for the theoretical study of the uranyl peroxide hydrates,

Received: January 22, 2017
Revised: February 23, 2017
Published: February 27, 2017

DOI: 10.1021/acs.jpcc.7b00699
J. Phys. Chem. C XXXX, XXX, XXX−XXX

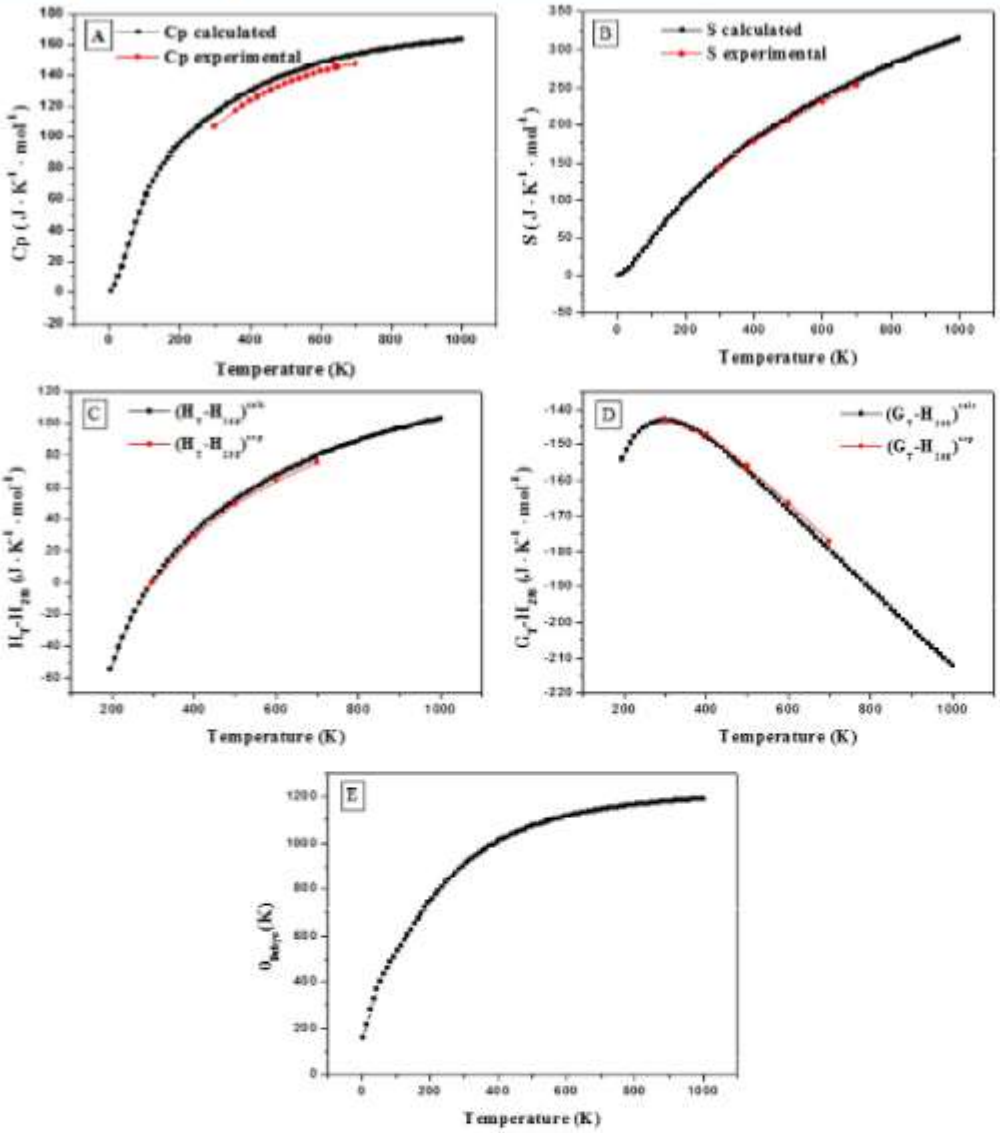

Figure 1. (A) Isobaric specific heat, (B) entropy, (C) enthalpy, (D) Gibbs free energy, and (E) Debye temperature. All functions are given as a function of temperature.

studtite, and metastudtite by Weck et al.,[21] no experimental or computational studies reporting data of this kind have been carried out to date. Theoretical methods may be advantageous to determining the thermodynamic and mechanical properties of these materials because they are free of the difficulties associated with their radiotoxicity. Although theoretical solid-state methods may be used to obtain these properties, the calculations required are very complex and expensive.[22,23] For this reason, there are very few such studies, and we may cite the recent works by Sassani et al.,[5] Weck and Kim,[24,25] Beridze and Kowalski,[23] and Weck et al.[21]

Uranium carbonate compounds and their importance in actinide environmental chemistry have been reviewed by Clark et al.[26] Because carbonate and bicarbonate, present in significant concentrations in many natural waters, are exceptionally strong complexing agents for actinide ions, carbonate complexes of actinide ions play an important role in the migration from nuclear waste repositories or in accidental site contamination. Because of the great relevance of uranyl carbonates, the rutherfordine mineral was studied using experimental and theoretical methods in our previous work.[27] As far as we are concerned, there is only a previous study[28] of this mineral by means of solid-state theoretical methods. However, the analysis of the results of this work reveals that the computed structure is not very precise. Therefore, the bulk modulus extracted from the equation of state of the rutherfordine mineral reported in that work may not be accurate because of structural deficiencies, and it deviates largely from the value reported in this article.

In this work, we study the thermodynamic and mechanical properties of mineral rutherfordine by means of computational density functional theory (DFT) calculations. In this way, we extend the previous study of this mineral[27] in which the structure, X-ray powder pattern, and Raman spectra were determined using a new norm-conserving relativistic pseudopotential for the uranium atom. All of the thermodynamic

DOI: 10.1021/acs.jpcc.7b00699
J. Phys. Chem. C XXXX, XXX, XXX−XXX

properties are evaluated as a function of temperature in the 0−1000 K range and are compared with experimental data in the 300−700 K range. This article is organized as follows. In Section II, the methods used are described. In Section III, the main results of our calculations of thermodynamic properties are given and compared to experimental data. The computed equation of state and mechanical properties are also reported in this section. Finally, in Section IV, the conclusions of this work are given.

II. METHODS

The rutherfordine unit cell has been modeled using the CASTEP code,[29] a module of the Materials Studio package.[30] The generalized gradient approximation (GGA) with the PBESOL functional[31,32] was used. Geometry optimization was carried out using the Broyden−Fletcher−Goldfarb−Shanno optimization scheme[33,34] with a convergence threshold on atomic forces of 0.01 eV/Å. The kinetic energy cutoff employed was 1000 eV, and the corresponding k-point mesh[35] adopted was 5 × 3 × 6 (18 K points). They were selected in our previous work[27] by performing calculations of increasing complexity. The above calculation parameters gave well-converged structures and were considered sufficient to determine the final material properties. The X-ray powder pattern was determined from the optimized structure. Also, in that work we used the linear response density functional perturbation theory (DFPT)[36−40] implemented in the CASTEP code in order to determine the Raman spectra of the rutherfordine mineral. All of these properties were evaluated for two different rutherfordine structures with symmetries *Imm*2 and *Pmmn*. For these structures, we obtained very close results for the energies and properties; therefore, we concluded that both could be simultaneously present in nature.[27] In present work, we have chosen the structure with *Imm*2 symmetry among these two nearly degenerate structures in order to determine the thermodynamic and mechanical properties.

The phonon spectrum at different points in the Brillouin zone can also be determined by DFPT as second-order derivatives of the total energy.[37] The knowledge of the entire phonon spectrum allows the phonon dispersion curves and density of states to be calculated and, from them, the evaluation of several important thermodynamic quantities in the quasi-harmonic approximation, such as free energies, enthalpies, entropies, specific heats, and Debye temperatures.[37,41]

The bulk modulus and its pressure derivative were calculated by fitting the lattice volumes and pressures to an equation of state. In the present study, the lattice volumes around the equilibrium were computed by optimizing the structure at several different pressures between −0.75 and 12 GPa, where negative pressure values mean traction or tension. The results were then fitted to a fourth-order Birch−Murnaghan equation of state[42] using the computed volume at 0 GPa as V_0 using EOSFIT 5.2 code.[43]

Elastic constants, needed for the calculation of mechanical properties and for the study of the mechanical stability of rutherfordine crystal structure, were calculated from stress−strain relations. For this purpose, the finite deformation technique is employed in CASTEP. In this technique, finite programmed symmetry-adapted strains[44] may be used to extract individual elastic constants from the stress tensor obtained as the response of the system to the applied strains. For the calculation of the elastic tensor, this stress-based method appears to be more efficient than the energy-based methods and the use of DFPT.[45]

The norm-conserving relativistic pseudopotential[46] for the uranium atom employed in the computations was generated in our previous work.[27] This paper and other publications[47] may be consulted to find the details of its construction and behavior for many different uranyl minerals. The pseudopotentials used for C and O atoms in the unit cell of the rutherfordine mineral were standard norm-conserving pseudopotentials[46] given in the CASTEP code (00PBE-OP type).

III. RESULTS AND DISCUSSION

III.1. Thermodynamic Properties. A phonon calculation was performed for the optimized rutherfordine structure (*Imm*2 symmetry) and with the same calculation parameters as in our previous work.[27] From it, the thermodynamic properties were evaluated. Figure 1A−D shows the isobaric heat capacity, entropy, enthalpy, and free-energy functions, respectively, compared to the experimental data of Hemingway.[1] Finally, Figure 1E shows the calculated Debye temperature function. More details about the Debye temperature function calculated in this work are given in Appendix B of the Supporting Information. Note that all enthalpy and free-energy values have been divided by the temperature to express these properties in the same units as entropy and heat capacity (J/(K·mol)).

The value obtained for the isobaric specific heat at zero pressure and 298 K is C_p = 115.0 J/(K·mol), which may be compared to the experimental value of Gurevich et al.[48,8] of 120.1 ± 0.1 J/(K·mol) and that of Hemingway[1] of 106.5 J/(K·mol). The agreement is quite good, with our value being between both experimental values and the deviations being about 4 and 8%, respectively. The heat capacity function is compared with that of Hemingway[1] in Figure 1A in the temperature range of 298−700 K. As can be appreciated, the calculated and experimental curves are closely parallel. The computed value at 700 K, near the limit of thermal stability,[1] C_p = 153.3 J/(K·mol), differs from the experimental value of 147.6 J/(K·mol) by only 3.9%. A precise comparison of the specific heat values at selected temperatures is given in Table 1.

To facilitate the use of the calculated heat capacity function, we have fitted it to a fifth-order polynomial, and the results are given in Table 2. The fit was carried out with 52 points, and it should be valid over a large range of temperature of 250−750 K. It has a very small sum of squared deviations (SSD) and a very good correlation factor (R). The calculated data may also be fitted, as usual, to a Haas−Fisher (HF) polynomial, $C_p(T) = a + bT + cT^{-2} + dT^{-0.5} + eT^2$, yielding coefficients a = 259.03119 J/(K·mol), b = −0.00101 J/(K^2·mol), c = 1.06343 × 10^6 J/(K^{-1}·mol), d = −2668.47225 J/(K$^{0.5}$·mol), and e = −1.28601 × 10^5 J/(K^3·mol). However, we prefer the polynomial fit because the SSD associated with the HF fit is 2 orders of magnitude larger (0.01091). The calculated heat capacity function over the temperature range of 0−1000 K is given in Appendix A of the Supporting Information. The last value of C_p calculated at a temperature of 1000 K, C_p = 162.8 J/(K·mol), is still well below the Dulong−Petit asymptotic value, $C_p = 3nR$ = 174.6 J/(K·mol).

The computed entropy value at zero pressure and a temperature of 298 K is S = 143.1 J/(K·mol). The agreement with the experimental value of Hemingway,[1] 142.7 J/(K·mol), is excellent. The value of entropy at 298 K given by Langmuir[49] was also 142.7 J/(K·mol). The estimate of Lemire and Tremaine[50] of 194 J/(K·mol) is ruled out because it is too

DOI: 10.1021/acs.jpcc.7b00699
J. Phys. Chem. C XXXX, XXX, XXX−XXX

Table 1. Comparison of Calculated and Experimental Isobaric Heat Capacity Functions[a]

T(K)	C_p^{exp}	C_p^{calc}
298.15	106.5	115.02
360	117.4	124.55
380	120.5	127.25
400	123.3	129.78
420	125.9	132.15
440	128.4	134.38
460	130.6	136.46
480	132.7	138.41
500	134.68	140.24
520	136.5	141.96
540	138.2	143.56
560	139.7	145.07
580	141.2	146.48
600	142.48	147.81
620	143.7	149.05
640	144.8	150.22
650	145.3	150.78
700	147.57	153.32

[a]All values are given in units of J/(K·mol). The experimental data are from Hemingway.[1]

large in comparison to the experimental values and the calculated one. Cordfunke and O'Hare[51] gave an estimation of 139 J/(K·mol). Although the errors are slightly larger at higher temperatures (Table 3), the entropy variation with temperature is very good. The calculated entropy function compared to the experimental one is displayed in Figure 1B. The differences with respect to Hemingway's experimental values range from 0.3% at 298 K to 2.3% at 700 K. The results of a fifth-order polynomial fit to the calculated entropy, valid from 250 to 750 K, are given in Table 2. The calculated entropy function over the full range of temperature, 0−1000 K, is given in Appendix A of the Supporting Information.

The calculated enthalpy value at zero pressure and temperature of 298.15 K is H_{298} = 70.95 J/(K·mol). The enthalpy variation with temperature is very good, as can be seen in Table 4, where the values of enthalpy relative to its value at 298.15 K ($H_T - H_{298}$) are compared to their experimental counterparts at 400, 500, 600, and 700 K. The calculated enthalpy function compared to the experimental one is displayed in Figure 1C. The computed value at 700 K, ($H_T - H_{298}$) = 79.3 J/(K·mol), deviates from experiment, ($H_T - H_{298}$) = 75.8 J/(K·mol), by 4.6%. The results of a fifth-order polynomial fit to the calculated enthalpy, valid from 250 to 750 K, are given in Table 2. The computed enthalpy function over the temperature range of 0−1000 K is given in Appendix A of the Supporting Information.

Table 3. Comparison of Calculated and Experimental Entropy Functions[a]

T(K)	S^{exp}	S^{calc}
298.15	142.70	143.11
400	176.50	179.10
500	205.32	209.24
600	230.61	235.52
700	252.99	258.74

[a]All values are given in units of J/(K·mol). The experimental data are from Hemingway.[1]

Table 4. Comparison of Calculated and Experimental Enthalpy Functions, $H_T - H_{298}$[a]

T(K)	$(H_T - H_{298})^{exp}$	$(H_T - H_{298})^{calc}$
298.15	0.00	0.0
400	29.400	31.3
500	49.382	52.0
600	64.292	67.5
700	75.854	79.3

[a]All values are given in units of J/(K·mol). The experimental data are from Hemingway.[1]

The variation of the free energy with temperature is also good, as can be seen in Table 5, where the calculated values relative to the enthalpy at 298 K ($G_T - H_{298}$) are compared with the corresponding experimental data at 298, 400, 500, 600, and 700 K. Computed values differ from experiment by 0.3 and 1.3% at 298 and 700 K, respectively. The calculated free-energy function compared to the experimental one is displayed in Figure 1D, and the results of a fifth-order polynomial fit to the calculated free energy, valid from 250 to 750 K, are given in Table 2. The calculated free-energy function over the

Table 5. Comparison of Calculated and Experimental Free-Energy Functions, $G_T - H_{298}$[a]

T(K)	$(G_T - H_{298})^{exp}$	$(G_T - H_{298})^{calc}$
298.15	−142.70	−143.11
400	−147.10	−147.81
500	−155.94	−157.20
600	−166.32	−168.06
700	−177.14	−179.44

[a]All values are given in units of J/(K·mol). The experimental data are from Hemingway.[1]

Table 2. Fifth-Order Polynomial Fit of the Calculated Heat Capacity, Entropy, Enthalpy, and Free-Energy Functions[a]

	C_T^{calc}	S^{calc}	$(H_T - H_{298})^{calc}$	$(G_T - H_{298})^{calc}$
A_0	32.31873	−20.33277	−299.5316	279.1873
A_1	0.4175506	0.7833474	2.078814	1.295351
$A_2 \times 10^3$	−0.5960663	−1.101300	−5.651087	−4.549320
$A_3 \times 10^6$	0.4846092	1.303643	8.807384	7.502775
$A_4 \times 10^9$	−0.2220333	−0.9440572	−7.225174	−6.280124
$A_5 \times 10^{12}$	0.04688578	0.2968067	2.418783	2.121575
SSD	0.00024	0.00051	0.05419	0.04450
R	1.00000	1.00000	1.00000	1.00000

[a]$F(T) = A_0 + A_1T + A_2T^2 + A_3T^3 + A_4T^4 + A_5T^5$). The A_i coefficients are given in J/(K^{i+1}·mol) units.

DOI: 10.1021/acs.jpcc.7b00699
J. Phys. Chem. C XXXX, XXX, XXX−XXX

temperature range of 0−1000 K is given in Appendix A of the Supporting Information.

III.2. Equation of State. Lattice volumes around equilibrium were calculated by optimizing the structure at 17 different applied pressures. The results are displayed in Figure 2.

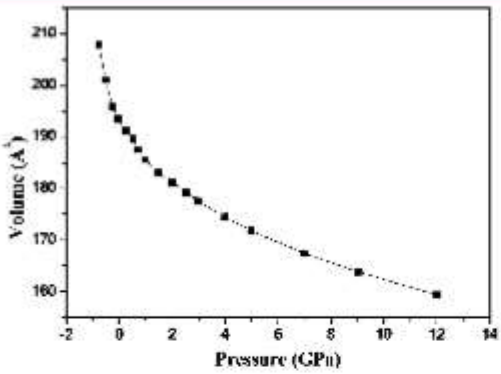

Figure 2. Rutherfordine unit cell volume versus applied pressure.

The calculated data were then fitted to a fourth-order Birch−Murnaghan equation of state (EOS) using the computed volume at 0 GPa (193.7 Å^3) as V_0 using the EOSFIT 5.2 code,[43]

$$P = 3Bf_E(1+2f_E)^{5/2}\left[1+\frac{3}{2}(B'-4)f_E + \frac{3}{2}\left\{BB'' + (B'-4)(B'-3) + \frac{35}{9}\right\}f_E^{\,2}\right]$$

In this equation,

$$f_E = \frac{1}{2}\left[\left(\frac{V_0}{V}\right)^{2/3} - 1\right]$$

and B, B', and B'' are the bulk modulus and its first and second derivatives, respectively, at the temperature of 0 K. The values found for B, B', and B'' were B = 19.03 (±0.36) GPa, B' = 15.34 (±0.72), and B'' = −7.43 (±1.32) GPa^{-1} (χ^2 = 0.003). The value obtained for the bulk modulus is very different to that computed previously by Matar.[28] Because our previous structural and spectroscopic results (Bonales et al.[27]) and the thermodynamic properties computed in this work are in very good agreement with experimental data, we believe that the present value of B is much more accurate.

III.3. Mechanical Properties and Stability. The elastic tensor, needed for the calculation of mechanical properties and to study the mechanical stability of the rutherfordine crystal structure, was calculated, at the optimized equilibrium structure, from stress−strain relations using the finite deformation technique implemented in CASTEP. Crystals with orthorhombic symmetry have nine nondegenerate elastic constants in the symmetric stiffness matrix,[44,21] which may be written as

$$C = \begin{pmatrix} C_{11} & C_{12} & C_{12} & 0 & 0 & 0 \\ C_{12} & C_{22} & C_{23} & 0 & 0 & 0 \\ C_{13} & C_{23} & C_{33} & 0 & 0 & 0 \\ 0 & 0 & 0 & C_{44} & 0 & 0 \\ 0 & 0 & 0 & 0 & C_{55} & 0 \\ 0 & 0 & 0 & 0 & 0 & C_{66} \end{pmatrix}$$

Here, we use the standard Voigt notation for the indices contracting a pair of Cartesian indices into a single integer $1 \le i \le 6$: $xx \to 1$, $yy \to 2$, $zz \to 3$, $yz \to 4$, $xz \to 5$, $xy \to 6$. The precise values of these constants obtained in our computations are given in Table 6.

For orthorhombic crystals, the necessary and sufficient Born criteria for mechanical stability are[52,21]

$$C_{ii} > 0 \ (i = 1, 4, 5, 6)$$

$$C_{11}C_{22} - C_{12}C_{12} > 0$$

$$C_{11}C_{22}C_{33} + 2C_{12}C_{13}C_{23} - C_{11}C_{23}C_{23} - C_{22}C_{13}C_{13} - C_{33}C_{12}C_{12} > 0$$

Because the above conditions are fulfilled by the elastic constants of rutherfordine reported in Table 6, its mechanical stability can be inferred. To analyze the stability of the material in a complete form, we must also study the dynamic stability. A structure is dynamically stable if and only if all of its phonon modes have positive frequencies for all wave vectors.[52] The satisfaction of this condition has also been verified from the phonon calculation utilized to determine the thermodynamic properties of rutherfordine.

The fact that C_{22}, the diagonal component of the C matrix along the b direction, is much smaller than either C_{11} or C_{33} suggests that the thermal expansion of the material will occur predominantly along this direction (perpendicular to rutherfordine sheets). Diagonal component C_{11} is the largest (along the a direction). A simple view of the elastic constants given in Table 6 shows that the mechanical properties are very different along the different directions. Therefore, the rutherfordine crystal structure is highly anisotropic. This anisotropy may be understood from the analysis of the structure, as illustrated in Figure 3. Although rutherfordine sheets, perpendicular to the b direction, are held together with weak van der Waals forces, the atoms within the sheets are linked with strong UO and CO bonds.

Bulk and shear moduli (B and G) of polycrystalline aggregates of rutherfordine crystals were determined from the elastic tensor according to Voigt, Reuss, and Hill schemes.[53−55] Relevant formulas for these approximations may be found in several sources (e.g., Weck et al.[21]). Large differences between these approximations are expected for crystalline systems with strong anisotropy, featuring large differences between elastic constants along different directions (Weck et al.[21]). The Reuss scheme gave the best comparison of the computed bulk

Table 6. Nine Independent Elastic Constants in the Stiffness Matrix for the Orthorhombic Lattice Structure of Rutherfordine[a]

C_{11}	C_{22}	C_{33}	C_{44}	C_{55}	C_{66}	C_{12}	C_{13}	C_{23}
259.88	23.03	165.27	9.85	65.88	15.06	−8.33	72.39	−5.18

[a]All values are in GPa.

DOI: 10.1021/acs.jpcc.7b00699
J. Phys. Chem. C XXXX, XXX, XXX−XXX

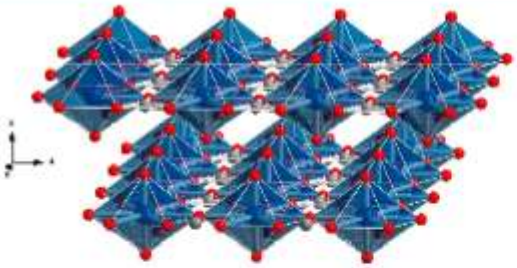

Figure 3. Crystal structure of rutherfordine.[27] Color code: U, blue; O, red; and C, gray.

modulus with that determined from the equation of state, given in the previous section. The bulk and shear moduli calculated in this approximation together with the values obtained for other mechanical properties are given in Table 7. The numerical

Table 7. Bulk, Modulus, Shear Modulus, Young Modulus, Poisson Ratio, Pugh's Ratio, and Vickers Hardness (B, G, E, ν, D, and H) Calculated in the Reuss Approximation[a]

property	value
B	17.97
G	19.47
E	42.92
ν	0.10
D	0.92
H	9.47

[a]Values of B, G, and E are given in GPa.

estimate of the error in the computed bulk modulus given by the CASTEP code is 0.94 GPa. Our value of the bulk modulus, B = 17.97 ± 0.94 GPa, agrees reasonably well with that obtained from the EOS, B = 19.03 ± 0.36 GPa.

In general, a large value of the shear modulus is an indication of the more pronounced directional bonding between atoms. The shear modulus represents the resistance to plastic deformation whereas the bulk modulus represents the resistance to fracture. The individual components of the bulk and Young's moduli may be derived from the elastic compliance matrix components.[56,21] The compliance matrix is the inverse of the stiffness C matrix. The corresponding values are given in Table 8. As can be seen, B_b is much smaller than

Table 8. Bulk and Young Moduli Components along the Crystallographic Axes[a]

	a axis	b axis	c axis
B	271.19	21.70	170.06
E	226.57	22.71	144.75

[a]All values are given in GPa.

either B_a or B_c. Also, component E_b is much smaller than E_a or E_c. Thus, the b direction, perpendicular to rutherfordine sheets, is the most compressible and least stiff, in agreement with the results of the components of the elastic C matrix.

Pugh[57] introduced the proportion of bulk into shear modulus of polycrystalline phases ($D = B/G$) as a measure of ductility by considering the interpretation of the shear and bulk moduli given above. A higher D value is usually associated with higher ductility, and the critical value that separates ductile and brittle materials is 1.75 (i.e., if $B/G > 1.75$, then the material behaves in a ductile manner; otherwise, the material behaves in a brittle manner[56]). Poisson's ratio,[57] ν, can also be utilized to measure the malleability of crystalline compounds and is related to Pugh's ratio given above by the relation $D = (3 - 6\nu)/(8 + 2\nu)$. Poisson's ratio is close to $^1/_3$ for ductile materials, but it is generally much less than $^1/_3$ for brittle materials. As it can be seen in Table 7, for rutherfordine we find small ratios D and ν corresponding to a brittle material. For comparison, both studtite and metastudtite were found to be ductile.[21]

The hardness of these systems is computed according to a recently introduced empirical scheme[58] that correlates the Vickers hardness and Pugh ratio ($D = B/G$). The Vickers hardness, H, of polycrystalline rutherfordine is given in Table 7. Its value, about 9.5, corresponds to material of intermediate hardness. For comparison, we can compute the hardness of studtite and metastudtite using the elasticity data of Weck et al.[21] These systems, characterized by much larger D ratios, have a much smaller hardness (smaller than 1).

To assess the elastic anisotropy of rutherfordine, shear anisotropic factors were obtained. These factors provide a measure of the degree of anisotropy in the bonding between atoms in different planes and are very important in the study of material durability. Shear anisotropic factors for the {100} (A_1), {010} (A_2), and {001} (A_3) crystallographic planes were computed using the formulas given by Bouhadda et al.[56] For an isotropic crystal, factors A_1, A_2, and A_3 must be 1, whereas any value smaller or greater than unity is a measure of the degree of elastic anisotropy possessed by the crystal. The computed values were 0.14, 1.33, and 0.20. Thus, the anisotropies are very large in the {100} and {001} planes. The {010} plane, containing rutherfordine sheets, is the least anisotropic.

In the recently introduced universal anisotropy index,[59] the departure of A^U from zero defines the extent of single-crystal anisotropy and accounts for both the shear and the bulk contributions unlike all other existing anisotropy measures. It must also be noted that A^U is independent of the scheme used to determine the polycrystalline elastic properties because it is defined in terms of the bulk and shear moduli in both Voigt and Reuss approximations. Thus, A^U represents a universal measure to quantify the single-crystal elastic anisotropy. It must be noted that the universal anisotropy index is defined in terms of the bulk and shear moduli in Voigt and Reuss schemes; therefore, it does not change upon selecting a particular scheme. Rutherfordine is characterized by a computed anisotropy index of 8.82, which is a rather large value (A^U = 0 corresponds to a perfectly isotropic crystal). For comparison, studtite and metastudtite exhibit anisotropy values[21] of 2.17 and 1.44, respectively.

IV. CONCLUSIONS

The thermodynamic and mechanical properties of the rutherfordine mineral were studied by means of first principles calculations based on density functional theory. These calculations extend the knowledge and interpretation of the structure and properties of this uranyl carbonate mineral reported in the previous study of this mineral (Bonales et al.[27]) and illustrate the power of theoretical methods as a predictive tool in the research of uranium-containing materials.

All of the thermodynamic properties, including the enthalpy, free energy, entropy, heat capacity, and Debye temperature, were evaluated as a function of temperature and compared to experimental data in the range of 300−700 K. Our calculations show very good agreement with experimental data. These

DOI: 10.1021/acs.jpcc.7b00699
J. Phys. Chem. C XXXX, XXX, XXX−XXX

thermodynamic properties were obtained in the extended range of 0−1000 K, including the full range of thermal stability, up to 700 K.[1] The computed values of the heat capacity, entropy, and free energy at 298 K deviate from experimental values by about 8, 0.2, and 0.5%, respectively. At 700 K, the corresponding differences remain very small, 3.9, 2.3, and 1.3%, respectively.

The equation of state and mechanical properties were also computed. The crystalline structure was shown to be mechanically and dynamically stable. Rutherfordine is shown to be a highly anisotropic and brittle material with very large compressibility along the direction perpendicular to the sheets characterizing its structure. The computed bulk modulus is very small, $B \approx 20$ GPa, in comparison to the values obtained in previous calculations.[28] This emphasizes the need for very high levels of theory in the computational treatment of uranium-containing materials because inaccuracies in the calculations may lead to imprecise results for material properties. A large amount of relevant mechanical data of the rutherfordine mineral is reported here, including bulk modulus derivatives, elastic coefficients, shear and Young moduli, Poisson ratios, ductility and hardness indices, and elastic anisotropy measures.

■ ASSOCIATED CONTENT

Supporting Information

The Supporting Information is available free of charge on the ACS Publications website at DOI: 10.1021/acs.jpcc.7b00699.

The calculated thermodynamic functions of rutherfordine (isobaric specific heat, entropy, enthalpy, free energy, and Debye temperature) in the range of temperature 0−1000 K are given in a series of tables in Appendix A. Details of the Debye temperature function calculated in this work are given in Appendix B. (PDF)

■ AUTHOR INFORMATION

Corresponding Author

*E-mail: vicente.timon@csic.es. Phone number: +34 915616800 ext. 941120.

ORCID

Francisco Colmenero: 0000-0003-3418-0735

Notes

The authors declare no competing financial interest.

■ ACKNOWLEDGMENTS

This work was supported by ENRESA in project no. 079000189 "Aplicación de técnicas de caracterización en el estudio de la estabilidad del combustible nuclear irradiado en condiciones de almacenamiento" (ACESCO) and project FIS2013-48087-C2-1-P. Supercomputer time at the CETA-CIEMAT, CTI-CSIC, and CESGA centers is also acknowledged. This work has been carried out in the context of a CSIC−CIEMAT collaboration agreement: "Caracterización experimental y teórica de fases secundarias y óxidos de uranio formados en condiciones de almacenamiento de combustible nuclear". We also thank Dr. Ana Ma. Fernández for reading the document and making many helpful comments.

■ REFERENCES

(1) Hemingway, B. S. *Thermodynamic Properties of Selected Uranium Compounds and Aqueous Species at 298.15 K and 1 bar and at Higher Temperatures - Preliminary Models for the Origin of Coffinite Deposits*; USGS Open-File Report, 1982, pp 82−619.

(2) Langmuir, D. *Aqueous Environmental Geochemistry*; Prentice-Hall: NJ, 1997; pp 486−557.

(3) Casas, I.; Bruno, J.; Cera, E.; Finch, R. J.; Ewing, R. C. *Kinetic and Thermodynamic Studies of Uranium Minerals Assessment of the Long-Term Evolution of Spent Nuclear Fuel*; SKB Technical Report 94-16; Swedish Nuclear Fuel and Waste Management Co.: Stockholm, Sweden, 1994.

(4) Navrotsky, A.; Shvareva, T. Y.; Guo, X.; Rock, P. A. *Thermodynamics of Uranium Minerals and Related Materials*; Mineralogical Association of Canada: Winnipeg, MB, Canada, May 2013; Short Course 43, Chapter 4.

(5) Sassani, D. C.; Jové-Colón, C. F.; Weck, P. F.; Jerden, J. L.; Frey, K. E.; Cruse, T.; Ebert, W. L.; Buck, E. C.; Wittman, R. S. *Used Fuel Degradation: Experimental and Modeling Report, Fuel Cycle Research and Development Report FCRD-UFD-2013-000404*; Sandia National Laboratories: Albuquerque, NM, October 17, 2013.

(6) Wanner, H., Forest, I., Eds.; *Chemical Thermodynamics of Uranium*; Elsevier Science Publishers B.V.: Amsterdam, North-Holland, 1992.

(7) Murphy, W. M.; Pabalan, R. T. *Review of Empirical Thermodynamic Data for Uranyl Silicate Minerals and Experimental Plan*; Nuclear Regulatory Commission Contract NRC-02-93-005; Center for Nuclear Waste Regulatory Analyses: San Antonio, TX, June 1995.

(8) Grenthe, I.; Fuger, J.; Konings, R. J. M.; Lemire, R. J.; Muller, A. B.; Nguyen-Trung, C.; Wanner, H. *Chemical Thermodynamics of Uranium*; Nuclear Energy Agency Organisation for Economic Co-Operation and Development, OECD: Issy-les-Moulineaux, France, 2004.

(9) Shvareva, T. Y.; Fein, J. B.; Navrotsky, A. Thermodynamic Properties of Uranyl Minerals: Constraints from Calorimetry and Solubility Measurements. *Ind. Eng. Chem. Res.* **2012**, *51*, 607−613.

(10) Guillaumont, N. Y. R.; Fanghänel, T.; Neck, V.; Fuger, J.; Palmer, D. A.; Grenthe, I.; Rand, M. H. *Update on the Chemical Thermodynamics of Uranium, Neptunium, Plutonium, Americium, and Technetium*; Mompean, F. J., Illemassene, M., Domenech-Orti, C., Ben Said, K., Eds.; OECD Nuclear Energy Agency, Data Bank: Issy-les-Moulineaux, France, 2003.

(11) Kubatko, K.-A.; Helean, K. B.; Navrotsky, A.; Burns, P. C. Stability of Peroxide-Containing Uranyl Minerals. *Science* **2003**, *302*, 1191−1193.

(12) Kubatko, K.-A. *Crystallography, Hyerarchy of Crystal Structures, and Chemical Thermodynamics of Selected Uranyl Phases*. Ph.D. Thesis, Graduate School of the University of Notre Dame, Notre Dame, IN, 2005.

(13) Armstrong, C. R.; Nyman, M.; Shvareva, T. Y.; Sigmon, G. E.; Burns, P. C.; Navrotsky, A. Uranyl Peroxide Enhanced Nuclear Fuel Corrosion in Seawater. *Proc. Natl. Acad. Sci. U. S. A.* **2012**, *109*, 1874−1877.

(14) Guo, X.; Ushakova, S. V.; Labs, S.; Curtius, H.; Bosbach, D.; Navrotsky, A. Energetics of Metastudtite and Implications for Nuclear Waste Alteration. *Proc. Natl. Acad. Sci. U. S. A.* **2014**, *111*, 17737−17742.

(15) Kubatko, K.-A.; Helean, K. B.; Navrotsky, A.; Burns, P. C. Thermodynamics of Uranyl Minerals: Enthalpies of Formation of Rutherfordine, UO_2CO_3, Andersonite, $Na_2CaUO_2(CO_3)_3(H_2O)_5$, and Grimselite, $K_3NaUO_2(CO_3)\cdot 3H_2O$. *Am. Mineral.* **2005**, *90*, 1284−1290.

(16) Gorman-Lewis, D.; Shvareva, T. Y.; Kubatko, K.-A.; Burns, P. C.; Wellman, D. M.; McNamara, B.; Szymanowsky, J. E. S; Navrotsky, A.; Fein, J. B. Thermodynamic Properties of Autunite, Uranyl Hydrogen Phosphate, and Uranyl Orthophosphate from Solubility and Calorimetric Measurements. *Environ. Sci. Technol.* **2009**, *43*, 7416−7422.

(17) Nguyen, S. N.; Silva, R. J.; Weed, H. C.; Andrews, L. E. Standard Gibbs Free Energies of Formation at the Temperature 303.15 K of Four Uranyl Silicates: Soddyite, Uranophane, Sodium Boltwoodite, and Sodium Weeksite. *J. Chem. Thermodyn.* **1992**, *24*, 359−376.

DOI: 10.1021/acs.jpcc.7b00699
J. Phys. Chem. C XXXX, XXX, XXX−XXX

(18) Gorman-Lewis, D.; Mazeina, L.; Fein, J. B.; Szymanowski, J. E. S.; Burns, P. C.; Navrotsky, A. Thermodynamic Properties of Soddyite from Solubility and Calorimetry Measurements. *J. Chem. Thermodyn.* **2007**, *39*, 568−575.
(19) Shvareva, T. Y.; Mazeina, L.; Gorman-Lewis, D.; Burns, P. C.; Szymanowski, J. E. S.; Fein, J. B.; Navrotsky, A. Thermodynamic Characterization of Boltwoodite and Uranophane: Enthalpy of Formation and Aqueous Solubility. *Geochim. Cosmochim. Acta* **2011**, *75*, 5269−5282.
(20) Guo, X.; Szenknect, S.; Mesbah, A.; Labs, S.; Clavier, N.; Poinssote, C.; Ushakova, S. V.; Curtius, H.; Bosbach, D.; Ewing, R. C.; Burns, P. C.; Dacheux, N.; Navrotsky, A. Thermodynamics of Formation of Coffinite, $USiO_4$. *Proc. Natl. Acad. Sci. U. S. A.* **2015**, *112*, 6551−6555.
(21) Weck, P. F.; Kim, E.; Buck, E. C. On the Mechanical Stability of Uranyl Peroxide Hydrates: Implications for Nuclear Fuel Degradation. *RSC Adv.* **2015**, *5*, 79090−79097.
(22) Crocombette, J. P.; Jollet, F.; Nga, L. T.; Petit, T. Plane-Wave Pseudopotential Study of Point Defects in Uranium Dioxide. *Phys. Rev. B: Condens. Matter Mater. Phys.* **2001**, *64*, 104107.
(23) Beridze, G.; Kowalski, P. M. Benchmarking the DFT+U Method for Thermochemical Calculations of Uranium Molecular Compounds and Solids. *J. Phys. Chem. A* **2014**, *118*, 11797−11810.
(24) Weck, P. F.; Kim, E. Layered Uranium(VI) Hydroxides: Structural and Thermodynamic Properties of Dehydrated Schoepite α-$UO_2(OH)_2$. *Dalton Trans.* **2014**, *43*, 17191−17199.
(25) Weck, P. F.; Kim, E. Uncloaking the Thermodynamics of the Studtite to Metastudtite Shear-Induced Transformation. *J. Phys. Chem. C* **2016**, *120*, 16553−16560.
(26) Clark, D. L.; Hobart, D. E.; Neu, M. P. Actinide Carbonate Complexes and Their Importance in Actinide Environmental Chemistry. *Chem. Rev.* **1995**, *95*, 25−48.
(27) Bonales, L. J.; Colmenero, F.; Cobos, J.; Timón, V. Spectroscopic Raman Characterization of Rutherfordine: a Combined DFT and Experimental Study. *Phys. Chem. Chem. Phys.* **2016**, *18*, 16575−16584.
(28) Matar, S. F. Lattice Anisotropy, Electronic and Chemical Structures of Uranyl Carbonate, UO_2CO_3, from First Principles. *Chem. Phys.* **2010**, *372*, 46−50.
(29) Clark, S. J.; Segall, M. D.; Pickard, C. J.; Hasnip, P. J.; Probert, M. I. J.; Refson, K.; Payne, M. C. First Principles Methods Using CASTEP. *Z. Kristallogr. - Cryst. Mater.* **2005**, *220*, 567−570.
(30) MaterialsStudio, http://accelrys.com/products/collaborative-science/biovia-materials-studio/, accessed Jan 20, 2017.
(31) Perdew, J. P.; Burke, K.; Ernzerhof, M. Generalized Gradient Approximation Made Simple. *Phys. Rev. Lett.* **1996**, *77*, 3865−3868.
(32) Perdew, J. P.; Ruzsinszky, A.; Csonka, G. I.; Vydrov, O. A.; Scuseria, G. E.; Constantin, L. A.; Zhou, X.; Burke, K. Restoring the Density-Gradient Expansion for Exchange in Solids and Surfaces. *Phys. Rev. Lett.* **2008**, *100*, 136406.
(33) Pfrommer, B. G.; Cote, M.; Louie, S. G.; Cohen, M. L. Relaxation of Crystals with the Quasi-Newton Method. *J. Comput. Phys.* **1997**, *131*, 233−240.
(34) Payne, M. C.; Teter, M. P.; Allan, D. C.; Arias, A.; Joannopoulos, J. D. Iterative Minimization Techniques for *Ab Initio* Total-Energy Calculations: Molecular Dynamics and Conjugate Gradients. *Rev. Mod. Phys.* **1992**, *64*, 1045−1097.
(35) Monkhorst, H. J.; Pack, J. D. Special Points for Brillonin-Zone Integration. *Phys. Rev. B* **1976**, *13*, 5188−5192.
(36) Baroni, S.; Giannozzi, P.; Testa, A. Green's-Function Approach to Linear Response in Solids. *Phys. Rev. Lett.* **1987**, *58*, 1861−1864.
(37) Baroni, S.; de Gironcoli, S.; Dal Corso, A. Phonons and Related Crystal Properties from Density-Functional Perturbation Theory. *Rev. Mod. Phys.* **2001**, *73*, 515−562.
(38) Gonze, X.; Allan, D. C.; Teter, M. P. Dielectric tensor, Effective Charges and Phonon in α-Quartz by Variational Density-Functional Perturbation Theory. *Phys. Rev. Lett.* **1992**, *68*, 3603−3606.
(39) Gonze, X.; Lee, C. Dynamical Matrices, Born Effective Charges, Dielectric Permittivity Tensors, and Interatomic Force Constants from Density-Functional Perturbation Theory. *Phys. Rev. B: Condens. Matter Mater. Phys.* **1997**, *55*, 10355−10368.
(40) Refson, K.; Tulip, P. R.; Clark, S. J. Variational Density-Functional Perturbation Theory for Dielectrics and Lattice Dynamics. *Phys. Rev. B: Condens. Matter Mater. Phys.* **2006**, *73*, 155114.
(41) Lee, C.; Gonze, X. Ab Initio Calculation of the Thermodynamic Properties and Atomic Temperature Factors of SiO_2 α-Quartz and Stishovite. *Phys. Rev. B: Condens. Matter Mater. Phys.* **1995**, *51*, 8610−8613.
(42) Birch, F. Finite Elastic Strain of Cubic Crystal. *Phys. Rev.* **1947**, *71*, 809−824.
(43) Angel, R. J. Equations of State. *Rev. Mineral. Geochem.* **2000**, *41*, 35−60. EOSFIT 5.2 software, http://www.ccp14.ac.uk/ccp/web-mirrors/ross-angel/rja/soft/.10.2138/rmg.2000.41.2
(44) Nye, J. F. *The Physical Properties of Crystals: Their Representation by Tensors and Matrices*; Oxford University Press: New York, 1985.
(45) Yu, R.; Zhu, J.; Ye, H. Q. Calculations of Single-Crystal Elastic Constants Made Simple. *Comput. Phys. Commun.* **2010**, *181*, 671−675.
(46) Troullier, N.; Martins, J. L. Efficient Pseudopotentials for Plane-Wave Calculations. *Phys. Rev. B: Condens. Matter Mater. Phys.* **1991**, *43*, 1993−2006.
(47) Colmenero, F.; Bonales, L. J.; Cobos, J.; Timón, V. Study of the Thermal Stability of Studtite by *In Situ* Raman Spectroscopy and DFT Calculations. *Spectrochim. Acta, Part A* **2017**, *174*, 245−253.
(48) Gurevich, V. M.; Sergeyeva, E. I.; Gavrichev, K. S.; Gorbunov, V. E.; Khodakovsky, I. L. Low-Temperature Specific Heat of UO_2CO_3. *Russ. J. Phys. Chem.* **1987**, *61*, 856−857.
(49) Langmuir, D. Uranium Solution-Mineral Equilibria at Low Temperatures with Applications to Sedimentary Ore Deposits. *Geochim. Cosmochim. Acta* **1978**, *42*, 547−570.
(50) Lemire, R. J.; Tremaine, P. R. Uranium and Plutonium Equilibria in Aqueous Solutions to 200°C. *J. Chem. Eng. Data* **1980**, *25*, 361−370.
(51) Cordfunke, E. H. P.; O'Hare, P. A. G. *The Chemical Thermodynamics of Actinide Elements and Compounds. Part 3. Miscellaneous Actinide Compounds*; International Atomic Energy Agency: Vienna, Austria, 1978.
(52) Mouhat, F.; Coudert, F.-X. Necessary and Sufficient Elastic Stability Conditions in Various Crystal Systems. *Phys. Rev. B: Condens. Matter Mater. Phys.* **2014**, *90*, 224104.
(53) Hill, R. The Elastic Behaviour of a Crystalline Aggregate. *Proc. Phys. Soc., London, Sect. A* **1952**, *65*, 349−354.
(54) Reuss, A. Berechnung der Fliessgrenze von Mischkristallen auf Grund der Plastizitatsbedingung fur Einkristalle. *Z. Angew. Math. Mech.* **1929**, *9*, 49−58.
(55) Voigt, W. *Lehrbuch der Kristallphysik*; Teubner: Leipzig, 1962.
(56) Bouhadda, Y.; Djella, S.; Bououdina, M.; Fenineche, N.; Boudouma, Y. Structural and Elastic Properties of LiBH4 for Hydrogen Storage Applications. *J. Alloys Compd.* **2012**, *534*, 20−24.
(57) Pugh, S. F. XCII. Relations between the Elastic Moduli and the Plastic Properties of Polycrystalline Pure Metals. *Philos. Mag.* **1954**, *45*, 823−843.
(58) Niu, H.; Wei, P.; Sun, Y.; Chen, C.-X.; Franchini, C.; Li, D.; Li, Y. Electronic, Optical, and Mechanical Properties of Superhard Cold-Compressed Phases of Carbon. *Appl. Phys. Lett.* **2011**, *99*, 031901.
(59) Ranganathan, S. I.; Ostoja-Starzewski, M. Universal Elastic Anisotropy Index. *Phys. Rev. Lett.* **2008**, *101*, 055504.

DOI: 10.1021/acs.jpcc.7b00699
J. Phys. Chem. C XXXX, XXX, XXX−XXX

SUPPORTING INFORMATION

Thermodynamic and Mechanical Properties of Rutherfordine Mineral Based on Density Functional Theory

Francisco Colmenero[a], *Laura. J. Bonales*[b], *J. Cobos*[b] *and Vicente Timón*[a]

[a] Instituto de Estructura de la Materia (CSIC). C/ Serrano, 113. 28006 – Madrid, Spain.

[b] Centro de Investigaciones Energéticas, Medioambientales y Tecnológicas (CIEMAT). Avda/ Complutense, 40. 28040 – Madrid, Spain.

APPENDIX A. Calculated thermodynamic functions.

Table A.1. Calculated isobaric heat capacity function. Temperature and heat capacity values are given in units K and J/(K·mol), respectively.

T	C_p	T	C_p	T	C_p	T	C_p
5	0.4293	256.26263	107.42752	507.52525	140.9014	758.78788	155.86372
15.05051	4.69165	266.31313	109.34672	517.57576	141.75582	768.83838	156.25559
25.10101	9.92651	276.36364	111.20344	527.62626	142.58284	778.88889	156.6362
35.15152	16.19379	286.41414	113.00071	537.67677	143.38339	788.93939	157.00595
45.20202	23.1633	296.46465	114.74107	547.72727	144.15838	798.9899	157.36521
55.25253	30.50212	306.51515	116.4267	557.77778	144.90867	809.0404	157.71434
65.30303	37.87873	316.56566	118.05953	567.82828	145.63512	819.09091	158.05368
75.35354	44.98538	326.61616	119.64127	577.87879	146.33856	829.14141	158.38357
85.40404	51.60986	336.66667	121.1735	587.92929	147.0198	839.19192	158.70433
95.45455	57.65034	346.71717	122.6577	597.9798	147.6796	849.24242	159.01626
105.50505	63.09102	356.76768	124.09527	608.0303	148.31871	859.29293	159.31968
115.55556	67.96931	366.81818	125.48755	618.08081	148.93788	869.34343	159.61485
125.60606	72.34877	376.86869	126.83582	628.13131	149.53779	879.39394	159.90206
135.65657	76.30095	386.91919	128.14135	638.18182	150.11913	889.44444	160.18157
145.70707	79.89487	396.9697	129.40538	648.23232	150.68256	899.49495	160.45363
155.75758	83.19186	407.0202	130.6291	658.28283	151.2287	909.54545	160.7185
165.80808	86.24375	417.07071	131.81372	668.33333	151.75817	919.59596	160.9764
175.85859	89.09284	427.12121	132.96039	678.38384	152.27156	929.64646	161.22756
185.90909	91.77295	437.17172	134.07026	688.43434	152.76944	939.69697	161.47221
195.9596	94.31063	447.22222	135.14447	698.48485	153.25235	949.74747	161.71055
206.0101	96.72654	457.27273	136.18413	708.53535	153.72082	959.79798	161.94278
216.06061	99.03665	467.32323	137.19031	718.58586	154.17535	969.84848	162.1691
226.11111	101.2533	477.37374	138.16409	728.63636	154.61645	979.89899	162.3897
236.16162	103.386	487.42424	139.10652	738.68687	155.04458	989.94949	162.60476
246.21212	105.44214	497.47475	140.01863	748.73737	155.46019	1000	162.81445

Table A.2. Calculated entropy function. Temperature and entropy values are given in units K and J/(K·mol), respectively.

T	S	T	S	T	S	T	S
5	0.1399	256.26263	126.39578	507.52525	211.30287	758.78788	271.12378
15.05051	2.34354	266.31313	130.2552	517.57576	214.19743	768.83838	273.05348
25.10101	5.92618	276.36364	134.59704	527.62626	217.09199	778.88889	275.46562
35.15152	10.23994	286.41414	138.45645	537.67677	219.50413	788.93939	277.39532
45.20202	15.14086	296.46465	142.31586	547.72727	222.39869	798.9899	279.32503
55.25253	20.5	306.51515	146.17527	557.77778	224.81082	809.0404	281.25474
65.30303	26.19866	316.56566	150.03469	567.82828	227.22295	819.09091	283.18444
75.35354	32.12238	326.61616	153.8941	577.87879	230.11751	829.14141	285.11415
85.40404	38.16646	336.66667	157.27109	587.92929	232.52964	839.19192	287.04386
95.45455	44.24378	346.71717	161.1305	597.9798	234.94178	849.24242	288.97356
105.50505	50.17237	356.76768	164.50749	608.0303	237.35391	859.29293	290.90327
115.55556	56.44392	366.81818	167.88447	618.08081	239.76604	869.34343	292.83298
125.60606	62.23304	376.86869	171.26146	628.13131	242.17818	879.39394	294.28026
135.65657	68.02216	386.91919	174.63845	638.18182	244.59031	889.44444	296.20996
145.70707	73.32885	396.9697	178.01543	648.23232	247.00244	899.49495	298.13967
155.75758	78.63554	407.0202	181.39242	658.28283	249.41458	909.54545	300.06938
165.80808	83.94224	417.07071	184.76941	668.33333	251.82671	919.59596	301.51666
175.85859	89.24893	427.12121	187.66397	678.38384	253.75642	929.64646	303.44636
185.90909	94.55562	437.17172	191.04095	688.43434	256.16855	939.69697	305.37607
195.9596	99.37989	447.22222	193.93551	698.48485	258.58068	949.74747	306.82335
206.0101	104.20416	457.27273	196.83007	708.53535	260.51039	959.79798	308.75306
216.06061	108.546	467.32323	199.72463	718.58586	262.92252	969.84848	310.20034
226.11111	113.37026	477.37374	202.61919	728.63636	264.85223	979.89899	312.13004
236.16162	117.7121	487.42424	205.51375	738.68687	267.26436	989.94949	313.57732
246.21212	122.05394	497.47475	208.40831	748.73737	269.19407	1000	315.0246

Table A.3. Calculated enthalpy function, H_T-H_{298}. Temperature and enthalpy values are given in units K and J/(K·mol), respectively.

T	H_T-H_{298}	T	H_T-H_{298}	T	H_T-H_{298}	T	H_T-H_{298}
5	-4230.55345	256.26263	-18.19806	507.52525	53.38394	758.78788	85.16243
15.05051	-1403.85635	266.31313	-13.4209	517.57576	55.09138	768.83838	86.08908
25.10101	-838.86425	276.36364	-8.92139	527.62626	56.75023	778.88889	86.99677
35.15152	-595.29722	286.41414	-4.67533	537.67677	58.36231	788.93939	87.88623
45.20202	-458.56999	296.46465	-0.65533	547.72727	59.92933	798.9899	88.75814
55.25253	-370.27469	306.51515	3.15613	557.77778	61.45458	809.0404	89.61256
65.30303	-308.02744	316.56566	6.77891	567.82828	62.93772	819.09091	90.45013
75.35354	-261.41186	326.61616	10.22747	577.87879	64.38264	829.14141	91.27205
85.40404	-224.96014	336.66667	13.51599	587.92929	65.78882	839.19192	92.07774
95.45455	-195.51736	346.71717	16.65838	597.9798	67.15984	849.24242	92.86776
105.50505	-171.13537	356.76768	19.66565	608.0303	68.49663	859.29293	93.64324
115.55556	-150.54794	366.81818	22.54625	618.08081	69.79932	869.34343	94.40411
125.60606	-132.88261	376.86869	25.30906	628.13131	71.07031	879.39394	95.15143
135.65657	-117.52901	386.91919	27.96325	638.18182	72.31109	889.44444	95.88457
145.70707	-104.03527	396.9697	30.51585	648.23232	73.52158	899.49495	96.60455
155.75758	-92.05683	407.0202	32.97321	658.28283	74.7039	909.54545	97.31127
165.80808	-81.34143	417.07071	35.3399	668.33333	75.85861	919.59596	98.00569
175.85859	-71.68073	427.12121	37.62457	678.38384	76.98692	929.64646	98.68821
185.90909	-62.91667	437.17172	39.82847	688.43434	78.08929	939.69697	99.35818
195.9596	-54.91619	447.22222	41.9592	698.48485	79.16754	949.74747	100.01702
206.0101	-47.57692	457.27273	44.01842	708.53535	80.222	959.79798	100.66407
216.06061	-40.81104	467.32323	46.01178	718.58586	81.25302	969.84848	101.3002
226.11111	-34.54423	477.37374	47.94142	728.63636	82.26221	979.89899	101.92574
236.16162	-28.72093	487.42424	49.81127	738.68687	83.24916	989.94949	102.54052
246.21212	-23.28489	497.47475	51.62497	748.73737	84.21606	1000	103.14537

Table A.4. Calculated free energy function, G_T-H_{298}. Temperature and free energy values are given in units K and J/(K·mol), respectively.

T	G_T-H_{298}	T	G_T-H_{298}	T	G_T-H_{298}	T	G_T-H_{298}
5	-4230.69326	256.26263	-144.47936	507.52525	-157.9626	758.78788	-186.04858
15.05051	-1406.19989	266.31313	-143.87075	517.57576	-159.02623	768.83838	-187.17491
25.10101	-844.78382	276.36364	-143.45653	527.62626	-160.10146	778.88889	-188.29941
35.15152	-605.53548	286.41414	-143.21455	537.67677	-161.18763	788.93939	-189.42034
45.20202	-473.71452	296.46465	-143.12241	547.72727	-162.28327	798.9899	-190.53842
55.25253	-390.77579	306.51515	-143.16538	557.77778	-163.38613	809.0404	-191.65318
65.30303	-334.22355	316.56566	-143.326	567.82828	-164.49753	819.09091	-192.76473
75.35354	-293.53158	326.61616	-143.59196	577.87879	-165.61451	829.14141	-193.87318
85.40404	-263.12314	336.66667	-143.95093	587.92929	-166.73679	839.19192	-194.9775
95.45455	-239.76001	346.71717	-144.39484	597.9798	-167.86329	849.24242	-196.07841
105.50505	-221.42423	356.76768	-144.91381	608.0303	-168.99382	859.29293	-197.17546
115.55556	-206.79981	366.81818	-145.50034	618.08081	-170.12738	869.34343	-198.26879
125.60606	-194.9882	376.86869	-146.14776	628.13131	-171.26384	879.39394	-199.35852
135.65657	-185.35352	386.91919	-146.84882	638.18182	-172.40155	889.44444	-200.44369
145.70707	-177.44201	396.9697	-147.59824	648.23232	-173.54118	899.49495	-201.52553
155.75758	-170.90458	407.0202	-148.39243	658.28283	-174.6812	909.54545	-202.60255
165.80808	-165.48557	417.07071	-149.22584	668.33333	-175.82157	919.59596	-203.67597
175.85859	-160.98497	427.12121	-150.09457	678.38384	-176.96229	929.64646	-204.74486
185.90909	-157.24606	437.17172	-150.99509	688.43434	-178.10264	939.69697	-205.80988
195.9596	-154.14424	447.22222	-151.92418	698.48485	-179.24263	949.74747	-206.87014
206.0101	-151.58394	457.27273	-152.87994	708.53535	-180.38092	959.79798	-207.92628
216.06061	-149.47842	467.32323	-153.8586	718.58586	-181.51826	969.84848	-208.97845
226.11111	-147.76704	477.37374	-154.8587	728.63636	-182.65401	979.89899	-210.02626
236.16162	-146.39129	487.42424	-155.87695	738.68687	-183.78759	989.94949	-211.06937
246.21212	-145.30814	497.47475	-156.91223	748.73737	-184.91909	1000	-212.10839

Table A.5. Calculated Debye temperature function, θ_{Debye}. All values are given in K units.

T	θ_{Debye}	T	θ_{Debye}	T	θ_{Debye}	T	θ_{Debye}
5	158.23	256.26263	842.37149	507.52525	1075.73832	758.78788	1157.37723
15.05051	214.53138	266.31313	857.59832	517.57576	1080.75916	768.83838	1159.3997
25.10101	277.57936	276.36364	872.15777	527.62626	1085.5786	778.88889	1161.30081
35.15152	326.97289	286.41414	886.07979	537.67677	1090.17826	788.93939	1163.10002
45.20202	367.46264	296.46465	899.38664	547.72727	1094.64686	798.9899	1164.94219
55.25253	401.73049	306.51515	912.0999	557.77778	1098.87066	809.0404	1166.67223
65.30303	431.72708	316.56566	924.24511	567.82828	1102.98162	819.09091	1168.28909
75.35354	459.04221	326.61616	935.84721	577.87879	1106.89878	829.14141	1169.953
85.40404	484.79819	336.66667	946.93037	587.92929	1110.68758	839.19192	1171.57989
95.45455	509.67735	346.71717	957.518	597.9798	1114.31904	849.24242	1173.0142
105.50505	534.07047	356.76768	967.63275	608.0303	1117.82105	859.29293	1174.49868
115.55556	558.14883	366.81818	977.29654	618.08081	1121.18344	869.34343	1176.03374
125.60606	581.95215	376.86869	986.53066	628.13131	1124.435	879.39394	1177.35057
135.65657	605.45267	386.91919	995.35589	638.18182	1127.54118	889.44444	1178.65186
145.70707	628.5858	396.9697	1003.7926	648.23232	1130.58062	899.49495	1180.00585
155.75758	651.27175	407.0202	1011.86095	658.28283	1133.44014	909.54545	1181.38281
165.80808	673.42886	417.07071	1019.58104	668.33333	1136.30635	919.59596	1182.49491
175.85859	694.98988	427.12121	1026.96269	678.38384	1138.92838	929.64646	1183.66134
185.90909	715.90842	437.17172	1034.01602	688.43434	1141.56286	939.69697	1184.88199
195.9596	736.14451	447.22222	1040.77113	698.48485	1144.05563	949.74747	1186.12396
206.0101	755.66778	457.27273	1047.24789	708.53535	1146.46135	959.79798	1187.09458
216.06061	774.45852	467.32323	1053.45179	718.58586	1148.87479	969.84848	1188.12049
226.11111	792.51401	477.37374	1059.37269	728.63636	1151.05262	979.89899	1189.20139
236.16162	809.84994	487.42424	1065.06239	738.68687	1153.26132	989.94949	1190.33694
246.21212	826.4595	497.47475	1070.53419	748.73737	1155.39245	1000	1191.23935

APPENDIX B. Temperature dependent Debye temperature.

Debye temperature, Θ_D, is an important quantity which gives a relative idea for a temperature scale above which the vibrations within a solid behave classically and the heat capacity follows the Dulong-Petit law[1]. Below the Debye temperature the quantum effects are important. Debye temperature may be estimated in terms of the mean sound velocity of a crystal or elasticity constants[2]. Thus, its temperature dependence comes from that of elasticity constants and it is very slight.

A popular representation of the experimental data on heat capacity is based on the comparison of the actual heat capacity to that predicted by the Debye model. This leads to the concept of the temperature dependent Debye temperature, $\Theta_D(T)$. The constant volume heat capacity in the Debye model is given by[1]

$$C_v^D = 9\,nk\left(\frac{T}{\Theta_D}\right)^3 \int_0^{\Theta_D/T} \frac{x^4 e^x}{(e^x-1)^2}\,dx$$

Where n is the number of atoms per cell and k is the Boltzmann constant. Once the actual heat capacity value at a given T is known, one may determine Θ_D at that temperature by inverting this equation.

REFERENCES

1. Ashcroft, N.W.; Mermin, N.D. *Solid State Physics*; Harcourt College Publishers: New York, 1976.

2. Anderson, O.L. A Simplified Method for Calculating the Debye Temperature from Elastic Constants. *J. Phys. Chem. Solids* **1963**, *24*, 909–917.

Soddyite: Structure, Mechanical Properties, Equation of State, and Raman Spectroscopy

Article: "*Structural, mechanical and vibrational study of uranyl silicate mineral soddyite by DFT calculations*", by F. Colmenero, L. J. Bonales, J. Cobos and V. Timón, J. Solid. State. Chem. 253, 249–257 (2017).

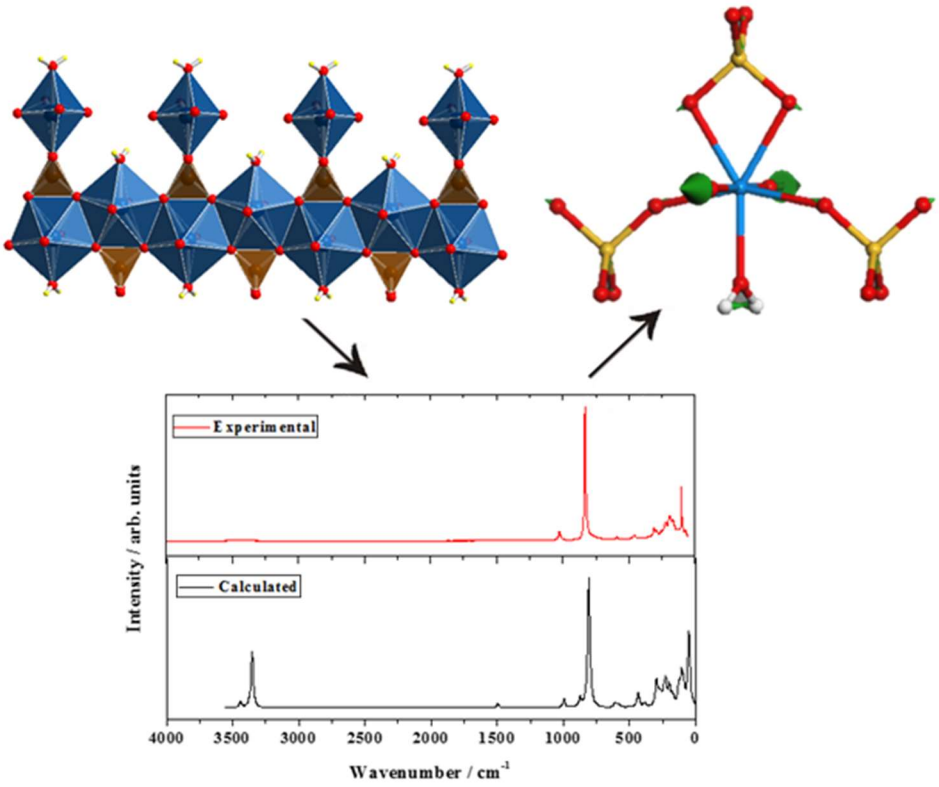

Journal of Solid State Chemistry 253 (2017) 249–257

Contents lists available at ScienceDirect

Journal of Solid State Chemistry

journal homepage: www.elsevier.com/locate/jssc

Structural, mechanical and vibrational study of uranyl silicate mineral soddyite by DFT calculations

Francisco Colmenero[a,*], Laura J. Bonales[b], Joaquín Cobos[b], Vicente Timón[a]

[a] Instituto de Estructura de la Materia, CSIC, C/ Serrano, 113, 28006 Madrid, Spain
[b] Centro de Investigaciones Energéticas, Medioambientales y Tecnológicas, CIEMAT, Avda/Complutense, 40, 28040 Madrid, Spain

ARTICLE INFO

Keywords:
Spent nuclear fuel
Soddyite
DFT
Mechanical properties
Raman spectroscopy

ABSTRACT

Uranyl silicate mineral soddyite, $(UO_2)_2(SiO_4)\cdot 2(H_2O)$, is a fundamental component of the paragenetic sequence of secondary phases that arises from the weathering of uraninite ore deposits and corrosion of spent nuclear fuel. In this work, soddyite was studied by first principle calculations based on the density functional theory. As far as we know, this is the first time that soddyite structure is determined theoretically. The computed structure of soddyite reproduces the one determined experimentally by X-Ray diffraction (orthorhombic symmetry, spatial group *Fddd O2*; lattice parameters a = 8.334 Å, b = 11.212 Å; c = 18.668 Å). Lattice parameters, bond lengths, bond angles and X-Ray powder pattern were found to be in very good agreement with their experimental counterparts. Furthermore, the mechanical properties were obtained and the satisfaction of the Born conditions for mechanical stability of the structure was demonstrated by means of calculations of the elasticity tensor. The equation of state of soddyite was obtained by fitting lattice volumes and pressures to a fourth order Birch-Murnahan equation of state. The Raman spectrum was also computed by means of density functional perturbation theory and compared with the experimental spectrum obtained from a natural soddyite sample. The results were also found in agreement with the experimental data. A normal mode analysis of the theoretical spectra was carried out and used in order to assign the main bands of the Raman spectrum.

1. Introduction

The resurgence of the use of nuclear energy is mainly driven by the need of more electricity for increasing populations and consumption, as well as the need of energy sources without CO_2 emissions and other greenhouse gases causing global warming [1–3]. However, the management of nuclear waste is a matter of concern because it can be a source of high ecological damage, in the same way as uranium ore mining [4] and nuclear accidents [5].

High-level nuclear waste, such as spent nuclear fuel (SNF) or reprocessed waste immobilized in a borosilicate glass [6], will be disposed of by burial in an underground geological repository. Contact of this waste with groundwater is expected after a time period of the order of some thousands of years [7] after closure, when the barriers that protect the waste will be breach [3]. The reducing conditions in the deep geological disposal at this time will not be maintained, and oxidized species near the spent fuel surface will increase due to the radiolysis of water caused by the ionizing radiation associated with the SNF [8–12]. Therefore, uranium in the matrix of the spent nuclear fuel, composed by uranium dioxide, $U^{IV}O_2$, could oxidize to U(VI) and dissolve into the water forming uranyl groups. These uranyl groups can precipitate forming secondary phases, *i.e.* alteration products, on the spent fuel surface depending on the local physico-chemical conditions and concentrations of reactive species present [12]. These secondary phases can reduce the release and environmental impact of the fission products and heavier actinides contents in the SNF to the biosphere [9,13]. The knowledge of the structures of these phases may be a key to evaluate the possible incorporation of fission products and transuranic elements into their crystal structures [13–19].

Uranyl secondary phases are usually studied by analyzing natural minerals containing the uranyl ion [20], $U^{VI}O_2^{2+}$, found as alteration products of uraninite [12], which is a natural analogue of the SNF matrix. The general trend of the temporal sequence of alteration products of natural uraninites at different geochemical conditions was first recognized by Frondel [21], and it is still widely accepted nowadays [12,22,23]. In this sequence, the uranyl oxide hydrates appear at the first place, then the uranyl silicates and, less frequently, the uranyl phosphates; although the specific alteration products depend on the local conditions. Therefore, the study of these uranyl

* Corresponding author.
E-mail address: francisco.colmenero@iem.cfmac.csic.es (F. Colmenero).

http://dx.doi.org/10.1016/j.jssc.2017.06.002
Received 2 May 2017; Received in revised form 31 May 2017; Accepted 3 June 2017

minerals is very important for understanding the long-term performance of a geological repository for nuclear waste.

One of the minerals found very often in nature as alteration product of uraninite is soddyite. Mineral soddyite is a hydrated uranyl nesosilicate which was found in Shinkolobwe Mine (Kasolo Mine), Shinkolobwe, Katanga Cooper Crescent, Katanga (Shaba), Democratic Republic of Congo (Zaire). It was first described by Schoep in 1922 [24]. In nature, soddyite occurs as fine grained pale-yellow aggregates or flat crystals or fibers having a color from greenish to canary yellow [25]. Soddyite, $(UO_2)_2(SiO_4)\cdot 2(H_2O)$, is the unique uranyl silicate mineral known characterized by a 2:1 uranium to silicon ratio [26]. Most uranyl silicate minerals have a 1:1 uranium to silicon ratio and contain sheets [14,20,26], except soddyite [27] and weeksite [17], which have framework crystal structures [14,15,27]. Soddyite is isostructural to the uranyl germanate mineral [26,27] studied by Legros et al. [28]. The crystal structure of $Na_2(UO_2)_2SiO_4F_2$ [29] is structurally related to soddyite. Its structure is very complex and includes 136 atoms in the unit cell, as well as 768 valence electrons. In oxidizing waters that contain uranyl and silicate ions, the solid uranyl orthosilicate may form as a solubility-controlling solid [30]. It has been synthetized in the laboratory, for example, by Legros et al. [31], Kuznetsov et al. [32,33] and Moll et al. [30]. The latter synthesized the uranyl orthosilicate with reproducible yields of about 81%, and phase purity.

The present state of knowledge about the crystal chemistry and bonding of the uranium ion in these systems is very incomplete. As noted by Weck et al. [34], the existence of a great amount of information on the formation, thermodynamic stability, and phase transformations of alteration phases formed at the SNF surface is in stark contrast with the paucity of data regarding the mechanical stability and properties of these phases. Saving the theoretical study of Weck et al. [34] on the uranyl peroxide hydrates, studtite and metastudtite, no experimental or computational studies have reported the mechanical properties (bulk and shear moduli, stiffness coefficients, anisotropy factors, etc.) of these phases [35]. Furthermore, the conditions of mechanical stability of their structures have not been analyzed. Whereas the lack of the experimental data could be related to the special care needed to handle these radioactive minerals, the computational data are scarce due to the difficulties in the application of theoretical methods to uranium containing solids. The calculations are very computationally demanding, not only due to the great size of the corresponding unit cells, but also to the high level of theory required to describe correctly these systems [36]. For example, there is very few published works on the theoretical vibrational spectra of uranium containing solids [37–40], and none of these works includes a complete determination of these spectra.

Despite the structure of soddyite have been determined by experimental X-ray diffraction techniques, it has never been confirmed by means of theoretical solid state calculations. In this paper, we perform a complete structural characterization of soddyite by theoretical solid state methods, which allow us to confirm the structure obtained experimentally. From the obtained structure, we had studied the mechanical properties and stability of soddyite structure, based on the elastic constants computed in this study. The elastic constant tensor of an inorganic compound provides a complete description of the response of the material to external stresses in the elastic limit [35]. The analysis of this tensor, which is usually correlated with many mechanical properties, allows to understand the nature of the bonding in the material. Soddyite equation of state is also reported. Besides, although the Raman spectrum of this mineral has been determined by experimental methods [41–44], a precise assignation of the main bands in the spectra is lacking, since they have been characterized incompletely and by using empirical arguments. The theoretical Raman spectrum of soddyite is reported here, including the computation of intensities and the assignment of the vibrational bands. We have performed the assignment of the experimental vibrational Raman bands since theoretical methods provide detailed microscopic scale views of the atomic vibrational motions in the corresponding normal modes. Computations were carried out by means of Density Functional Theory [45] (DFT) based on plane waves and pseudopotentials [46]. A norm conserving relativistic pseudopotential for uranium atom [47] developed in a previous paper [48] was used.

2. Materials and methods

2.1. Experimental

The mineral sample studied in this work [49] is a natural mineral from Sierra Albarrana (Córdoba, Spain) whose structure corresponds to the ideal gummite occurrence [21] (central core black and a yellow surrounding zone, formed by several minerals). The sample contains a mixture of alteration phases of natural uraninite: rutherfordine, soddyite, uranophane and kasolite. Soddyite prevails in the inner part of the sample.

A polished section of the sample was analyzed by Raman using a Horiba LabRam HR evolution spectrometer (Jobin Yvon Technology). A red laser of HeNe with a wavelength of 632.81 nm and an operation power of 20 mW was used as excitation source. The laser was focused onto the sample by using 100x objective at the confocal microscope BX4 with confocal 800 mm; the scatter light was collected with the same objective and then dispersed with a Jobin-Yvon spectrometer (600 grooves/mm), and detected with a Peltier cooled CCD detector (256 × 1024 pixel). The spectral resolution was about 1 cm^{-1} per pixel.

2.2. Theoretical DFT calculations

CASTEP code [50], a module of the Materials Studio package [51], was employed to model soddyite structure. The generalized gradient approximation (GGA) together with PBE functional [52] and Grimme empirical dispersion correction [53], called the DFT-D2 approach, were used. The Grimme dispersion correction was included to describe correctly the hydrogen bonds present in the soddyite structure. The pseudopotentials used for H, O and Si atoms in the unit cell of soddyite mineral were standard norm-conserving pseudopotentials [47] given in CASTEP code (00PBE-OP type). The norm-conserving relativistic pseudopotential for U atom was generated from first principles as shown in a previous work [48].

Geometry optimization was carried out by using the Broyden–Fletcher–Goldfarb–Shanno optimization scheme [46,54] with a convergence threshold on atomic forces of 0.01 eV/Å. The kinetic energy cut-off and k-point mesh [55] was adopted to ensure good convergence for computed structures and energies. Soddyite structure was optimized in calculations with increasing complexity by increasing these parameters. The optimization performed with a cut-off of 930 eV and a K mesh of 3 × 2 × 1 gave a well converged structure, and it was used to determine the final results.

Elastic constants, used for the calculation of mechanical properties and to study the mechanical stability of soddyite crystal structure, were calculated from stress-strain methodology. With this purpose, finite deformation technique is employed in CASTEP. In this technique, finite programmed symmetry-adapted strains [35] are applied to the equilibrium conformation generating a set of distorted structures. The individual elastic constants are then extracted from the stress tensor obtained as response of the system to the applied strains. For the calculation of elastic tensor, this stress-based method appears to be more efficient than the energy-based methods and the use of DFPT [56].

Bulk modulus and its pressure derivatives were also calculated by fitting the lattice volumes and pressures to an equation of state. In the present study, the lattice volumes around the equilibrium were calculated by optimizing the structure at several different pressures −1.0, −0.75, −0.50, −0.25, 0.0, 0.25, 0.50, 0.75, 1.0, 1.5, 2.0, 3.0, 4.0,

5.0, 7.0, and 9.0 GPa, where negative pressure values mean traction or tension. The results were then fitted to a fourth-order Birch-Murnaghan equation of state [57] using EOSFIT 5.2 code [58].

For the calculations of vibrational properties, the linear response density functional perturbation theory (DFPT) [59–61], implemented in the CASTEP code, was used in the same way as in previous works [48,62].

3. Results and discussion

The unit cell parameters and internal atomic positions were first optimized using an initial atomistic model based in the atomic coordinates given by Demartin et al. [27] From the optimized structure, we have obtained both the structural parameters as well as the X-Ray powder pattern. The elastic tensor was calculated, for the optimized equilibrium structure, from the stress-strain relationships by using the finite deformation technique implemented in CASTEP. From the elastic tensor, mechanical properties such as elastic modulus, shear modulus, Vickers hardness and anisotropy index were then computed. Besides, the soddyite equation of state was obtained by fitting lattice volumes and pressures to a fourth order Birch-Murnahan equation of state. Finally, the vibrational Raman spectrum was predicted as a list of wavenumbers and intensity values for each normal mode [61]. Experimental Raman spectrum was then compared with the computed one, and the assignment of main fundamental band frequencies was carried out.

3.1. Structure

Stohl and Smith [26] categorized the naturally occurring uranyl silicates according to the uranium to silicon ratio, which in part determines the structure of these minerals. Most uranyl silicate minerals, as uranophane and boltwoodite, are sheet silicates with a 1:1 uranium to silicon ratio [14,20,26]. The sheets are composed of $[(UO_2)_2(SiO_4)_2]^{1-}$ units bound at the equatorial edges. Charge compensating cations, as calcium in uranophane and potassium in boltwoodite, lie in the interlayer space between the sheets. Soddyite [27] and weeksite [17] have uranium to silicon ratios of 2:1 and 2:5, respectively, and their structure involve frameworks of U^{6+} polyhedra [14,15,27]. In soddyite, charge compensation for the uranyl silicate groups is not required as the basic building unit is neutral $[(UO_2)_2(SiO_4)]$ [63].

The computed structure is shown in Fig. 1. Fig. 1A shows a view of the unit cell from [001]. Fig. 1B is a view of a 2 × 2 × 1 supercell along [110]. Fig. 1C is a view of the latter cell where only a subset of atoms is retained in order to show a clearer view of the soddyite structure. As can be seen, U atoms display pentagonal bipyramid coordination, $UO_6(H_2O)$, and Si atoms present tetrahedral coordination, SiO_4. The U bipyramids are connected by sharing two non-adjacent edges of the equatorial plane to form zigzag chains (see Fig. 1C). The single unshared equatorial vertex of the bipyramid is occupied by H_2O. The chains are parallel to [110] plane and are cross bonded through two opposite edges of the SiO_4 tetrahedra; *i.e.* adjacent uranyl silicate chains are directly linked as each tetrahedron shares two edges with bipyramids from two different chains. Moreover, the cohesion of the structure is enhanced by a pattern of hydrogen bonds involving the water molecules and the uranyl O atoms.

As mentioned, the structure of soddyite was determined in calculations with increasing complexity. Table 1 gives the final lattice parameters, volumes and densities obtained compared with the experimental ones from Demartin et al. [27]. As it can be seen, theoretical and experimental results are in good agreement. The computed volume and density differ from the corresponding experimental values by about 0.3%.

Tables A.1 and A.2 of Appendix A of the Supplementary Information give a comparison of the more important geometric

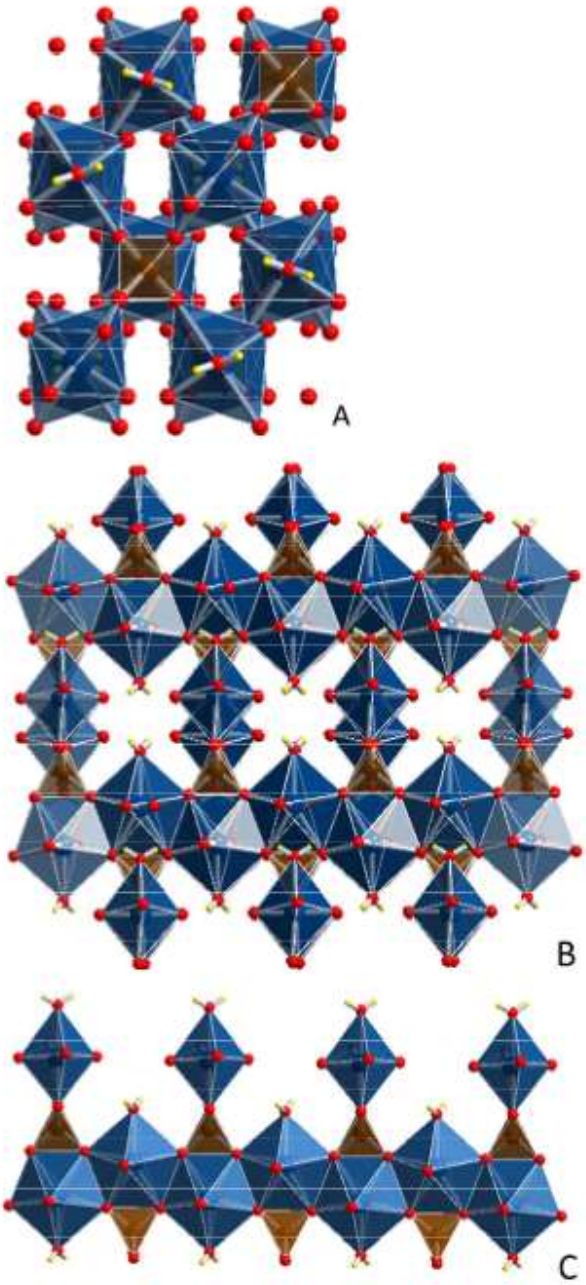

Fig. 1. Structure of soddyite mineral: A) View of the unit cell from [001]; B) View of a 2 × 2 × 1 supercell from [110]; C) View of a 2 × 2 × 1 supercell from [110], retaining only a subset of atoms (a single chain of U bipyramids cross bonded to other chains through two opposite edges of the SiO_4 tetrahedra is shown). Color code: U-Blue, Si-Brown, O-Red, H-Yellow. (For interpretation of the references to color in this figure legend, the reader is referred to the web version of this article).

Table 1
Lattice parameters.

Parameter	a (Å)	b (Å)	c (Å)	α	β	γ	Vol. (Å^3)	Dens. (g/cc)
Calc.	8.0780	11.4253	18.8380	90	90	90	1738.6	5.104
Exp. [27]	8.334	11.212	18.668	90	90	90	1744.4	5.088

parameters (bond distances and angles) obtained with the corresponding experimental data of Demartin et al. [27]. Soddyite has only one structurally (symmetrically) identical U^{6+} ion and one structurally (symmetrically) identical Si^{4+} ion in its crystal structure. The two O atoms in the uranyl group, UO_2^{2+} (O1 and its symmetry related companion), are in apical positions of the pentagonal bipyramids at a distance of 1.781 Å. The calculated value is 1.801 Å. The remaining five O atoms (four O2 and OW) lie in the equatorial plane which U-O distances which range from 2.313 to 2.424 Å (calculated 2.312–2.436 Å). The distances between adjacent O atoms range from 2.462 to 3.126 Å (calculated 2.467–3.166 Å), the shortest values corresponding to the shared edges with other U centered bipyramids and SiO_4 groups. The SiO_4 tetrahedron is markedly irregular, the O-Si-O angles ranging from 98.0 to 119.0 degrees (calculated 98.1 and 119.6 degrees). The O-O distances range from 2.462 to 2.811 Å (calculated 2.487 and 2.846 Å). The Si-O distances, 1.631 Å, are within the normal range, the calculated value being of 1.647 Å. The geometry and orientation of the plane of water molecule is mainly determined by the hydrogen bond interaction, directed towards O1. The OW-H-O1 angle determined experimentally is 156 degrees, which is satisfactorily reproduced in our calculations, 149 degrees.

The X-Ray powder diffractogram of soddyite was computed from the experimental [27] and computed structures [64] using CuK_α radiation (λ = 1.540598 Å). The most intense lines (I > 10%) are compared in Fig. 2. As it can be seen, the agreement in line positions and intensities is very good. The use of spectra derived directly from the experimental and computed structures allows for a fair comparison of the results free of interferences and possible artefacts, as the presence of sample impurities, because both are determined under the identical conditions. Nevertheless, the use of an experimental pattern also leads to an excellent agreement. Computer program XPowder [65] using the PDF-2 database [66] recognizes the computed spectrum as that of soddyite (pattern 77–0604, which corresponds to synthetic soddyite sample, see Nozik and Kuznetsov [33]). The values of the main reflections are given in Table A.3 of Appendix A of the Supplementary Information.

3.2. Mechanical properties and stability

Elastic tensor, used for the calculation of mechanical properties and for analyzing the mechanical stability of soddyite crystal structure, was calculated for the optimized equilibrium structure, from the stress-strain relations by using the finite deformation technique implemented in CASTEP. Crystals with orthorhombic symmetry have 9 non-degenerate elastic constants in the symmetric stiffness matrix [34,35], which may be written as:

$$C = \begin{pmatrix} C_{11} & C_{12} & C_{13} & 0 & 0 & 0 \\ C_{12} & C_{22} & C_{23} & 0 & 0 & 0 \\ C_{13} & C_{23} & C_{33} & 0 & 0 & 0 \\ 0 & 0 & 0 & C_{44} & 0 & 0 \\ 0 & 0 & 0 & 0 & C_{55} & 0 \\ 0 & 0 & 0 & 0 & 0 & C_{66} \end{pmatrix}$$

Here, we use the standard Voigt notation for the indices contracting a pair of Cartesian indices into a single integer $1 \le i \le 6$: xx → 1, yy → 2, zz → 3, yz → 4, xz → 5, xy → 6. The precise values of these constants obtained in our computations are given in Table 2.

Table 2
The nine independent elastic constants in the stiffness matrix for the orthorhombic lattice structure of soddyite. All values are given in GPa.

C_{11}	C_{22}	C_{33}	C_{44}	C_{55}	C_{66}	C_{12}	C_{13}	C_{23}
81.65	120.92	161.54	40.99	25.93	42.14	35.61	22.59	49.84

For orthorhombic crystals, the necessary and sufficient Born criteria for mechanical stability are [34,67]:

$C_{11}>0 (i = 1, 4, 5, 6)$
$C_{11}C_{22}-C_{12}C_{12}>0$
$C_{11}C_{22}C_{33}+2C_{12}C_{13}C_{23}-C_{11}C_{23}C_{23}-C_{22}C_{13}C_{13}-C_{33}C_{12}C_{12}>0$

Since the above conditions are fulfilled by the elastic constants of soddyite reported in Table 2, its mechanical stability can be inferred. The generic necessary and sufficient Born criterion that all eigenvalues of the C matrix be positive [67] was also checked. The C matrix was diagonalized numerically, and all eigenvalues were found to be positive, as expected. The lowest eigenvalue was about 0.026, so that the soddyite structure is far from instability.

The fact that C_{11}, the diagonal component of the C matrix along a direction, is much smaller than either C_{22} or C_{33}, suggests that the thermal expansion of the material will occur predominantly along this

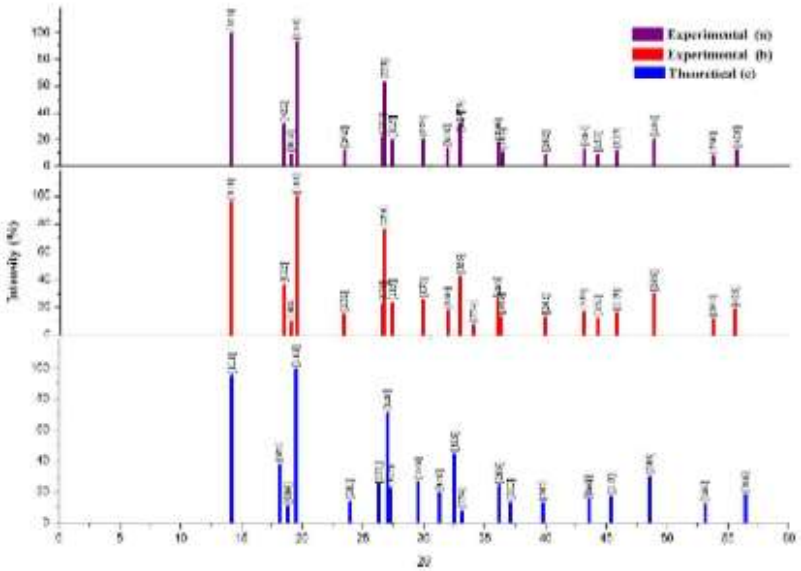

Fig. 2. X-Ray powder pattern of soddyite using CuKα radiation: a) Experimental pattern (pattern 77–0604 in the PDF-2 database); b) X-Ray powder pattern computed from experimental geometry [27]; c) X-Ray powder pattern computed from calculated geometry.

Table 3
Bulk, modulus, shear modulus, Young modulus, Poisson ratio, Pugh's ratio, and Vickers hardness (B, G, E, ν, D, and H) calculated in the Voigt, Reuss, and Hill approximations. Values of B, G and E are given in GPa.

Property	Voigt	Reuss	Hill
B	64.4615	58.4136	61.4375
G	38.8807	36.0015	37.4411
E	97.1164	89.5976	93.3586
ν	0.2489	0.2444	0.2467
D	1.6579	1.6225	1.6409
H	6.4217	6.2374	6.3280

direction (contained in the plane of the soddyite chains). C_{33} is the largest diagonal component (along the perpendicular direction to soddyite chains).

If single crystal samples are not available, the measurement of the individual elastic constants cannot be possible. Instead, the polycrystalline bulk modulus (B) and shear modulus (G) may be determined experimentally. The Voigt and Reuss [35] schemes were used to compute the isotropic elastic properties of soddyite polycrystalline aggregates. As shown by Hill [68], the Reuss and Voigt approximations result in lower and upper limits, respectively, of polycrystalline constants, and practical estimates of the polycrystalline bulk and shear moduli in the Hill approximation can be computed using average formulas. Relevant formulae for these approximations may be found in several sources (see for example Weck et al. [34]). The bulk and shear moduli and other mechanical properties computed in these approximations are given in Table 3.

The numerical estimate of the error in the computed bulk modulus given by the CASTEP code is 2.312 GPa, quite similar to the difference of the values in the Hill and Voigt/Reuss schemes, 3.024 GPa. Voigt and Reuss methods yield quite small differences for soddyite. Larger differences are expected for crystalline systems with strong anisotropy, featuring large differences between elastic constants along different directions [34]. The values of the bulk modulus computed by Weck et al. [34] for studtite and metastudtite (about 30 and 42 GPa, respectively) are smaller than the value obtained here for soddyite.

In general, a large value of the shear moduli is an indication of the more pronounced directional bonding between atoms. The shear modulus G represents the resistance to plastic deformation, while the bulk modulus represents the resistance to fracture [69]. Young modulus defines the relationship between stress (force per unit area) and strain (proportional deformation) in a material, that is, $E = \sigma/\varepsilon$. The individual components of Bulk and Young's moduli may be derived from the elastic compliance matrix components [34,70]. Compliance matrix is the inverse of stiffness C matrix. For example, the E components along a, b, and c directions can be expressed as $E_a = S_{11}^{-1}$, $E_b = S_{22}^{-1}$ and $E_c = S_{33}^{-1}$. The corresponding values are given in Table 4. As it can be seen, B_c is larger than either B_a or B_b. Thus, c direction is the least compressible. Also, the component E_c is much larger (stiffer) than E_a and E_b. Thus, the direction perpendicular to the plane containing the chains is the stiffest, in agreement with the results of the stiffness C matrix.

Pugh [71] introduced the proportion of bulk to shear modulus of polycrystalline phases ($D = B/G$) as a measure of ductility by considering the interpretation of the shear and bulk modulus given above. A higher D value is usually associated with a higher ductility. The critical value which separates ductile and brittle materials is 1.75, *i.e.*, if $B/G > 1.75$, the material behaves in a ductile manner, otherwise the material behaves in a brittle manner [70]. The Poisson's ratio, ν, can also be utilized to measure the malleability of crystalline compounds [71], and is related to the Pugh's ratio given above by the relationship $D = (3 - 6\nu)/(8 + 2\nu)$. The Poisson's ratio is close to 1/3 for ductile materials, while it is generally much less than 1/3 for brittle materials. As it can be seen in Table 3, for soddyite we found ratios D and ν about 1.65 and 0.25, respectively. These values are only slightly smaller than 1.75 and 1/3, respectively. Therefore, soddyite corresponds to a brittle material. For comparison, both studtite and metastudtite minerals were found to be ductile [34].

Hardness of these systems was computed according to a recently introduced empirical scheme [72], which correlates the Vickers hardness and the Pugh's ratio ($D = B/G$). Vickers hardness, H, of polycrystalline soddyite is given in Table 3. Its value, about 6.3, corresponds to a material of intermediate hardness. For comparison, we computed the hardness of studtite and metastudtite by using the elasticity data of Weck et al. [34]. These systems, characterized by much larger D ratios, have much smaller hardness (smaller than one).

In order to assess the elastic anisotropy of soddyite, shear anisotropic factors were obtained. These factors provide a measure of the degree of anisotropy in the bonding between atoms in different planes, and are very important to study material durability. Shear anisotropic factors for the {100} (A_1), {010} (A_2), and {001} (A_3) crystallographic planes and percentages of anisotropy in compression and shear (A_{comp} and A_{shear}) were computed by using the formulae given by Ravindran et al. [69]. For an isotropic crystal, the factors A_1, A_2, and A_3 must be one, while any value smaller or greater than unity is a measure of the degree of elastic anisotropy possessed by the crystal. For percentage anisotropies, a value of 0% represents a perfectly isotropic crystal. For soddyite (see Table 5), the anisotropies grow in the planes {100}, {001}, and {010} ($A_1 < A_3 < A_2$). The {010} plane is shown to be the most anisotropic one. Percentage anisotropies in compression and shear were about 5% and 4%, respectively.

In the recently introduced universal anisotropy index [73], the departure of A^U from zero defines the extent of single crystal anisotropy and accounts for both the shear and the bulk contributions unlike all other existing anisotropy measures. Thus, A^U represents a universal measure to quantify the single crystal elastic anisotropy. Soddyite is characterized by an anisotropy index of 0.50, which is a rather small value ($A^U = 0$ corresponds to a perfectly isotropic crystal). For comparison, studtite and metastudtite exhibit much larger anisotropies, the values computed by Weck et al. [34] being of 2.17 and 1.44, respectively.

A set of fundamental physical properties may be estimated using the calculated elastic constants. For example, V_L and V_T, the transverse and longitudinal elastic wave velocities of the polycrystalline materials, may be determined in terms of the bulk and shear moduli [34]. The values obtained were 2.708 and 4.671 km/s, respectively, by using the calculated crystal density of 5.104 g/cc (see Table 1).

3.3. Equation of state

Lattice volumes around the equilibrium were calculated by optimizing the structure at sixteen different applied pressures. The results are displayed in Fig. 3.

The calculated data were fitted to a fourth-order Birch-Murnaghan

Table 4
Bulk and Young moduli components along the crystallographic axes. All values are given in GPa.

Property	a axis	b axis	c axis
B	105.10	251.92	275.08
E	70.68	95.09	140.12

Table 5
Shear anisotropy factors (A_1, A_2 and A_3), percentages of anisotropy in compression and shear (A_{comp} and A_{shear}), and universal anisotropy index (A^U).

A_1	A_2	A_3	A_{comp} (%)	A_{shear} (%)	A^U
0.8282	0.5674	1.2836	4.9220	3.8449	0.5034

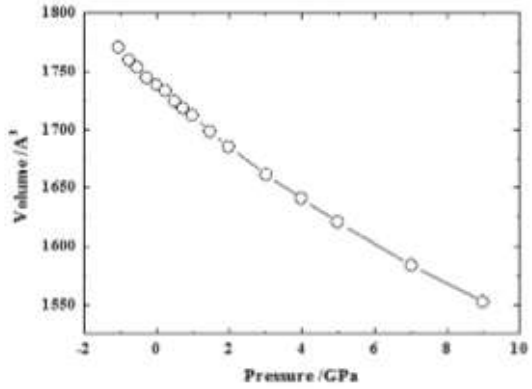

Fig. 3. Soddyite unit cell volume vs. applied pressure.

equation of state [57] (EOS) using the volume at 0 GPa (1738.6 Å^3) as V_0 with the EOSFIT 5.2 code [58]:

$$P = 3Bf_E(1+2f_E)^{\frac{5}{2}}\left[1+\frac{3}{2}(B'-4)f_E+\frac{3}{2}\left\{BB''+(B'-4)(B'-3)+\frac{35}{9}\right\}f_E^2\right]$$

In this equation,

$$f_E = \frac{1}{2}\left[\left(\frac{V_0}{V}\right)^{\frac{2}{3}}-1\right]$$

and B, B' and B'' are the bulk modulus and its first and second derivatives, respectively, at the temperature of 0 K. The values found for the bulk modulus and its derivatives were B = 60. 07(±0. 67) GPa, B' = 4. 19(±0. 60), and B'' = 0. 25(±0. 20) GPa^{-1} (χ^2 = 0.001). The bulk modulus found agrees very well with those determined from calculated elastic constants given in Table 3. As in other works [74], the agreement is better with the bulk modulus obtained in the Reuss approximation (B = 58. 41 ± 2. 31 GPa). This is due to the fact that values of B obtained from the EOS are generally smaller than those obtained from elastic tensor. The explanation can be found in that in this case the cell shapes are relaxed, whereas the cell shapes are kept fixed in the determinations of the elastic constants [75].

3.4. Raman spectra and band assignment

The theoretical Raman spectrum in the wavenumber range of 3600–0 cm^{-1} is compared with the one obtained experimentally in Fig. 4. As can be seen in this figure, the calculated spectrum is quite similar to the experimental one. The theoretical spectrum was computed at T = 298 K, λ = 532 nm, FWHM = 20 cm^{-1}. Pictures of the atomic motions in the Raman active vibrational modes are given in Appendix B of Supplementary Information (Fig. B.1).

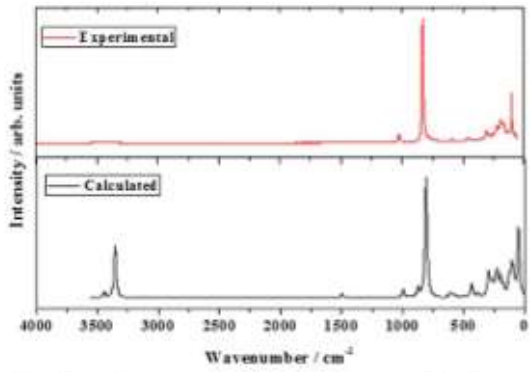

Fig. 4. Experimental and calculated Raman spectra of soddyite mineral.

In order to calculate the number of contributions of a given band in the experimental spectrum, we carry out the analysis by using the second derivative method [48,49]. In Fig. 5, we show the experimental and theoretical Raman spectra divided in four regions: (A) OH stretching vibration region from 3800 to 3000 cm^{-1} (Fig. 5. A); (B) H_2O bending region 1800–1300 cm^{-1} (Fig. 5. B); (C) uranyl UO_2^{2+} and silicate SiO_4^{4-} fundamental vibrations region from 1400 to 700 cm^{-1} (Fig. 5. C); and (D) low wavenumber region from 700 to 0 cm^{-1} (Fig. 5. D). The wavenumber of both spectra along with the corresponding calculated intensities and assignments are given in Table 6. The Raman shifts and assignments performed by Frost et al. [44] are also given in this table for comparison. The results obtained in each region are described in the next paragraphs.

(A) *OH stretching vibrations region*

In the hydroxyl stretching region we found one broad band with two contributions at about 3488 cm^{-1} and 3398 cm^{-1}. The corresponding computed Raman shifts are 3443 and 3353 cm^{-1}. These bands were assigned to antisymmetric and symmetric water stretching vibrations, ν^a(OH) and ν^s(OH), respectively. Although the difference of computed and experimental shifts is quite large, it must be noted that the infrared OH stretching frequencies calculated for uranyl silicate clusters have much larger differences with respect to the experimental data [76]. Note that the low intensity contribution band at wavenumber 3147 cm^{-1} is not found in the calculated spectrum. This band was also found by Frost et al. [44] at 3158 cm^{-1}.

(B) *H_2O bending vibration region*

The Raman shift associated to the water bending vibration, δ(H_2O), was found to be placed at about 1584 cm^{-1}, comparable to the calculated wavenumber of 1495 cm^{-1}. Note that Frost et al. [44] found a shoulder at 1596 cm^{-1}. This was attributed to water absorbed on the sample surface [30].

(C) *Uranyl UO_2^{2+} and silicate SiO_4^{4-} fundamental vibrations region*

The experimental band at 1024 cm^{-1} corresponds to the band calculated at 995 cm^{-1}, which was assigned to the SiO_4^{4-} asymmetric stretching vibration, $\nu^a(SiO_4)^{4-}$ (see vibrational mode picture in Appendix B of the Supporting Information). Similar wavenumbers were found by Frost et al. [44] and Biwer et al. [42] (1025 and 1018 cm^{-1}, respectively).

The most intense band in the Raman spectrum is found experimentally at about 830 cm^{-1}, and calculated at 807 cm^{-1}. This band was found to be placed at 824, 830, and 828 cm^{-1} by Biwer et al. [42], Amme et al. [43] and Frost et al. [44]. As it can be observed in the vibrational mode picture in Appendix B, it was assigned to UO_2^{2+} symmetric stretching vibration, $\nu^s(UO_2)^{2+}$.

It should be noted that in the computed spectrum appears two very close bands at 874 and 873 cm^{-1}. Frost et al. [44] also found two bands in this region at 909 and 897 cm^{-1}, which were attributed to the $\nu^a(UO_2)^{2+}$ vibration. Based in our computed results we think that the band at 909 cm^{-1} corresponds to the calculated vibration at 873 cm^{-1}, which is attributed to the symmetric stretching SiO_4^{4-} vibration. Additionally, Frost et al. [44] found a band at 791 cm^{-1}, which was assigned it to water librational vibrations. This band is close to the computed one at 799 cm^{-1}, assigned to $\nu^s(UO_2)^{2+}$ vibration.

(D) *Low wavenumber region*

The bands computed at 610 and 579 cm^{-1} are comparable to the experimental value of 592 cm^{-1}. They were assigned to the water librational vibrations (twisting and rocking, respectively). In the experimental work of Frost et al. [44], the 591 cm^{-1} band was assigned to a silicate bending vibration, δ(SiO_4)$^{4-}$. This kind of vibration appears in the theoretical spectrum at 431 cm^{-1}, which is comparable to the experimental band at 460 cm^{-1}. The corresponding values found by Biwer et al. [42], Amme et al. [43] and

Frost et al. [44], are 457, 455 and 459 cm^{-1}, respectively. While Biwer et al. [42], attribute this band to an equatorial UO stretching vibration, Frost et al. [44], assign this band to $\delta(SiO_4)^{4-}$ vibration in agreement with the data from this work. The free ion value for this vibration is 527 cm^{-1} [77,78].

The bands calculated at 299, 296 and 295 cm^{-1} were assigned mainly to a silicate translation the first, and the other ones to different silicate deformation vibrations, $t(SiO_4)^{4-}$ and $\rho(SiO_4)^{4-}$ (twisting and rocking). They are comparable to the experimental band at about 289 cm^{-1}.

Finally, the band calculated at 50 cm^{-1} can be approximately mapped to the experimental shift of 103 cm^{-1}.

4. Conclusions

In this work, soddyite structure was determined theoretically for the first time. The calculations have been performed by using the CASTEP module of Materials Studio software. The pseudopotentials used for H, O and Si atoms in the unit cell of soddyite mineral were standard norm-conserving pseudopotentials, whereas the pseudopotential for U atom was generated from first principles in a previous paper [48].

These calculations, based on density functional theory, show the role of water in the structural and vibrational properties of the uranyl silicate mineral soddyite. Water molecules enter in the structure of soddyite as structural water forming part of the coordination structure of uranium atom, that is, within the pentagonal bipyramids, $UO_6(H_2O)$. Structural optimization performed by using the GGA-PBE exchange-correlation functional, taking into account a dispersion correction scheme, has given unit cell lattice parameters, atomic bond distances and angles in excellent agreement with experimental data. The computed X-Ray powder pattern was also in very good agreement with the experimental pattern.

Elastic tensor was calculated from stress-strain relationships by using the finite deformation technique implemented in CASTEP for the optimized equilibrium structure. The analysis of the calculated elasticity stiffness tensor has revealed that the soddyite structure satisfies properly the mechanical stability conditions. Furthermore, mechanical properties of this mineral, for which there are not experimental data to compare with, were predicted. Mechanical data reported here include the bulk modulus, elastic coefficients, shear and Young moduli, Poisson

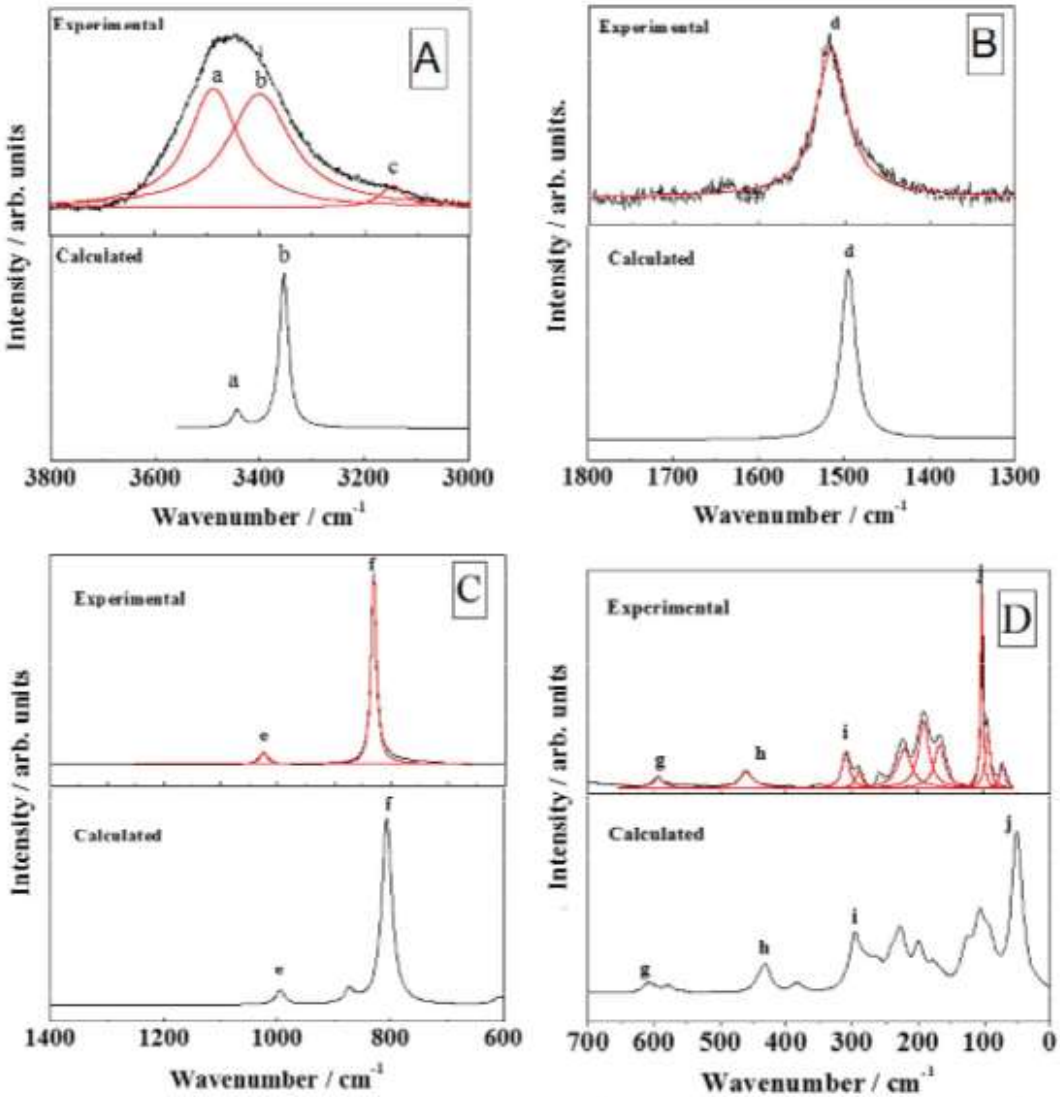

Fig. 5. Experimental and theoretical Raman spectra of soddyite mineral. (A) Region: 3800–3000 cm^{-1}; (B) Region: 1800–1300 cm^{-1}; (C) Region: 1400–700 cm^{-1}; (D) Region: 700–0 cm^{-1}.

Table 6
Experimental and calculated Raman band wavenumbers, calculated intensities and assignations. Raman shifts and assignments performed by Frost et al. [44] are also given in this table for comparison.

Band Name	Exp. Raman shift (cm^{-1}) (This work)	Exp. Raman shift (cm^{-1}) (Frost et al. [44]) shift/assignation	Calc. Raman shift (cm^{-1})	Irr. Rep. (D_{2h})	Int. ($Å^4$)	Assignment
OH stretching region						
a	3488	3516/ν(OH)	3443	B_{2g}	3229.1	$\nu^a(OH)$
b	3398	3414/ν(OH)	3353	A_g	27,818.8	$\nu^s(OH)$
c	3147	3158/ν(OH)	–	–	–	–
H_2O bending region						
d	1584	1584,1596/δ(H_2O)	1495	A_g	433.8	δ(H_2O)
UO_2^{2+} and SiO_4^{4-} fundamental vibrations region						
e	1024	1025/$\nu^s(SiO_4)^{4-}$	995	B_{1g}	750.1	$\nu^a(SiO_4)^{4-}$
	–	909,897/$\nu^s(UO_2)^{2+}$	874	B_{2g}	53.5	$\nu^s(UO_2)^{2+}$+ρ(H_2O)
			873	A_g	583.7	$\nu^s(SiO_4)^{4-}$
f	830	838,828,820/$\nu^a(UO_2)^{2+}$	807	A_g	8054.0	$\nu^s(UO_2)^{2+}$
	–	791/l(H_2O)	799	B_{1g}	387.3	$\nu^s(UO_2)^{2+}$
Low wavenumber region						
g	592	591/δ(SiO_4)$^{4-}$	610	A_g	168.6	t(H_2O)
			579	B_{2g}	138.4	ρ(H_2O)
h	460	459/δ(SiO_4)$^{4-}$	431	A_g	323.3	δ(SiO_4)$^{4-}$
i	289	310	299	B_{1g}	54.8	T(SiO_4)$^{4-}$
			296	A_g	39.6	t(SiO_4)$^{4-}$
			295	B_{3g}	308.3	ρ(SiO_4)$^{4-}$
j	103	111,102	50	B_{2g}	54.5	δ^{op}(U-OH_2)

ratios, ductility and hardness indices and elastic anisotropy measures.

Soddyite equation of state was obtained by fitting lattice volumes and pressures to a fourth order Birch-Murnahan equation of state.

Raman spectrum was also computed and compared with their experimental counterpart. The normal mode analysis of the theoretical spectra was carried out and used to assign the main bands of the Raman spectra. It should be also noted that some bands, as that placed at 3147 cm^{-1}, were not found in the theoretical spectrum. Thus, they may correspond to other phases present in the natural mineral under study.

This work verifies that the DFT method is a reliable tool to analyse the structure, mechanical properties and vibrational spectra of uranyl silicate minerals.

Supplementary data

Supplementary data associated with this article contain two appendices. Appendix A contains additional details about the optimized soddyite structure. Pictures of the atomic motions in the Raman active vibrational modes of soddyite mineral are given in Appendix B.

Acknowledgements

This work was supported by ENRESA in the project: No 079000189 "Aplicación de técnicas de caracterización en el estudio de la estabilidad del combustible nuclear irradiado en condiciones de almacenamiento" (ACESCO) and project FIS2013-48087-C2-1-P. Supercomputer time by the CETA-CIEMAT, CTI-CSIC and CESGA centers are also acknowledged. This work has been carried out in the context of a CSIC–CIEMAT collaboration agreement: "Caracterización experimental y teórica de fases secundarias y óxidos de uranio formados en condiciones de almacenamiento de combustible nuclear". We also want to thank to Dr. Rafael Escribano for his help in the assignment of the bands of the Raman spectrum.

Appendix A. Supporting information

Supplementary data associated with this article can be found in the online version at doi:10.1016/j.jssc.2017.06.002.

References

[1] J. Bruno, R.C. Ewing, Spent nuclear fuel, Elements 2 (2006) 343–349.
[2] R.C. Ewing, The nuclear fuel cycle: a role for mineralogy and geochemistry, Elements 2 (2006) 331–334.
[3] R.C. Ewing, Long-term storage of spent nuclear fuel, Nat. Mater. 14 (2015) 252–256.
[4] G. Geipel, M. Thieme, Determination of inorganic species in seepage water of uranium mining rockpiles and in related media, J. Radio. Inorg. Nucl. Chem. 183 (1984) 139–145.
[5] P.C. Burns, R.C. Ewing, A. Navrotsky, Nuclear fuel in a reactor accident, Science 335 (2012) 1184–1188.
[6] R.C. Ewing, W.J. Weber, J. Lian, Nuclear waste disposal – pyrochlore ($A_2B_2O_7$): nuclear waste form for the immobilization of plutonium and "minor" actinides, J. Appl. Phys. 95 (2004) 5949–5971.
[7] SKB-91, Final Disposal Of Spent Nuclear Fuel. Importance Of The Bedrock For Safety, SKB Report 92-20, Swedish Nuclear Fuel and Waste Management Co., May 1992SKB-91, Final Disposal of Spent Nuclear Fuel. Importance of the Bedrock for Safety, SKB Report 92-20, Swedish Nuclear Fuel and Waste Management Co., May 1992.
[8] H. Christensen, S. Sunder, An evaluation of layer water thickness effective in the oxidation of UO_2 fuel due to radiolysis of water, J. Nucl. Mater. 238 (1996) 70–77.
[9] D.W. Shoesmith, Fuel corrosion processes under waste disposal conditions, J. Nucl. Mater. 282 (2000) 1–31.
[10] S. Sunder, Calculation of radiation dose rates in a water layer in contact with used CANDU UO_2 Fuel, Nucl. Technol. 122 (1998) 211–221.
[11] O. Roth, M. Jonsson, Oxidation of UO_2 (s) in aqueous solution, Cent. Eur. J. Chem. 6 (2008) 1–14.
[12] J. Plasil, Oxidation-hydration weathering of uraninite: the current state-of knowledge, J. Geosci. 59 (2014) 99–114.
[13] P.C. Burns, R.C. Ewing, M.L. Miller, Incorporation mechanisms of actinide elements in to the structures of U^{6+} phases formed during the oxidation of spent nuclear fuel, J. Nucl. Mater. 245 (1997) 1–9.
[14] P.C. Burns, U^{6+} minerals and inorganic compounds: insights into an expanded structural hierarchy of crystal structures, Can. Mineral. 43 (2005) 1839–1894.
[15] P.C. Burns, The crystal chemistry of uranium, Rev. Mineral. 38 (1999) 23–90.
[16] a) P.C. Burns, The structure of botwoodite and implications of solid solution towards sodium boltwoodite, Can. Mineral. 36 (1998) 1069–1075;
b) P.C. Burns, Cs boltwoodite obtained by ion exchange from single crystals: implications for radionuclide release in a nuclear repository, J. Nucl. Mater. 265 (1999) 218–223;
c) P.C. Burns, A new uranyl silicate sheet in the structure of haiweeiteand comparison to other uranyl silicates, Can. Mineral. 39 (2001) 1153–1160.
[17] J.M. Jackson, P.C. Burns, The re-evaluation of the structure of weeksite: a uranyl silicate framework mineral, Can. Mineral. 39 (2001) 187–195.
[18] a) P.C. Burns, K.M. Deely, S. Skanthakumar, Neptunium incorporation into uranyl compounds that form as alteration products of spent nuclear fuel: implications for geologic repository performance, Radiochim. Acta 92 (2004) 151–159;
b) P.C. Burns, R.C. Ewing, F.C. Hawthorne, The crystal chemistry of hexavalent uranium: polyhedron geometries, bond-valence parameters, and polymerization of polyhedra, Can. Mineral. 35 (1997) 1551–1570;
c) P.C. Burns, M.L. Miller, R.C. Ewing, U^{6+} minerals and inorganic phases: a comparison and hierarchy of crystal structures, Can. Mineral. 34 (1996) 845–880.
[19] A.L. Klingensmith, P.C. Burns, Neptunium substitution in synthetic uranophane and soddyite, Am. Mineral. 92 (2007) 1946–1951.
[20] I. Grenthe, J. Drozdzynski, T. Fujino, E.C. Buck, T.E. Albrecht-Schmitt, S.F. Wolf, Uranium, in: L.R. Morss, N.M. Edelstein, J. Fuger (Eds.), , The Chemisty of Actinide and Transactinide Elements I, Springer Science and Business Media, Berlin, 2006, pp. 253–638.

[21] a) C. Frondel, Mineral composition of gummite, Am. Mineral. 41 (1956) 539–568; b) C. Frondel, Systematic mineralogy of uranium and thorium, U.S. Geol. Surv. Bull. 1064 (1958); c) R.J. Finch, R.C. Ewing, The corrosion of uraninite under oxidizing conditions, J. Nucl. Mater. 190 (1992) 133–156.

[22] E.C. Pearcy, J.D. Prikryl, W.M. Murphy, B.W. Leslie, Alteration of uraninite from the Nopal I deposit, Peña Blanca District, Chihuahua, Mexico, compared to degradation of spent nuclear fuel in the proposed US high-level nuclear waste repository at Yucca Mountain, Nevada, Appl. Geochem. 9 (1994) 713–732.

[23] a) D.J. Wronkiewicz, J.K. Bates, T.J. Gerding, E. Veleckis, B.S. Tani, Uranium release and secondary phase formation during unsaturated testing of UO_2 at 90 °C, J. Nucl. Mater. 190 (1992) 107–127; b) D.J. Wronkiewicz, J.K. Bates, S.F. Wolf, E.C. Buck, Ten-year results from unsaturated drip tests with UO_2 at 90 °C: implications for the corrosion of spent nuclear fuel, J. Nucl. Mater. 238 (1996) 78–95.

[24] A. Schoep, La Soddite, Nouveau Minéral radioactive, Comptes Rendus Acad. Sci. 174 (1922) 1066–1067.

[25] D.H. Gorman, Studies of radioactive compounds: V – soddyite, Am. Mineral. 37 (1952) 386–393.

[26] F.V. Stohl, D.K. Smith, The crystal chemistry of the uranyl silicate minerals, Am. Mineral. 66 (1981) 610–624.

[27] F. Demartin, C.M. Gramaccioli, T. Pilati, The Importance of accurate crystal structure determination of uranium minerals. II. Soddyite $(UO_2)_2(SiO_4)\cdot 2H_2O$, Acta Crystallogr. C 48 (1992) 1–4.

[28] J.P. Legros, Y. Jeannin, Coordination de l'Uranium par l'Ion Germanate. II. Structure du Germanate d'Uranyle Dihydraté $(UO_2)_2GeO_4(H_2O)_2$, Acta Crystallogr. B 31 (1975) 1140–1143.

[29] N. Blaton, R. Vochten, O.M. Peeters, K. van Springel, The crystal structure of $Na_2(UO_2)_2SiO_4F_2$, a compound structurally related to soddyite, and formed during uranyl silicate synthesis in Teflonlined Bombs, Neues Jahrbuch fuer Mineralogie, Monatshefte 6 (1999) 253–264.

[30] H. Moll, W. Matz, G. Schuster, E. Brendler, G. Bernhard, H. Nitsche, Synthesis and characterization of uranyl orthosilicate $(UO_2)_2SiO_4\cdot 2H_2O$, J. Nucl. Mater. 227 (1995) 40–49.

[31] J.P. Legros, R. Legros, E. Masdupuy, Sur un Silicate d'Uranyle, Isomorphe du Germanated Uranyle, et sur les Solutions Solides Correspondantes. Application a l'Etude Structurale du Germanated Uranyle, Bull. Soc. Chim. Fr. 8 (1972) 3051.

[32] L.M. Kuznetsov, A.N. Tsvigunov, E.S. Makarov, Hydrothermal synthesis and physico-chemical study of the synthetic analog of soddyite, Geochimiya 10 (1981) 1493.

[33] Y.Z. Nozik, L.M. Kuznetsov, Neutron diffraction study of synthetic soddyite by the full-profile analysis technique, Kristallografiya 35 (1990) 1563–1564.

[34] P.F. Weck, E. Kim, E.C. Buck, On the mechanical stability of uranyl peroxide hydrates: implications for nuclear fuel degradation, RSC Adv. 5 (2015) 79090–79097.

[35] J.F. Nye, The Physical Properties of Crystals: Their Representation by Tensors and Matrices, Oxford University Press, New York, 1985.

[36] a) J.P. Crocombette, F. Jollet, L.T. Nga, T. Petit, Plane-wave pseudopotential study of point defects in uranium dioxide, Phys. Rev. B 64 (2001) 104107; b) G. Beridze, P.M. Kowalski, Benchmarking the DFT+U method for thermochemical calculations of uranium molecular compounds and solids, J. Phys. Chem. A 118 (2014) 11797–111810.

[37] a) Z.-G. Mei, M. Stan, J. Yang, First-principles study of thermophysical properties of uranium dioxide, J. Alloy. Compd. 603 (2014) 282–286; b) Z.-G. Mei, M. Stan, B. Pichler, First-principles study of structural, elastic, electronic, vibrational and thermodynamic properties of UN, J. Nucl. Mater. 440 (2013) 63–69.

[38] B.T. Wang, P. Zhang, R. Lizarraga, I. Di Marco, O. Eriksson, Phonon spectrum, thermodynamic properties, and pressure-temperature phase diagram of uranium dioxide, Phys. Rev. B 88 (2013) 104107.

[39] Q. Yin, S.Y. Savrasov, Origin of low thermal conductivity in nuclear fuels, Phys. Rev. Lett. 100 (2008) 225504.

[40] Y. Yun, D. Legut, P.M. Oppeneer, Phonon spectrum, thermal expansion, and heat capacities of UO_2 from first principles, J. Nucl. Mater. 423 (2012) 109–114.

[41] a) D.E. Giammar, Geochemistry of Uranium at Mineral-Water Interfaces: Rates of Sorption Desorption and Dissolution-Precipitation Reactions (Ph.D. thesis), California Institute of Technology, Pasadena, California, 2001; b) D.E. Giammar, J.G. Hering, Equilibrium and kinetic aspects of soddyite dissolution and secondary phase precipitation in aqueous suspension, Geochim. Cosmochim. Acta 66 (2002) 3235–3245.

[42] D.M. Biwer, W.L. Ebert, J.K. Bates, The Raman spectra of several uranyl-containing minerals using a microprobe, J. Nucl. Mater. 175 (1990) 188–193.

[43] M. Amme, B. Renker, B. Schmid, M.P. Feth, H. Bertagnolli, W. Döbelin, Raman microspectrometric identification of corrosion products formed on UO_2 nuclear fuel during leaching experiments, J. Nucl. Mater. 306 (2002) 202–212.

[44] R.L. Frost, J. Cejka, M.L. Weier, W.A. Martens, Raman and infrared spectroscopic study of the uranyl silicates–weeksite, soddyite and haiweeite: Part 2, Spectrochim. Acta A 63 (2002) 305–312.

[45] a) P. Hohenberg, W. Kohn, Inhomogeneous electron gas, Phys. Rev. 136 (1964) B864–B871; b) W. Kohn, L.J. Sham, Self-consistent equations including exchange and correlation effects, Phys. Rev. 140 (1965) A1133–A1138; c) R.G. Parr, W. Yang, Density-Functional Theory of Atoms and Molecules, Oxford University Press, New York, 1989.

[46] M.C. Payne, M.P. Teter, D.C. Allan, A. Arias, J.D. Joannopoulos, Iterative minimization techniques for ab initio total-energy calculations: molecular dynamics and conjugate gradients, Rev. Mod. Phys. 64 (1992) 1045–1097.

[47] N. Troullier, J.L. Martins, Efficient pseudopotentials for plane-wave calculations, Phys. Rev. B 43 (1991) 1993–2006.

[48] L.J. Bonales, F. Colmenero, J. Cobos, V. Timón, V. Spectroscopic Raman, Characterization of Rutherfordine: combined DFT and experimental study, Phys. Chem. Chem. Phys. 18 (2016) 16575–16584.

[49] L.J. Bonales, C. Menor-Salvan, J. Cobos, Study of the alteration products of a natural uraninite by raman spectroscopy, J. Nucl. Mater. 462 (2015) 296–303.

[50] a) S.J. Clark, M.D. Segall, C.J. Pickard, P.J. Hasnip, M.I.J. Probert, K. Refson, M.C. Payne, First principles methods using CASTEP, Z. Kristallogr. 220 (2005) 567–570; b) V. Milman, K. Refson, S.J. Clark, C.J. Pickard, J.R. Yates, S.-P. Gao, P.J. Hasnip, M.I.J. Probert, A. Perlov, M.D. Segall, Electron and vibrational spectroscopies using DFT, plane waves and pseudopotentials: CASTEP implementation, J. Mol. Struct. Theochem. 954 (2010) 22–35.

[51] Materials Studio, ⟨http://accelrys.com/products/materials-studio⟩, (2014).

[52] J.P. Perdew, K. Burke, M. Ernzerhof, Generalized gradient approximation made simple, Phys. Rev. Lett. 77 (1996) 3865–3868.

[53] S. Grimme, Semiempirical GGA-type density functional constructed with a long-range dispersion correction, J. Comput. Chem. 27 (2006) 1787–1799.

[54] B.G. Pfrommer, M. Cote, S.G. Louie, M.L. Cohen, Relaxation of crystals with the Quasi-Newton method, J. Comput. Phys. 131 (1997) 233–240.

[55] H.J. Monkhorst, J.D. Pack, Special points for Brillonin-zone integration, Phys. Rev. B 13 (1976) 5188–5192.

[56] R. Yu, J. Zhu, H.Q. Ye, Calculations of single-crystal elastic constants made simple, Comput. Phys. Commun. 181 (2010) 671–675.

[57] F. Birch, Finite elastic strain of cubic crystal, Phys. Rev. 71 (1947) 809–824.

[58] R.J. Angel, Equations of State, Rev. Mineral. Geochem. 41, 2000. 35–60. EOSFIT 5. 2 software, ⟨http://www.ccp14.ac.uk/ccp/webmirrors/ross-angel/rja/soft/.10.2138/rmg.2000.41.2⟩.

[59] a) S. Baroni, S. de Gironcoli, A. Dal Corso, Phonons and related crystal properties from density-functional perturbation theory, Rev. Mod. Phys. 73 (2001) 515–562; b) S. Baroni, P. Giannozzi, A. Testa, Green's-function approach to linear response in solids, Phys. Rev. Lett. 58 (1987) 1861–1864.

[60] a) X. Gonze, D.C. Allan, M.P. Teter, Dielectric tensor, effective charges and phonon in α-quartz by variational density-functional perturbation theory, Phys. Rev. Lett. 68 (1992) 3603–3606; b) X. Gonze, C. Lee, Dynamical matrices, born effective charges, dielectric permittivity tensors, and interatomic force constants from density-functional perturbation theory, Phys. Rev. B 55 (1997) 10355–10368.

[61] K. Refson, P.R. Tulip, S.J. Clark, Variational density-functional perturbation theory for dielectrics and lattice dynamics, Phys. Rev. B 73 (2006) 155114.

[62] F. Colmenero, L.J. Bonales, J. Cobos, V. Timón, Study of the thermal stability of studtite by in situ raman spectroscopy and DFT calculations, Spectrochim. Acta A 174 (2017) 245–253.

[63] E.L. Belokoneva, V.I. Mokeeva, L.M. Kuznetsov, M.A. Simonov, E.S. Makarov, N.V. Belov, Crystal structure of synthetic soddyite, $(UO_2)_2[SiO_4](H_2O)_2$, Dokl. Akad. Nauk SSSR 246 (1979) 93–96.

[64] R.T. Downs, K.L. Bartelmehs, G.V. Gibbs, M.B. Boisen, Interactive software for calculating and displaying x-ray or neutron powder diffractometer patterns of crystalline materials, Am. Mineral. 78 (1993) 1104–1107.

[65] J.D. Martin, XPowder12, Ver. 04.13, 2012.

[66] ICDD, The International Center for Diffraction Data, PDF-2 Database, 2003.

[67] F. Mouhat, F.-X. Coudert, Necessary and sufficient elastic stability conditions in various crystal systems, Phys. Rev. B 90 (2014) 224104.

[68] R. Hill, The elastic behaviour of a crystalline aggregate, Proc. Phys. Soc. Lond. 65 (1952) 349–354.

[69] P. Ravindran, L. Fast, P.A. Korzhavyi, B. Johansson, J. Wills, O. Eriksson, Density functional theory for calculation of elastic properties of orthorhombic crystals: application to $TiSi_2$, J. Appl. Phys. 84 (1998) 4891–4904.

[70] Y. Bouhadda, S. Djella, M. Bououdina, N. Fenineche, Y. Boudouma, Structural and elastic properties of $LiBH_4$ for hydrogen storage applications, J. Alloy. Compd. 534 (2012) 20–24.

[71] S.F. Pugh, XCII. Relations between the elastic moduli and the plastic properties of polycrystalline pure metals, Philos. Mag. 45 (1954) 823–843.

[72] H. Niu, P. Wei, Y. Sun, C.-X. Chen, C. Franchini, D. Li, Y. Li, Electronic, optical, and mechanical properties of superhard cold-compressed phases of carbon, Appl. Phys. Lett. 99 (2011) 031901.

[73] S.I. Ranganathan, M. Ostoja-Starzewski, Universal elastic anisotropy index, Phys. Rev. Lett. 101 (2008) 055504.

[74] G. Ulian, S. Tosoni, G. Valdre, The compressional behaviour and the mechanical properties of talc $[Mg_3Si_4O_{10}(OH)_2]$: a density functional theory investigation, Phys. Chem. Miner. 41 (2014) 639–650.

[75] S. Shang, Y. Wang, Z.K. Liu, First-principles elastic constants of α-and θ-Al_2O_3, Appl. Phys. Lett. 90 (2007) 101909.

[76] V. Wheaton, D. Majumdar, K. Balasubramanian, L. Chauffe, P.G.A. Allen, Comparative theoretical study of uranyl silicate complexes, Chem. Phys. Lett. 371 (2003) 349–359.

[77] K. Nakamoto, Infrared and Raman Spectra of Inorganic and Coordination Compounds, J. Wiley and Sons, New York, 1986.

[78] J. Cejka, Infrared spectroscopy and thermal analysis of the uranyl minerals, Rev. Mineral. Geochem. 38 (1999) 521–622.

Supplementary Information

Structural, Mechanical and Vibrational Study of Uranyl Silicate Mineral Soddyite by DFT Calculations

F. Colmenero[a], L.J. Bonales[b], J. Cobos[b], V. Timón[a]

[a]*Instituto de Estructura de la Materia, CSIC. C/ Serrano, 113. 28006 Madrid, Spain*

[b]*Centro de Investigaciones Energéticas, Medioambientales y Tecnológicas, CIEMAT. Avda/ Complutense, 40. 28040 Madrid, Spain*

Appendix A. Additional details about the optimized soddyite structure.

Table A.1. Bond distances (in Å)

Bond	Experimental [1]	Calculated
Tetrahedron around Si		
Si-O2	1.631	1.647
O2-O2a x2	2.811	2.846
O2-O2b x2	2.705	2.722
O2-O2c x2	2.462	2.487
Pentagonal Bipyramid around U		
U1-O1 x2	1.781	1.801
U1-O2 x2	2.313	2.312
U1-O2d x2	2.424	2.377
U1-OW	2.406	2.436
O1-O2d x2	3.126	3.166
O1-O2e x2	2.925	2.931
O1-O2f x2	2.916	2.910
O1-O2 x2	2.906	2.926
O1-OW x2	2.974	2.969
O2-O2d x2	2.745	2.764
O2d-O2f	2.462	2.467
O2-OW x2	3.003	2.972
Water molecule		
OW-H	0.76	0.980
H-O1	2.22	1.881

Table A.2 Bond angles (in deg)

Bond	Experimental [1]	Calculated
Tetrahedron around Si		
O2-Si-O2a x2	119.0	119.58
O2-Si-O2b x2	112.0	111.48
O2-Si-O2c x2	98.0	98.06

Pentagonal Bipyramid around U		
O1-U-O2d x2	94.8	95.54
O1-U-O2e x2	90.3	90.00
O1-U-O2f x2	86.5	85.37
O1-U-O2 x2	89.5	89.79
O1-U-OW x2	89.2	89.47
O2-U-O2d x2	70.8	71.13
O2d-U-O2f	61.1	61.39
O2-U-OW x2	79.0	78.64
O1-U-O1'	178.5	178.95
Water molecule		
H-OW-H'	121	111.50
OW-H-O1	156	148.67

Table A.3 Main reflections in the X-Ray powder pattern of soddyite: a) Experimental diffractogram (pattern 77-0604 in the PDF-2 database [2]); b) X-Ray powder pattern computed from experimental geometry [1]; c) X-Ray powder diffractogram computed from calculated geometry.

Experimental (a)				Experimental (b)			Theoretical		
2Θ	**d(Å)**	**I (%)**	**hkl**	**2Θ**	**d(Å)**	**I (%)**	**2Θ**	**d(Å)**	**I (%)**
14.087	6.281	100.0	[111]	14.054	6.297	96.394	14.216	6.225	95.455
18.440	4.807	32.131	[022]	18.447	4.806	36.467	18.147	4.884	38.067
19.008	4.665	9.409	[004]	19.001	4.667	10.215	18.828	4.709	11.333
19.496	4.549	93.493	[113]	19.468	4.556	100.0	19.503	4.548	100.0
23.449	3.790	12.412	[202]	23.360	3.805	15.597	23.953	3.712	14.158
26.556	3.354	22.723	[131]	26.550	3.355	22.569	26.279	3.389	24.626
26.705	3.335	63.063	[220]	26.633	3.344	75.999	27.015	3.298	71.489
27.360	3.257	20.320	[115]	27.334	3.260	23.500	27.237	3.271	22.776
29.861	2.990	20.420	[133]	29.853	2.990	25.564	29.553	3.020	27.392
31.881	2.805	14.014	[040]	31.902	2.803	18.360	31.291	2.856	20.156
32.902	2.720	32.332	[026]	32.897	2.720	42.632	32.515	2.751	44.763
32.986	2.713	24.424	[224]	33.972	2.718	7.788	33.135	2.701	7.846
36.064	2.488	18.318	[206]	35.995	2.493	25.637	36.209	2.479	24.403
36.413	2.465	11.011	[313]	36.280	2.474	13.661	37.142	2.419	13.768
39.954	2.255	9.509	[242]	39.946	2.257	13.473	39.788	2.264	13.243
43.170	2.094	13.213	[333]	43.062	2.099	17.153	43.580	2.075	16.420
44.246	2.045	9.109	[153]	44.253	2.045	12.778	43.578	2.075	14.099
45.789	1.980	11.811	[119]	45.762	1.981	16.559	45.424	1.995	17.433
48.890	1.861	20.420	[246]	48.851	1.863	30.247	48.592	1.872	30.517
53.728	1.705	8.308	[260]	53.715	1.705	12.017	53.132	1.722	12.959
55.682	1.649	12.412	[426]	55.509	1.654	19.025	56.477	1.628	18.638

Appendix B. Raman active normal modes of soddyite.

Figure B.1 The atomic motions associated to each Raman active vibrational normal mode of soddyite.

Mode ν=3442 cm^{-1} – ν(OH) – Antisymmetric OH stretching.

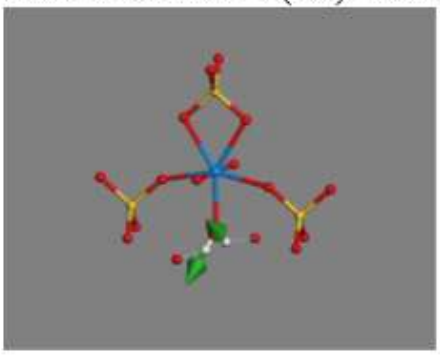

Mode ν=3374 cm^{-1} – ν(OH) - Symmetric OH stretching.

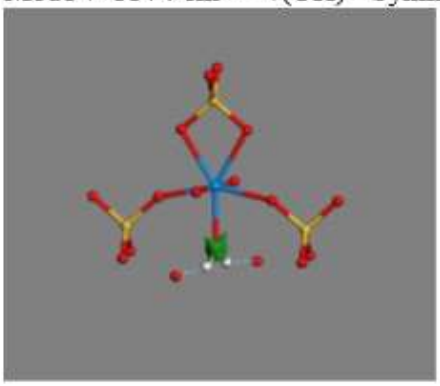

Mode ν=3353 cm^{-1} – ν(OH) - Symmetric OH stretching.

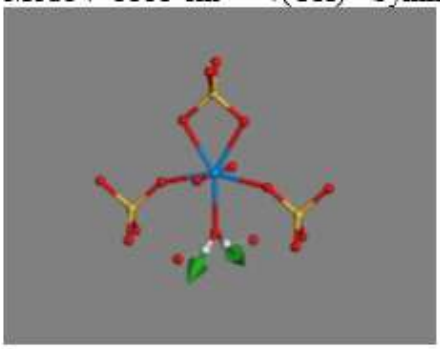

Mode ν=1495 cm^{-1} – $\delta(H_2O)$ – H_2O bending.

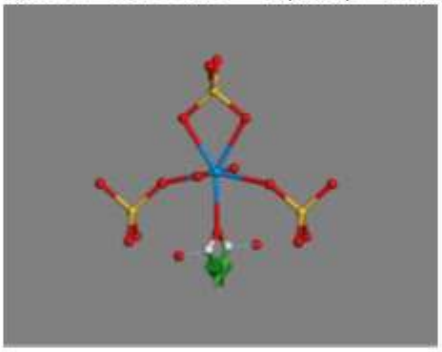

Mode ν=1494 cm^{-1} – $\delta(H_2O)$ – H_2O bending.

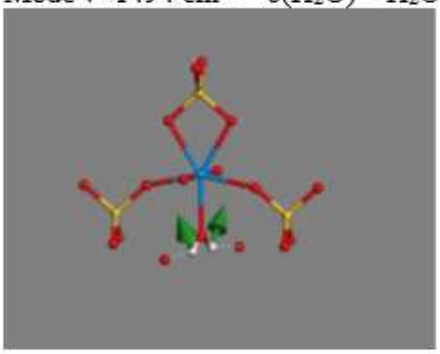

Mode ν=995 cm^{-1} – $\nu^a(SiO_4)^{4-}$ – Asymmetric $(SiO_4)^{4-}$ stretching.

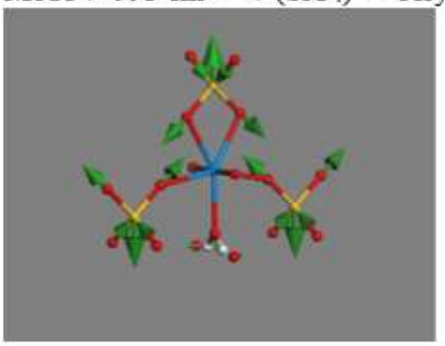

Mode ν=874 cm^{-1} – $\nu^a(UO_2)^{2+}+\rho(H_2O)$ – Asymmetric $(UO_2)^{2+}$ stretching plus H_2O rocking vibration.

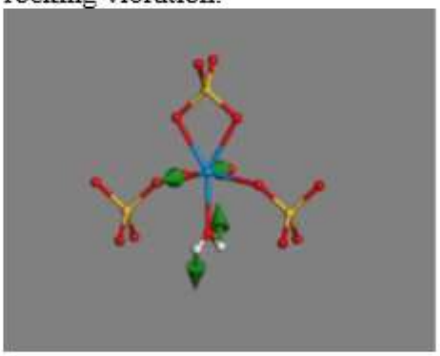

Mode ν=873 cm^{-1} – $\nu^{s}(SiO_4)^{4-}$ – Symmetric $(SiO_4)^{4-}$ stretching.

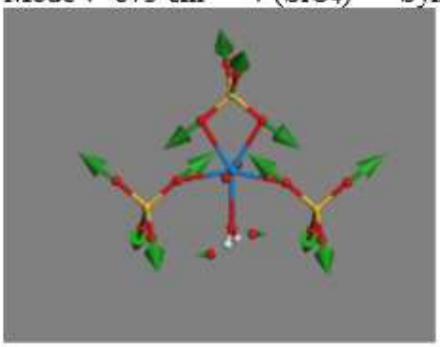

Mode ν=852 cm^{-1} – $\nu^{a}(UO_2)^{2+}$ – Asymmetric $(UO_2)^{2+}$ stretching.

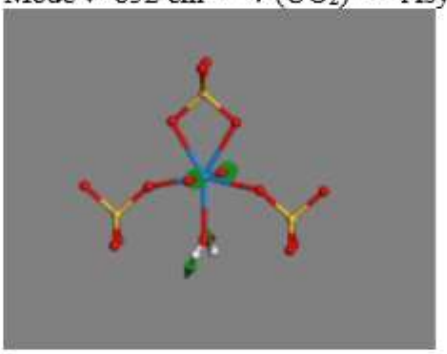

Mode ν=846 cm^{-1} – $\nu^{a}(SiO_4)^{4-}$ – Asymmetric $(SiO_4)^{4-}$ stretching.

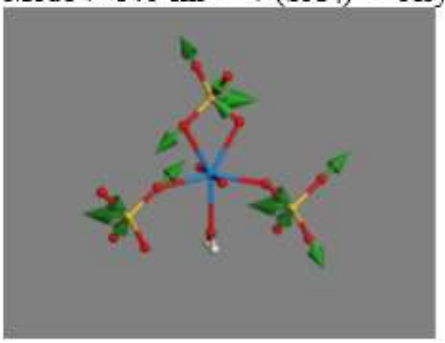

Mode ν=810 cm^{-1} – $\nu^{a}(SiO_4)^{4-}$– Asymmetric $(SiO_4)^{4-}$ stretching.

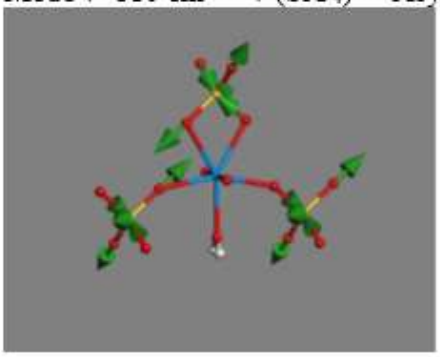

Mode ν=807 cm^{-1} – $\nu^s(UO_2)^{2+}$– Symmetric $(UO_2)^{2+}$ stretching.

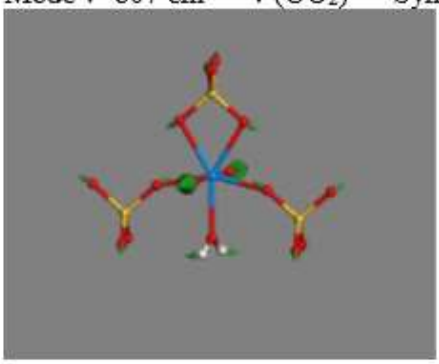

Mode ν=799 cm^{-1} – $\nu^s(UO_2)^{2+}$ – Symmetric $(UO_2)^{2+}$ stretching.

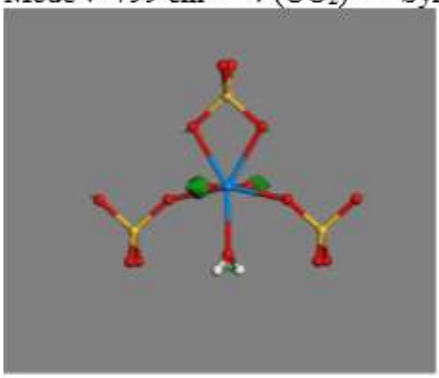

Mode ν=610 cm^{-1} – $t(H_2O)$ – H_2O twisting.

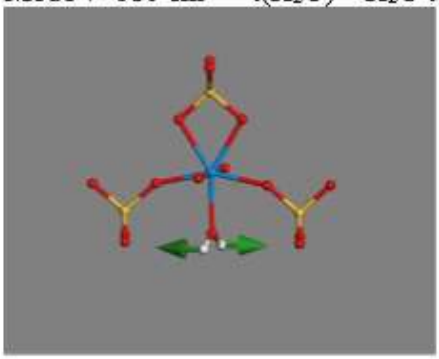

Mode ν=602 cm^{-1} – $t(H_2O)$ – H_2O twisting.

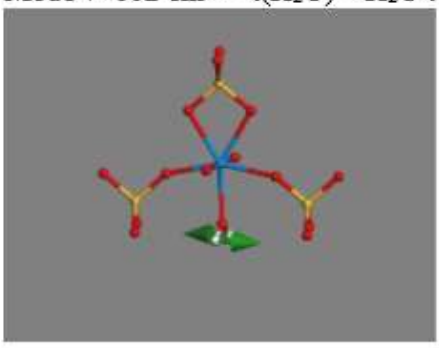

Mode ν=579 cm^{-1} – ρ(H_2O) – H_2O rocking.

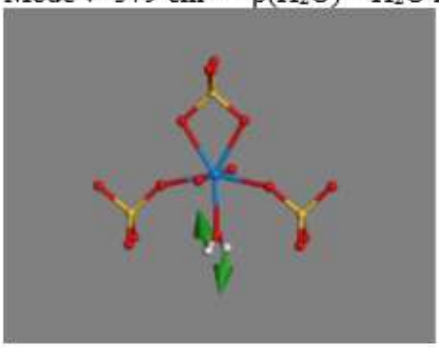

Mode ν=555 cm^{-1} – δ$(SiO_4)^{4-}$ – Silicate $(SiO_4)^{4-}$ symmetric bending.

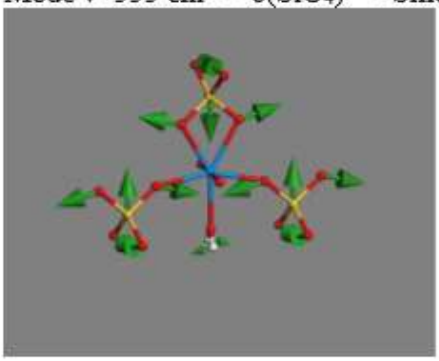

Mode ν=507 cm^{-1} – ω(H_2O) – H_2O wagging.

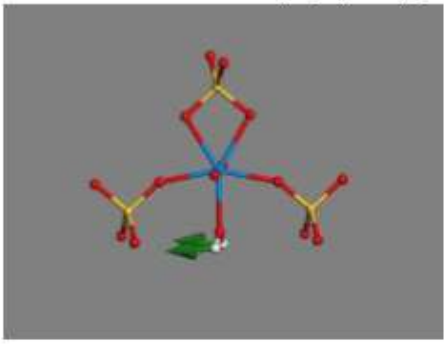

Mode ν=491 cm^{-1} – ω(H_2O) – H_2O wagging.

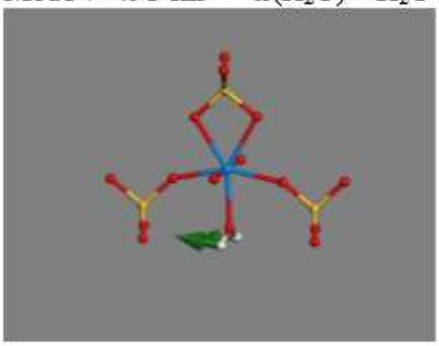

Mode ν=445 cm^{-1} – ω(H_2O) – H_2O wagging.

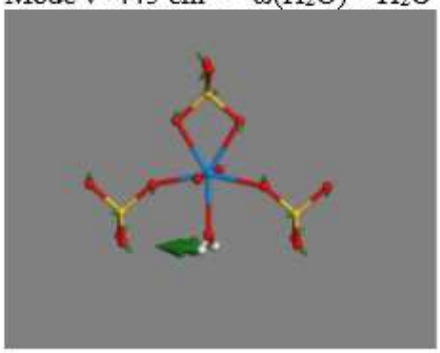

Mode ν=438 cm^{-1} – ω(H_2O) – H_2O wagging.

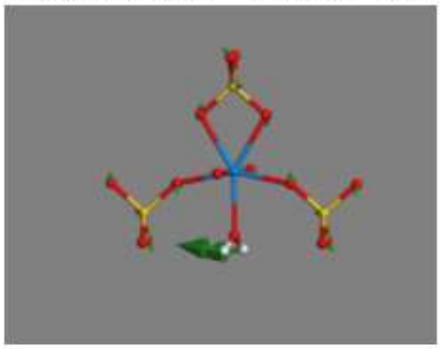

Mode ν=431 cm^{-1} – δ$(SiO_4)^{4-}$ – Silicate $(SiO_4)^{4-}$ symmetric bending.

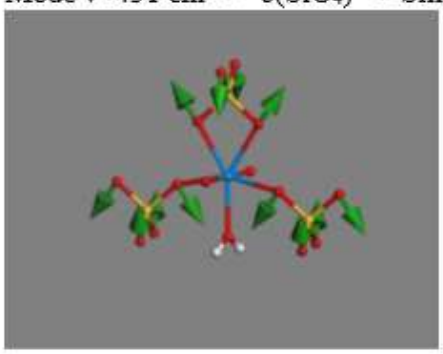

Mode ν=384 cm^{-1} – ν(UO_{aqua})/T(H_2O) – UO_{aqua} stretching/H_2O translation.

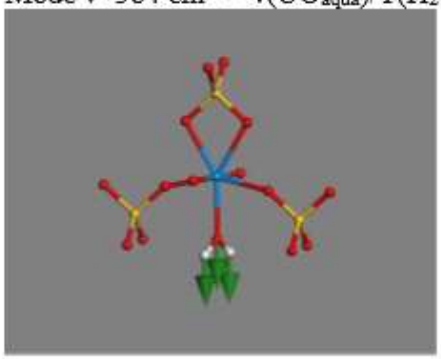

Mode ν=299 cm^{-1} – $T(SiO_4)^{4-}$– Silicate $(SiO_4)^{4-}$ translation.

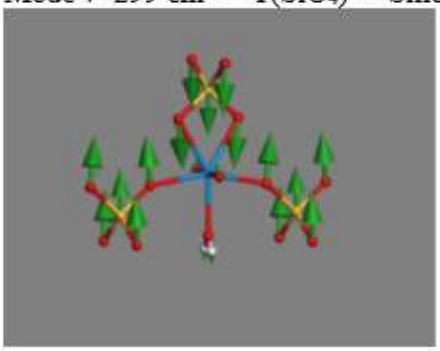

Mode ν=296 cm^{-1} – $t(SiO_4)^{4-}$ – Silicate $(SiO_4)^{4-}$ twisting vibration.

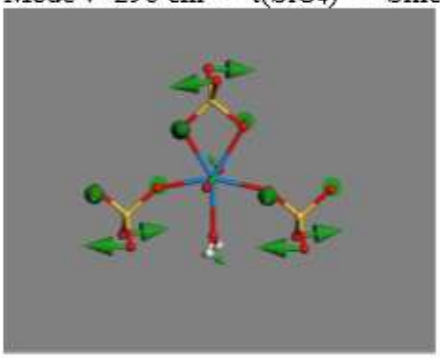

Mode ν=295 cm^{-1} – $\rho(SiO_4)^{4-}$ – Silicate $(SiO_4)^{4-}$ rocking vibration.

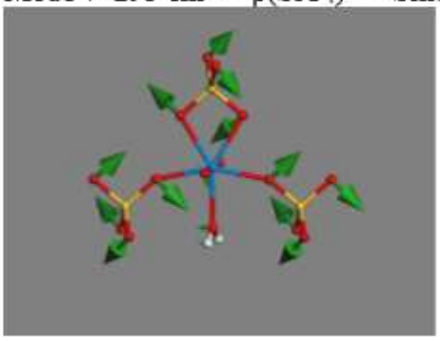

Mode ν=282 cm^{-1} – $t(SiO_4)^{4-}$ – Silicate $(SiO_4)^{4-}$ twisting vibration.

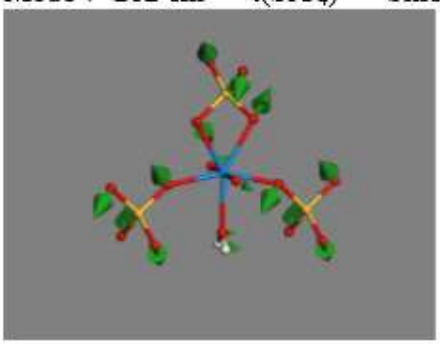

Mode ν=272 cm^{-1} – $\delta(UO_2)^{2+}$ + $T(SiO_4)^{4-}$– Uranyl $(UO_2)^{2+}$ bending vibration plus silicate $(SiO_4)^{4-}$ translation.

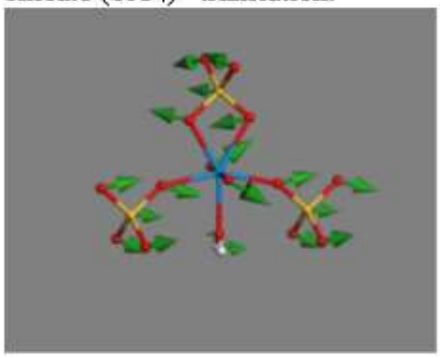

Mode ν=261 cm^{-1} – $\delta(UO_2)^{2+}$ – Uranyl $(UO_2)^{2+}$ bending vibration.

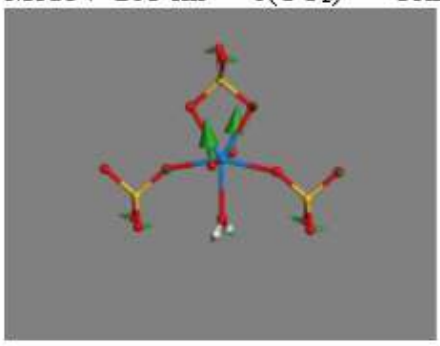

Mode ν=240 cm^{-1} – $\delta(UO_2)^{2+}$+ $\omega(H_2O)$ – Uranyl $(UO_2)^{2+}$ bending vibration plus H_2O wagging vibration.

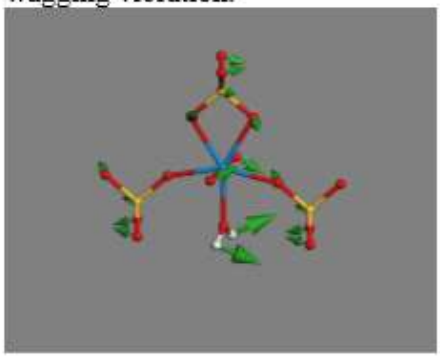

Mode ν=228 cm^{-1} – $\delta(UO_2)^{2+}$ – Uranyl $(UO_2)^{2+}$ bending vibration.

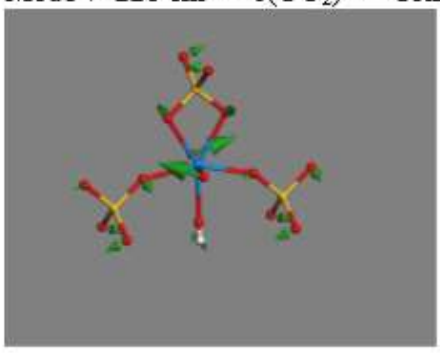

Mode ν=225 cm^{-1} – $\rho(UO_2)^{2+}$+ $T(SiO_4)^{4-}$+ $\omega(H_2O)$ – Uranyl $(UO_2)^{2+}$ rocking plus silicate $(SiO_4)^{4-}$ translation and water wagging.

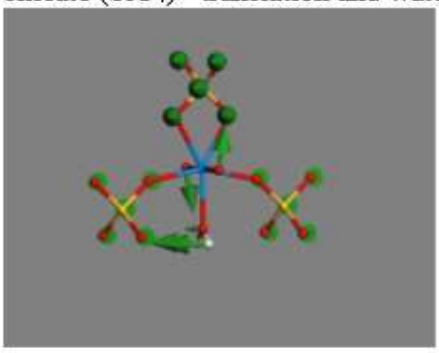

Mode ν=198 cm^{-1} – $\rho(UO_2)^{2+}$ – Uranyl $(UO_2)^{2+}$ rocking.

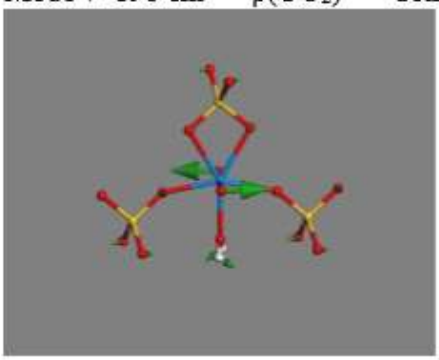

Mode ν=177 cm^{-1} – $\rho(UO_2)^{2+}$ – Uranyl $(UO_2)^{2+}$ rocking.

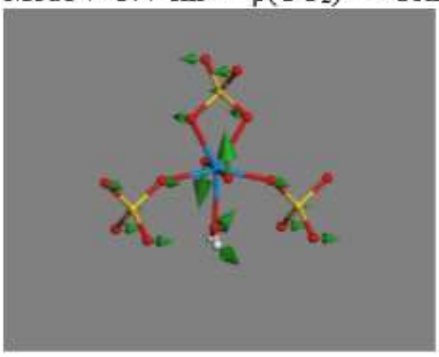

Mode ν=165 cm^{-1} – $\rho(UO_2)^{2+}$+$\delta^{ip}(U\text{-}OH_2)$ – Uranyl $(UO_2)^{2+}$ rocking and U-O_{aqua} in plane bending vibrations.

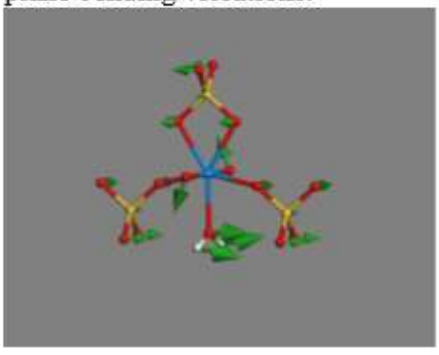

Mode ν=129 cm^{-1} – $\delta^{ip}(U\text{-}OH_2)$ – $U\text{-}O_{aqua}$ in plane bending vibration.

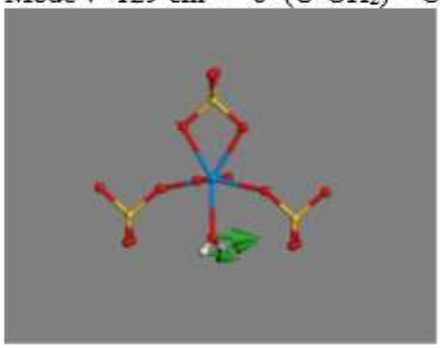

Mode ν=126 cm^{-1} – $\delta^{op}(U\text{-}OH_2)$ – $U\text{-}O_{aqua}$ out of plane bending vibration.

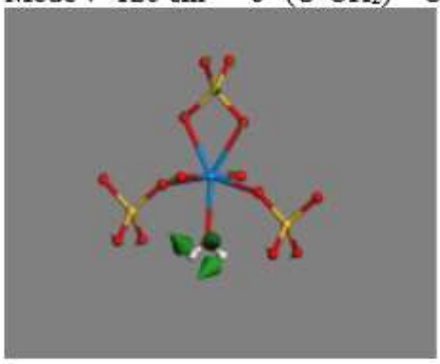

Mode ν=107 cm^{-1} – $T(UO_2)^{2+}$+ $T(H_2O)$ – $(UO_2)^{2+}$and H_2O translation.

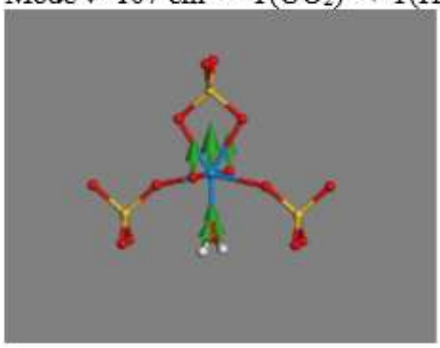

Mode ν=90 cm^{-1} – $\delta^{op}(U\text{-}OH_2)$ – $U\text{-}O_{aqua}$ out of plane bending vibration.

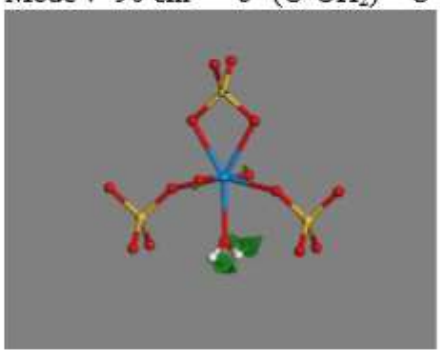

Mode ν=50 cm^{-1} – δ^{op}(U-OH_2) – U-O_{aqua} out of plane bending vibration.

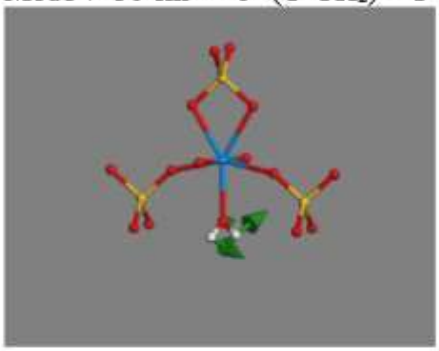

References

[1] F. Demartin, C. M. Gramaccioli, T. Pilati, The Importance of Accurate Crystal Structure Determination of Uranium Minerals. II. Soddyite $(UO_2)_2(SiO_4)\cdot 2H_2O$, Acta Crystallogr. C 48 (1992) 1–4.

[2] ICDD, The International Center for Diffraction Data, PDF-2 Database, 2003.

Studtite: Structure, Raman Spectroscopy and Thermal Stability

Article: *"Study of the thermal stability of studtite by in situ Raman spectroscopy and DFT calculations",* by F. Colmenero, L. J. Bonales, J. Cobos and V. Timón, Spectrochim. Acta A 174, 245–253 (2017).

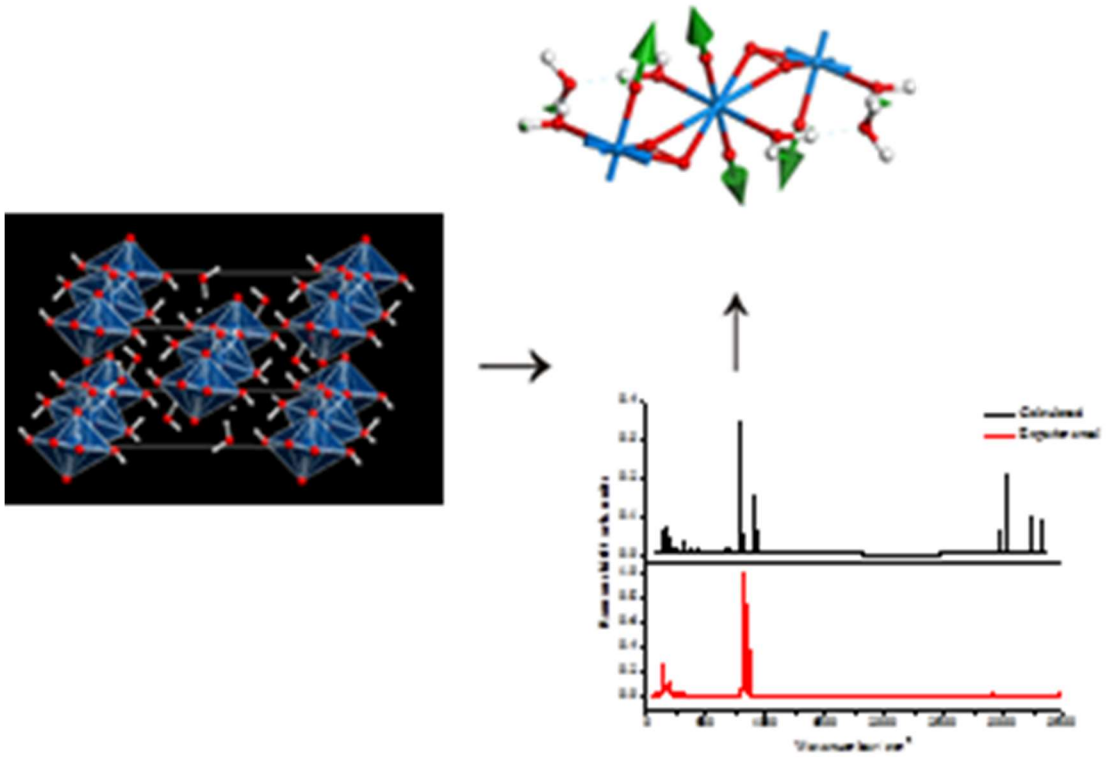

Spectrochimica Acta Part A: Molecular and Biomolecular Spectroscopy 174 (2017) 245–253

Contents lists available at ScienceDirect

Spectrochimica Acta Part A: Molecular and Biomolecular Spectroscopy

journal homepage: www.elsevier.com/locate/saa

Study of the thermal stability of studtite by *in situ* Raman spectroscopy and DFT calculations

Francisco Colmenero [a,*], Laura J. Bonales [b], Joaquín Cobos [b], Vicente Timón [a]

[a] Instituto de Estructura de la Materia, CSIC. C/Serrano, 113, 28006 Madrid, Spain
[b] Centro de Investigaciones Energéticas, Medioambientales y Tecnológicas, CIEMAT. Avda/Complutense, 40, 28040 Madrid, Spain

ARTICLE INFO

Article history:
Received 26 September 2016
Received in revised form 16 November 2016
Accepted 24 November 2016
Available online 29 November 2016

Keywords:
Spent fuel
Studtite
Raman spectroscopy
DFT
Structure thermal stability

ABSTRACT

The design of a safe spent nuclear fuel repository requires the knowledge of the stability of the secondary phases which precipitate when water reaches the fuel surface. Studtite is recognized as one of the secondary phases that play a key-role in the mobilization of the radionuclides contained in the spent fuel. Thereby, it has been identified as a product formed under oxidation conditions at the surface of the fuel, and recently found as a corrosion product in the Fukushima-Daiichi nuclear plant accident. Thermal stability is one of the properties that should be determined due to the high temperature of the fuel.

In this work we report a detailed analysis of the structure and thermal stability of studtite. The structure has been studied both by experimental techniques (SEM, TGA, XRD and Raman spectroscopy) and theoretical DFT electronic structure and spectroscopic calculations. The comparison of the results allows us to perform for the first time the Raman bands assignment of the whole spectrum. The thermal stability of studtite has been analyzed by *in situ* Raman spectroscopy, with the aim of studying the effect of the heating rate and the presence of water. For this purpose, a new cell has been designed. The results show that studtite is stable under dry conditions only at temperatures below 30 °C, in contrast with the higher temperatures published up to date (~130 °C). Opposite behaviour has been found when studtite is in contact with water; under these conditions studtite is stable up to 90 °C, what is consistent with the encounter of this phase after the Fukushima-Daiichi accident.

1. Introduction

Nuclear fuel, commonly composed of UO_2 pellets enriched from 0.7 to 3–5% of ^{235}U [1], is obtained from natural minerals found in the rocks of the Earth's crust. After its irradiation (one or more irradiation cycles) the fuel is considered as spent nuclear fuel (SNF) and must be managed as waste. The SNF is composed of a UO_2 matrix (>95%) and other radioactive elements. The latter are very hazardous, making the waste management difficult. Their hazard progressively decreases by natural processes (radioactive decay) leading, after several millions of years, to a total radioactivity that equals the radioactivity of natural uranium [2]. Therefore, it has been proposed that the most appropriate and natural way of managing this waste is to return it to the Earth's crust. For this aim, the generally agreed solution is the burial of the SNF in the so called deep geological disposal of radioactive wastes for a period, at least, as long as the radioactive decay time.

The design of a deep geological repository must avoid the reach of these radionuclides to the biosphere for such a long time, and the best recognized option for this purpose is the use of a multi-barrier system which, in general, involves containing the radioactive waste inside canisters, then a buffer that protects the canisters and, finally the whole system is surrounded by geological natural barriers. Despite the barriers, it is well-known that, at such a long time, water could be the vehicle that interacts with the barriers and could mobilize radionuclides. Therefore, the studies about the reaction between SNF and groundwater under the possible repository conditions are of great interest [3].

Although the groundwater conditions in a repository are generally reducing, in a layer near the fuel surface, *i.e.* within <50 μm of the fuel surface, an oxidative environment has been postulated [4]. This ambient is produced by the radiolysis of water due to the ionizing radiation associated with the fuel [5–7]. The radiolysis of groundwater results in the production of oxidants as H_2O_2 among others [8], which in contact with UO_2 leads to the formation of uranyl peroxides [9–14]. Studtite: $(UO_2)(O_2)\cdot 4H_2O$, and its dehydration product metastudtite: $(UO_2)(O_2)\cdot 2H_2O$, are the only known uranyl peroxides [15–17] and both were found as corrosion products of SNF [12–14] in two-year experiments with deionized water.

From this foundings, different essays have been performed highlighting that studtite plays an important role in the SNF corrosion process. For example, Amme [18] showed the precipitation of studtite by direct leaching of UO_2 with H_2O_2, and Kubatko et al. [15] showed that studtite may be formed even at very low peroxide concentrations

* Corresponding author.
E-mail address: francisco.colmenero@iem.cfmac.csic.es (F. Colmenero).

http://dx.doi.org/10.1016/j.saa.2016.11.040
1386-1425/

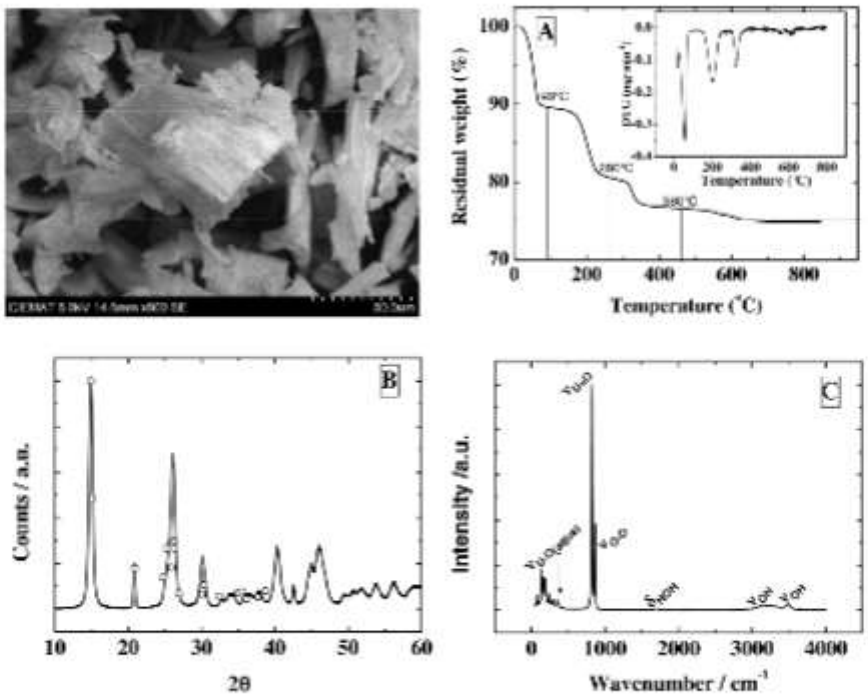

Fig. 1. Synthetic studtite characterization: SEM image of the precipitated crystals, and graphics corresponding to: (A) TGA curve and DTG (thermogravimetric derivative curve), (B) X-ray powder diffraction pattern and (C) Raman spectrum.

$(1.1 \cdot 10^{-14}$ M $H_2O_2)$, created by the alpha flux of natural uranium ores. Forbes et al. [19] found that studtite could be the alteration product of other uranyl hydrates as schoepite and soddyite, recognized as the fundamental secondary phases of SNF. Furthermore, studtite has been recently proposed as a corrosion product in sea water after the Fukushima-Daiichi nuclear plant accident [20–22]. Despite the

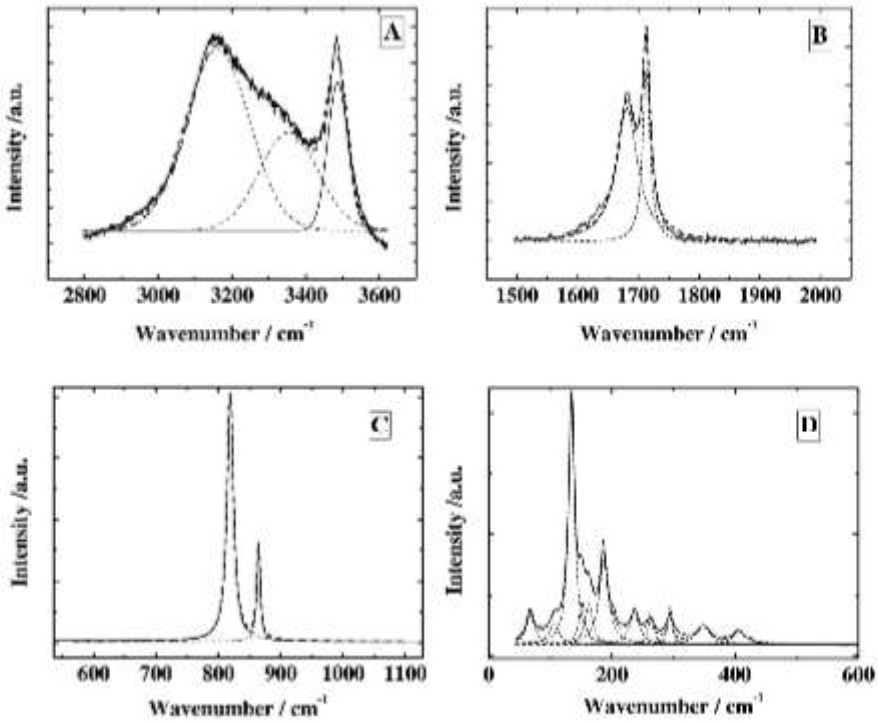

Fig. 2. Experimental Raman spectra obtained for studtite at STP conditions: A) OH stretching region: 2800–3600 cm^{-1}, B) OH bending region: 1500–2000 cm^{-1}, C) Uranyl and peroxo stretching region: 600–1100 cm^{-1}, and D) low frequency region: 50–600 cm^{-1}.

importance of this uranyl mineral, there is still some doubt concerning its formation process and crystal structure [17].

The structures of uranyl peroxide hydrates have been investigated by means of theoretical methods in several previous works. The first study was that of Ostanin and Zeller [23] in which the structures of studtite and metastudtite were determined by means of density functional theory (DFT) methods using ultrasoft pseudopotentials. Studtite and the incorporation of neptunium into its structure were later investigated by Shuller [24] using the same kind of techniques and pseudopotentials. These calculations were refined by Weck et al. [25,26] by using DFT techniques and the projector augmented wave (PAW) method to describe the interaction between valence electrons and ionic cores. These authors also researched the mechanical stability of uranyl peroxide hydrates. Walshe et al. [27] have studied the local electronic structure of the hydrated uranium peroxides by means of *ab initio* quantum chemical calculations based on the real space Green function calculations. Studies of atomic clusters closely related to these systems have been reported by Odoh et al. [28,29].

In this work we study the structure of synthetic studtite by both experimental techniques (SEM, TGA, XRD and Raman spectroscopy) and computational density functional theory calculations. The DFT results were obtained by using a norm-conserving relativistic pseudopotential for uranium atom reported and validated for this kind of materials in a previous work [30]. As far as we know, there is not any published theoretical study on the vibrational spectra of these materials. Comparison of the experimental and computed Raman spectra allows us to assign the different Raman bands that form the whole spectra. The thermal stability of studtite has been analyzed at different conditions by *in situ* Raman spectroscopy. Specifically, we have studied the effect of the heating rate and the presence of liquid water on the studtite irreversible dehydration of studtite.

2. Materials and Methods

2.1. Experimental

Synthetic studtite, $UO_2(O_2)\cdot 4H_2O$, was precipitated at room temperature by adding dropwise a solution of 1 M H_2O_2 (Sigma-Aldrich) over a solution of 10^{-4} M uranyl nitrate hexahydrate $UO_2(NO_3)_2\cdot 6H_2O$ (Sigma-Aldrich). This reaction yields yellow crystals, which were rinsed with cold water and dried before experiments. The precipitate was characterized by thermogravimetry (TG), scanning electron microscopy (SEM), X-ray diffraction (XRD) and Raman spectroscopy (RS).

A Q50 thermo-balance (TA Instruments, Spain) was used in synthetic air for the TG analysis. Texture of the sample was analyzed with a Jeol 5600-LV scanning electron microscope (SEM) equipped with an Oxford Industries INCA X-sight energy dispersive X-ray spectrometer. XRD was conducted using a Philips PANalytical X'Pert MPD diffractometer using Cu K_{α_1} radiation ($\lambda = 1.54056$ Å) and operating at 45 kV and 40 mA. A Bragg–Brentano configuration geometry was used. The 2θ range covered was from 20° to 120°, with a scanning step of 0.02° and an overall exposure time of 18 h. Horiba LabRam HR evolution spectrometer (Jobin Yvon Technology) was used in order to acquire the Raman spectra. A red laser of HeNe with a wavelength of 632.81 nm and a nominal power of 20 mW was used as excitation source. The grating used has 600 grooves/mm leading to a resolution better than 1 cm^{-1}/pixel. The details of this equipment are described elsewhere [31].

In situ Raman characterization of the dehydration of studtite was carried out by using a Linkam temperature controlled pressure stage, THMS-600, coupled with the BX4 Olympus microscope of the Raman spectrometer. The mechanical design and electronics of the Linkam stage provided precise control and temperature stability better than 0.2 K. Spectra were collected with a 50× long-range objective through a silica window (used in place of the standard quartz optical window) on the top of the stage.

A simple home cell had been specifically used to perform the *in situ* Raman measurements of studtite in contact with liquid water. This cell was mainly composed by two borosilicate glass cover slides separated

Table 1
Raman shift, width and area of the Raman spectrum bands of studtite. Assignments given by Bastians et al. [49] are included for comparison. Numbers in bold indicate the bands that are not found in our measurements.

Center (cm^{-1})	Width (cm^{-1})	Area (a.u²)	Center (cm^{-1}) [49]	Assignment [49]
67.7 (0.3)	16(1)	30,503(1504)	–	–
106 (1)	20 (1)	25,115(1220)	–	–
134.61 (0.04)	11.8(0.1)	182,953(2184)	–	–
151.3 (0.4)	11(1)	31,312(57111)	–	–
162.8 (0.6)	15(2)	37,993.0(6203)	–	–
186.9 (0.2)	18.9(0.6)	100,069(2865)	–	–
236.8 (0.4)	25 (1)	39,209 (1461)	238	–
263.4 (0.4)	14.2 (0.8)	16,543 (1275)	261	–
294.3 (0.2)	24.5 (0.9)	30,935 (1031)	294	–
348.11 (0.8)	33 (1)	27,889(1035)	351	$\nu^5(UO_{equa})$
405.6 (0.9)	29 (1)	18,670 (940)	405	–
–	–	–	**433**	–
–	–	–	**815**	–
819.05 (0.02)	12.33 (0.05)	778,663 (2133)	819	$\nu^5(UO_2^{2+})$
–	–	–	**840**	–
864.40 (0.03)	6.48 (0.09)	154,047 (1491)	864	$\nu(OO)$
1681.1 (0.2)	43.0 (0.7)	116,513 (1811)	1648	$\delta(H_2O)$
1713.04 (0.07)	14.6 (0.3)	51,439 (1010)	1710	$\delta(H_2O)$
3161(2)	174 (2)	546,238 (12150)	3085	$\nu(OH)$
3354 (3)	161 (6)	273,672 (14514)	–	–
3487.1 (0.8)	55.6 (0.8)	143,344 (3601)	3450	$\nu(OH)$

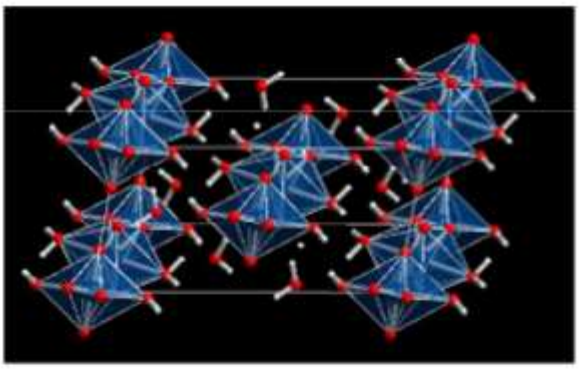

Fig. 3. General view of the studtite structure $(UO_2)(O_2)\cdot 4H_2O$: Color code: U-Blue, O-Red, H-Grey. (For interpretation of the references to color in this figure legend, the reader is referred to the web version of this article.)

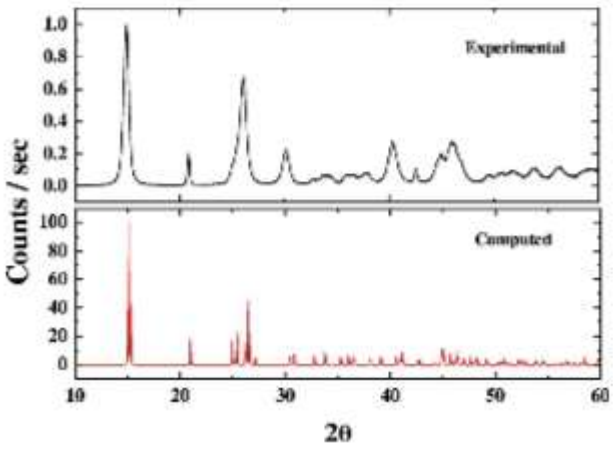

Fig. 4. Comparison of experimental and computed XRD patterns.

Table 2
Studtite lattice parameters.

Parameters	a (Å)	b (Å)	c (Å)	α	β	γ	Vol. (Å^3)	Density (g/cm^3)
This work	13.813	6.804	8.496	90.0	122.951	90.0	669.98	3.708
DFT [26]	13.93	6.84	8.55	90.0	122.7	90.0	685.6	–
DFT [24]	13.96	6.88	8.53	90.0	122.55	90.0	689.9	–
Exp. [17]	14.068	6.721	8.428	90	123.356	90	665.6	3.733

by an O-ring. Therefore, the sample with water was housed between the two cover slides, separated by the O-ring. A detailed description of this cell and its set up can be found in the Appendix A of the Supplementary Information.

2.2. Theoretical DFT Calculations

Studtite models of unit cells have been calculated using the CASTEP code [32], a module of the Materials Studio package [33]. The generalized gradient approximation (GGA) together with PBE functional [34] was used. Grimme empirical dispersion correction, the DFT-D2 approach [35] was used in order to describe properly the hydrogen bonding present in the system studied in this work. Geometry optimization was carried out using the Broyden–Fletcher–Goldfarb–Shanno optimization scheme [36,37] with a convergence threshold on atomic forces of 0.01 eV/Å. The different kinetic energy cutoffs and k-point meshes [38], must be adopted to ensure good convergence for computed structures and energies. Studtite structure was optimized in calculations with increasing complexity by increasing these parameters. The

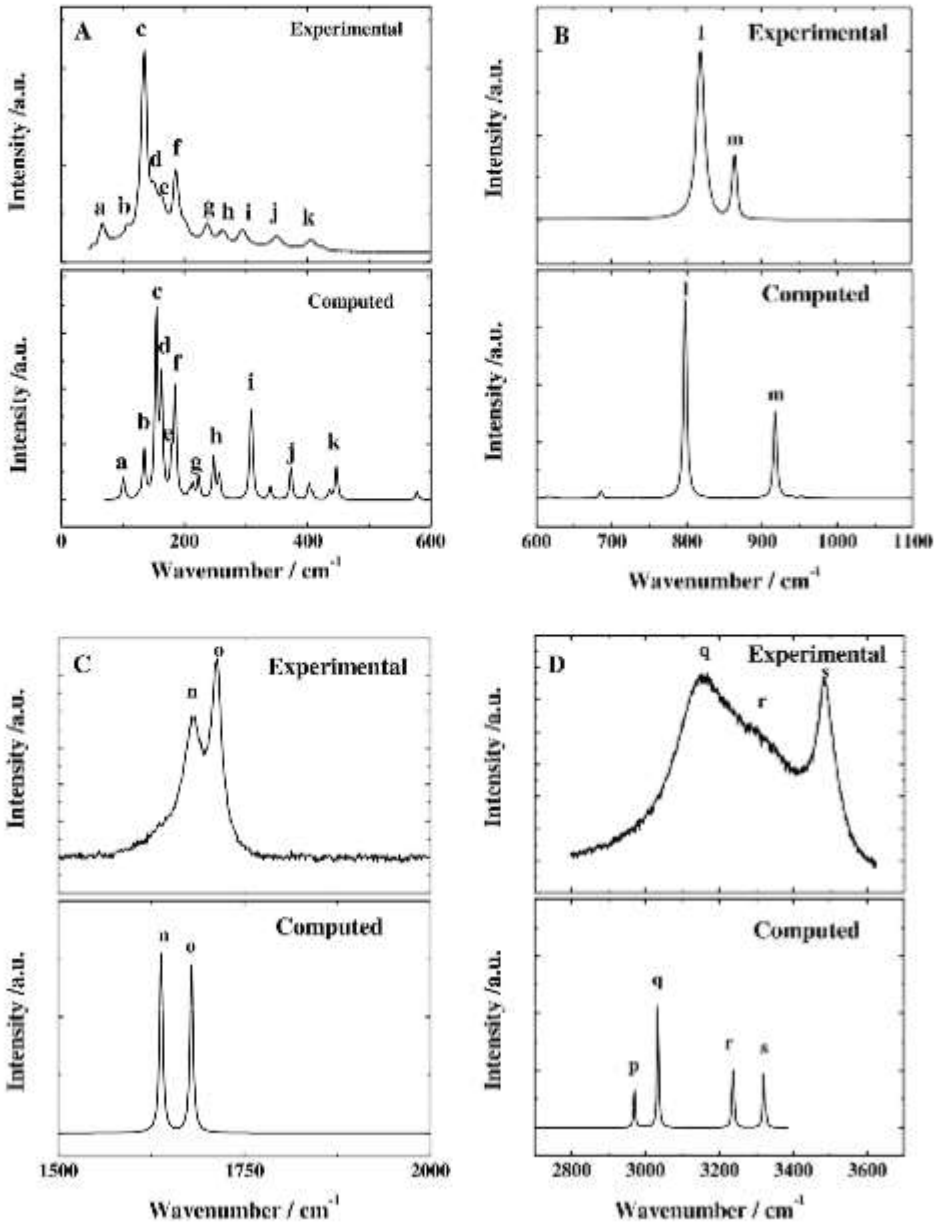

Fig. 5. Experimental and computed Raman spectra obtained for studtite at STP conditions: A) Low frequency region: 50–600 cm^{-1}, B) Uranyl and peroxo stretching region: 600–1100 cm^{-1}, C) HOH bending region: 1500–2000 cm^{-1}, and D) OH stretching region: 2800–3600 cm^{-1}.

optimization performed with a cutoff of 1000 eV and a K mesh of 2 × 4 × 4 (8 K points) gave a well converged structure and was used to determine the final results.

For the calculations of vibrational properties, the linear response density functional perturbation theory (DFPT) [39–41] implemented in the CASTEP code was used, where the phonon frequencies at the gamma point of the Brillouin zone were computed using atomic displacement perturbations. Raman intensities are third-order derivatives of total energy with respect to vibrational mode (atomic position) and laser field (electric field, twice). These are calculated in CASTEP [42] by using a combination of perturbation theory (second derivative with respect to field) and finite differences (third derivative with respect to atomic displacement). The frequencies presented in this work have not been scaled to correct for anharmonicity and remaining errors of the theoretical treatment employed, such as incomplete treatment of electron correlation and basis set truncation [43]. They correspond to the harmonic approximation of the force field. Since the effects of these defects tend to cancel out, the scale factor should be near to unity.

The pseudopotential for uranium atom used is a scalar relativistic GGA-PBE Troullier-Martins [44] type norm-conserving pseudopotential. Its generation was described in a previous work [30].

3. Results and Discussion

3.1. Experimental Characterization

The synthesized studtite was analyzed by different techniques: scanning electron microscopy (SEM), TGA, X-Ray diffraction (XRD) and Raman spectroscopy (RS). Results are shown in Fig. 1.

SEM micrographs reveal the high crystallinity of the rod-shaped sample, as the general morphology of studtite.

The curve shown in Fig. 1. A was obtained by placing a few milligrams (~8 mg) of the sample in the platinum TGA balance, and increasing the temperature up to 850 °C at a rate of 5 °C/min, in a synthetic air flow of 60 mL/min. The TGA results (see the DTG curve in the inset of Fig. 1.A) show a reasonable agreement with the literature data [45], *i.e.* the initial studtite loses two molecules of water from 22 to 90 °C (Eq. (1)). Between 90 and 260 °C the decrease in weight can be associated with a loss of one oxygen and two molecules of water forming UO_3 (Eq. (2)), which is not stable and forms U_3O_8 (Eq. (3)) at temperatures higher than 570 °C.

$$UO_2(O_2)\cdot 4H_2O \rightarrow UO_2(O_2)\cdot 2H_2O\ (-2H_2O;\ 22\text{–}90\ ^\circ C) \quad (1)$$

$$UO_2(O_2)\cdot 2H_2O \rightarrow UO_3\ (-O, -2H_2O;\ 90\text{–}260\ ^\circ C) \quad (2)$$

$$UO_3 \rightarrow U_3O_8 \quad (3)$$

The XRD pattern showed in Fig. 1.B can be identified as that of studtite [46,47], $UO_2(O_2)\cdot 4H_2O$, in agreement with the data published by the International Center of Diffraction Data [48] (open symbols in Fig. 1.B correspond to the ICDD 98-016-7992 studtite pattern).

The Raman spectrum of the sample, shown in Fig. 1.C, corresponds to the typical spectrum of studtite in agreement with the published ones [27,49,50]. The only band assignment so far, was performed by Bastians et al. [49] and, therefore, in the following discussion we have used the band assignment given in this reference. Four regions can be distinguished in the spectrum. From 3000 to 3600 cm^{-1} two broad bands are assigned to the OH stretching vibrations of water. Around 1600 cm^{-1} the two small bands are assigned to the water bending vibrations. The strongest bands appear in the intermediate region, from 700 to 900 cm^{-1}. The one at 819 cm^{-1} corresponds to the symmetric uranyl stretch, $\nu^s(UO_2^{2+})$, and the one at 865 cm^{-1} to the peroxo stretch, $\nu(OO)$, of the bridging peroxo ligands. The band at about 348 cm^{-1} was assigned to a symmetric stretching, $\nu^s(UO_{aqua})$.

In Fig. 2 the experimental analysis of the spectrum is presented. The fit, shown in this figure (dashed line), was obtained as follows: first, determining the number of contributions of a given band from the experimental spectrum by the second derivate method; and second, performing a Lorentzian fit. Results are summarized in Table 1, in which they are compared with some published data of this mineral phase [49].

As can be seen, the data obtained are in good agreement with those previously published, except for the bands at 433, 815 and 840 cm^{-1}. It should be noted that these bands could be due to the presence of impurities, since the bands at 433 and 815 cm^{-1} appear only in the spectrum of the synthetic sample, and they are not present in the natural one. Besides, these bands are very weak. The band at 840 cm^{-1} can be related to metastudtite, and therefore it is probably associated to the partial dehydration of studtite by natural processes or due to heating of the Raman excitation laser.

Table 3
Studtite experimental and calculated Raman shifts, calculated intensities and assignations.

Exp. wavenumber (cm^{-1})	Calc. wavenumber (cm^{-1})	Irr. rep. (C_{2h})	Intensity ($Å^4$)	Assignation
(a) 67.7 (0.3)	(a)101	Ag	2.39	$\rho(OUO_{aqua}) + \rho(UO_2^{2+}) + T(H_2O\text{-cr.})$
(b) 106 (1)	(b)135	Ag	9.16	$\rho(OUO_{aqua}) + \rho(UO_2^{2+}) + T(H_2O\text{-cr.})$
(c) 134.61 (0.04)	(c)154	Ag	43.42	$\rho(OUO_{aqua}) + \rho(UO_2^{2+}) + \rho(OUO_{perox}) + T(H_2O\text{-cr.})$
(d) 151.3 (0.4)	(d)163	Bg	29.06	$T(H_2O\text{-cr})$
(e) 162.8 (0.6)	(e)179	Bg	10.48	$\rho(UO_2^{2+})$
(f) 186.9 (0.2)	(f)185	Ag	34.17	$\rho(UO_2^{2+}) + \rho(OUO_{aqua}) + \rho(OUO_{perox}) + T(H_2O\text{-cr.})$
(g) 236.8 (0.4)	(g1)213	Ag	5.66	$\rho(UO_2^{2+}) + \rho(OUO_{aqua}) + T(H_2O\text{-cr.})$
	(g2)223	Bg	9.864	$\rho(OUO_{aqua}) + \rho(UO_2^{2+}) + \rho(OUO_{perox})$
(h) 263.4 (0.4)	(h_1)247	Ag	21.54	$\rho(UO_2^{2+}) + \rho(OUO_{aqua}) + T(H_2O\text{-cr.})$
	(h_2)257	Bg	12.76	$\rho(UO_2^{2+}) + \rho(OUO_{aqua}) + \rho(OUO_{perox}) + T(H_2O\text{-cr.})$
(i) 294.3 (0.2)	(i_1)308	Ag	40.90	$\rho(OUO_{perox})$
	(i_2)309	Ag	32.93	$\rho(OUO_{aqua}) + T(H_2O\text{-cr.})$
(j) 348.11 (0.8)	(j)373	Bg	30.48	$\rho(OUO_{perox})$
(k) 405.6 (0.9)	(k)402	Ag	17.42	$\rho(OUO_{perox})$
(l) 819.05 (0.01)	(l)798	Ag	2537.86	$\nu^s(UO_2^{2+})$
(m) 864.40 (0.03)	(m)917	Ag	1344.38	$\nu(OO)$
(n) 1681.1 (0.2)	(n)1638	Ag	142.66	$\delta(H_2O)$
(o) 1713.04 (0.07)	(o)1679	Ag	139.50	$\delta(H_2O)$
(p) –	(p)2970	Ag	2993.29	$\nu(OH)$
(q) 3161 (2)	(q)3033	Ag	10,233.49	$\nu(OH)$
(r) 3354 (3)	(r)3238	Ag	4734.37	$\nu(OH)$
(s) 3487.1 (0.8)	(s)3319	Ag	5109.120	$\nu(OH)$

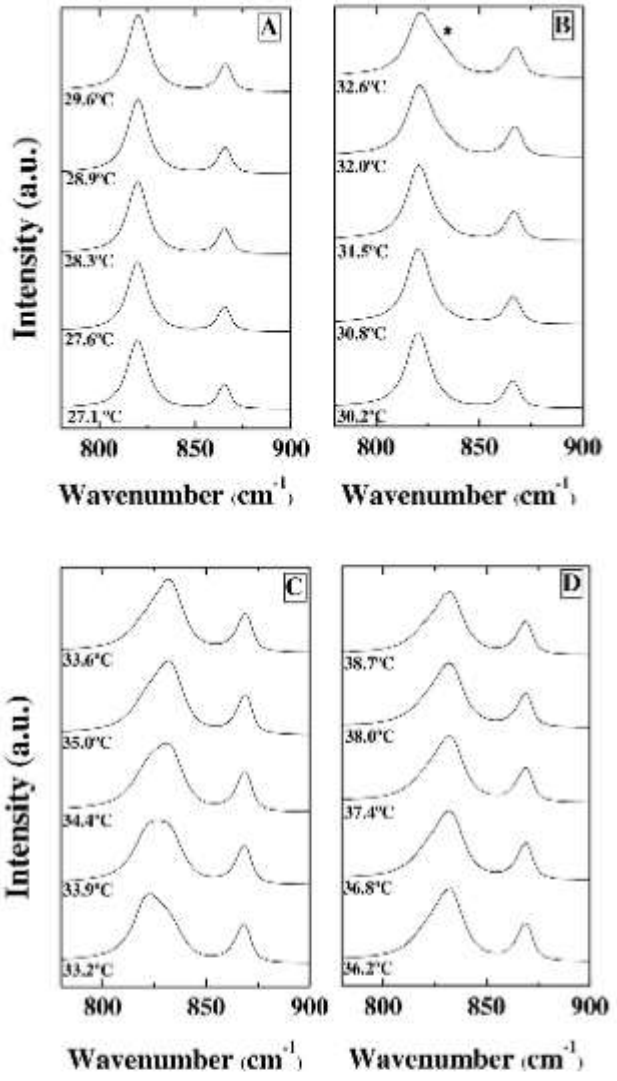

Fig. 6. Evolution of the Raman spectrum along a 1 °C/min heating process, obtained by the use of Raman microscopy in conjunction with a Linkam thermal stage. Fig. 6.A corresponds to spectra from 27.1 °C to 29.6 °C, Fig. B from 30.2 °C to 32.6 °C, Fig. C from 33.2 °C to 35.6 °C and Fig. D from 36.2 °C to 38.7 °C.

3.2. DFT Calculations

3.2.1. Structure

The optimized studtite structure is displayed in Fig. 3. As can be observed, uranium atom displays hexagonal bipyramid coordination. Two oxygen atoms are in apical positions and the six equatorial oxygen atoms are two peroxo groups (four oxygen atoms) forming opposite edges of the hexagon and two water molecule oxygen atoms. The different bipyramids are linked by sharing the peroxo equatorial edges and form zig-zag chains. The studtite structure has two kinds of water molecules in the structure, one half being the structural ones and the other crystallization water molecules; thus, the structure is more correctly formulated as $[(UO_2)O_2(H_2O)_2]\cdot 2H_2O$. The chains are held together by means of a network of hydrogen bonds between these water molecules. Each water molecule forming part of the uranyl polyhedra (structural water, also called terminal aqua groups) donates two hydrogen bonds with other water molecules which do form part of the bipyramids (crystallization water).

The X-Ray pattern of studtite was computed from the calculated structure using the program REFLEX, a module of Materials Studio Package [33] and compared with an experimental one in Fig. 4. As can be seen, the agreement in line positions and intensities is quite satisfactory.

Studtite optimized lattice parameters, volumes and densities compared with those obtained in previous theoretical studies [23–26] and experimental results [17] are shown in Table 2. As it can be seen, the agreement is excellent. The computed volume is larger than experimental value by only about 0.7%. Overestimation of volume and bond distances (see Appendix B of Supplementary Information) is a general trend in DFT calculations [51,52].

A more complete description and additional data about the calculated studtite structure and its X-Ray powder spectra is given in Appendix B of Supplementary Information.

3.2.2. Raman Spectrum and Band Assignment

The Raman spectrum of studtite was calculated at T = 298 K, λ = 532 nm, FWHM = 5 cm^{-1} and compared with the experimental one in Fig. 5. The experimental and calculated wavenumbers, the calculated intensities and the assignments derived from the calculations are shown in Table 3. The atomic motions associated to each vibrational normal mode are shown in the Appendix C of Supplementary Information.

The two bands at the highest wavenumbers are mainly attributed to OH stretching vibrations for the crystallization water molecules and the ones at the lowest wavenumbers to the structural water molecules (see vibrational mode pictures of the Appendix B of Supplementary Information). The two bands placed at about 1650 cm^{-1} represent water

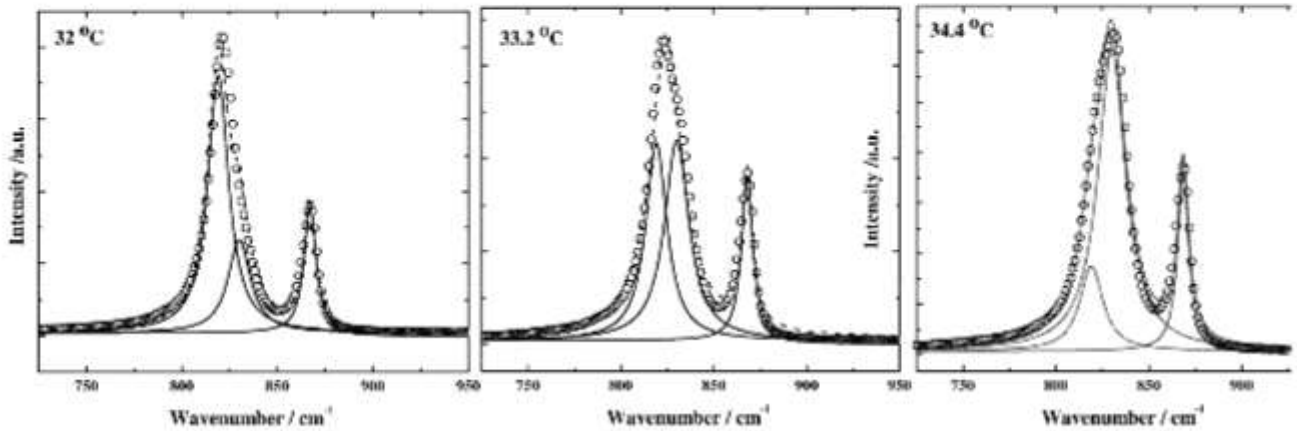

Fig. 7. Lorentzian fit of the Raman spectra obtained at three temperatures in the phase transition region.

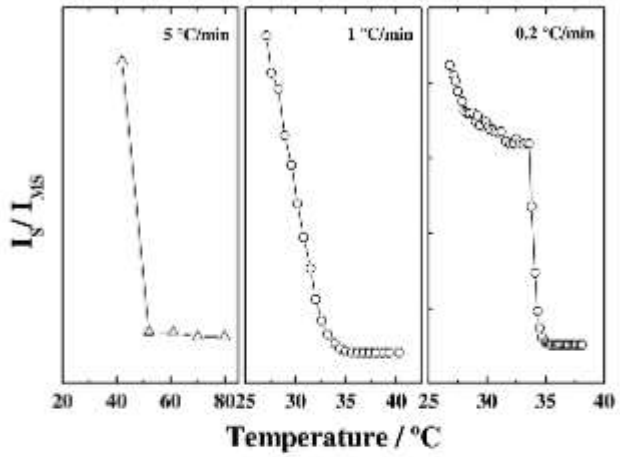

Fig. 8. I_S/I_{MS} ratio as a function of temperature for three different heating rates. I_S and I_{MS} correspond to the symmetric uranyl stretch ($\nu^S_{O=U=O}$) intensity band for studtite and metastudtite, respectively.

bending vibrations, $\delta(H_2O)$. The band at lower wavenumber corresponds mainly to the bending of crystallization water molecules whereas the band at higher wavenumber should be associated to the structural water molecules.

The experimental band at about 864 cm^{-1} is shifted in the computed spectra by nearly 53 cm^{-1} (calculated value is 917 cm^{-1}). It is assigned to peroxo group O—O stretching, $\nu(OO)$. The most intense band in the Raman spectrum appears at 819 cm^{-1} and the calculated wavenumber is 798 cm^{-1}. It is attributed to the uranyl symmetric stretching vibration $\nu^S(UO_2^{2+})$.

The bands placed at 405 and 348 cm^{-1} have theoretical counterparts of 402 and 373 cm^{-1} and are assigned to a $\rho(OUO_{perox})$ vibration. With the symbol ρ we denote an antisymmetric motion of O atoms belonging to equatorial peroxo groups at opposite sides of U atom. Since the O—U—O atoms form an angle of nearly 180° and the central U atom does not move during the motion, the result can be described as a planar rotation similar to a rocking vibration, usually denoted with symbol ρ (see the corresponding vibrational mode pictures in Appendix C of Supplementary Information). However, the last band was assigned to an asymmetric U—O_{aqua} stretching, $\nu^{as}(UO_{aqua})$ in the experimental work performed by [49]. In this work, the symmetric U—O_{aqua} stretching band appears at a higher wavenumber, at 446 cm^{-1} (see Appendix C of Supplementary Information).

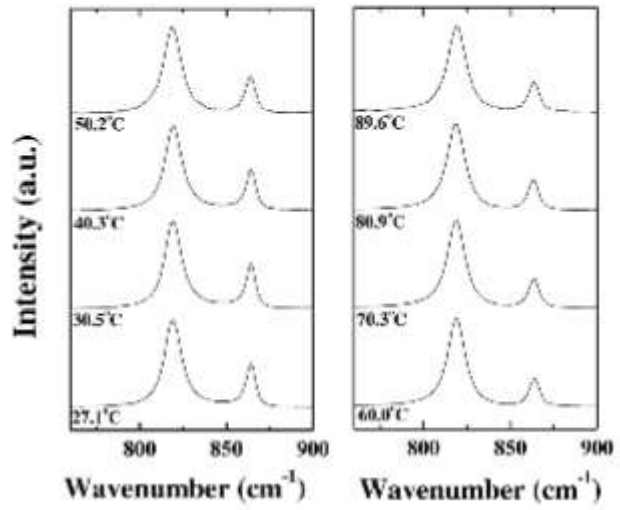

Fig. 9. Evolution of the Raman spectrum of studtite in contact with liquid water during heating experiments in the designed cell with a Linkam thermal stage.

The band located at 294 cm^{-1} is associated with two nearly coincident theoretical bands at 308 and 309 cm^{-1}. The first is assigned to $\rho(OUO_{perox})$. Since in this case the two O atoms of the peroxide group of each side of U atom perform the same vibrations, the peroxide group motion is nearly a translation. The second band is mainly assigned to $\rho(OUO_{aqua})$, that is, now, the O atoms involved are those belonging to equatorial aqua groups. It must be noted that the H atoms in the aqua groups performs similar motions as O atom. Crystallization water molecules nearly translate in this mode.

Bands placed at 263, 184 and 135 cm^{-1} are determined at 257, 185, and 154 cm^{-1}, and attributed to a combination of ρ(O-U-O) vibrations, axial $\rho(UO_2^{2+})$ and equatorial $\rho(OUO_{perox})$ and $\rho(OUO_{aqua})$, and crystallization water molecules translations. For the bands at 237, 203, 107 and 67 cm^{-1} we obtained theoretical values of 247, 223, 135, and 101 cm^{-1}, associated with uranyl axial $\rho(UO_2^{2+})$ and equatorial $\rho(OUO_{aqua})$ vibrations and crystallization water molecules translations. Finally, the ones at 164 and 150 cm^{-1} are calculated at 179 and 163 cm^{-1}. The first is assigned to uranyl axial $\rho(UO_2^{2+})$ vibration and the second one to crystallization water molecules translations.

3.3. Thermal Stability of Studtite

It is well-known that studtite loses two water molecules forming metastudtite with the rise of temperature (see TGA results in Fig. 1.A). In this section the stability of studtite is studied with the aim of knowing the effect of: 1) the heating rate, and 2) the presence of water in the dehydration process.

3.3.1. Heating Rate Effect

In order to study the heating rate effect on the stability of studtite, different dehydration processes at three different heating rates in dry air were performed in the Linkam stage. The processes were analyzed by *in situ* Raman spectroscopy. Fig. 6 shows, as an example, some of the Raman spectra obtained at different temperatures when a small amount of studtite is heated at 1 °C/min. Fig. 6.A shows the spectra from 27.1 °C to 29.6 °C, Fig. B from 30.2 °C to 32.6 °C, Fig. C from 33.2 °C to 35.6 °C and Fig. D from 36.2 °C to 38.7 °C.

As can be appreciated, a new band appears as a shoulder at ~830 cm^{-1} (see asterisk in Fig. 6.B) when the temperature reaches 32.6 °C. From this temperature on, the intensity of such new band, previously attributed to the metastudtite symmetric uranyl stretch ($\nu^S_{O=U=O}$) [49], increases. Opposite behaviour is shown for the band corresponding to $\nu^S_{O=U=O}$ of studtite at ~819 cm^{-1}. At 33.9 °C the intensity of both bands are very similar, leading to a symmetric broad band centered at ~827 cm^{-1}. The intensity of the ($\nu^S_{O=U=O}$) band corresponding to studtite vanishes at temperatures above 35.6 °C. In Fig. 6, a shift to higher frequencies of the peroxo stretch ν_{O-O} of the bridging peroxo ligands can also be observed at ~865 cm^{-1}. This behaviour reflects a phase transition from studtite to metastudtite.

Fig. 7 shows the analysis of the Raman spectra obtained at three temperatures in the phase transition region.

As can be seen, the band at around ~827 cm^{-1} can be understood as the direct sum of the symmetric uranyl stretch ($\nu^S_{O=U=O}$) of studtite (819 cm^{-1}) and metastudtite (830 cm^{-1}).

From this analysis, it becomes clear that it is possible to analyze the phase transition by analyzing the intensities of the mentioned bands. Therefore, the relative intensity I_S/I_{MS}, (where I_S and I_{MS} corresponds to the symmetric uranyl stretch ($\nu^S_{O=U=O}$) intensity band for studtite and metastudtite, respectively) are shown in Fig. 8 as a function of temperature for heating rates of 0.2, 1 and 5 °C/min.

By considering the temperature at which the $I_S/I_{MS} \sim 0$, the transition temperatures, T_t, are 50, 35 and 35 °C for the rate studies; *i.e.*, at low heating rates (0.2 °C/min) the transition temperature is around 35 °C, whereas at a high rate (5 °C/min) the T_t is higher. This increase in T_t

could be due to the fact that the system is out of equilibrium at such a high heating rate and, therefore, T_t at equilibrium should be obtained in experiments at heating rates below 1 °C/min.

3.3.2. Presence of Liquid Water

The effect of water molecules in contact with the mineral on the studtite thermal stability was studied by placing a few mg of studtite covered with liquid water in the designed cell. The cell was housed in the Linkam stage in which the temperature of the system was increased at 0.2 °C/min. Fig. 9 shows some of the Raman spectra obtained in the *in situ* analysis of these experiments.

As can be observed, all spectra correspond to the studtite structure, i.e., in presence of liquid water the dehydration of the molecule does not take place in the temperature range studied. This behaviour (higher thermal stability against dehydration than that in air) has been shown in other systems [53].

4. Conclusions

In this work studtite was synthetized and characterized by scanning electron microscopy (SEM), TGA, X-Ray diffraction (XRD) and Raman spectroscopy. The structure was besides analyzed by computed DFT calculations. The computed X-ray diffractogram, in agreement with the experimental one, indicates that the optimized structure of studtite describes accurately the experimental studtite structure. Moreover, the computed Raman spectrum shows a correspondence to the experimental bands and, therefore, they could be assigned to specific vibrational motions. The OH stretching and bending bands were found to be associated to specific types of water molecules (crystallization and structural).

The thermal stability of studtite was studied by *in situ* Raman spectroscopy, performing the dehydration of studtite at different heating rates (5, 1 and 0.2 °C/min) and in presence of water. For this work, a new cell was designed. The results show how the temperature of the dehydration process at low heating rates takes place around 33–34 °C. However, when the experiments were performed at a higher heating rate (5 °C/min) the temperature increased at 50 °C. This discrepancy may be due to the fact that the system is out of equilibrium at such a high heating rate, which would explain the TGA results, and the previous published ones, which shows a high loss of water at low temperatures (<90 °C), and points out the importance of applying low heating rates in this kind of studies.

From the experiments performed in presence of water, the studtite is stable up to 90 °C, what is consistent with the founding of this phase after the Fukushima-Daiichi accident [20–22]. More studies are needed to be done in order to clarify the moisture effect on the thermal stability of this mineral phase.

Acknowledgements

This work was supported by ENRESA in the project: N° 079000189 "Aplicación de técnicas de caracterización en el estudio de la estabilidad del combustible nuclear irradiado en condiciones de almacenamiento" (ACESCO) and project CGL2013-48415-C2-1-R. Supercomputer time by the CETA-CIEMAT, CTI-CSIC and CESGA centers are also acknowledged. We also want to thank to Dr. Rafael Escribano for his help in the assignment of the bands of the Raman spectrum and Dr. Ana María Fernández for reading the manuscript and many helpful comments.

Appendix A. Supplementary Data

Supplementary data associated with this article contain three appendices to the present article. Appendix A contains a description of the home cell used to perform the in situ Raman measurements of studtite in contact with water. Appendix B provides additional details on the theoretical DFT calculations reported in this work. Appendix C gives graphical pictures of the Raman normal modes of studtite. Supplementary data associated with this article can be found in the online version, at http://dx.doi.org/10.1016/j.saa.2016.11.040.

References

[1] G. Choppin, J.O. Liljenzin, J. Rydberg, Radiochemistry and Nuclear Chemistry, Reed Educational and Professional Publishing Ltd, Oxford, 1995.
[2] A. Hedin, Spent Nuclear Fuel – How Dangerous Is It? SKB Technical Report 97-13, Swedish Nuclear Fuel and Waste Management Co., 1997
[3] SKB-91, Final Disposal of Spent Nuclear Fuel. Importance of the Bedrock for Safety, SKB Report 92-20, 1992.
[4] H. Christensen, S. Sunder, An evaluation of water layer thickness effective in the oxidation of UO_2 fuel due to radiolysis of water, J. Nucl. Mater. 238 (1996) 70–77.
[5] D.W. Shoesmith, Fuel corrosion processes under waste disposal conditions, J. Nucl. Mater. 282 (2000) 1–31.
[6] S. Sunder, Calculation of radiation dose rates in a water layer in contact with used CANDU UO_2 fuel, Nucl. Technol. 122 (1998) 211–221.
[7] A.O. Allen, The Radiation Chemistry of Water and Aqueous Solutions, D. Van Nostrand Co. Inc., Princeton, 1961.
[8] R. Wang, Y.B. Katayama, Dissolution mechanisms for UO_2 and spent fuel, Nucl. Chem. Waste Manage. 3 (1982) 83–90.
[9] G. Sattonnay, C. Ardois, C. Corbel, J.F. Lucchini, M.F. Barthe, F. Garrido, D. Gosset, Alpha-radiolysis effects on UO_2 alteration in water, J. Nucl. Mater. 288 (2001) 11–19.
[10] M. Amme, B. Renker, B. Schmid, M.P. Feth, H. Bertagnolli, W. Döbelin, Raman microspectrometric identification of corrosion products formed on UO_2 nuclear fuel during leaching experiments, J. Nucl. Mater. 306 (2002) 202–212.
[11] F. Clarens, J. de Pablo, I. Díez-Pérez, I. Casas, J. Giménez, M. Rovira, Formation of studtite during the oxidative dissolution of UO_2 by hydrogen peroxide: a SFM study, Environ. Sci. Technol. 38 (2004) 6656–6661.
[12] B. McNamara, E. Buck, B. Hanson, Observation of studtite and metastudtite on spent fuel, MRS Online Proceedings Library Archive 757 (2002) II9.7 (6 pages).
[13] B.D. Hanson, B. McNamara, E.C. Buck, J.I. F., E. Jenson, K. Krupka, B.W. Arey, Corrosion of commercial spent nuclear fuel. 1. Formation of studtite and metastudtite, Radiochim. Acta 93 (2005) 159–168.
[14] B. McNamara, B.D. Hanson, E.C. Buck, C. Soderquist, Corrosion of commercial spent nuclear fuel. 2. Radiochemical analyses of metastudtite and leachates, Radiochim. Acta 93 (2005) 169–175.
[15] K.-A.H. Kubatko, K.B. Helean, A. Navrotsky, P.C. Burns, Stability of peroxide-containing uranyl minerals, Science 302 (2003) 1191–1193.
[16] K.-A. Kubatko, Crystallography, Hierarchy of Crystal Structures, and Chemical Thermodynamics of Selectes Uranyl Phases(PhD Thesis) Graduate School of the University of Notre Dame, Illinois, 2005.
[17] P.C. Burns, K.-A. Hughes, Studtite, $[(UO_2)(O_2)(H_2O)_2](H_2O)_2$: the first structure of a peroxide mineral, Am. Mineral. 88 (2003) 1165–1168.
[18] M. Amme, Contrary effects of the water radiolysis product H_2O_2 upon the dissolution of nuclear fuel in natural ground water and deionized water, Radiochim. Acta 90 (2002) 399–406.
[19] T.Z. Forbes, P. Horan, T. Devine, D. McInnis, P.C. Burns, Alteration of dehydrated schoepite and soddyite to studtite, $[(UO_2)(O_2)(H_2O)_2](H_2O)_2$, Am. Mineral. 96 (2010) 202–206.
[20] C.R. Armstrong, M. Nyman, T. Shvareva, G.E. Sigmon, P.C. Burns, A. Navrotsky, Uranyl peroxide enhanced nuclear fuel corrosion in seawater, Proc. Natl. Acad. Sci. U. S. A. 109 (2012) 1874–1877.
[21] P.C. Burns, R.C. Ewing, A. Navrotsky, Nuclear fuel in a reactor accident, Science 335 (2012) 1184–1188.
[22] J. Giménez, J. de Pablo, I. Casas, X. Martínez-Lladó, M. Rovira, A. Martínez Torrents, Solubility study and point of zero charge of studtite ($UO_2O_2{\cdot}4H_2O$), Appl. Geochem. 49 (2014) 42–45.
[23] S. Ostanin, P. Zeller, Ab initio study of uranyl peroxides: electronic factors behind the phase stability, Phys. Rev. B 75 (2007) 073101.
[24] L.C. Shuller, Atomistic modeling of the solid-state chemistry of actinide materials(PhD Thesis) University of Michigan, 2010.
[25] P.F. Weck, E. Kim, E.C. Buck, On the mechanical stability of uranyl peroxide hydrates: implications for nuclear fuel degradation, RSC Adv. 5 (2015) 79090–79097.
[26] P.F. Weck, E. Kim, C.F. Jove-Colon, D.C. Sassani, Structures of uranyl peroxide hydrates: a first-principles study of studtite and metastudtite, Dalton Trans. 41 (2012) 9748–9752.
[27] A. Walshe, T. Pru, Vitova, R.J. Baker, An EXAFS and HR-XANES study of the uranyl peroxides $[UO_2(\eta^2\text{-}O_2)(H_2O)_2]{\cdot}nH_2O$ (n = 0, 2) and uranyl (oxy)hydroxide $[(UO_2)_4O(OH)_6]{\cdot}6H_2O$, Dalton Trans. 43 (2014) 4400–4407.
[28] S.O. Odoh, G. Schreckenbach, DFT study of uranyl peroxo complexes with H_2O, F^-, OH^-, CO_3^{2-}, and NO_3^-, Inorg. Chem. 52 (2013) 5590–5602.
[29] S.O. Odoh, J. Shamblin, C.A. Colla, S. Hickam, H.L. Lobeck, R.A.K. Lopez, T. Olds, J.E.S. Szymanowski, G.E. Sigmon, J. Neuefeind, W.H. Casey, M. Lang, L. Gagliardi, P.C. Burns, Structure and reactivity of X-ray amorphous uranyl peroxide, U_2O_7, Inorg. Chem. 55 (2016) 3541–3546.
[30] L.J. Bonales, F. Colmenero, J. Cobos, V. Timon, Spectroscopic Raman characterization of rutherfordine: a combined DFT and experimental study, Phys. Chem. Chem. Phys. 18 (2016) 16575–16584.
[31] L.J. Bonales, C. Menor-Salván, J. Cobos, Study of the alteration products of a natural uraninite by Raman spectroscopy, J. Nucl. Mater. 462 (2015) 296–303.
[32] S.J. Clark, M.D. Segall, C.J. Pickard, P.J. Hasnip, M.I.J. Probert, K. Refson, M.C. Payne, First principles methods using CASTEP, Z. Kristallograph. 220 (2005) 567–570.
[33] Materials Studio, http://accelrys.com/products/materials-studio, (2014).

[34] J.P. Perdew, K. Burke, M. Ernzerhof, Generalized gradient approximation made simple, Phys. Rev. Lett. 77 (1996) 3865–3868.
[35] S. Grimme, Semiempirical GGA-type density functional constructed with a long-range dispersion correction, J. Comput. Chem. 27 (2006) 1787–1799.
[36] B.G. Pfrommer, M. Côté, S.G. Louie, M.L. Cohen, Relaxation of crystals with the quasi-Newton method, J. Comput. Phys. 131 (1997) 233–240.
[37] M.C. Payne, M.P. Teter, D.C. Allan, T.A. Arias, J.D. Joannopoulos, Iterative minimization techniques for *ab initio* total-energy calculations: molecular dynamics and conjugate gradients, Rev. Mod. Phys. 64 (1992) 1045–1097.
[38] H.J. Monkhorst, J.D. Pack, Special points for Brillouin-zone integrations, Phys. Rev. B 13 (1976) 5188–5192.
[39] S. Baroni, S. de Gironcoli, A. Dal Corso, P. Giannozzi, Phonons and related crystal properties from density-functional perturbation theory, Rev. Mod. Phys. 73 (2001) 515–562.
[40] X. Gonze, C. Lee, Dynamical matrices, born effective charges, dielectric permittivity tensors, and interatomic force constants from density-functional perturbation theory, Phys. Rev. B 55 (1997) 10355–10368.
[41] K. Refson, P.R. Tulip, S.J. Clark, Variational density-functional perturbation theory for dielectrics and lattice dynamics, Phys. Rev. B 73 (2006) 155114.
[42] V. Milman, K. Refson, S.J. Clark, C.J. Pickard, J.R. Yates, S.P. Gao, P.J. Hasnip, M.I.J. Probert, A. Perlov, M.D. Segall, Electron and vibrational spectroscopies using DFT, plane waves and pseudopotentials: CASTEP implementation, J. Mol. Struct. (THEOCHEM) 954 (2010) 22–35.
[43] W.J. Hehre, L. Radom, P.V.R. Schleyer, J.A. Pople, Ab Initio Molecular Orbital Theory, Wiley, New York, 1986.
[44] N. Troullier, J.L. Martins, Efficient pseudopotentials for plane-wave calculations, Phys. Rev. B 43 (1991) 1993–2006.
[45] A. Rey, I. Casas, J. Giménez, J. Quiñones, J. de Pablo, Effect of temperature on studtite stability: thermogravimetry and differential scanning calorimetry investigations, J. Nucl. Mater. 385 (2009) 467–473.
[46] P.C. Debets, X-ray diffraction data on hydrated uranium peroxide, J. Inorg. Nucl. Chem. 25 (1963) 727–730.
[47] K. Walenta, On studtite and its composition, Am. Mineral. 59 (1974) 166–171.
[48] ICDD, The International Center for Diffraction Data, PDF-2 Database, 2003.
[49] S. Bastians, G. Crump, W.P. Griffith, R. Withnall, Raspite and studtite: Raman spectra of two unique minerals, J. Raman Spectrosc. 35 (2004) 726–731.
[50] S. Labs, Secondary Uranium Phases of Spent Nuclear Fuel - Coffinite, USiO4, and Studtite, $UO_4 \cdot 4H_2O$ - Synthesis, Characterization, and Investigations Regarding Phase Stability, Forschungszentrum Jülich GmbH Verlag, Zentralbibliothek, 2015.
[51] I. Grinberg, N.J. Ramer, A.M. Rappe, Quantitative criteria for transferable pseudopotentials in density functional theory, Phys. Rev. B 63 (2001) 201102.
[52] W. Kohn, Y. Meir, D.E. Makarov, van der Waals energies in density functional theory, Phys. Rev. Lett. 80 (1998) 4153–4156.
[53] I.-M. Chou, R.R. Seal, B.S. Hemingway, Determination of melanterite-rozenite and chalcanthite-bonattite equilibria by humidity measurements at 0.1 MPa, Am. Mineral. 87 (2002) 108–114.

Supplementary Information

Study of the thermal stability of studtite by *in situ* Raman spectroscopy and DFT calculations

F. Colmenero[a], L.J. Bonales[b], J. Cobos[b], V. Timón[a]

[a]*Instituto de Estructura de la Materia, CSIC. C/ Serrano, 113. 28006 Madrid, Spain*

[b]*Centro de Investigaciones Energéticas, Medioambientales y Tecnológicas, CIEMAT. Avda/ Complutense, 40. 28040 Madrid, Spain*

Appendix A. Home-made cell

A very simple home-made cell had been used to perform the *in situ* Raman measurements of studtite in contact with liquid water. This cell is composed by two borosilicate glass cover slides of 22 mm diameter and 0.25 mm thickness separated by an O-ring of 20 mm diameter. See Fig. A.1

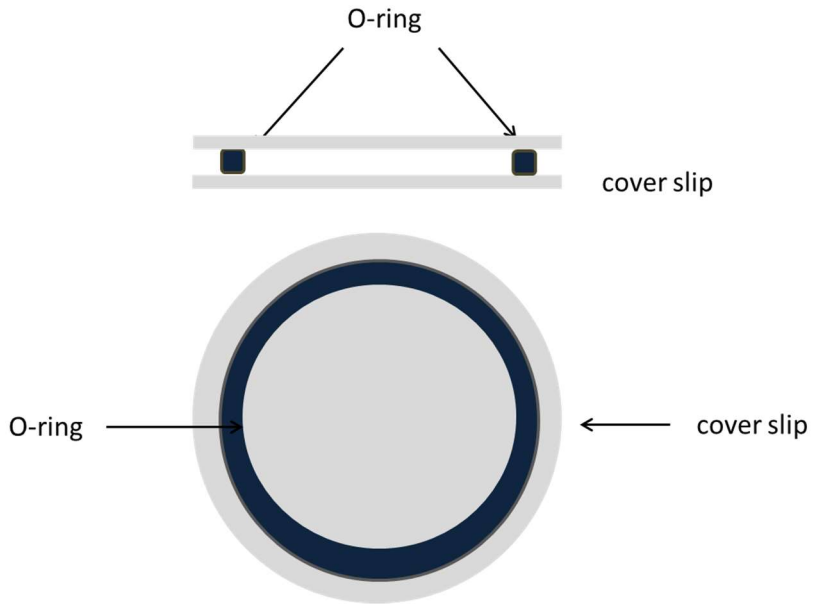

Fig. A1. Home-made cell sketch.

In Figure A.2 the setup it is shown. First, we place an O-ring on top of a cover slip (1), then some milligrams (10-20 mg) of the solid sample is disposed on the surface of a cover slide provided with the O-ring, and a few drops of water are added over the solid (2) and, finally, the other cover slide was placed on the top the sample (studtite and water) (3). Therefore, the sample was housed between the two cover slides, separated by the O-ring

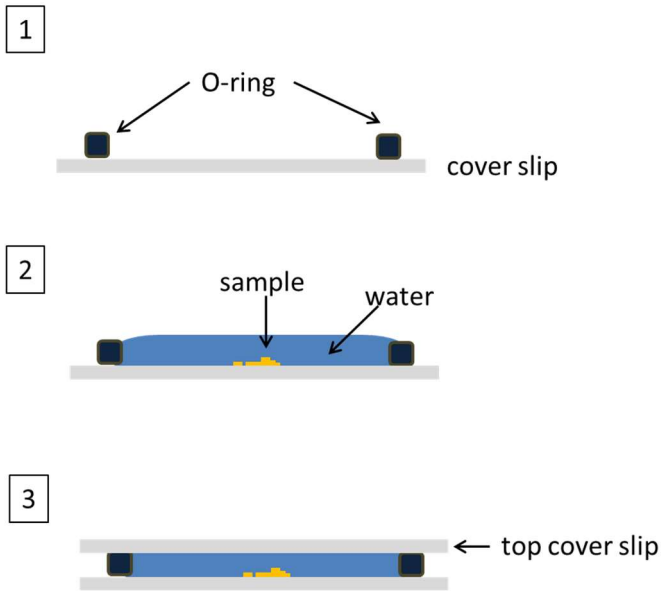

Fig. A.2. Home-made cell setup.

Appendix B. Studtite DFT calculations.

The mineral studtite was originally described in 1947 by Vaes [1] as a hydrated carbonate of uranium from a qualitative chemical analysis. Subsequent chemical and powder XRD investigations by Walenta [2] demonstrated that mineral studtite is identical to synthetic $(UO_2)O_2 \cdot 4H_2O$ [3-6]. Subsequent analyses of studtite from the type locality (Shinkolobwe) by Cejka *et al*. [7] confirmed Walenta's unit-cell determination. The structure of studtite was finally reported in 2003 by [8], which showed that its unit cell is approximately twice the size of the previously accepted unit-cell. The structure is displayed in Fig. B.1. Equilibrium structure is monoclinic and crystallizes in the space group C2/c (Z=4). [9], also reported the thermodynamic stability of the peroxide-containing uranyl minerals.

In studtite, uranium atom displays hexagonal bipyramid coordination. Two oxygen atoms are in apical positions forming with uranium atom nearly linear uranyl UO_2^{2+} uranyl ions. The six equatorial oxygen atoms are two peroxo groups (four oxygen atoms) forming opposite edges of the hexagon and two water molecule oxygen atoms. The different bipyramids are linked by sharing the peroxo equatorial edges and form zig-zag chains along [001] direction.

Most uranyl minerals including uranium as the only high-valence cation invariably contain sheets. However, some minerals as studtite are not based upon sheet of uranyl polyhedra, but contain polymerized uranyl polyhedra in only one dimension. The occurrence of chains rather sheets in U(VI) minerals is usually due to distortions in the polyhedra [10]. The presence of peroxide at the equatorial positions of the uranyl polyhedra results in distorted hexagonal bipyramids, with the peroxide O–O edge length (about 1.46 Å) being much shorter than the typical O–O edge length in uranyl hexagonal bipyramid (about 2.4 Å) This distortion may prevent the formation of two-dimensional layer structures.

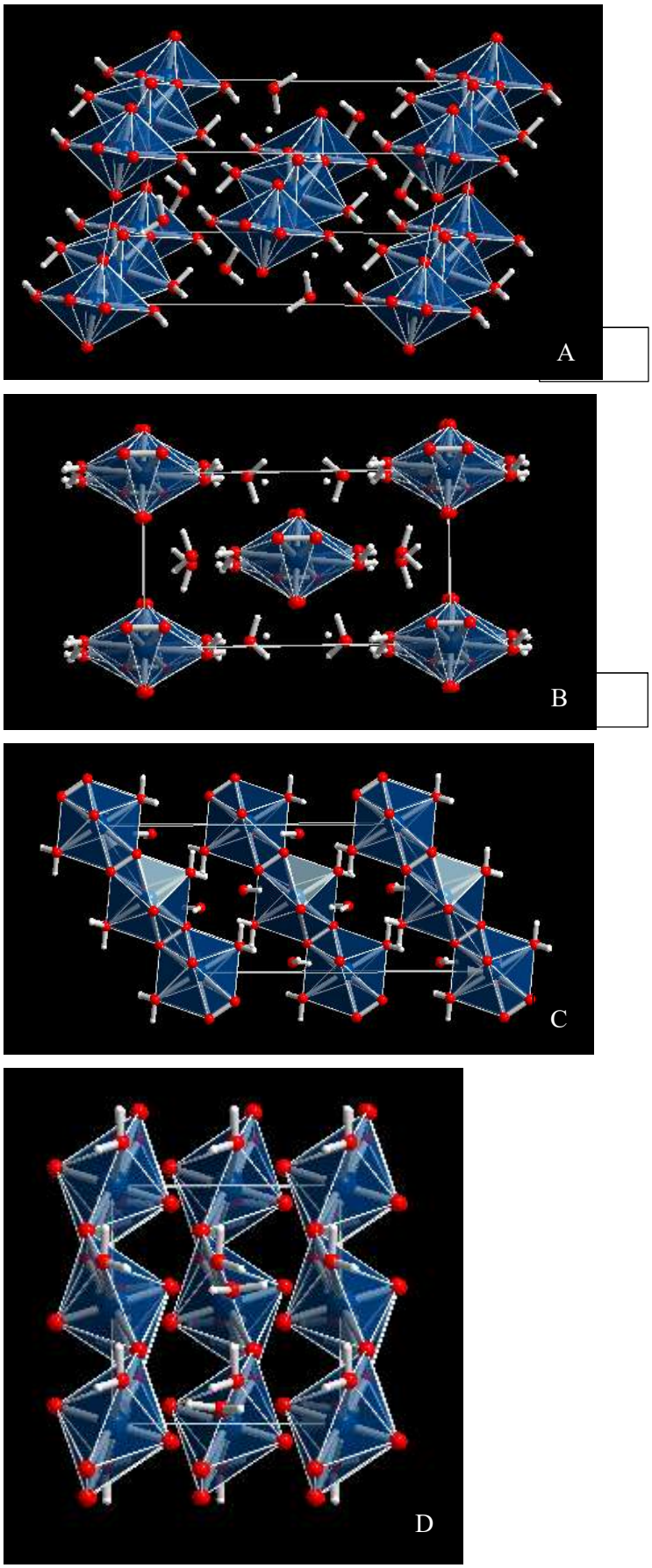

Fig. B.1. Structure of studtite, $(UO_2)(O_2)\cdot 4H_2O$: a) General view of the studtite structure; b) view from [001]; c) view from [010]; d) view from [100]. Color code: U-Blue, O-Red, C-Carbon.

The chains are held together by means of a network of hydrogen bonds. The hydrogen bond structure is show in detail in Fig. B.2. Each water molecule forming part of the uranyl polyhedra (structural water, also called terminal aqua groups) donate two hydrogen bonds with other water molecules which do form part of the bipyramids (crystallization water). The last two molecules participate in four hydrogen bonds. They are acceptors of two hydrogen bonds donated by structural water molecules of two subsequent bipyramids of a chain and are donors of two hydrogen bonds, one with a uranyl oxygen atom and one with a peroxide oxygen atom. These oxygen atoms belong to upper and lower chains. The uranyl oxygen atom is acceptor of one hydrogen bond and the two oxygen atoms in a peroxide group are each one also acceptors of one hydrogen bond. Thus, the network of hydrogen bonds enforces the structure by linking the chains at the same height and upper and lower chains. In studtite two subsequent bipyramids are linked not only by sharing a peroxo O-O edge but also through hydrogen bonds with an intermediate molecule outer of the bipyramids. The outer molecule receives these hydrogen bonds and donates hydrogen bonds to upper and lower chains.

Since there are two kinds of water molecules in the structure, one half being the structural ones and the other crystallization water molecules, the structure is more correctly formulated as $[(UO_2)O_2(H_2O)_2]\cdot 2H_2O$. Due to the fact that peroxo groups are side-bonded (η^2) to the uranium atoms, the structure is commonly referred to as $[(UO_2)(\eta^2\text{-}O_2)(H_2O)_2]\cdot 2H_2O$. However, the notation $[(UO_2)(\mu^2\text{-}O_2)(H_2O)_2]\cdot 2H_2O$ may also be used, indicating that peroxo atoms are μ^2-bridging between symmetry related uranium metal centers.

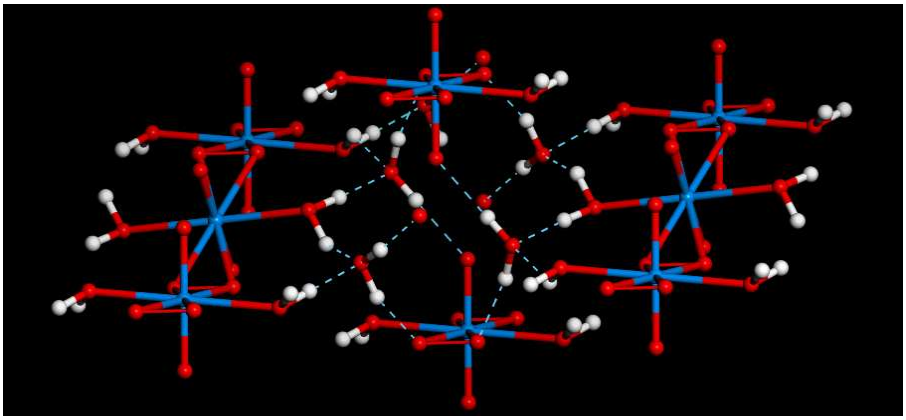

Fig. B.2. Detailed view of the hydrogen bond structure of studtite.

In this work, studtite structure was optimized in the calculations by increasing the different parameters (larger kinetic energy cutoffs and K meshes), i.e., increasing complexity. The optimization performed with a cutoff of 1000 eV and a K mesh of 2 x 4 x 4 (8 K points) gave a well converged structure and was used to determine the final material properties. Calculated lattice parameters, volumes and densities compared with the results of other calculations and the experimental results are given in table 2 of the main part of this paper. The corresponding bond distances and angles are given in Tables B.1 and B.2. Present results are comparable in accuracy with those of Weck *et al*. [11, 12].

Table B.1. Studtite bond angles (in deg).

Bond	**Exp.** [8]	**This work**	**DFT** [11]
U1-O1	1.769	1.807	1.83
U1-O2	1.769	1.807	1.83
U1-O3	2.352	2.383	2.38
U1-O3’	2.365	2.395	2.38
U1-O4	2.395	2.400	2.41
U1-U1	4.214	4.248	4.21
O3-O3’	1.464	1.430	1.46
O4-H1	0.978	0.999	1.00
O4-H2	0.975	1.000	1.00
H1..OH2	1.722	1.647	1.62
H2..OH2	1.959	1.644	1.66
O3..H2O	1.757	1.771	1.71
O2..H2O	1.956	1.795	1.79

Table B.2. Studtite bond angles (in deg).

Bond angle	**Exp.** [8]	**This work**	**DFT** [11]
O1-U1-O2	180.0	180.0	180.0
O1-U1-O3	89.73	89.00	88.2
O1-U1-O4	86.53	88.71	86.5
O2-U1-O3	90.27	90.54	92.3
O2-U1-O4	93.47	91.00	87.7
O3-U1-O3’	36.17	34.84	35.5
O3-U1-O3’’’	180.0	180.0	180.0
O3-U1-O3’’’’	143.83	145.16	144.4
O3-U1-O4	71.32	72.53	71.4
U1-O3-U1’’	126.60	125.52	124.0
O4-U1-O3’	107.25	107.35	106.9
O4-U1-O4’	180.0	180.0	180.0
O1-U1-U1’-O1’’	5.99	0.00	0.2

The powder X-ray powder spectrum of studtite was computed from the experimental and computed structures [13]. The most intense lines are compared in Fig. B.3 and, as can be seen, the agreement in line positions and intensities is very good. The use of spectra derived directly from the experimental and computed structures allows for a fair comparison of the results free of interferences as the experimental conditions or possible artefacts as the presence of sample impurities since both are determined under the identical conditions. Nevertheless, agreement with the experimental pattern of Debets [6] (see also [2] is also good. The main results are given in Table B.3. The pattern computed with program REFLEX, a module of Materials Studio package [14], is given in the main part of this paper.

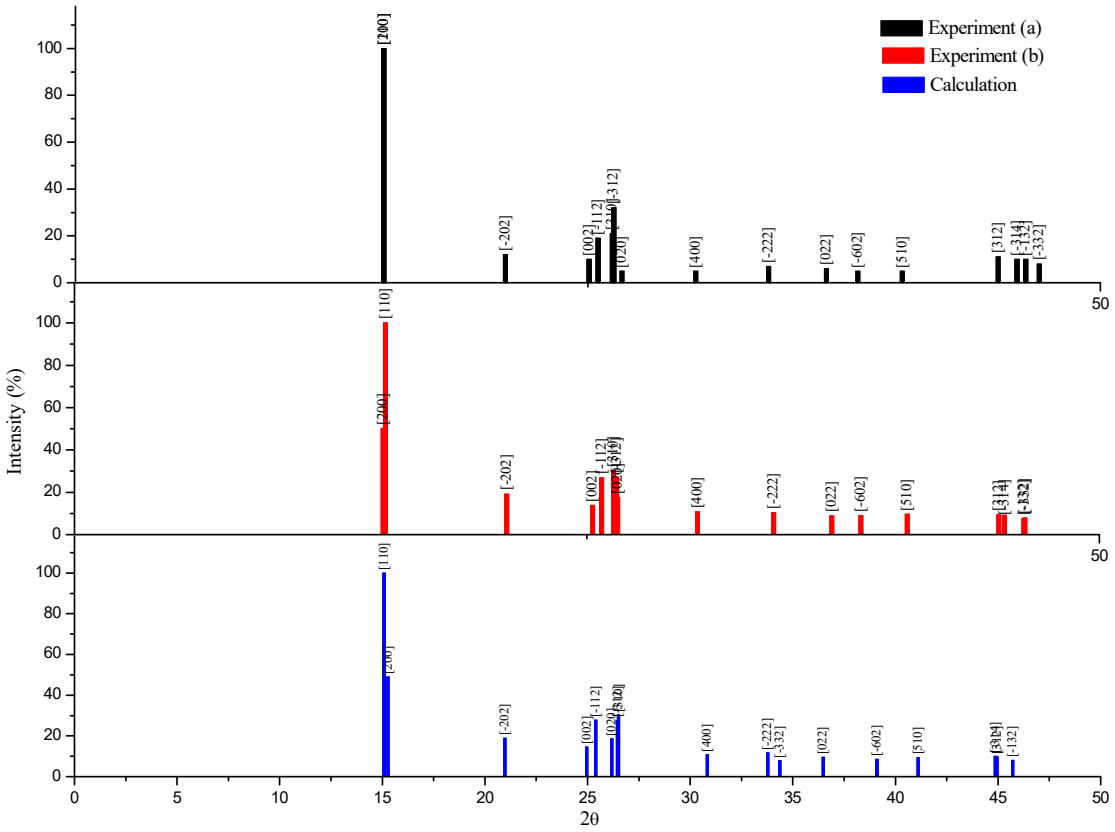

Fig. B.3. X-ray powder spectrum of studtite using CuK$_\alpha$ radiation: a) Experimental spectrum [6]; b) X-ray powder spectrum computed form experimental geometry [8]; c) X-ray powder spectrum computed from calculated geometry.

Table B.3. Main reflections in the X-ray powder spectrum of studtite. The experimental data are from a synthetic sample [6]

	Experimental reflections			Calculated reflections (Experimental geometry)			Calculated reflections (Calculated geometry)		
2θ	d(Å)	I (%)	hkl	2θ	d(Å)	I (%)	2θ	d(Å)	I (%)
15.055	5.88	100	200	15.067	5.8753	50.252	15.276	5.7955	48.977
15.055	5.88	100	110	15.174	5.8341	100.0	15.087	5.8675	100.0
20.984	4.23	12	-202	21.102	4.2067	19.182	20.971	4.2327	18.937
25.063	3.55	10	002	25.282	3.5198	13.810	24.960	3.5645	14.485
25.501	3.49	19	-112	25.723	3.4605	26.910	25.395	3.5045	27.734
26.188	3.40	21	310	26.314	3.3841	30.183	26.509	3.3597	30.472
26.267	3.39	32	-312	26.460	3.3658	27.202	26.465	3.3651	27.537
26.667	3.34	5	020	26.502	3.3605	17.568	26.175	3.4018	18.623
30.272	2.95	5	400	30.403	2.9376	10.744	30.832	2.8978	10.927
33.823	2.648	7	-222	34.121	2.6256	10.455	33.777	2.6516	11.681
36.634	2.451	6	022	36.953	2.4306	8.821	36.481	2.4610	9.587
38.167	2.356	5	-602	38.361	2.3446	9.070	39.096	2.3022	8.485
40.339	2.234	5	510	40.636	2.2184	9.721	41.102	2.1943	9.367
45.020	2.012	11	312	45.095	2.0089	9.365	44.949	2.0150	9.713
45.935	1.974	10	-314	45.368	1.9974	9.246	44.867	2.0185	10.023
46.358	1.957	10	-132	46.312	1.9589	7.398	45.711	1.9832	8.074
47.019	1.931	8	-332	46.362	1.9569	7.822	46.362	1.9569	7.822

Appendix C. Raman modes of studtite.

Fig. C.1. The atomic motions associated to Raman active vibrational normal modes of studtite.

Mode 3319 cm^{-1} – ν(OH) – OH stretching for crystallization H_2O molecules

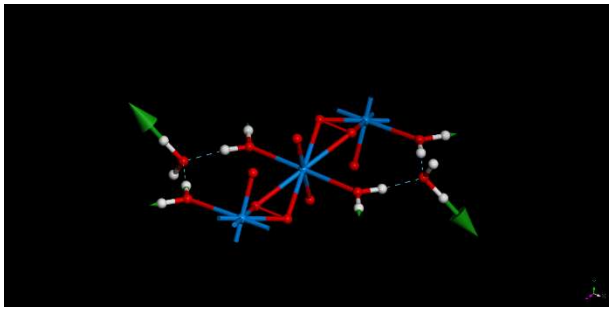

Mode 3238 cm^{-1} – ν(OH) – OH stretching for crystallization H_2O molecules

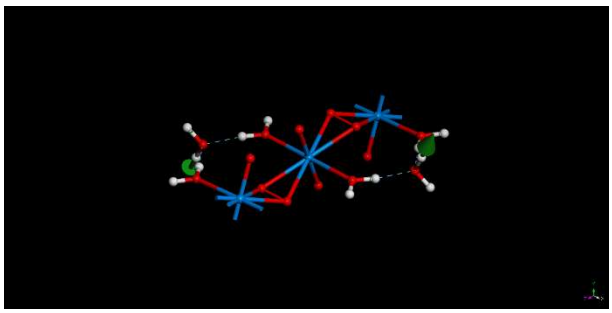

Mode 3033 cm^{-1} – ν(OH) – OH stretching for structural H_2O molecules

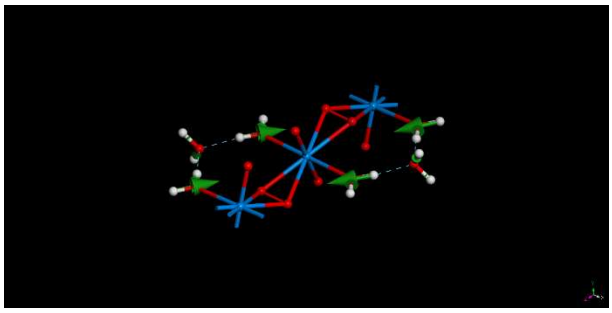

Mode 2970 cm^{-1} – ν(OH) – OH stretching for structural H_2O molecules

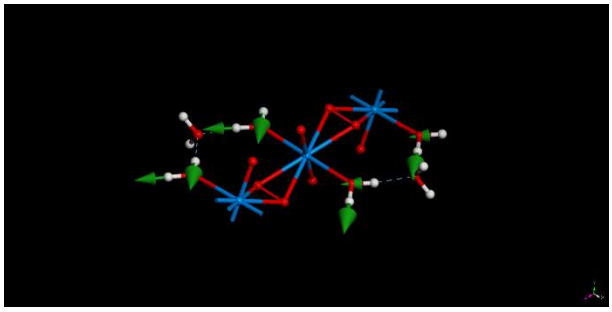

Mode 1679 cm^{-1} – $\delta(H_2O)$ – H_2O bending for structural H_2O molecules

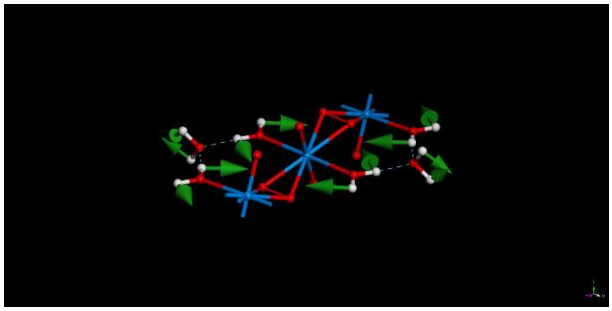

Mode 1638 cm^{-1} – $\delta(H_2O)$ – H_2O bending for crystallization H_2O molecules

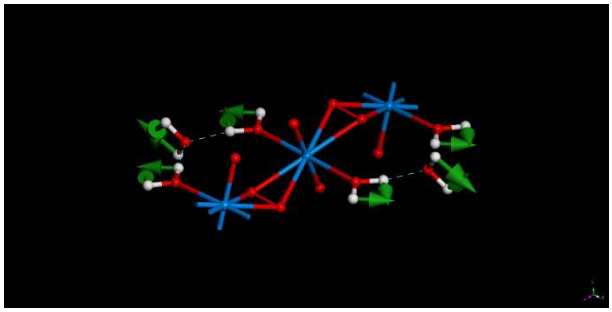

Mode 917 cm^{-1} – $\nu(OO)$ – Peroxo O-O stretching

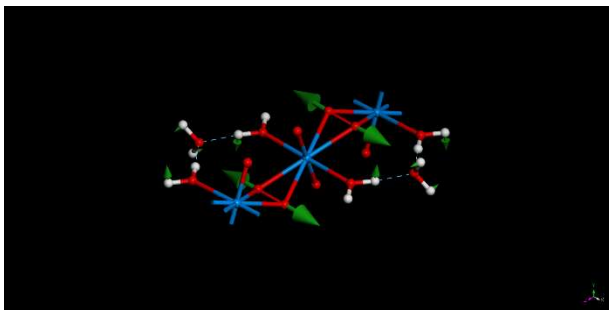

Mode 798 cm^{-1} – $\nu^s(UO_2^{2+})$ – Symmetric UO_2^{2+} stretching

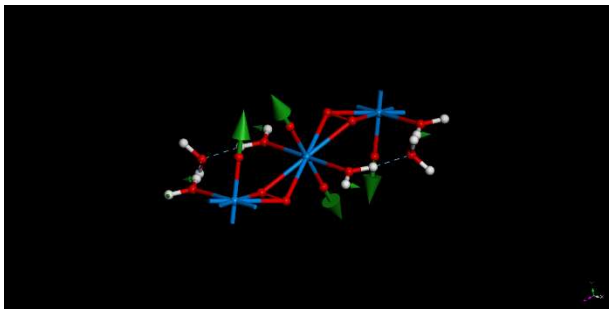

Mode 686 cm^{-1} – $\rho(H_2O\text{-st.})+ \omega(H_2O\text{-cr.})$ – H_2O librations. Rocking vibrations for structural H_2O molecules and wagging vibrations for crystallization H_2O molecules

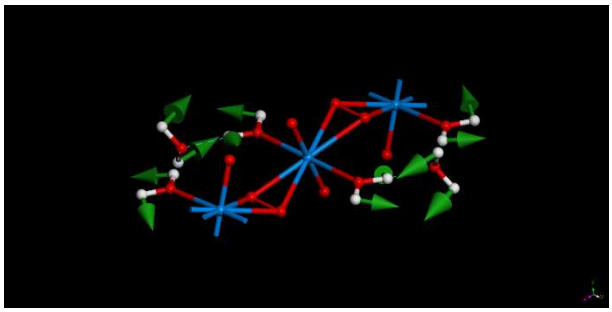

Mode 446 cm^{-1} – $\nu^{s}(UO_{aqua})$ – Symmetric UO_{aqua} stretching (H_2O-str. translation)

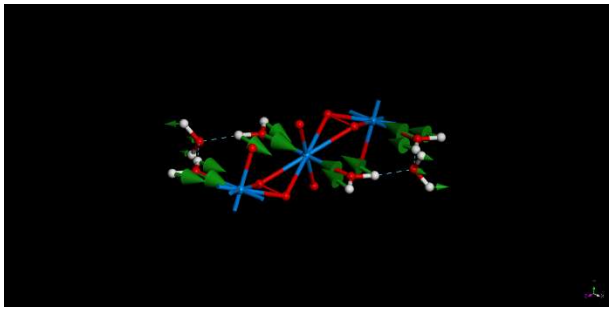

Mode 402 cm^{-1} – $\rho(OUO_{perox})$ – OUO_{perox} rocking

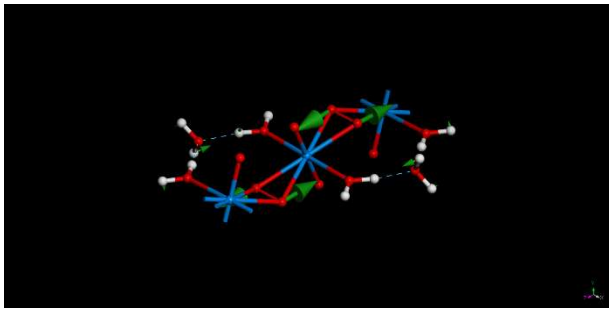

Mode 372 cm^{-1} – $\rho(OUO_{perox})$ – OUO_{perox} rocking

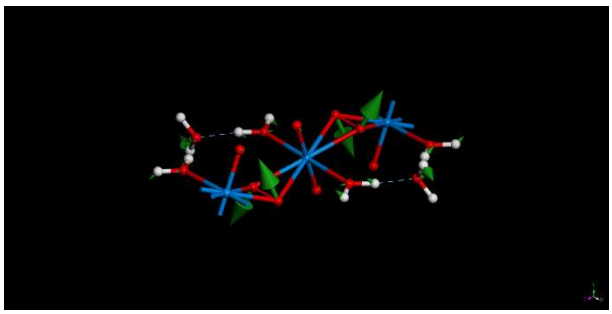

Mode 309 cm^{-1} – $\rho(OUO_{aqua})$+T(H_2O-cr.) – OUO_{aqua} rocking plus crystallization H_2O translation

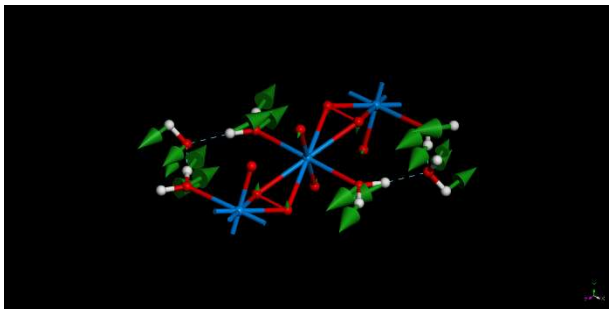

Mode 307 cm^{-1} – $\rho(OUO_{perox})$ – OUO_{perox} rocking

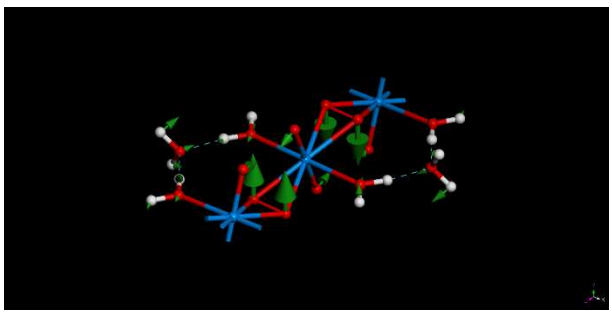

Mode 256 cm^{-1} – $\rho(UO_2^{2+})$ + $\rho(OUO_{aqua})$+$\rho(OUO_{perox})$+T(H_2O-cr.) – Uranyl, OUO_{aqua}, and OUO_{perox} rocking plus crystallization H_2O molecules translation

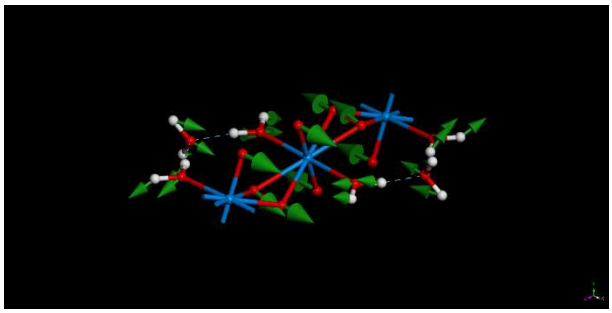

Mode 247 cm^{-1} – $\rho(UO_2^{2+})$ + $\rho(OUO_{aqua})$+T(H_2O-cr.) – Uranyl and OUO_{aqua} rocking plus crystallization H_2O molecules translation

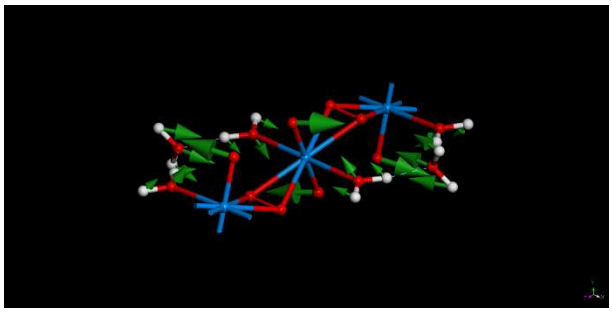

Mode 223 cm^{-1} – $\rho(OUO_{aqua})$+$\rho(UO_2^{2+})$+$\rho(OUO_{perox})$ – OUO_{aqua}, OUO_{perox}, and uranyl rocking

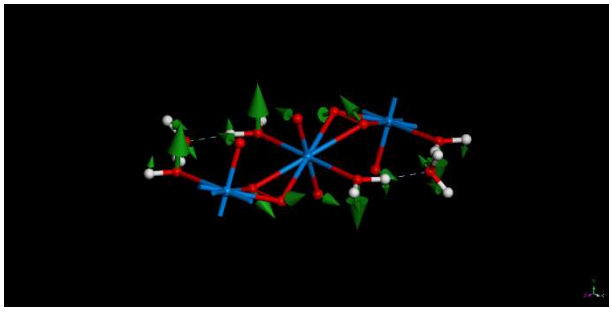

Mode 213 cm^{-1} – $\rho(UO_2^{2+})$+ $\rho(OUO_{aqua})$+T(H_2O-cr.) – Uranyl and OUO_{aqua} rocking plus crystallization H_2O molecules translation

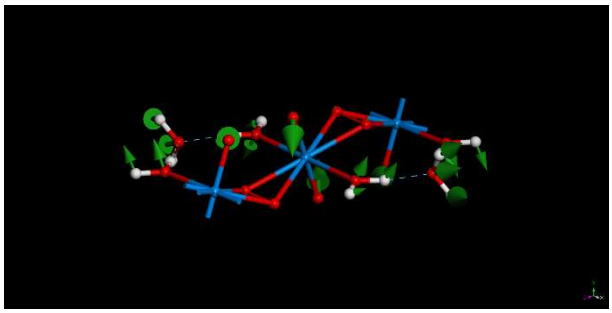

Mode 185 cm^{-1} – $\rho(UO_2^{2+})$+ $\rho(OUO_{aqua})$+$\rho(OUO_{perox})$+$T(H_2O\text{-cr.})$ – Uranyl, OUO_{aqua}, and OUO_{perox} rocking plus crystallization H_2O molecules translation

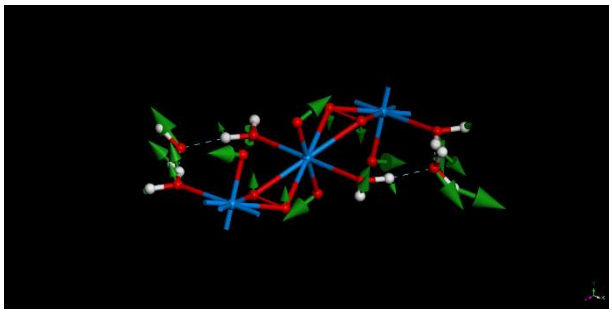

Mode 179 cm^{-1} – $\rho(UO_2^{2+})$ – uranyl UO_2^{2+} rocking

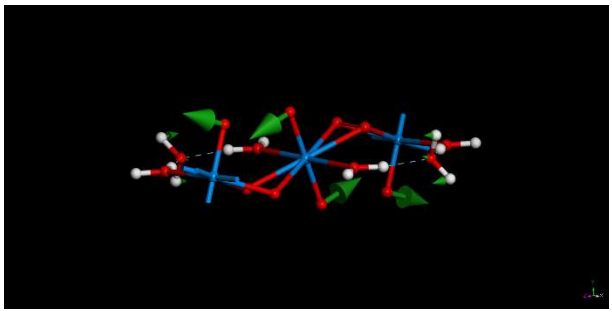

Mode 163 cm^{-1} – $T(H_2O\text{-cr.})$ – crystallization H_2O molecules translation

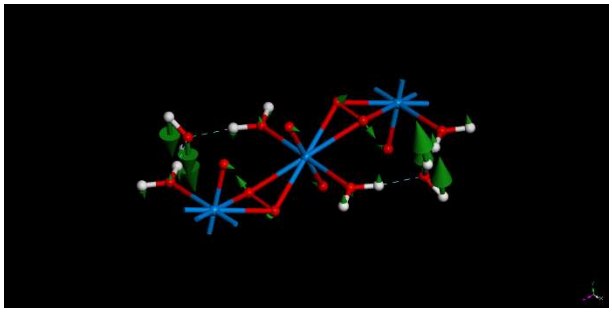

Mode 154 cm^{-1} – $\rho(OUO_{aqua})$+$\rho(UO_2^{2+})$+$\rho(OUO_{perox})$+$T(H_2O\text{-cr.})$ – $OUO_{aqua,}$, OUO_{perox}, and uranyl rocking plus crystallization H_2O molecules translation

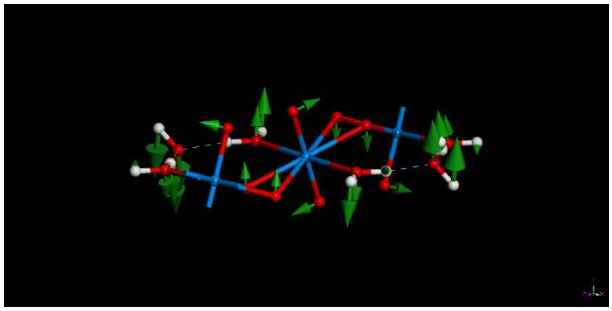

Mode 135 cm^{-1} – $\rho(OUO_{aqua})+\rho(UO_2^{2+})+T(H_2O\text{-cr.})$ – OUO_{aqua} and uranyl rocking plus crystallization H_2O molecules translation

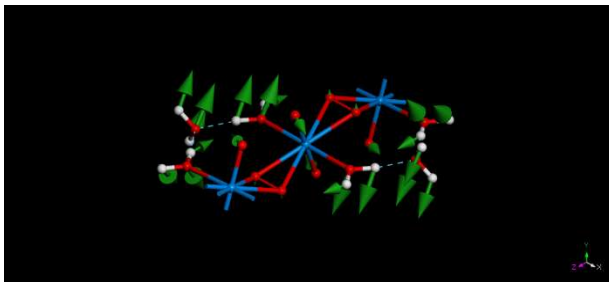

Mode 101 cm^{-1} – $\rho(OUO_{aqua})+\rho(UO_2^{2+})+T(H_2O\text{-cr.})$ – OUO_{aqua} and uranyl rocking plus crystallization H_2O molecules translation

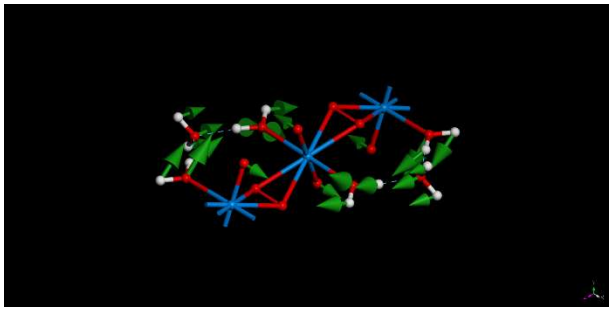

References

[1] J.F. Vaes, Six nouveaux min´eraux d'urane provenant de Shinkolobwe (Katanga), Ann. Soc. Geol. Belg., 70 (1947) B212–B229.

[2] K. Walenta, On Studtite and lts Composition, Am. Mineral., 59 (1974) 166–171.

[3] T. Sato, Thermal decomposition of uranium peroxide hydrate, Naturwissenschaften, 48 (1961) 693-693.

[4] T. Sato, Uranium peroxide hydrates, Naturwissenschaften, 48 (1961) 668-668.

[5] T. Sato, Preparation of uranium peroxide hydrates, J. Appl. Chem., 13 (1963) 361-365.

[6] P.C. Debets, X-ray diffraction data on hydrated uranium peroxide, J. Inorg. Nucl. Chem., 25 (1963) 727-730.

[7] J. Cejka, J. Sejkora, M. Deliens, New data on studtite, $UO_4{\cdot}4H_2O$, from Shinkolobwe, Shaba, Zaire, Neues Jahrbuch fuer Mineralogie, Monatshefte, 3 (1996) 125–134.

[8] P.C. Burns, K.-A. Hughes, Studtite, $[(UO_2)(O_2)(H_2O)_2](H_2O)_2$: The first structure of a peroxide mineral, Am. Mineral., 88 (2003) 1165-1168.

[9] K.-A.H. Kubatko, K.B. Helean, A. Navrotsky, P.C. Burns, Stability of Peroxide-Containing Uranyl Minerals, Science, 302 (2003) 1191-1193.

[10] I. Grenthe, J. Drożdżynński, T. Fujino, E.C. Buck, T.E. Albrecht-Schmitt, S.F. Wolf, Uranium, in: The chemistry of the actinide and transactinide elements, Springer Netherlands, 2008, pp. 253-698.

[11] P.F. Weck, E. Kim, C.F. Jove-Colon, D.C. Sassani, Structures of uranyl peroxide hydrates: a first-principles study of studtite and metastudtite, Dalton Trans., 41 (2012) 9748-9752.

[12] P.F. Weck, E. Kim, E.C. Buck, On the mechanical stability of uranyl peroxide hydrates: implications for nuclear fuel degradation, RSC Adv., 5 (2015) 79090-79097.

[13] R.T. Downs, K.L. Bartelmehs, G.V. Gibbs, M.B. Boisen, Interactive software for calculating and displaying X-ray or neutron powder diffractometer patterns of crystalline materials, Am. Mineral., 78 (1993) 1104-17107.

[14] MaterialsStudio, http;//accelrys.com/products/materials-studio, (2014).

Structural, Mechanical and Raman Spectroscopic Characterization of Layered Uranyl Silicate Mineral Uranophane-α by DFT Methods

Article: "*Structural, Mechanical and Raman Spectroscopic Characterization of Layered Uranyl Silicate Mineral Uranophane-α by DFT Methods*" by F. Colmenero, V. Timón, L. J. Bonales, and J. Cobos, Clay Minerals (2017, submitted).

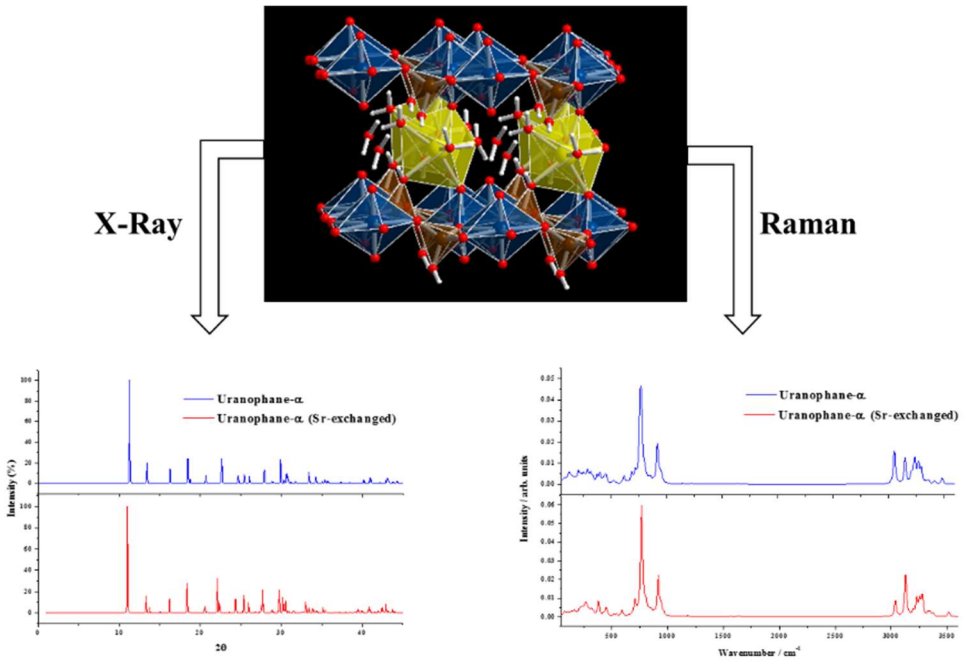

Structural, Mechanical and Raman Spectroscopic Characterization of Layered Uranyl Silicate Mineral Uranophane-α by DFT Methods

Francisco Colmenero[a], Vicente Timón[a], Laura J. Bonales[b], Joaquín Cobos[b]

[a]*Instituto de Estructura de la Materia, CSIC. C/ Serrano, 113. 28006 Madrid, Spain*

[b]*Centro de Investigaciones Energéticas, Medioambientales y Tecnológicas, CIEMAT. Avda/ Complutense, 40. 28040 Madrid, Spain*

Abstract

Layered uranyl silicate mineral uranophane-α, $Ca(UO_2)_2(SiO_3OH)_2{\cdot}5H_2O$, was studied by first principle calculations based on density functional theory method. Its structure, present in nature in a wide variety of compounds having the *uranophane sheet anion-topology* is confirmed here for the first time by means of rigorous theoretical solid state calculations. Computed lattice parameters, bond lengths, bond angles, and X-ray powder spectrum reproduce accurately their experimental counterparts. Mechanical properties of uranophane are predicted and the satisfaction of the mechanical stability Born conditions of the structure is demonstrated by means of calculations of the elasticity tensor. The Raman spectrum was computed by means of density functional perturbation theory and compared with the experimental spectrum. Since the comparison was satisfactory, a normal mode analysis of the theoretical spectra was carried out and used with the aim of assigning the main bands of the Raman spectrum. Theoretical methods allowed us to assign the Raman spectrum bands to vibrations localized in different fragments within the crystal unit cell. Finally, the structure, X-Ray powder pattern and Raman spectrum of Sr-exchanged uranophane are studied.

Keywords: Spent nuclear fuel, Uranophane-α, DFT calculations, uranyl silicate minerals, Raman spectroscopy

1. Introduction

Uranyl silicates are very important materials because they form as alteration phases during hydration-oxidation weathering of uraninite [1-2] and spent nuclear fuel (SNF) [3-6] which is mainly composed of uranium dioxide, UO_2. The contact of groundwaters containing dissolved silicate with dissolved uranyl, is expected to result in the formation of uranyl silicate minerals [3-5]. Ubiquity of uranophane-α suggests that the uranyl silicates are among the most important phases controlling uranium concentrations in groundwater [2].

Mineral uranophane-α, $Ca(UO_2)_2(SiO_3OH)_2 \cdot 5H_2O$, is one of the earliest known uranyl minerals. It is a hydrated uranyl nesosilicate which was first described by Websky [6]. Since then, it has been identified in nearly all major and most of the minor uranium deposits in the world. Its β polymorph, also monoclinic, is much more infrequent and was observed for the first time by Novacek [7]. In nature, uranophane, when well crystallized, is always fibrous and, usually, the fibers consist of several crystals in parallel growth [8]. A cluster of single crystals rarely is found. Where uranophane occurs as radiating fibers, it is yellow and has a vitreous luster, but more commonly it occurs as massive crusts which are pale yellow to yellow-orange and have a waxy luster. Uranophane-α has been synthetized in the laboratory, for example, by Nguyen *et al.* [9], Cesbron *et al.* [10], Vochten *et al.* [11], and Wall *et al.* [12]. Wall *et al.* [12] presented a detailed, optimized technique to synthesize this layered uranyl silicate using aqueous solutions of uranyl acetate, calcium acetate, and sodium metasilicate as starting materials. So far, nobody has succeeded in preparing β-uranophane. Other uranyl silicates, as boltwoodite, can be synthesized only if calcium is virtually absent.

Uranophane-α is characterized by a 1:1 uranium to silicon ratio [13]. Its structure is very complex and includes 68 atoms in the unit cell, as well as 320 valence electrons. Uranyl silicate minerals having this ratio contain sheets [13-15]. Nine uranyl silicate minerals (uranophane-α and β, sklodowskite, cuprosklodowskite, boltwoodite, sodium boltwoodite, kasolite, oursinite and swamboite) have been classified as members of the uranophane group on the basis of the uranium to silicon ratio and a similar uranophane anion sheet topology [14-17]. Structural connectivities of uranophane-β polymorph differ substantially from those of uranophane-α [18,17]. Soddyite has 2:1 uranium to silicon ratio and framework crystal structure [19, 13-14]. The ratio 2:5 was found in the crystal structures of weeksite [20], haiweeite [21] and coutinhoite [22], and probably also in some uranyl silicate minerals from Russia that are not approved [23]. Some synthetic framework uranyl silicates have also been described [24-25].

Uranyl silicate minerals are mostly layered uranyl silicates that behave much like clay minerals. The layers are composed of sheets having a net negative charge which stack up with cations in the interlayer spaces to provide charge balance within the structure [26-28,14-15]. Uranyl cation in the sheet could be replaced by other non-uranyl cations, similar to cation substitution in the sheets of clay minerals, providing a mechanism for incorporation of transuranic elements into these phases [16, 29-33]. Also, other cations can be substituted into the interlayer spaces via ion exchange, providing a mechanism of incorporation of fission products as cesium or strontium [26-28, 16]. Thus, these mineral phases formed at the SNF surface may potentially act as an additional barrier to radionuclide migration through the accessible environment via mineral sorption reactions. The incorporation mechanisms seem to be more favorable in structures with charged sheets and cations in the interlayer than in structures with electroneutral sheets since coupled substitutions involving the interlayer may be a charge-balancing mechanism that permits the substitution [32]. The incorporation of fission products as ^{137}Cs and ^{90}Sr into the structure of uranophane was studied by Douglas *et al.* [28]. Incorporation of Cs into the structure of the closely related mineral boltwoodite was previously reported by Burns [26]. Also, the substitution of uranium by neptunium in uranophane was studied by Douglas *et al.* [30], Murphy and Grambow [31], Burns and Klingensmith [32].

While the structure of uranophane has been determined by experimental X-Ray diffraction techniques [34], it has never been confirmed by means of theoretical solid state calculations. Although classical molecular dynamics methods based in empirical force fields have been employed to study the uranophane-water interface as well as the interfacial reactivity of this

uranyl silicate [35], rigorous first principles methods have only been used to study uranyl silicate clusters [35-36]. Also, as far as we know, no experimental or computational studies have been reported of the mechanical properties of uranophane, and the conditions of mechanical stability of its structure have not been studied. The confirmation of the structure and stability of the uranophane structure by means of first principles methods is also relevant because this structure represents one of the most fundamental anion topologies in the U(VI) minerals, referred to as the *uranophane sheet anion-topology* in the literature [14-17]. This topology is also at the basis of the structure of a large series of phosphates, arsenates, vanadates and molybdates [15,37-40].

Radiotoxicity of these substances complicates its handling under security conditions and, therefore, its characterization. The proper characterization techniques to analyze these materials must be non-destructive, should not require any special sample preparation, and must allow the analysis of very small amount of sample. A technique satisfying these requirements is Raman spectroscopy [41-44]. Raman spectra of uranyl silicate minerals have been given by Frost *et al.* [41-42], Amme *et al.* [43] and Bonales *et al.* [44]. A very complete characterization study of uranophane including scanning electron microscopy (SEM), X-Ray diffraction (XRD), thermogravimetric analysis (TGA), surface area and charge determination, and Raman spectroscopy, was carried out by Wall *et al.* [12]. Although the Raman spectra of this mineral has been determined experimentally, a precise assignation of the main bands in the spectra is lacking. Theoretical methods allow for a complete characterization of these materials free of all the difficulties associated to the experimental techniques associated to its radiotoxicity. The assignment of the experimental vibrational bands is possible since these methods provide detailed microscopic scale views of the atomic vibrational motions in the corresponding normal modes. However, the application of theoretical methods to uranium containing solids is very complicated and computationally demanding, not only due to the great size of the corresponding unit cells but also to the high level of theory required to describe correctly these systems In our previous paper [45] a norm conserving relativistic pseudopotential [46] for uranium atom was generated. Studies of uranyl containing materials carried out with this pseudopotential are the theoretical studies of rutherfordine [45,47] studtite [48] and soddyite [49] minerals.

In this paper uranophane-α was studied by DFT calculations. The paper is organized as follows. In section 2, the methods used in this work are described. Then, in section 3, theoretical results are presented and compared with experimental data. Finally, the conclusions of this work are presented in section 4.

2. Methods: Theoretical DFT calculations.

CASTEP code [50], a module of the Materials Studio package [51], was employed to model uranophane-α structure as in our previous papers [45,47-49]. Also, the generalized gradient approximation (GGA) together with PBE functional [52] and Grimme empirical dispersion correction, the DFT-D2 approach [53], were employed. The introduction of dispersion corrections produces a remarkable improvement of the results for systems in which the accurate description of non-bonded interactions is important [54]. The methods employed for geometry optimization and calculation of vibrational Raman spectra, mechanical properties and equation of state were the same as in our previous works [45,47-49] and their description will be not repeated here. However, present uranophane computations required larger kinetic energy cutoffs and K-point meshes to ensure good convergence for computed structures and energies. A kinetic energy cutoff of 1000 eV and a K mesh of 3 x 3 x 1 (4 K points) were selected to determine the final results.

3. Results and discussion

3.1. Structure

The unit cell of uranophane-α, $Ca(UO_2)_2(SiO_3OH)_2 \cdot 5H_2O$, has monoclinic symmetry, spatial group $P2_1$ ($Z=4$). It contains 68 atoms: 4 U, 4 Si, 2 Ca, 34 O and 24 H. In our computations, 320 valence electrons should be described explicitly.

Stohl and Smith [13] categorized naturally occurring uranyl silicates according to the uranium to silicon ratio, which in part determines the structures of these minerals. Most uranyl silicate minerals have 1:1 uranium to silicon ratio and are sheet silicates [13-15]. The uranyl silicate sheets are composed of $[(UO_2)_2(SiO_4)_2]^{-4}$ units bound at the equatorial edges (see Figs. 1.A and 1.B). A sheet, $[(UO_2)(SiO_4)]_n^{-2n}$, contains UO_7 pentagonal bipyramids and SiO_3OH tetrahedra. Charge compensating cations, calcium in uranophane, lie in the interlayer space between the sheets (see Fig. 1.C). Two uranyl silicate sheets are connected by $CaO_2(OH)(H_2O)_4$ polyhedra (distorted pentagonal bipyramid). The Ca atom ligands are four water molecules, two uranyl oxygen atoms belonging to the upper and the lower sheets, and one OH group of a SiO_3OH tetrahedra. One water molecule is out of the Ca polyhedra. While this water molecule is described as free or crystallization water, the four water molecules belonging to Ca atom coordination sphere are referred to as structural water. Hydrogen bonds reinforce the bonding between the uranyl silicate sheets, the Ca atom, and the free water. As it can be seen in Fig. 1.C, the upper sheet SiO_3OH tetrahedra have free OH groups pointing downwards and the lower sheet tetrahedra have OH groups pointing upwards which belong to the Ca atom coordination sphere.

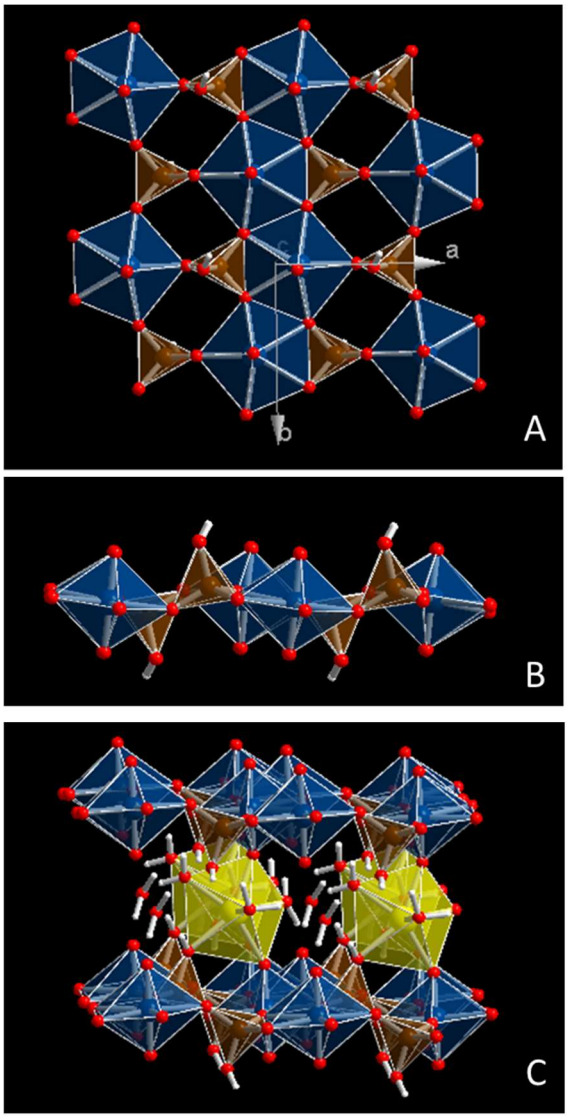

Figure 1. Structure of uranophane-α mineral: a) View of a 2 x 2 x 2 supercell from [001] showing a uranyl silicate sheet $[(UO_2)(SiO_4)]_n^{-2n}$ composed of UO_7 pentagonal bipyramids and SiO_3OH tetrahedra; b) The same view as in a) from [010]; c) View of a 2 x 2 x 2 supercell from [010] showing two uranyl silicate sheets connected by $CaO_2(OH)(H_2O)_4$ polyhedra (distorted pentagonal bipyramid). One water molecule is out of the Ca polyhedra (free water). Color code: U-Blue, Si-Brown, O-Red, H-White, Ca-Yellow.

The structure of uranophane-α was determined in calculations with increasing complexity in order to obtain a set of calculation parameters yielding good convergence for computed structures and energies. Table 1 gives the final lattice parameters, volumes and densities obtained compared with the corresponding experimental values of Ginderow [34].

Table 1. Lattice parameters.

Parameter	*a* (Å)	*b* (Å)	*c* (Å)	α	β	γ	Vol. (Å^3)	Dens. (g/cm^3)
Calculated	6.6689	7.0022	15.8684	90.0	98.0748	90.0	733.6520	3.8766
Exp. [34]	6.665	7.002	15.909	90.0	97.27	90.0	736.478	3.8618

Table 2 give a comparison of the more important geometric parameters (bond distances) obtained with the corresponding experimental data of Ginderow [34]. Uranophane-α has two structurally (symmetrically) identical U^{6+} ions and two structurally (symmetrically) identical Si^{4+} ions in its crystal structure. However, the two non-symmetrically related uranyl and silicate polyhedra are nearly the same. The two O atoms in the uranyl group, UO_2^{2+}, are in apical positions of the pentagonal bipyramids at distances of 1.801 and 1808 Å for both U1 and U2. The calculated values are 1.828 and 1.843 Å for U1 and 1.825 and 1.829 Å for U2, respectively. The remaining five O atoms lie in the equatorial plane which U-O distances which range from 2.241 to 2.463 Å (calculated 2.214 to 2.457 for U1 and 2.236 to 2.462 Å for U2, respectively). The Si-O distances, ranging from 1.601 to 1.638 Å, are within the normal range (calculated 1.621 to 1.663 Å for Si1 and 1.620 to 1.666 for Si2, respectively). Ca-O distances in the distorted pentagonal bipyramid are satisfactorily reproduced and range from 2.371 to 2.445 Å (calculated 2.372 to 2.509 Å).

We conclude that the experimental geometrical parameters and our theoretical values agree quite well in spite of the complexity of the uranophane-α structure.

The X-Ray powder pattern of uranophane-α was computed from the experimental [34] and computed structures [55] using CuK_α radiation (λ=1.540598 Å). The most intense lines (I > 10%) are compared in Figures 2.b and 2.c, and, as can be seen, the agreement in line positions and intensities is very good. The use of spectra derived directly from the experimental and computed structures allows for a fair comparison of the results free of interferences as the experimental conditions or possible artifacts as the presence of sample impurities since both are determined under the identical conditions. Nevertheless, the use of an experimental pattern also leads to an excellent agreement. Computer program XPowder [56] using the PDF-2 database [57] recognizes the computed pattern as that of uranophane-α (pattern 78-1840, from Ginderow [34]). The experimental X-Ray powder pattern can be seen in Figure 2.a where it is compared with the previously described spectra. The precise values of the main reflections for are given in Table 3.

3.2 Mechanical properties and stability

As noted by Weck *et al.* [58], the existence of a great amount of information on the formation, thermodynamic stability, and phase transformations of alteration phases formed at the SNF surface is in stark contrast with the paucity of data regarding the mechanical stability and properties of these phases. Saving this theoretical study of the uranyl peroxide hydrates, studtite and metastudtite, none experimental or computational studies have reported, for example, the bulk and shear moduli, stiffness coefficients, or anisotropy factors for these phases, and their conditions of mechanical stability remain to be analyzed. This appears particularly surprising since the underlying atomistic deformation modes and interactions determine thermodynamic phase stability and transformation.

Elastic tensor, needed for the calculation of mechanical properties and to study the mechanical stability of uranophane crystal structure, was calculated, at the optimized equilibrium structure, from stress-strain relations using the finite deformation technique implemented in CASTEP. Crystals with monoclinic symmetry have 13 non-degenerate elastic constants in the symmetric stiffness matrix [58-59], which may be written as:

$$C = \begin{pmatrix} C_{11} & C_{12} & C_{13} & 0 & C_{15} & 0 \\ C_{12} & C_{22} & C_{23} & 0 & C_{25} & 0 \\ C_{13} & C_{23} & C_{33} & 0 & C_{35} & 0 \\ 0 & 0 & 0 & C_{44} & 0 & C_{46} \\ C_{15} & C_{25} & C_{35} & 0 & C_{55} & 0 \\ 0 & 0 & 0 & C_{46} & 0 & C_{66} \end{pmatrix}$$

Table 2. Bond distances (in Å).

Bond	Experimental [34]	Calculated
U-1 pentagonal dipyramids		
U1-O3	1.801	1.828
U1-O1	1.808	1.843
U1-O9	2.241	2.214
U1-O7	2.294	2.286
U1-O5	2.296	2.281
U1-O7’	2.437	2.455
U1-O5’	2.463	2.457
Average	2.346	2.339
U-2 pentagonal dipyramids		
U2-O4	1.801	1.825
U2-O2	1.808	1.829
U2-O10	2.241	2.236
U2-O8	2.294	2.296
U2-O6	2.296	2.276
U2-O8’	2.437	2.441
U2-O6’	2.463	2.462
Average	2.346	2.342
Tetrahedron around Si-1		
Si1-O9	1.601	1.621
Si1-O7	1.617	1.644
Si1-O5	1.626	1.642
Si1-O11	1.638	1.663
Average	1.621	1.642
Tetrahedron around Si-2		
Si2-O10	1.601	1.620
Si2-O6	1.617	1.639
Si2-O8	1.626	1.643
Si2-O12	1.638	1.666
Average	1.621	1.642
Ca pentagonal bipyramid		
Ca-OW1	2.371	2.372
Ca-OW2	2.387	2.509
Ca-OW3	2.387	2.446
Ca-O3	2.396	2.387
Ca-O11	2.429	2.420
Ca-O2	2.432	2.382
Ca-OW4	2.445	2.474
Average	2.407	2.427

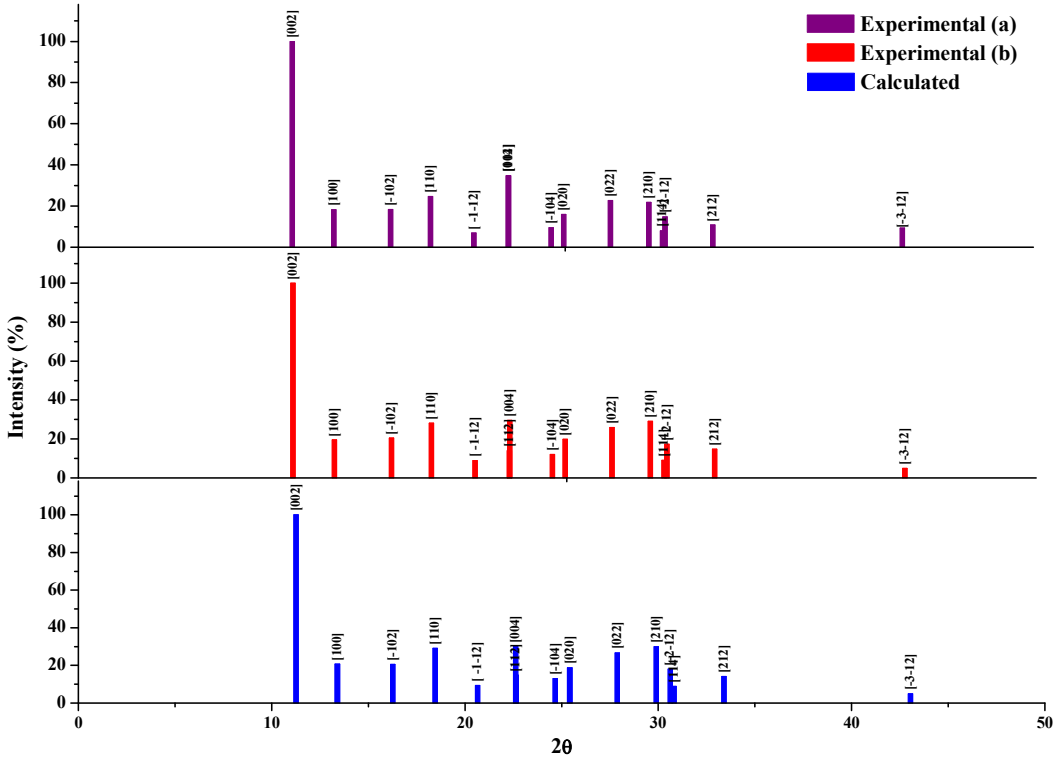

Figure 2. X-Ray powder spectrum of uranophane-α using CuK_α radiation: a) Experimental spectrum (pattern 78-1840 in the PDF-2 database); b) X-Ray powder spectrum computed from experimental geometry (Ginderow [34]); c) X-Ray powder spectrum computed from calculated geometry. The results for the main reflections are also given in Table 3.

Table 3. Main reflections in the X-Ray powder pattern of uranophane-α: a) Experimental spectrum (pattern 78-1840 in the PDF-2 database); b) X-Ray powder pattern computed from experimental geometry (Ginderow [34]); c) X-Ray powder pattern computed from calculated geometry.

Experimental (a)				Experimental (b)			Theoretical		
2Θ	**d(Å)**	**I(%)**	**hkl**	**2Θ**	**d(Å)**	**I(%)**	**2Θ**	**d(Å)**	**I(%)**
11.205	7.8906	100.0	[002]	11.205	7.890	100.0	11.255	7.8555	100.0
13.381	6.6114	19.618	[100]	13.381	6.611	18.218	13.399	6.6028	20.808
16.353	5.4163	20.554	[-102]	16.353	5.416	18.418	16.265	5.4452	20.638
18.442	4.8071	28.222	[110]	18.442	4.807	24.725	18.454	4.8039	29.147
20.716	4.2842	8.832	[-1-12]	20.716	4.284	6.907	20.647	4.2985	9.434
22.508	3.9471	13.933	[112]	22.518	3.945	34.835	22.644	3.9237	14.800
22.518	3.9453	29.656	[004]	22.518	3.945	34.835	22.620	3.9278	30.001
24.753	3.5939	12.114	[-104]	24.753	3.594	9.509	24.672	3.6055	13.054
25.421	3.5010	19.901	[020]	25.421	3.501	16.016	25.420	3.5011	18.783
27.857	3.2001	25.850	[022]	27.857	3.200	22.723	27.877	3.1979	26.584
29.865	2.9893	29.178	[210]	29.865	2.989	21.822	29.898	2.9861	29.875
30.583	2.9207	9.016	[114]	30.583	2.921	8.008	30.818	2.8990	8.899
30.722	2.9078	17.358	[-2-12]	30.723	2.908	14.815	30.623	2.9171	18.113
33.215	2.6951	14.807	[212]	33.215	2.695	10.811	33.402	2.6804	14.121
43.142	2.0952	4.943	[-3-12]	43.142	2.095	9.309	43.041	2.0999	4.943

Here we use the standard Voigt notation for the indices contracting a pair of Cartesian indices into a single integer $1 \leq i \leq 6$: xx → 1, yy → 2, zz → 3, yz → 4, xz → 5, xy → 6. The precise values of these constants obtained in our computations are (all values are given in GPa):

$$C = \begin{pmatrix} 156.59 & 44.77 & 17.85 & 0 & -6.84 & 0 \\ 44.77 & 152.19 & 14.46 & 0 & 0.60 & 0 \\ 17.85 & 14.46 & 94.34 & 0 & 2.46 & 0 \\ 0 & 0 & 0 & 23.93 & 0 & 2.27 \\ -6.84 & 0.60 & 2.46 & 0 & 27.71 & 0 \\ 0 & 0 & 0 & 2.27 & 0 & 34.54 \end{pmatrix}$$

For monoclinic crystals, a set of necessary (but not sufficient) Born criteria for mechanical stability were given in terms of the stiffness matrix elements, for example, by Weck *et al.* [58]. These conditions are fully satisfied. The generic necessary and sufficient Born criterion is that all eigenvalues of the C matrix be positive [60]. The C matrix was diagonalized numerically and all eigenvalues were found to be positive. Since the above condition is satisfied, uranophane-α mechanical stability can be inferred.

The fact that C_{33}, the diagonal component of C matrix along c direction, is much smaller than either C_{11} or C_{22} suggest that thermal expansion of the material will occur predominantly along direction perpendicular to the uranyl silicate sheets. This is consistent with the fact that intersheet space containing the hydrated Ca ions and free water molecules will increase as temperature increases. The diagonal component C_{11} (a direction contained in the plane of the uranyl silicate sheets, see Fig.1.A) is the largest.

If single crystal samples are not available, the measure of the individual elastic constants cannot be possible. Instead, the polycrystalline bulk modulus (B) and shear modulus (G) may be determined experimentally. The Voigt [61] and Reuss [62] schemes were used to compute the isotropic elastic properties of soddyite polycrystalline aggregates. As shown by Hill [63], the Reuss and Voigt approximations result in lower and upper limits, respectively, of polycrystalline constants and practical estimates of the polycrystalline bulk and shear moduli in the Hill approximation can be computed using average formulas. Relevant formulae for these approximations may be found in several sources (see for example [58,64]). The bulk and shear moduli and other mechanical properties computed in these approximations are given in Table 4.

Table 4. Bulk, modulus, shear modulus, Young modulus, Poisson ratio, Pugh's ratio, and Vickers hardness (B, G, E, ν, D, and H) calculated ind the Voigt, Reuss, and Hill approximations. Values of B, G and E, are given in GPa.

Property	Voigt	Reuss	Hill
$\boldsymbol{B}$	61.9215	56.4799	59.2007
$\boldsymbol{G}$	38.9723	34.0691	36.5207
$\boldsymbol{E}$	96.6419	85.0969	90.8752
$\boldsymbol{\nu}$	0.2399	0.2489	0.2442
$\boldsymbol{D}$	1.5889	1.6578	1.6210
$\boldsymbol{H}$	6.9163	5.7218	6.3253

The numerical estimate of the error in the computed bulk modulus given by the CASTEP code is 2.455 GPa, is reasonable and very similar to the the difference of the values in the Hill and Voigt/Reuss schemes, 2.721 GPa. Thus, we estimate the error to be about 5%. Voigt and Reuss methods yield quite small differences for uranophane-α. Larger differences are expected for crystalline systems with strong anisotropy, featuring large differences between elastic constants along different directions [58,47].

In general, a large value of shear moduli is an indication of the more pronounced directional bonding between atoms [65]. Shear modulus represents the resistance to plastic deformation while

the bulk modulus represents the resistance to fracture [64-65]. Young modulus defines the relationship between stress (force per unit area) and strain (proportional deformation) in a material, that is, $E = \sigma/\varepsilon$. The individual components of of Bulk and Young's moduli may be derived from the elastic compliance matrix components [58,64-65]. Compliance matrix is the inverse of stiffness C matrix. For example, the E components along the a, b, and c directions can be expressed as $E_a = S_{11}^{-1}$, $E_b = S_{22}^{-1}$, and $E_c = S_{33}^{-1}$. The corresponding values are given in Table 5. As it can be seen, B_c, is much smaller than either B_a or B_b. Thus, c direction is the most compressible one. Also, the component E_c is much smaller (less stiff) than E_a and E_b. Thus, direction perpendicular to the plane containing the uranyl silicate sheets is the most compressible and least stiff in agreement with results of elasticity C matrix.

Table 5. Bulk and Young moduli components along the crystallographic axes. All values are given in GPa.

Property	*a* axis	*b* axis	*c* axis
B	246.35	221.84	109.43
E	139.47	138.26	91.33

Pugh [66] introduced the proportion of bulk to shear modulus of polycrystalline phases ($D = B/G$) as a measure of ductility by considering the interpretation of the shear and bulk modulus given above. A higher D value is usually associated with higher ductility and the critical value which separates ductile and brittle materials is 1.75, i.e., if $B/G > 1.75$, the material behaves in a ductile manner, otherwise the material behaves in a brittle manner [64]. The Poisson's ratio, ν, can also be utilized to measure the malleability of crystalline compounds and is related to the Pugh's ratio given above by the relation $D = (3 - 6\nu) / (8 + 2\nu)$. The Poisson's ratio is close to 0.33 (1/3) for ductile materials, while it is generally much less than 0.33 for brittle materials. As it can be seen in Table 4, for uranophane we find ratios D and ν about 1.62 and 0.24, respectively. These values are only slightly smaller than 1.75 and 0.33, respectively, corresponding to a brittle material. For comparison, both studtite and metastudtite were found to be ductile (Weck *et al.* [58]).

Hardness of these systems is computed according to a recently introduced empirical scheme [67] which correlates the Vickers hardness and the Pugh's ratio ($D = B/G$). Vickers hardness, H, of polycrystalline uranophane is given in Table 4. Its value, about 6.3, corresponds to material of intermediate hardness. For comparison, we can compute the hardness of studtite and metastudtite using the elasticity data of Weck *et al.* [58]. These systems, characterized by much larger D ratios, have much smaller hardnesses (smaller than one). Uranophane has a hardness close to that of soddyite uranyl silicate mineral for which we have computed a hardness value about 6.3 (Colmenero *et al.* [49]).

In order to assess the elastic anisotropy of uranophane, shear anisotropic factors were obtained. These factors provide a measure of the degree of anisotropy in the bonding between atoms in different planes and are very important to study material durability [64-65]. Shear anisotropic factors for the $\{100\}$ (A_1), $\{010\}$ (A_2), and $\{001\}$ (A_3), crystallographic planes and percentages of anisotropy in compression and shear (A_{comp} and A_{shear}) were computed using the formulae given by Ravindran *et al.* [65]. For an isotropic crystal, the factors A_1, A_2, and A_3 must be one, while any value smaller or greater than unity is a measure of the degree of elastic anisotropy possessed by the crystal. For percentage anisotropies, a value of 0% represents a perfectly isotropic crystal. For uranophane (see Table 6), the anisotropies grow in the planes $\{100\}$, $\{010\}$, and $\{001\}$ ($A_1 < A_2 < A_3$). The $\{100\}$ plane is shown to be the most anisotropic one. Percentage anisotropies in compression and shear are about 5 and 7 %, respectively.

In the recently introduced universal anisotropy index [68], the departure of A^U from zero defines the extent of single crystal anisotropy and accounts for both the shear and the bulk contributions unlike all other existing anisotropy measures. Thus, A^U represents a universal measure to quantify the single crystal elastic anisotropy. Uranophane is characterized by an anisotropy index of 0.81, which is a rather small value ($A^U = 0$ corresponds to a perfectly

isotropic crystal). For comparison, studtite and metastudtite exhibit much larger anisotropies. The values computed by Weck *et al.* [58] are 2.17 and 1.44, respectively. Soddyite mineral calculations result in a value of A^U of 0.50 [49]. Therefore, soddyite and uranophane uranyl silicate minerals are characterized by small anisotropies.

Table 6. Shear anisotropy factors (A_1, A_2, and A_3), percentages of anisotropy in compression and shear (Acomp and Ashear), and universal anisotropy index (A^U).

A_1	A_2	A_3	A_{comp} (%)	A_{shear} (%)	A^U
0.4448	0.5094	0.6301	4.5959	6.7129	0.8159

A set of fundamental physical properties may be estimated using the calculated elastic constants. For example, V_L and V_T, the transverse and longitudinal elastic wave velocities of the polycrystalline materials may be determined in terms of the bulk and shear moduli (Weck *et al.* [58]). The values obtained are 3.069 and 5.276 km/s, respectively, using the calculated crystal density of 3.8766 gr/cc (see Table 1).

3.3. Equation of state

Lattice volumes around the equilibrium were calculated by optimizing the structure at seventeen different applied pressures between -1.0 and 12.0 GPa. The calculated volume and pressure data were then fitted to a fourth-order Birch-Murnaghan [69] equation of state (EOS) using the computed volume at 0 GPa (733.6 Å^3) as V_0 using EOSFIT 5.2 code [70],

$$P = 3\,B\,f_E\,(1+2f_E)^{\frac{5}{2}}\left[1+\frac{3}{2}(B'-4)f_E+\frac{3}{2}\left\{B\,B''+(B'-4)(B'-3)+\frac{35}{9}\right\}{f_E}^2\right]$$

In this equation,

$$f_E=\frac{1}{2}\left[\left(\frac{V_0}{V}\right)^{\frac{2}{3}}-1\right]$$

and B, B', and B'' are the bulk modulus and its first and second derivatives, respectively, at the temperature of 0 K. The values found for B, B', and B'' were $B = 59.96\ (\pm 2.1)$ GPa, $B' = 2.29\ (\pm 1.11)$, and $B'' = -0.25\ (\pm 0.19)$ ($\chi 2 = 0.014$). The value obtained for the bulk modulus agrees very well with that determined from elastic constants. For comparison, the bulk modulus obtained in the Hill approximation is $B = 59.20 \pm 2.45$ GPa.

3.4. Raman spectra and band assignment

In this section, we analyze the theoretically determined Raman spectrum and compare the main band wavenumbers obtained with the corresponding values found experimentally in the literature [41-42] for this mineral phase. Additional information about the Raman spectrum of uranophane can be found in Amme *et al.* [43], Bonales *et al.* [44], and Wall *et al.* [12]. The experimental band wavenumbers of Frost *et al.* [41-42] are given in Table 7, being their assignments also given in this Table. Experimental and calculated Raman shifts, calculated intensities and assignations are given in Table 8. For the purpose of visual comparison, the spectrum computed at T=298 K, λ=532 nm, FWHM=20 cm^{-1} is shown in Figure 3, where it is compared with an experimental spectrum of RRUFF database (Downs [82]; record RRUFF-050380). As can be seen in Figure 3, the calculated spectrum is very similar to the experimental one. Pictures of the atomic motions in some of the Raman active vibrational modes are given in Appendix A of Supplementary information (Figure A.1).

Although the bands in the OH stretching region seems to be quite variable from one sample to another, most bands are well reproduced theoretically. Wavenumbers of the bands observed in the experimental samples are generally comparable but not identical [41-42]. This supports the presence of mobile protons that may be exchanged between the uranyl silicate sheets and the interlayer and influence the hydrogen-bonding networks in their crystal structures [72,42]. We find experimental bands centered at about 3492, 3463, 3358, 3326, 3310, 3216 and 3142, cm^{-1}, which can be compared with the calculated wavenumbers of 3485, 3478, 3357, 3295, 3272, 3238, and 3149 cm^{-1}. It should be underlined that theoretical methods allow to distinguish the origin of these bands which may be assigned to specific stretching vibrations. The first two ones are attributed to OH stretching vibrations of crystallization water molecules (labelled as *cr* in Table 8). The next three bands are instead due to vibrations localized on structural (coordinated) water molecules (labelled as *st* in Table 8). The next one is ascribed to vibrations in crystallization and structural water molecules and OH stretching vibrations in SiO_3OH fragments including OH groups which do not form part of the Ca atom coordination sphere (referred to as *fr* in Table 8). Finally, the last band is assigned to vibrations in structural water molecules and SiO_3OH fragments including OH groups which are not coordinated with interlayer Ca atoms. In previous experimental works, all these bands were attributed without specification to OH stretching vibrations in the water molecules. As it can be seen, the bands at lower wavenumbers contain also contributions from OH stretching vibrations in the free SiO_3OH fragments. Frost *et al.* [41], placed these vibrations at wavenumbers higher than 3600 cm^{-1}. However, in other works (see Frost *et al.* [41-42]), OH stretching vibrations at SiO_3OH groups at about 3200 cm^{-1} are reported on the basis of the infrared spectra.

The water bending vibration is not observed in the experimental Raman spectra and, accordingly, the corresponding computed band, at 1639 cm^{-1}, has a very small intensity (see vibrational mode picture in Appendix A of Supplementary information).

Experimental bands located at 1272 and 1156 cm^{-1} are placed at 1222 and 1146 cm^{-1} in the computed spectrum. These are assigned, respectively, to SiOH bending vibrations localized in SiO_3OH fragments including OH groups which are coordinated with interlayer Ca atoms (referred to as *co*, in Table 8), and in free SiO_3OH fragments (referred to as *fr* in Table 8, as it has already been mentioned), respectively.

The experimental bands at 960 and 950 cm^{-1} are close the theoretical ones located at wavenumbers 958 and 942 cm^{-1}, respectively. These bands are ascribed to SiOH bending vibrations localized in SiO_3OH fragments including coordinated OH groups, δ(*co*-SiOH), and water librations. These bands were however assigned to silicate symmetric stretching vibrations, $\nu^s(SiO_4^{4-})$ (ν_1), by Frost *et al.* [41]. This assignation seems to be incorrect. It must also be noted that the correspondence with symmetric vibrations of the free silicate group are lost for uranophane (monoclinic symmetry) as it can be seen in the vibrational mode pictures in Appendix A of Supplementary information. The contribution of SiO_3OH group vibrations to these modes is very small. A band appears in the calculated spectrum at 915 cm^{-1} which is assigned to SiO stretching vibrations of the SiO_3OH fragments with coordinated OH groups (see vibrational mode picture in Appendix A of Supplementary information). Thus, silicate stretching vibrations appears at smaller wavenumbers than those reported by Frost *et al.* [41].

The band placed at 886 cm^{-1} is obtained theoretically at 884 cm^{-1} and that at 839 cm^{-1} is calculated to be at 837 cm^{-1}. Both bands are assigned to SiOH bending vibrations (localized in *fr* and *co* SiO_3OH fragments) and water librations.

The band placed at 797 cm^{-1} is the most intense of the Raman spectrum and it is calculated to be at 776 cm^{-1}. This band is assigned by Frost *et al.* [41], to symmetric uranyl stretching vibrations $\nu^s(UO_2^{2+})$. However, our calculations show that it is the result of a combination of vibrations including SiOH vibrations localized in *fr*-SiO_3OH fragments, uranyl stretching vibrations, and water librations. The uranyl vibrations make one a small contribution to this mode. As it has already been mentioned the symmetry of this vibration is lost and therefore the term symmetric should not be used. A weak band at 786 cm^{-1} is also observed and it is comparable to calculated bands at 760 and 766 cm^{-1} having the same assignation that the intense band at 798 cm^{-1}.

For the bands at 711, 627, 544, 525, 469, 444, and 399 cm^{-1} we obtain the theoretical counterparts 717, 618, 539, 519, 452, 434, and 399 cm^{-1} which correspond to different *fr* and *co*

SiOH bending vibrations. The band placed at 544 cm^{-1} and found at 539 cm^{-1} it is attributed to water librational vibrations only.

Uranyl bending vibrations begin to appear at about 376 cm^{-1}. Bands at wavenumbers 376, 347, 325, 306, 289, 280, 250, 214, 205, 167, 139, 137, 122 and 112 cm^{-1} are close to the calculated bands at 374, 333, 317, 316, 289, 276, 256, 226, 206, 186, 137, 135, 126, and 119 cm^{-1}. Most of them are assigned to a combination of silicate, SiO_3OH, deformations (localized in *fr* or *co* groups), uranyl bending vibrations and water librations. The bands in this region were assigned by Frost *et al.* [41] to uranyl bending vibrations. However, it must be pointed out that uranyl bending vibration is only a contribution, generally small, to these modes and is accompanied by silicate deformation vibrations and water librations. The precise assignations are given in Table 8.

It must be emphasized that band assignment is a very difficult task in the case of complex systems having low symmetry. While the assignations made by correlating the bands with those of free fragments [73,72] are generally very useful to understand the origin of the bands which are experimentally found, these correspondences cannot always be made, especially for many systems with low symmetry (monoclinic in this case). For example, as it is shown here, vibrations with specific motions similar to those of free silicate fragment ($\nu_3(SiO_4^{4-})$, $\nu_1(SiO_4^{4-})$, $\nu_4(SiO_4^{4-})$ and $\nu_2(SiO_4^{4-})$) and free uranyl fragment ($\nu_3(UO_2^{2+})$, $\nu_1(UO_2^{2+})$ and $\nu_2(UO_2^{2+})$) are not found for uranophane-α.

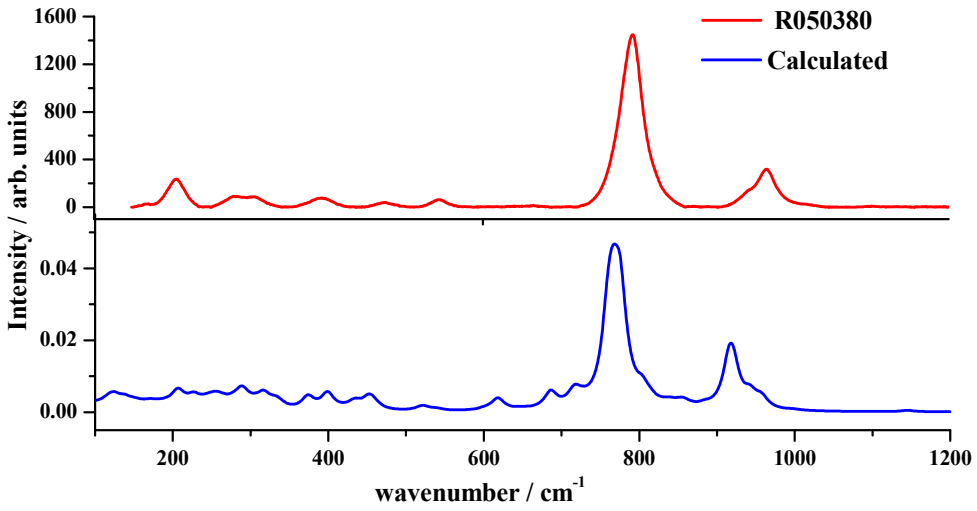

Figure 3. Raman spectra of uranophane-α mineral. a) RRUFF-050380 [82]; b) Calculated.

Table 7. Comparison of experimental Raman shifts (cm^{-1}).

Frost *et al.* [41] (Sample-m31300)	**Frost *et al.* [42] Sample-Shaba - 77 K**	**Frost *et al.* [42] Sample-Eagle - 77 K**	**Assignation**
3492	3494	3534	ν(OH)
3463	3437	3434	ν(OH)
3358	3382	3381	ν(OH)
-	3326	3322	
-	3310	-	
3216	-	3224	ν(OH)
-	-	3142	
2900	-	-	
2729	-	-	
2477	-	-	
2137	-	-	
	1905	1905	
-	1371	1499	
-	1272	1314	
-	1169	1164	
1005	-	995	$\nu^{a}(SiO_4^{4-})$ (ν_3)
964	-	-	
960	965	964	$\nu^{s}(SiO_4^{4-})$ (ν_1)
950	954	955	
886	886	886	
839	-	822	
797	800	800	$\nu^{s}(UO_2^{2+})$
793	789	788	
786	-	-	
-	-	761	
711	716	715	
-	627	629	
545	547	547	$\nu_4(SiO_4^{4-})$
-	525	522	
469	469	471	$\nu_2(SiO_4^{4-})$
-	-	444	
-	402	406	
399	397	398	$\nu_2(SiO_4^{4-})$
376	382	-	
347	335	334	
325	323	323	$\delta(UO_2^{2+})$
306	307	307	
289	296	296	$\delta(UO_2^{2+})$
280	286	286	$\delta(UO_2^{2+})$
250	257	268	$\delta(UO_2^{2+})$
-	235	256	
-	225	225	
214	212	212	$\delta(UO_2^{2+})$
205	196	195	
167	-	-	
139	-	-	
137	-	-	
122	-	-	
112	-	-	

Table 8. Experimental and calculated Raman band frequencies, calculated intensities and assignations.

Exp. Raman shift (cm^{-1})	Calc. Raman shift (cm^{-1})	Irr. Rep. (C_{2v})	Intensity (Å^4)	Assignation
3492 (a)	3485	B	543.453	ν(OH) [*cr*-H_2O]
3463 (a)	3478	A	234.841	
3358 (a)	3359	B	206.215	ν(OH) [*st*-H_2O]
	3357	A	241.922	
3326 (b)	3295	B	1298.612	
3310 (b)	3272	B	1627.297	
3216 (a)	3238	B	2003.074	ν(OH) [*cr*- and *st*-H_2O and *fr*-SiOH]
	3222	B	638.256	
3142 (b)	3149	B	2468.104	ν(OH) [*st*-H_2O and *fr*-SiOH]
1272 (b)	1222	B	22.349	δ(*co*-SiOH)
1169 (b)	1146	B	13.621	δ(*fr*-SiOH)
964, 960 (a)	958	B	102.979	δ(co-SiOH)+l(H_2O)
950 (a)	942	B	126.692	
886 (a)	884	B	25.099	δ(SiOH)+l(H_2O)
839 (a)	857	A	23.425	ν(fr-SiO)+l(H_2O)
	837	B	25.221	δ(SiOH)+l(H_2O)
	813	B	29.204	δ(SiOH)+l(H_2O)+ν(UO_2)
797, 793 (a)	804	B	113.942	δ(SiOH)+l(H_2O)+ν(UO_2)
	776	B	767.503	δ(fr-SiOH)+l(H_2O)+ν(UO_2)
786 (a)	766	B	504.625	δ(fr-SiOH)+l(H_2O)+ν(UO_2)
	760	B	521.123	
711 (a)	717	B	103.711	δ(fr-SiOH)+l(H_2O)
	686	B	104.691	
627 (b)	618	B	72.848	δ(co-SiOH)+l(H_2O)
545 (a)	539	B	8.337	l(H_2O)
525 (b)	524	B	9.467	δ(co-SiO_3OH)+l(H_2O)
	519	B	15.642	δ(fr-SiO_3OH)+l(H_2O)
469 (a)	459	B	21.980	δ(co-SiO_3OH)+l(H_2O)
	452	B	48.164	δ(fr-SiO_3OH)+l(H_2O)
444 (b)	434	B	29.965	δ(co-SiO_3OH)+l(H_2O)
399 (a)	399	B	61.655	δ(co-SiO_3OH)+l(H_2O)
376 (a)	374	B	44.165	δ(fr-SiO_3OH)+δ(UO_2)+l(H_2O)
347 (a)	333	A	11.578	δ(fr-SiO_3OH)+δ(UO_2)+l(H_2O)
325 (a)	317	B	12.801	δ(SiO_3OH)+ δ(UO_2)+l(H_2O)
306 (a)	316	A	23.824	δ(co-SiO_3OH)+δ(UO_2)+l(H_2O)
289 (a)	289	A	18.128	δ(co-SiO_3OH)+δ(UO_2)+l(H_2O)
	288	B	9.997	δ(SiO_3OH)+δ(UO_2)+l(H_2O)
280 (a)	276	A	11.180	δ(fr-SiO_3OH)+δ(UO_2)+l(H_2O)
250 (a)	256	B	13.132	δ(SiO_3OH)+δ(UO_2)+l(H_2O)
214 (a)	226	A	17.045	δ(SiO_3OH)+δ(UO_2)+l(H_2O)
205 (a)	206	B	18.514	δ(SiO_3OH)+δ(UO_2)+l(H_2O)
167 (a)	186	A	4.163	δ(SiO_3OH)+δ(UO_2)+l(H_2O)
	175	B	3.374	δ(SiO_3OH)+δ(UO_2)+l(H_2O)
139 (a)	138	B	4.891	δ(co-SiO_3OH)+δ(UO_2)+l(H_2O)
137 (a)	135	A	1.229	δ(co-SiOH)+l(H_2O)
122 (a)	126	B	7.777	δ(SiO_3OH)+δ(UO_2)+l(H_2O)
112 (a)	119	B	4.741	δ(SiO_3OH)+δ(UO_2)+l(H_2O)

(a) R.L. Frost, *et al.* [41].
(b) R.L. Frost, *et al.* [42].

3.5. Sr-exchanged uranophane-α

The possibility of incorporation of Strontium in the structure of uranophane-α was investigated by Douglas *et al.* [28]. This research was made in order to analyze if this 1:1 uranyl silicate may serve as a host for the incorporation of fission products by substitution of Ca^{2+} in the interlayer spaces in the solid. Uranophane-α was synthetized by these authors and Ca^{2+} was exchanged completely or partially in the structure. The resulting solid was then characterized by X-Ray diffraction, scanning electron microscopy (SEM) and elemental analysis. The Sr^{2+} analog of uranophane yielded a diffractogram that resembles the XRD pattern obtained for synthetic uranophane, although the morphology of the solid is different from uranophane.

Theoretical methods allow to study this incorporation in a simple way free of the difficulties associated to the radiotoxicity of these materials. We have studied the Sr-exchanged uranophane material by replacing the Ca^{2+} ion by Sr^{2+} in the structure of uranophane and performing a structural reoptimization with the same calculation parameters as those used for the calculations of normal uranophane (kinetic energy cutoff and K-mesh). The structure experimented very small variations upon exchange and the interlayer cation solvation structure was very similar to that of normal uranophane. The same structure was obtained when the calculations were made from different initial forms of the hydrogen bond structure in the interlayer space. The corresponding lattice parameters are given in Table 9. As it can be seen, the main variation is the increase of the interlayer space, corresponding to an increase of 0.35 Å of the *c* lattice parameter. The change of *a* and *b* lattice parameters was only of about 0.02 Å. The volume is increased approximately 3%. These results may be compared with those of Berghout *et al.* [74] for the Ca- and Sr-exchanged two layer montmorillonites. In this case, the computed increase in the *c* lattice parameter was of 0.21 Å and the unit cell volume increased by 2.4%.

Table 9. Lattice parameters of normal and Sr-exchanged uranophane-α.

Parameter	*a* (Å)	*b* (Å)	*c* (Å)	α	β	γ	Vol. (Å^3)	Dens. (g/cm^3)
Calculated (Ca)	6.6689	7.0022	15.8684	90.0	98.0748	90.0	733.65	3.877
Calculated (Sr)	6.6959	7.0233	16.2127	90.0	97.3650	90.0	756.15	3.970

The X-Ray powder diffractograms of normal and Sr-exchanged uranophane were obtained from the optimized atomistic positions using program REFLEX included in Materials Studio package [51]. As expected from the study of Douglas *et al.* [28], the diffractograms of both forms is very similar and are given in Figure 4.

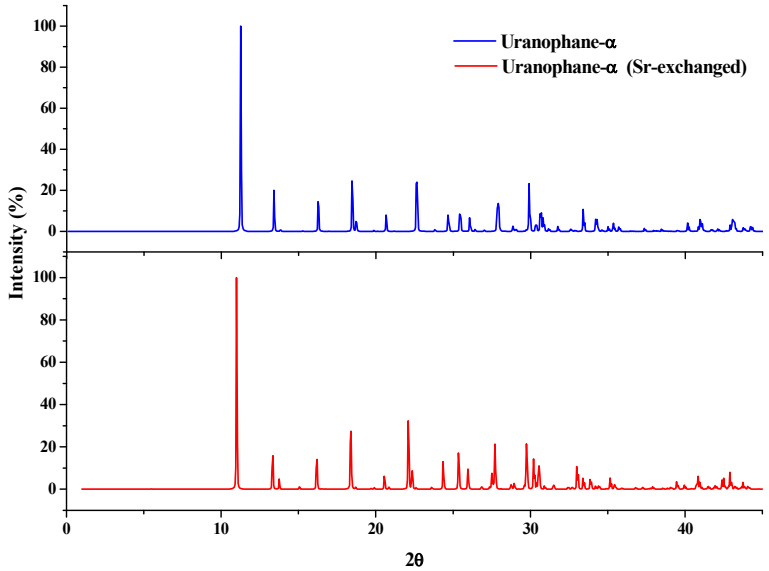

Figure 4. Computed X-Ray powder diffractograms of normal and Sr-exchanged uranophane

In order to know whether we can differentiate these materials by Raman spectroscopy we computed the corresponding spectra of Sr-exchanged uranophane using Density Functional Perturbation Theory. The corresponding spectra, were again very similar and are given in Figure 5.

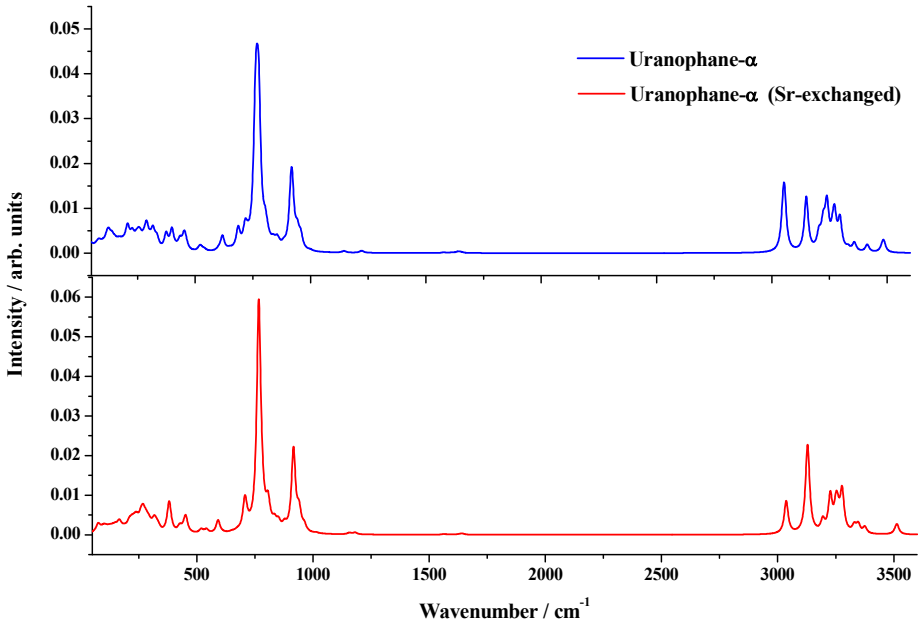

Figure 5. Computed Raman spectra of normal and Sr-exchanged uranophane.

3. Conclusions

The DFT results show the important role of water in the structural and vibrational properties of uranyl silicate mineral uranophane-α. Water molecules enter in the structure of uranophane-α as structural and crystallization water. Structural water molecules form part of the coordination structure of calcium ion present in the interlayer space between the uranyl silicate sheets, that is, within the distorted pentagonal bipyramids, $CaO_2(OH)(H_2O)_4$. Crystallization water molecules are also localized in the interlayer space but are free, that is, they do not coordinate the calcium ions. Present calculations confirm several important issues related to uranophane structure as the presence of five interlayer neutral water molecules (instead of four) and the absence of interlayer hydronium $(H_3O)^+$ ions [34]. Structural optimization performed using the GGA-PBE exchange-correlation functional taking into account a dispersion correction scheme has produced unit cell lattice parameters and atomic bond distances in excellent agreement with experimental data. The computed X-Ray powder spectrum is also in very good agreement with experiment.

An analysis of the calculated elasticity stiffness tensor has revealed that uranophane-α structure satisfies properly the mechanical stability conditions. Furthermore, mechanical properties of this mineral, for which there are not experimental data to compare with, are predicted. Uranophane-α is brittle and is characterized by small anisotropy and large hardness in comparison with those of other uranyl containing materials. The equation of state of uranophane-α was obtained by fitting lattice volumes and pressures to a fourth order Birch-Murnahan equation of state.

Raman spectrum was also computed by means of density functional perturbation theory and compared with its experimental counterpart. The results were also found to be in good agreement well the experimental data. A normal mode analysis of the theoretical spectrum was carried out and used in order to assign the main bands of the Raman spectra. Theoretical methods allowed us to assign the bands to vibrations localized in different fragments within the crystal unit cell.

Main band used as fingerprints to identify uranophane-α are those placed at wavenumbers 797 and 960 cm^{-1}. The corresponding values resulting from our computations are quite close to the experimental values, 776 and 958 cm^{-1}. The first band is assigned to a combination of SiOH bending vibrations localized in *fr* SiO_3OH fragments, uranyl UO stretching vibrations, and water librations. The second one is assigned to a combination of SiOH bending vibrations localized in *co* SiO_3OH fragments and water librations. In the experimental works, these bands were attributed to uranyl symmetric stretching, $\nu^s(UO_2)^{2+}$, and silicate symmetric stretching, $\nu^s(SiO_4)^{4-}$, vibrations. As indicated by our theoretical calculations, these assignations are incorrect or incomplete since they do not include several contributions, as those coming from vibrations arising from the ubiquitous water molecules and SiOH fragments. These contributions underline the role of the hydrogen bond structure in uranophane-α and its impact in the vibrational spectra. Further, the correlation of these bands with those of free fragments is lost due to the low crystal symmetry.

The bands situated at wavenumbers 545, 469, and 399 cm^{-1} are also satisfactorily reproduced theoretically, the corresponding values being 539, 459 and 399 cm^{-1}. The first band is ascribed to water librational vibrations only and the other ones represent SiOH bending vibrations localized in SiO_3OH fragments with coordinated OH groups and water librational vibrations. Previous assignments of these bands are not correct since involve silicate group deformations, $\nu_4(SiO_4^{4-})$ and $\nu_2(SiO_4^{4-})$. Further, as it has already been said, the correspondence with free silicate group vibrations cannot be performed for uranophane.

In the low wavenumber region, we have four main bands located at wavenumbers 289, 250, 205 and 167 cm^{-1} which are determined theoretically to be placed at 289, 256, 206 and 186 cm^{-1}, respectively. These were mainly attributed to uranyl bending vibrations. Theoretical calculations indicate that these bands correspond to a combination of silicate (SiO_3OH) deformations, uranyl bending vibrations and water librations. The uranyl bending vibration appears to be only a small contribution.

In the OH stretching region most bands are well reproduced theoretically, in spite of the fact that the bands in this region are quite variable from one sample to another. The theoretical analysis allows to assign these bands to vibrations localized in different fragments of the unit cell. The bands at higher wavenumber are attributed to OH stretching vibrations in crystallization water molecules. The bands at medium wavenumber are due to OH stretching vibrations localized in structural water molecules. Finally, the bands with lowest wavenumbers contain contributions from OH stretching vibrations localized in the SiOH fragments containing OH groups out of the coordination sphere of interlayer calcium ions.

For the bands placed at 1272 and 1156 cm^{-1} (comparable to the theoretical bands located at 1222 and 1146 cm^{-1}, respectively) the band assignment reveals that while both are attributable to SiOH bending vibrations, these vibrations are localized in different SiO_3OH fragments (the higher wavenumber one in *co* SiO_3OH fragments and the lower one in *fr* fragments).

Finally, the possibility of incorporation of Strontium into the structure of uranophane-α was investigated. The structure of Sr-exchanged uranophane and the structure of the solvation sphere of the interlayer cation are showed to be very similar to that of normal uranophane, the main difference being, as in the case of montmorillonite clay mineral [74], the increase of in the interlayer space (the *c* parameter increased by about 0.35 Å). The X-Ray powder pattern and Raman spectrum of Sr-exchanged uranophane are also showed to be extremely close to those of normal uranophane. These findings agree with the results of the experimental study of Douglas *et al.* [28].

Acknowledgements

This work was supported by ENRESA in the project: Nº 079000189 "Aplicación de técnicas de caracterización en el estudio de la estabilidad del combustible nuclear irradiado en condiciones de almacenamiento" (ACESCO) and project CGL2013-48415-C2-1-R. Supercomputer time by the CETA-CIEMAT, CTI-CSIC and CESGA centers are also acknowledged. We also want to thank to Dr. Ana María Fernández for reading the manuscript and many helpful comments.

SUPPLEMENTARY DATA

Supplementary data associated with this article contain an appendix to the present article which contain graphical pictures of the Raman normal modes of uranophane-α.

References

[1] C. Frondel, Mineral composition of gummite, Am. Mineral. 41 (1956) 539–568.

[2] R. J. Finch, R. C. Ewing, The corrosion of uraninite under oxidizing conditions, J. Nucl. Mater. 190 (1992) 133–156.

[3] a) D. J. Wronkiewicz, J. K. Bates, T. J. Gerding, E. Veleckis, B. S. Tani, Uranium release and secondary phase formation during unsaturated testing of UO_2 at 90°C, J. Nucl. Mater. 190 (1992) 107–127; b) D. J. Wronkiewicz, J. K. Bates, S. F. Wolf, E. C. Buck, Ten-year results from unsaturated drip tests with UO_2 at 90°C: implications for the corrosion of spent nuclear fuel, J. Nucl. Mater. 238 (1996) 78–95.

[4] E. C. Pearcy, J. D. Prikryl, W. M. Murphy, B. W. Leslie, Alteration of uraninite from the Nopal I deposit, Peña Blanca District, Chihuahua, Mexico, compared to degradation of spent nuclear fuel in the proposed U.S. high-level nuclear waste repository at Yucca Mountain, Nevada, Appl. Geochem. 9 (1994) 713–732.

[5] J. Plasil, Oxidation-hydration weathering of uraninite: the current state-of-knowledge, J. Geosci. 59 (2014) 99–114.

[6] a) M. Websky, Über die geognostichen Verhaltnisse der Erzlagerstäten von Kupferberg u. Rudelstadt in Schlesien, Zs. d. Deutsch. Geol. Ges. V (1853) 391; b) M. Websky, Ueber Uranophan, Zs. d. Deutsch. Geol. Ges. XI (1859) 384.

[7] R. Novacek, Study of some secondary uranium minerals, Vesnik Kral. Ceske. Spol. Nauk II, No. 7 (1935) 36 pp., 2 pls.

[8] a) D. H. Gorman, E. W. Nuffield, Studies of Radioactive Compounds: VIII-Uranophane, Am. Mineral. 40 (1955) 634–645; b) D. K. Smith, J. W. Gruner, W. N. Lipscomb, The crystal structure of Uranophane, $[Ca(H_3O)_2](UO_2)_2(SiO_4)_2 \cdot 3H_2O$, Am. Mineral. 42 (1957) 594–618.

[9] S. N. Nguyen, R. J. Silva, H. C. Weed, J. E. Andrews, Standard Gibbs free energies of formation at the temperature 303.15 K of four uranyl silicates: soddyite, uranophane, sodium boltwoodite, and sodium weeksite, J. Chem. Thermodyn. 24 (1992) 359–376.

[10] F. Cesbron, P. Ildefonse, M. C. Sichere, New mineralogical data on uranophane and β-uranophane; synthesis of uranophane, Mineral. Mag. 57 (1993) 301–308.

[11] R. Vochten, N. Blaton, O. Peeters, K. van Springel, L. van Haverbeke, A new method of synthesis of boltwoodite and of formation of sodium boltwoodite, uranophane, sklodowskite and kasolite from boltwoodite, Can. Mineral. 35 (1997) 735–741.

[12] N. A. Wall, S. B. Clark, J. L. McHale, Synthesis and characterization of 1:1 layered uranyl silicate mineral phases, Chem. Geol. 274 (2010) 149–157.

[13] F. V. Stohl, D. K. Smit, The crystal chemistry of the uranyl silicate minerals, Am. Mineral. 66 (1981) 610–624.

[14] P. C. Burns, U^{6+} minerals and inorganic compounds: insights into an expanded structural hierarchy of crystal structures, Can. Mineral. 43 (2005) 1839–1894.

[15] I. Grenthe, J. Drozdzynski, T. Fujino, E. C. Buck, T. E. Albrecht-Schmitt, S. F. Wolf, *Uranium*, in "The chemistry of the actinide and transactinide elements", Chapter V, Vol. I; L. R. Morss, N. M. Edelstein, J. Fuger, (eds.); Springer Science and Business Media, Berlin, 2006; pp. 253–638.

[16] a) P. C. Burns, M. L. Miller, R. C. Ewing, U^{6+} minerals and inorganic phases: a comparison and hierarchy of crystal structures, Can. Mineral. 34 (1996) 845–880; b) P. C. Burns, R. C. Ewing, F. C Hawthorne, The crystal chemistry of hexavalent uranium; polyhedron geometries, bond-valence parameters, and polymerization of polyhedra, Can. Mineral. 35 (1997) 1551–1570; c) P. C. Burns, The structure of boltwoodite and implications of solid solution toward sodium boltwoodite, Can. Mineral. 36 (1998) 1069–1075.

[17] P. C. Burns, The crystal chemistry of uranium, Rev. Mineral. 38 (1999) 23-90.

[18] K. Viswanathan, O. Harneit, Refined crystal structure of beta-uranophane, $Ca(UO_2)_2(SiO_3OH)_2 \cdot 5H_2O$, Am. Mineral. 71 (1986) 1489–1493.

[19] F. Demartin, C. M. Gramaccioli, T. Pilati, The Importance of Accurate Crystal Structure Determination of Uranium Minerals. II. Soddyite $(UO_2)_2(SiO_4)\cdot 2H_2O$, Acta Crystallogr. C 48 (1992) 1–4.

[20] J. M. Jackson, P. C. Burns, A re-evaluation of the structure of weeksite, a uranyl silicate framework mineral, Can. Mineral. 39 (2001) 187–195.

[21] P. C. Burns, A new uranyl silicate sheet in the structure of haiweeite and comparison to other uranyl silicates, Can. Mineral. 39 (2001) 1153–1160.

[22] D. Atencio, F. M. S. Carvalho, P. A. Matioli, Coutinhoite, a new thorium uranyl silicate hydrate, from Urucum mine, Galiléia, Minas Gerais, Brazil, Am. Mineral. 89, (2004) 721–724.

[23] a) G. A. Sidorenko, I. K. Moroz, I. G. Zhiltsova, Zapiski Vsesoyuznogo Mineralogicheskogo Obshchestva 104 (1975) 559; b) G. A. Sidorenko, N. V. Chukanov, I. S. Naumova, Mineral. Z. 23 (2001) 55.

[24] P. C. Burns, F. C. Hill, A new uranyl sheet in $K_5[(UO_2)_{10}O_8(OH)_9](H_2O)$: New insight into sheet anion-topologies, Can. Mineral. 38 (2000) 163–173.

[25] J. Huang, X. Wang, A. J. Jacobson, Hydrothermal Synthesis and Structures of the New Open-Framework Uranyl Silicates $Rb_4(UO_2)_2(Si_8O_{20})$ (USH-2Rb), $Rb_2(UO_2)(Si_2O_6)\cdot H_2O$ (USH-4Rb) and $A_2(UO_2)(Si_2O_6)\cdot 0.5H_2O$ (USH-5A, A=Rb,Cs), J. Mater. Chem. 13 (2003) 191–196.

[26] P. C. Burns, Cs boltwoodite obtained by ion exchange from single crystals: Implications for radionuclide release in a nuclear repository, J. Nucl. Mater. 265 (1999) 218–223.

[27] P. C. Burns, Y. Li, The structures of becquerelite and Sr-exchanged becquerelite, Am. Mineral. 87 (2002) 550–557.

[28] M. Douglas, S. B. Clark, S. Utsunomiya, R. C. Ewing Cesium and Strontium Incorporation into Uranophane, $Ca[(UO_2)(SiO_3OH)]_2\cdot 5H_2O$, J. Nucl. Sci. Technol. Suppl. 3 (2002) 504–507.

[29] a) P.C. Burns, R. C. Ewing, M. L. Miller, Incorporation mechanisms of actinide elements into the structures of U^{6+} phases formed during the oxidation of spent nuclear fuel, J. Nucl. Mater. 245 (1997) 1–9; b) P.C. Burns, K. M. Deely, S. Skanthakumar, Neptunium incorporation into uranyl compounds that form as alteration products of spent nuclear fuel: Implications for geologic repository performance, Radiochim. Acta 92 (2004) 151–159.

[30] M. Douglas, S. B. Clark, J. I. Friese, B. W. Arey, E. C. Buck, B. D. Hanson, S. Utsunomiya, R. C. Ewing, Microscale characterization of uranium(VI) silicate solids and associated neptunium(V), Radiochim. Acta 93 (2005) 265–272.

[31] W. M. Murphy, B. Grambow, Thermodynamic interpretation of neptunium coprecipitation in uranophane for application to the Yucca Mountain repository, Radiochim. Acta 96 (2008) 563–567.

[32] a) P. C. Burns, A. L. Klingensmith, Uranium mineralogy and Neptunium mobility, Elements 2 (2006) 351–356; b) A. L. Klingensmith, P. C. Burns, Neptunium substitution in synthetic uranophane and soddyite. Am. Mineral. 92 (2007) 1946–1951.

[33] a) L. C. Shuller, R. C. Ewing, U. Becker, Quantum-mechanical evaluation of Np-incorporation into studtite, Am. Mineral. 95 (2010) 1151–1160; b) L. C. Shuller, R. C. Ewing, U. Becker, Np-incorporation into uranyl phases: A quantum–mechanical evaluation, J. Nucl. Mater. 434 (2013) 440–450; c) L.C. Shuller, W. M. Bender, S. M. Walker, U. Becker, Quantum-Mechanical Methods for Quantifying Incorporation of Contaminants in Proximal Minerals, Minerals 4 (2014) 690–715.

[34] D. Ginderow, Structure de l'Uranophane Alpha, $Ca(UO_2)_2(SiO_3OH)_2.5H_2O$, Acta Crystallogr. 44 (1988) 421–424.

[35] J. Kuta, Z. Wang, K. Wisuri, M. C. F. Wander, N. A. Wall, A. E. Clark, The surface structure of α-uranophane and its interaction with Eu(III) – An integrated computational and fluorescence spectroscopy study, Geochim. Cosmochim. Acta 103 (2013) 184–196.

[36] V. Wheaton, D. Majumdar, K. Balasubramanian, L. Chauffe, P. G. Allen, A comparative theoretical study of uranyl silicate complexes, Chem. Phys. Lett. 371 (2003) 349–359.

[37] a) L. Jouffret, M. Rivenet, F. Abraham, U(VI) oxygen polyhedra as pillars for building frameworks from uranophane-type layers, IOP Conf. Series: Mat. Sci. Eng. 9 (2010) 012028; b) L. Jouffret, Z. Shao, M. Rivenet, F. Abraham, New three-dimensional inorganic frameworks based on the uranophane-type sheet in monoamine templated uranyl-vanadates, J. Solid State

Chem. 183 (2010) 2290–2297; c) L. Jouffret, M. Rivenet, F. Abraham, A new series of pillared uranyl-vanadates based on uranophane-type sheets in the uranium-vanadium-linear alkyl diamine systems, J. Solid State Chem. 183 (2010) 84–92.

[38] T. Z. Forbes, P. C. Burns, $Ba(NpO_2)(PO_4)(H_2O)$, its relationship to the uranophane group, and implications for Np incorporation in uranyl minerals, Am. Mineral. 91 (2006) 1089–1093.

[39] G. B. Jin, S. Skanthakumar, L. Soderholm, Two New Neptunyl(V) Selenites: A Novel Cation-Cation Interaction Framework in $(NpO_2)_3(OH)(SeO_3)(H_2O)_2 \cdot H_2O$ and a Uranophane-Type Sheet in $Na(NpO_2)(SeO_3)(H_2O)$, Inorg. Chem. 50 (2011) 6297–6303.

[40] A. Mer, S. Obbade, M. Rivenet, C. Renard, F. Abraham, $[La(UO_2)V_2O_7][(UO_2)(VO_4)]$ the first lanthanum uranyl-vanadate with structure built from two types of sheets based upon the uranophane anion-topology, J. Solid State Chem. 185 (2012) 180–186.

[41] R. L. Frost, J. Cejka, M. L. Weier, W. Martens, Molecular structure of the uranyl silicates—a Raman spectroscopic study, J. Raman Spectrosc. 37 (2006) 538–551.

[42] R. L. Frost, J. Cejka, M. L. Weier, W. N. Martens, Raman spectroscopy study of selected uranophanes, J. Mol. Struct. 788 (2006) 115–125.

[43] M. Amme, B. Renker, B. Schmid, M. P. Feth, H. Bertagnolli, W. Döbelin, Raman microspectrometric identification of corrosion products formed on UO_2 nuclear fuel during leaching experiments, J. Nucl. Mater. 306 (2002) 202–212.

[44] L. J. Bonales, C. Menor-Salván, J. Cobos, Study of the alteration products of a natural uraninite by Raman spectroscopy. J. Nucl. Mater. 462 (2015) 296–303.

[45] L. J. Bonales, F. Colmenero, J. Cobos, V. Timon, Spectroscopic Raman characterization of rutherfordine: a combined DFT and experimental study, Phys. Chem. Chem. Phys. 18 (2016) 16575–16584.

[46] N. Troullier, J. L. Martins, Efficient pseudopotentials for plane-wave calculations, Phys. Rev. B 43 (1991) 1993–2006.

[47] F. Colmenero, L. J. Bonales, J. Cobos, V. Timón, Thermodynamic and Mechanical Properties of the Rutherfordine Mineral Based on Density Functional Theory, J. Phys. Chem. C 121 (2017) 5994–6001.

[48] F. Colmenero, L. J. Bonales, J. Cobos, V. Timón, Study of the Thermal Stability of Studtite by In Situ Raman Spectroscopy and DFT Calculations, Spectrochim. Acta. A 174 (2017) 245–253.

[49] F. Colmenero, L. J. Bonales, J. Cobos, V. Timón, Structural, mechanical and vibrational study of uranyl silicate mineral soddyite by DFT calculations, J. Phys. Chem. C, to be published, 2017.

[50] S. J. Clark, M. D. Segall, C. J. Pickard, P. J. Hasnip, M. I. J. Probert, K. Refson, M. C. Payne, First principles methods using CASTEP, Z. Kristallogr. 220 (2005) 567–570.

[51] MaterialsStudio, http://accelrys.com/products/collaborativescience/biovia-materials-studio/, accessed Jan 20, 2017.

[52] J. P. Perdew, K. Burke, M. Ernzerhof, Generalized Gradient Approximation Made Simple, Phys. Rev. Lett. 77 (1996) 3865–3868; ibid. 78 (1997) 1396 (E).

[53] S. Grimme, Semiempirical GGA-type density functional constructed with a long-range dispersion correction, J. Comp. Chem. 27 (2006) 1787–1799.

[54] D. Tunega, T. Bucko, A. Zaoui, Assessment of ten DFT methods in predicting structures of sheet silicates: importance of dispersion corrections, J. Chem. Phys. 137 (2012) 114105.

[55] R. T. Downs, K. L. Bartelmehs, G. V. Gibbs, M. B. Boisen, Interactive software for calculating and displaying X-ray or neutron powder diffractometer patterns of crystalline materials, Am. Mineral. 78 (1993) 1104–1107.

[56] J.D. Martin, XPowder12, Ver. 04.13 (2012)

[57] ICDD, The international center for diffraction data. PDF-2 database (2003).

[58] P. F. Weck, E. Kim, E. C. Buck, On the mechanical stability of uranyl peroxide hydrates: Implications for nuclear fuel degradation, RSC Adv. 5 (2015) 79090–79097.

[59] J. F. Nye, The Physical Properties of Crystals: Their Representation by Tensors and Matrices, Oxford University Press, New York, 1985.

[60] F. Mouhat, F.-X. Coudert, Necessary and sufficient elastic stability conditions in various crystal systems, Phys. Rev. B 90 (2014) 224104.

[61] W. Voigt, Lehrbuch der Kristallphysik, Leipzig, Teubner, 1928.

[62] A. Reuss, Berechnung der Fliessgrenze von Mischkristallen auf Grund der Plastizitatsbedingung fur Einkristalle, Z. Angew. Math. Mech. 9 (1929) 49–58.

[63] R. Hill, The Elastic Behaviour of a Crystalline Aggregate, Proc. Phys. Soc. London 65 (1952) 349–354.

[64] Y. Bouhadda, S. Djella, M. Bououdina, N. Fenineche, Y. Boudouma, Structural and elastic properties of $LiBH_4$ for hydrogen storage applications, J. Alloys Compd. 534 (2012) 20–24.

[65] P. Ravindran, L. Fast, P. A. Korzhavyi, B. Johansson, J. Wills, O. Eriksson, Density functional theory for calculation of elastic properties of orthorhombic crystals: Application to $TiSi_2$. J. Appl. Phys. 84 (1998) 4891–4904.

[66] S. F. Pugh, XCII. Relations between the elastic moduli and the plastic properties of polycrystalline pure metals, Philos. Mag. 45 (1954) 823–843.

[67] a) H. Niu, P. Wei, Y. Sun, X.-Q. Chen, C. Franchini, D. Li, Y. Li, Electronic, optical, and mechanical properties of superhard cold-compressed phases of carbon. Appl. Phys. Lett. 99 (2011) 031901; b) X.-Q. Chen, H. Niu, D. Li, Y. Li, Modeling hardness of polycrystalline materials and bulk metallic glasses, Intermetallics 19 (2011) 1275–1281.

[68] S. L. Ranganathan, M. Ostoja-Starzewski, Universal Elastic Anisotropy Index, Phys. Rev. Lett. 101 (2008) 055504.

[69] F. Birch, Finite Elastic Strain of Cubic Crystal, Phys. Rev. 71 (1947) 809–824.

[70] R. J. Angel, Equations of State, Rev. Mineral. Geochem. 41 (2001) 35–60. EOSFIT 5.2 software, http://www.ccp14.ac.uk/ccp/webmirrors/ross-angel/rja /soft/.

[71] R. T. Downs, The RRUFF Project: an integrated study of the chemistry, crystallography, Raman and infrared spectroscopy of minerals, Program and Abstracts of the 19th General Meeting of the International Mineralogical Association in Kobe, Japan, 2006. O03-13; RRUFF database, http://rruff.info/uranophane. Record RRUFF-050380 corresponds to a natural mineral sample from Grafton County, New Hampshire, USA.

[72] J. Cejka, Infrared spectroscopy and thermal analysis of the uranyl minerals, Rev. Mineral. Geochem. 38 (1999) 521–622.

[73] K. Nakamoto, Infrared and Raman Spectra of Inorganic and Coordination Compounds, J. Wiley and Sons, New York, 1986.

[74] A. Berghout, D. Tunega, A. Zaoui, Density functional theory (DFT) study of the hydration steps of $Na^+/Mg^{2+}/Ca^{2+}/Sr^{2+}/Ba^{2+}$-exchanged montmorillonites, Clays Clay Miner. 58 (2010) 174–187.

Supplementary Information

Structural, Mechanical and Raman Spectroscopic Characterization of Layered Uranyl Silicate Mineral Uranophane-α by DFT Methods

Francisco Colmenero[a], Vicente Timón[a], Laura J. Bonales[b], Joaquín Cobos[b]

[a]*Instituto de Estructura de la Materia, CSIC. C/ Serrano, 113. 28006 Madrid, Spain*

[b]*Centro de Investigaciones Energéticas, Medioambientales y Tecnológicas, CIEMAT. Avda/ Complutense, 40. 28040 Madrid, Spain*

Appendix A. Raman active normal modes of Uranophane-α.

Figure A.1 The atomic motions associated to some Raman active vibrational normal modes of Uranophane-α.

Note that the abbreviations *cr* and *st* will be used to distinguish crystallization and structural water molecules. Note also that the labels *fr* and *co* will be employed to denote SiO_3OH fragments with free and coordinated OH groups. If none of these labels is given *both* kinds of fragments are involved.

Mode ν=3485 cm^{-1} – ν(OH) [cr-H_2O] – OH stretching.

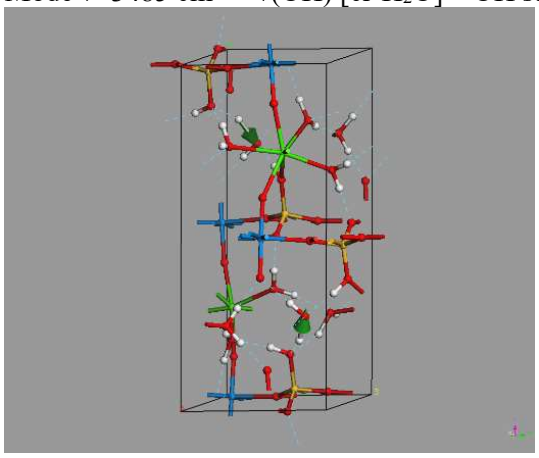

Mode ν=3357 cm^{-1} – ν(OH) [st-H_2O] – OH stretching.

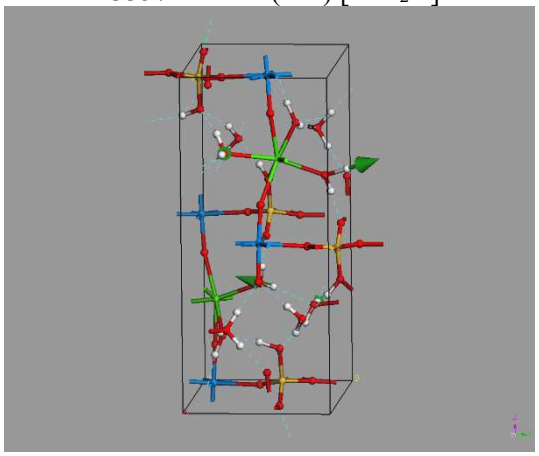

Mode ν=3238 cm^{-1} – ν(OH) [cr- and st-H_2O and fr-SiOH] – OH stretching.

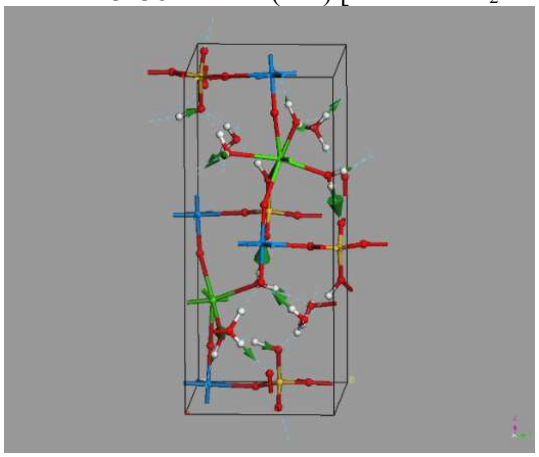

Mode ν=3149 cm^{-1} – ν(OH) [st-H_2O and fr-SiOH] – OH stretching.

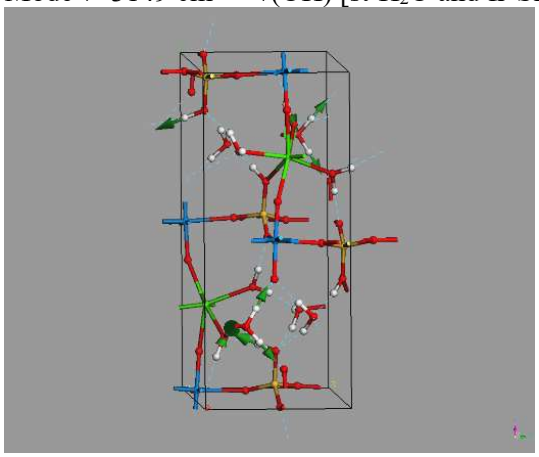

Mode ν=1639 cm^{-1} – δ(H_2O) – H_2O bending.

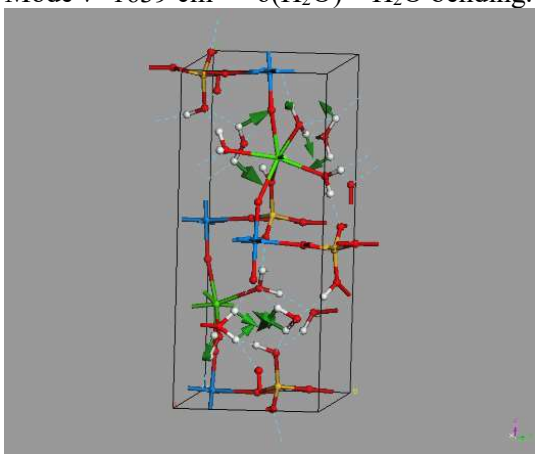

Mode ν=1222 cm^{-1} – δ(co-SiOH) – SiOH bending.

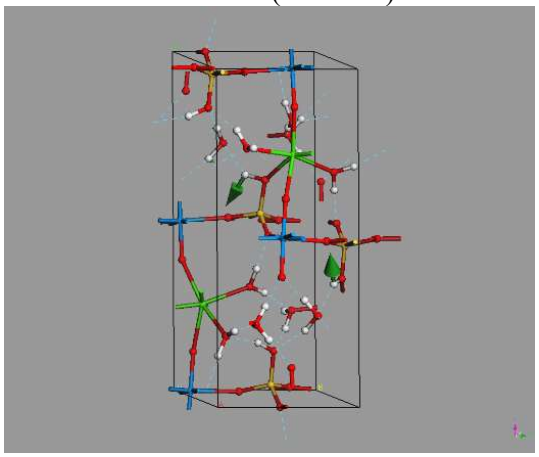

Mode ν=1146 cm^{-1} – δ(fr-SiOH) – SiOH bending.

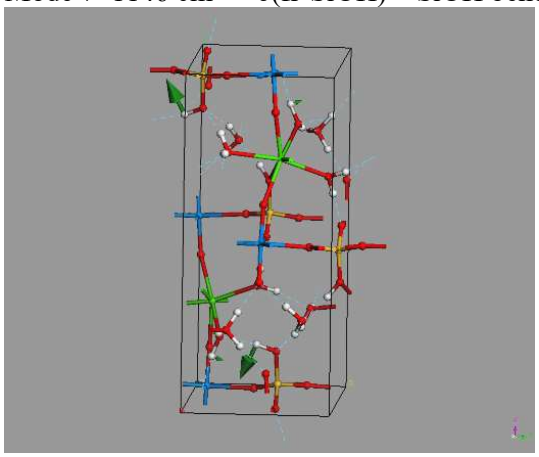

Mode ν=942 cm^{-1} – δ(co-SiOH)+l(H_2O) – SiOH bending plus water librations.

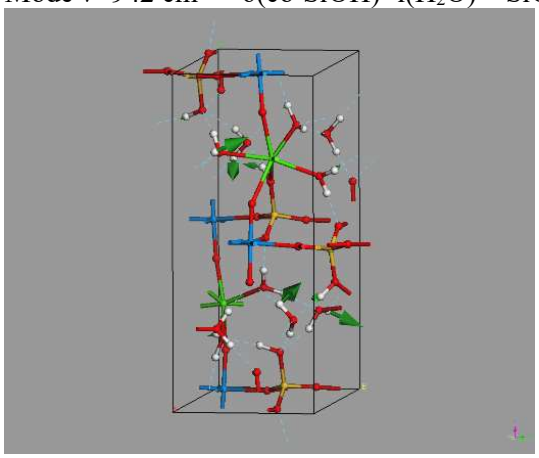

Mode ν=915 cm^{-1} – ν(co-SiO)+l(H_2O) – SiO stretching plus water librations.

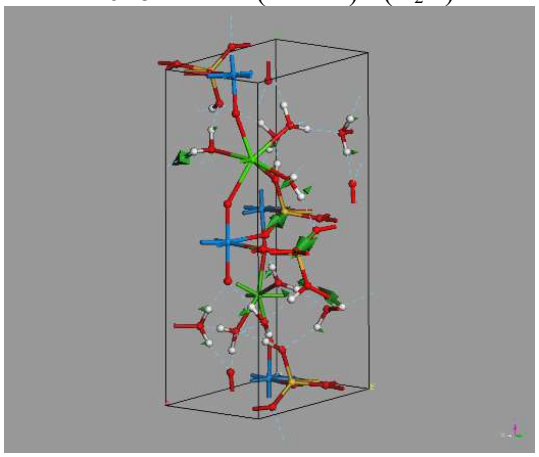

Mode ν=837 cm^{-1} – δ(SiOH)+l(H_2O) – SiOH bending plus water librations.

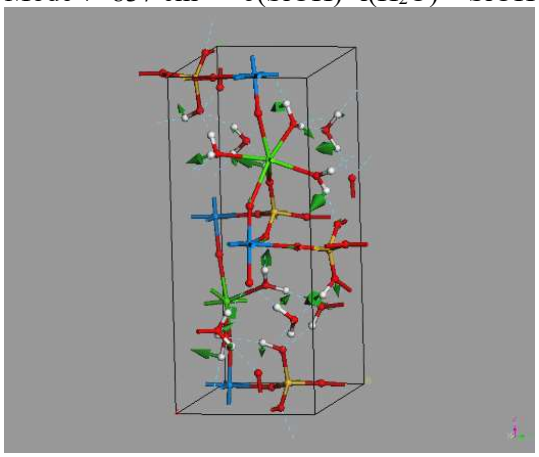

Mode ν=776 cm^{-1} – δ(fr-SiOH)+l(H_2O)+ν(UO_2) – SiOH bending + water librations + uranyl UO stretching.

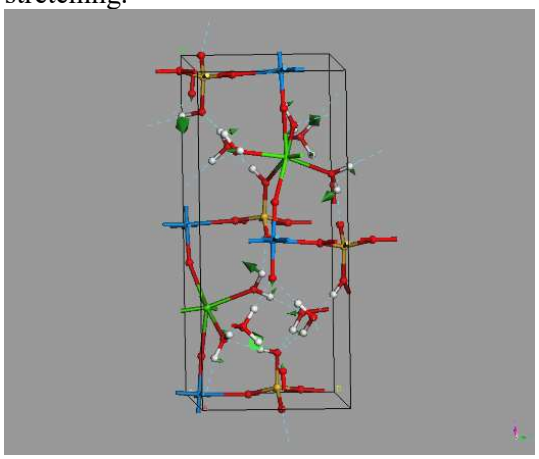

Mode ν=686 cm^{-1} – δ(fr-SiOH)+l(H_2O) – SiOH bending plus water librations.

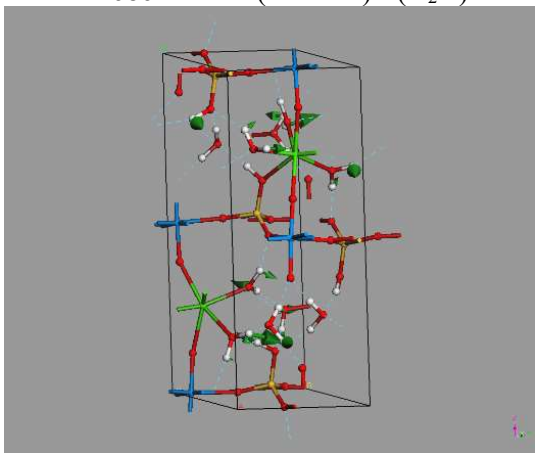

Mode ν=618 cm^{-1} – δ(co-SiOH)+l(H_2O) – SiOH bending plus water librations.

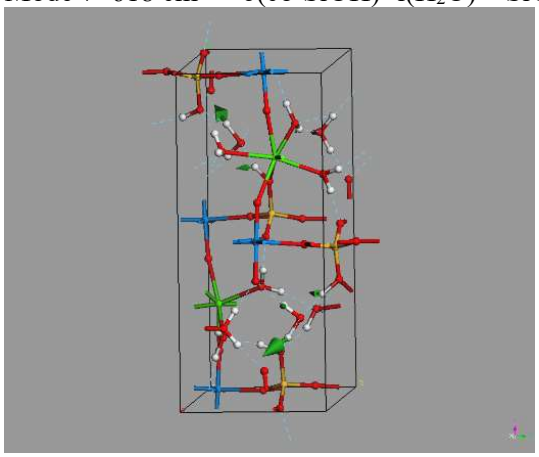

Mode ν=539 cm^{-1} – l(H_2O) – water librations.

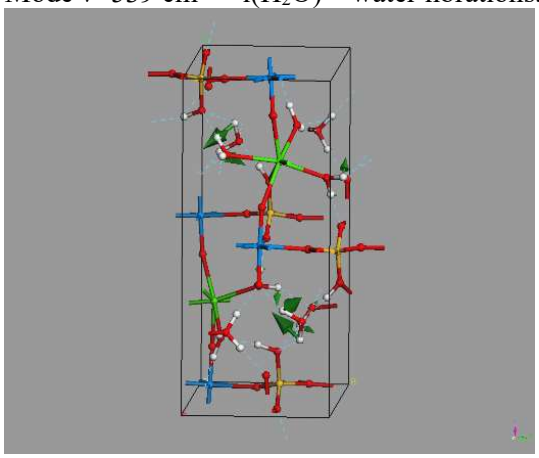

Mode ν=524 cm^{-1} – δ(co-SiO_3OH)+l(H_2O) – SiO_3OH deformation + water librations.

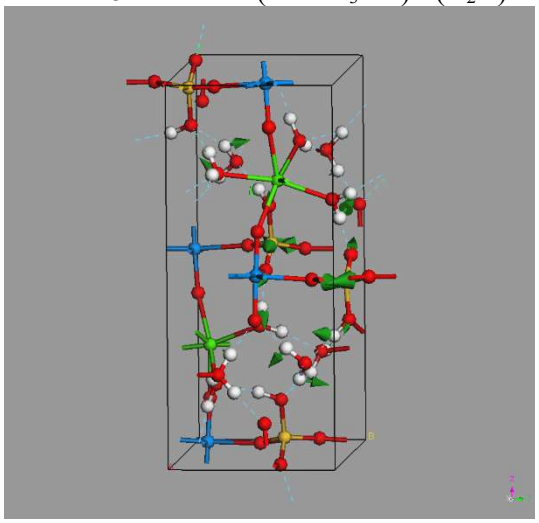

Mode ν=519 cm^{-1} – δ(fr-SiO_3OH)+l(H_2O) – SiO_3OH deformation + water librations.

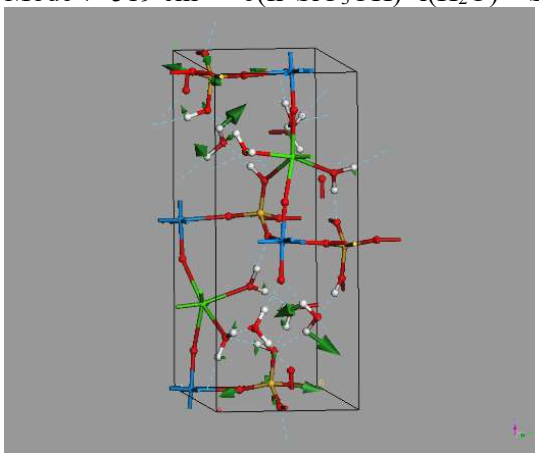

Mode ν=459 cm^{-1} – δ(co-SiO_3OH)+l(H_2O) – SiO_3OH deformation + water librations.

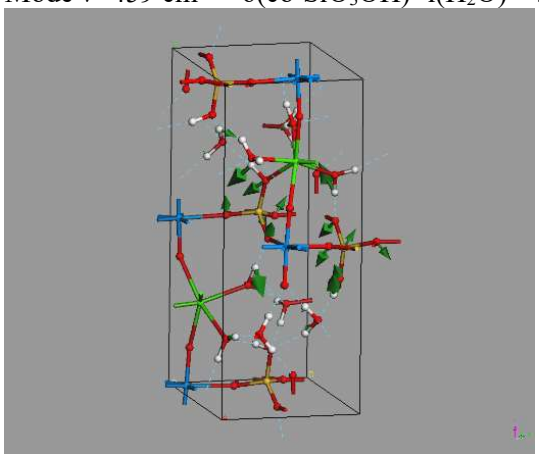

Mode ν=452 cm^{-1} – δ(fr-SiO_3OH)+l(H_2O) – SiO_3OH deformation + water librations.

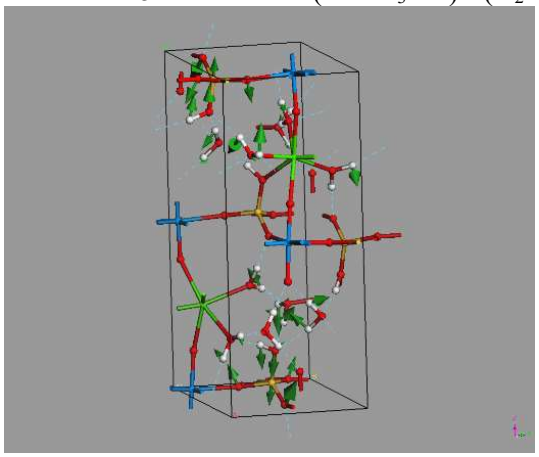

Mode ν=374 cm^{-1} – δ(fr-SiO_3OH)+δ(UO_2)+l(H_2O) – SiO_3OH deformation + UO_2 bending + water librations.

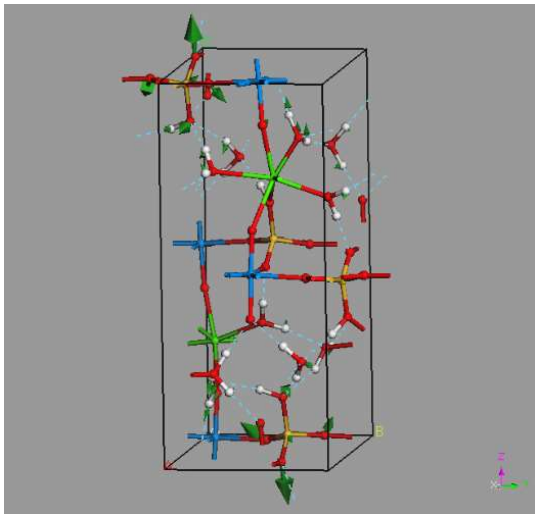

Mode ν=317 cm^{-1} – δ(SiO_3OH)+δ(UO_2)+l(H_2O) – SiO_3OH deformation + UO_2 bending + water librations.

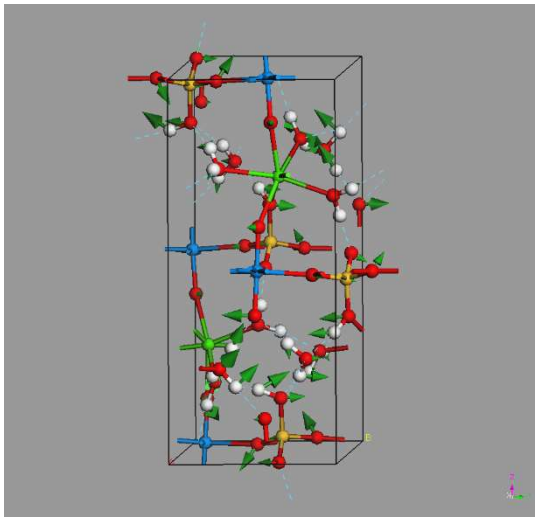

Mode ν=289 cm^{-1} – δ(co-SiO_3OH)+δ(UO_2)+l(H_2O) – SiO_3OH deformation + UO_2 bending + water librations.

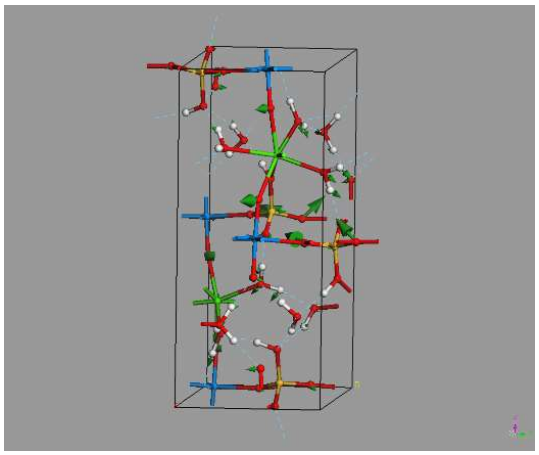

Uranium-Oxygen Bond-Length to Uranyl Symmetric Stretching Raman Shift relationship

Article: "*Relation of uranium-oxygen bond length and uranyl symmetric stretching Raman shift obtained from theoretical DFT calculations*", by F. Colmenero, L. J. Bonales, J. Cobos and V. Timón, J. Mol. Struct. (2017, to be submitted)

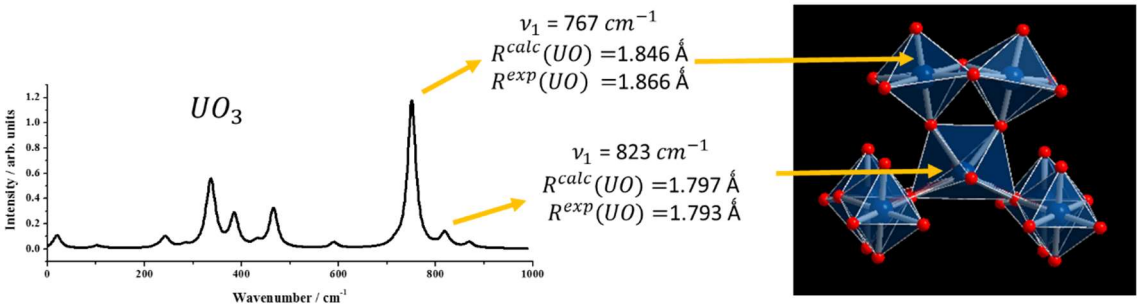

Relation of uranium-oxygen bond length and uranyl symmetric stretching Raman shift obtained from theoretical DFT calculations

Francisco Colmenero[a3], Laura J. Bonales[b], Joaquín Cobos[b], Vicente Timón[a]

[a]*Instituto de Estructura de la Materia, CSIC. C/ Serrano, 113. 28006 Madrid, Spain*

[b]*Centro de Investigaciones Energéticas, Medioambientales y Tecnológicas, CIEMAT. Avda/ Complutense, 40. 28040 Madrid, Spain*

Abstract

An expression for the uranium-oxygen bond length in terms of the uranyl symmetric stretching Raman shift was obtained by means of a least-squares fit of data from theoretical solid state Density Functional Theory calculations of a small set of uranyl containing materials. The resulting expression provides bond-lengths with an accuracy comparable to that obtained previously from a large set of experimental results. The average deviation of calculated bond-length values with respect to experimental ones for a large set of materials is 3.5 pm.

Keywords: Uranyl containing compounds; Uranium-oxygen bond-length; Raman spectroscopy; DFT

[3] Corresponding author. Tel.+34 915616800 Ext. 941033
E-mail address: francisco.colmenero@iem.cfmac.csic.es

1. Introduction

Based in Badger's relation [1], approximate expressions relating the uranium-oxygen bond length with spectroscopy data have been derived [2-8] and used extensively in the research of uranyl containing systems [9-30]. The most widely used of these expressions is that of Bartlett and Cooney [8] relating the uranium-oxygen bond length with the uranyl symmetric stretching Raman shift. These relations have been employed by many research groups [9-19] in order to rationalize the results of Raman and Infrared spectroscopy of solid materials by correlating them with the uranyl group geometries obtained from X-Ray diffraction. However, these expressions are particularly useful to investigate solid materials in which crystallographic methods are difficult to apply and in the study of uranyl complexes in solution [20-21]. They may also be used, for example, to follow the changes in UO bond upon variations of the experimental conditions, i.e. temperature and pressure (for instance in dehydration experiments), or along the course of chemical reactions [20-30] using in situ spectroscopic measurements.

In this communication, we report an expression relating uranium-oxygen bond length and the uranyl symmetric stretching Raman shift similar to that of Bartlett and Cooney [8], deduced from a least squares fit to a set of data obtained from theoretical density functional theory (DFT) [36] calculations on uranyl containing materials [31-35]. These calculations were carried out employing plane waves and pseudopotentials [37]. A new norm conserving relativistic pseudopotential [38] for uranium atom generated from first principles in our previous work [31] was employed opening the possibility of performing complete theoretical solid-state calculations of the Raman spectra of uranyl containing materials. The methods used are presented in Section 2. In Section 3, our relation is reported and discussed. Finally, the conclusions of this work are given Section 4.

2. Methods

We use a UO bond length to wavenumber relation of the form:

$$R_{UO} = a{\cdot}{\nu_1}^{-b} + c$$

where $b = \frac{2}{3}$. In order to obtain approximate values of the remaining parameters a and c, we use a least squares analysis of the data presented in Table 1. The values given in this table were obtained from ab initio theoretical solid state DFT calculations [31-35].

Table 1. UO bond lengths and UO symmetric stretching uranyl symmetric stretching Raman shifts used in the least squares analysis.

System	$\nu_1\ (cm^{-1})$	$R_{UO}(pm)$
Rutherfordine	886.5	176.4
Studtite	797.6	180.7
Soddyite	806.8	180.1
Uranophane-α	775.6	183.1
α-$UO_2(OH)_2$	819.3	179.2
ϒ-UO_3	751.9	188.6
ϒ-UO_3	818.0	179.4

The calculations include six different uranyl containing materials: the uranyl carbonate rutherfordine, UO_2CO_3 [31], the uranyl peroxide studtite, $(UO_2)(O_2){\cdot}4H_2O$ [32], the uranyl silicates soddyite, $(UO_2)_2(SiO_4){\cdot}2(H_2O)$ [33], and uranophane-α, $Ca(UO_2)_2(SiO_3OH)_2{\cdot}5H_2O$ [35],

the uranyl hydroxide dehydrated schoepite, α-$UO_2(OH)_2$ [35], and the uranyl oxide, ϒ-UO_3 [34]. The unit cells of these materials were modelled with the help of CASTEP code [39], a module of Materials Studio package [40].

The generalized gradient approximation (GGA) together with two different functionals were employed [41]. In the case of rutherfordine and uranium trioxide, the PBESOL functional [42] was utilized. For the remaining four materials, the PBE functional [41], together with the Grimme empirical dispersion correction, the DFT-D2 approach [43] was used in order to describe properly the hydrogen bonding present in the systems. Geometry optimization was carried out using the Broyden–Fletcher–Goldfarb–Shanno optimization scheme [44,37] with a convergence threshold on atomic forces of 0.01 eV/Å. The different kinetic energy cutoffs and k-point meshes [45] adopted were selected to ensure good convergence for computed structures and energies.

For the calculations of vibrational properties, the linear response density functional perturbation theory (DFPT) [46] implemented in the CASTEP code was used, where the phonon frequencies at the gamma point of the Brillouin zone were computed by using atomic displacement perturbations. These are calculated in CASTEP [47] using a combination of perturbation theory (second derivative with respect to field) and finite differences (third derivative with respect to atomic displacement). The wavenumbers presented in this work have not been scaled to correct for anharmonicity and remaining errors of the theoretical treatment employed, such as incomplete treatment of electron correlation and basis set truncation [48]. They correspond to the harmonic approximation of the force field. Since the effects of these defects tend to cancel out, the scale factor should be near to unity.

The pseudopotentials used for H, C, O, Si, and Ca atoms in the unit cells of these materials were standard norm-conserving pseudopotentials [38] given in CASTEP code (00PBE-OP type). The norm-conserving relativistic pseudopotential for U atom was generated from first principles in our previous work [31] and the reader may consult this reference for more details about its construction and performance. The pseudopotential must be norm conserving; otherwise vibrational spectra cannot be determined with CASTEP software.

3. Results and discussion

The least squares fit to the data given in Table 1 is showed if Figure 1, and the resulting parameters are given in Table 2, compared with those of Bartlett and Cooney [8].

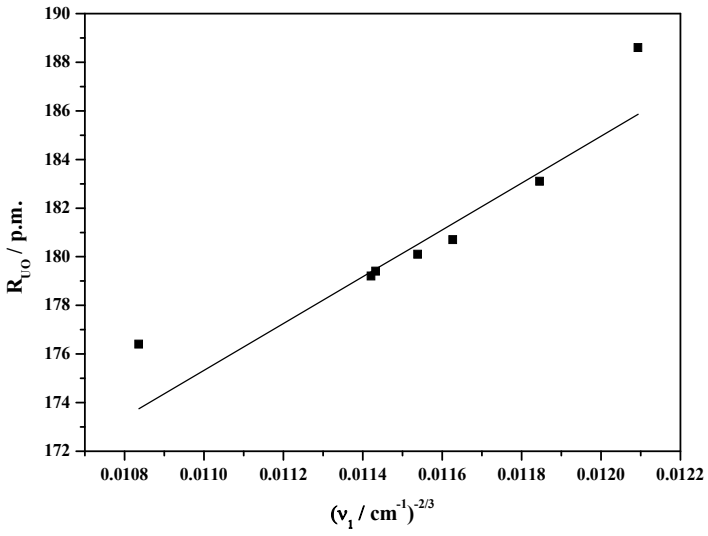

Fig. 1. Least squares fit to $(R_{UO}, {\nu_1}^{-2/3})$ data points. The data used in the fit is given in Table 1.

Table 2. Least squares fit results. The a and c parameters obtained in this work are compared with those of Bartlett and Cooney [8].

Reference	a	c
This work	9096.149	76.081
Bartlett and Cooney [4]	10650	57.5

By using these parameters and those of Bartlett and Cooney [8], we can obtain the values of the uranium-oxygen bond distance for the same set of experimental uranyl symmetric stretching frequencies as in Ref [8]. The resulting bond lengths are given in Table 3, compared with the experimental values. The averaged deviation of the calculated values (the sum of the absolute values of the errors divided by the number of systems considered) is 3.5 pm for both the relation obtained in this work and that of Bartlett and Cooney [8]. This fact is quite surprising since while this is the set used by these authors to derive the relation we have used only a small set of data derived from ab initio DFT theoretical calculations. It must be noted that the errors obtained by using the parameters obtained in this work seems to be smaller when the UO bond length is large and greater when the UO bond is short.

Larger order fits were also carried out in order to adjust the initial data in a more accurate way. However, the resulting fits gave distance-wavenumber relations providing similar averaged deviations with respect to experiment.

Since we are interested in the secondary phases appearing as products of alteration (hydration-oxidation weathering) of spent nuclear fuel (SNF), we have made a comparison of the bond-lengths obtained from these relations for some of the most important secondary phases. The results are given in Table 4. In these cases, we have several band wavenumbers assigned to uranyl symmetric stretching vibrations. For each of these bands, the corresponding UO distances are obtained and compared with the experimental average UO length determined from the distances obtained from X-ray single-crystal structure analyses. The averaged deviation of the calculated values is 1.3 pm for the relation obtained in this work and 1.4 pm for that of Bartlett and Cooney [8].

4. Conclusions

The purpose of this work was to derive the parameters of the expression relating the uranium-oxygen bond-length and symmetric stretching Raman shift, from a small set of results derived from first principle calculations, that is without using any experimental information. The resulting parameters gave an expression with essentially the same accuracy as that derived by Bartlett and Cooney [8] employing a large set of experimental results.

Similar relations could be obtained for bonds involving different elements using data obtained from first principles methods. However, it should be noted that, although the number of theoretical calculations required may be small, the corresponding calculations are computationally time-consuming if one desires to reach a good level of accuracy in the computed vibrational spectra.

The present study suggests that the relation given in this work and by Bartlett and Cooney [8] provide bond lengths whose accuracy is limited only by the approximate character of the distance-wavenumber relation. Relations deduced from larger sets of data or from expressions of larger order aiming to adjust the initial data in a more accurate way do not provide better averaged deviations with respect to the corresponding experimental data.

Table 3. Bond lengths obtained for a series of uranyl ion containing systems. Raman shifts and bond-lengths are given in units of cm^{-1} and pm respectively. The references for the experimental data may be found in the work of Bartlett and Cooney [4].

System	ν_1^{Exp}	R_{UO}			Errors	
		This work	Bartlett and Cooney [4]	Exp.	This work	Bartlett and Cooney [4]
$UO_2Cl_2 \cdot 3H_2O$	879	175.2	173.6	165	-10.2	-8.6
UO_2CO_3	870	175.9	174.4	169	-6.9	-5.4
α-$UO_2(OH)_2$	848	177.6	176.4	170	-7.6	-6.4
$Na[UO_2(Ac)_3]$	856	177.0	175.6	171	-6.0	-4.6
$(Ph_3AsO)_2(UO_2)(NO_3)_2$	818	180.1	179.3	171	-9.1	-8.3
UO_2F_2	872	175.7	174.2	174	-1.7	-0.2
UO_2Cl_2	852	177.3	176.0	174	-3.3	-2.0
$[Et_4N]\ [UO_2(S_2PMe_2)]Cl$	861	176.6	175.2	175	-1.6	-0.2
$UO_2(NO_3)_2 \cdot 6H_2O$	869	176.0	174.5	176	0.0	1.5
$K_3[UO_2F_5]$	803	181.4	180.8	176	-5.4	-4.8
$(Ph_3PO)_2UO_2(NO_3)_2$	848	177.6	176.4	176	-1.6	-0.4
$[(UO_2)_2(NO_3)_4(H_2O)_2] \cdot [C_3H_4N_2]_2$	856	177.0	175.6	177	0.0	1.4
$Rb(UO_2)(NO_3)_2$	879	175.2	173.6	178	2.8	4.4
$Na_3[(UO_2)_2F_7] \cdot 6H_2O$	840	178.3	177.1	178	-0.3	0.9
$[(UO_2)_4O_2Cl_8(H_2O)_2]^{4-}$	833	178.8	177.8	178	-0.8	0.2
ϒ-UO_3	829	179.2	178.2	179	-0.2	0.8
$K_5(UO_2)_2F_9$	807	181.0	180.4	179	-2.0	-1.4
$(UO_2)_2(OH)_2Cl_2(H_2O)_4$	848	177.6	176.4	179	1.4	2.6
$UO_2(S_2PPh_2)_2 \cdot EtOH$	868	176.0	174.5	180	4.0	5.5
$Cs_3[UO_2F_5]$	784	183.1	182.8	180	-3.1	-2.8
β-$UO_2(OH)_2$	821	179.8	179.0	181	1.2	2.0
ϒ-$UO_2(OH)_2$	821	179.8	179.0	181	1.2	2.0
$[UO_2(NH_2O)_2(H_2O)_2] \cdot H_2O$	783	183.2	182.9	181	-2.2	-1.9
$Cs_2[UO_2Cl_4]$	831	179.0	178.0	181	2.0	3.0
UO_2Cl_2	766	184.7	184.7	181	-3.7	-3.7
$(NH_4)_2UO_2(SO_4)_2 \cdot 2H_2O$	836	178.6	177.5	182	3.4	4.5
$[Cs_4[(UO_2)_2F_8] \cdot 2H_2O$	814	180.4	179.7	184	3.6	4.3
$[Rb_4[(UO_2)_2F_8] \cdot 2H_2O$	813	180.5	179.8	184	3.5	4.2
Li_2UO_4	725	188.8	189.5	189	0.2	-0.5
α-Na_2UO_4	737	187.6	188.0	190	2.4	2.0
$(NH_4)_3UO_2F_5$	819	180.0	179.2	190	10.0	10.8

Table 4. Bond lengths obtained for a series of uranyl ion containing systems. Raman shifts and bond-lengths are given in units of cm^{-1} and pm respectively. The references for the experimental data (Raman shifts and average UO distances) may be found in the first column of the table.

System	ν_1^{Exp}	R_{UO}			Errors	
		This work	Bartlett and Cooney [4]	Exp.	This work	Bartlett and Cooney [4]
Rutherfordine [31,49]	882.3	174.96	173.27	174.4	-0.56	1.13
Studtite [32,50]	819.05	179.99	179.16	176.9	-3.09	-2.26
Soddyite [33,51]	830.0	179.07	178.09	178.1	-0.97	0.01
Uranophane-α [35,52]	798.3	181.78	181.26	180.45	-1.33	-0.81
Becquerelite [9,53]	838.3	178.39	177.29	179.39	1.00	2.10
	831.1	178.98	177.98		0.41	1.41
	813.7	180.44	179.69		-1.05	-0.31
Schoepite [9,54]	838.7	178.36	177.25	177.9	-0.46	0.65
	826.2	179.39	178.46		-1.49	-0.55
	817.1	180.15	179.35		-2.25	-1.45
	802.3	181.43	180.85		-3.53	-2.95
Billietite [9,55]	830.7	179.02	178.02	180.14	1.12	2.12
	830.3	179.05	178.06		1.09	2.08
	810.0	180.76	180.06		-0.62	0.08
	794.6	182.11	181.64		-1.97	-1.50
Curite [9,56]	803.0	181.37	180.77	182.50	1.13	1.73
	791.0	182.43	182.02		0.07	0.48
Vandendriesscheite [9,57]	852.3	177.27	175.97	179.55	2.28	3.58
	840.6	178.21	177.07		1.34	2.48
	831.9	178.92	177.90		0.63	1.65
	819.4	179.96	179.12		-0.41	0.43

Acknowledgements

This work was supported by ENRESA in the project: Nº 079000189 "Aplicación de técnicas de caracterización en el estudio de la estabilidad del combustible nuclear irradiado en condiciones de almacenamiento" (ACESCO) and project CGL2013-48415-C2-1-R. Supercomputer time by the CETA-CIEMAT, CTI-CSIC and CESGA centers are also acknowledged.

References

[1] R. M. Badger, The Relation Between the Internuclear Distances and Force Constants of Molecules and Its Application to Polyatomic Molecules, J. Chem. Phys. 3 (1935) 710-714.

[2] L. H. Jones, Determination of U-O bond distance in uranyl complexes from their infrared spectra, Spectrochim. Acta 15 (1959) 409-411; Systematics in the vibrational spectra of uranyl complexes, Spectrochim. Acta 10 (1958) 395-403.

[3] S. P. McGlynn, J. K. Smith, and W. C. Neely, Electronic Structure, Spectra, and Magnetic Properties of Oxycations. III. Ligation Effects on the Infrared Spectrum of the Uranyl Ion, J. Chem. Phys. 35 (1961) 105-116.

[4] W. T. Carnall, S. J. Neufeldt, A. Walker, Reactions in Molten Salt Solutions. I. Uranate and Neptunate Formation in Molten Lithium Nitrate-Sodium Nitrate, Inorg. Chem. 4 (1965) 1808-1813.

[5] J. I. Bullock, Raman and infrared spectroscopic studies of the uranyl ion: the symmetric stretching frequency, force constants, and bond lengths, J. Chem. Soc. A (1969) 781-784.

[6] B. W. Veal, D. J. Lam, W. T. Carnall, and H. R. Hoekstra, X-ray photoemission spectroscopy study of hexavalent uranium compounds, Phys. Rev. B 12 (1975) 5651-5663.

[7] B. W. Veal, D. J. Lam, W. T. Carnall, and H. R. Hoekstra, X-ray photoemission spectroscopy study of hexavalent uranium compounds, Phys. Rev. B 12 (1975) 5651-5663.

[8] J. R. Bartlett, R. P. Cooney, On the determination of uranium-oxygen bond lengths in dioxouranium(VI) compounds by Raman spectroscopy, J. Mol. Struct. 193 (1989) 295-300.

[9] R. L. Frost, J. Cejka, M. L. Weier, Raman spectroscopic study of the uranyl oxyhydroxide hydrates: becquerelite, billietite, curite, schoepite and vandendriesscheite, J. Raman Spectrosc. 38 (2007) 460-466.

[10] R.L. Frost, M. L. Weier, T. Bostrom, J. Cejka, Molecular structure of the uranyl mineral zippeite - an XRD, SEM and Raman spectroscopic study, Neues Jahrbuch fuer Mineralogie 181 (2005) 271-279.

[11] R. L. Frost, J. Cejka, M. J. Dickfos, Raman spectroscopic study of the uranyl minerals vanmeersscheite $U(OH)_4[(UO_2)_3(PO_4)_2(OH)_2]\cdot 4H_2O$ and arsenouranylite $Ca(UO_2)[(UO_2)_3(AsO_4)_2(OH)_2].(OH)_2\cdot 6H_2O$, Spectrochim. Acta 71 (2009) 1799-1803.

[12] R. L. Frost, J. Cejka, M. J. Dickfos, Raman and infrared spectroscopic study of the molybdate containing uranyl mineral calcurmolite, J. Raman Spectrosc. 39 (2006) 779-785.

[13] R. L. Frost, M. L. Weier, W. N. Martens, J. T. Kloprogge, J. Kristof, Thermo-Raman spectroscopic study of the uranium mineral sabugalite, J. Raman Spectrosc. 36 (2006) 797-805.

[14] R. L. Frost, J. Cejka, G. Ayoko, Raman spectroscopic study of the uranyl phosphate minerals phosphuranylite and yingjiangite, J. Raman Spectrosc. 39 (2008) 495-502.

[15] R. L. Frost, O. Carmody, K. L. Erickson, M. L. Weier, D. O. Henry, J. Cejka, Molecular structure of the uranyl mineral uranopilite - A Raman spectroscopic study, J. Mol. Struct. 733 (2005) 203-210.

[16] R. L. Frost, J. Cejka, G. Ayoko, M. Dickfos, Raman spectroscopic study of the multi-anion uranyl mineral schroeckingerite. J. Raman Spectrosc. 38 (2007) 1609-1614

[17] J. Plasil, F. Veselovsky, J. Hlousek, R. Skoda, M. Novak, J. Sejkora, J. Cejka, P. Skacha, A. V. Kasatkin, Mathesiusite, $K_5(UO_2)_4(SO_4)_4(VO_5)(H_2O)_4$, a new uranyl vanadate-sulfate from Jachymov, Czech Republic, Am. Mineral. 99 (2013) 625-632.

[18] H.R. Hoekstra, S. Siegel, The uranium-oxygen system U3O8-UO3, J. Inorg. Nucl. Chem. 1961, 18, 154-165.

[19] E. Faulques, N. Kalashnyk, F. Massuyeau, D. L. Perry, Spectroscopic markers for uranium(VI) phosphates: A vibronic study, RSC Adv. 5 (2015) 71219-71227.

[20] K. Ohwada, Laser Raman Spectra and Normal Coordinate Analysis of Some Uranyl Tetrachloride Complexes, Appl. Spectrosc. 34 (1980) 327-331.

[21] M. Gal, P.L. Goggin and J. Mink, Mid-, far-infrared and Raman spectra of uranyl complexes in aqueous solutions, J. Mol. Struct. 114 (1984) 459-462.

[22] Y. Zhang, M. Bhadbhade, J. R. Price, I. Karatchevtseva, D. Collison, G. R. Lumpkin, Kinetics vs thermodynamics: A unique crystal transformation from a uranyl peroxo-nanocluster to a nanoclustered uranyl polyborate, RSC Adv. 4 (2014) 34244-34247.

[23] N. D. Shepherd, Y. Zhang, I. Karatchevtseva, J. R. Price, L. Kong, N. Scales, G. R. Lumpkin, One-dimensional uranium(VI) coordination polymers with pyridinecarboxylate ligands, Polyhedron 113 (2016) 88-95.

[24] S. Biswas, R. Steudtner, M. Schmidt, C. McKenna, L. L. Vintro, B. Twamley, R. J. Baker, An investigation of the interactions of Eu^{3+} and Am^{3+} with uranyl minerals: implications for the storage of spent nuclear fuel, Dalton Trans. 45 (2016) 6383-6393.

[25] K. Servaes, C. Hennig, I. Billard, C. Gaillard, K. Binnemans, C. Gorller-Walrand, R. Van Deun, Speciation of Uranyl Nitrato Complexes in Acetonitrile and in the Ionic Liquid 1-Butyl-3-methylimidazolium Bis(trifluoromethylsulfonyl)imide, Eur. J. Inorg. Chem. 32 (2007) 5120–5126.

[26] F. D. M. Ramirez, K. Palomares-Castillo, B. Ocampo-Garcia, E. Morales-Avila, S. Varbanov, Physicochemical behaviour of a dinuclear uranyl complex formed with an octaphosphinoylated para-tert-butylcalix[8]arene. Spectroscopic studies in solution and in the solid state, Polyhedron 123 (2017) 75-89.

[27] C. Falaise, J. Delille, C. Volkringer, H. Vezin, P. Rabu, T. Loiseau, Series of Hydrated Heterometallic Uranyl-Cobalt(II) Coordination Polymers with Aromatic Polycarboxylate Ligands: Formation of U=O-Co Bonding upon Dehydration Process, Inorg. Chem. 55 (2016) 10453-10466.

[28] N. P. Martin, C. Falaise, C. Volkringer, N. Henry, P. Fargen, C. Falk, E. Delahaye, P. Rabu, T. Loiseau, Hydrothermal Crystallization of Uranyl Coordination Polymers Involving an Imidazolium Dicarboxylate Ligand: Effect of pH on the Nuclearity of Uranyl-Centered Subunits, Inorg. Chem. 55 (2016) 8697-8705.

[29] N. Henry, M. Lagrenee, T. Loiseau, N. Clavier, N. Dacheux, F. Abraham, Tetrameric entity resulting from two distinct dinuclear uranyl-centered motifs bridged through μ_2-OH and pyridazine-3,6-dicarboxylate, Inorg. Chem. Commun. 14 (2011) 429-432.

[30] Y. Hao, V. V. Klepov, G. L. Murphy, G. Modolo, D. Bosbach, T. E. Albrecht-Schmitt, B. J. Kennedy, S. Wang, E. V. Alekseev, Influence of Synthetic Conditions on Chemistry and Structural Properties of Alkaline Earth Uranyl Borates, Cryst. Growth Des. 16 (2016) 5923-5931.

[31] L.J. Bonales, F. Colmenero, J. Cobos, V. Timón, Spectroscopic Raman characterization of rutherfordine: a combined DFT and experimental study, Phys. Chem. Chem. Phys. 18 (2016) 16575-16584.

[32] F. Colmenero, L.J. Bonales, J. Cobos, V. Timón, Study of the thermal stability of studtite by in situ Raman spectroscopy and DFT calculations, Spectrochim. Acta. A 174 (2017) 245-253.

[33] F. Colmenero, L.J. Bonales, J. Cobos, V. Timón, Structural, mechanical and vibrational study of uranyl silicate mineral soddyite by DFT calculations, to be published, 2017.

[34] F. Colmenero, L.J. Bonales, J. Cobos, V. Timón, Density functional theory study of the structural, thermodynamic and vibrational properties of γ-UO3 polymorph, to be published, 2017.

[35] F. Colmenero, L.J. Bonales, J. Cobos, V. Timón, to be published, 2017.

[36] P. Hohenberg, W. Kohn, Phys. Rev. 136 (1964) B864-B871; W. Kohn, L.J. Sham, Phys. Rev. 140 (1965) A1133-A1138; R.G. Parr, W. Yang, Density-Functional Theory of Atoms and Molecules, Oxford University Press, USA, 1994.

[37] M. C. Payne. M. P. Teter and D. C. Ailan, A. Arias, J. D. Joannopoulos, Iterative minimization techniques for ab initio total-energy calculations: molecular dynamics and conjugate gradients, Rev. Mod. Phys. 64 (1992) 1045-1097.

[38] N. Troullier, J. L. Martins, Efficient pseudopotentials for plane-wave calculations, Phys. Rev. B 43 (1991) 1993-2006.

[39] S. J. Clark, M. D. Segall, C. J. Pickard, P. J. Hasnip, M. I. J. Probert, K. Refson and M. C. Payne, First principles methods using CASTEP, Z. Kristallogr. 220 (2005) 567-570.

[40] MaterialsStudio, http://accelrys.com/products/materials-studio, 2017.

[41] J.P. Perdew, K. Burke and M. Ernzerhof, Generalized Gradient Approximation Made Simple, Phys. Rev. Lett. 77 (1996) 3865-3868.

[42] J.P. Perdew, A. Ruzsinszky, G.I. Csonka, O.A. Vydrov, G.E. Scuseria, L.A. Constantin, X. Zhou and K. Burke, Restoring the Density-Gradient Expansion for Exchange in Solids and Surfaces, Phys. Rev. Lett. 100 (2008) 136406.

[43] S. Grimme, Semiempirical GGA-type density functional constructed with a long-range dispersion correction. J. Comput. Chem. 27 (2006) 1787-1799.

[44] B.G. Pfrommer, M. Cote, S.G. Louie, M.L. Cohen, Relaxation of Crystals with the Quasi-Newton Method, J. Comput. Phys. 131 (1997) 233-240.

[45] H.J. Monkhorst, J.D. Pack, Special points for Brillouin-zone integrations, Phys. Rev. B 13 (1976) 5188-5192.

[46] S. Baroni, S. de Gironcoli, A. Dal Corso, P. Giannozzi, Phonons and related crystal properties from density-functional perturbation theory. Rev. Mod. Phys. 73 (2001) 515-562.

[47] V. Milman, K. Refson, S.J. Clark, C.J. Pickard, J.R. Yates, S.P. Gao, P.J. Hasnip, M.I.J. Probert, A. Perlov, M.D. Segall, Electron and vibrational spectroscopies using DFT, plane waves and pseudopotentials: CASTEP implementation, J. Mol. Struct. (Theochem) 954 (2010) 22-35.

[48] W.J. Hehre, L. Radom, P.V.R. Schleyer, J.A. Pople, Ab Initio Molecular Orbital Theory, Wiley, New York, 1986.

[49] R.J. Finch, M.A. Cooper, F.C. Hawthorne, R.C. Ewing, Refinement of the crystal structure of rutherfordine, Can. Mineral. 37 (1999) 929-938.

[50] P.C. Burns, K.-A. Hughes, Studtite, $[(UO_2)(O_2)(H_2O)_2](H_2O)_2$: The first structure of a peroxide mineral, Am. Mineral. 88 (2003) 1165-1168.

[51] F. Demartin, C.M. Gramaccioli, T. Pilati, The Importance of Accurate Crystal Structure Determination of Uranium Minerals. II. Soddyite $(UO_2)_2(SiO_4)\cdot 2H_2O$, Acta Cryst. C 48 (1992) 1-4.

[52] D. Ginderow, Structure de I'Uranophane Alpha, $Ca(UO_2)_2(SiO_3OH)_2\cdot 5H_2O$, Acta Cryst. C 44 (1988) 421-424.

[53] P.C. Burns, Y. Li, The structures of becquerelite and Sr-exchanged becquerelite, Am. Mineral. 87 (2002) 550-557; M.K. Pagoaga, D.E. Appleman, J.M. Stewart, Crystal structures and crystal chemistry of the uranyl oxide hydrates becquerelite, billietite, and protasite, Am. Mineral. 72 (1987) 1230-1238.

[54] R.J. Finch, M.A. Cooper, F.C. Hawthorne, R.C. Ewing, The crystal structure of schoepite $[(UO_2)_8O_2(OH)_{12}](H_2O)_{12}$, Can. Mineral. 34 (1996) 1071-1088.

[55] R.J. Finch, P.C. Burns, F.C. Hawthorne, R.C. Ewing, Refinement of the crystal structure of billietite $Ba[(UO_2)_6O_4(OH)_6](H_2O)_8$, Can. Mineral. 44 (2006) 1197-1205.

[56] Y. Li, P.C. Burns, Investigations of crystal-chemical variability in lead uranyl oxide hydrates. I. Curite, Can. Mineral. 38 (2000) 727-735.

[57] P.C. Burns, A new uranyl oxide hydrate sheet in vandendriesscheite: Implications for mineral paragenesis and the corrosion of spent nuclear fuel, Am. Mineral. 82 (1997) 1176-1186.